CHARACTERIZATION OF THE INFLUENCE OF A FAVORABLE PRESSURE GRADIENT ON THE BASIC STRUCTURE OF A MACH 5.0 HIGH REYNOLDS NUMBER SUPERSONIC TURBULENT BOUNDARY LAYER

A Dissertation

by

NATHAN RYAN TICHENOR

Submitted to the Office of Graduate Studies of
Texas A&M University
in partial fulfillment of the requirements for the degree of

DOCTOR OF PHILOSOPHY

August 2010

Major Subject: Aerospace Engineering

CHARACTERIZATION OF THE INFLUENCE OF A FAVORABLE PRESSURE GRADIENT ON THE BASIC STRUCTURE OF A MACH 5.0 HIGH REYNOLDS NUMBER SUPERSONIC TURBULENT BOUNDARY LAYER

A Dissertation

by

NATHAN RYAN TICHENOR

Submitted to the Office of Graduate Studies of
Texas A&M University
in partial fulfillment of the requirements for the degree of

DOCTOR OF PHILOSOPHY

Approved by:

Chair of Committee,	Rodney D.W. Bowersox
Committee Members,	Sharath Girimaji
	Simon W. North
	Othon K. Rediniotis
Head of Department,	Dimitris Lagoudas

August 2010

Major Subject: Aerospace Engineering

ABSTRACT

Characterization of the Influence of a Favorable Pressure Gradient on the Basic Structure of a Mach 5.0 High Reynolds Number Supersonic Turbulent Boundary Layer. (August 2010)

Nathan Ryan Tichenor, B.S., Texas A&M University;

M.S., Texas A&M University

Chair of Advisory Committee: Dr. Rodney D.W. Bowersox

High-speed high Reynolds number boundary layer flows with mechanical non-equilibrium effects have numerous practical applications; examples include access-to-space ascent, re-entry and descent, and military hypersonic systems. However, many of the basic turbulent flow processes in this regime are poorly understood and are beyond the realm of modern direct numerical simulations Previous studies have shown that curvature driven pressure gradients significantly alter the state of the turbulence in high-speed boundary layers; the turbulence levels have been shown to decrease by large amounts (up to 100%) and the Reynolds shear stress has been shown to change sign. However, most of our understanding is based on point measurement techniques such as hot-wire and Laser Doppler anemometry acquired at low to moderate supersonic Mach numbers (i.e., M = 2-3). After reviewing the available literature, the following scientific questions remain unanswered pertaining to the effect of favorable pressure gradients:

(1) How is state of the mean flow and turbulence statistics altered?

(2) How is the structure of wall turbulence; break-up, stretch or a combination?

(3) How are the Reynolds stress component production mechanisms altered?

(4) What is the effect of Mach number on the above processes?

To answer these questions and to enhance the current database, an experimental analysis was performed to provide high fidelity documentation of the mean and turbulent flow properties using two-dimensional particle image velocimetry (PIV) along with flow visualizations of a high speed ($M = 4.88$), high Reynolds number ($Re_\theta \approx 36,000$) supersonic turbulent boundary layer with curvature-driven favorable pressure gradients (a nominally zero, a weak, and a strong favorable pressure gradient). From these data, detailed turbulence analyses were performed including calculating classical mean flow and turbulence statistics, examining turbulent stress production, and performing quadrant decomposition of the Reynolds stress for each pressure gradient case.

It was shown that the effect of curvature-driven favorable pressure gradients on the turbulent structure of a supersonic boundary layer was significant. For the strong pressure gradient model, the turbulent shear stress changed sign throughout the entire boundary layer; a phenomena was not observed to this magnitude in previous studies. Additionally, significant changes were seen in the turbulent structure of the boundary layer. It is believed that hairpin vortices organized within the boundary layer are stretched and then broken up over the favorable pressure gradient. Energy from these hairpin structures is transferred to smaller turbulent eddies as well as back into the mean flow creating a fuller mean velocity profile. It was determined that the effects of favorable pressure gradients on the basic structure of a turbulent Mach 5.0 boundary layer were significant, therefore increasing the complexity of computational modeling.

DEDICATION

I dedicate this dissertation to my wife, Sarah, my mother, Diane, and to all of my family and friends who have guided and supported me throughout my years of education.

ACKNOWLEDGMENTS

Firstly, I would like to thank my advisor, Dr. Rodney Bowersox, for continually guiding me and supporting me throughout my education and research. I also thank my committee members, Dr. Sharath Girimaji, Dr. Othon Rediniotis and Dr. Simon North, for their support and advice throughout this project

I would like to thank my fellow graduate students involved in this project, Michael Semper, TJ Fuller, Andrea Hsu, Jerrod Hofferth and Scott Peltier for their help and support. Additionally, I would like to thank Ray Humble, a post-doc whose knowledge and experience proved invaluable to this endeavor.

I thank Jorge Martinez and the rest of the Oran W. Nicks Low Speed Wind Tunnel staff for their help and cooperation.

Finally, I would like to thank Dr. John Schmisseur from the Air Force Office of Scientific Research for the generous grant that allowed this research to be possible.

TABLE OF CONTENTS

Page

ABSTRACT…. iii

DEDICATION.. v

ACKNOWLEDGMENTS vi

TABLE OF CONTENTS vii

LIST OF FIGURES x

LIST OF TABLES xx

CHAPTER I: INTRODUCTION 1

Motivation 1
Synopsis of Favorable Pressure Gradient Mechanical Non-equilibrium Effects 6
Scientific Questions 9
Research Approach 10
Research Contributions 11
Additional Technical Contribution 11
Dissertation Overview 12

CHAPTER II: COMPRESSIBLE TURBULENT BOUNDARY LAYERS 13

Compressible Turbulent Boundary Layers 13
Pressure Gradients 16

CHAPTER III: EXPERIMENTAL FACILITIES 21

Infastructure 21
SHR Tunnel 50
Tunnel Operating Conditions 50
Settling Chamber 52
Mach 5 Nozzle Adapter 53
Nozzle 54
Test Section 57
Diffuser 62
Wind Tunnel Models 63

Page

CHAPTER IV: EXPERIMENTAL TECHNIQUES....65

Particle Image Velocimetry....65
Hardware and Operation....66
Experimental Setup....70
System Timing....81
Data Processing....85
Conventional Methods....88

CHAPTER V: RESULTS AND DISCUSSION....92

Measurement Normalization....92
Inflow Characterization....94
Flow Visualization....98
PIV Valid Vectors....104
Mean Flow Measurements....109
Mean Velocity Measurements....109
Mean Velocity Gradient Measurements....130
Turbulent Flow Measurements....147
Turbulence Intensities....148
Turbulent Shear Stress....154
Turbulent Stress Production....159
Turbulent Stress Principal Axes Analysis....178
Reynolds Stress Quadrant Decomposition....184
Two-Point Correlations....203

CHAPTER VI: CONCLUSIONS AND RECOMMENDATIONS....207

Hypersonic Boundary Layer Study....207
Conclusions....207
Recommendations....214
ACE Hypersonic Wind Tunnel Facility Development....216
Conclusions....216
Recommendations....216

REFERENCES....218

ADDITIONAL REFERENCES....226

APPENDIX A: SOFTWARE PARAMETERS....227

APPENDIX B: PIV CODES....234

Page

APPENDIX C: PIV UNCERTAINTY ANALYSIS.....279

APPENDIX D: ADDITIONAL DATA PLOTS.....282

APPENDIX E: TABULATED PROFILE DATA.....298

APPENDIX F: ACE HYPERSONIC WIND TUNNEL FACILITY DEVELOPMENT.....311

APPENDIX G: SAFE OPERATING PROCEDURES.....420

VITA 425

LIST OF FIGURES

Page

Figure 1: NASA X-43 in Flight (Artist's Concept) 3

Figure 2: NASA X-43 Labeled Diagram 3

Figure 3: X-15 Hypersonic Test Aircraft 4

Figure 4: X-15 Shock Impingement Damage[5] 5

Figure 5: Representative Sketch of the Present Flow Field 8

Figure 6: Schematic of Energy Cascade[6] 9

Figure 7: Chicago Pneumatic Compressors 22

Figure 8: Compressor Pressure Switches 23

Figure 9: After Cooler SolidWorks Drawing and Photograph 24

Figure 10: Cyclone Separator SolidWorks Drawing and Photograph 25

Figure 11: Filter Assembly 26

Figure 12: Donaldson High Pressure Air Dryer 27

Figure 13: Donaldson High Pressure Air Dryer Specifications 28

Figure 14: A. D. Smith High Pressure Storage Tank 29

Figure 15: New Tank Exit Contraction Section 30

Figure 16: Steel Pipelines 31

Figure 17: Original Actuator and Ball Valve 32

Figure 18: Final 4" Actuator, Ball Valve, and Solenoid 33

Figure 19: 4" Ball Valve Specifications 34

Figure 20: 4" Actuator Mounting Shaft 35

Page

Figure 21: ASCO 3-Way Solenoid Valve....36
Figure 22: Actuator Air Supply Compressor and Dryer....37
Figure 23: Swagelok Tank Pressure Gauges....38
Figure 24: Swagelok Line Pressure Gauges....39
Figure 25: High Pressure Hydroseal Safety Relief Valve....40
Figure 26: 2" High Pressure Ball Valve....41
Figure 27: 2" Tank Actuator....42
Figure 28: 2" Actuator, Solenoid, and Ball Valve....43
Figure 29: 3" Rupture Disk System....44
Figure 30: 2" High Pressure Ball Valves....45
Figure 31: Heater Room Regulator, Ball Valve, and Actuator....47
Figure 32: Chromalox Heater....48
Figure 33: Heater Room Safety Relief Valves....49
Figure 34: KTM 3" Ball Valve....50
Figure 35: SolidWorks Drawing of Mach 5 Nozzle Adapter....54
Figure 36: Mach 5 Nozzle Contour....55
Figure 37: Installed Mach 5 Nozzle....57
Figure 38: Test Section Assembly - Front View....58
Figure 39: Test Section Front Wall Dimensioned Drawing....58
Figure 40: Fused Silica Window in Window Frame....59
Figure 41: Test Section Top Plate....60

Page

Figure 42: Test Section Top Plate Dimensioned Drawing 60
Figure 43: Test Section Complete Assembly 61
Figure 44: Installed Test Section 61
Figure 45: Disassembled Diffuser 62
Figure 46: Installed Diffuser 62
Figure 47: Pressure Gradient Model Wall Geometry 63
Figure 48: Original PIV Beam Combination Optics 67
Figure 49: Modified PIV Beam Combination Optics 68
Figure 50: PIV Beam Combination Optics Reflections 69
Figure 51: PIV Laser Frame Platform 71
Figure 52: High-Speed PIV Optics Rail 72
Figure 53: Razor Blade Cutoff 73
Figure 54: Example PIV Image 74
Figure 55: High Pressure PIV Seeder 75
Figure 56: PIV Seeder Connection Tubing 76
Figure 57: Slotted Seed Injection Sting 77
Figure 58: Slotted Seed Injection Sting (Zoom) 77
Figure 59: Cooke Camera System 78
Figure 60: Aluminum Dot Card 80
Figure 61: Aluminum Dot Card (Close Up) 80
Figure 62: Pulse Generator 82

Page

Figure 63: PIV Timing Schematic 84

Figure 64: Cooke Camera Double-Shutter Timing 85

Figure 65: PIV Correlation Process 86

Figure 66: Omega PX303 Pressure Transducer 89

Figure 67: MKS Series 902 Pressure Transducer 89

Figure 68: MKS Transducer and Omega Thermocouple Displays 90

Figure 69: LabVIEW DAQ Interface Screenshot 91

Figure 70: Spanwise Survey $\bar{u}$ (m/s) Contour Plots 95

Figure 71: Spanwise *U* Velocity Profiles 96

Figure 72: Three Dimensional Spanwise Contours with Iso-Surfaces 97

Figure 73: Sample Flow Visualization Images 99

Figure 74: ZPG Flow Visualization Survey 100

Figure 75: WPG Flow Visualization Survey 102

Figure 76: SPG Flow Visualization Survey 103

Figure 77: Contour Plots of Percentage of Valid Vectors 105

Figure 78: Profile Plot of Percentage of Valid Vectors 107

Figure 79: Profile Plot of Percentage of Valid Vectors (Cropped) 108

Figure 80: ZPG Mean Velocity Contours at 1st Measurement Location
a) Wide View, b) Zoom View 110

Figure 81: Zero Pressure Gradient Mean Velocity Profiles 111

Figure 82: ZPG Law of the Wall Plot 113

Figure 83: ZPG Defect Law Plot 114

Page

Figure 84: SPG Mean Velocity Contours at 1st Measurement Location 115

Figure 85: Raw PIV Image of WPG Model at 2nd Measurement Location 116

Figure 86: WPG Mean Velocity Contours at 2nd Measurement Location (Wall Normal Coordinate System).....117

Figure 87: WPG Mean Velocity Vectors in a) Wall Normal Coordinate System, b) Global Coordinate System 118

Figure 88: WPG Mean Velocity Contours at 2nd Measurement Location (Global Coordinate System).....118

Figure 89: WPG Velocity Profiles - Upstream Side.....120

Figure 90: WPG Velocity Profiles – Center 121

Figure 91: WPG Velocity Profiles - Downstream Side 122

Figure 92: Raw PIV Image of SPG Model at 2nd Measurement Location.....123

Figure 93: SPG Mean Velocity Contours at 2nd Measurement Location (Wall Normal Coordinate System).....124

Figure 94: SPG Mean Velocity Vectors in a) Wall Normal Coordinate System, b) Global Coordinate System 125

Figure 95: SPG Mean Velocity Contours at 2nd Measurement Location (Global Coordinate System).....126

Figure 96: SPG Velocity Profiles - Upstream Side 127

Figure 97: SPG Velocity Profiles - Center 128

Figure 98: SPG Velocity Profiles - Downstream Side 129

Figure 99: ZPG Wide View Mean Velocity Gradient Contours at 1st Measurement Location.....132

Figure 100: ZPG Zoom View Mean Velocity Gradient Contours at 1st Measurement Location.....133

Page

Figure 101: WPG Mean Velocity Gradient Contours at 2nd Measurement Location (Wall Normal Coordinate System) 135

Figure 102: WPG Mean Velocity Gradient Contours at 2nd Measurement Location (Global Coordinate System).....136

Figure 103: SPG Mean Velocity Gradient Contours at 2nd Measurement Location (Wall Normal Coordinate System) 138

Figure 104: SPG Mean Velocity Gradient Contours at 2nd Measurement Location (Global Coordinate System).....139

Figure 105: $d\bar{u}/dx$ Velocity Gradient Profiles.....141

Figure 106: $d\bar{u}/dy$ Velocity Gradient Profiles.....142

Figure 107: $d\bar{v}/dx$ Velocity Gradient Profiles.....143

Figure 108: $d\bar{v}/dy$ Velocity Gradient Profiles.....145

Figure 109: $\left(d\bar{v}/dx - d\bar{u}/dy\right)$ Velocity Gradient Profiles.....146

Figure 110: $\left(d\bar{v}/dx + d\bar{u}/dy\right)$ Velocity Gradient Profiles.....147

Figure 111: ZPG Turbulence Intensities Contours at 1st Measurement Location a) Wide View, b) Zoom View.....149

Figure 112: WPG Turbulence Intensities Contours at 2nd Measurement Location (Wall Normal Coordinate System) 150

Figure 113: WPG Turbulence Intensities Contours at 2nd Measurement Location (Global Coordinate System).....150

Figure 114: SPG Turbulence Intensities Contours at 2nd Measurement Location (Wall Normal Coordinate System) 151

Figure 115: SPG Turbulence Intensities Contours at 2nd Measurement Location (Global Coordinate System).....152

Figure 116: Axial Turbulence Intensity Profiles 153

Page

Figure 117: Transverse Turbulence Intensity Profiles 154

Figure 118: ZPG Turbulent Shear Stress Contours at 1st Measurement Location a) Wide View, b) Zoom View 155

Figure 119: WPG Turbulent Shear Stress Contours at 2nd Measurement Location a) Wall Normal Coordinate System, b) Global Coordinate System 156

Figure 120: SPG Turbulent Shear Stress Contours at 2nd Measurement Location a) Wall Normal Coordinate System, b) Global Coordinate System 157

Figure 121: Turbulent Shear Stress Profiles 158

Figure 122: Turbulent Shear Stress Profiles (Wall Normal) 159

Figure 123: ZPG (Wide View) Contours of P_{xx}, P_{yy} and Their Components at 1st Measurement Location 162

Figure 124: ZPG (Wide View) Contours of P_{xy} and Its Components at 1st Measurement Location 163

Figure 125: ZPG (Zoom View) Contours of P_{xx}, P_{yy} and Their Components at 1st Measurement Location 164

Figure 126: ZPG (Zoom View) Contours of P_{xy} and Its Components at 1st Measurement Location 165

Figure 127: WPG Contours of P_{xx}, P_{yy} and Their Components at 2nd Measurement Location (Wall Normal Coordinate System) 166

Figure 128: WPG Contours of P_{xy} and Its Components at 2nd Measurement Location (Wall Normal Coordinate System) 167

Figure 129: WPG Contours of P_{xx}, P_{yy} and Their Components at 2nd Measurement Location (Global Coordinate System) 168

Figure 130: WPG Contours of P_{xy} and Its Components at 2nd Measurement Location (Global Coordinate System) 169

Page

Figure 131: SPG Contours of P_{xx}, P_{yy} and Their Components at 2nd Measurement Location (Wall Normal Coordinate System) 171

Figure 132: SPG Contours of P_{xy} and Its Components at 2nd Measurement Location (Wall Normal Coordinate System) 172

Figure 133: SPG Contours of P_{xx}, P_{yy} and Their Components at 2nd Measurement Location (Global Coordinate System) 173

Figure 134: SPG Contours of P_{xy} and Its Components at 2nd Measurement Location (Global Coordinate System) 174

Figure 135: Axial Turbulent Stress Production, P_{xx} Profiles 175

Figure 136: Transverse Turbulent Stress Production, P_{yy} Profiles 177

Figure 137: Turbulent Shear Stress Production, P_{xy} Profiles 178

Figure 138: Sketch of Turbulence Stress Orientation[55] 179

Figure 139: ZPG Contours of Turbulent Stress-Turning Angle at 1st Measurement Location 180

Figure 140: WPG Contours of Turbulent Stress-Turning Angle at 2nd Measurement Location 181

Figure 141: SPG Contours of Turbulent Stress-Turning Angle at 2nd Measurement Location 182

Figure 142: Turbulent Stress-Turning Angle Profiles 183

Figure 143: Sketch of a Hairpin Vortex and the Induced Motion[60] 185

Figure 144: ZPG (Wide View) Quadrant Decomposition at y/δ_{ref} =1.4 at 1st Measurement Location 187

Figure 145: ZPG (Wide View) Quadrant Decomposition at y/δ_{ref} =1.2 at 1st Measurement Location 187

Figure 146: ZPG (Wide View) Quadrant Decomposition at y/δ_{ref} =1.0 at 1st Measurement Location 188

Page

Figure 147: ZPG (Wide View) Quadrant Decomposition at y/δ_{ref} =0.8 at 1st Measurement Location 189

Figure 148: ZPG (Wide View) Quadrant Decomposition at y/δ_{ref} =0.6 at 1st Measurement Location 189

Figure 149: ZPG (Wide View) Quadrant Decomposition at y/δ_{ref} =0.4 at 1st Measurement Location 190

Figure 150: ZPG (Wide View) Quadrant Decomposition at y/δ_{ref} =0.2 at 1st Measurement Location 191

Figure 151: ZPG (Wide View) Quadrant Decomposition at y/δ_{ref} =0.1 at 1st Measurement Location 191

Figure 152: WPG Quadrant Decomposition at y/δ_{ref} =1.4 at 2nd Measurement Location (Wall Normal Coordinate System) 192

Figure 153: WPG Quadrant Decomposition at y/δ_{ref} =1.2 at 2nd Measurement Location (Wall Normal Coordinate System) 193

Figure 154: WPG Quadrant Decomposition at y/δ_{ref} =1.0 at 2nd Measurement Location (Wall Normal Coordinate System) 194

Figure 155: WPG Quadrant Decomposition at y/δ_{ref} =0.8 at 2nd Measurement Location (Wall Normal Coordinate System) 195

Figure 156: WPG Quadrant Decomposition at y/δ_{ref} =0.6 at 2nd Measurement Location (Wall Normal Coordinate System) 195

Figure 157: WPG Quadrant Decomposition at y/δ_{ref} =0.4 at 2nd Measurement Location (Wall Normal Coordinate System) 196

Figure 158: WPG Quadrant Decomposition at y/δ_{ref} =0.2 at 2nd Measurement Location (Wall Normal Coordinate System) 197

Figure 159: WPG Quadrant Decomposition at y/δ_{ref} =0.1 at 2nd Measurement Location (Wall Normal Coordinate System) 197

Figure 160: SPG Quadrant Decomposition at y/δ_{ref} =1.4 at 2nd Measurement Location (Wall Normal Coordinate System) 198

Page

Figure 161: SPG Quadrant Decomposition at y/δ_{ref} =1.2 at 2nd Measurement Location (Wall Normal Coordinate System) 199

Figure 162: SPG Quadrant Decomposition at y/δ_{ref} =1.0 at 2nd Measurement Location (Wall Normal Coordinate System) 199

Figure 163: SPG Quadrant Decomposition at y/δ_{ref} =0.8 at 2nd Measurement Location (Wall Normal Coordinate System) 200

Figure 164: SPG Quadrant Decomposition at y/δ_{ref} =0.6 at 2nd Measurement Location (Wall Normal Coordinate System) 200

Figure 165: SPG Quadrant Decomposition at y/δ_{ref} =0.4 at 2nd Measurement Location (Wall Normal Coordinate System) 201

Figure 166: SPG Quadrant Decomposition at y/δ_{ref} =0.2 at 2nd Measurement Location (Wall Normal Coordinate System) 201

Figure 167: SPG Quadrant Decomposition at y/δ_{ref} =0.1 at 2nd Measurement Location (Wall Normal Coordinate System) 202

Figure 168: ZPG Streamwise Autocorrelation Map 204

Figure 169: WPG Streamwise Autocorrelation Map.....204

Figure 170: SPG Streamwise Autocorrelation Map 205

Figure 171: Streamwise Autocorrelation at y/δ=0.5.....206

LIST OF TABLES

Page

Table 1: Mach 5 Nozzle Coordinates 56

Table 2: Model Geometry and Pressure Gradient Parameters 64

Table 3: Pressure Gradient Strength Parameters 64

Table 4: Data Set Camera Resolutions 81

Table 5: Pulse Generation Channel Allocation 82

Table 6: Pulse Generator Settings 83

Table 7: Defined Normalization Quantities 94

Table 8: Valid Streamwise Field of View 106

Table 9: Valid Wall Normal Ranges 108

CHAPTER I

INTRODUCTION

Motivation

Accurate prediction of high-speed, high Reynolds number turbulent gaseous flow is an essential step in the design of future aerospace flight systems[1]. As fundamental scientific understanding and technologies continue to advance, aerospace vehicles are being designed to push previously established performance limits. Hypersonic (Mach>5) flight vehicles have been and will continue to be a long term focus of research and development, where an increasing number of future aerospace vehicles will be operating in this regime. According to the Air Force Office of Scientific Research in their Broad Agency Announcement (AFOSR BAA) 2006-11 in the Unsteady Aerodynamics and Hypersonics section, hypersonic aerodynamics research is critical to the Air Force's renewed interest in long-range and space operations. Because of the harshness of the thermal environment, designers must rely heavily on numerical simulations as part of the design process. However, limited understanding of key physical processes, such as high-speed turbulence with mechanical non-equilibrium effects, leads to large design uncertainties. Hence, improved knowledge of hypersonic viscous flows is required[2].

When a vehicle is traveling at hypersonic velocity, a thin boundary layer is formed on the surface. Since realistic flight vehicles are not flat plates, the boundary

---

This dissertation follows the format of the *AIAA Journal.*

layer will experience mechanical non-equilibrium effects. The already complicated flow physics in a high speed boundary layer are further complicated in these regions and are not very well understood[3]. To efficiently design future aerospace vehicles for hypersonic flight, these flow characteristics must be accounted for and predicted because of their impact on the vehicle.

The flow over an actual vehicle in a real fluid is complex at any speed. In the hypersonic flow regime, realistic flight vehicles will experience a range of complicated flow features including streamline curvature, separation regions, shock/shock and shock/boundary layer interactions. Areas that might create these flow structures include control surfaces, flame holders, and inlets. These phenomena can greatly impact the aerodynamic characteristics of hypersonic vehicles and therefore are an interest to many researchers[4].

To demonstrate the practical importance of high-speed turbulent boundary layers with mechanical non-equilibrium, consider the NASA X-43 shown in Figure 1. A labeled diagram of the X-43 showing important mechanical non-equilibrium effects is given in Figure 2. As indicated these mecahnical non-equilibrium effects are prevalent, and have the potential to adversely affect the component performance.

Figure 1: NASA X-43 in Flight (Artist's Concept)

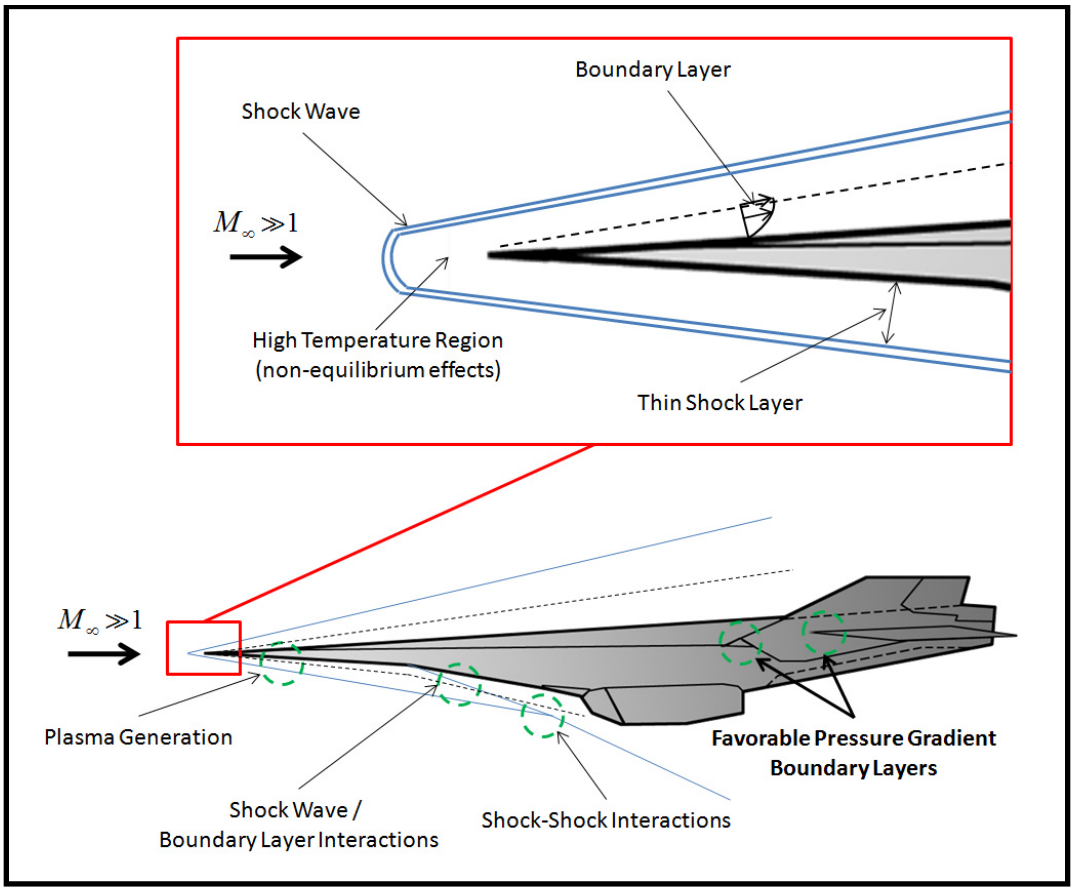

Figure 2: NASA X-43 Labeled Diagram

In areas of shock impingement, the surface of the vehicle can experience high localized aerodynamic and aerothermal loads which could affect the vehicle. Particularly in hypersonic flow, aerodynamic heating is a major factor because local heat transfer in these interaction regions can be extremely severe[3,4]. An example of this intense heating was shown during testing of the X-15, which is shown in Figure 3. During one of the flight tests in 1967, extreme heating caused by shock impingement was experienced at Mach 6 to 7, severely damaging the test article and the aircraft. A labeled photograph of the melted Inconel pylon that resulted from the interaction heating damage is shown in Figure 4. As indicated, the consequences can be catastrophic. In this case, the test article fell from the aircraft during the flight test.

Figure 3: X-15 Hypersonic Test Aircraft

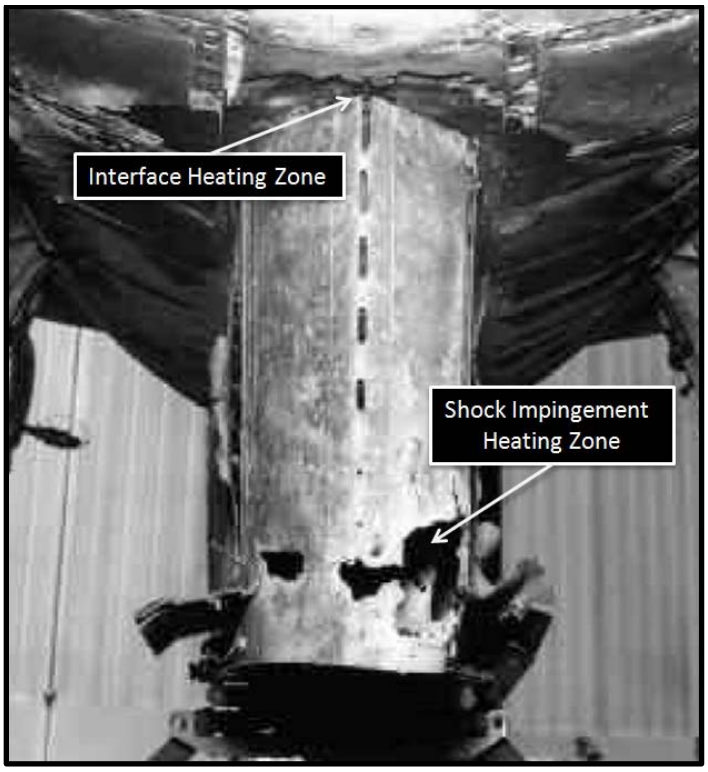

Figure 4: X-15 Shock Impingement Damage[5]

To date, the basic flow turbulent processes in this regime are poorly understood and are beyond the realm of direct numerical simulation. Thus, to predict high Reynolds number complex geometry problems, simulations are limited to either the Reynolds Averaged Navier-Stokes (RANS) or partially averaged Navier-Stokes methods such as Large-Eddy Simulations (LES), and for both, turbulence modeling is a key limiting factor in the solution accuracy. Providing improved understanding of the underlying mechanisms is one of the fundamental aims of turbulence research. Turbulence models vary in complexity and the extensive research on the development of these models is well documented[5,6,7,8,9,10]; a literature review is given in Chapter II. The majority of the

second order transport models that have been developed for compressible flow regimes are largely extensions of incompressible models[11,12,13]. In some cases this approach yields positive results. However, compressible flow inherently contains phenomenon that are not present in incompressible flow and therefore are not accounted for in these models without empirical corrections.

Synopsis of Favorable Pressure Gradient Mechanical Non-equilibrium Effects

The available literature (see Chapter II) suggests the following trends for the effects of streamline curvature driven favorable pressure gradients on high-speed turbulent boundary layers:

- Favorable pressure gradients and concave wall curvature both have a stabilizing effect on the boundary layer structure, where the turbulent Reynolds stress in the boundary layer can dramatically decrease; *o*(100%) and the Reynolds shear stress can change sign.
- The “extra” production can result in an overall negative production indicating that energy may flow back to the mean flow, which could lead to relaminarization.
- Intermittency changes indicating that the large-scale turbulence structure is altered.
- Many of the characteristic trends of subsonic and supersonic turbulent boundary layers, with respect to pressure gradients and wall curvature, have opposite orientation.

The above trends suggest that underlying structure of the wall turbulence is altered as the flow experiences wall curvature driven favorable pressure gradients[13]. Two scenarios are proposed schematically in Figure 5. It can be seen that the turbulent structures (represented as the black shapes) within the boundary layer are organized and growing upstream of the favorable pressure gradient curvature. As the flow moves over the favorable pressure gradient, one scenario has large-scale structures stretching and breaking up into smaller turbulent structures (indicated with the black shapes). For the second model, the turbulent structures elongate, but remain intact (grey shapes). The manner in which structure is altered remains uncertain.

Also shown in Figure 5 is the Reynolds stress transport equation. The terms that are altered by the presence of the wall curvature are highlighted. First, the additional strain rates ($\partial u/\partial x$, $\partial v/\partial x$, and $\partial v/\partial y$) result in "extra" production, P_{ij}. Second, the mean pressure gradients result in pressure-work, PW_{ij}, and the altering of the structures may result in significant changes in the pressure and density fluctuation, which alters the pressure-strain, R_{ij}. Lastly, if the large-scale structure are altered, it is reasonable to expect a significant change in the turbulence dissipation, ε_{ij}. The basic understanding of these transport processes is insufficient to construct reliable models.

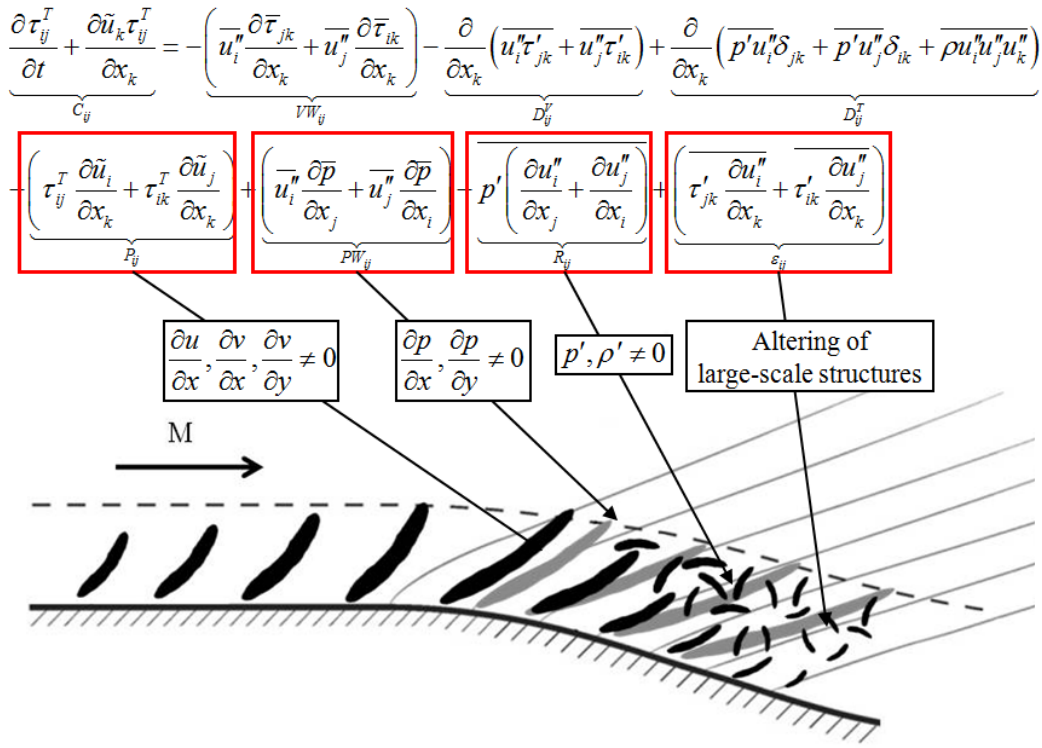

Figure 5: Representative Sketch of the Present Flow Field

The concept of the energy cascade from larger to smaller turbulent scales is well-known and well-accepted. Energy is typically transferred from the larger, energy-containing eddies down to the very small eddies where the structures experience significant viscous effects and account for nearly all of the dissipation in the flow. A schematic of the energy cascade is shown in Figure 6. The favorable pressure gradient alters the large-scale structure of the turbulent boundary layer therefore changing the typical energy cascade process. The effect of the favorable pressure gradient on the energy cascade is important, especially to LES models which require accurate prediction of the energy-containing length scales for model accuracy.

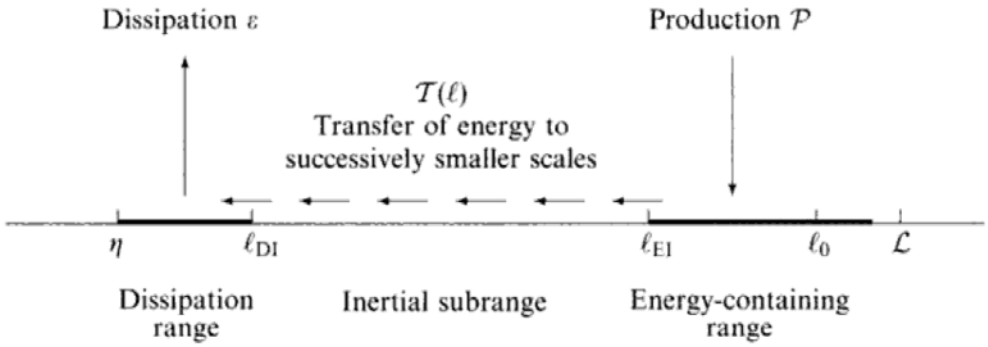

Figure 6: Schematic of Energy Cascade[6]

Scientific Questions

The aim of this dissertation is to answer the following questions:

(1) How is the state of the mean flow and turbulence statistics altered by curvature driven favorable pressure gradients at high Mach numbers?

(2) How is the structure of wall turbulence altered by curvature driven favorable pressure gradients; break-up, stretch or a combination of both?

(3) How are the Reynolds stress component production mechanisms altered by curvature driven favorable pressure gradients?

(4) What is the effect of Mach number on the above processes?

Answering these questions is an important step toward building improved models to predict this class of flow.

.

Research Approach

The overarching research objective for the proposed research project is to improve our basic understanding and prediction capabilities of a high Mach high Reynolds number boundary layer over curvature driven pressure gradients. To address this objective, detailed studies of Mach 5.0, high Reynolds number (Re_θ =36,000) flow over curved walls, similar to that shown in Figure 5 were performed. Analyses were performed to answer the questions listed above.

To accomplish the measurements, an existing high-speed wind tunnel research facility was modified to allow for high quality flow measurements. Specifically, a Mach 5 nozzle was installed, a new test section was designed and built and a new data acquisition system was installed to monitor the tunnel operating conditions. The wind tunnel models from Ekoto et al (2009) were refurbished and readied for high resolution diagnostic testing, including a zero pressure gradient (ZPG) model, a weak favorable pressure gradient model (WPG) and a strong favorable pressure gradient model (SPG). The Ekoto et al study was performed at Mach 2.9. Hence, comparison between Ekoto et al and the present Mach 5.0 study will provide information on the Mach number effects.

Flow visualizations and high quality two-dimensional particle image velocimetry (PIV) data were gathered to quantify the mean velocity flow fields over these pressure gradient models. The measurement resolution for the planar particle image velocimetry was 0.4 mm x 0.4 mm, and data were accomplished in the outer 85% of the boundary layer. From the mean velocity data, turbulence statistics including turbulence intensities and Reynolds shear stress were calculated as well as turbulent stress production terms.

Turbulent stress principal axes analyses were performed as well as Reynolds stress quadrant decomposition.

Research Contributions

The research contributions for this study based on the acquired data are as follows:

1. Improved basic understanding of the hypersonic flow properties found in a high Reynolds number turbulent boundary layer over curvature driven favorable pressure gradients.
2. Extensive addition to the current supersonic turbulent boundary layer experimental database. The data from the present study will be used to quantify flow field characteristics and will provide invaluable information for future theoretical studies and model comparison.

Additional Technical Contribution

In parallel with the current study, a new actively controlled expansion hypersonic wind tunnel was developed. This new facility will enable additional studies (e.g., low Reynolds number effects, thermal non-equilibrium, unsteady hypersonics, etc.) by future students at Texas A&M University.

Dissertation Overview

Brief descriptions of the research motivation, theoretical background and framework, objectives and approach, and contributions are presented above in Chapter I. In Chapter II a review of supersonic boundary layer literature is provided as a basis for the present study. In Chapter III the experimental facilities used for the present study are described in detail while the experimental diagnostic techniques are described in Chapter IV. In Chapter V the experimental results for the present study are presented and discussed. In Chapter VI, conclusions and recommendations for future research are presented. Appendix A provides the software settings while appendix B presents the in-house post-processing codes used for the particle image velocimetry measurements. Appendix C discusses the PIV uncertainty for the present study. In appendix D, the remaining data plots not shown in the main body of the dissertation while in appendix E, profile data is presented in tabular form. In appendix F, the design and construction of the new ACE hypersonic wind tunnel facility are described in detail. Finally, the safe operating procedures for the SHR and ACE high speed wind tunnel facilities are given for reference.

CHAPTER II

COMPRESSIBLE TURBULENT BOUNDARY LAYERS

One of the key challenges in developing and validating turbulence models for high-speed flow is the lack of experimental data that includes both mean and turbulence statistics. Much research has been done on mechanical non-equilibrium hypersonic flows especially in the context of aero braking of re-entry vehicles using continuum computational fluid dynamics (CFD) and molecular-dynamics methods such as direct-simulation Monte Carlo (DSMC). The study of non-equilibrium gases relevant to high-speed aerodynamics and or combustion has also received considerable theoretical attention[3,14,15,16,17,18]. Modern computational methods have provided valuable tools for the prediction of both internal and external flows over high-speed aerospace vehicles[19,20,21,22,23]. However, important computational limitations exist, which ultimately lead to reduced fidelity modeling in turbulence.

Compressible Turbulent Boundary Layers

The focus of the present study is to investigate the effects of mechanical non-equilibrium in the form of contour driven favorable pressure gradients on a high Reynolds number, M=4.88 supersonic turbulent boundary layer. Incompressible smooth wall zero pressure gradient turbulent boundary layers are very well understood; semi-empirical correlations such as the law of the wall, defect law, and turbulent kinetic energy transport data are routinely used to validate turbulence modeling concepts

including high speed, compressible flows. These flows have been the focus of many previous studies and have been comprehensively reviewed[5,8,9,10,24,25].

However, the fundamental thermodynamic characteristics for compressible flow fields are inherently different than their incompressible counterparts. The shear stress and Reynolds shear stress tensors are defined as:

$$\tau_{ij} = \mu\left(\frac{\partial u_i}{\partial x_j} + \frac{\partial u_j}{\partial x_i}\right) - \frac{2}{3}\mu\frac{\partial u_k}{\partial x_k}, \qquad \tau_{ij}^T = -\overline{\rho}\overline{u_i^{"}u_j^{"}} \tag{2.1}$$

The complete compressible form of the Reynolds Stress Transport Equation is then given as:

$$\begin{aligned}
&\underbrace{\frac{\partial \tau_{ij}^T}{\partial t} + \frac{\partial \tilde{u}_k \tau_{ij}^T}{\partial x_k}}_{C_{ij}} = \underbrace{-\left(\tau_{ij}^T \frac{\partial \tilde{u}_i}{\partial x_k} + \tau_{ik}^T \frac{\partial \tilde{u}_j}{\partial x_k}\right)}_{P_{ij}} - \underbrace{\left(\overline{u_i''}\frac{\partial \overline{\tau}_{jk}}{\partial x_k} + \overline{u_j''}\frac{\partial \overline{\tau}_{ik}}{\partial x_k}\right)}_{VW_{ij}} + \\
&\underbrace{\left(\overline{u_i''}\frac{\partial \overline{p}}{\partial x_j} + \overline{u_j''}\frac{\partial \overline{p}}{\partial x_i}\right)}_{PW_{ij}} - \underbrace{\overline{p'\left(\frac{\partial u_i''}{\partial x_j} + \frac{\partial u_j''}{\partial x_i}\right)}}_{R_{ij}} - \underbrace{\frac{\partial}{\partial x_k}\left(\overline{u_i''\tau_{jk}'} + \overline{u_j''\tau_{ik}'}\right)}_{D_{ij}^V} + \\
&\underbrace{\frac{\partial}{\partial x_k}\left(\overline{p'u_i''}\delta_{jk} + \overline{p'u_j''}\delta_{ik} + \overline{\rho u_i'' u_j'' u_k''}\right)}_{D_{ij}^T} + \underbrace{\left(\overline{\tau_{jk}'\frac{\partial u_i''}{\partial x_k}} + \overline{\tau_{ik}'\frac{\partial u_j''}{\partial x_k}}\right)}_{\varepsilon_{ij}}
\end{aligned} \tag{2.2}$$

The term on the left side C_{ij} of the equation represents the convection of the turbulent stresses. The first term on the right hand side P_{ij} is the turbulent stress production. The second and third terms VW_{ij} and PW_{ij} are the viscous and pressure work terms

respectively. The fourth term on the right hand side of the equation R_{ij} is the pressure strain redistribution term. The fifth and sixth terms D_{ij}^{V} and D_{ij}^{T} are the viscous diffusion and turbulent diffusion respectively. The last term on the right side of the equation ε_{ij} is the viscous dissipation.

Morkovin first observed that many of the differences in the turbulent statistical properties across supersonic and subsonic zero pressure gradient, flat plate boundary layers could be correlated by using the thermodynamic property variations across the layers[11]. This observation, termed Morkovin's hypothesis, was based on limited smooth wall zero pressure gradient data and the flat plate form of the turbulent kinetic energy transport equation, has provided the rationale for using incompressible turbulence models for flows up to Mach 5. Van Driest developed compressibility scaling that has been found to correlate the mean velocity of high-speed data with the low-speed database across smooth boundary layers[26]. Although Morkovin's hypothesis is generally accepted and used often in modeling compressible flows, more recent analysis of turbulent smooth wall data indicates that the current database was insufficient to confirm turbulent property scaling and therefore the realm of applicability of Morkovin's hypothesis might be more restrictive than originally believed[2,27,28,29,30]. Additionally, supersonic flows often possess features that are not present in subsonic flow fields such as shock-boundary layer interactions which Morkovin's hypothesis does not apply.

Pressure Gradients

The effects of pressure gradients on low-speed boundary layers have also been the subject of numerous studies[8,10,31]. The inner region boundary layer scaling (i.e., law of the wall) has been shown to hold in the presence of favorable and adverse pressure gradients. However near separation, the inner scaling breaks down. Additionally, the logarithmic region termination height depends on the strength of the pressure gradient; for favorable pressure gradients, the height increases and for adverse pressure gradients it decreases. The outer region of the boundary layer is very sensitive to pressure gradient, and in general the defect law does not hold. However, Clauser defined a pressure gradient strength parameter β as the product of the axial pressure gradient dp_e/dx and the ratio of the boundary layer displacement thickness δ^* and wall shear stress τ_{wall} as:

$$\beta = \left(\frac{\delta^*}{\tau_{wall}} \right) \left(\frac{dp_e}{dx} \right)$$

When β is constant, the boundary layers are in equilibrium; (i.e., the defect scaling laws hold and the corresponding profiles are independent of axial location)[32]. Coles used this idea to generalize the law of the wall for equilibrium pressure gradient flows by developing a wake function[33].

For diffusers and nozzles, favorable pressure gradients without wall curvature (i.e., accelerating flows) reduce turbulence levels; the opposite is true for adverse pressure gradients. Concave and convex curvature, with and without an associated

pressure gradient, have been shown to have de-stabilizing and stabilizing effects, respectively on the turbulent flow properties across low-speed boundary layers[31,34,35]. For convex curvatures, the turbulence levels, turbulent shear stresses and wall friction all decrease relative to canonical flat surface values while the opposite is observed for concave curvatures. These trends are explained by simple angular momentum arguments. The angular momentum terms in the Navier-Stokes equations for planar flow over curved surfaces are on the order of the ratio of the boundary layer thickness and radius of curvature of the wall turning; hence, the effects are first order. For laminar flow, the effects have been shown to be first order. However for turbulent flows, the effects of wall curvature are significantly larger (approximately a factor of 10) than expected. Heuristic empirical corrections are therefore required in order to account for this effect in predictions[35,36]. The effects of wall curvature are most pronounced in the outer region of the boundary layer, where for strong wall curvatures (e.g., ratio of the boundary thickness and wall radius of curvature of order 0.1), negative Reynolds shear stresses have been observed [37]. Additionally, it was reported that the turbulent heat flux was affected by curvature more than the turbulent shear stress[38].

Many of the observed differences between distorted supersonic and subsonic boundary layers can be explained in terms of the fluid property changes across the boundary layers[28,36,39]. However, supersonic flows possess phenomena that do not have incompressible counterpart such as expansion or shock wave boundary layer interactions. In these cases the longitudinal pressure gradients can lead to compression

or dilatation, which in turn affects the velocity, pressure and density fluctuations. This type of phenomenon is not present in subsonic flow.

When a streamwise favorable pressure gradient is imposed on a supersonic boundary layer, the flow is distorted by both the effects of pressure gradient and by the bulk pressure gradient[31]. A distortion is generally considered mild if $d_{\max} \approx 0.01$ and strong for $d_{\max} \approx 0.1$[29]. If the distortion is applied for a time that is comparable to an eddy lifetime, then the impulse parameter *I*, defined as the time-integrated strain rate, may be a better choice for the distortion classification[39]. For an impulsive perturbation resulting from a region of bulk compression, $I_p = \ln(p_2/p_1)/\gamma$ and for an impulse as a result of curvature, $I_\phi = \Delta\phi$[29,39,40]. Even though the interactions between the strain rates are most likely nonlinear, the linear addition of the perturbation strengths is usually accepted for crude comparisons among different flows. A generalization of the pressure gradient strength definition is provided in Luker *et al.*[41].

Collectively, the available turbulence data indicate that the axial turbulence intensities decrease by 70-90% for I_p and I_ϕ values $\in$ (-0.4,-1.0) and (-0.1,-0.3), respectively[34,42,43,44,45]. Because of reductions in the fluctuating properties as well as reductions in the skin friction and heat transfer, favorable pressure gradients are often characterized as having a stabilizing effect. Relaminarization of part of the boundary layer is believed to be possible if the favorable pressure gradient is strong enough[28,44]. Other work estimated, using a rapid distortion analysis, that the majority of the turbulence reduction was the result of mean bulk dilatation[42,45].

Other work showed that the overall magnitude of the kinematic Reynolds shear stress was dramatically decreased across the entire boundary layer for 7.0 and 14.0 deg. centered and gradual expansions[46]. They further defined an "apparent reverse transition," where the normal energy transfer from the mean flow had been reversed, to describe a sign changing of the Reynolds shear stress. Although this study provided detailed turbulence information throughout the expansion, the axial spacing was not refined enough to resolve the streamwise strain rates.

Other studies have performed detailed investigations of the influence of the wall curvature driven pressure gradients on the turbulent flow field including the turbulent shear stress transport[41,47,48]. For favorable pressure gradient flows, the previous turbulence data showed that the presence of a favorable pressure gradient had the expected stabilizing effect on the turbulent quantities. The magnitude of the Reynolds shear stress was also reduced by the favorable pressure gradient; in the near-wall region it was approximately 25% of the zero pressure gradient value, and in the outer region $(y/\delta > 0.5)$, the kinematic Reynolds shear stresses were negative and the principle strain rates were positive. The three-dimensional strain rate measurements and the associated extra production terms indicated that the overall turbulence production was also negative in the outer half of the favorable pressure gradient boundary layer. The use of a body-intrinsic coordinate system contributed to the reduced shear stress levels. Overall, the current database indicated that the favorable pressure gradient was disintegrating the large-scale eddies into smaller ones. This redistribution of energy increased the amount of turbulent energy available for dissipation by the flow, which in

turn had the observed stabilizing effect on the boundary layer. Numerical simulations using two-equation turbulence modeling demonstrated that the eddy viscosity approach was inadequate for even these very mild pressure gradient flows.

CHAPTER III

EXPERIMENTAL FACILITIES

In this section, the experimental facilities utilized for this project are described. First, the high-speed experimental facility is described, beginning with the infrastructure followed by a detailing of the tunnel components. The general wind tunnel configuration was designed using *High-Speed Wind Tunnel Testing*[49] as an engineering reference along with the computer-aided design software SolidWorks.

Infastructure

The high pressure air used to drive the high-speed blow-down tunnel was supplied by two four-stage Chicago Pneumatic TCB-4 compressors that were formerly installed in a NASA rocket vehicle test facility. Each unit is powered by a 112 kilowatt motor and is rated to provide a mass flow rate of 0.13 kg/s at 24.0 MPa (500 SCFM). The maximum discharge pressure for each compressor is limited to 15.51 MPa (2250 psig). The compressors can be seen in Figure 7 below.

Figure 7: Chicago Pneumatic Compressors

Electronic pressure switches were installed in line to automatically control the normal operation of the compressors. For a tank pressure of 0 – 10.34 MPa (0 – 1500 psig), both compressors run to charge the tank as quickly as possible. However, above 15.51 MPa (2250 psig), if both compressors are running, the back pressure increases and

begins to discharge through safety pop off valves. To prevent this, a pressure switch unloads one compressor at 15.51 MPa (2250 psig). The maximum pressure that the tank was charged to was 16.54 MPa (2400 psig) at which point a second pressure switch would unload the second compressor. As a master kill, if the pressure ever reached 17.92 MPa (2600 psig), a third pressure switch would turn off power to both compressors. When the tank pressure dropped below the set pressures, the switches would load one or both of the compressors until the tank reaches maximum pressure. The pressure switches are shown in Figure 8.

Figure 8: Compressor Pressure Switches

The high pressure air from the compressors is first passed through an after cooler composed of approximately 15.24 meters (50 feet) of 2.54 cm (1 inch) SCH 80 carbon steel pipe with a 0.455 cm (0.179 inch) wall thickness and an inner diameter of 2.070 cm (0.815 inches). Tap water was passed through a trough in which the pipe was submerged in order to cool the temperature of the high pressure air and to allow additional moisture to be condensed from the air. A SolidWorks model as well as a picture of the installed after cooler are shown in Figure 9.

Figure 9: After Cooler SolidWorks Drawing and Photograph

After the air was cooled, the air passed through a cyclone separator to remove the majority of the condensed liquid. The cyclone separator was designed in-house and was constructed from 7.62 cm (3 inch) SCH 160 carbon steel pipe and fittings. The cyclone

separator was sized to meet the high pressure and the mass flow requirements of the other components in the air supply system. A SolidWorks model of the cyclone separator as well as a picture of the installed cyclone separator is shown in Figure 10.

Figure 10: Cyclone Separator SolidWorks Drawing and Photograph

Immediately after the cyclone separator, the high pressure air was passed through two cartridge filters to further scrub the air of particulates. Additionally, glycerin filled gages were installed before and after each filter to monitor the pressure drop through each filter. If the pressure drop became significant, it would indicate the filter cartridge was beginning to clog and would need to be replaced. A standard Omega K-type

thermocouple probe was installed in the filter assembly to monitor the high pressure air temperature prior to it entering the dryer. The entire filter assembly is shown in Figure 11.

Figure 11: Filter Assembly

The remaining moisture, oil, and other particulates produced by the compressors were removed by passing the air through a Donaldson AHLD-500 High Pressure Heatless Regenerative Air Dryer. The dryer was a high pressure dual tower heatless regenerative desiccant air dryer. The high pressure air was dried by the desiccant in one tank while

the other tank was regenerated. The tanks were alternated from a drying cycle to a regeneration cycle and vice-versa automatically every 5 minutes. The rated mass flow rate of the dryer was 0.13 kg/s at 24.0 MPa (500 SCFM); however, approximately one third of the mass flow was passed through the regenerating tower to dry the desiccant. This resulted in an effective mass flow rate of 333 SCFM into the storage tank. The dryer's rated inlet pressure and temperature were 13.79 MPa (2000 psi) and 311 K (100 °F) respectively while the maximum inlet pressure and temperature were 20.68 MPa (3000 psi) and 322 K (120 °F) respectively. The dryer and the dryer specifications can be seen in Figure 12 and Figure 13.

Figure 12: Donaldson High Pressure Air Dryer

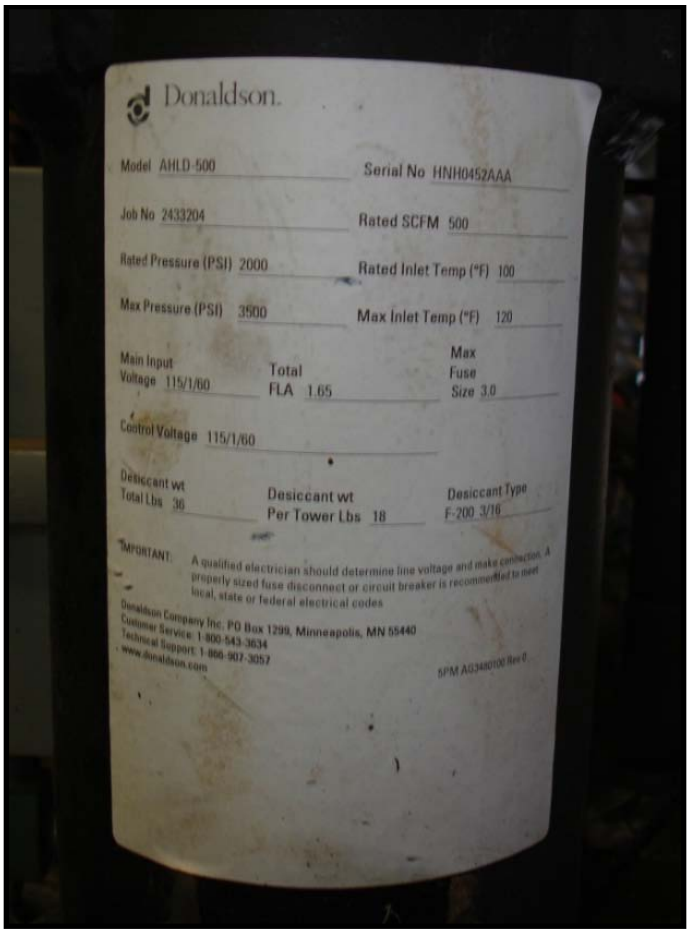

Figure 13: Donaldson High Pressure Air Dryer Specifications

The clean, dry compressed air was stored in an A. D. Smith high pressure storage tank, shown in Figure 14, which had an internal volume of 23.3 cubic meters (825 ft^3) and a maximum operating pressure of 19.3 MPa (2800 psi). The tank was located adjacent to the compressor building and was connected to the 5.08 cm (2 inch) pipeline and to the 10.16 cm (4 inch) pipeline on each end.

Figure 14: A. D. Smith High Pressure Storage Tank

While in the process of developing the infrastructure needed for the high-speed wind tunnel facility, the section of pipe connected to the storage tank on the 10.16 cm (4 inch) pipeline side was replaced. The original section of pipe had a smaller inner diameter than the tank exit pipe which could increase pressure losses during running. To solve this problem, a new section of pipe was designed and custom built in house. A 7.62 cm (3 inch) 1500# and a 10.16 cm (4 inch) 1500# RTJ weld neck flange were machined into socket-weld flanges with custom bored inner diameters to allow for a smooth transition from the 7.62 cm (3 inch) tank exit pipe to the 10.16 cm (4 inch) knife valve that isolates the tank from the 10.16 (4 inch) pipeline. A SolidWorks drawing and a picture of the new tank exit contraction section are shown in Figure 15.

Figure 15: New Tank Exit Contraction Section

The air to the wind tunnel facility was originally ran through approximately 65 m (213 feet) of 10.16 cm (4 inch) SCH XX A105 carbon steel pipe. It had an outer diameter of 11.43 cm (4.5 inches), an inner diameter of 8.00 cm (3.152 inches), and a maximum rated pressure of 27.55 MPa (3994 psig) at a factor of safety of 1.5. This pipeline was welded and was originally the sole source of high pressure air from the storage tank to the high-speed experimental laboratory. However, due to laboratory improvements and expansions, a cleaner air line was required from the storage tank to the laboratory. A secondary pipeline was installed parallel to the original 10.16 cm (4 inch) pipeline. This pipeline was made of 5.08 cm (2 inch) SCH 80 stainless steel pipe and was threaded together. It had an outer diameter of 6.03 cm (2.375 inches), an inner diameter of 4.93 cm (1.939 inches), and a maximum rated pressure of 16.87 MPa (2448 psig) at a factor of safety of 1.5. Stainless steel was chosen to avoid introducing rust into

the air flow of the high-speed experimental facility. Both pipelines can be seen in Figure 16.

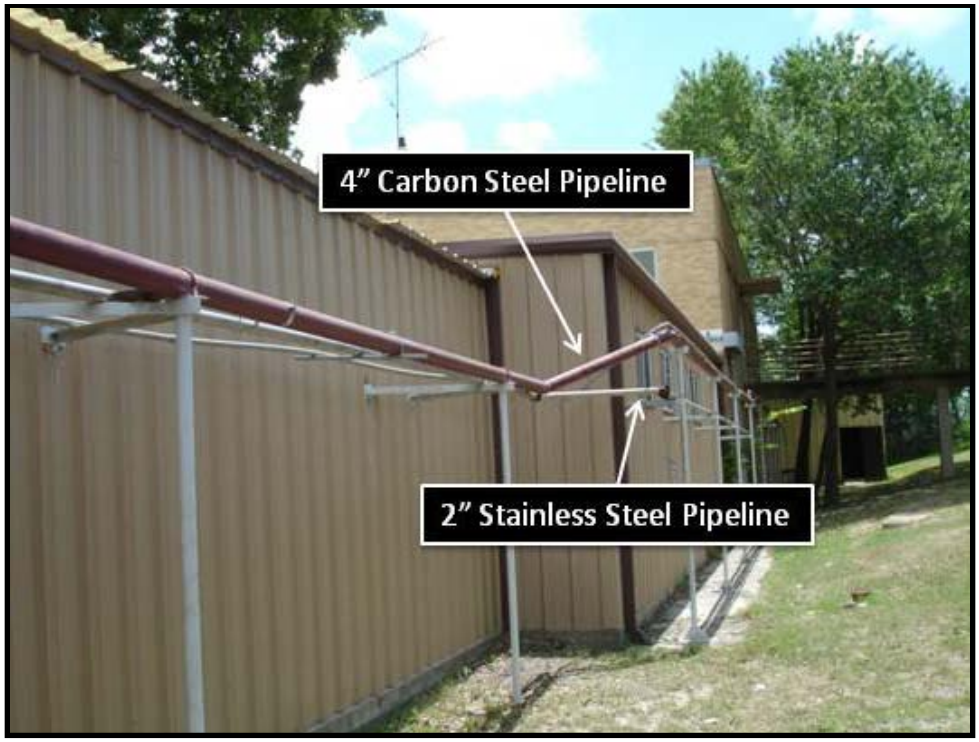

Figure 16: Steel Pipelines

Originally, the wind tunnel facility used the above described 10.16 cm (4 inch) pipeline and was controlled using, a 4-1500 full bore Virgo Engineers Trunion Mounted Ball Valve. The ball valve was 54.61 cm (21.5 inches) long and had 10.16 cm (4 inch) 1500# RTJ flange connections with a rated pressure of 25.92 MPa (3760 psig) at 311 K (100 °F) and 22.90 MPa (3322 psig) at 422 K (300 °F). The ball valve was initially controlled by a B-270U-S100 Morin Series B pneumatic actuator. The original configuration is shown in Figure 17. This actuator was a quarter-turn, spring return

model with 316 stainless steel cylinders and two pistons. At a 0.83 MPa (120 psig) air supply pressure, the specified minimum opening torque was 1653.42 Nm (14634 in. lb.) with a closing spring torque of 1012.80 Nm (8964 in. lb.).

Figure 17: Original Actuator and Ball Valve

However, the actuator malfunctioned and could no longer fully close the ball valve. A replacement actuator was ordered, but the lead time required to obtain the exact model was prohibitive. To get back up and running as quickly as possible, a similar actuator was purchased. The replacement actuator was a B-270U-S80 Morin Series B pneumatic actuator. This actuator was also quarter-turn, spring return model with 316 stainless steel cylinders and two pistons however it had a smaller spring than the first installed actuator. Also, when the actuator was replaced, the 1.27 cm (0.5 inch) aluminum tubing

air supply lines to the actuator were also replaced with 1.27 cm (0.5 inch) stainless steel braided hoses to allow for easier connection. The specified minimum opening torque at 0.83 MPa (120 psig) was 2091.69 Nm (18513 in. lb.) while the closing spring torque was 810.44 Nm (7173 in. lb.) due to the smaller spring size. The final 10.16 cm (4 inch) pipeline assembly and the 10.16 cm (4 inch) ball valve specifications are shown below in Figure 18 and Figure 19 respectively.

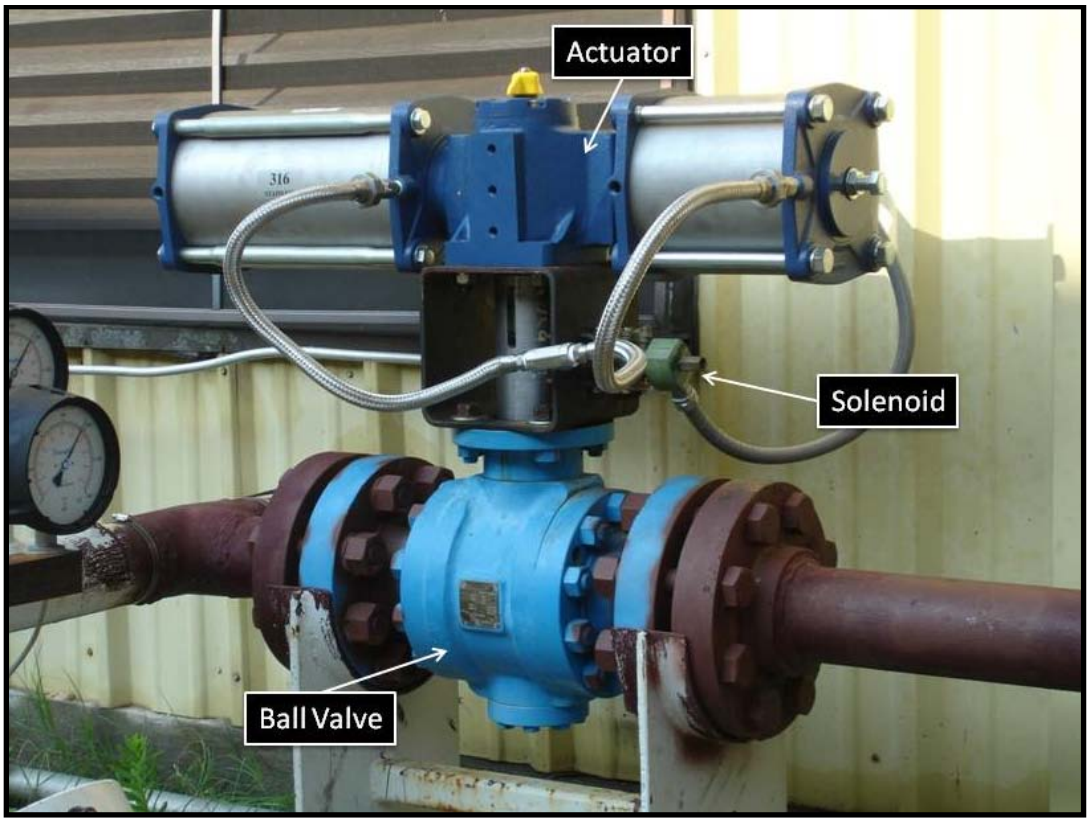

Figure 18: Final 4" Actuator, Ball Valve, and Solenoid

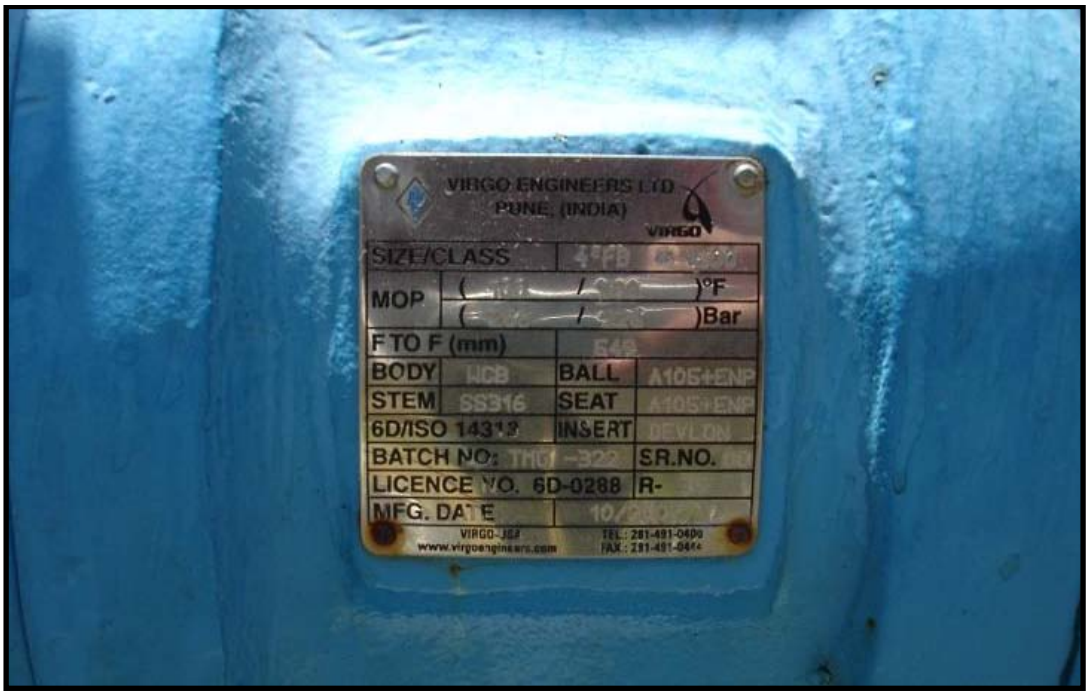

Figure 19: 4" Ball Valve Specifications

Additionally, when the new actuator was installed, a new mounting shaft was designed and built from 304 Stainless Steel. This mounting shaft featured slotted key ways to allow the actuator to be securely mounted to the ball valve and to eliminate slipping during operation. A picture of the new actuator mounting shaft can be seen in Figure 20.

Figure 20: 4” Actuator Mounting Shaft

Both actuators required a supply pressure of 0.83 MPa (120 psig) which was controlled by an ASCO Red Hat 3-way normally-closed high flow solenoid valve model 8316G004. The solenoid had 1.27 cm (0.5 inch) NPT pipe connections, a 1.59 cm (0.625 inch) orifice size and a rated pressure of 0.10-1.03 MPa (15-150 psig). The solenoid valve is shown in Figure 21.

Figure 21: ASCO 3-Way Solenoid Valve

An Ingersoll Rand model 2475N5 single-stage air compressor was used to provide the 120 psig operating air to the actuator. The compressor had a 5 hp motor, a 302.83 L (80 gallon) vertical tank, a maximum pressure of 1.21 MPa (175 psig) and a maximum mass flow rate of 16.8 cfm at 1.21 MPa (175 psig). To dry the air before entering the actuators, a desiccant air dryer was installed. The dryer featured a zinc body with an aluminum bowl filled with silica gel desiccant, a maximum flow rate of 25 scfm and a dew point of 230 K (-45 °F). The shop air compressor and the desiccant air dryer for the actuator air supply are shown in Figure 22.

Figure 22: Actuator Air Supply Compressor and Dryer

To monitor the tank and 4” line pressures, a series of Swagelok model PGI-160P-PG3000-LAP1-J gauges were installed near the 10.16 cm (4 inch) ball valve and actuator. These industrial processes gauges had 15.24 cm (6 inch) dial faces, a pressure range of 0-20.68 MPa (0-3000 psig) and were glycerin filled. They are shown in Figure 23 and Figure 24.

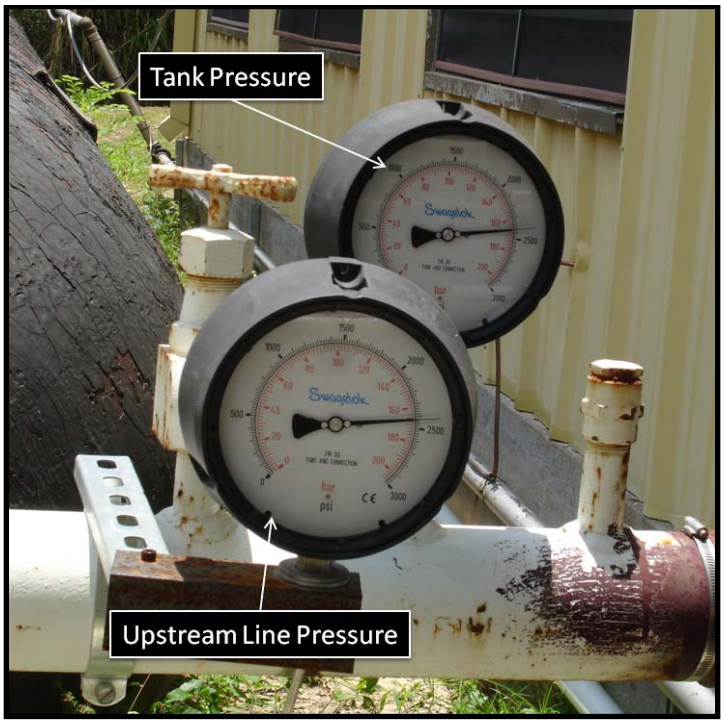

Figure 23: Swagelok Tank Pressure Gauges

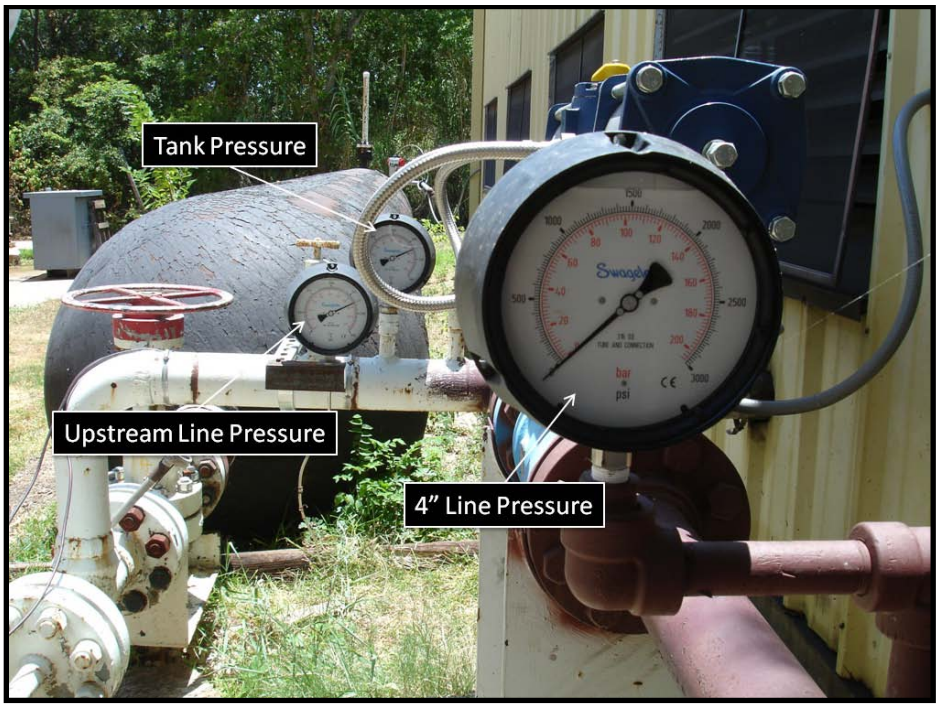

Figure 24: Swagelok Line Pressure Gauges

Also, in order to prevent the 10.16 cm (4 inch) line from over pressurizing, a Hydroseal safety relief valve, model SFTN0L/G5 was installed after the ball valve. The valve had a 1.27 cm (0.5 inch) orifice diameter, had a set pressure of 17.23 MPa (2500 psig) and is shown in Figure 25.

Figure 25: High Pressure Hydroseal Safety Relief Valve

The air for the present study was supplied to the wind tunnel facility via the 5.08 cm (2 inch) pipeline. A manually operated high pressure ball valve was installed immediately after the storage tank, allowing the pipeline to be isolated from the storage tank when the wind tunnel was not in operation. The valve was a Cameron WKM Dynaseal 5.08 cm (2 inch) full bore 3-piece ball valve model 310C5 and had a pressure rating of 20.68 MPa (3000 psig) at 295 K (72 °F) and 18.74 MPa (2719 psig) at 377 K (220 °F). The valve is shown in Figure 26.

Figure 26: 2" High Pressure Ball Valve

A duplicate Cameron WKM Dynaseal 5.08 cm (2 inch) full bore 3-piece ball valve was placed approximately 30.48 cm (12 inches) downstream of the first valve and was fitted with an actuator. This valve served as the control valve for the high-speed experimental facility. The actuator for the 5.08 cm (2 inch) ball valve was a Bray Controls pneumatic actuator model 92-1180-11300-532. The actuator was a double-acting pneumatic actuator that had a maximum operating pressure of 0.97 MPa (140 psig) and was controlled with the same shop air system previously discussed. A picture of the 5.08 cm (2 inch) tank actuator is shown in Figure 27.

Figure 27: 2" Tank Actuator

To enable electrical control of the actuator, a Bray Controls 4-Way Series 63 solenoid was mounted directly to it. The pneumatic actuator, 4-way solenoid and the high pressure ball valve are shown in Figure 28.

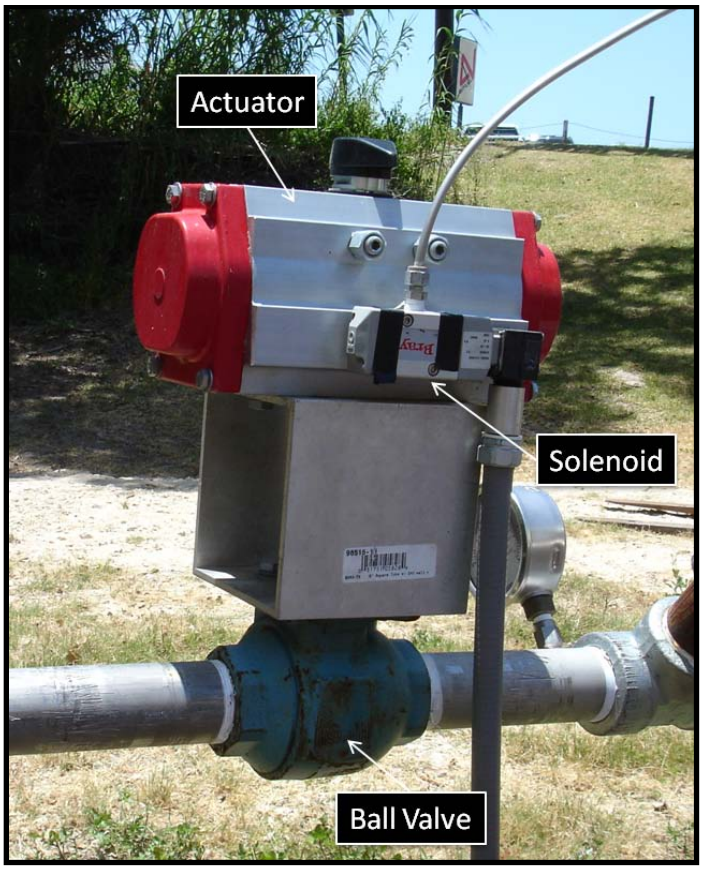

Figure 28: 2" Actuator, Solenoid, and Ball Valve

To prevent over-pressuring of the tank and other components, a 7.62 cm (3 inch) rupture disk system was installed. The rupture disk was rated at 17.23 MPa (2500 psig) at 491 K (425 °F) and 23.28 MPa (3378 psig) at 295 K (72 °F). The rupture disk mounting system is shown in Figure 29.

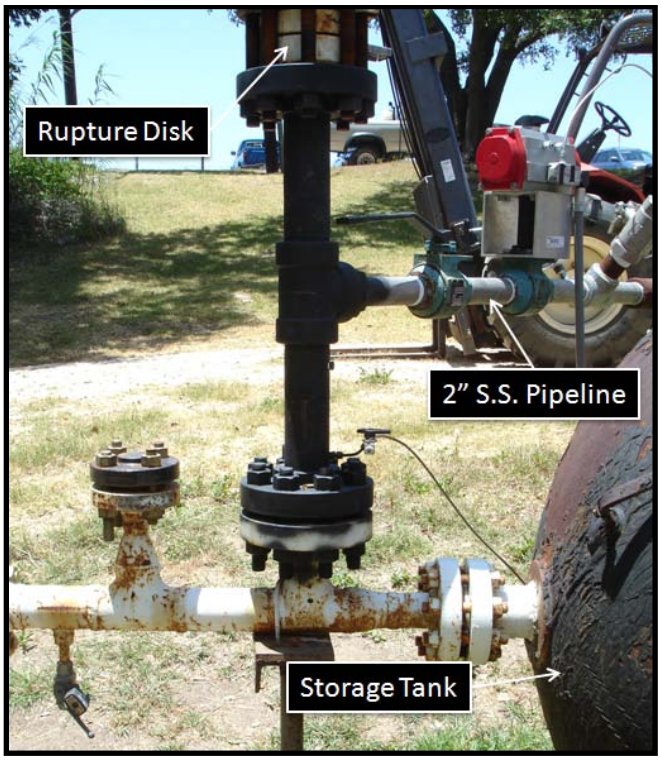

Figure 29: 3" Rupture Disk System

An exhaust port was added to the 5.08 cm (2 inch) stainless steel line to enable the line to be depressurized when needed. A Warren W36 series 5.08 cm (2 inch) high pressure reduced port ball valve was used to seal the exhaust line. This ball valve had a rated pressure of 24.81 MPa (3600 psig) at 310 K (100 °F). All three high pressure ball valves on the 5.08 cm (2 inch) line near the storage tank can be seen in Figure 30.

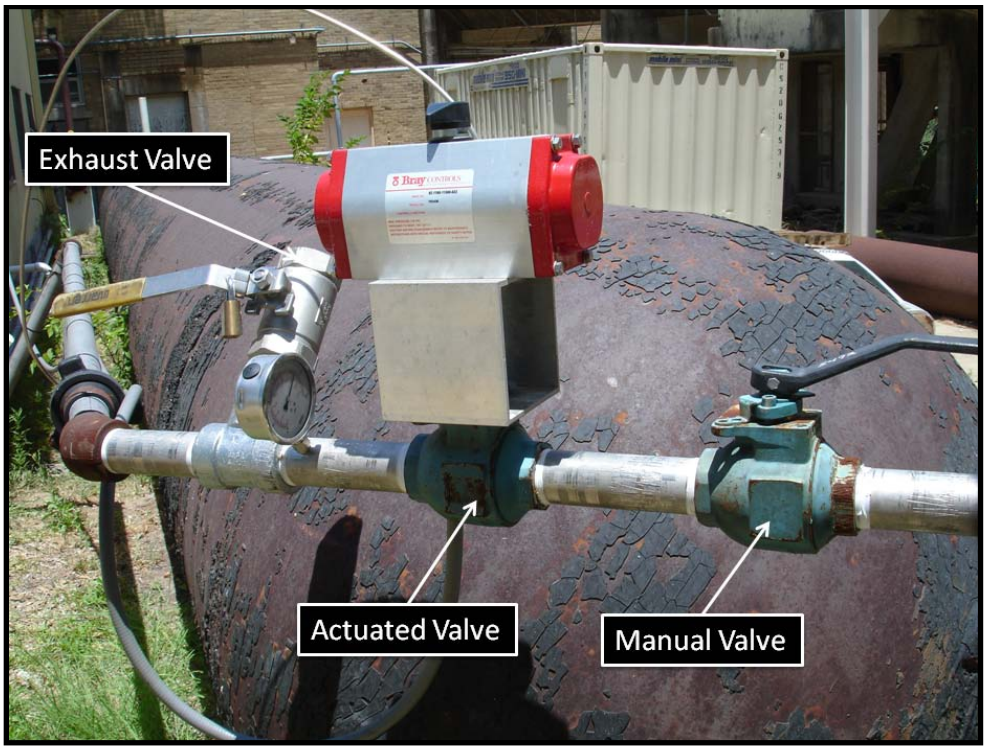

Figure 30: 2" High Pressure Ball Valves

The high pressure air through the 5.08 cm (2 inch) pipeline was originally regulated down in the heater room using two stainless steel Stra-Val dome loaded pressure regulators. Both regulators had a 5.08 cm (2 inch) FNPT inlet and outlet while the first regulator had a Cv value of 33.0 and the second had a Cv value of 33.5. The high pressure air from the 5.08 cm (2 inch) pipeline was regulated down through the first regulator to approximately 3.45 MPa (500 psig). Immediately downstream of the first pressure regulator, was an actuated high pressure ball valve. The ball valve was Cameron WKM Dynaseal 5.08 cm (2 inch) full bore 3-piece ball valve and was actuated with a Bray Controls pneumatic actuator model 92-1180-11300-532. This combination was the exact setup used for the 5.08 cm (2 inch) pipeline near the storage tank. A Bray

Controls 4-Way Series 63 solenoid was again mounted directly to the actuator and was supplied with shop air from the laboratory and the air compressor described in the low-speed experimental facility section. Downstream of the actuated ball valve, the second Stra-Val pressure regulator was installed before the heater entrance and regulated the incoming 3.45 MPa (500 psig) air down to approximately 1.24 MPa (180 psig). The purpose of having two regulators in series was to minimize output pressure drop as the storage tank pressure dropped. However, when initially testing the high-speed experimental facility, large scale pressure oscillations were observed. After tedious inspections and many test runs, it was determined that the second Stra-Val regulator was chattering, most likely due to unforeseen dynamic interaction with the first pressure regulator. To solve this problem, the second Stra-Val regulator was simply removed from the line and replaced with a standard, high pressure 5.08 cm (2 inch) steel pipe elbow. In the final configuration, the sole remaining regulator was readjusted to regulate the high pressure air down to preferred settling chamber pressure. The final configuration including the single Stra-Val pressure regulator, the high pressure ball valve, and the pneumatic actuator is shown in Figure 31.

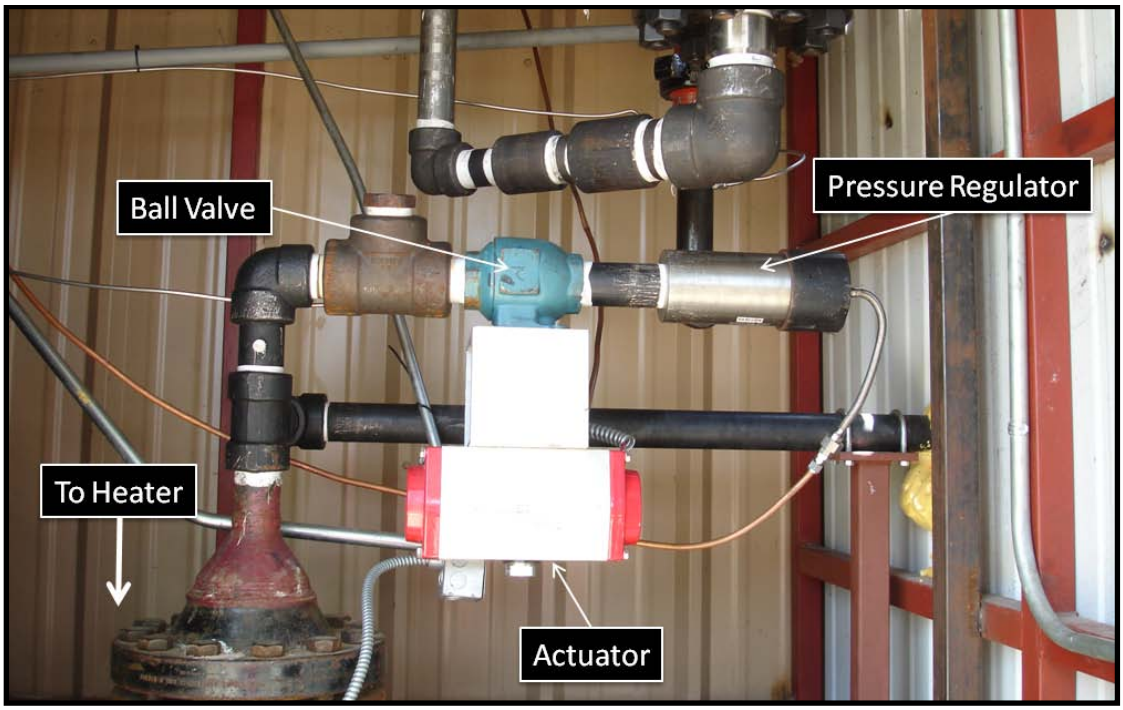

Figure 31: Heater Room Regulator, Ball Valve, and Actuator

When operating the wind tunnel facility, the incoming air must be heated to avoid liquefaction. To achieve this, the incoming air from the 5.08 cm (2 inch) pipeline was heated using a Chromalox 535 kW circulation heater model GCHI-108-535P-E4, shown in Figure 32.

Figure 32: Chromalox Heater

The maximum rated input pressure for the heater was 5.17 MPa (750 psig) at 533 K (500 °F). To ensure that the heater was never over-pressured, four safety relief valves were installed near the heater inlet. Two Stra-Val valves, model RVC0520T-N1642, and two Hydroseal valves, model 7HCN01/F5, were mounted in a manifold to enable sufficient mass flow and mounted outside of the heater room to minimize damage in the event of over-pressurization of the line. All of the valves had a set pressure of 5.17 MPa (750 psig). The safety relief valves are shown in Figure 33 below.

Figure 33: Heater Room Safety Relief Valves

After the air is regulated down to the desired pressure, it flows through the heater and into the laboratory through 7.62 cm (3 inch) carbon steel pipe. Inside the lab, the pipe is split between the various wind tunnel facilities. For the high-speed experimental wind tunnel test facility discussed in this dissertation, a 7.62 cm (3 inch) KTM EB12 full bore ball valve was installed to isolate the tunnel from the pipeline and is shown in Figure 34.

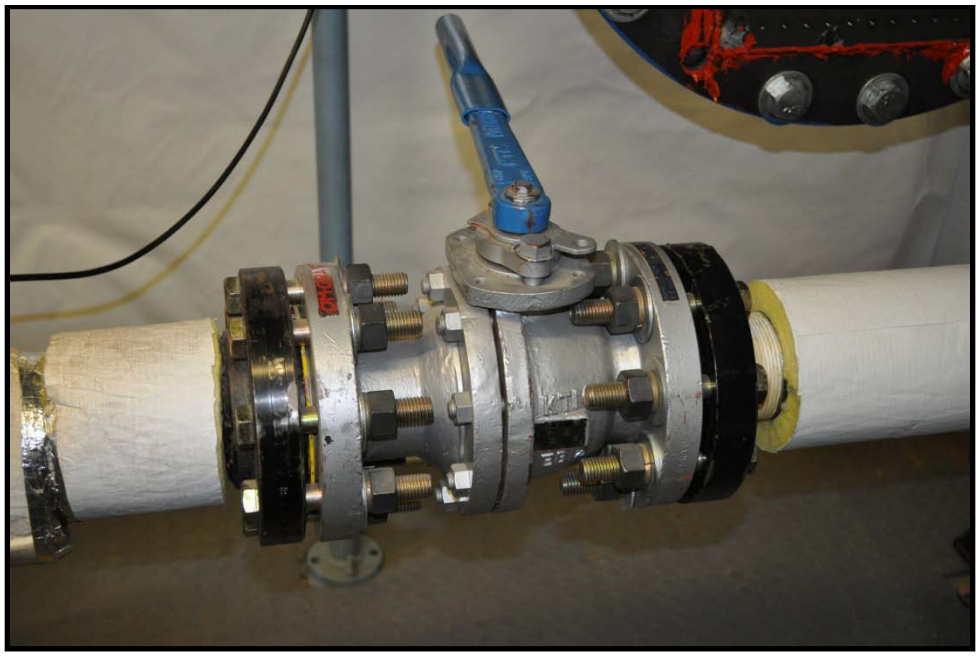

Figure 34: KTM 3" Ball Valve

This ball valve had a carbon steel body and a stainless steel stem and ball. It had an ASME Class 300 pressure rating and 7.62 cm (3 inch) 300# flanged connections. When the wind tunnel facility was not in use, this valve remained closed as an additional safety measure.

SHR Tunnel

Tunnel Operating Conditions

The wind tunnel facility used for the present study was also the focus of previous work described in Ekoto 2006 [52]. In order to run a Mach 5 wind tunnel facility, a pressure ratio (settling chamber total pressure / exit pressure) of approximately 40 is needed. Since the present facility exhausts to atmospheric pressure, a nominal running

stagnation pressure in the setting chamber was 2.55 MPa (370 psig). In order to avoid liquefaction and to prevent heat transfer from model surface, the incoming air was heated using the above described electric heater to approximately 375K (215 °F). The adiabatic wall temperature is found by the following relation between adiabatic wall, boundary layer edge, and stagnation temperatures:

$$r = \frac{T_{aw} - T_\infty}{T_0 - T_\infty} \tag{3.1}$$

Where r is the adiabatic recovery factor approximated as $r \approx \sqrt[3]{\Pr}$ and Pr is the turbulent Prandtl number. For air and Mach 4.88, $\Pr \approx 0.71$ and therefore $r \approx 0.892$. The boundary layer edge temperature can be calculated in terms of the stagnation temperature using the isentropic temperature relation.

$$\frac{T_o}{T_\infty} = 1 + \frac{\gamma - 1}{2} M^2 \tag{3.2}$$

Combining equations (3.1) and (3.2) gives the following relation for the adiabatic wall temperature in terms of the total temperature, the adiabatic recovery factor, and the freestream Mach number:

$$\frac{T_{aw}}{T_0} = \frac{1 + r\frac{(\gamma - 1)}{2} M^2}{1 + \frac{(\gamma - 1)}{2} M^2} \tag{3.3}$$

Due to the long tunnel run times, it was assumed that the boundary layer adiabatic wall temperature closely matched the actual wall temperature.

Settling Chamber

Smooth uniform flow was produced by passing the high pressure air a through a settling chamber. The external structure of the settling chamber is constructed of 35.56 cm (14 inch) SCH 160 pipe carbon steel pipe 91.44 cm (36 inch) long, 35.56 cm (14 inches) in diameter, and with a wall thickness of 3.57 cm (1.406 inches). It was designed for a maximum working pressure of 6.89 MPa (1000 psig). The settling chamber exterior is capped at each end by class 1500 blind and slip-on flanges. The inlet flange has a 7.62 cm (3 inch) NPT hole placed where it connects with the main air line, and the exit blind flange has a 7.62 cm x 7.62 cm (3 inch x 3 inch) square hole for the transition to the nozzle. Initially air was passed through a 12.7 cm (5 inch) diameter cylinder that was 12.7 cm (5 inches) long in order to quickly redistribute the mass of the air away from the chamber centerline. It had 56 evenly spaced holes that were 1.27 cm (0.5 inch) in diameter. The flow was straightened by passing it through a reverse cone that had 225 evenly spaced 0.48 cm (0.1875 inch) diameter holes. Finally the turbulence intensities were minimized by passing the flow through 3 wire mesh screens evenly spaced 3.81 cm (1.5 inches) apart. The mesh was made of woven stainless steel wire with a diameter of 88.9 μm (0.0035 inches) with 28 x 28 strands per square centimeter (71 x 71 strands per square inch). The open area of the mesh was 55%. The exit was constructed of 4 pieces of pipe that had been halved along their centerline, cut at 45 degree angles, and joined together to form a square. The outer diameter of the pipe was 6.02 cm (2.37 inches), the dimension of the inner square was 7.62 cm x 7.62 cm (3 inches x 3 inches), and the dimension of the outer square was 16.19 cm x 16.19 cm

(6.375 inches x 6.375 inches). It was designed so that the inviscid core of the pipe flow would be allowed to pass through, so that boundary layer growth doesn't begin until the inlet of the nozzle.

Mach 5 Nozzle Adapter

As described in detail in the previous section, the settling chamber exit port had a cross section of 7.62 cm x 7.62 cm (3 inches x 3 inches) and was sized to fit an existing Mach 3 nozzle. However, for the present study, an existing Mach 5 nozzle was used (described below). The inlet cross section of the Mach 5 nozzle was 3.81 cm x 7.62 cm (1.5 inches x 3 inches). Because of this, a nozzle adapter was designed to allow for a smooth transition from the settling chamber exit dimensions to the Mach 5 nozzle inlet dimensions. The overall length of the adapter was 10.16 cm (4 inches) and was constructed out of 1.27 cm (0.5 inch) carbon steel plate. A SolidWorks drawing of the adapter section with a side wall removed is shown in Figure 35.

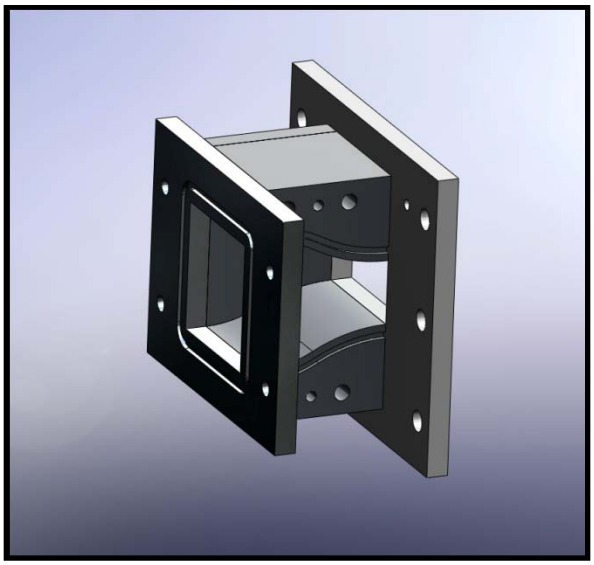

Figure 35: SolidWorks Drawing of Mach 5 Nozzle Adapter

The nozzle adapter was originally designed to be bolted together with O-rings used for sealing. However, it was observed that the seams leaked profusely and could not be sealed. To solve this, the entire adapter was simply welded together. A picture of the final Mach 5 nozzle adapter installed in the wind tunnel facility is shown in Figure 36.

Nozzle

The nozzle used for the present study was a Mach 4.89 hypersonic nozzle with exit cross-sectional dimensions of 7.62 cm x 7.62 cm (3 inches x 3 inches). The nozzle was designed and constructed as part of a previous study using the standard method of characteristics for supersonic flow[50]. The nozzle was machined out of Type 347 stainless steel and bolted together. It was also shown that the nozzle exhibits good flow

field uniformity at the exit. A schematic of the nozzle contour is provided below in Figure 36 and the coordinates are provided in tabular form in Table 1.

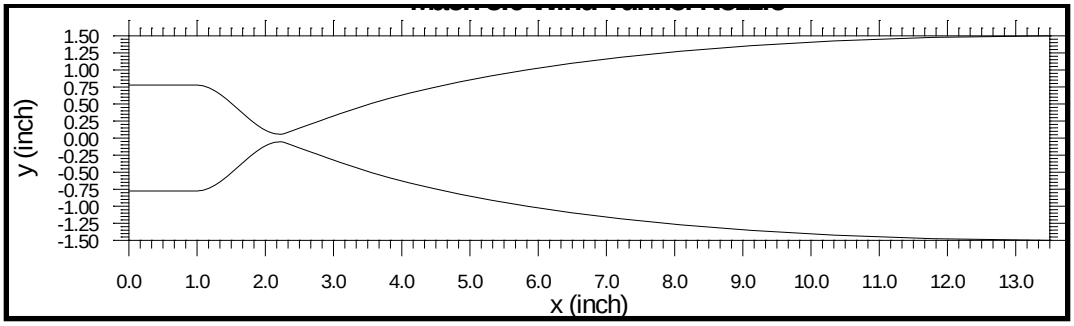

Figure 36: Mach 5 Nozzle Contour

Table 1: Mach 5 Nozzle Coordinates

X (inch)	Y_{top} (inch)	Y_{bot} (inch)	X (inch)	Y_{top} (inch)	Y_{bot} (inch)
0.0000	-0.7770	0.7770	2.4565	-0.1295	0.1295
1.0000	-0.7770	0.7770	2.4920	-0.1425	0.1425
1.0870	-0.7665	0.7665	2.5310	-0.1565	0.1565
1.1735	-0.7370	0.7370	2.5755	-0.1725	0.1725
1.2605	-0.6920	0.6920	2.6255	-0.1900	0.1900
1.3470	-0.6340	0.6340	2.6825	-0.2105	0.2105
1.4340	-0.5665	0.5665	2.7480	-0.2340	0.2340
1.5205	-0.4925	0.4925	2.8245	-0.2615	0.2615
1.6075	-0.4160	0.4160	2.9145	-0.2935	0.2935
1.6945	-0.3390	0.3390	3.0200	-0.3315	0.3315
1.7810	-0.2650	0.2650	3.0750	-0.3510	0.3510
1.8680	-0.1975	0.1975	3.5585	-0.5085	0.5085
1.9545	-0.1395	0.1395	3.8190	-0.5825	0.5825
2.0415	-0.0945	0.0945	4.1155	-0.6590	0.6590
2.1280	-0.0650	0.0650	4.4575	-0.7395	0.7395
2.2150	-0.0545	0.0545	4.8530	-0.8245	0.8245
2.2255	-0.0550	0.0550	5.3140	-0.9120	0.9120
2.2330	-0.0555	0.0555	5.8515	-1.0025	1.0025
2.2410	-0.0565	0.0565	6.4810	-1.0945	1.0945
2.2495	-0.0580	0.0580	7.2200	-1.1850	1.1850
2.2575	-0.0595	0.0595	8.0900	-1.2740	1.2740
2.2660	-0.0620	0.0620	9.1200	-1.3555	1.3555
2.2745	-0.0645	0.0645	10.335	-1.4250	1.4250
2.3390	-0.0875	0.0875	11.780	-1.4765	1.4765
2.3945	-0.1075	0.1075	13.500	-1.5000	1.5000

The nozzle was bolted to seed injection block on the upstream side and to the test section on the downstream side. A picture showing the installed Mach 5 nozzle is shown in Figure 37.

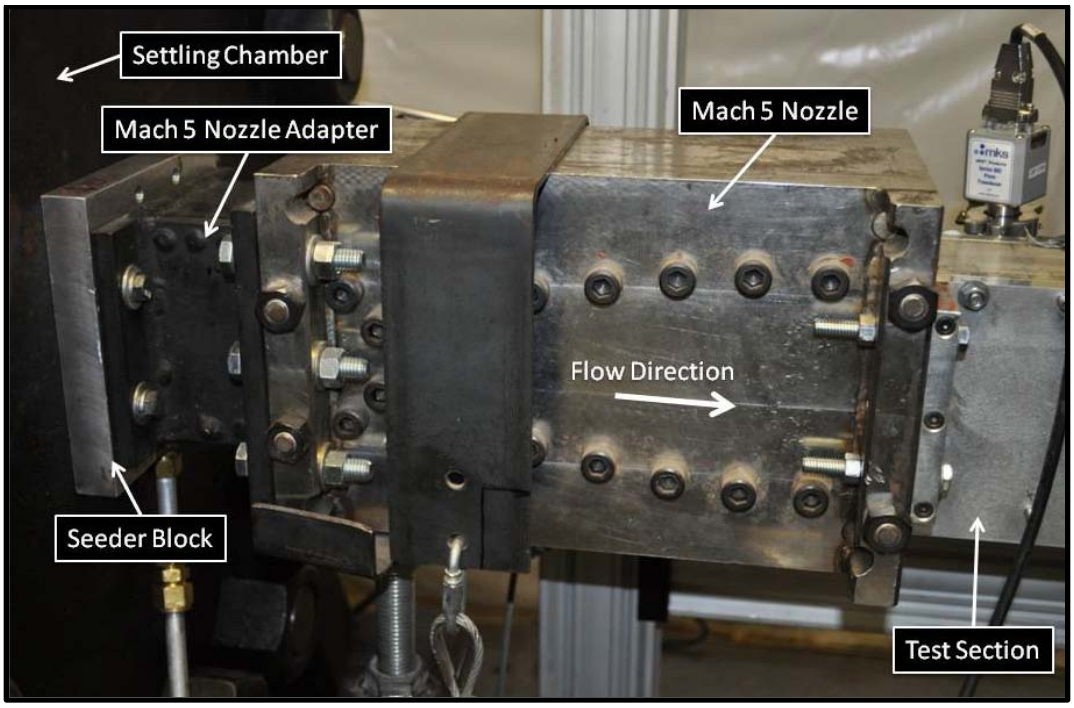

Figure 37: Installed Mach 5 Nozzle

Test Section

The test section was designed so that PIV measurements could be accurately and efficiently obtained. The sidewalls were constructed of aluminum and were 71.12 cm (28.0 inches) long, 14.61 cm (5.75 inches) wide and 1.27 cm (0.5 inches) thick. Symmetric mounting brackets were used to connect the sidewall to the nozzle exit and diffuser inlet. A SolidWorks drawing of front view of the test section assembly is shown in Figure 38.

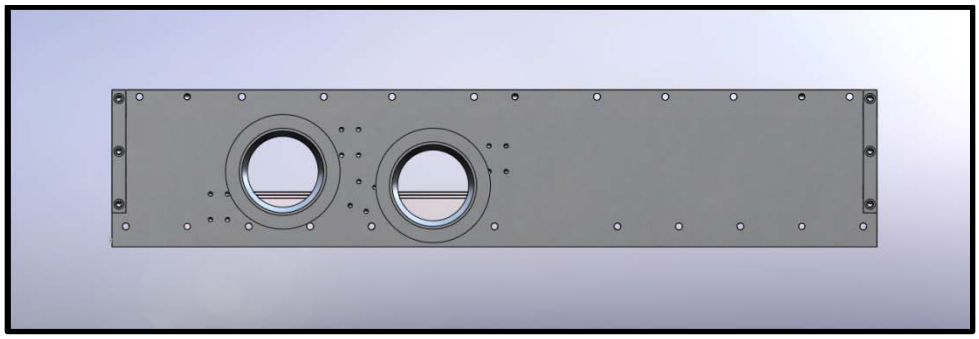

Figure 38: Test Section Assembly - Front View

To allow optical access into the test section, two large holes were machined into the front and back walls. The diameters of the holes were 9.65 cm (3.8 inches) and they were staggered to allow for better access to pressure gradient models. The upstream window location was 15.88 cm (6.25 inches) from the nozzle exit and 7.62 cm (3.0 inches) from the outer surface of the test section. The downstream window location was 29.85 cm (11.75 inches) from the nozzle exit and 8.89 cm (3.5 inches) from the outer surface of the test section. A dimensioned drawing of the test section front wall is given in Figure 39.

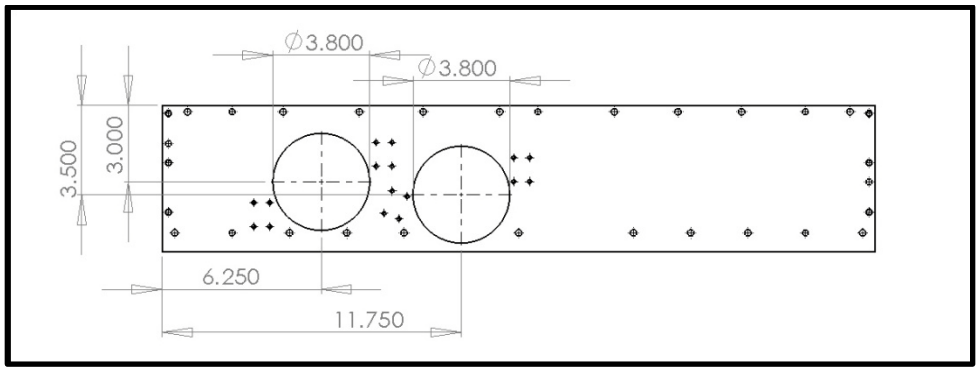

Figure 39: Test Section Front Wall Dimensioned Drawing

In order to mount the windows to the side walls, a window frames were designed and machined from aluminum. The window frames slide into the 9.652 cm (3.80 inch) diameter holes in the front and back test section walls and are sealed by an O-ring. Fused silica optical windows with a diameter of 7.62 cm (3 inches) were mounted into the window frames with the inner surface flush. This allowed the windows to seamlessly fit with the inner surface of the test section walls. A picture of one of the fused silica windows mounted in a window frame is shown in Figure 40.

Figure 40: Fused Silica Window in Window Frame

The top plate of the test section was fabricated out of 1.91 cm (0.75 inch) aluminum with overall dimensions of 71.12 cm x 7.62 cm (28.0 inches x 3.0 inches). An O-ring groove was machined along the edges to allow the test section to seal properly. In order to pass the laser into the test section for PIV measurements, two holes were machined into the top plate to allow for windows. The upstream hole was located at

15.88 cm (6.25 inches) from the nozzle exit and the downstream hole was located 29.85 cm (11.75 inches) from the nozzle exit. The holes were beveled to allow the windows to be flush mounted and had a thru hole diameter of 4.06 cm (1.6 inches). Two 5.08 cm (2 inch) beveled fused windows were glued into place to guarantee the inner surface was as smooth as possible. A SolidWorks drawing of the top plate is shown in Figure 41 and a dimensioned drawing is given in Figure 42.

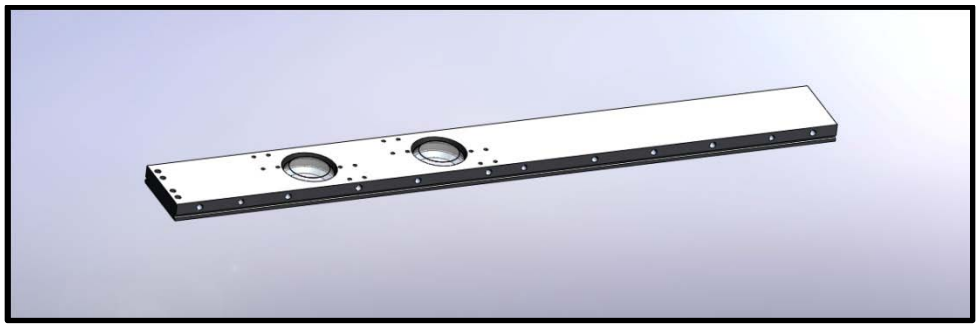

Figure 41: Test Section Top Plate

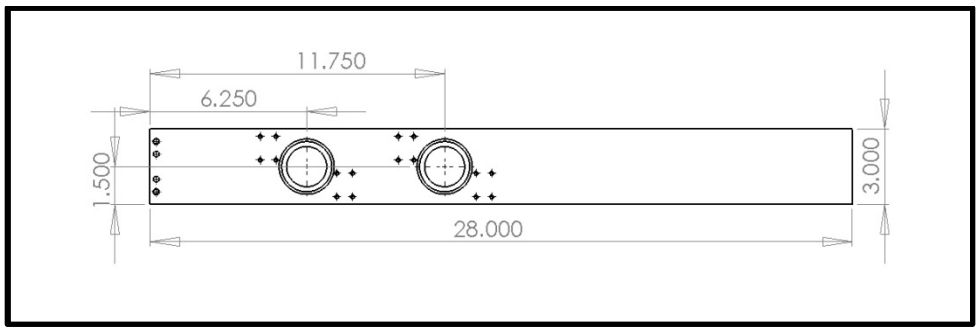

Figure 42: Test Section Top Plate Dimensioned Drawing

This test section designed allowed the floor models to easily be swapped with minimal disassembly. A SolidWorks drawing of the complete test section assembly is shown in Figure 43 and a picture of the installed test section is given in Figure 44.

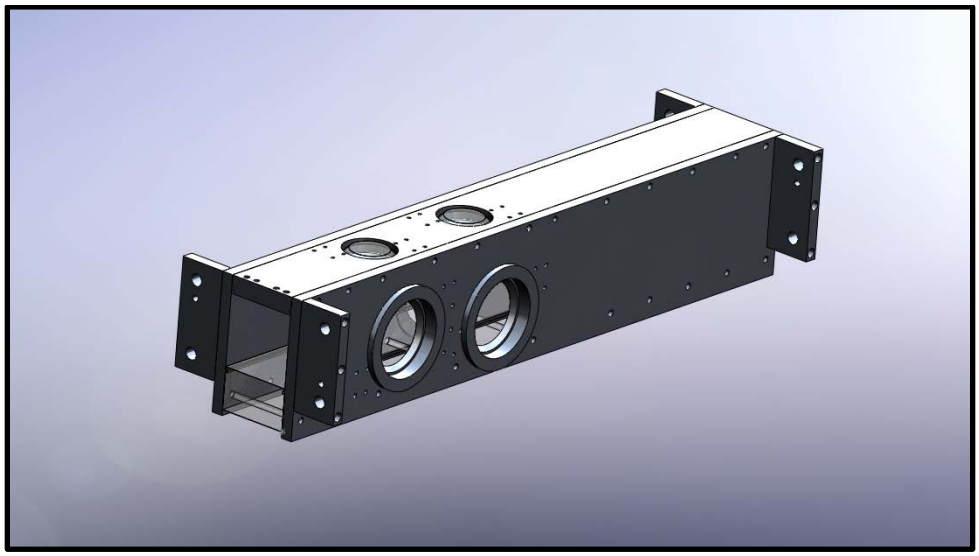

Figure 43: Test Section Complete Assembly

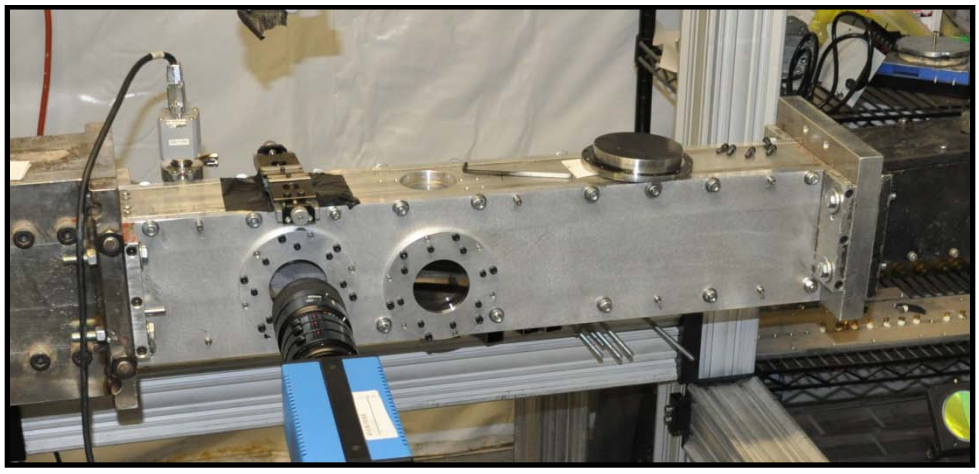

Figure 44: Installed Test Section

Diffuser

A variable throat diffuser was used to reduce the required stagnation pressure required for running the wind tunnel facility. The inlet height of the diffuser is 7.62 cm (3 inches) and the exit height increases to 13.97 cm (5.5 inches). The diffuser is shown disassembled in Figure 45 and installed in Figure 46 below.

Figure 45: Disassembled Diffuser

Figure 46: Installed Diffuser

Wind Tunnel Models

The wind tunnel models for the present study were designed to incorporate the effects of a curvature driven favorable pressure gradient on a Mach 5 hypersonic turbulent boundary layer.

A flat plate zero pressure gradient (ZPG) model, weak pressure gradient (WPG) model, and strong pressure gradient (SPG) model were created using the following third order polynomial: $y = A(x - x_1)^3 + B(x - x_1)^2$, where x_1 is the axial location where the curvature begins. The geometry boundary conditions were that the slope at the start and end points were zero, while the curvature began at 0 and ended and -1.91 cm in the y-direction. A sketch of the WPG and SPG model geometries are shown in Figure 47 while Table 2 lists the model geometry parameters including the beginning and ending axial locations and the polynomial coefficients for the WPG and SPG models. The pressure gradient models used for the present study are the same models described in Ekoto 2006 in detail[51].

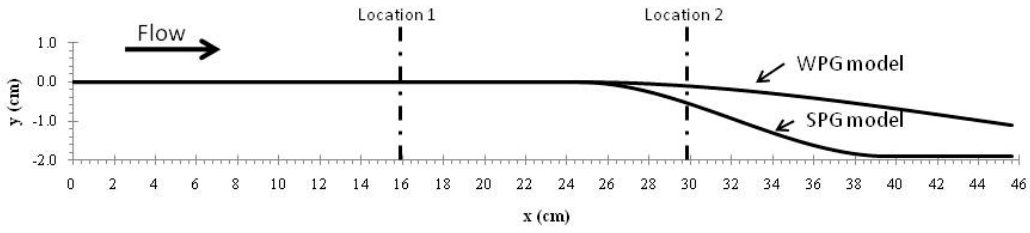

Figure 47: Pressure Gradient Model Wall Geometry

Table 2: Model Geometry and Pressure Gradient Parameters

	x_1(cm)	x_2(cm)	A	B
WPG	24.54	63.54	6.42×10^{-5}	-3.757×10^{-3}
SPG	24.54	39.64	1.107×10^{-3}	-2.507×10^{-2}

The pressure gradient strength parameter described in Chapter II was determined for two favorable pressure gradient models used in the present study. A single downstream surface pressure tap was utilized for the SPG model while the β parameter for the WPG model was determined using estimated values. The values are presented in Table 3.

Table 3: Pressure Gradient Strength Parameters

Model	β
WPG	-0.50
SPG	-1.09

CHAPTER IV

EXPERIMENTAL TECHNIQUES

Particle Image Velocimetry

Particle image velocimetry (PIV) is an extremely powerful non-intrusive diagnostic tool used to measure instantaneous velocity fields. Acquiring PIV data in the high-speed wind tunnel was the main focus of this study. Two-dimensional PIV was utilized because the flow field under observation did not necessitate the increased complication of stereoscopic PIV to resolve the third velocity vector. The basic process involves the use of a double-pulsed laser light source to illuminate seed particles in the flow. Scattered light from these particles is collected and recorded, usually on a digital camera equipped with a charge-coupled device (CCD) array. A correlation process is then carried out on each image pair. A small area (interrogation window) of the primary image is analyzed by computing an intensity map. Another interrogation window then sweeps the second image, and intensity peaks are matched to determine the displacement of the particles from the first to the second image. With the known displacement and the time between laser pulses, velocities can then be calculated. Subtracting averaged velocity from the instantaneous velocity resulted in the instantaneous fluctuating velocity. A large number of image pairs are typically recorded to reach statistical convergence in the fluctuating velocities. A detailed description of the application of particle image velocimetry on the high-speed wind tunnel is discussed below.

Hardware and Operation

The PIV measurements were taken using a dual port/dual head variable frequency New-Wave Solo 120XT PIV laser system. The system provided a stable, high-energy light pulse at 532 nm. The maximum energy output was 120 mJ per head with a pulse width of 4 ns (± 1 ns). The two pulses from each head (laser-one and laser-two) were originally combined by introducing a half-wave plate made of crystal quartz in the path of laser-one, which induced perpendicular polarization. Each pulse was then passed through a high-energy polarizing cube beam-splitter which passed the perpendicularly polarized pulse from laser-one and turned the unmodified pulse from laser-two, combining the beam paths of each laser pulse. The beam combination optics setup is shown in Figure 48. This setup worked well but the polarized laser beam produced much higher scatter than the non-polarized beam. For the present study where the measurements very close to the wall are critical, this was not acceptable.

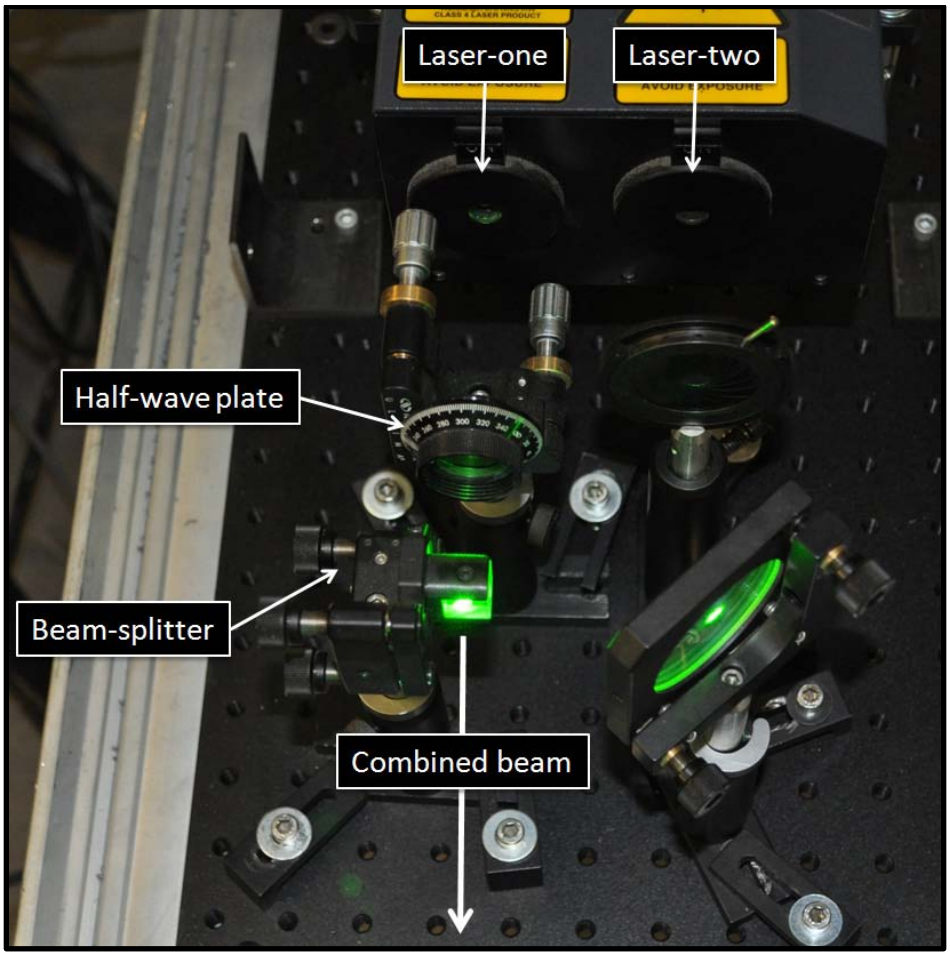

Figure 48: Original PIV Beam Combination Optics

In order to eliminate the different laser polarizations, a new set of beam combination optics were installed. The half-wave plate and the polarizing beam-splitting cube were replaced with two 50-50 beam splitters. These optics pass 50 percent of the laser power and reflect 50 percent. By arranging two optics at the outlets of the two lasers, they can be used to align the laser beams into a single path as seen in Figure 49. This setup eliminated the different beam polarizations; however, it does waste half of the laser power. For the present study, this available laser power was sufficient to

produce good results. The lasers and combination optics were mounted to small optics breadboard adjacent to the wind tunnel facility.

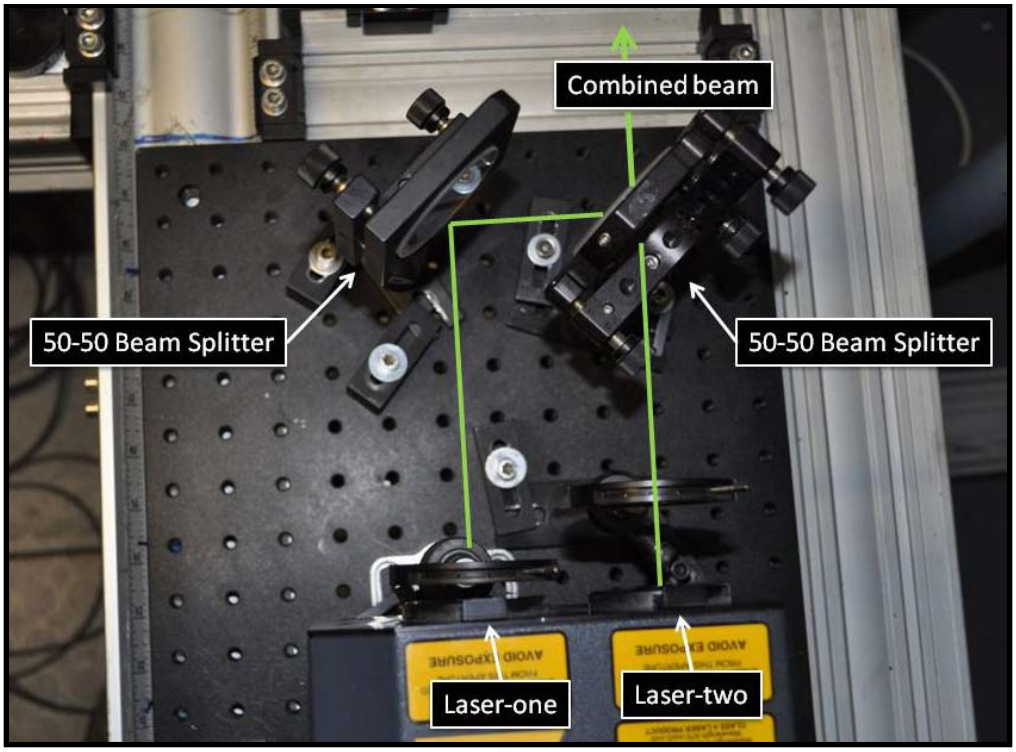

Figure 49: Modified PIV Beam Combination Optics

Note that only laser-one had adjustable power output and it was optimal for the intensity of each image to be approximately equal. It was possible to modify the power output by adjusting the timing between the flash-lamp and q-switch. The combination optics were rotated slightly with respect to the exit beam axes. This was done so that reflected light did not re-enter the laser system and harm any internal optics or other hardware. The irises located at the exit ports of the lasers were used as both an

alignment tool (to be explained later) as well as a beam block for the reflected light. The reflections can be seen below in Figure 50.

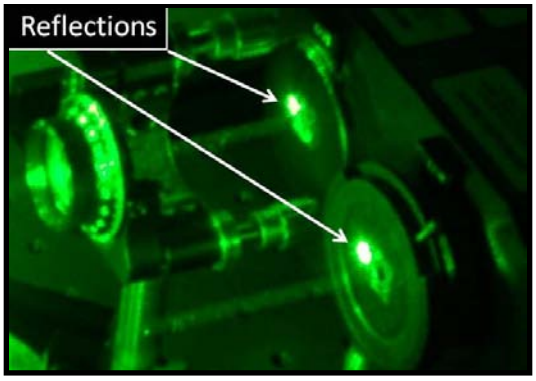

Figure 50: PIV Beam Combination Optics Reflections

The most important step in the operation of the New-Wave Solo 120XT PIV laser system is optical setup and laser alignment. The dual-head configuration requires diligence in alignment of laser-one and laser-two to ensure that the sheets are both parallel and coincident at the measurement location. First, it is important to be certain that laser-one and laser-two are exiting the exit ports parallel to one another. This was checked by measuring the distance between the two beams at the exit ports, and then measuring that distance again at a location relatively far away (across the room). If they are not parallel, the internal optic (last mirror before the laser exits) of laser-two should be modified until the two lasers are parallel. The next step was to make certain that all optics were square when initially setting up the system. The optics will also change as they absorb energy from the laser, so it is advisable to allow the optical system to reach an equilibrium temperature before carrying out the final alignment step. This was done

by running the system on high power for 10 minutes. The final step was to ensure sheet alignment by carrying out near-field/far-field calibration. The system was operated in internal mode at a rep-rate of two to three hertz. Slowing the rep-rate allows the user to isolate the beams and visually amplifies any misalignment (jitter) between the two lasers. The beams were compared at a location just after they are combined through the combination optics. The orientations of these optics were then modified until the two lasers were exactly aligned. The irises near the exit port of the lasers were then contracted to be able to better distinguish between each laser. Once the beams were aligned at the near-field location, the beams were then compared at the far-field location. The farther away the far-field location (within reason), the more accurate the alignment will be. The near-field/far-field alignment process was repeated until no changes were required.

Experimental Setup

For the experimental facility, the PIV laser system and optics were mounted on a frame constructed of XT95 rail sections connected using XT95 sliders. A platform shown in Figure 51, was created using the XT95 rail approximately 60.96 cm (24 inches) above the floor on which the small laser breadboard was mounted.

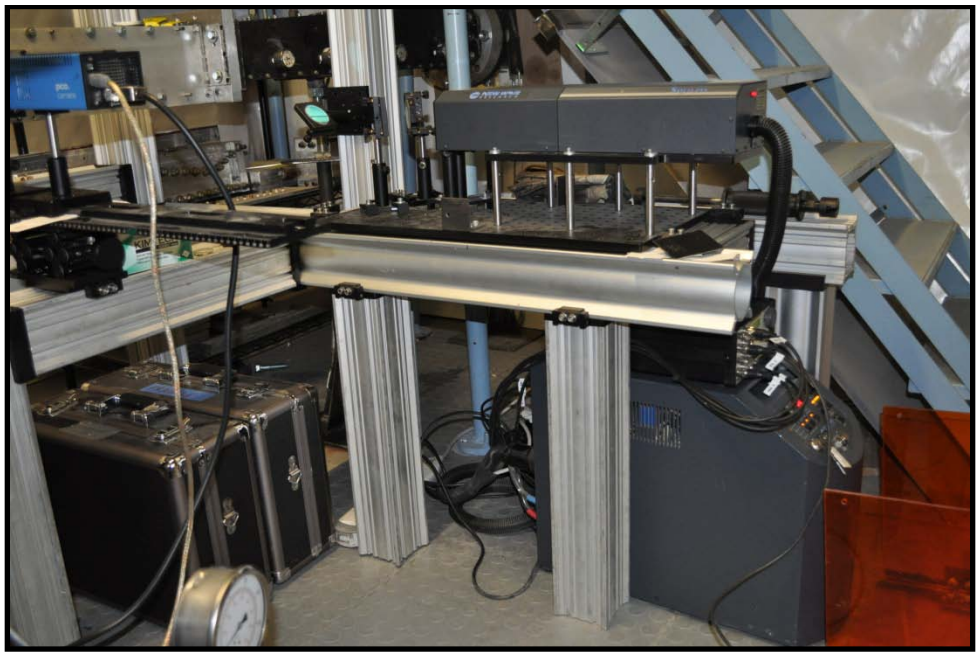

Figure 51: PIV Laser Frame Platform

The combined beam was directed to the test section through a series of 532 nm mirrors (5.08 cm (2 inch), 45°) that were mounted to a frame system. Once the beam was above the tunnel, it was directed over the test section using a series of optics mounted to a PRL-24 dovetail rail that was mounted on a XT95 slider riding on an upper horizontal XT95 rail section. Each optic was mounted in a post holder attached to a PRC-1 slider mounted on the PRL-24 section. A convex spherical lens (500 mm focal length) was used to control the location of the beam waist, and a convex cylindrical lens (150 mm focal length) was used to form the laser sheet. The rail with the sheet forming optics can be seen in Figure 52.

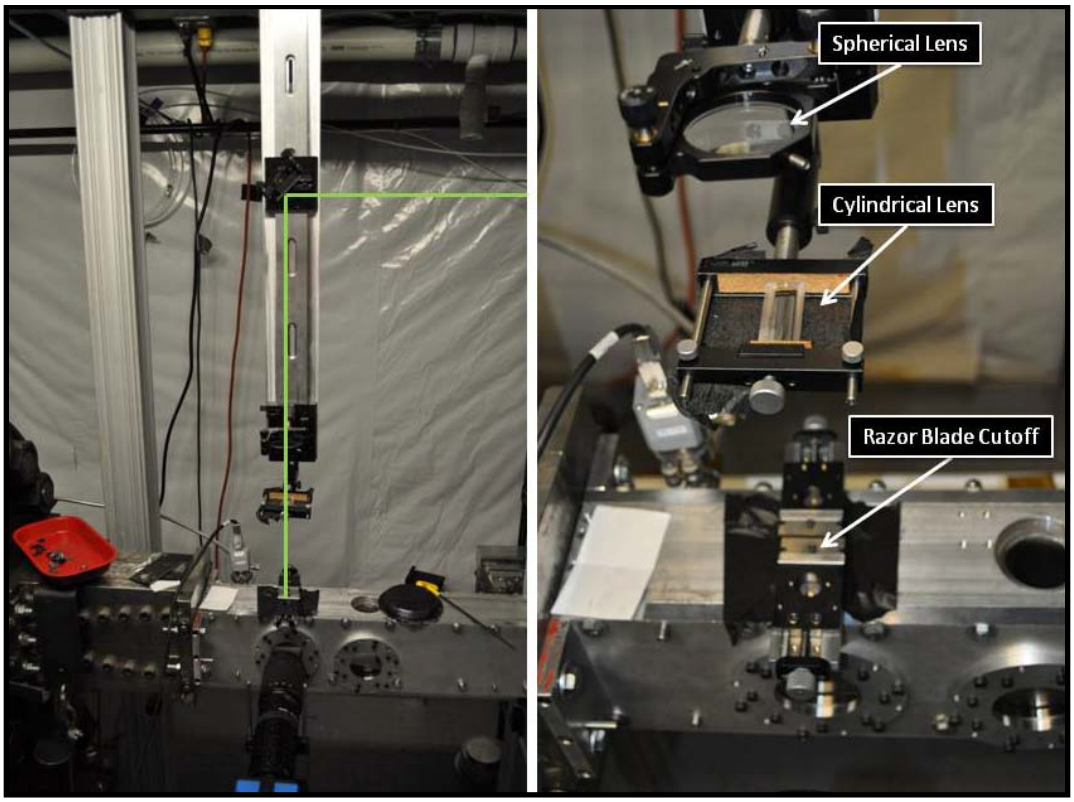

Figure 52: High-Speed PIV Optics Rail

To produce a laser sheet that was sufficiently sized for accurate measurements, the cylindrical lens was positioned to create a sheet that was approximate 50.8 mm (2 inches) wide and 2.54 mm (0.10 inches) thick at the top of the test section. The focal point was adjusted using the spherical lens position. Two razor blades were mounted to linear translation stages and bolted above the top test section window. The blades were mounted parallel to each other and were moved towards each other to clip the outer part of the laser sheet. This allowed the effective sheet within the measurement location to be well controlled and very uniform. A picture of the razor blade cutoff arrangement is shown in Figure 53.

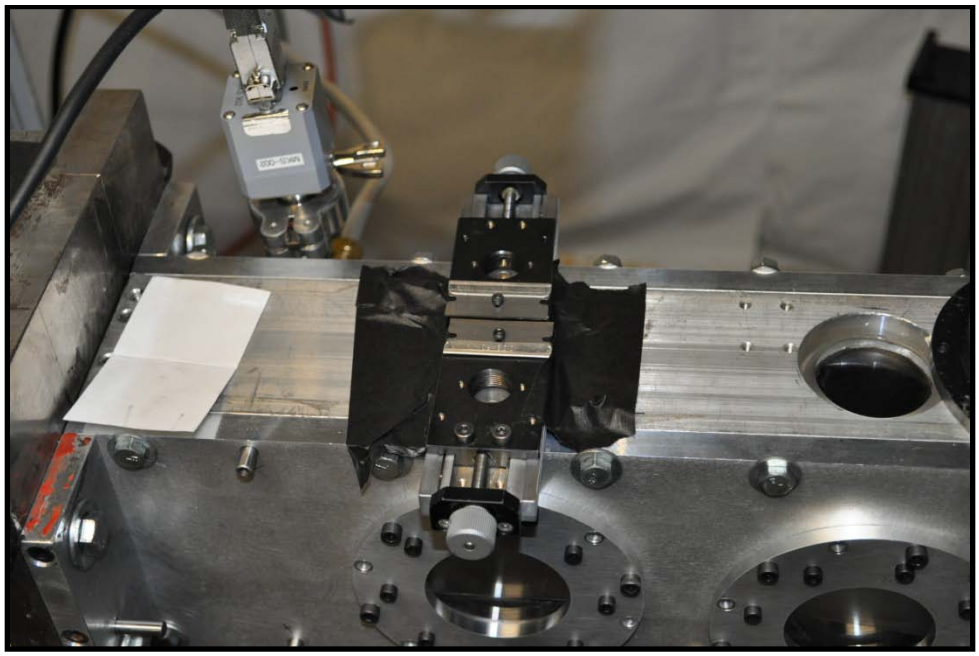

Figure 53: Razor Blade Cutoff

Since the wind tunnel models were made of transparent Plexiglas, the reflections at the wall were very small. This allowed for accurate measurements close to the lower surface. An example of a typical raw PIV image is shown in Figure 54.

Figure 54: Example PIV Image

Dioctyl phthalate (DOP) was used for the seed particle compound in the high-speed experimental facility. The liquid was atomized using a TSI model 9306 six-jet atomizer which each created DOP particles with an average diameter of 250 nm[52]. The atomizer was housed inside of a welded steel box that allowed the entire seeder to be pressurized above the tunnel settling chamber pressure. The seeder was connected to the settling chamber using 1.27 cm (0.5 inch) aluminum tubing that was connected to seeding strut block. The seeder and the seeder connection can be seen in Figure 55 and Figure 56.

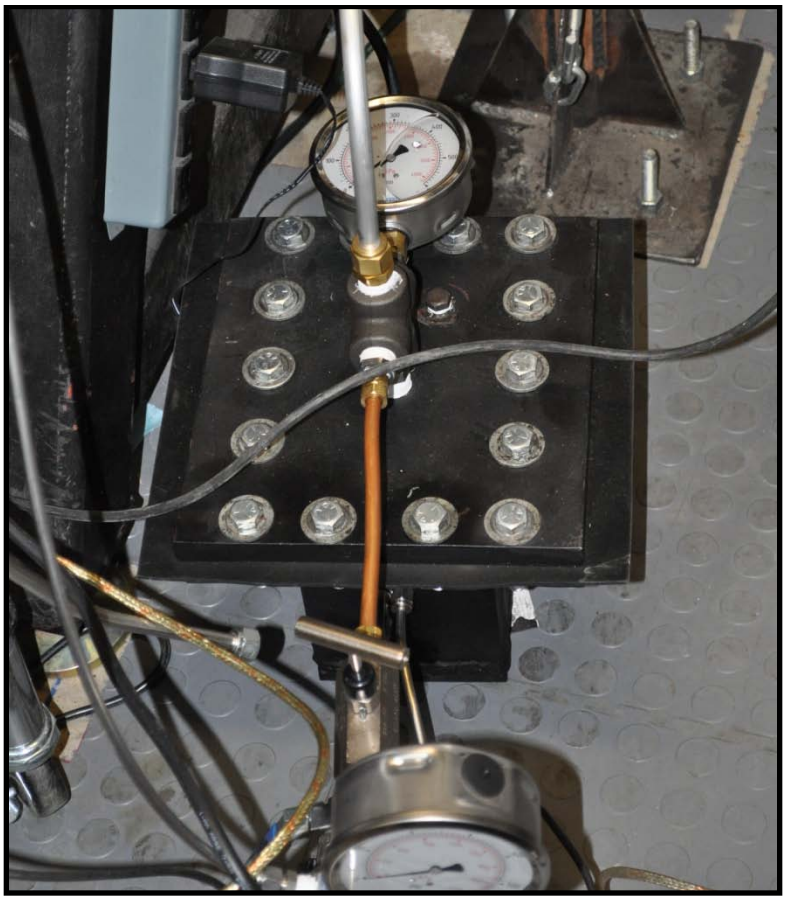

Figure 55: High Pressure PIV Seeder

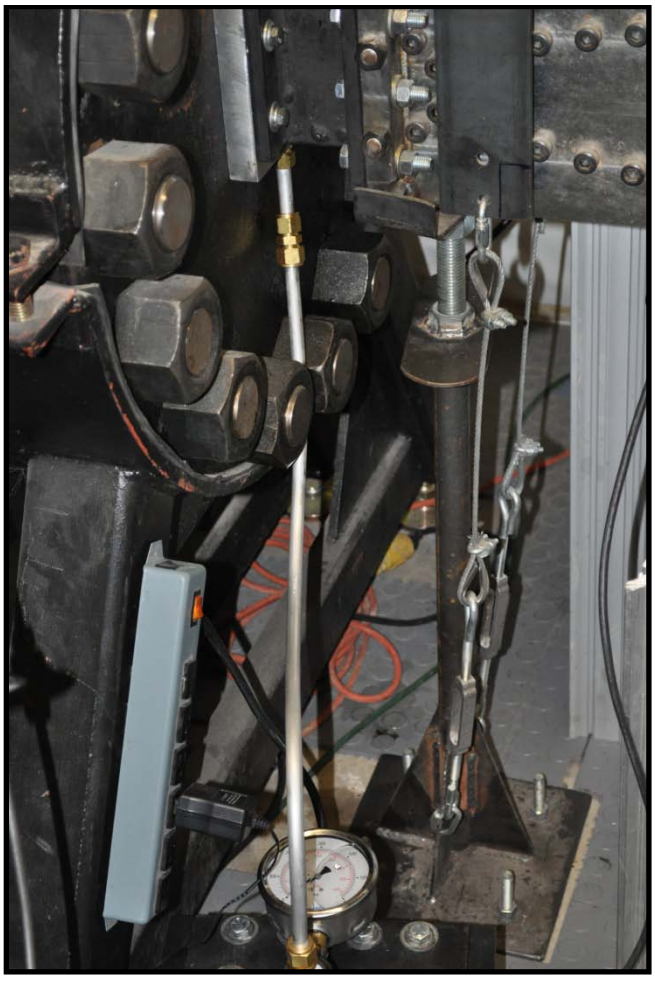

Figure 56: PIV Seeder Connection Tubing

The seed particles were injected directly into the bulk flow just upwind of the nozzle throat. The system consisted of a 1.27 cm (0.5 inch) aluminum tube partially flattened to increase aerodynamic efficiency. This tube was slotted near the bottom wall to produce as much seed near the focus region as possible. The tunnel seed injector is shown in Figure 57 and Figure 58.

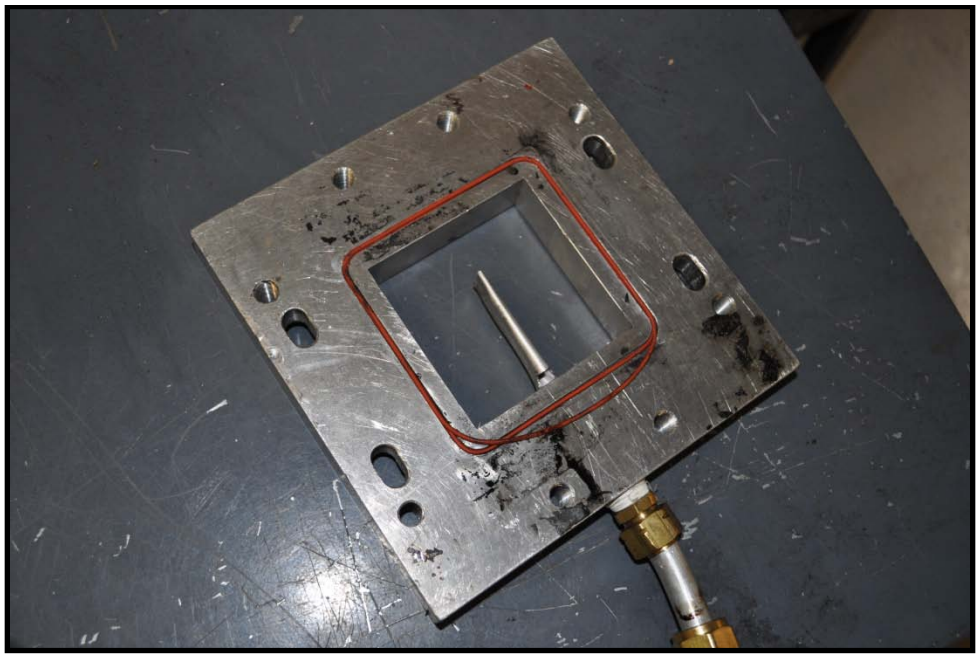

Figure 57: Slotted Seed Injection Sting

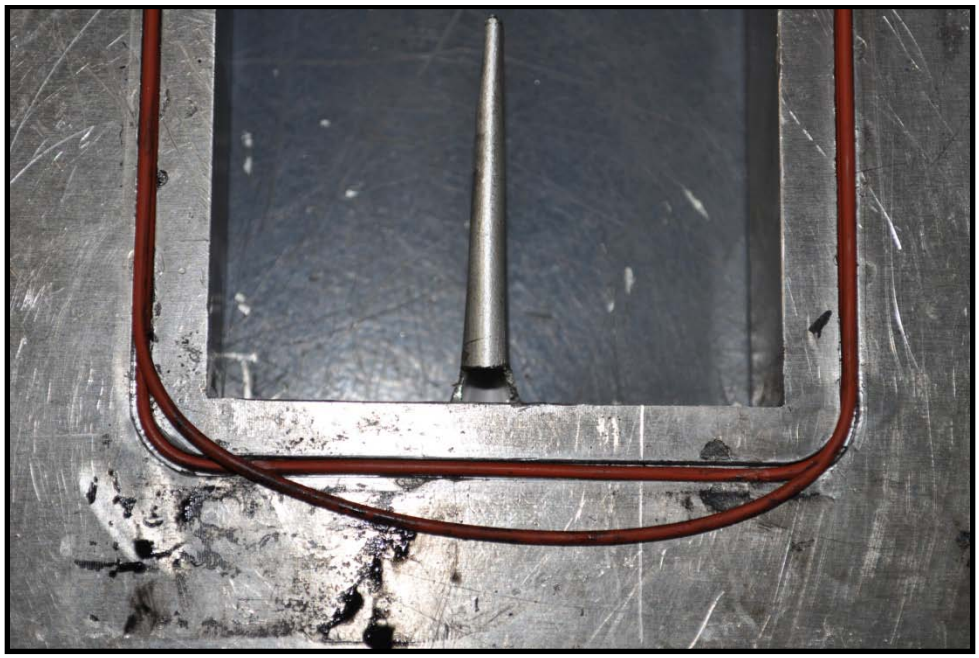

Figure 58: Slotted Seed Injection Sting (Zoom)

To record the Mie scattering from the particles, a Cooke Corporation PCO 1600 CCD camera system was mounted with a Nikon AF Micro-NIKKOR 60mm f/2.8D lens. A f-stop of 5.6 was optimal to maximize signal as well as depth of field. The camera was mounted on a post which was bolted to a Newport PRC-3 rail slider mounted to a PRL-24 dovetail rail section. The rail section was mounted to an elevating scissor jack which allowed the camera to be raised and lowered to the desired measurement location. The jack was mounted to a XT95 rail slider on a horizontal section of XT95 rail. This configuration allowed the camera to be rotated as well as translated along all three coordinate axes. The camera system can be seen below in Figure 59.

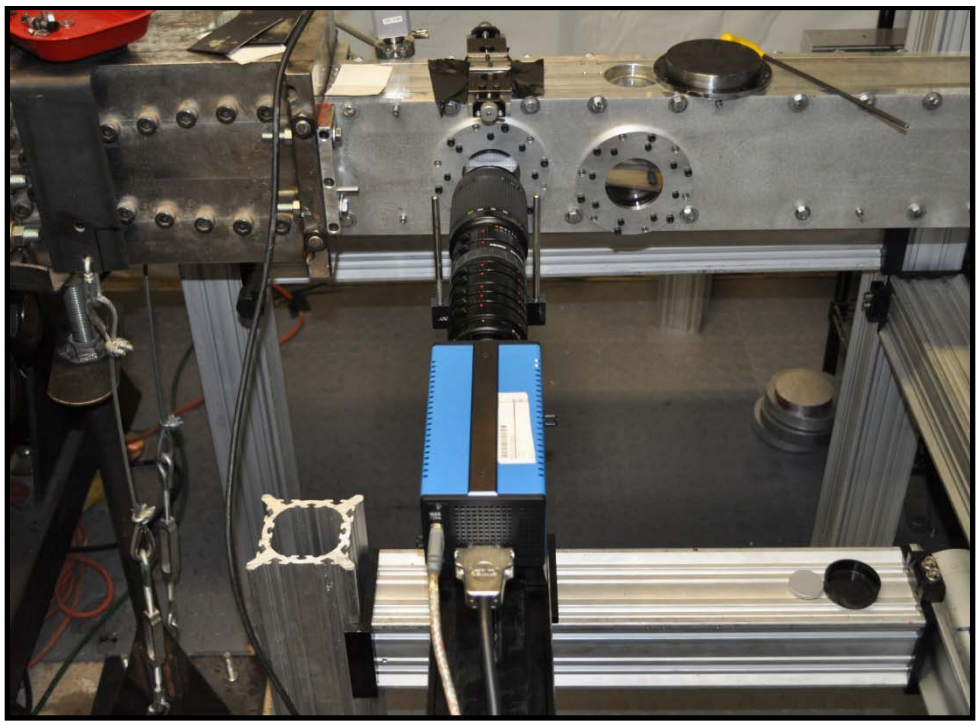

Figure 59: Cooke Camera System

The camera was controlled using Cooke CamWare software (v. 2.19, build 0141) and screen captures of all settings used in CamWare are located in Appendix A. The most important setting is the exposure time which must be set just prior to the second laser pulse. The camera system operates by saving the images to onboard RAM as they are recorded. Therefore, recording times were limited by onboard memory capacity (2 GB) and recording frequency. A data acquisition rate of 10 Hz was used. Therefore a data acquisition sequence took 35 seconds to acquire, followed by transfer of images to the computer hard-drive which took approximately 2 minutes.

Physical scale of the images was determined using a dot card made of aluminum plate with (0.16 cm (0.0625 inch) diameter holes drilled every 0.32 cm (0.125 inches). The overall dimensions were 10.16 cm x 2.54 cm x 0.95 cm (4 inches x 1.0 inches x 0.375 inches). The dot card was positioned in the laser sheet after each run and an image was taken of the illuminated dot card. In the post processing, the dot card image was used to determine the pixels/mm resolution of each image. The dot card is shown in Figure 60 and Figure 61. The camera resolution for each data set was different. In order to provide a concise location for the various resolutions obtained in the present study, Table 4 is shown below.

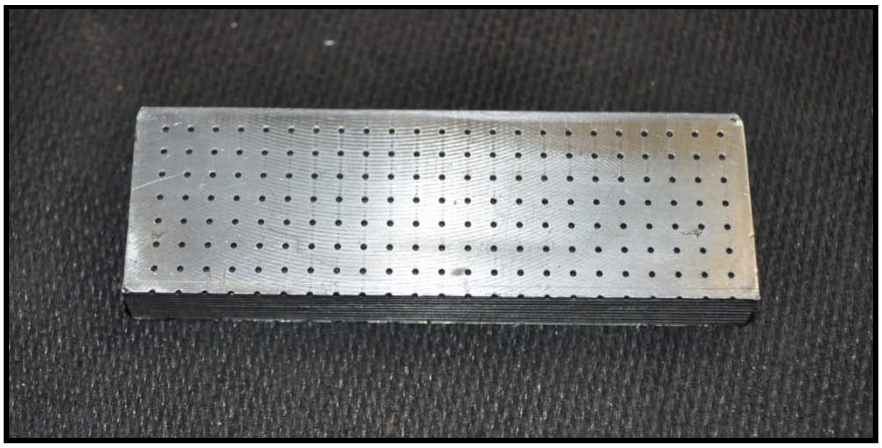

Figure 60: Aluminum Dot Card

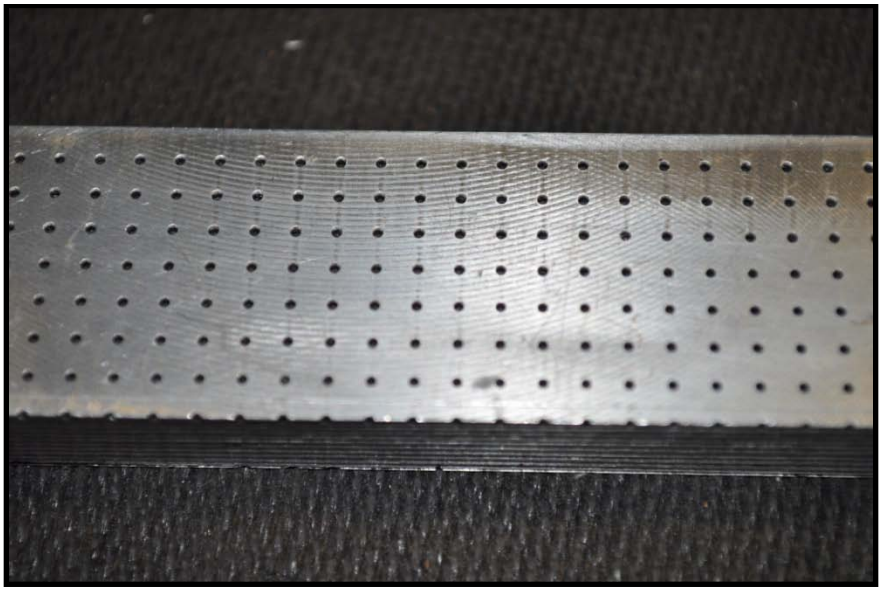

Figure 61: Aluminum Dot Card (Close Up)

Table 4: Data Set Camera Resolutions

Data Set	Resolution (pixels / mm)	Field of View (W x H) (mm)
Spanwise survey at 1st location	80.9	19.8 x 14.8
ZPG Flow Visualization at 1st location	78.4	20.4 x 15.3
WPG Flow Visualization at 2nd Location	46.0	34.8 x 26.1
SPG Flow Visualization at 2nd Location	46.0	34.8 x 26.1
ZPG (Wide View) at 1st location	78.4	20.4 x 15.3
ZPG (Zoom View) at 1st location	120.8	13.2 x 9.9
WPG at 2nd Location	65.1	24.6 x 18.4
SPG at 2nd Location	65.2	25.5 x 18.4

System Timing

The timing of each laser pulse and the camera was driven by a Quantum Composers, Inc. Model 9618 Digital Delay-Pulse Generator, shown in Figure 62. Each laser pulse was triggered by two separate signal pulses. The first pulse signals the flash-lamp to fire which produces the initial laser pulse. This light is then amplified internally until the q-switch signal is received, releasing the final laser pulse to the exit port. The power of the final laser pulse when plotted versus internal delay time follows a bell-curve. Once the lasers were properly warmed up, a power meter was used to tweak this internal delay to achieve maximum power output. This delay for each laser was set to 195.5 μs. The channels were allocated to system signals as shown in

Table 5 and the settings for each channel of the signal generator are listed below in Table 6.

Figure 62: Pulse Generator

Table 5: Pulse Generation Channel Allocation

4Channel	Signal
1	-
2	Flash-lamp 1 (FL 1)
3	Flash-lamp 2 (FL 2)
4	Q-Switch 1 (QS 1)
5	Q-Switch 2 (QS 2)
6	Cooke Camera Trigger
7	*not enabled*
8	*not enabled*

Table 6: Pulse Generator Settings

Settings									
Ch	*Sync*	*Delay (μs)*	*Width (μs)*	*Mode*	*Wait*	*Polarity*	*Amplitude (V)*	*MUX*	*Gate*
T1	T0	0.5	120	Normal	0 Pulses	Active High	5.00	T8-0000 0001-T1	Disabled
T2	T0	0	120	Normal	0 Pulses	Active High	5.00	T8-0000 0010-T1	Disabled
T3	T1	0	120	Normal	0 Pulses	Active High	5.00	T8-0000 0100-T1	Disabled
T4	T2	195.5	120	Normal	0 Pulses	Active High	5.00	T8-0000 1000-T1	Disabled
T5	T3	195.5	120	Normal	0 Pulses	Active High	5.00	T8-0001 0000-T1	Disabled
T6	T0	189.9	120	Normal	0 Pulses	Active High	5.00	T8-0010 0000-T1	Disabled

The timing was set up in this way – utilizing channel one as a dummy – in order to be able to change the time delay (Δt) for each laser by modifying only one channel setting. It is important to be able to change this delay easily during a PIV experiment as it directly controls the pixel displacement between image pairs. The optimal pixel displacement to maximize accuracy is 15-30 pixels. The time delay (Δt) was modified by changing the delay on T1. The internal laser pulse delay was set at 195.5 μs (T4 and

T5). The camera delay was set at 189.9 μs. A schematic of the timing setup is shown below in Figure 63.

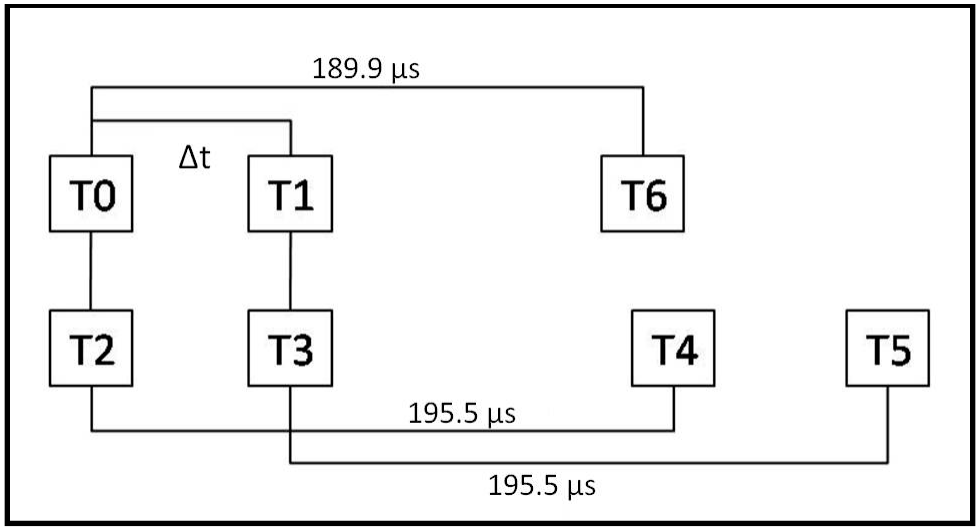

Figure 63: PIV Timing Schematic

The 5.6 μs difference between the camera delay (T6) and the first laser pulse (T4) was a result of an intrinsic 5.3 μs internal delay between the time the Cooke camera receives the trigger signal and the time the shutter actually opens. When operating in double-shutter mode (as was done for PIV), the shutter stays open for the length of the exposure time, closes (saving the first image), and then re-opens for the entire remaining read time (saving the second image). The full read time at a pixel clock of 40 MHz with two ADC was 208 ms. A timing schematic for the Cooke PCO.1600 camera operating in double-shutter mode is shown in Figure 64.

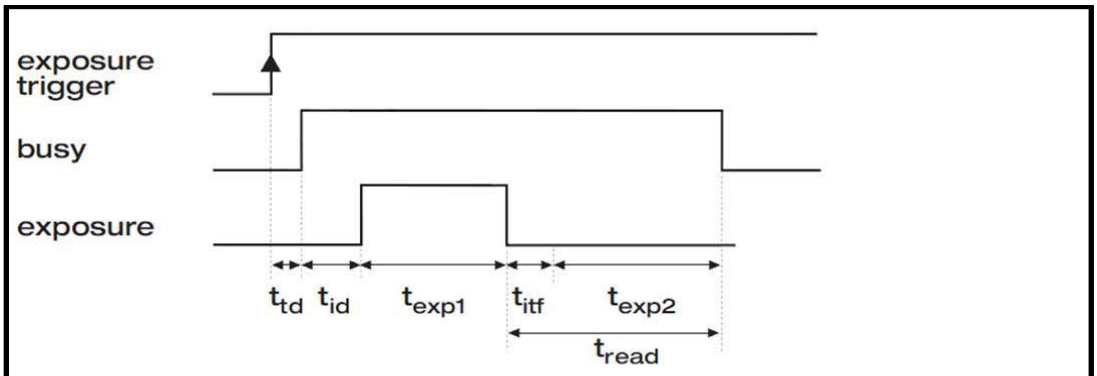

time	description	pco.1600	pco.2000	pco.4000	pco.1200hs
t_{td}	trigger ackn. delay	200±13ns	200±13ns	200±13ns	220±16ns/ 200±13ns (66MHz/86MHz)
t_{id}	intrinsic delay	5.3µs	5.3µs	6.4µs	4.8µs/3.7µs (66MHz/86MHz)
t_{exp}	exposure time	0.5µs..49d	0.5µs..49d	5µs..49d	0.05µs..5s
t_{read}	readout time (full frame)	33ms..208ms (10MHz/1ADC.. 40MHz/2ADC)	68ms..452ms (10MHz/1ADC.. 40MHz/2ADC)	199ms..1390ms (8MHz/1ADC.. 32MHz/2ADC)	2.1ms/1.6ms (66MHz/86MHz)
t_{itf}	interframing time	180ns	180ns	180ns	75ns

Figure 64: Cooke Camera Double-Shutter Timing

Data Processing

In previous studies, the first step in reconstructing velocity fields was to carry out background subtraction of all images. This process increased the number of vectors by eliminating weak reflections and a portion of the strong reflections very near the surfaces, leaving the particle scattering to be correlated. However, for the present study, no background subtraction was needed due to the low surface reflections.

In order to more accurately locate the wall surface, the raw PIV images were first cropped so that the surface was exactly at the lower edge of the image. Additionally, the

top of the images were cropped so that the total pixel height of each image remained a multiple of 16 pixels to ensure that the PIV processing software would analyze the entire image.

From the PIV images, velocity fields were computed. This was done by cross-correlation analysis of each image pair. The basic process is as follows. A small interrogation window is fixed at a point in image one. An intensity map is then calculated for this small area. Centered on that same coordinate location in image two, an interrogation window of the same size sweeps the area, calculating intensity maps. A cross-correlation function of the intensities is computed for each interrogation paring. A peak in this array of cross-correlation data corresponds to the interrogation window pair that is the most similar. Hence, the location of the interrogation window in image two is the location that the particles have traveled. This distance along with a known time delay results in a velocity vector. A simple graphic showing this process is given in Figure 65.

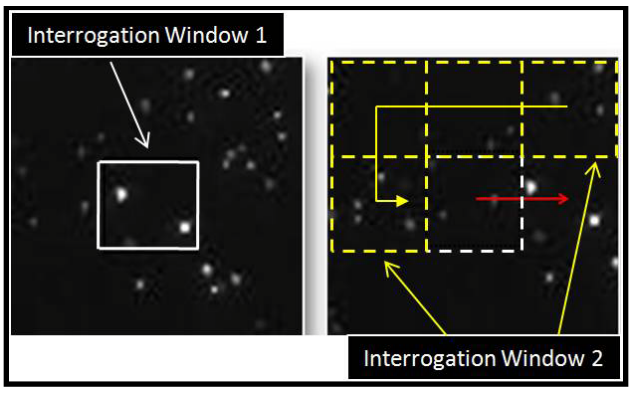

Figure 65: PIV Correlation Process

Velocity field reconstruction was accomplished using Innovative Scientific Solutions, Inc. (ISSI) dPIV 32-bit analysis code version 2.1[53]. A three-step adaptive correlation calculation using successive rectangular interrogation window sizes of 128x128, 64x64, and 32x32 pixels with 50% overlap was used. Correlation multiplication was activated on all four maps adjacent to the center map. When this option was turned on, the target correlation map was multiplied by the center correlation map prior to determining peak location (and hence, pixel location). This had the effect of smoothing the data similar to what a Gaussian filter would do. The consistency filter was also turned on with Min. (minimum number of vectors) set to 2 and Radius (absolute distance) set to 2. This filter operated by computing the absolute distance between the current center vector and its surrounding eight neighbors. If the absolute distance was less than the user selected radius, a counter was incremented. If the counter value was greater than the user selected minimum once all eight neighbors were checked, then the current vector was good and would not be filtered. The dPIV parameters used to process the PIV data are fully documented in Appendix A.

Averages and turbulent quantities were computed using an in-house computer code written in FORTRAN. This code read in the .dat files generated by dPIV and computed average and fluctuating velocities. This code also carried out a simple outlier based filter with a user-set threshold of 2-sigma which simply cleaned up the data without altering the results. The PIV averaging codes are provided in full in Appendix B.

Conventional Methods

In addition to the techniques described above, conventional pressure measurements were also used in the current study. A series of pressure transducers were purchased for in order to accurately monitor and measure the operating pressures of the wind tunnel facility.

For supersonic testing, it is important to monitor the settling chamber total pressure, and the test section static pressure. The settling chamber total pressure was measured via a pitot probe using an Omega PX303 voltage output pressure transducer. The transducer is capable of measuring 0-3.45 MPa (0-500 psig) and outputs a voltage between 0.5 – 5.5 volts DC. The total temperature was measured using an Omega JQSS model thermocouple and the signal was amplified by an OMNI AMP-IV thermocouple amplifier. To measure the test section static pressure, a MKS series 902 piezo vacuum (~0-0.133 MPa (0-1000 torr)) pressure transducer was connected to a pressure tap in the test section sidewall, 6.35 cm (2.5 inches) downstream of the nozzle exit plane. To monitor the output, the MKS transducer was connected to a MKS display model PDR900-1 which was then connected to the DAQ. The Omega and MKS transducers are shown in Figure 66 and Figure 67 respectively and the MKS and thermocouple displays are shown in Figure 68.

Figure 66: Omega PX303 Pressure Transducer

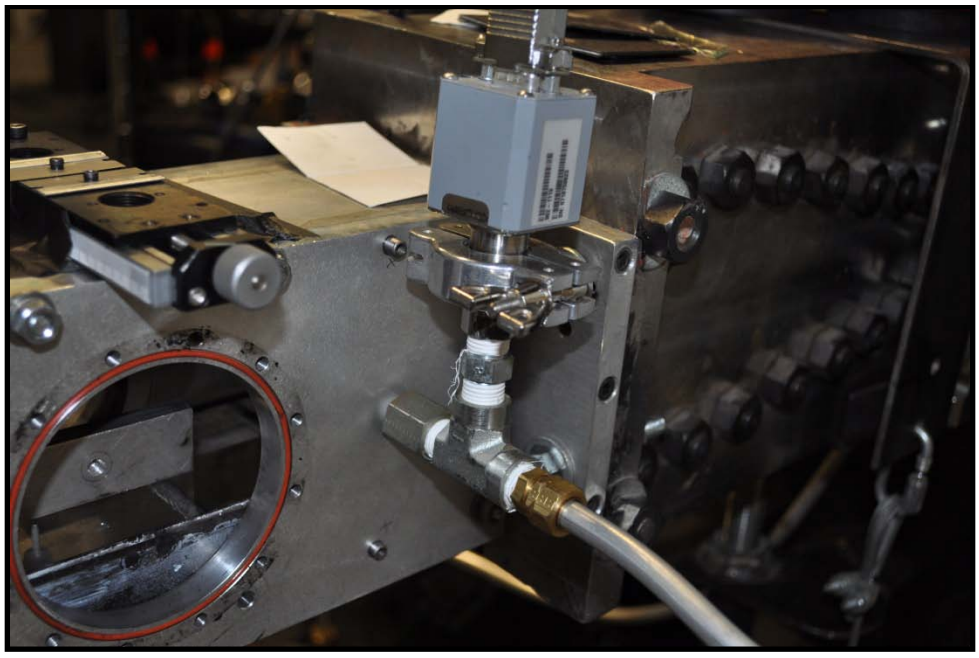

Figure 67: MKS Series 902 Pressure Transducer

Figure 68: MKS Transducer and Omega Thermocouple Displays

Data signals from the pressure transducers and thermocouple were passed through a National Instruments signal conditioning connector block, model SC-2345 which was connected to a National Instruments PCIe-6321 data acquisition board with a sampling rate of 250 KS/s. The board has 16 bit resolution and can support up to 16 single ended or 8 differential channels. LabVIEW version 9.0f3 was used to write the DAQ interface and to record the measurements from the pressure transducers and thermocouple. A screenshot of the LabVIEW DAQ interface is shown in Figure 69.

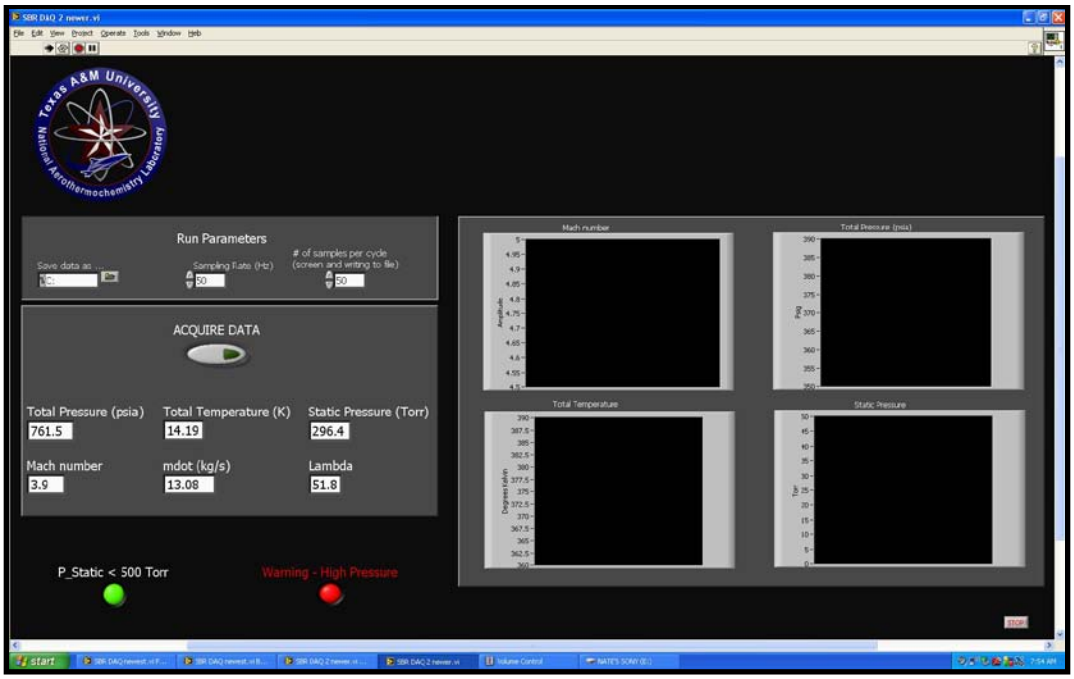

Figure 69: LabVIEW DAQ Interface Screenshot

CHAPTER V

RESULTS AND DISCUSSION

The primary object of this study was to improve the understanding of the fundamental physics of a supersonic turbulent boundary layer over curvature driven favorable pressure gradients. To achieve this goal, high fidelity quantitative experiments were performed. In the first results section, *Measurement Normalization*, a description of how the data was normalized and presented is given. In the next section, *Inflow Characterization*, the properties of the incoming flow are addressed and quantified. In the third section, *Flow Visualization*, qualitative flow visualization images from the wind tunnel testing are presented. In the fourth section, *PIV Valid Vectors*, the validity of the particle image velocimetry is addressed prior to discussing the results. In the next section, *Mean Flow Data*, the quantitative mean flow measurements from the PIV experiments are described. Finally in the last section, *Turbulent Flow Data*, the calculated classical turbulence statistics are presented. Additionally, principal turbulent stress axes analyses as well as Reynolds stress quadrant decomposition analyses are described in the final section.

Measurement Normalization

Two different normalization techniques were utilized in the present study. For all of the proceeding two-dimensional contour plots, quantities were normalized using the reference velocity U_{ref} which was the freestream velocity of the zero pressure

gradient model at the upstream measurement location. For the present study this value was measured to be 788.5 m/s. Also for the contour plots, the length scales were normalized by the reference boundary layer thickness δ_{ref} which was the boundary layer thickness for the zero pressure gradient model at the upstream measurement location at $U/U_{ref} = 99.5\%$. For the present study this value was measured to be 8.57 mm.

In order to allow for a more useful comparison between the different pressure gradient models, a local normalization standard was used. Since the freestream velocity was hard to quantify with the obtained data sets, the traditional boundary layer thickness criteria could not be used for the pressure gradient models. Instead, the calculated spanwise vorticity ω_z was used to define a boundary layer thickness. For the ZPG model at the upstream measurement location, $\omega_z = -4.22\times10^3 \left[(m/s)/m\right]$ at $y = \delta_{ref}$ ($\omega_z \approx -5.0\times10^{-2}$ when normalized by (δ_{ref}/U_{ref})). From this criteria, a boundary layer thickness δ_{ω_z} was defined for each model. Additionally, a local edge velocity U_e was defined at $y = \delta_{\omega_z}$ for each model. All of the proceeding profile plots were normalized using δ_{ω_z} and U_e. Table 7 shows the defined normalization quantities, δ_{ω_z} and U_e for each pressure gradient model.

Table 7: Defined Normalization Quantities

Model	δ_{ω_z} (mm)	U_e (m/s)
ZPG (Wide View)	8.57	788.5
ZPG (Zoom View)	8.08	788.6
WPG	11.80	777.5
SPG	16.40	774.9

For convenience the ω_z subscript will be dropped and $\delta \equiv \delta_{\omega_z}$ from here after.

Inflow Characterization

The purpose of the inflow characterization was to provide the inflow conditions for comparison of pressure gradient effects and for numerical simulations. In particular, the state of the freestream turbulence was quantified, the flow was demonstrated to be two-dimensional, and the state of the boundary layer was shown to be representative of an equilibrium zero pressure gradient boundary layer.

In order to sufficiently characterize the incoming flow properties of the wind tunnel facility used in the present study, a series of tests were performed. At the first measurement location (15.88 cm from the nozzle exit) a spanwise flow survey was conducted to insure that the tunnel flow was two-dimensional. Four locations were probed, z=+5.0 ,0.0, -5.0 and -7.5 mm where z=0.0 was the tunnel centerline. The streamwise velocity (m/s) contour plots for each measurement plane are given in Figure 70.

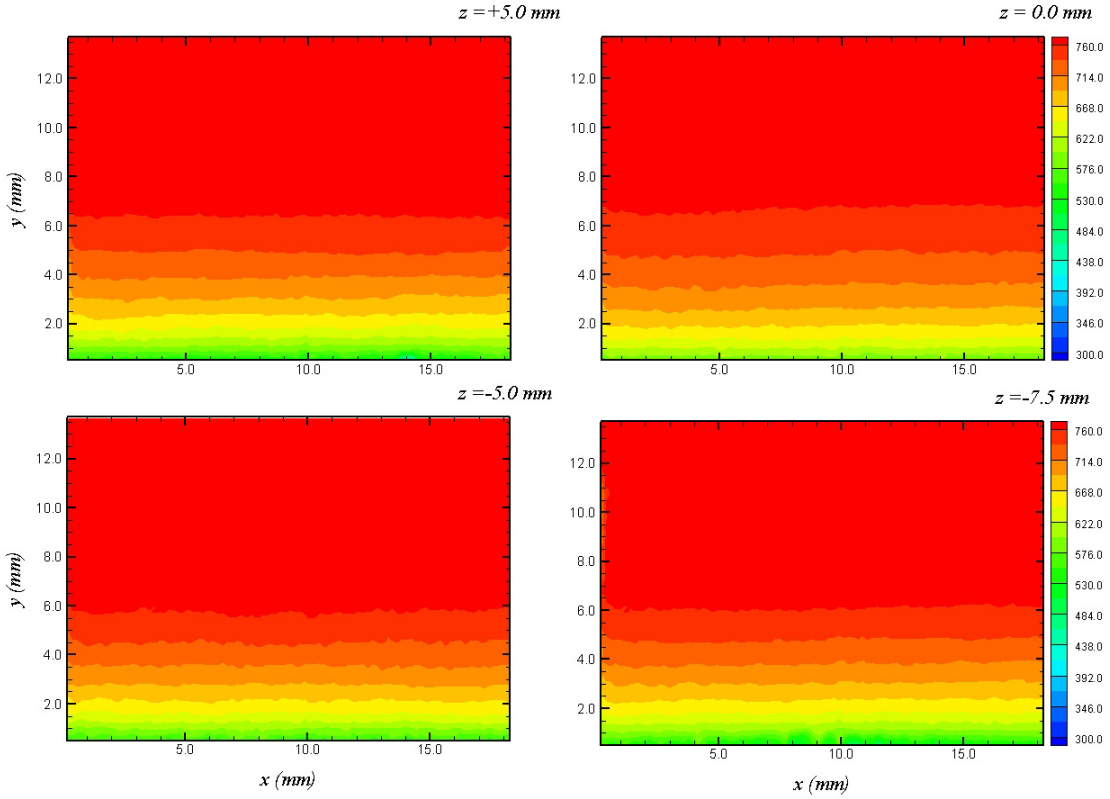

Figure 70: Spanwise Survey $\bar{u}$ (m/s) Contour Plots

It can clearly be seen that the flow looks identical at each spanwise measurement location with a freestream velocity of approximately 785 m/s. Velocity profiles were created from the contour plots by averaging across the field of view for each measurement location. All four $\bar{u}$ velocity profiles are plotted in Figure 71.

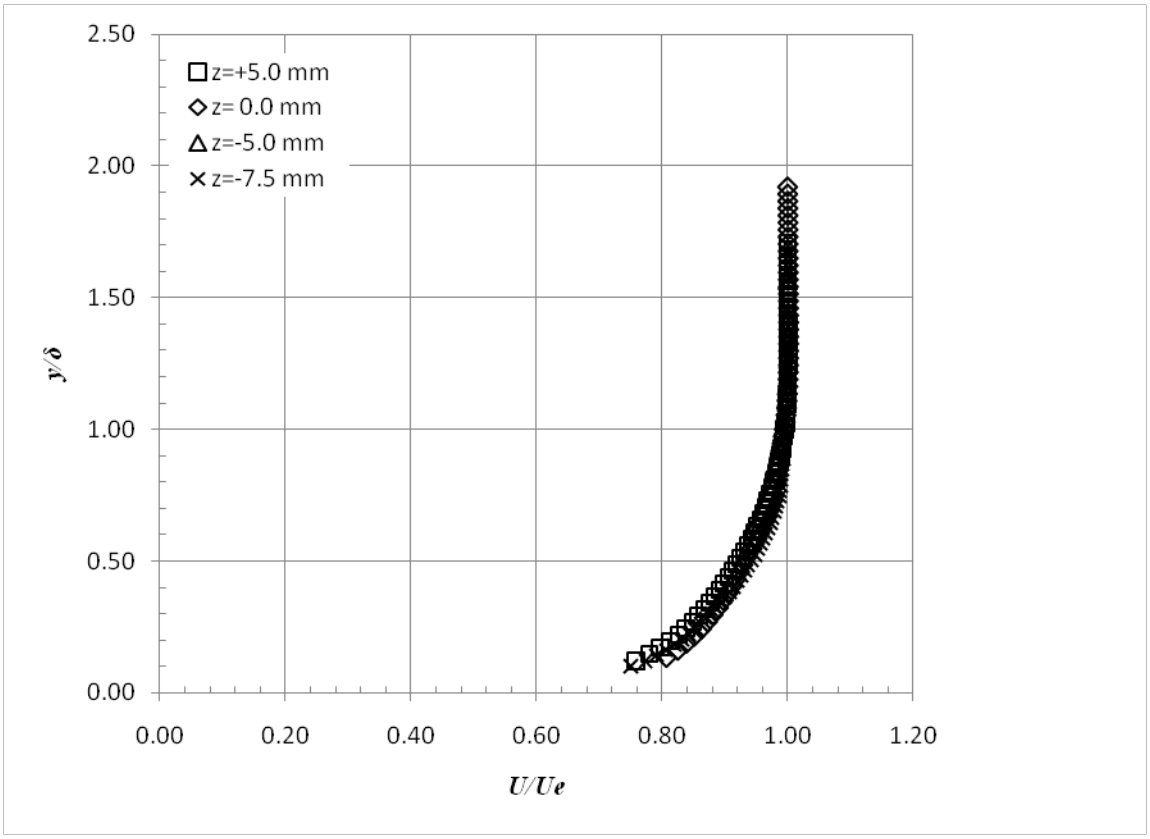

Figure 71: Spanwise *U* Velocity Profiles

Quantitatively it can be seen from the profiles that the mean $\overline{u}$ velocity across the spanwise survey locations is very uniform, with a maximum variation of 5% near the wall and 1.5% in the freestream. This analysis verified that the tunnel inflow was sufficiently uniform near the center-line and therefore could be considered two dimensional for the present study.

Finally, the contours for each spanwise measurement location were compiled in three-dimensional space. Iso-surfaces were generated from the two dimensional data to give an additional estimate of the spanwise flow uniformity. It can be seen from Figure

72 that the flow is very uniform across the measured region and is considered two dimensional for the present study. From the inflow characterization measurements, it was determined that the freestream turbulence intensity was approximately 1.2% of the freestream velocity in both the streamwise and wall normal directions.

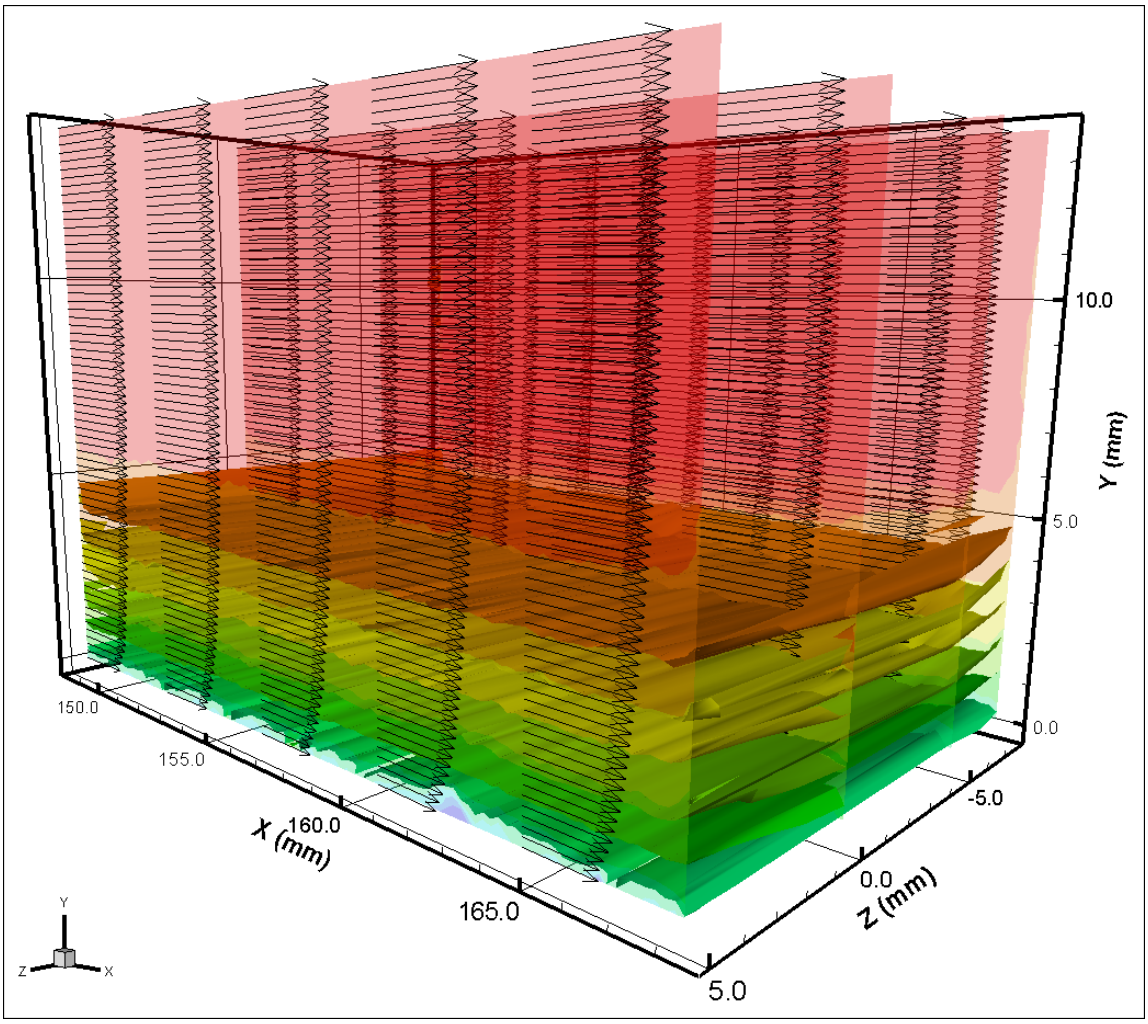

Figure 72: Three Dimensional Spanwise Contours with Iso-Surfaces

Flow Visualization

In order to provide a qualitative assessment of the effect of pressure gradient of the large-scale structures, flow visualization were utilized. These results were collected in order address scientific question 2 described in Chapter I.

The wind tunnel facility was started by pressurizing the settling chamber. Once the tunnel was running properly, the electric heater was powered and the air temperature began to rise. Five minutes were allotted to allow the air temperature to equalize and reach the desired level. While the air was still below the liquefaction point, the PIV laser was turned on and images were recorded of the scattered light off of the liquefied oxygen in the freestream air flow. The camera memory was filled once (345 image pairs) for each location. Two of these images are shown in Figure 73. This process was repeated with each measurement location and with each model to allow for a qualitative comparison of the turbulence characteristics of the boundary layer for each case. The size of the boundary layer as well as the boundary layer intermittency was compared for the ZPG, WPG, and SPG cases. Additionally, movies were created from the series of images to get a qualitative feel of the movement of the turbulent boundary layer for each model and location.

It can easily be seen when the incoming air is not heated above the required liquefaction temperature, liquefied oxygen droplets can easily be seen in freestream Mach 4.88 flow. However, in the turbulent boundary layer, the temperature is significantly higher and therefore vaporizes the incoming liquid oxygen. This is why the freestream flow is bright and the boundary layer is dark; there are no droplets to scatter the laser light. This

technique allows for an easy way to visualize the turbulent boundary layer and previous published work has been performed using images similar to these for data analyses[54]. A survey of images from the ZPG case is shown in Figure 74. For this field of view, the camera resolution was approximately 79 pixels / mm and the camera was horizontal.

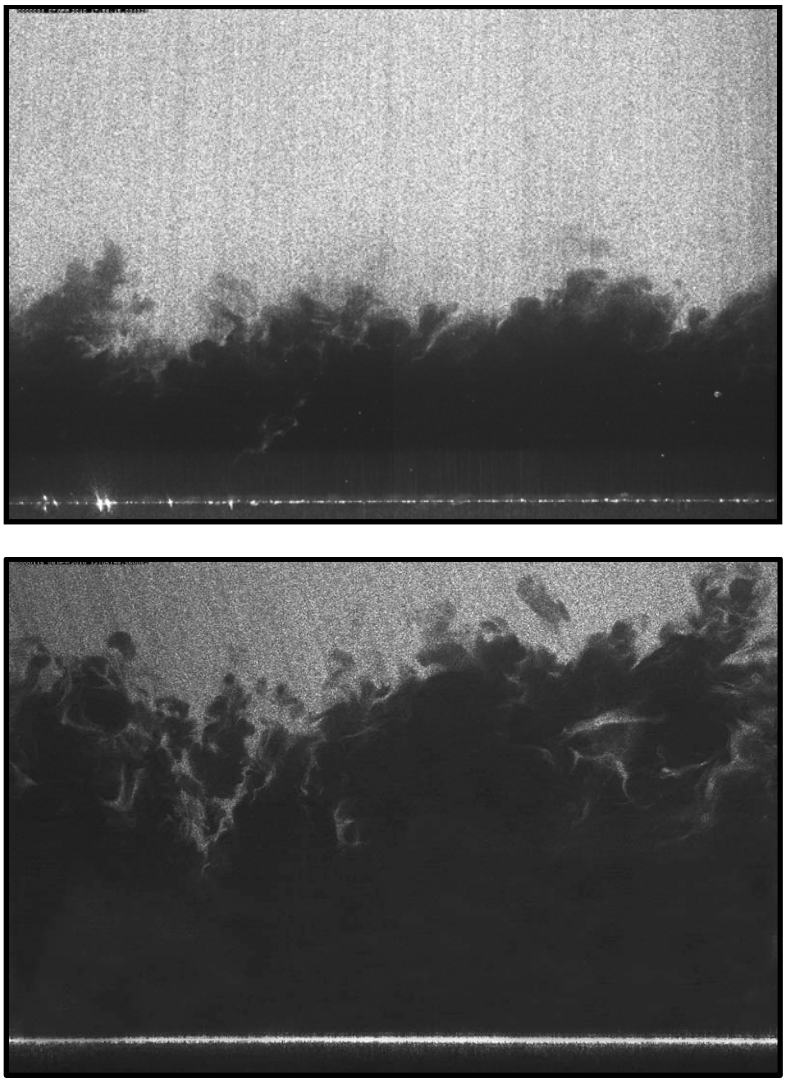

Figure 73: Sample Flow Visualization Images

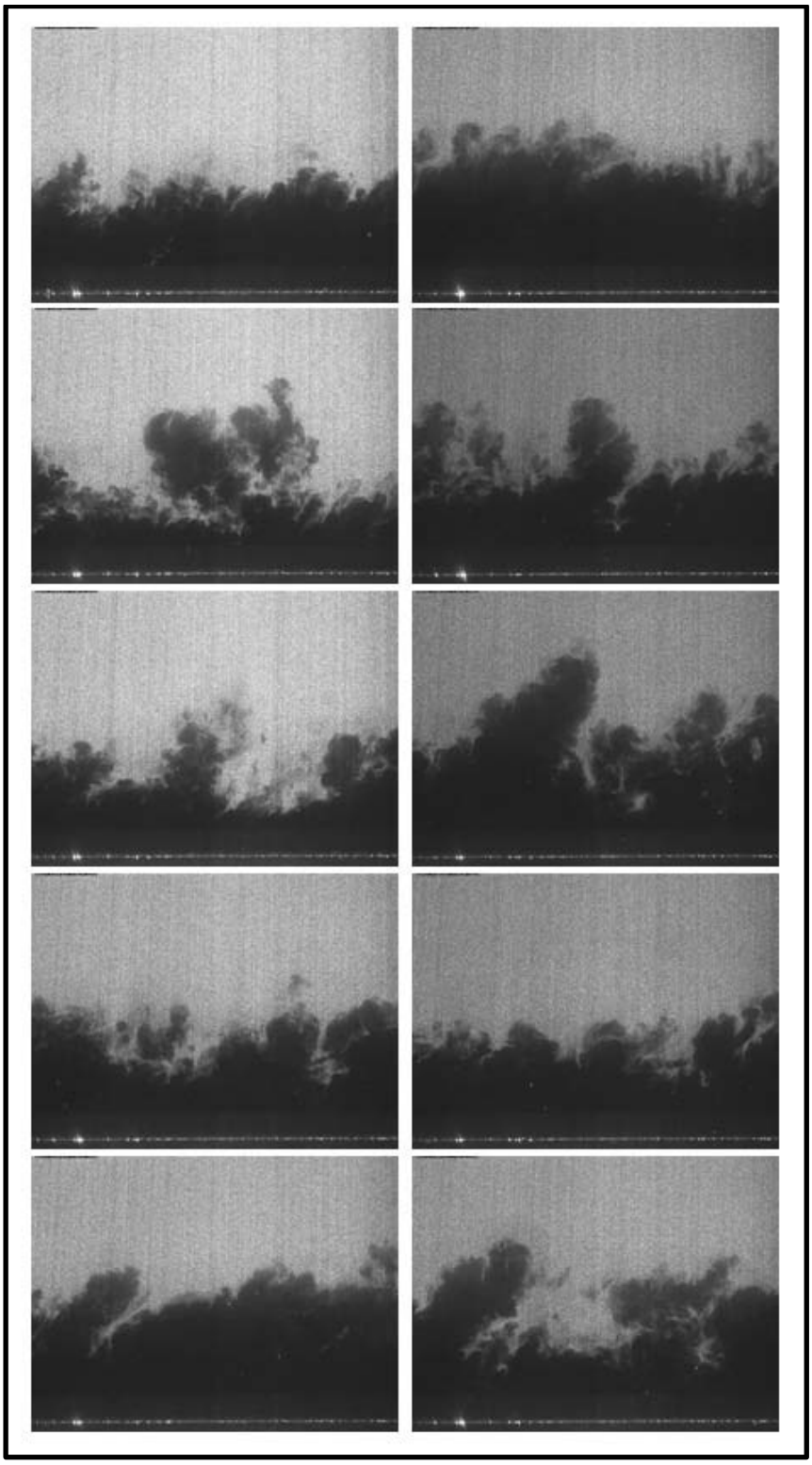

Figure 74: ZPG Flow Visualization Survey

The same procedure was repeated for each pressure gradient model. The camera was rotated to match the local wall angle in order to maximize resolution near the surface. The camera zoom was also adjusted to allow for the larger boundary layer present downstream of the favorable pressure gradient curvature. The aim was to have the total height of the field of view to be approximate 2δ. A flow visualization survey of the WPG model is shown in Figure 75. For this run, the camera resolution was approximately 46 pixels / mm and the camera was rotated 1.6 degrees. It can qualitatively be seen that the boundary layer structure is slightly different from the ZPG case. As the flow moves over the favorable pressure gradient, the flow accelerates and the boundary layer expands. Larger structures can be seen compared to the ZPG case. Also, the boundary layer intermittency increases over the favorable pressure gradient. The flow visualization survey of the SPG model is shown in Figure 76. For this run the camera resolution was approximately 46 pixels / mm and the camera was rotated 10.3 degrees. It can be seen that the boundary layer is even larger than the WPG case as expected. Additionally, very large structures can clearly be seen being ejected from the main boundary layer. This movement of large chunks of boundary layer fluid make the boundary layer much more intermittent compared to the WPG or ZPG cases.

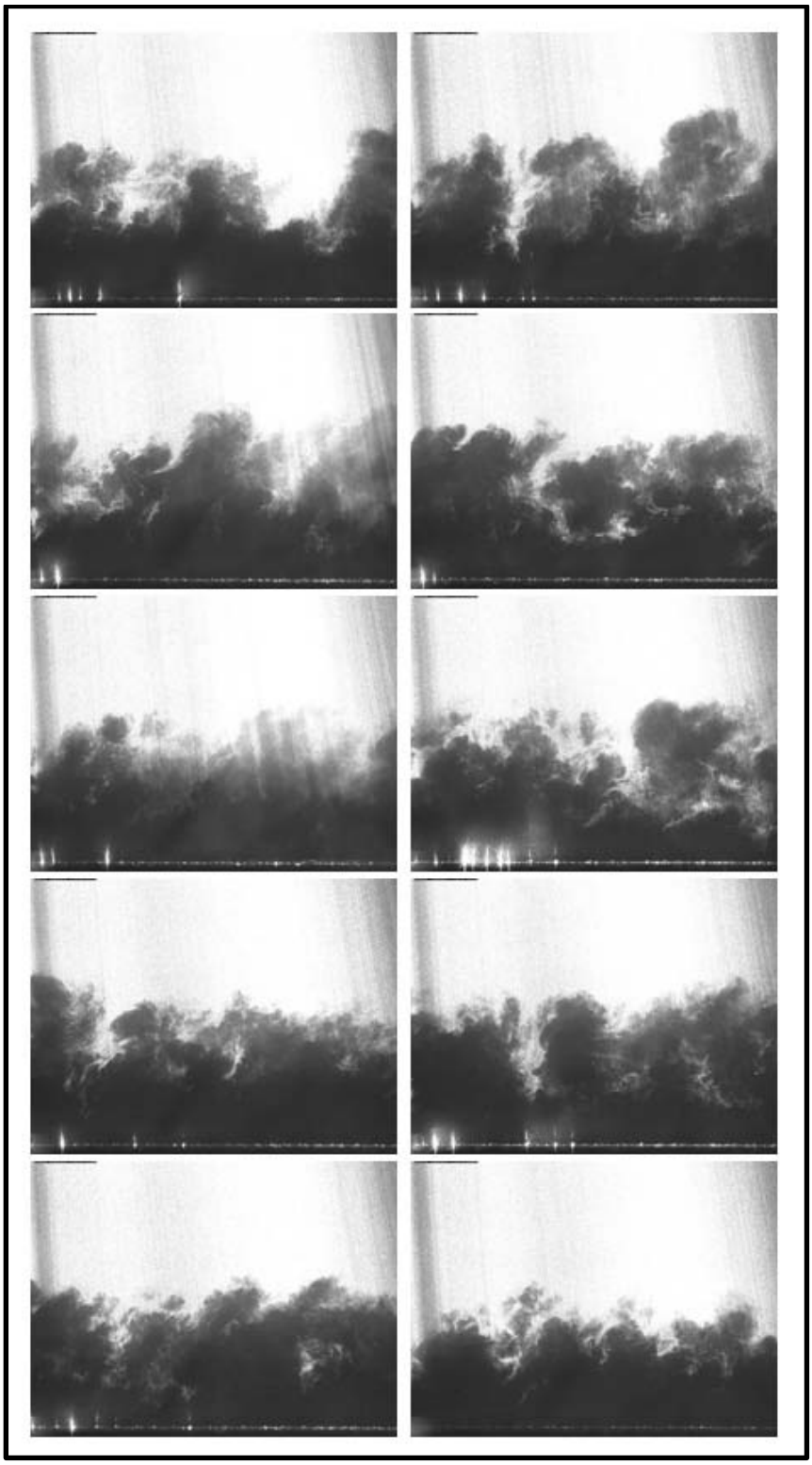

Figure 75: WPG Flow Visualization Survey

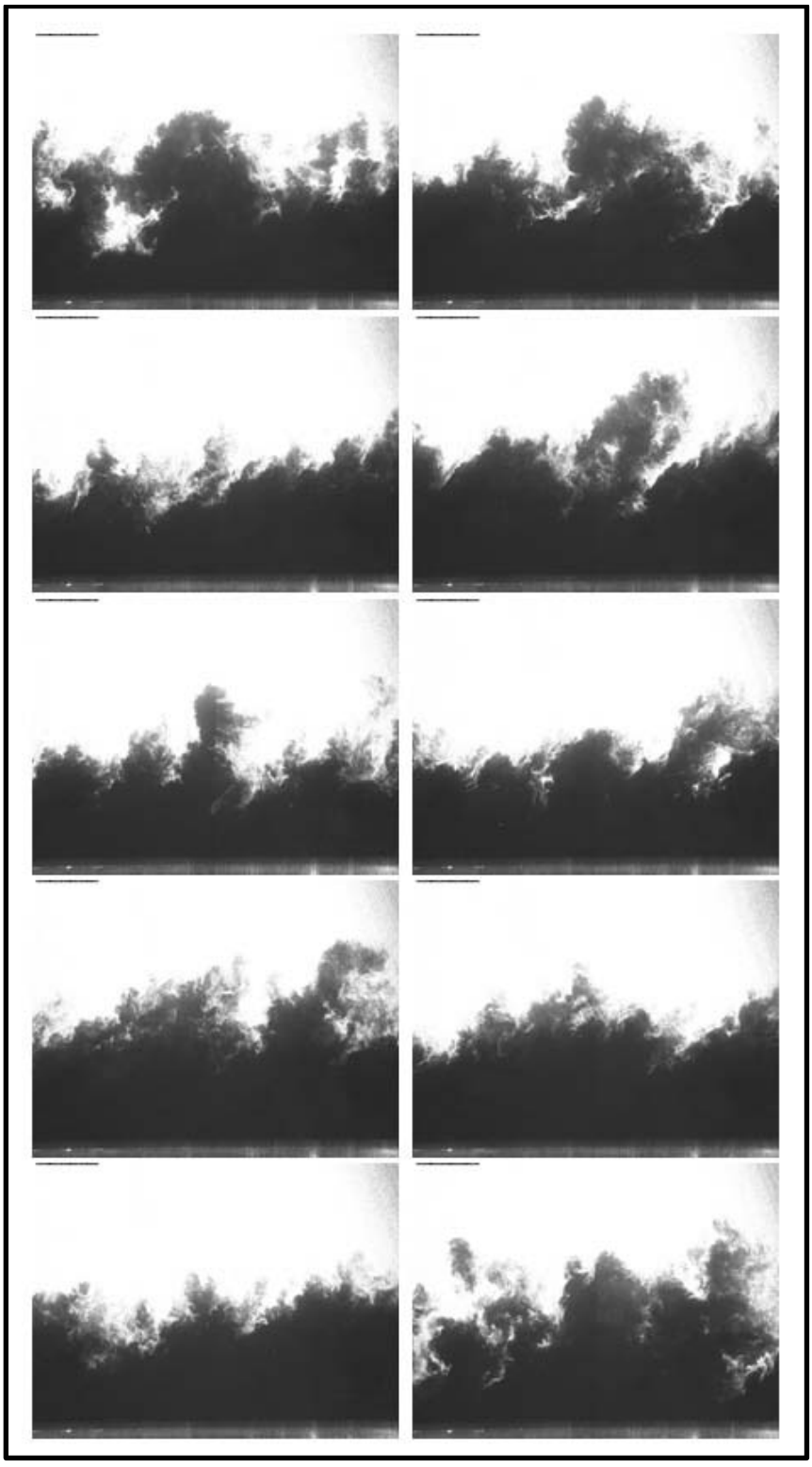

Figure 76: SPG Flow Visualization Survey

The qualitative flow visualization agreed well with predicted behavior of the turbulent boundary layer over curvature driven favorable pressure gradients. It was clearly seen that the boundary layer structure was altered and the boundary layer intermittency was decreased for the WPG and SPG cases. The boundary layer thickness grew over the pressure gradients as expected. In the ZPG boundary layer, large vortical structures could be seen in the instantaneous snap shots. Additionally, the visual edge of the boundary layer remained fairly constant over the course of the visualization run. For the WPG case, showed fewer large structures there were easily seen and the visual edge of the boundary layer varied slightly from image to image. For the SPG mode, large vortical structures were much more rare and the boundary layer fluid height was not changing significantly from image to image.

PIV Valid Vectors

Once the flow in the wind tunnel facility was characterized and determined to be two dimensional, the flow over the various pressure gradient models was visualized as described above. After the qualitative flow properties were determined, data was collected using particle image velocimetry as described in Chapter IV. Both measurement locations as well as all three pressure gradient models were probed with PIV to quantitatively measure the supersonic turbulent boundary layer properties. Through the post-processing, some vectors were determined not to be valid and were thrown out. Contour plots of the percentage of valid vectors to the total number of possible vectors are shown in Figure 77.

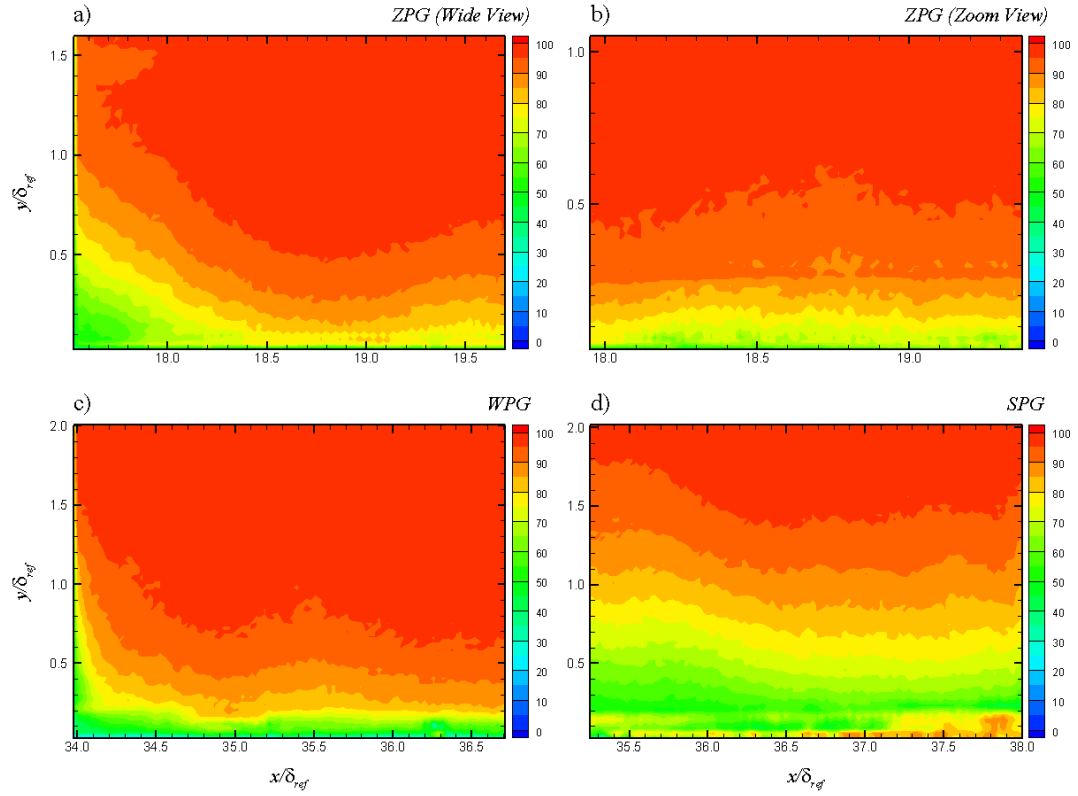

Figure 77: Contour Plots of Percentage of Valid Vectors

In the freestream, the percentage of valid vectors is above 95%, however the percentage decreases closer to the wall. This is mainly due to lower fluid density and therefore lower particle seed density as well as wall reflections very near the wall. The fluid density effects are amplified for the WPG and SPG cases where the flow is accelerating and therefore the density is decreasing. For the WPG case, the percentage of valid vectors below $0.2\ y/\delta_{ref}$ is only approximately 50%. For the SPG case, the fluid density near the wall is even lower and therefore fewer valid vectors are present with about 75% valid vectors at $0.6\ y/\delta_{ref}$ and 50% at $0.3\ y/\delta_{ref}$. Additionally, as seen in

the contour plots, the ZPG (wide view) and the WPG cases show a reduced number of valid vectors in the upstream side of the field of view. This is likely due to non-uniformities in the laser beam profile. For the remainder of the present study, the ZPG (wide view) and WPG contour plots will be cropped to omit these regions of lower validity. Table 8 presents the valid streamwise ranges for each pressure gradient model.

Table 8: Valid Streamwise Field of View

Model	Upstream x / δ_{ref}	Downstream x / δ_{ref}
ZPG (Wide View)	18.2	19.7
ZPG (Zoom View)	18.0	19.4
WPG	34.5	36.7
SPG	35.3	38.0

A profile plot was created from the contour plots by averaging over the center of each field of view. The profiles are shown in Figure 78.

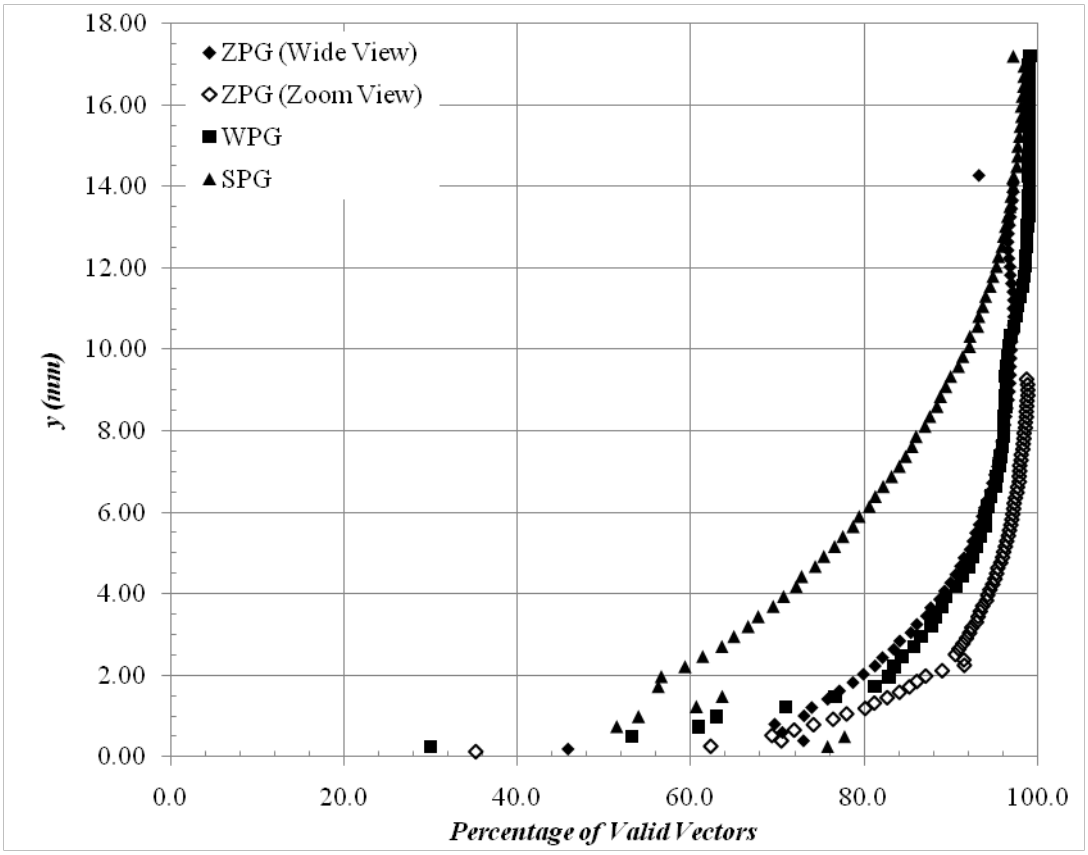

Figure 78: Profile Plot of Percentage of Valid Vectors

The profile plot clearly shows the trends visible in the above contour plots. The ZPG and WPG cases are all very similar in the percentage of valid vectors, due to the low turning angle of the WPG model. However, the SPG case shows an appreciable reduction in the number of valid vectors near the wall. Due to this reduced number of valid vectors near the wall for the various models, the error in the measurements was greatly increased. In order to maintain high quality statistics, data profiles and conclusions for each pressure gradient model were limited to the ranges listed in Table 9; however the full wall normal data ranges are shown in the contour plots.

Table 9: Valid Wall Normal Ranges

Model	y (mm)
ZPG (Wide View)	> 1.0
ZPG (Zoom View)	> 0.8
WPG	> 1.5
SPG	> 2.0

A modified profile plot of the valid vectors with the cropped data sets is shown in Figure 79. By eliminating the bad data points, the data is much cleaner and the results will be easier to analyze.

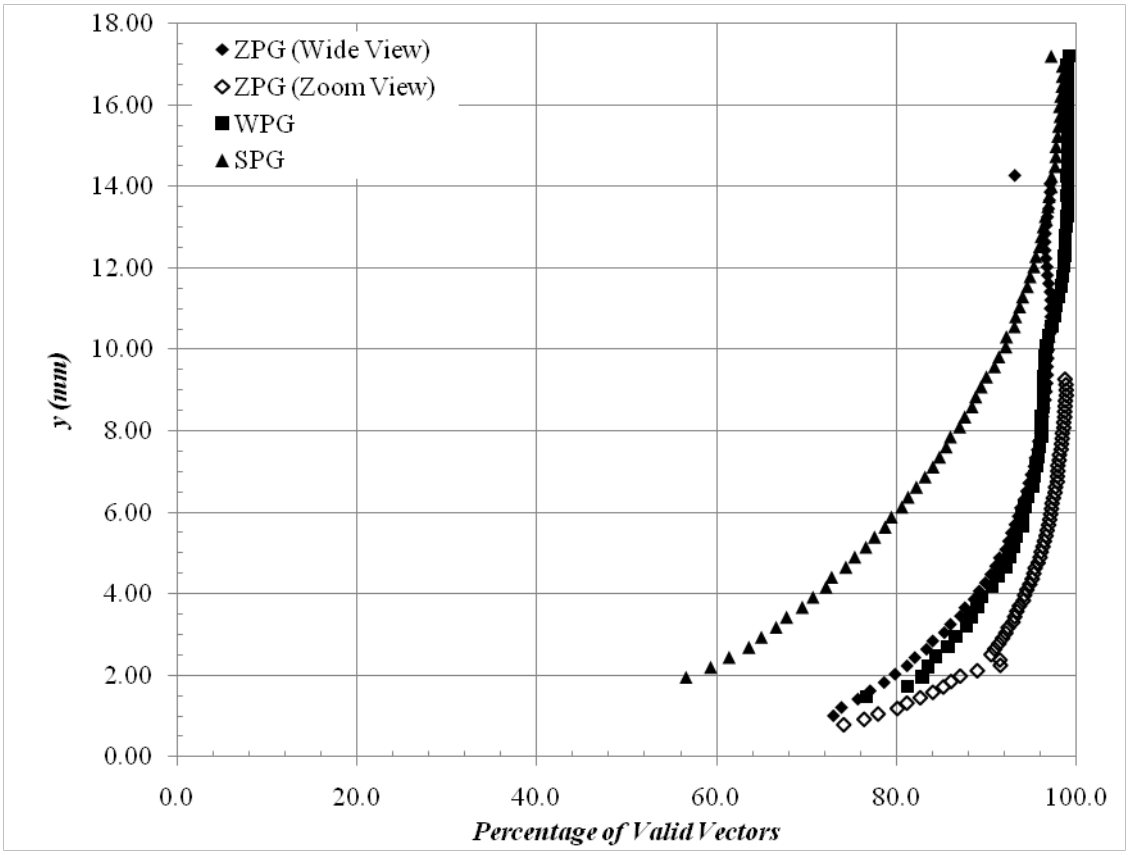

Figure 79: Profile Plot of Percentage of Valid Vectors (Cropped)

Mean Flow Measurements

This section presents the mean flow measurements obtained in the present study. A detailed discussion of the mean velocity fields is given as well as velocity gradient information. Contours and profiles for each model and location are provided and discussed.

Mean Velocity Measurements

The purpose of these data were to provide a quantitative measurement of the effect of favorable pressure gradients on the mean flow. These measurements were collected to address scientific question 1 discussed in Chapter I.

Mean velocity fields were measured using particle image velocimetry as discussed in Chapter IV. Contour plots were generated for both $\overline{u}$ and $\overline{v}$ velocity components for each measurement location and model. The velocity components were normalized by the reference velocity $\left(1/U_{ref}\right)$ and the length scales were normalized by the reference boundary layer thickness δ_{ref}. For the zero pressure gradient model, two different fields of view were used at the upstream measurement location. The wide view had a resolution of approximately 78.5 pixels / mm (1994 pixels / inch) and physical field of view of approximately 20.38 mm x 15.29 mm (0.80 inches x 0.60 inches). A second data set was collected with a zoomed in field of view in efforts to collect data closer to the tunnel floor. This data set had a resolution of approximately 120.9 pixels / mm (3071 pixels / inch) and a physical field of view of 13.23 mm x 9.93 mm (0.52

inches x 0.39 inches). The contour plots for the zero pressure gradient model mean velocities ($\bar{u}$, $\bar{v}$) at the first measurement location are given in Figure 80.

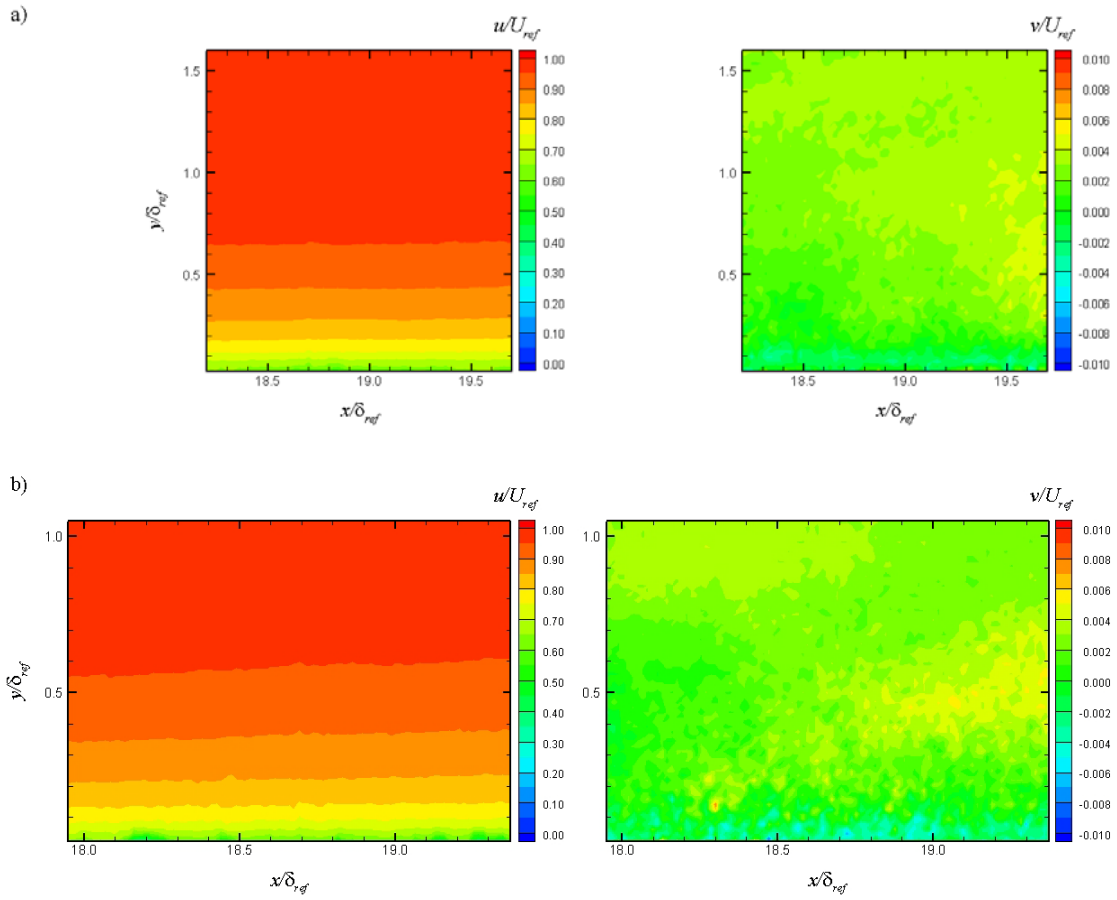

Figure 80: ZPG Mean Velocity Contours at 1st Measurement Location a) Wide View, b) Zoom View

From the contour plots, it can easily be seen that the $\bar{u}$ velocity fields are very uniform across the measurement area. The boundary layer is clearly visible and does not grow much due to the small field of view. The $\bar{v}$ velocity fields show that the velocity normal to the wall is practically zero for the purposes of this study.

Profiles were extracted from the contour plots normal to the wall surface. In order to generate more accurate profiles, the data was averaged over approximately 1.0 δ_{ref} in the streamwise direction to create the profiles. The velocity components were normalized by the local edge velocity $(1/U_e)$ and the length scales were normalized by the local boundary layer thickness δ defined above. The mean zero pressure gradient velocity profiles are shown in Figure 81. The measured velocity profiles for the zero pressure gradient model in the first window location compares very well with flat plate theory.

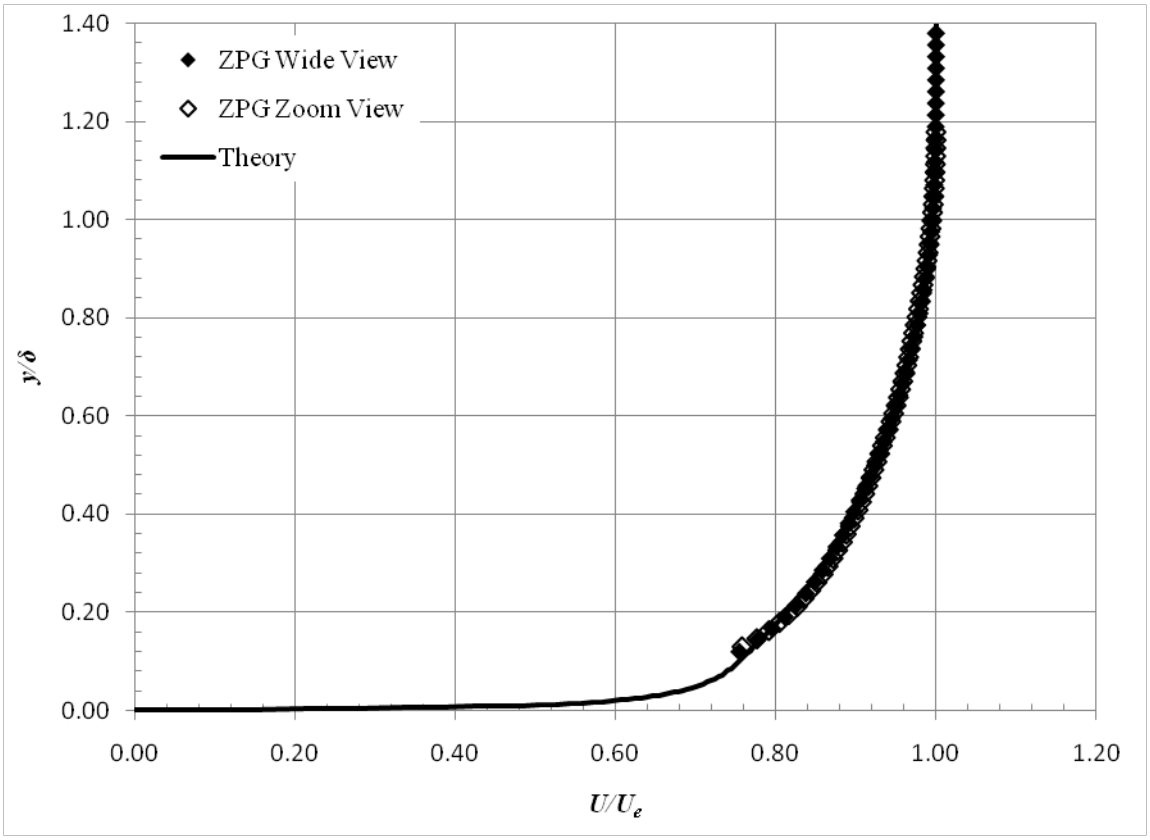

Figure 81: Zero Pressure Gradient Mean Velocity Profiles

In order to compare the zero pressure gradient data from the present study to incompressible data, Van Driest II scaling was used[9].

$$\overline{u}_{eff} = \frac{\overline{u}_e}{a}\left(\sin^{-1}\frac{2a^2\dfrac{\overline{u}}{\overline{u}_e} - b}{Q} + \sin^{-1}\frac{b}{Q} \right) \tag{4.1}$$

where

$$a = \left(\frac{\gamma - 1}{2} M_e^2 \frac{T_e}{T_w} \right)^{1/2}; \quad b = \left(\frac{T_{aw}}{T_w} - 1 \right); \quad Q = \left(b^2 + 4a^2 \right)^{1/2}$$

But for adiabatic walls (4.1) reduces to

$$\overline{u}_{eff} = \frac{\overline{u}_e}{a} \sin^{-1}\left(a\frac{\overline{u}}{\overline{u}_e} \right) \tag{4.2}$$

where

$$a^2 = 1 - \frac{T_e}{T_{aw}}$$

Law-of-the-wall correlation scaling was used to plot the mean velocity.

$$\overline{u}^+_{eff} = \begin{cases} y^+, & y^+ < 10 \\ \dfrac{1}{\kappa}\ln\left(y^+\right) + B + \dfrac{2\Pi}{\kappa}\sin^2\left(\dfrac{\pi}{2}\dfrac{y}{\delta}\right), & y^+ \geq 10 \end{cases} \tag{4.3}$$

where $B \approx 5.5$, $\kappa = 0.40$, and $\Pi \approx 0.55$. The wide and zoom data sets for the zero pressure gradient model at the upstream window location were plotted in viscous units versus theory. The data falls reasonably well on the theory curve and was deemed sufficient for the present study. The inner scaling law-of-the-wall plot is shown in Figure 82.

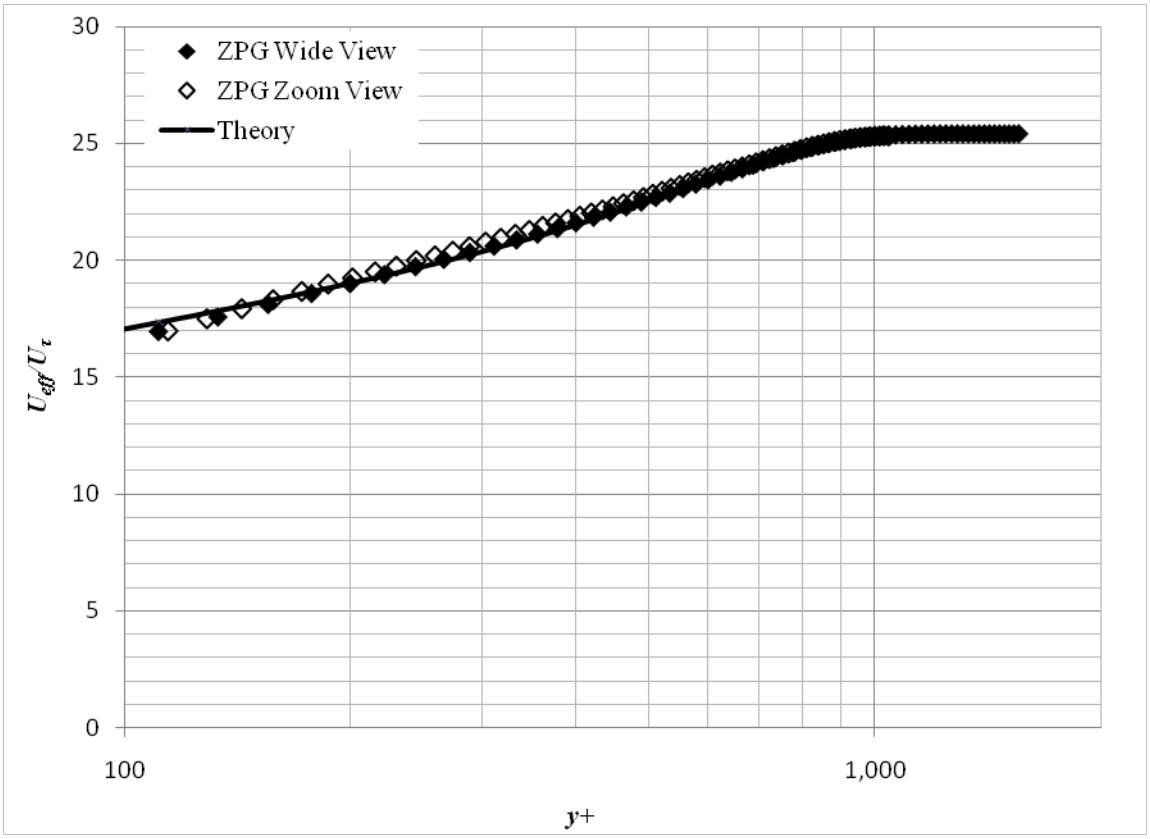

Figure 82: ZPG Law of the Wall Plot

Outer law scaling or defect law is given by

$$\frac{\overline{u}_{eff} - \overline{u}_{e,eff}}{u^*} = \frac{1}{\kappa}\ln\left(\frac{y}{\delta}\right) - \frac{2\Pi}{\kappa}\left[1 - \sin^2\left(\frac{\pi}{2}\frac{y}{\delta}\right)\right] \tag{4.4}$$

where again $B \approx 5.5$, $\kappa = 0.40$, and $\Pi \approx 0.55$. The defect law plot for the zero pressure gradient model at the upstream window location is shown in Figure 83. The PIV data

from both data sets collapse onto the incompressible theory regardless of the field of view.

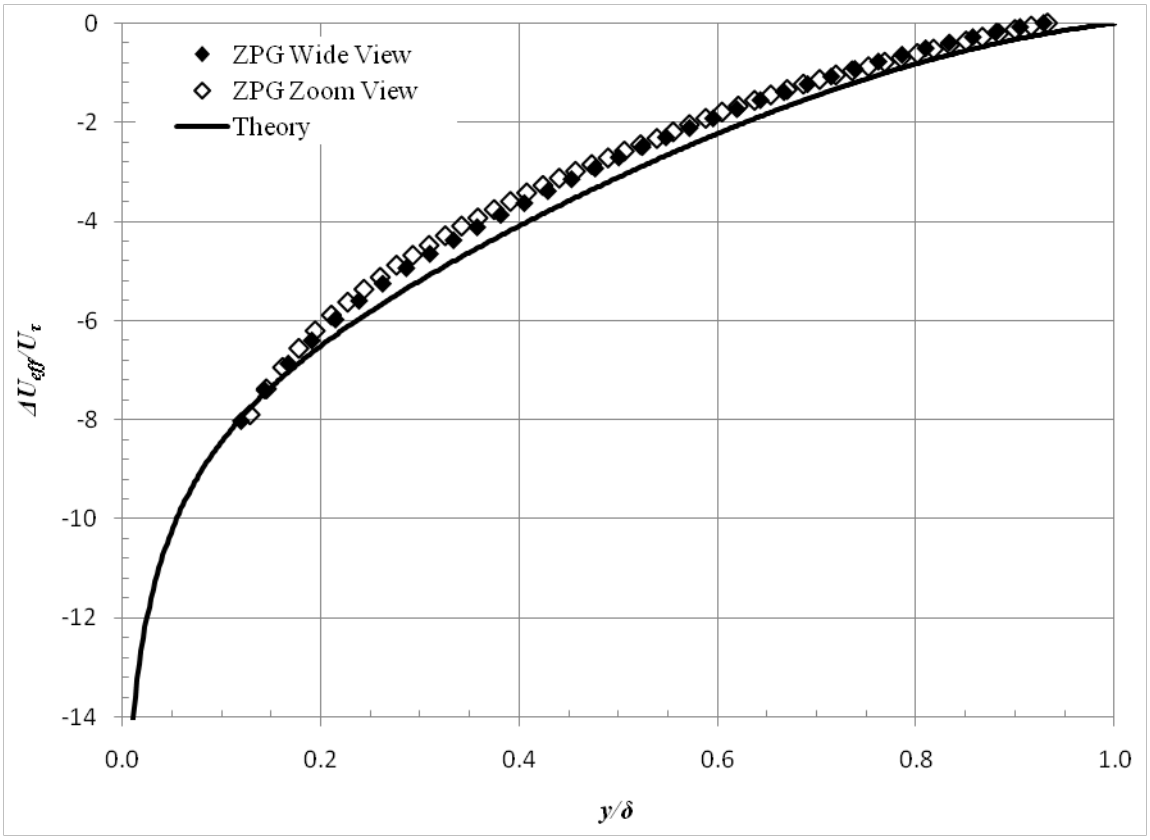

Figure 83: ZPG Defect Law Plot

In addition to the above described data from the zero pressure gradient model, one data set was collected using the wide view settings for the upstream window location of the strong pressure gradient model. This was done to verify that the boundary layer at the upstream measurement location was independent of the model that was installed. Mean velocity contours for the strong pressure gradient model at the

upstream measurement location are shown in Figure 84. For this data set, the resolution was 78.9 pixels / mm (2004 pixels / inch) with a physical field of view of 20.28 mm x 15.21 mm (0.80 inches x 0.60 inches).

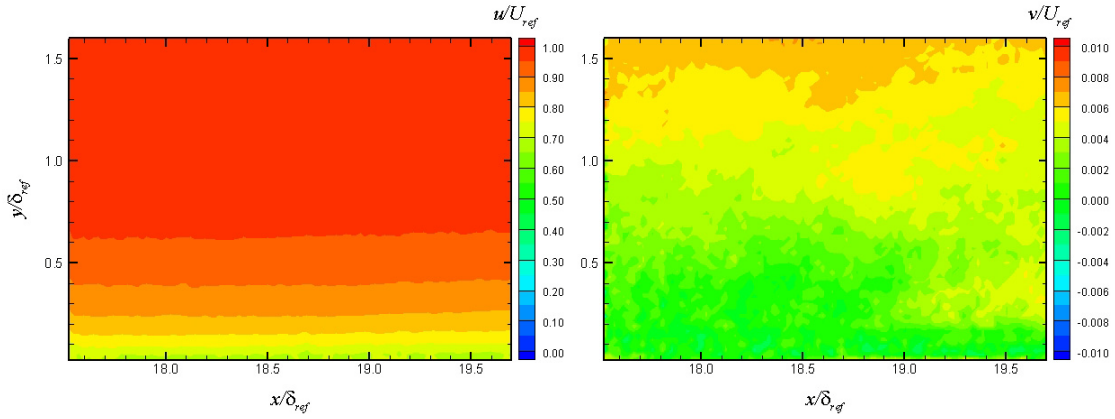

Figure 84: SPG Mean Velocity Contours at 1st Measurement Location

It can be seen that the $\bar{u}$ velocity field is again very uniform across the measurement area. The boundary layer is clearly visible and does not grow much due to the small field of view. The $\bar{v}$ velocity field shows that the velocity normal to the wall is again practically negligible. By performing this measurement with the strong pressure gradient model installed, it was shown that the first measurement location 15.88 cm (6.25 inches) downstream from the nozzle exit was independent of the installed tunnel model. The above contour plots, profiles, and incompressible scaling discussion sufficiently characterized and described the mean velocity of the boundary layer at the first measurement location; therefore data were not obtained for the weak pressure gradient model at the first measurement location. Additionally, data was not collected

for the zero pressure gradient model at the second measurement location because the upstream zero pressure gradient boundary layer was sufficiently characterized.

For the weak pressure gradient model, data was collected at the downstream measurement location. The camera was rotated 1.6 degrees so that the field of view was parallel to the model surface. The model surface can barely be seen in the raw PIV image shown in Figure 85. The bright white spot at the bottom right corner of the image is a glare off of the wall and the model surface runs parallel to the bottom of the image through the glare point. For this data set, the resolution was 65.1 pixels / mm (1654 pixels / inch) with a physical field of view of 24.58 mm x 18.43 mm (0.97 inches x 0.73 inches).

Figure 85: Raw PIV Image of WPG Model at 2nd Measurement Location

Because the camera was rotated to be parallel to the model surface, the local coordinate system no longer aligns with the tunnel coordinate system. The $\overline{u}$ and $\overline{v}$ mean velocity contours for the weak pressure gradient model at the second measurement location are shown in Figure 86.

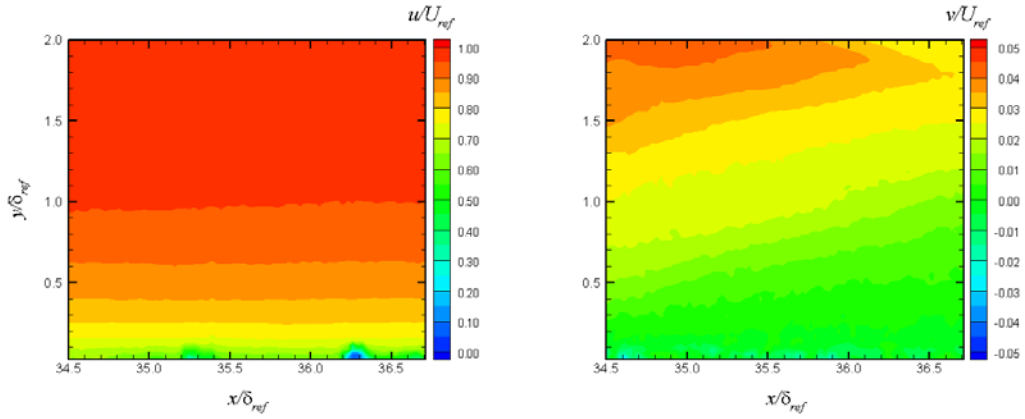

Figure 86: WPG Mean Velocity Contours at 2nd Measurement Location (Wall Normal Coordinate System)

As expected, the boundary layer begins to grow as it travels over the pressure gradient. The mean $\overline{u}$ velocity is still along the wall surface while the $\overline{v}$ mean velocity is negligible near the wall and increases towards the freestream. This is because the $\overline{v}$ velocity is normal to the wall and has a component in the global streamwise direction.

Using the post-processing FORTRAN code, the velocity vectors were transformed from the wall coordinate system to the global wind tunnel coordinate system by rotating each vector by the camera angle 1.6 degrees. A comparison of the mean velocity vectors in each coordinate system can be seen in Figure 87.

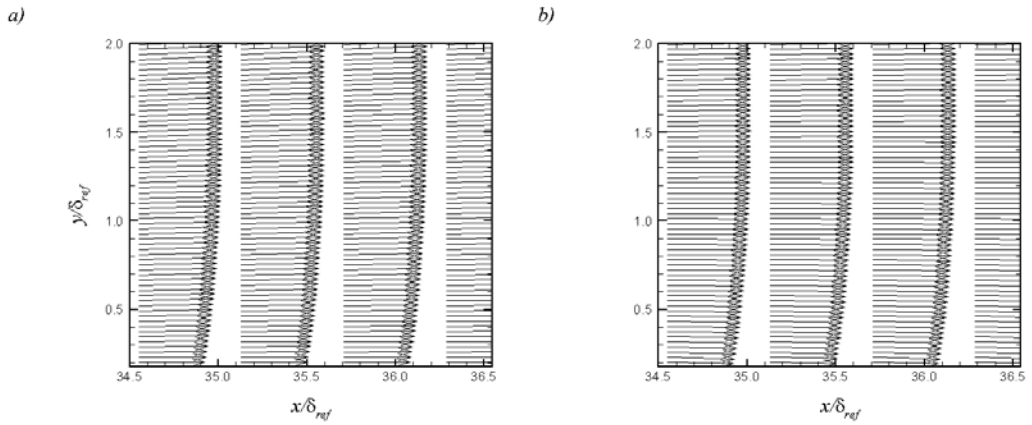

Figure 87: WPG Mean Velocity Vectors in a) Wall Normal Coordinate System, b) Global Coordinate System

Since the camera rotation angle was so small, the difference in the mean velocity vectors is difficult to detect. Contour plots were again generated for the mean $\overline{u}$ and $\overline{v}$ velocities in the global coordinate system and are shown in Figure 88.

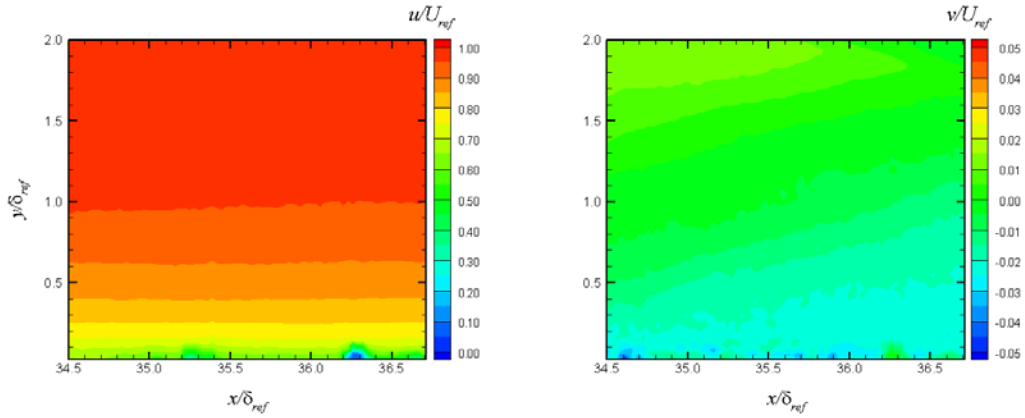

Figure 88: WPG Mean Velocity Contours at 2nd Measurement Location (Global Coordinate System)

Again, due to the small camera rotation angle, the contours are very similar to the previous set. The $\overline{u}$ velocity clearly shows the boundary layer growth and is of the same magnitude as before. The $\overline{v}$ velocity contour plot shows that now near the wall, $\overline{v}$ in the global coordinate system is negative and away from the wall, $\overline{v}$ in the global coordinate system is zero. This is expected as the flow along the wall would have a negative $\overline{v}$ velocity and flow in the freestream would have a zero $\overline{v}$ velocity in the global coordinate system.

Velocity profiles were generated for the weak pressure gradient model at the second measurement location. For this measurement location, the profiles were created by averaging in the streamwise direction approximately 1.0 δ_{ref}. Three sets of velocity profiles were created for the weak pressure gradient model. Profiles from the upstream side of the image (approximately 34-35 x/δ_{ref}) are shown in Figure 89 while profiles from the center of the image (approximately 35-36 x/δ_{ref}) are given in Figure 90. Finally, velocity profiles from the downstream side of the image (approximately 36-37 x/δ_{ref}) are shown in Figure 91. All of the velocity profiles are plotted in both coordinate systems as well as with the ZPG velocity profile from the upstream measurement location for reference. It can be seen that the $\overline{u}$ mean velocity profiles match the ZPG case very well and do not change significantly over the field of view for the weak pressure gradient model at the downstream measurement location. However the mean velocity profiles were slightly fuller downstream signified by a higher velocity closer to the wall.

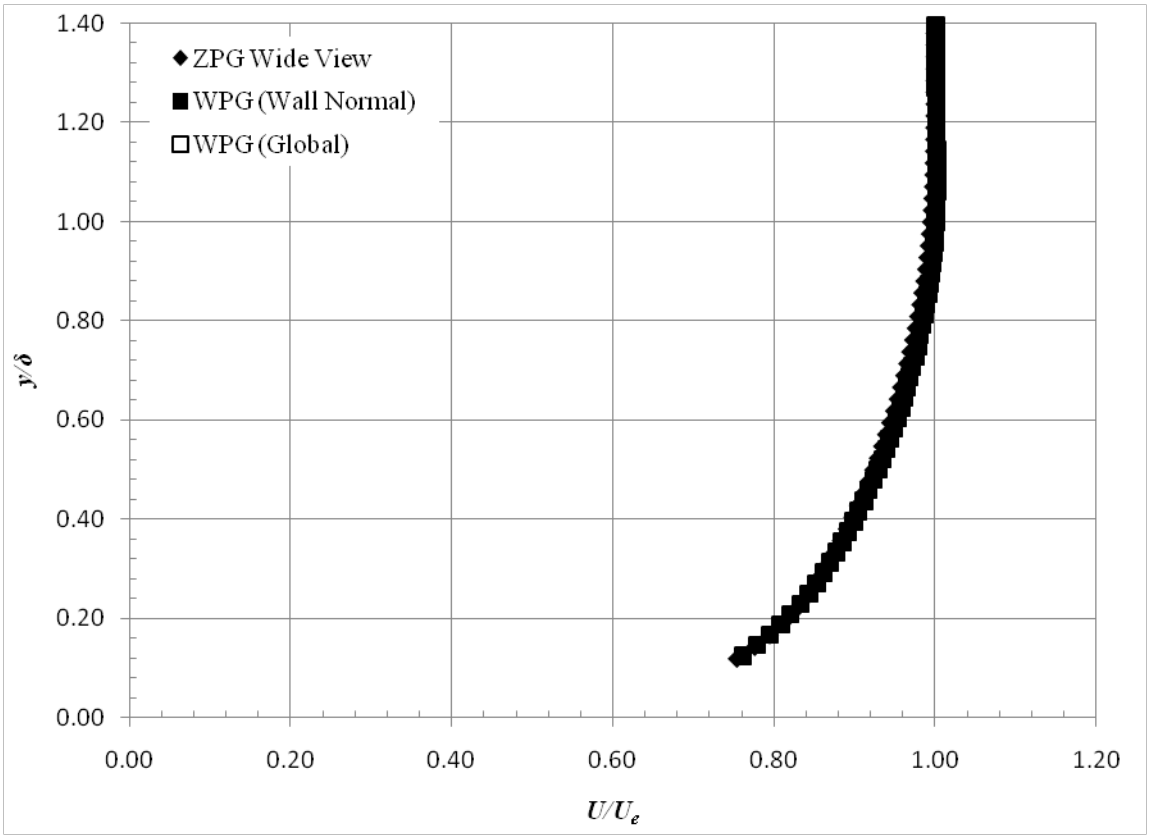

Figure 89: WPG Velocity Profiles - Upstream Side

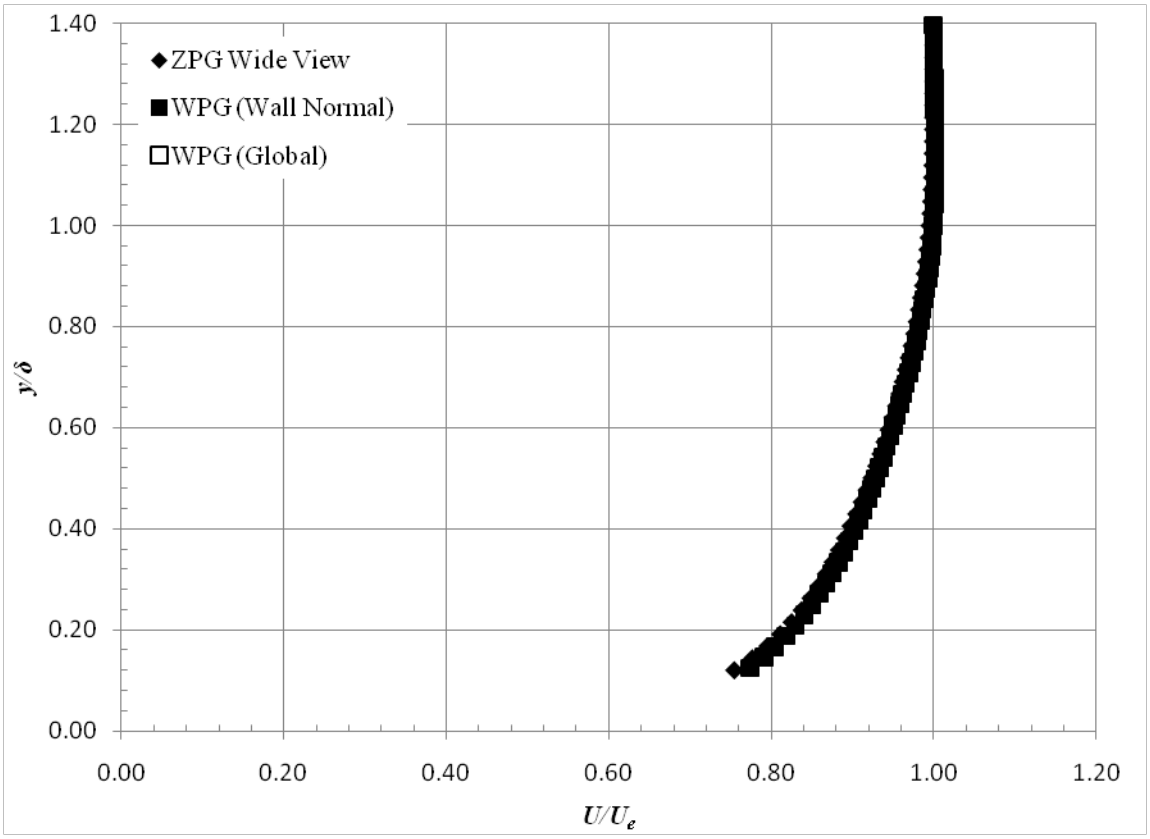

Figure 90: WPG Velocity Profiles – Center

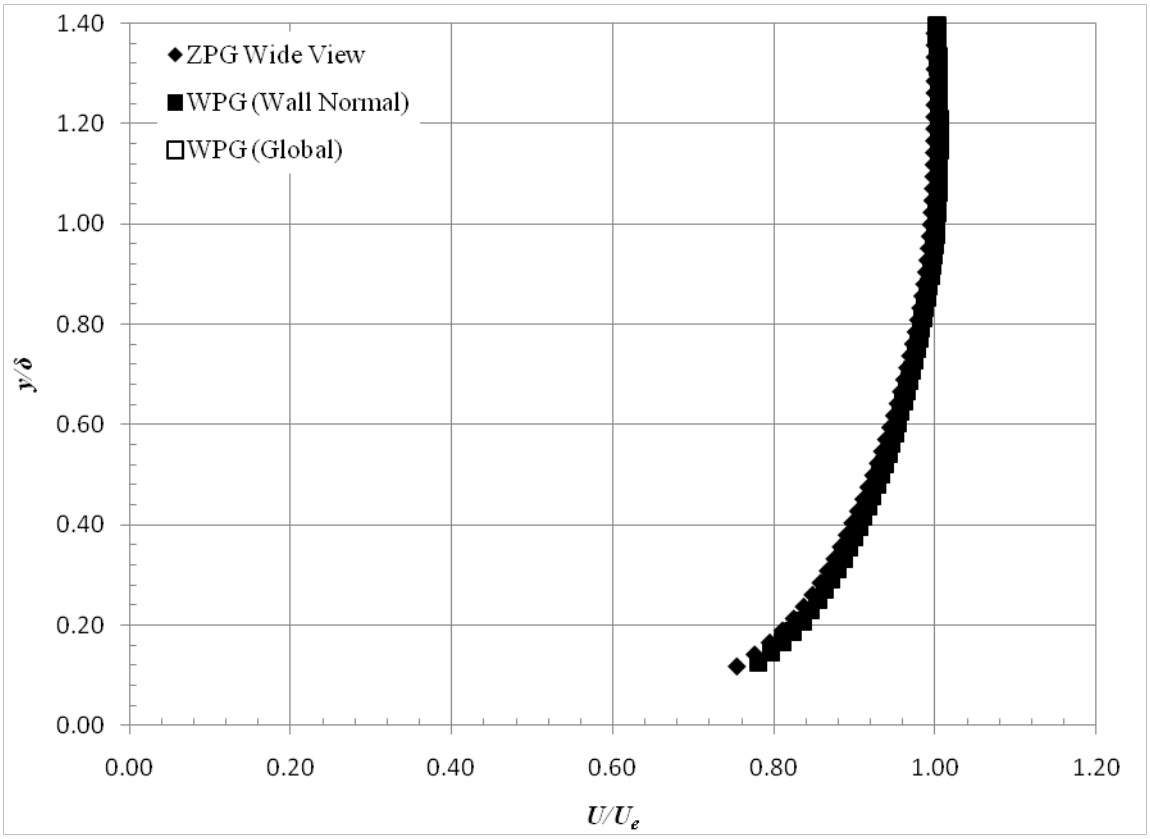

Figure 91: WPG Velocity Profiles - Downstream Side

For the strong pressure gradient model, data was collected at the downstream measurement location. The camera was rotated 10.3 degrees so that the field of view was again parallel to the model surface. A raw PIV image is shown in Figure 92. The wall can easily be seen as a thin white line across the bottom of the image and a slight glare appeared in the bottom right corner of the image. As seen in the following contour plots, this glare caused errors in the PIV correlations therefore contaminating the data in that region. For this data set, the resolution was 65.2 pixels / mm (1656 pixels / inch) with a physical field of view of 24.54 mm x 18.40 mm (0.97 inches x 0.72 inches).

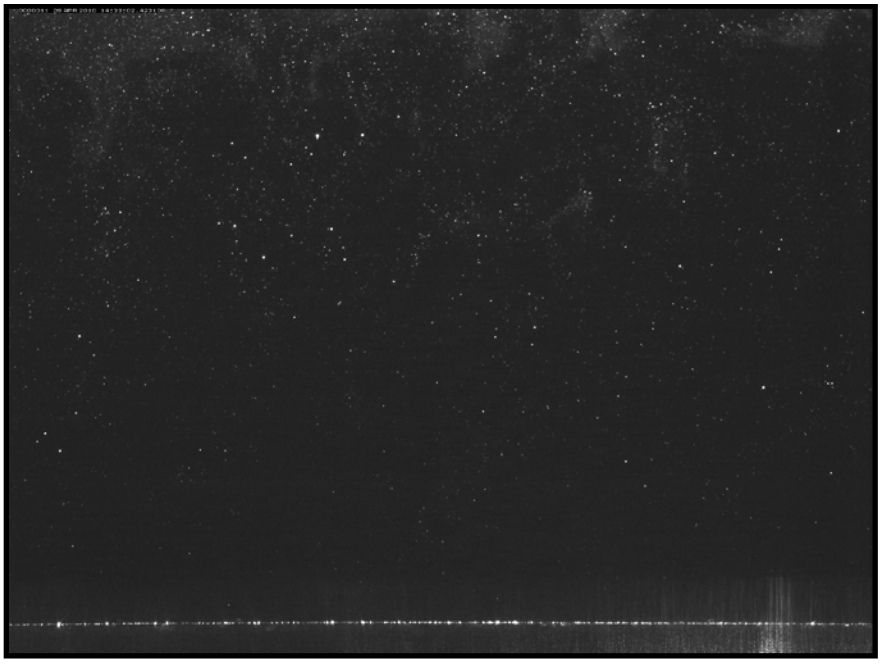

Figure 92: Raw PIV Image of SPG Model at 2nd Measurement Location

Because the camera was rotated to be parallel to the model surface, the local coordinate system no longer aligned with the tunnel coordinate system. The $\bar{u}$ and $\bar{v}$ mean velocity contours in the wall normal coordinate system for the strong pressure gradient model at the second measurement location are shown in Figure 93.

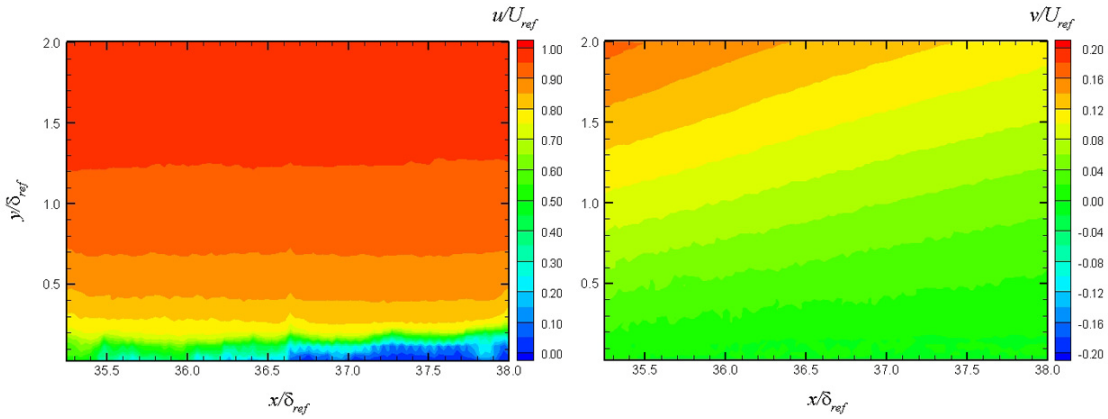

Figure 93: SPG Mean Velocity Contours at 2nd Measurement Location (Wall Normal Coordinate System)

As expected, the boundary layer grows as it travels over the pressure gradient and it is larger than the WPG model. The mean $\overline{u}$ velocity is still primarily along the wall surface while the $\overline{v}$ mean velocity is negligible near the wall and increases to a larger value towards the freestream when compared to the WPG model. As with the weak pressure gradient model, the positive $\overline{v}$ velocity away from the wall in the freestream is due to the local wall normal coordinate system. A larger component of the $\overline{v}$ velocity is in the global streamwise direction compared to the WPG model due to the larger surface curvature angle.

Again using the post-processing FORTRAN code, the velocity vectors were transformed from the wall coordinate system into the global wind tunnel coordinate system by rotating each vector by the camera angle of 10.3 degrees. A comparison of the mean velocity vectors in each coordinate system can be seen in Figure 94.

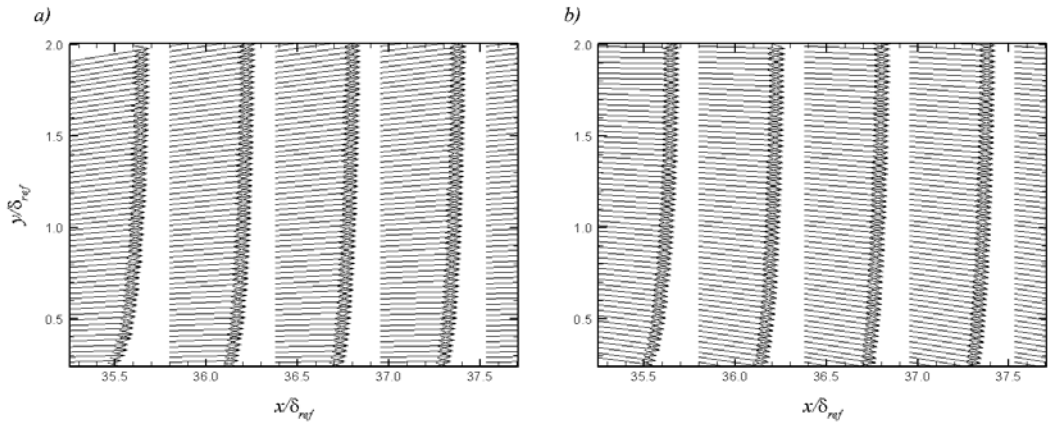

Figure 94: SPG Mean Velocity Vectors in a) Wall Normal Coordinate System, b) Global Coordinate System

Since the camera rotation angle was much larger than the WPG model, the difference in the mean velocity vectors is much easier to see. In the wall normal coordinate system, the vectors move away from the wall while in the global coordinate system, the vectors move towards the wall. Contour plots were again generated for the mean $\overline{u}$ and $\overline{v}$ velocities in the global coordinate system and are shown in Figure 95.

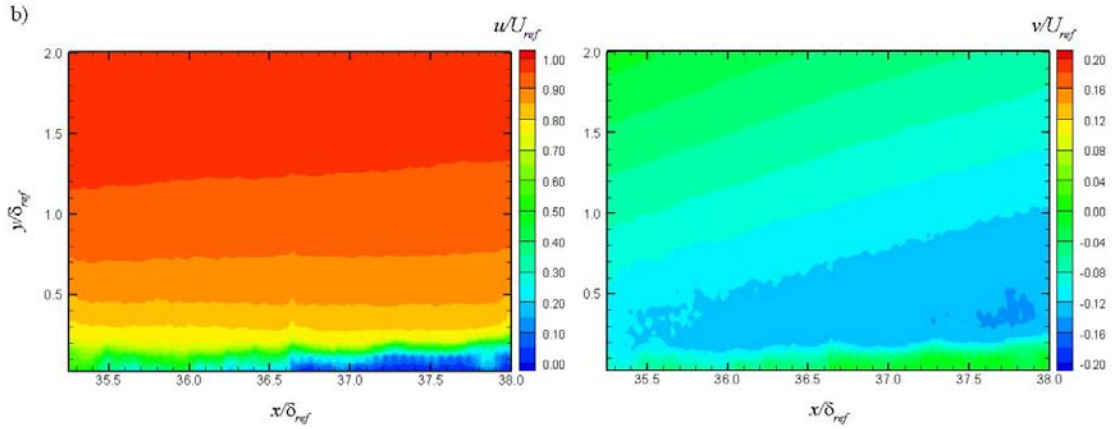

Figure 95: SPG Mean Velocity Contours at 2nd Measurement Location (Global Coordinate System)

The $\overline{u}$ velocity clearly shows the boundary layer growth and is of the same magnitude as before. The $\overline{v}$ velocity contour plot shows that now near the wall, $\overline{v}$ in the global coordinate system is negative and away from the wall, $\overline{v}$ in the global coordinate system is zero. This is expected as the flow along the wall would have a negative $\overline{v}$ velocity and flow in the freestream would have a zero $\overline{v}$ velocity in the global coordinate system.

Velocity profiles were also generated for the strong pressure gradient model at the second measurement location. As with the weak pressure gradient model, the velocity profiles were created by averaging in the streamwise direction approximately 1.0 δ_{ref}. Three sets of velocity profiles were created for the weak pressure gradient model. Profiles from the upstream side of the image (approximately 34-35 x/δ_{ref}) are shown in Figure 96 while profiles from the center of the image (approximately 35-36 x/δ_{ref}) are given in Figure 97. Finally, velocity profiles from the downstream side of

the image (approximately 36-37 x/δ_{ref}) are shown in Figure 98. All of the velocity profiles are plotted in both coordinate systems as well as with the ZPG velocity profile from the upstream measurement location for reference. It can be seen that the $\overline{u}$ mean velocity profile near the wall does again becomes slightly fuller as the flow moves downstream. This result corresponds to the prediction that energy from the turbulence is being channeled back into the mean velocity, therefore increasing the velocity near the wall.

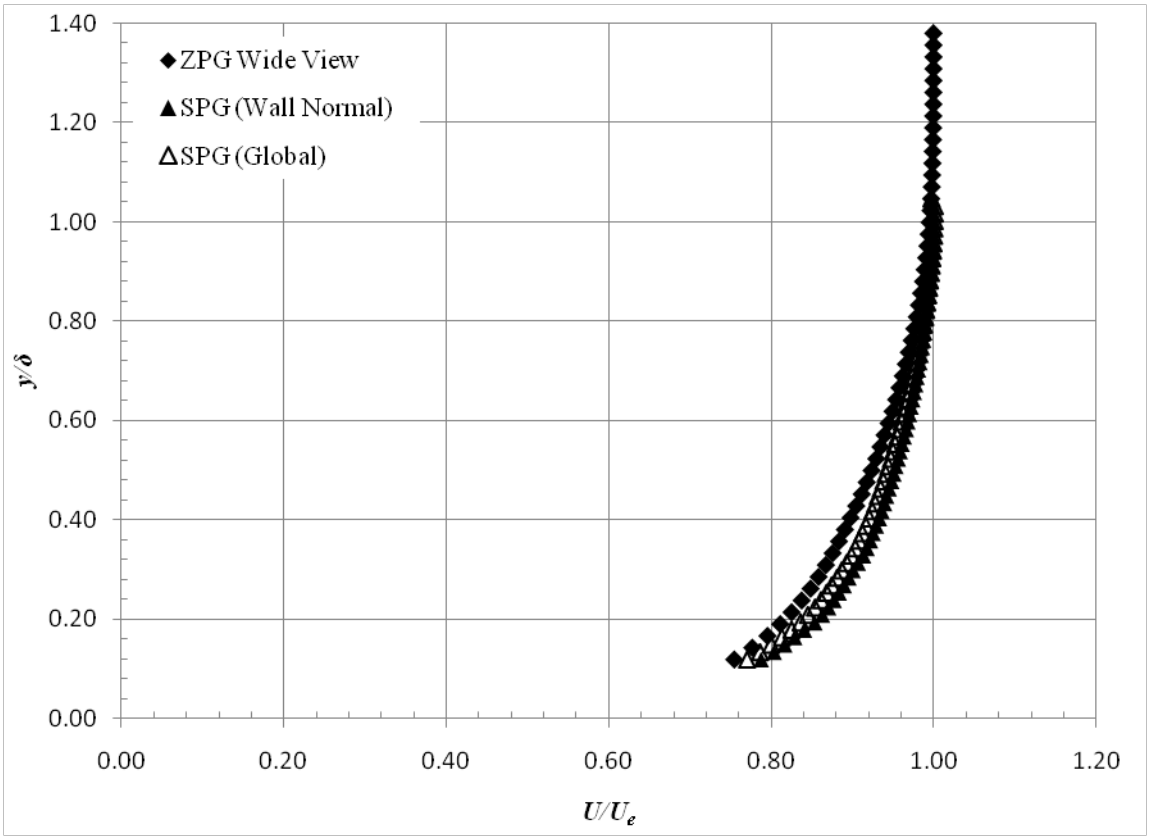

Figure 96: SPG Velocity Profiles - Upstream Side

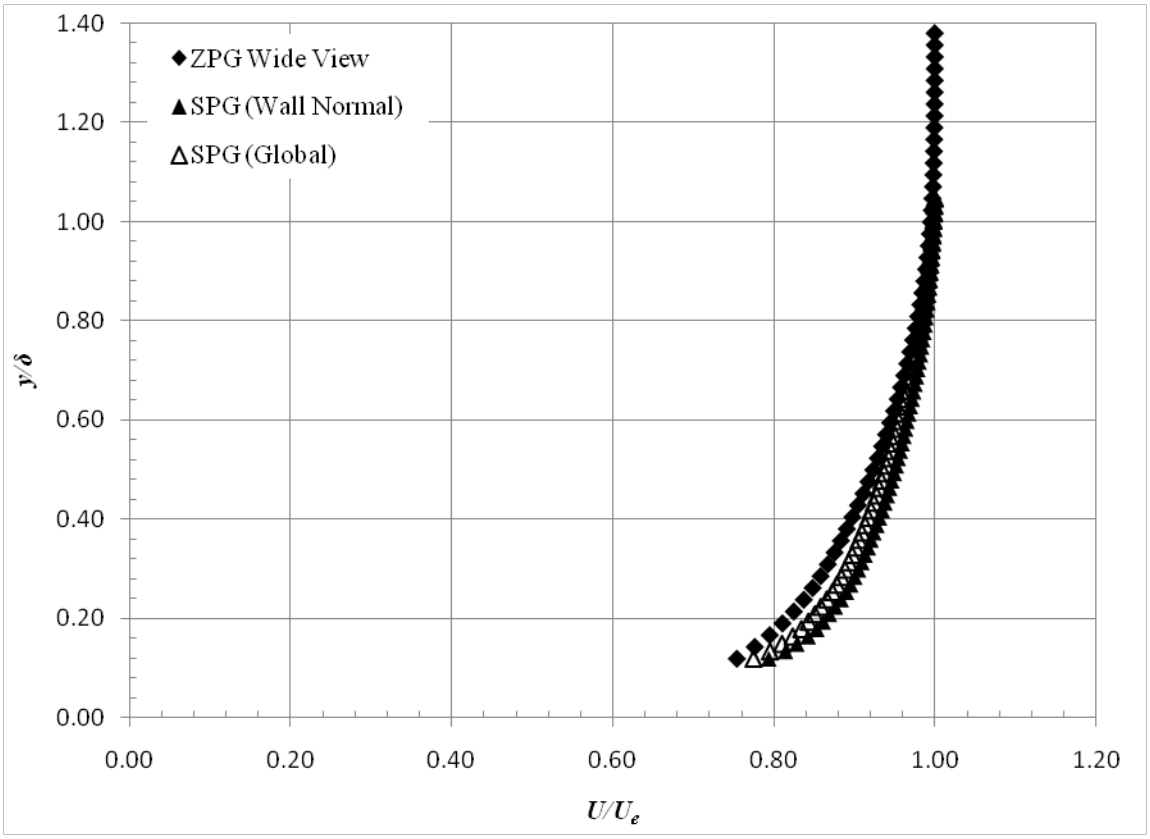

Figure 97: SPG Velocity Profiles - Center

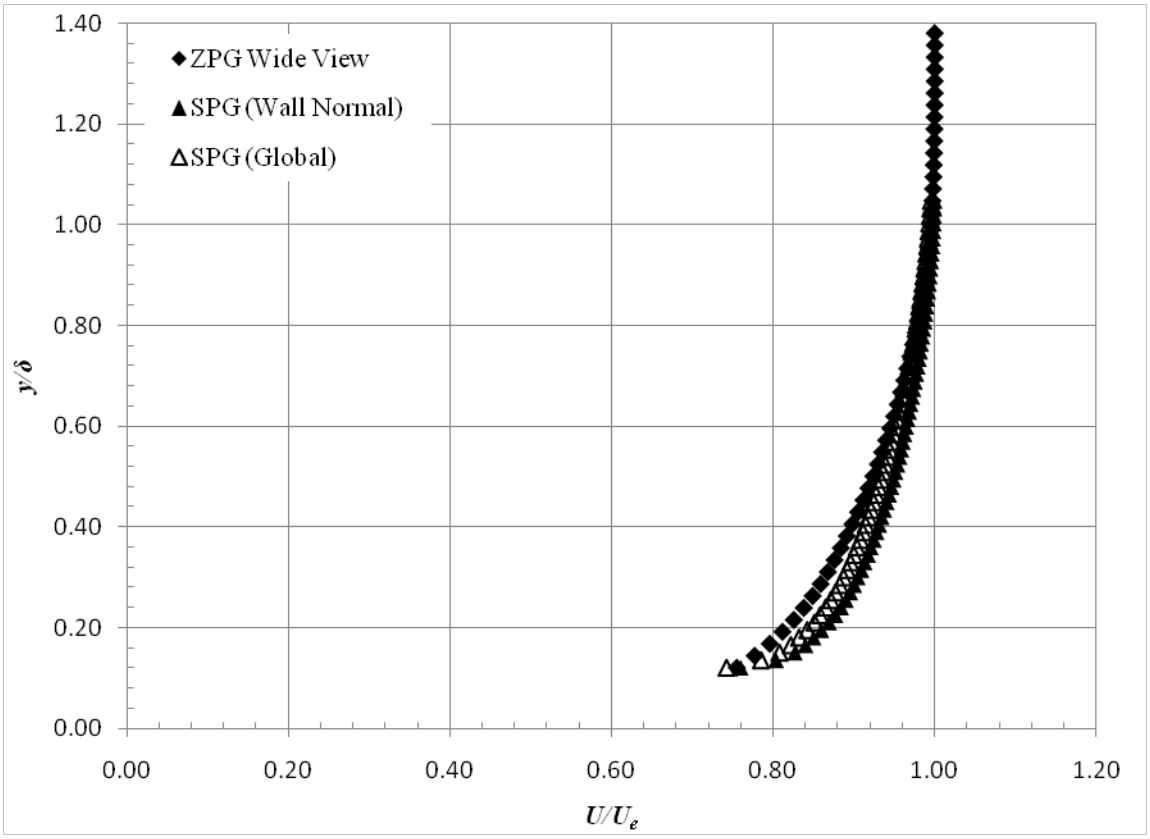

Figure 98: SPG Velocity Profiles - Downstream Side

For both the weak and strong pressure gradients, the coordinate system did not have much of an effect on the velocity profiles. However, transforming the vectors from the local wall normal coordinate system to the global coordinate system did change the sign of the mean $\overline{v}$ velocity and slightly alter the magnitude of the $\overline{u}$ velocity. Additionally, these data were compared to Mach 3 data from Ekoto et al. For the present study, the WPG model exhibited a 1.2% increase in mean velocity at y/δ_{ref} =0.25 while the SPG exhibited a 6.0% increase. The previous study showed a 5.6% increase and a 12.7% increase for the WPG and SPG models respectively. Therefore, to address scientific question 4 described in Chapter I, the mean velocity is effected less by the favorable pressure gradient due to the increased Mach number.

Mean Velocity Gradient Measurements

Velocity gradient data were measured using particle image velocimetry as discussed in Chapter IV. Streamwise and transverse mean velocity gradients for the $\overline{u}$ and $\overline{v}$ velocity components were created using an explicit central differencing scheme.

$$f'(x) \approx \frac{f(x+h) - f(x-h)}{2h}$$

From the mean velocity gradients, the mean strain rate and vorticity were calculated.

$$\text{mean strain rate} = \frac{d\overline{v}}{dx} + \frac{d\overline{u}}{dy} \tag{4.5}$$

$$\text{vorticity} = \frac{d\overline{v}}{dx} - \frac{d\overline{u}}{dy} \tag{4.6}$$

Contour plots of the primary velocity gradient $d\bar{u}/dy$, and the extra strain rates $d\bar{u}/dx$, $d\bar{v}/dx$, $d\bar{v}/dy$ were created for each pressure gradient model and measurement location. The velocity gradient contours were normalized by the reference length scale δ_{ref} and the reference velocity U_{ref} while the profiles were normalized by δ and U_e.

The contour plots for the zero pressure gradient model wide view and zoom view at the first measurement location are shown in Figure 99 and Figure 100 respectively. The largest velocity gradient is the primary gradient while the extra strain rates are all close to zero for both fields of view. Closer to the wall, the extra strain rates increased slightly, but were still not of the same order as the primary velocity gradient. The vorticity and the mean strain rate were nearly zero in the freestream as expected. The vorticity became increasingly negative closer to the wall and the mean strain rate became increasing positive, with a normalized value of -0.50 and 0.50 respectively near the wall.

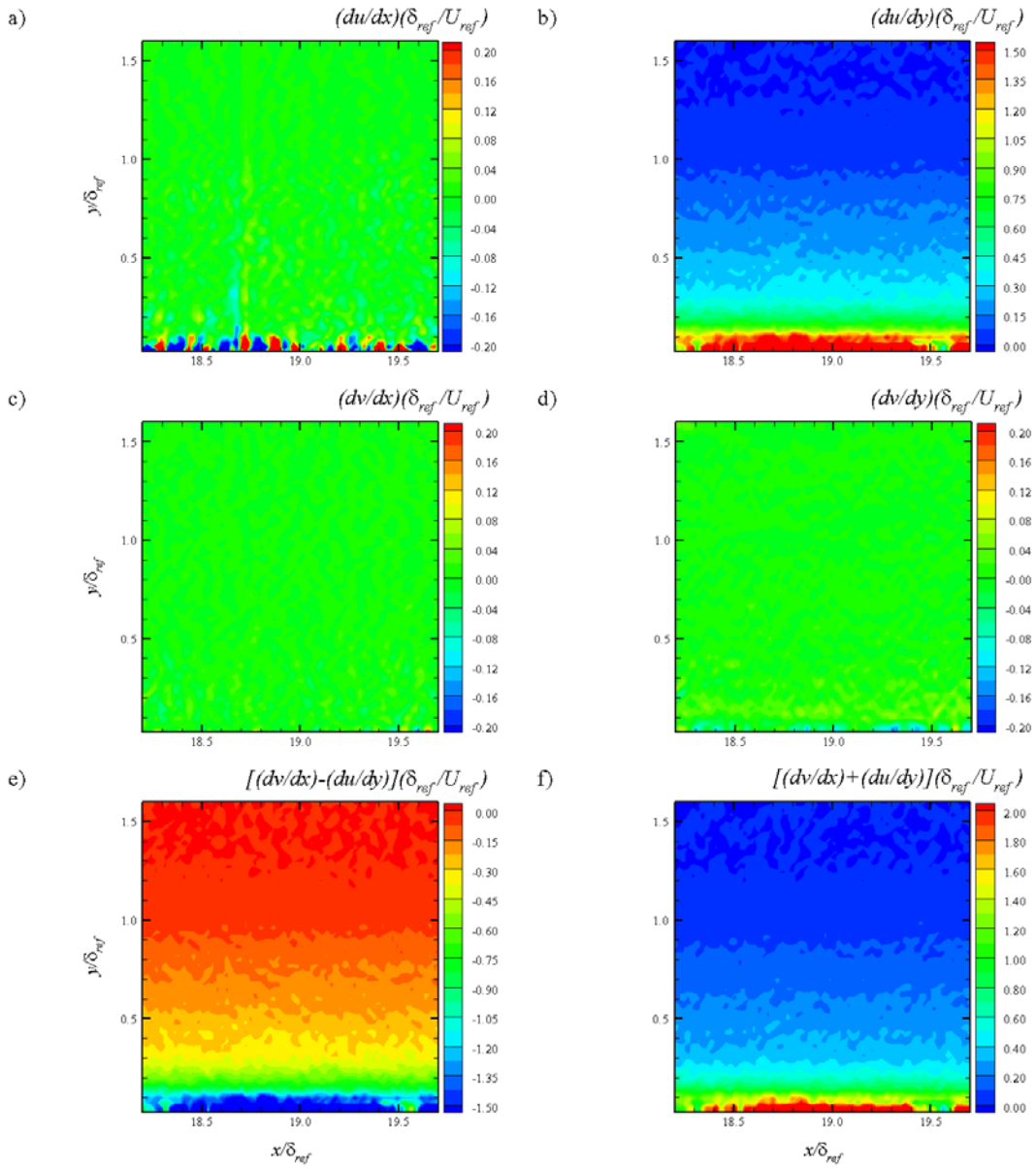

Figure 99: ZPG Wide View Mean Velocity Gradient Contours at 1st Measurement Location

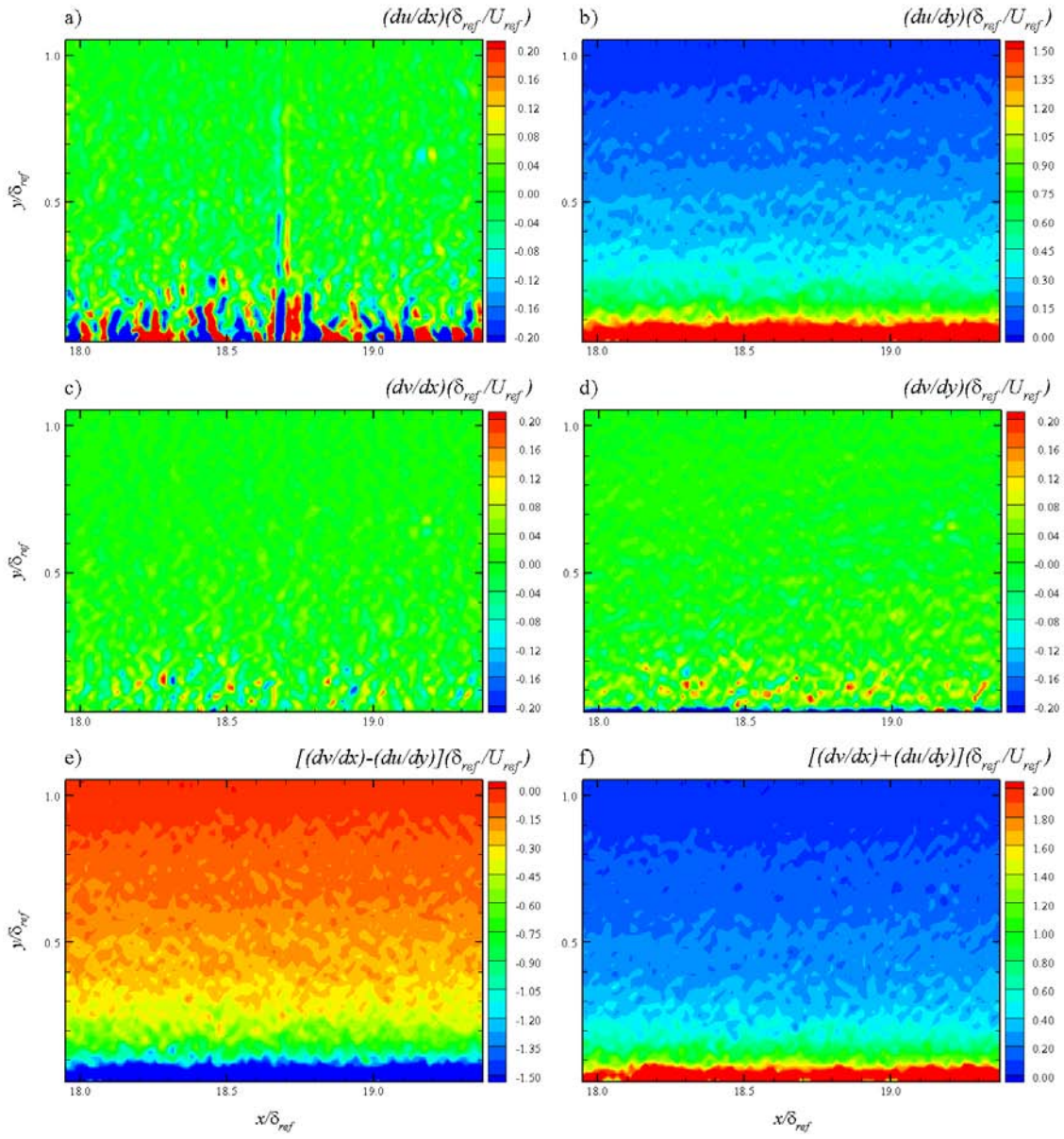

Figure 100: ZPG Zoom View Mean Velocity Gradient Contours at 1st Measurement Location

The contour plots for the weak pressure gradient model mean velocity gradients are shown in Figure 101 in the wall normal coordinate system and Figure 102 in the global coordinate system. It can clearly be seen that both sets of contour plots look identical, regardless of the coordinate system; this is due to the small model surface angle of 1.6 degrees. As with the ZPG case the dominant velocity gradient is $d\bar{u}/dy$ while the other gradients are nearly zero for the entire field of view. Again a slight increase in the extra strain rates can be seen close to the wall, but not of the same order of the primary gradient. The vorticity and mean strain are near zero in the freestream. Near the surface, the vorticity becomes more negative with a minimum value of -0.50, the same as the ZPG case. The mean strain rate becomes more positive closer to the wall with a maximum value of 0.50 at the wall. Again, this is comparable to the maximum value for the ZPG case. If the reader looks closely at the contours plots, it will be noticed that all of the velocity gradient contours show a discrepancy in the data below $y/\delta \approx 0.2$. The author believes these areas are due to the lack of good data vectors near the wall because of sparse PIV seeding density. This explains the areas of solid blue or red in the contour plots below.

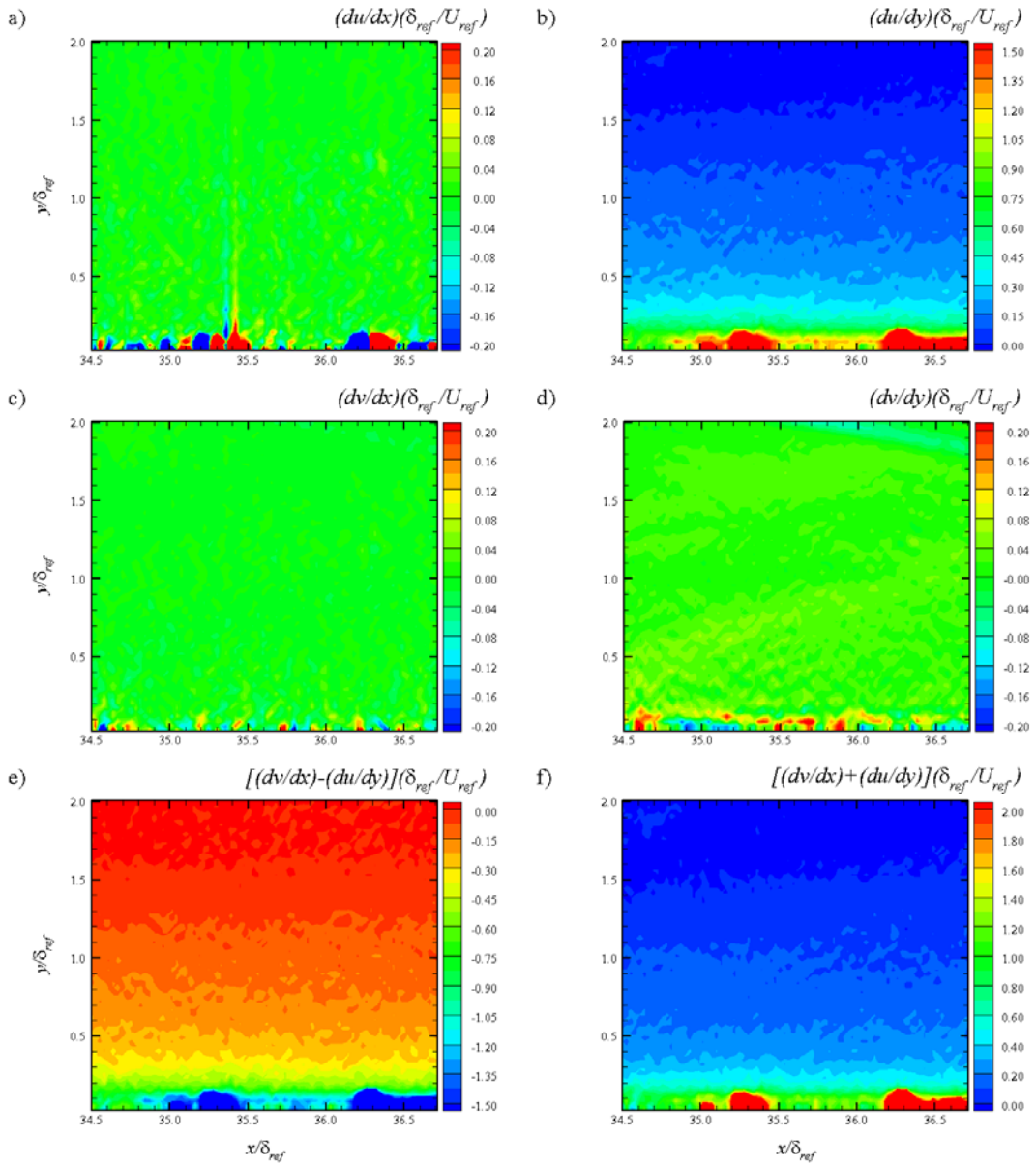

Figure 101: WPG Mean Velocity Gradient Contours at 2nd Measurement Location (Wall Normal Coordinate System)

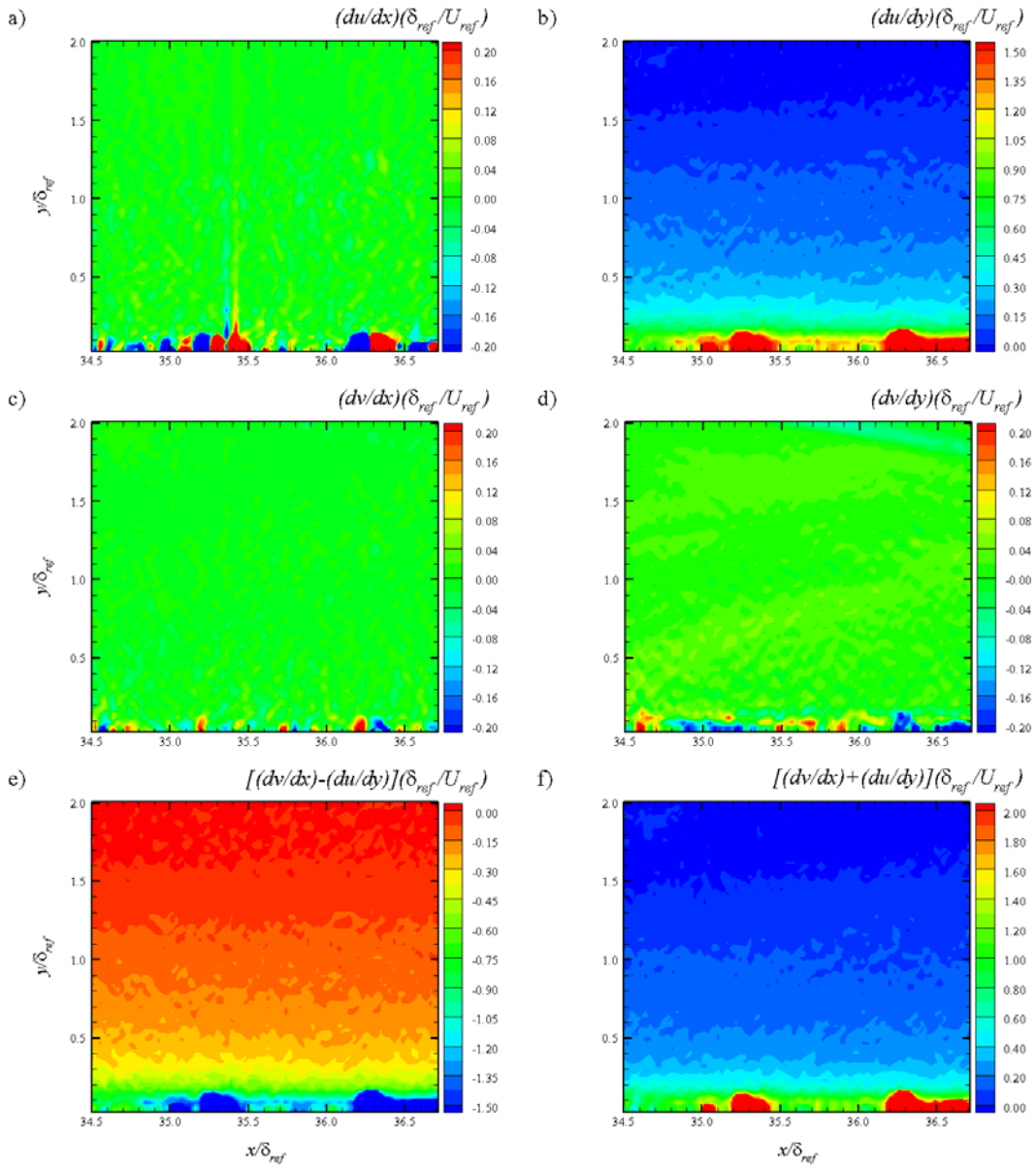

Figure 102: WPG Mean Velocity Gradient Contours at 2nd Measurement Location (Global Coordinate System)

The contour plots of the strong pressure gradient model at the second measurement location for the wall coordinate system and global coordinate system are shown in Figure 103 and Figure 104 respectively. As with the ZPG and WPG cases, the mean velocity gradients for the strong pressure gradient model are all close to zero except for the primary gradient, $d\bar{u}/dy$. For the wall normal coordinate system, $d\bar{v}/dy$ shows a larger magnitude increase near the wall than for the WPG case. This is expected because the coordinate axes are rotated by the camera angle of 10.3 degrees with respect to the freestream axes. Therefore, there is a larger velocity component in the $\bar{v}$ direction due to the global $\bar{u}$ velocity. The vorticity and mean strain rate follow the same trend as the ZPG and WPG cases, however near the wall, the vorticity only has a minimum value of approximately -0.40 and the mean strain rate has a maximum value of approximately 0.40. This shows that in the wall normal coordinate system, the vorticity and mean strain rate are lower for the SPG case than for the ZPG and WPG cases. This follows previous studies that the turbulence decreases over the favorable pressure gradient and therefore the vorticity and mean strain rate should also decrease. It is believed that this trend was also exhibited on the WPG model, but due to the small wall curvature angle, the decrease in vorticity and mean strain rate were difficult to detect.

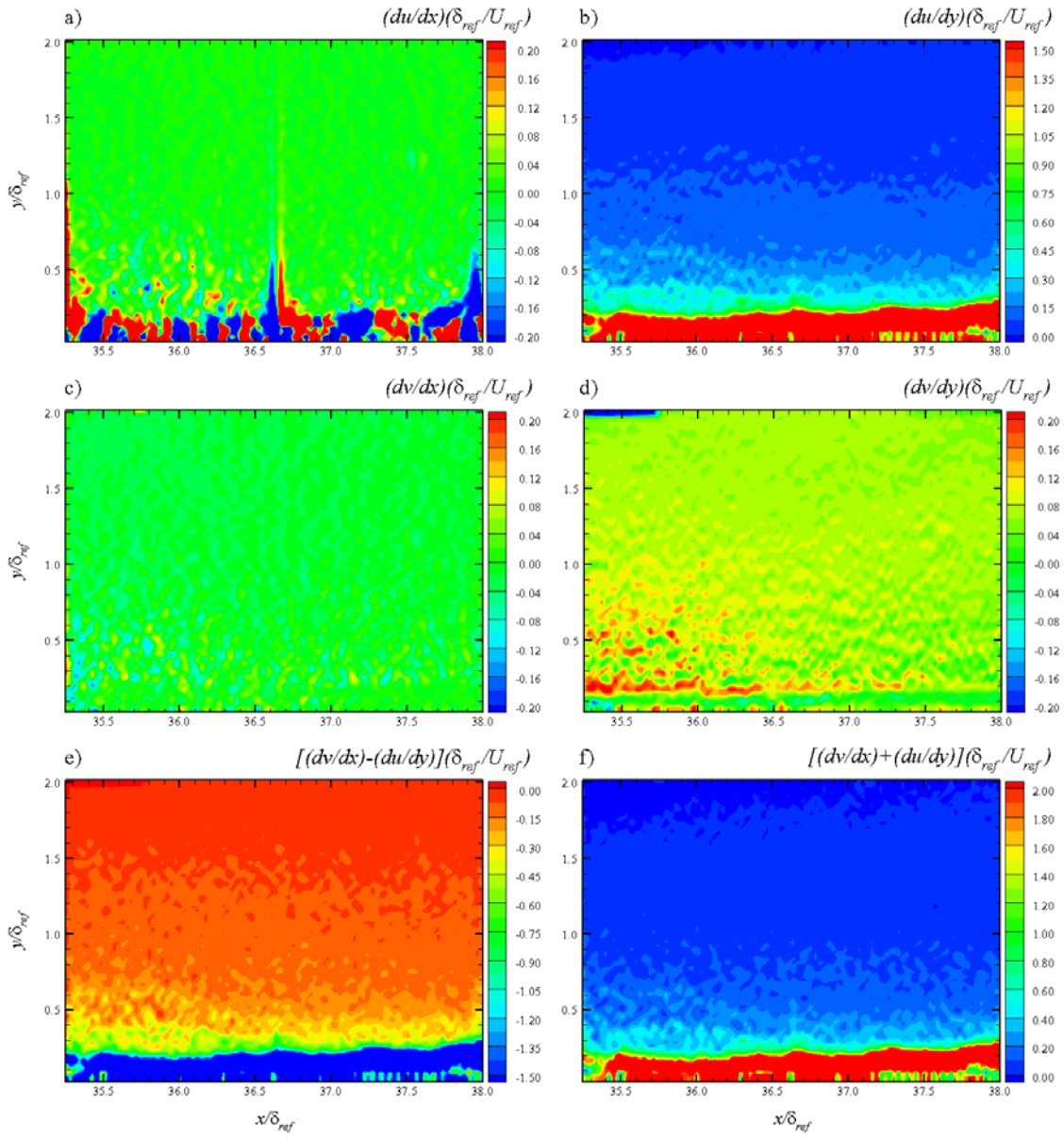

Figure 103: SPG Mean Velocity Gradient Contours at 2nd Measurement Location (Wall Normal Coordinate System)

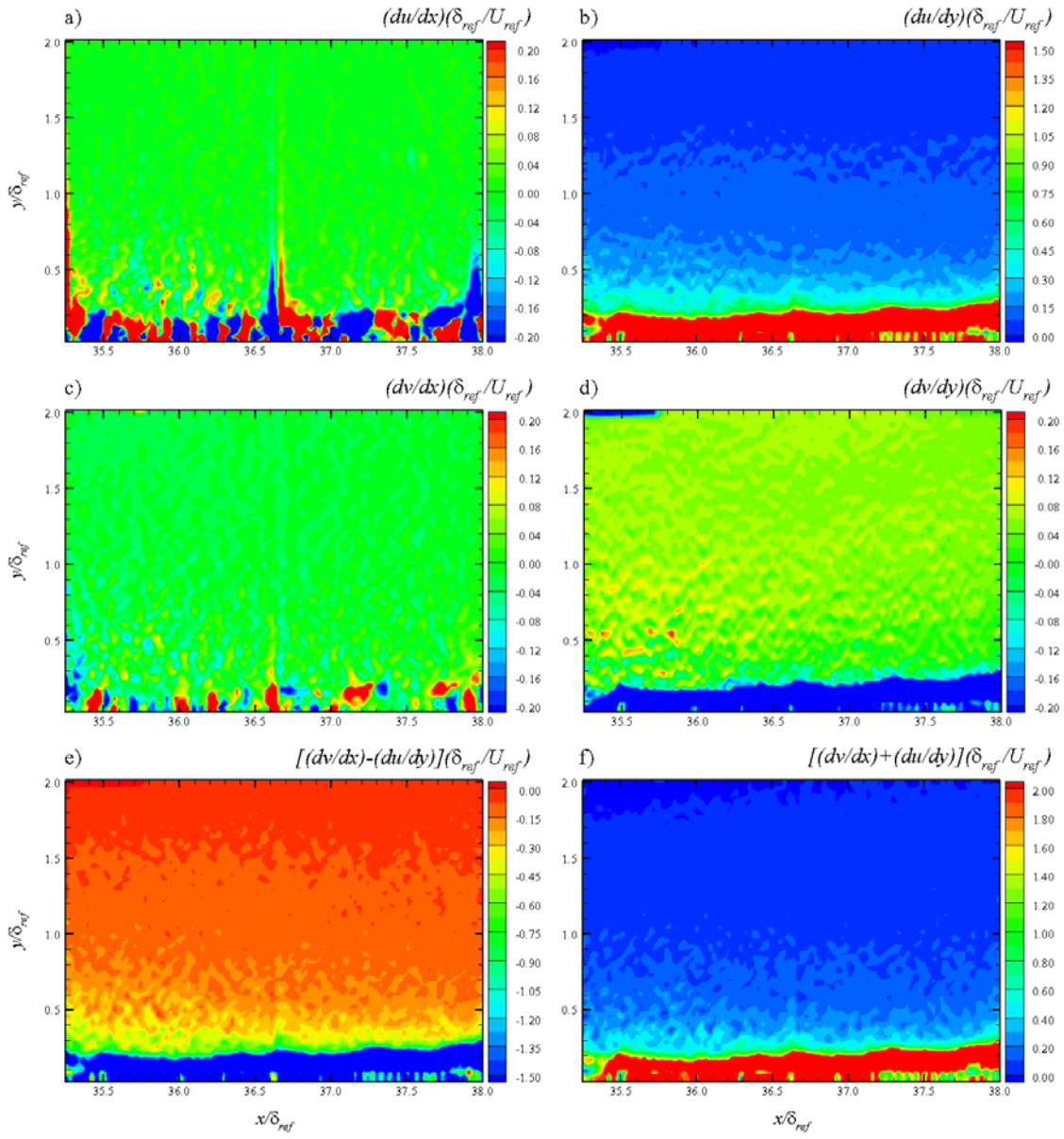

Figure 104: SPG Mean Velocity Gradient Contours at 2nd Measurement Location (Global Coordinate System)

Mean velocity gradient profiles were extracted from the above contours by averaging over 1.0 δ_{ref} in the streamwise direction at the center of each field of view. For comparison, all of the pressure gradient model results were plotted on the same axes for each velocity gradient. The velocity gradient profiles provide a quantitative comparison between the different models and can be easier to read than the above contour plots. The $d\overline{u}/dx$ velocity gradient is shown in Figure 105. For the ZPG model at the first measurement location, the $d\overline{u}/dx$ velocity gradient is very slightly negative but can be considered to be zero. For the WPG, the gradient is slightly negative in the freestream but approaches zero and actually becomes slightly positive close to the wall. Finally, for the SPG model, the $d\overline{u}/dx$ velocity gradient is very near zero in the freestream and becomes increasingly positive closer to the wall. A trend for the $d\overline{u}/dx$ velocity gradient can be seen; for increased favorable pressure gradient, the $d\overline{u}/dx$ velocity gradient increases, especially near the wall.

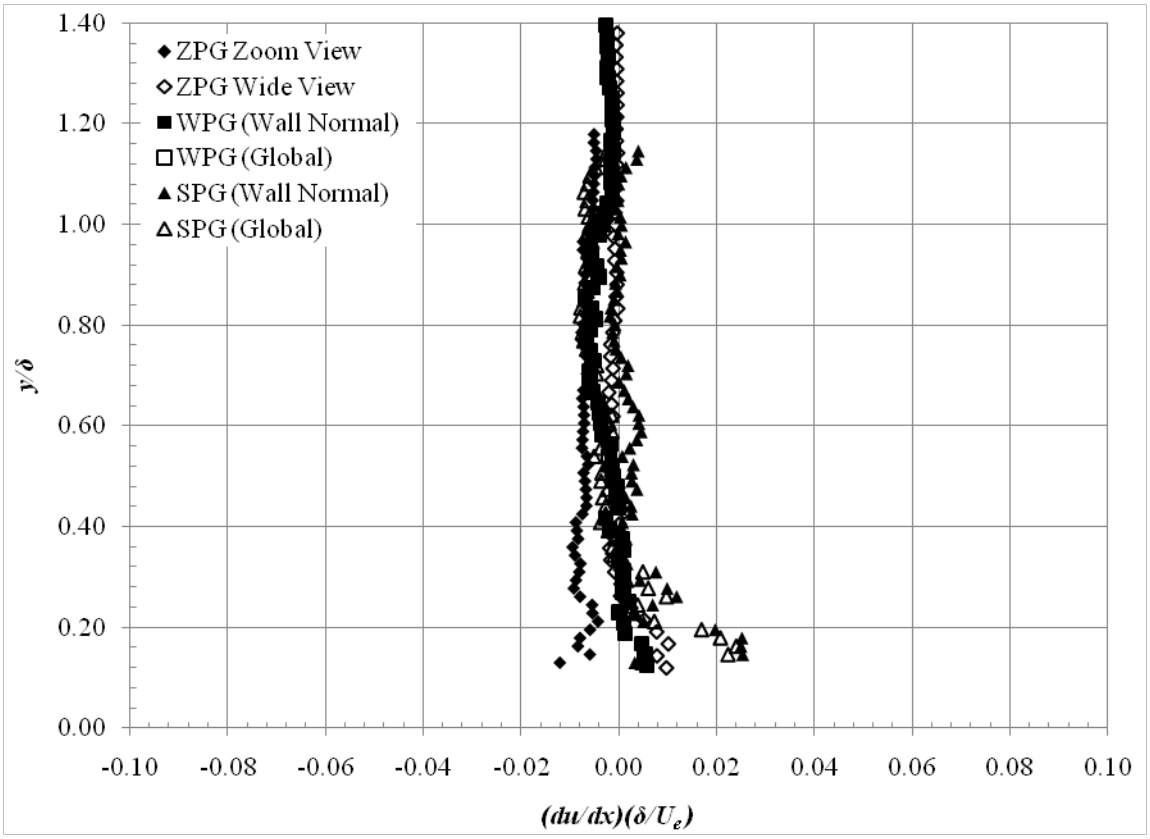

Figure 105: $d\bar{u}/dx$ **Velocity Gradient Profiles**

The $d\bar{u}/dy$ mean velocity gradient profile is shown in Figure 106. This is the primary velocity gradient and is much larger than the extra strain rates for all cases. The ZPG and WPG models displayed similar results for the $d\bar{u}/dy$ velocity gradient. In the freestream, the $d\bar{u}/dy$ velocity gradient is close to zero, but still larger than other velocity gradients and increases in magnitude closer to the wall. For the SPG case, the $d\bar{u}/dy$ velocity gradient is nearly the same as the ZPG and WPG models, but the gradient does increase slightly more near the wall when compared to the ZPG and WPG cases.

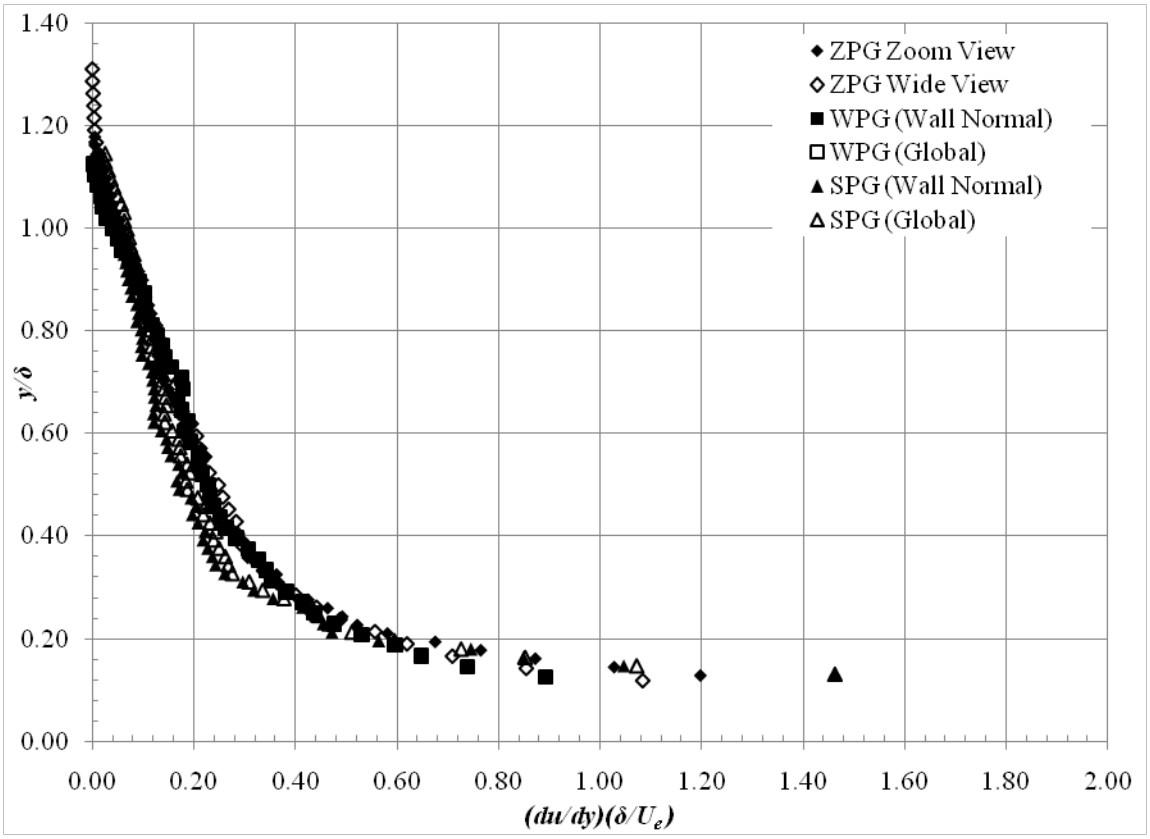

Figure 106: $d\bar{u}/dy$ **Velocity Gradient Profiles**

The $d\bar{v}/dx$ mean velocity gradient profiles for each pressure gradient model are shown in Figure 107. For the zero pressure gradient model, the $d\bar{v}/dx$ gradient is very near zero all the way to the wall. For the WPG model, the $d\bar{v}/dx$ velocity gradient is close to zero in the freestream and near the wall, but becomes slightly negative with a peak at approximately $0.50\ y/\delta$. For the SPG model, the $d\bar{v}/dx$ velocity gradient is more negative in the freestream and approaches zero near the wall. This is due to the larger wall curvature which is turning the air and changing the local flow direction.

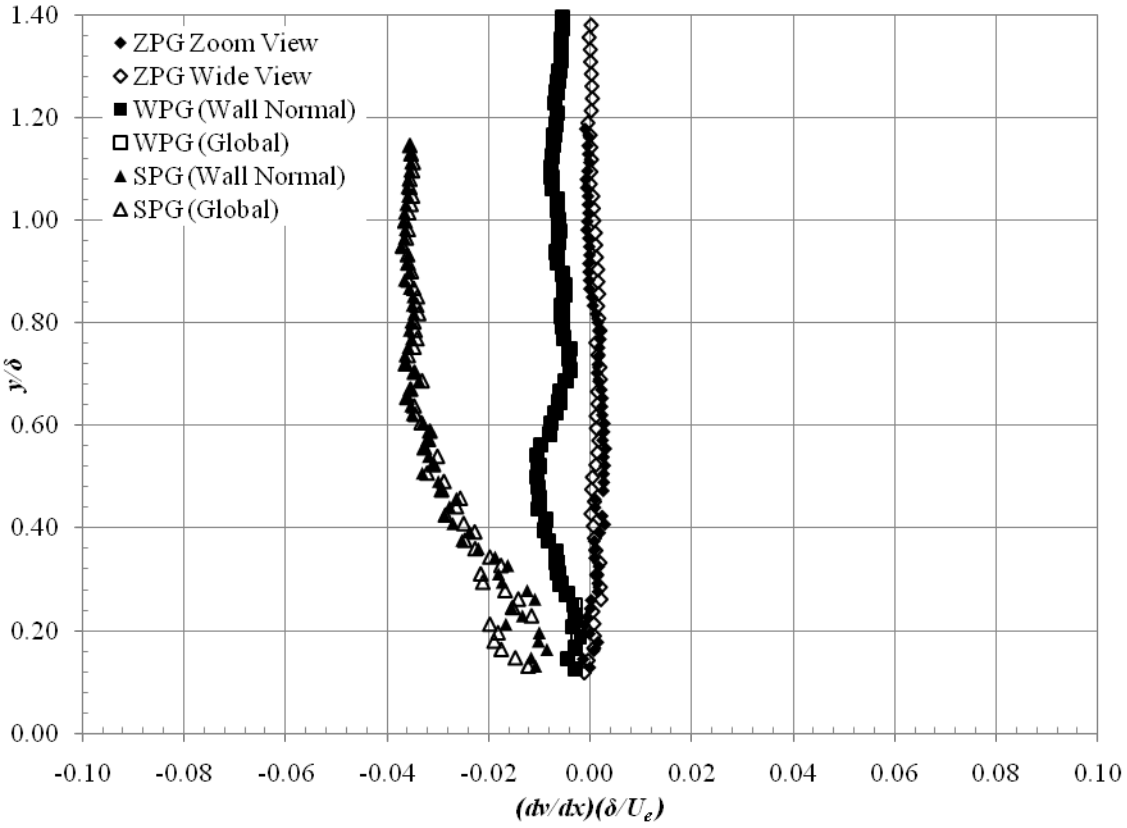

Figure 107: $d\bar{v}/dx$ **Velocity Gradient Profiles**

The $d\overline{v}/dy$ mean velocity gradient profile for all pressure gradient models is shown in Figure 108. For the ZPG model, the $d\overline{v}/dx$ velocity gradient profile is close to zero through the entire field of view. The scatter increases near the wall and the velocity gradient becomes slightly positive. For the WPG mode, the $d\overline{v}/dx$ velocity gradient exhibits a cyclical pattern from the freestream to the wall with a maximum value near $0.50\ y/\delta$; at $0.9\,y/\delta$ the $d\overline{v}/dx$ velocity gradient is minimized. The velocity does not change between the two coordinate systems for the WPG model due to the small angle difference. For the SPG model, the $d\overline{v}/dx$ velocity gradient changes significantly on the coordinate system. For the wall normal coordinate system, the $d\overline{v}/dx$ velocity gradient is relatively large compared to the ZPG and WPG models, with a normalized value between 0.10 and 0.15 for much of the field of view. Nearer the wall, the scatter increases and the nominal value is more difficult to determine. For the SPG case transformed into global coordinate, the $d\overline{v}/dx$ velocity gradient is much smaller and negative for the entire field of view. In the freestream the velocity gradient has the lowest value and slightly approaches zero nearer the wall. The large difference for the two coordinate systems is due to the definition of the $\overline{v}$ velocity. In the wall normal coordinate system, the $\overline{v}$ velocity has a component in the freestream direction that significantly changes the computed gradient.

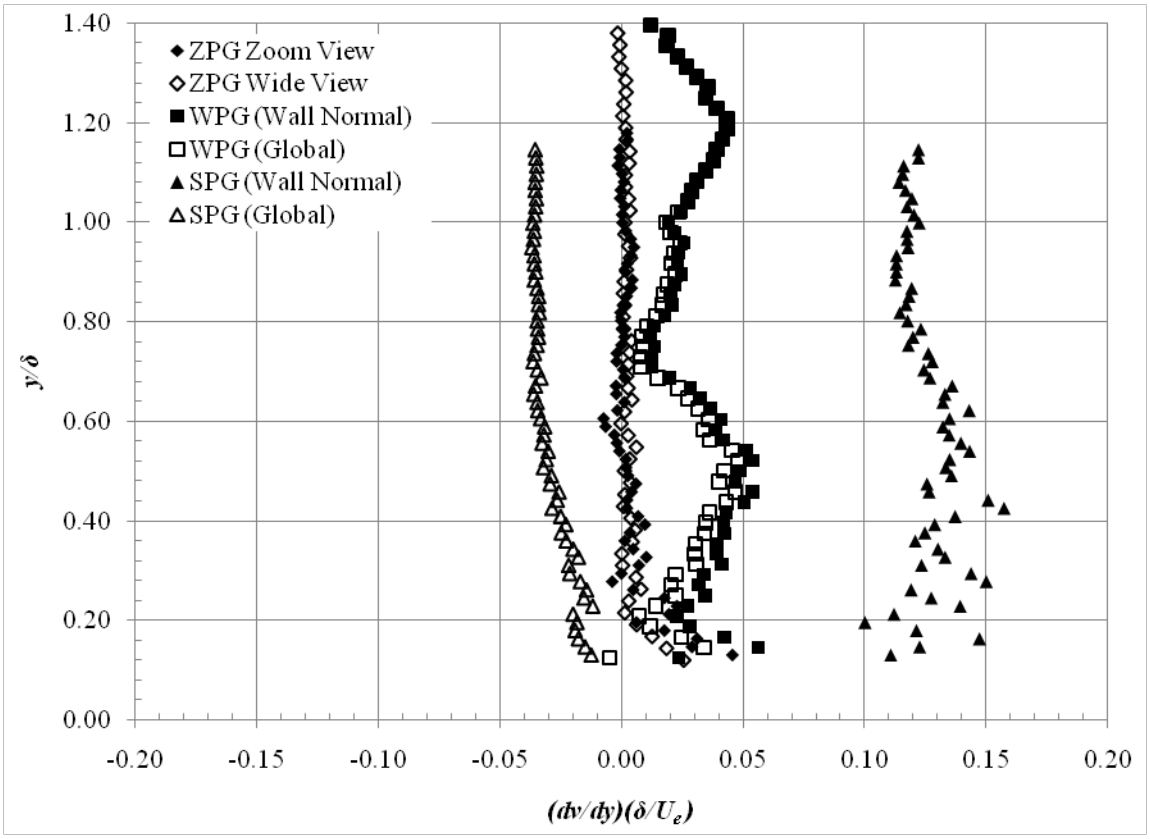

Figure 108: $d\bar{v}/dy$ **Velocity Gradient Profiles**

The vorticity $\left(d\bar{v}/dx - d\bar{u}/dy\right)$ profile plot is shown in Figure 109. This quantity was expected to be negative because the primary velocity gradient $d\bar{u}/dy$ is much larger than the extra strain rate $d\bar{v}/dx$. In the freestream, the vorticity approaches zero for all pressure gradient models. Because the flow is more isentropic in the freestream, this was expected. Approaching the wall, the vorticity becomes more negative with stronger values for the SPG compared to the ZPG and WPG models. It can also be seen that vorticity is fairly independent of the coordinate system for the WPG and SPG cases.

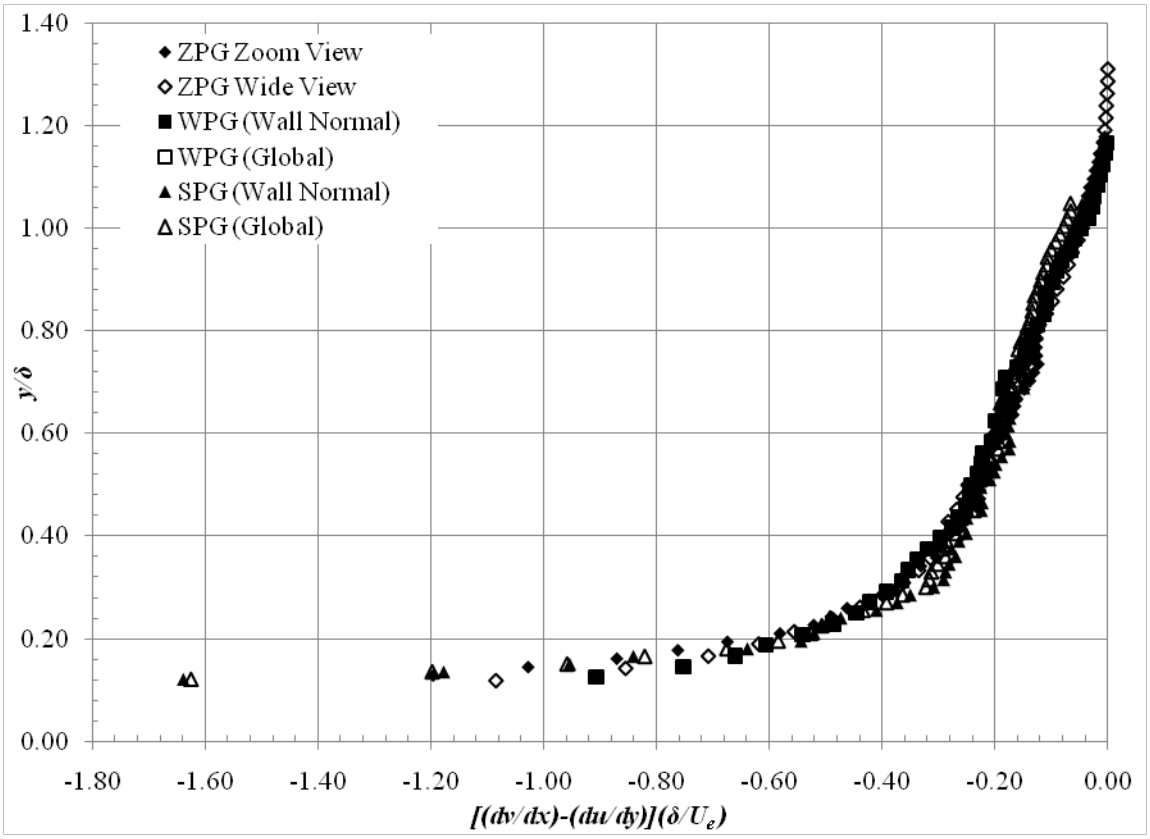

Figure 109: $\left(d\bar{v}/dx - d\bar{u}/dy\right)$ **Velocity Gradient Profiles**

The profile plot of the mean strain rate $\left(d\bar{v}/dx + d\bar{u}/dy\right)$ for all of the pressure gradient models is given in Figure 110. Again, the primary velocity gradient $d\bar{u}/dy$ is much larger than the extra strain rate $d\bar{v}/dx$ and therefore the mean strain rate follows closely with $d\bar{u}/dy$. In the freestream, the mean strain rate is near zero as expected, but closer to the wall, the mean strain rate increases. Again, the ZPG and WPG models are very similar and the SPG case shows the mean strain rate increasing farther from the model surface and to a larger value close to the wall. This is expected because the mean

strain rate is closely dependent on the $d\bar{u}/dy$ mean velocity gradient which increases near the wall.

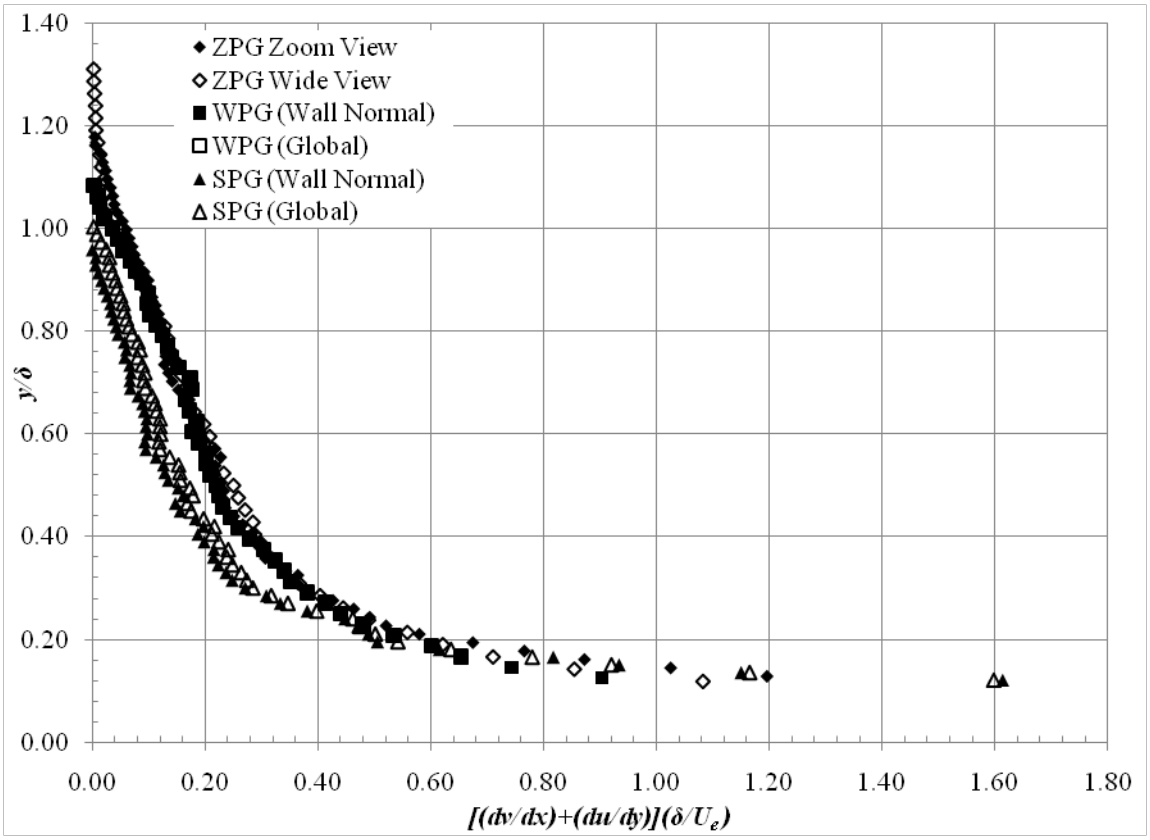

Figure 110: $\left(d\bar{v}/dx + d\bar{u}/dy\right)$ **Velocity Gradient Profiles**

Turbulent Flow Measurements

All of the turbulent flow quantities were calculated based on the particle image velocimetry data described in Chapter IV. The first and second order turbulent statistics are presented in the first two subsections. The turbulent stress production and all of its components are presented in the third subsection. In the next subsection, turbulent stress

principal axes analyses are presented. Finally, the instantaneous velocity fields are used to perform quadrant decomposition analyses of the Reynolds stresses in the last subsection.

Turbulence Intensities

The purpose of these measurements were to determine the effect of the favorable pressure gradients on the boundary layer turbulence intensities. These data addressed scientific question 1 described in Chapter I.

The turbulence intensities were measured using particle image velocimetry. The velocity fluctuations were determined by subtracting the instantaneous velocity fields from the mean velocity field using the in-house FORTRAN post-processing code. Contour plots of *u* and *v* turbulence intensities were created for each pressure gradient model and the turbulence intensities were normalized by taking their square root and non-dimensionalizing by the reference velocity $(1/U_{ref})$ described above.

The contour plots for the *u* and *v* turbulence intensities for the zero pressure gradient model at the first measurement location are shown in Figure 111. For both the wide and zoom field of view, the turbulence intensities approach zero in the freestream as should be expected. The axial turbulence intensity, $\sqrt{\overline{u'^2}}$, was twice as high as the normal turbulence intensity, $\sqrt{\overline{v'^2}}$, for the entire field.

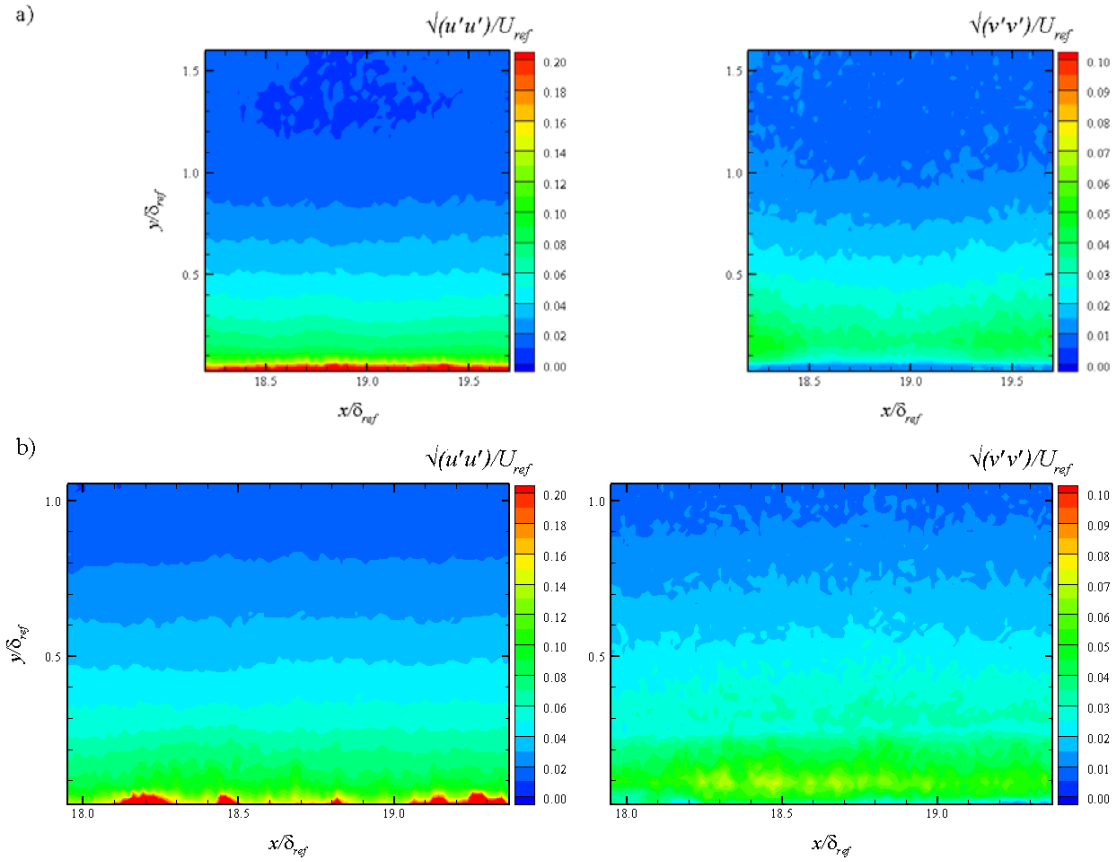

Figure 111: ZPG Turbulence Intensities Contours at 1st Measurement Location a) Wide View, b) Zoom View

The turbulence intensities contour plots for the weak pressure gradient model at the downstream measurement location are shown in Figure 112 and Figure 113 for wall normal and global coordinates respectively. Again, it can be seen that both the *u* and *v* turbulence intensities approach zero in the freestream. The levels near the wall are similar to those seen for the ZPG case. This is due to the small wall curvature of the weak pressure gradient model. However, it can clearly be seen that the turbulence begins to increase at a larger y/δ_{ref} location than the ZPG model due to the increased

boundary layer thickness. Additionally, the *u* and *v* turbulence intensities seem to be independent of the coordinate system; again attributed to the small wall curvature angle.

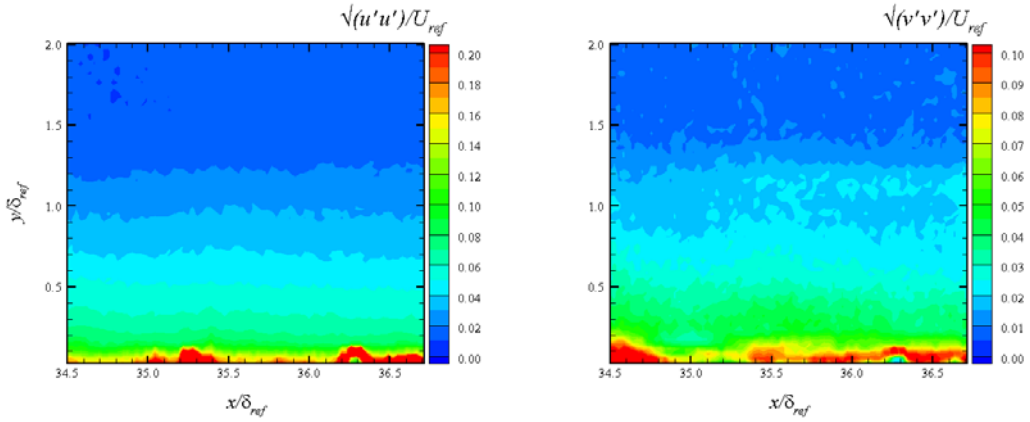

Figure 112: WPG Turbulence Intensities Contours at 2nd Measurement Location (Wall Normal Coordinate System)

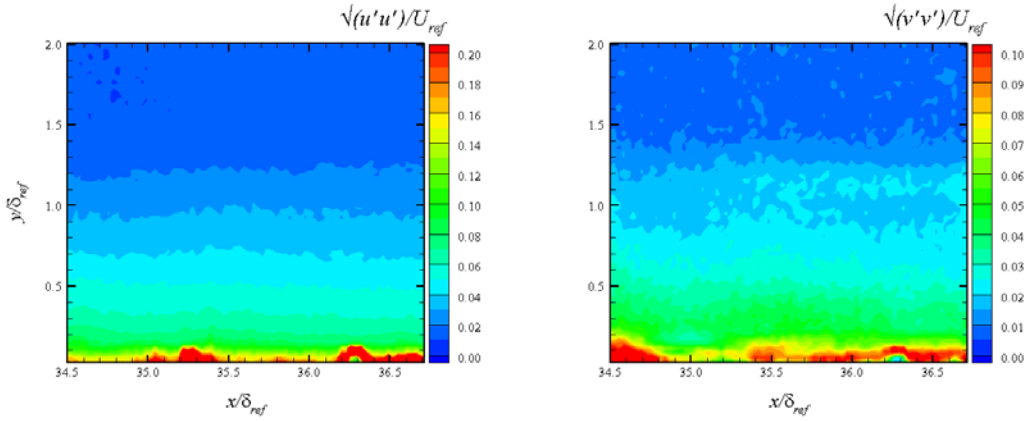

Figure 113: WPG Turbulence Intensities Contours at 2nd Measurement Location (Global Coordinate System)

The contour plots of the *u* and v turbulence intensities for the strong pressure gradient model at the downstream measurement location are given in Figure 114 and

Figure 115 for the wall normal and the global coordinate system respectively. Again, similar overall trends are seen in the SPG case. The large red regions in the contour plots are due to bad data and should omitted. The turbulence intensities decrease towards the freestream, however not to the level seen in the ZPG and WPG cases. This is due to the large boundary layer growth over the strong favorable pressure gradient and the physical field of view. The local freestream flow is out of the current SPG field of view so the turbulence intensities cannot be compared to the other models, but the trend is obvious and comparable to the ZPG and WPG models. The expansion of the flow due to the strong pressure gradient is clearly seen in the *u* turbulence intensity contour plots from the expansion of the color levels from left to right. Even with a rotation of over ten degrees, the *u* and *v* turbulence intensities do not change significantly from one coordinate system to the other.

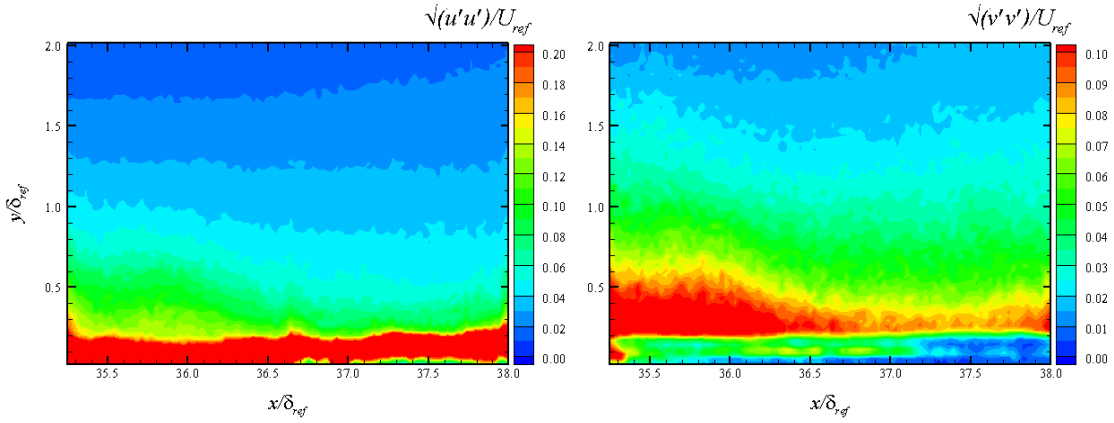

Figure 114: SPG Turbulence Intensities Contours at 2nd Measurement Location (Wall Normal Coordinate System)

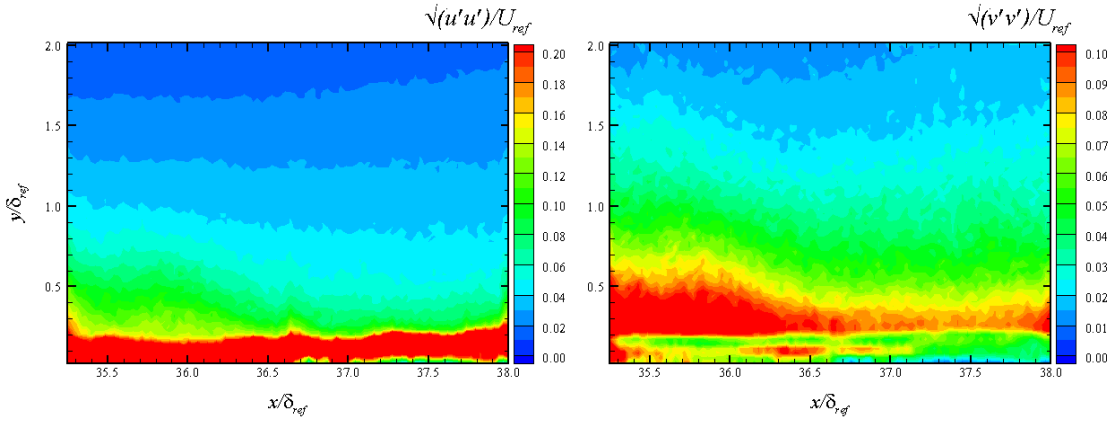

Figure 115: SPG Turbulence Intensities Contours at 2nd Measurement Location (Global Coordinate System)

From the contour plots, turbulence intensity profiles for both the *u* and *v* turbulence intensities for each pressure gradient model were extracted normal to the wall. The profiles for the turbulence intensities for all of the pressure gradient models are shown in Figure 116 and Figure 117 . The profiles clearly show the trends discussed for the contour plots. The WPG model shows lower overall turbulence levels than the ZPG case. The SPG has a even lower turbulence intensity than the ZPG and WPG models except near the wall. These results compare well with theory that the presence of the favorable pressure gradients reduce turbulence intensities. Additionally, these data correspond with the mean velocity data discusses above that energy from the turbulence is feeding back into the mean flow, therefore decreasing local turbulence intensities and increasing the local mean velocity.

For the present study, the WPG model decreased the axial turbulence intensity by 3.8% and the transverse turbulence intensity by 18.89%. For the SPG case, the axial was decreased by 13.6% while the transverse component was increased by 15.2%. These

results were compared to Mach 3 data from Ekoto et al in response to scientific question 4 discussed in Chapter I. For the lower Mach number, the WPG model exhibited approximately a 1.0% decrease in both the axial and transverse directions while the SPG case showed a 2.5% decrease in the axial component and a 3.0% increase in transverse. Therefore it was determined that the effect of the favorable pressure gradients on the turbulence intensities is increased with increasing Mach number.

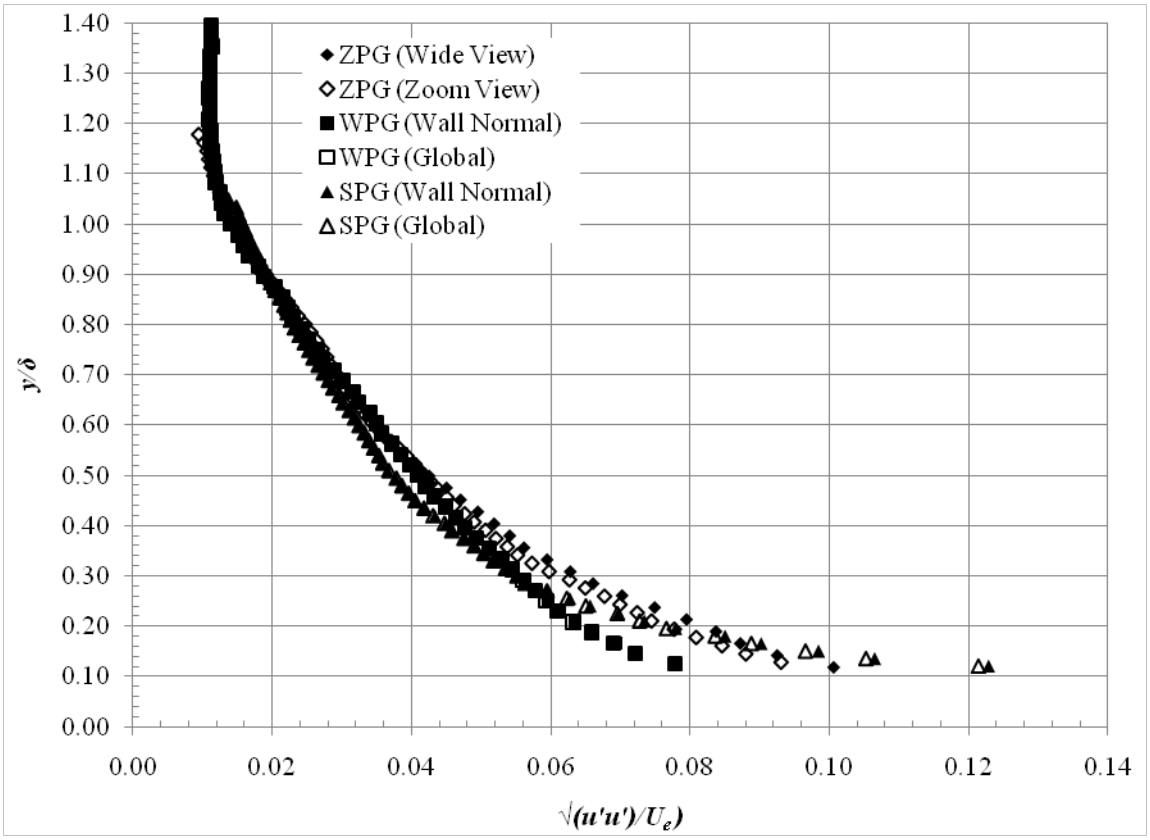

Figure 116: Axial Turbulence Intensity Profiles

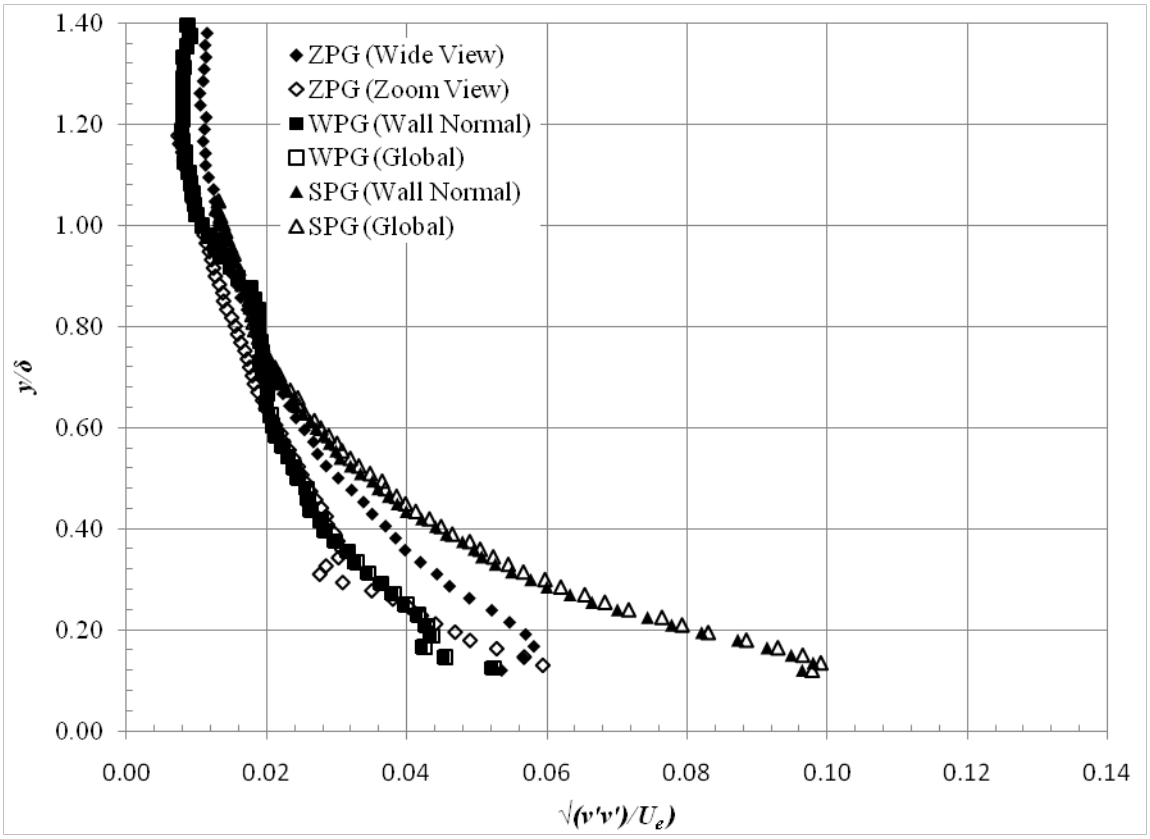

Figure 117: Transverse Turbulence Intensity Profiles

Turbulent Shear Stress

The purpose of these measurements was to measure the effect of favorable pressure gradients on the turbulence shear stress within the boundary layer. These data addressed scientific question 1 described in Chapter I.

The turbulent shear stress was determined from the particle image velocimetry data described in Chapter IV. The velocity fluctuations were determined by subtracting the instantaneous velocity fields from the mean velocity field using the in-house FORTRAN post-processing code. Contour plots of the turbulent shear stress were

created for each pressure gradient model and were normalized by the square of the reference velocity $(1/U_{ref}^2)$ described above.

The contour plots for the ZPG model at the upstream measurement location are shown in Figure 118. The shear stress approaches zero in the freestream flow for all cases. For both the ZPG fields of views, the turbulent shear stress has a normalized value of approximately 8.0×10^{-4}. Additionally, the shear stress gradient for both views agree very well. The contour plots for the WPG model are shown in Figure 119. Compared to the ZPG case, the weak pressure gradient exhibits decreased shear stress, due to the small wall curvature angle. The shear stress near the wall is slightly higher in the global coordinate system than in the wall normal system, but is nearly the same in the freestream for both coordinate systems.

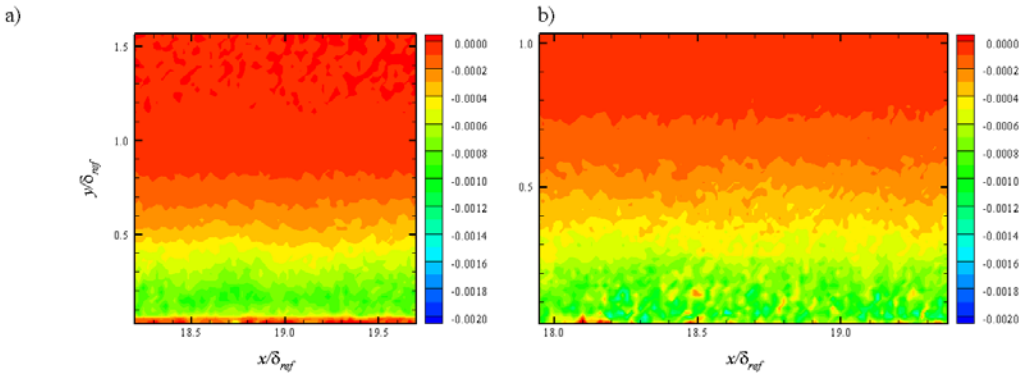

Figure 118: ZPG Turbulent Shear Stress Contours at 1st Measurement Location a) Wide View, b) Zoom View

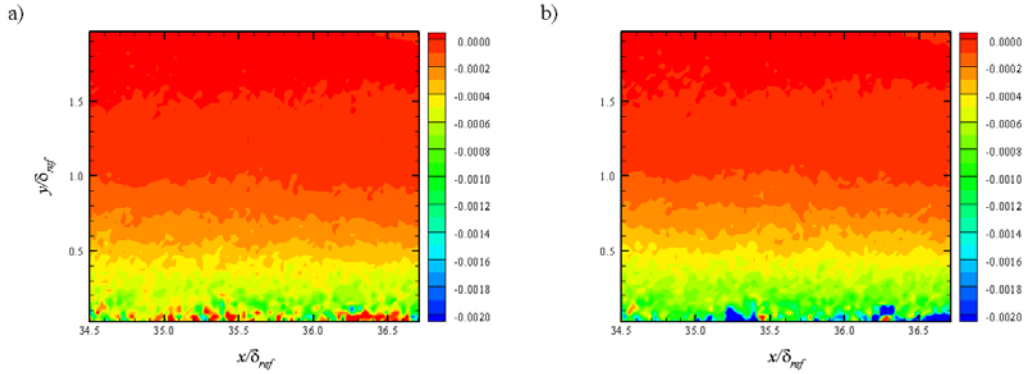

Figure 119: WPG Turbulent Shear Stress Contours at 2nd Measurement Location a) Wall Normal Coordinate System, b) Global Coordinate System

The contour plots of the turbulent shear stress for the SPG case are shown in Figure 120 for both the wall normal and global coordinate systems. In the wall normal coordinate system, the turbulent shear stress actually changes sign from all of the previous cases. This is a significant characteristic of the strong pressure gradient wall curvature. In the global coordinate system, the turbulent shear stress follows similar trends to the ZPG and WPG cases, with the shear stress near zero towards the freestream. Upon close analysis it can be seen that the shear stress at the top of the field of view is not quite to the same level as the freestream shear as seen in the ZPG and WPG fields of view due to the larger boundary layer thickness over the SPG curvature.

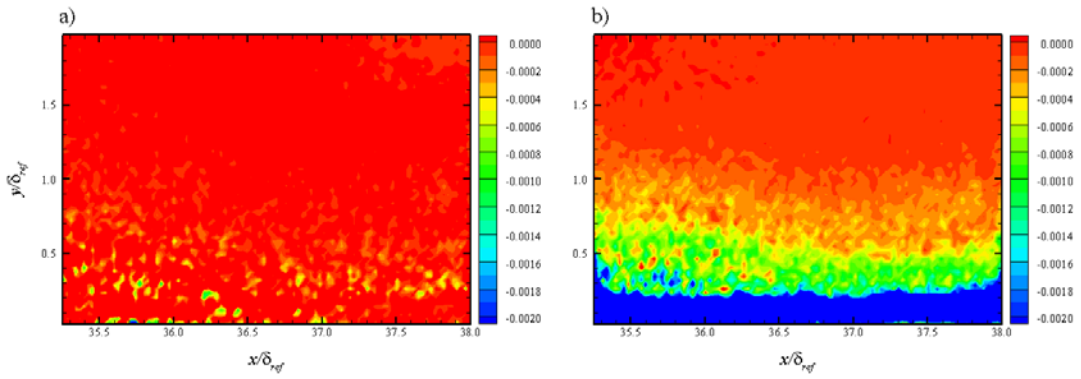

Figure 120: SPG Turbulent Shear Stress Contours at 2nd Measurement Location a) Wall Normal Coordinate System, b) Global Coordinate System

From the contour plots, turbulent shear stress profiles were extracted normal to the wall. The profiles for each pressure gradient model are shown in Figure 121. The profiles for the ZPG and WPG models are very similar. A slight decrease in the turbulent shear stress can be seen for the WPG versus the ZPG case. The turbulent shear stress profiles for the SPG exhibit a significant dependence on the coordinate system. In the global coordinate system, the SPG turbulent shear stress is the same sign and is larger than the ZPG and WPG cases. In the wall normal coordinate system, the turbulent shear stress for the SPG showed a significant result by switching sign compared to ZPG and WPG models.

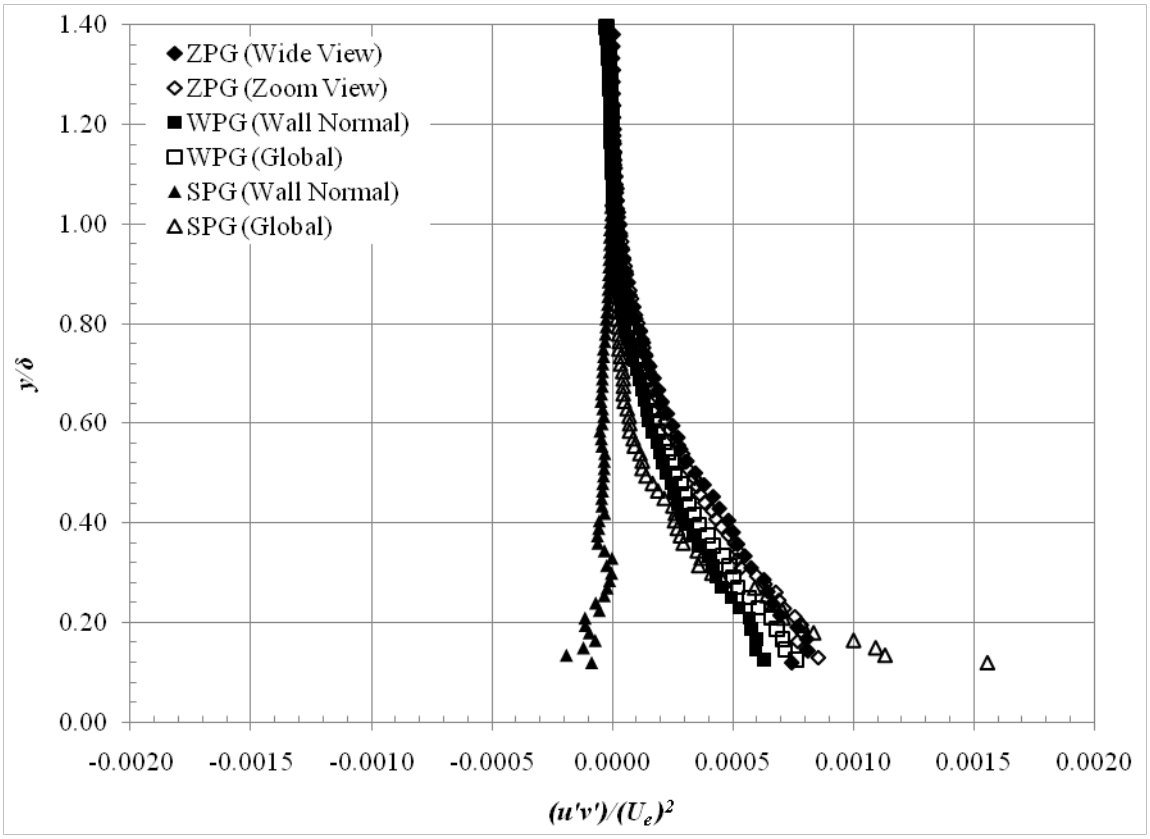

Figure 121: Turbulent Shear Stress Profiles

The profiles for each model in the wall normal coordinate system are shown in Figure 122 in order to more easily see the significant change in the SPG case. In the wall normal coordinate system, the SPG turbulent shear is a different sign all the way to the freestream. This is a new result not seen in previous studies at lower Mach numbers. Compared to Mach 3 data from Ekoto et al, the response was increased with Mach number, therefore addressing scientific question 4 described in Chapter I.

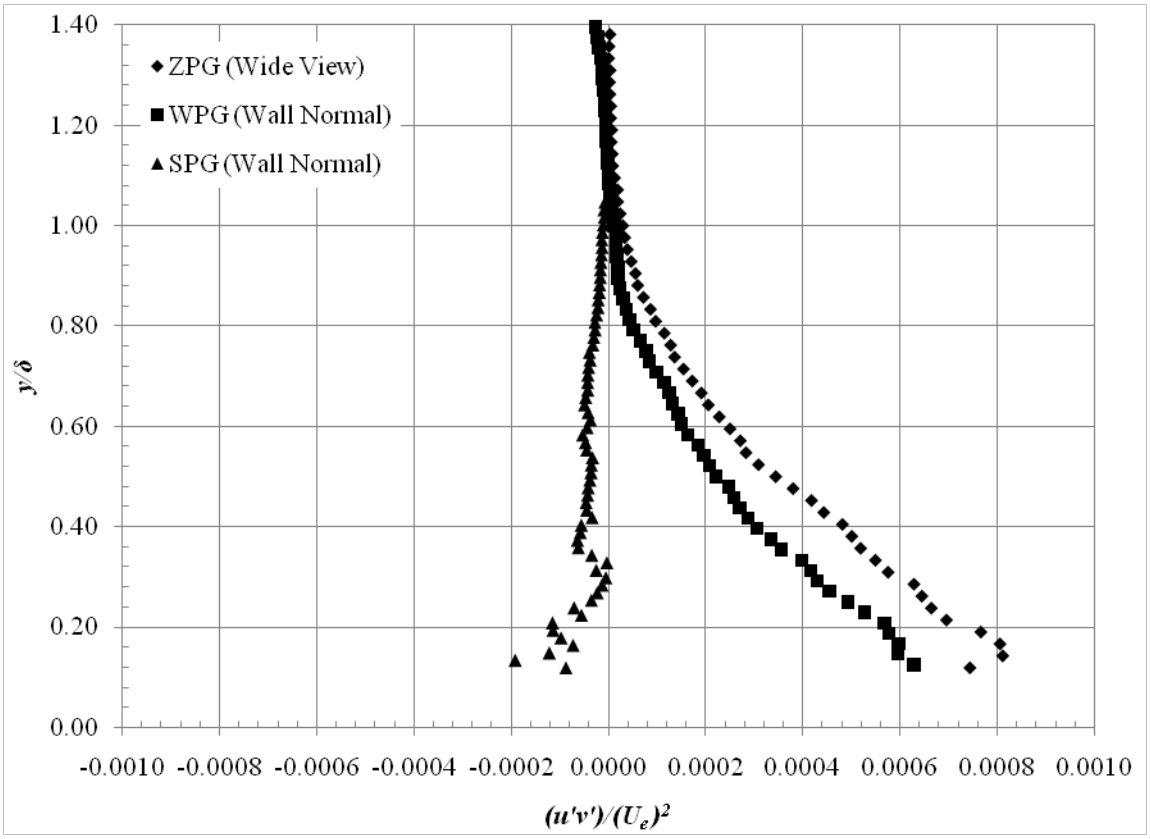

Figure 122: Turbulent Shear Stress Profiles (Wall Normal)

Turbulent Stress Production

The purpose of these data was to provide quantitative measurements of the effect of favorable pressure gradients on the turbulent stress production terms. These measurements addressed scientific question 3 described in Chapter I.

The turbulent stress production was measured using particle image velocimetry described in Chapter IV. In order to calculate the turbulent production, the mean flow gradients as well as the turbulent stress measurements were required. The calculation of

the turbulent stress production terms were performed with the in-house FORTRAN post-processing code. The general equation for the turbulent stress production is

$$P_{ij} = -\left[\tau_{jk}^{T} \frac{\partial \overline{u}_i}{\partial x_k} + \tau_{ik}^{T} \frac{\partial \overline{u}_j}{\partial x_k} \right] \tag{4.7}$$

Based on the incoming flow characterization provided above, it was assumed that the lateral velocity as well as the lateral velocity gradients were negligible. With these assumptions, only 3 of the 9 production terms remain: the axial turbulent stress production P_{xx}, the transverse turbulent stress production P_{yy}, and the turbulent shear stress production P_{xy}. From (4.7) and applying the assumptions, these production terms become

$$P_{xx} = -2\left[\tau_{xx}^{T} \frac{\partial \overline{u}}{\partial x} + \tau_{xy}^{T} \frac{\partial \overline{u}}{\partial y} \right]$$

$$P_{yy} = -2\left[\tau_{xy}^{T} \frac{\partial \overline{v}}{\partial x} + \tau_{yy}^{T} \frac{\partial \overline{v}}{\partial y} \right]$$

$$P_{xy} = -\left[\tau_{xy}^{T} \frac{\partial \overline{u}}{\partial x} + \tau_{yy}^{T} \frac{\partial \overline{u}}{\partial y} + \tau_{xx}^{T} \frac{\partial \overline{v}}{\partial x} + \tau_{xy}^{T} \frac{\partial \overline{v}}{\partial y} \right]$$

Contour plots of the turbulent stress production were created for each pressure gradient model. The contour plots were normalized by the reference length scale divided by the reference velocity cubed $(\delta_{ref} / U_{ref}^{3})$.

The contour plots of the production terms and their components for the ZPG wide view are shown in Figure 123 and Figure 124 and while the contour plots for the

ZPG zoom view are given in Figure 125 and Figure 126. For both ZPG fields of view, P_{xx} and P_{xy} were of the same order, but P_{xx} was the more dominant term. The transverse turbulent stress production term P_{yy} was significantly smaller than the other two. This was due to the P_{xx} and P_{xy} production terms dependence on the primary velocity gradient $d\bar{u}/dy$. All of the production term components for the ZPG model are very small compared to the primary velocity gradient component.

The contour plots of the production terms and their component for the WPG model are shown in Figure 127 Figure 128 for the wall normal coordinate system and in Figure 129 and Figure 130 for the global coordinate system. The axial production term is very close to the ZPG case however the transverse term P_{yy} is slightly larger for the WPG than for the ZPG model. This is due to the small expansion over the WPG wall curvature and the flow in the wall normal transverse direction. The turbulent shear stress production term appears to be smaller for the WPG model compared to the upstream ZPG case with the term nearly zero in the freestream. This result is expected again due to the expansion of the boundary layer over the wall curvature. The effect of the coordinate transformation from wall normal to global coordinates for the WPG model has negligible effect on the turbulent stress production terms or their components. This is expected because of the small wall curvature angle.

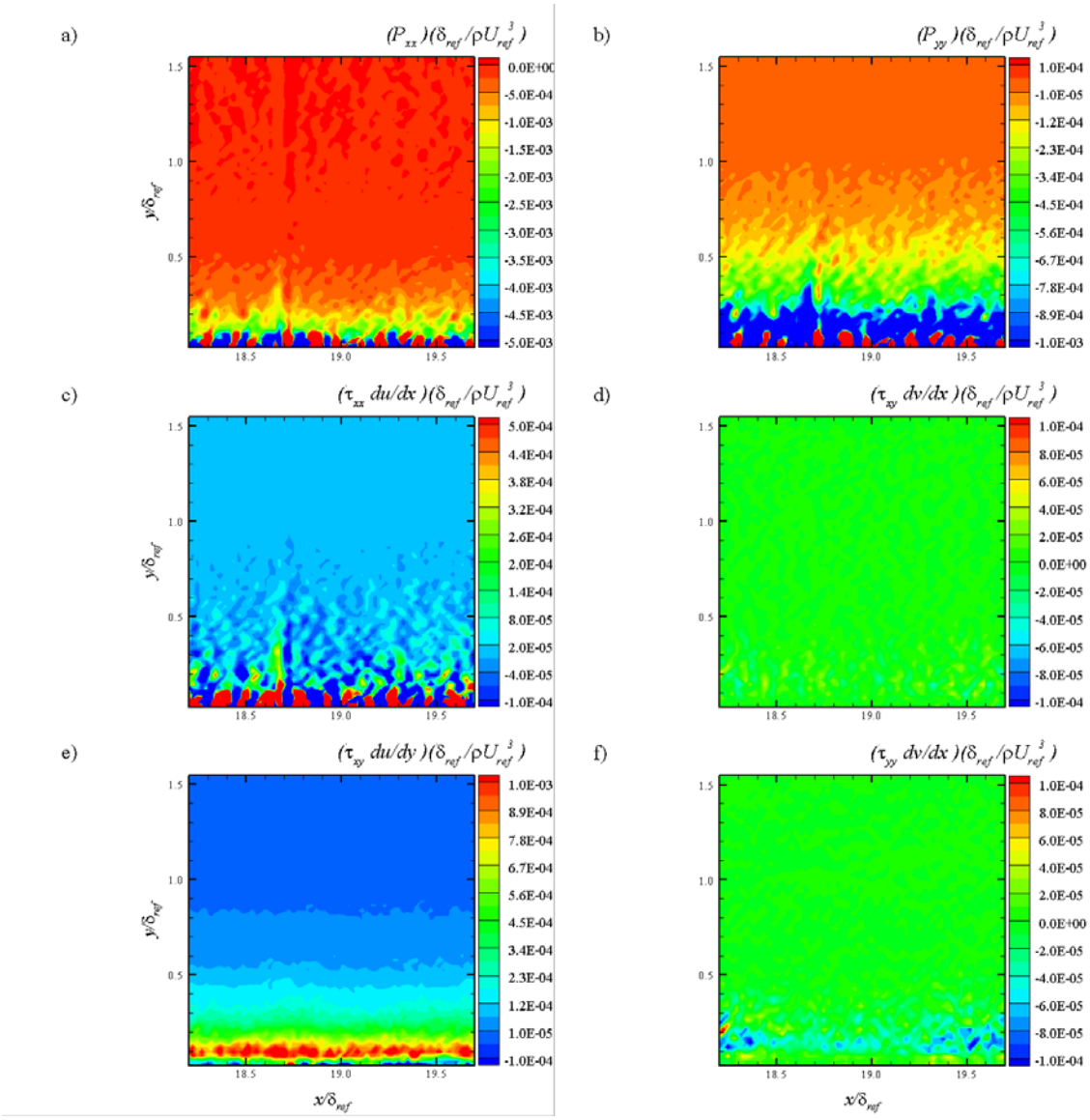

Figure 123: ZPG (Wide View) Contours of P_{xx}, P_{yy} and Their Components at 1st Measurement Location

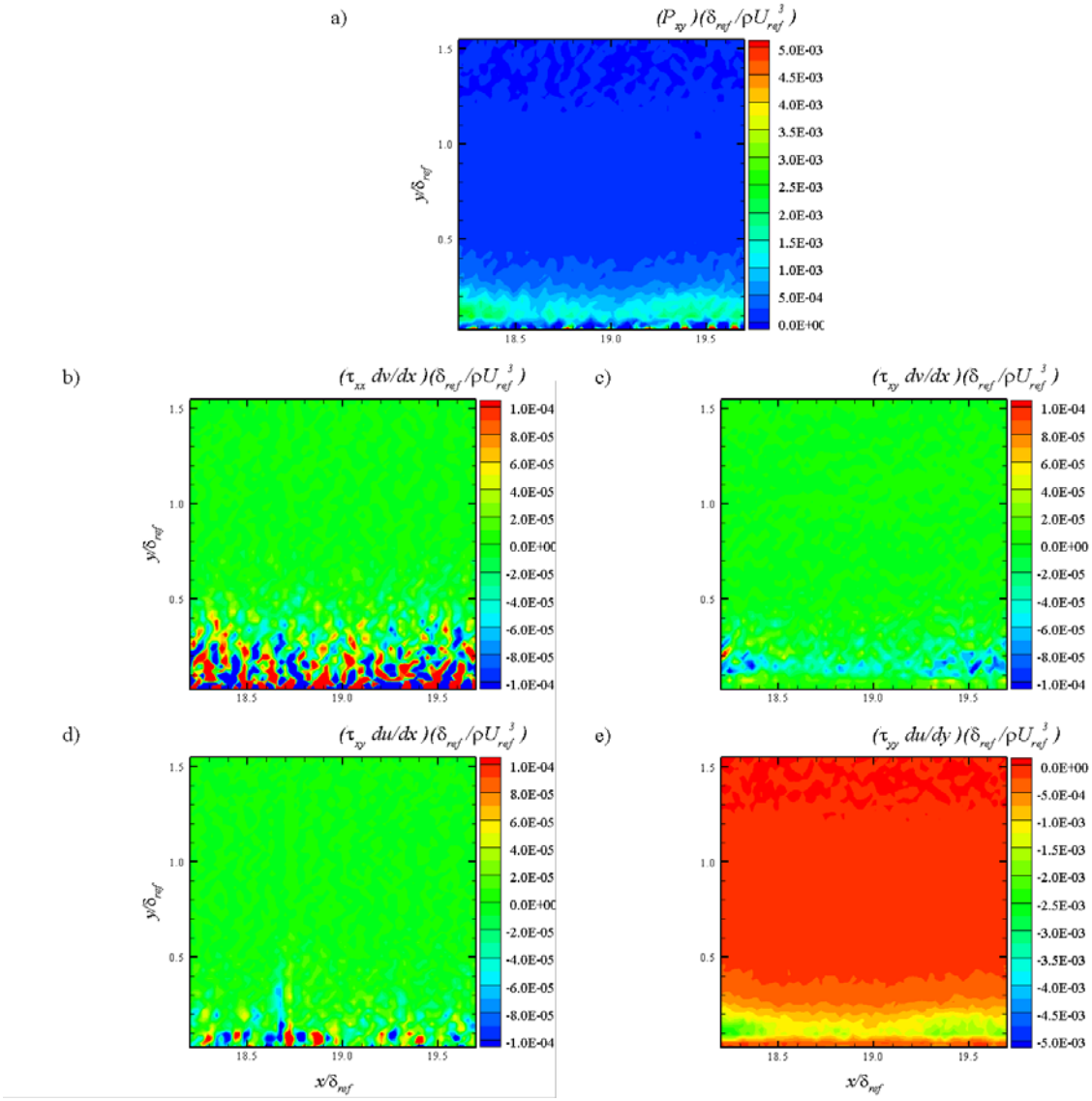

Figure 124: ZPG (Wide View) Contours of P_{xy} and Its Components at 1st Measurement Location

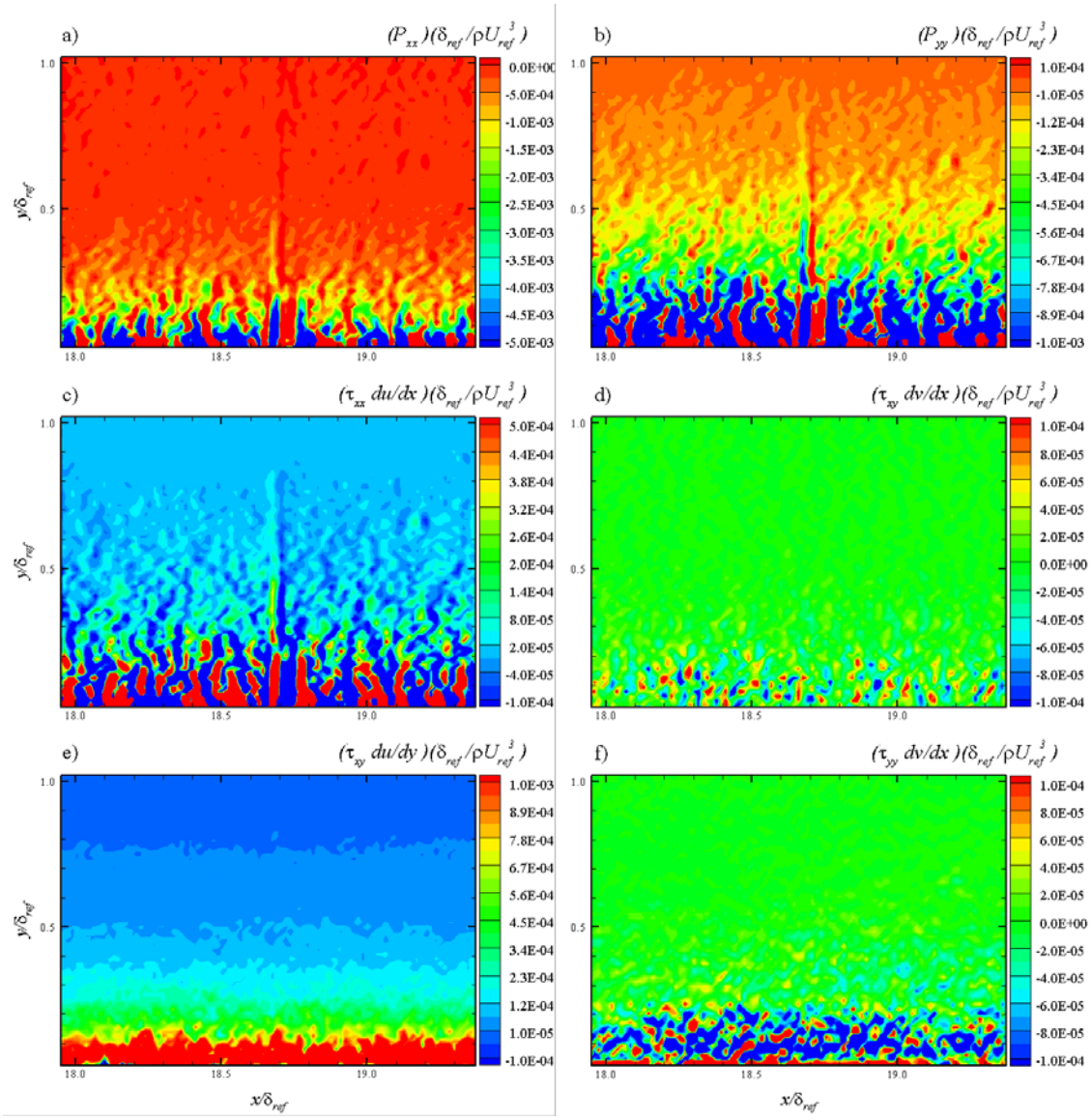

Figure 125: ZPG (Zoom View) Contours of P_{xx}, P_{yy} and Their Components at 1st Measurement Location

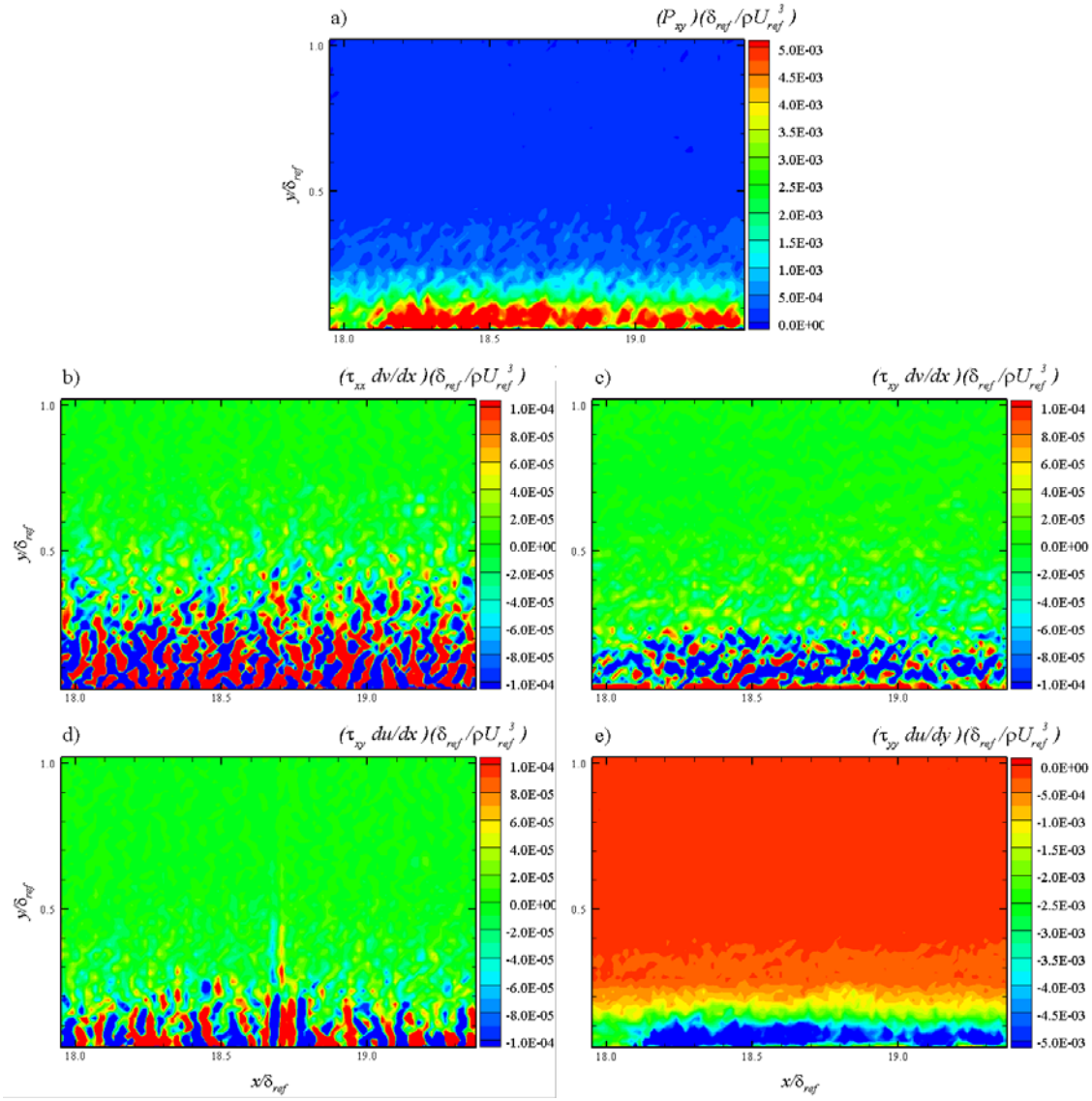

Figure 126: ZPG (Zoom View) Contours of P_{xy} and Its Components at 1st Measurement Location

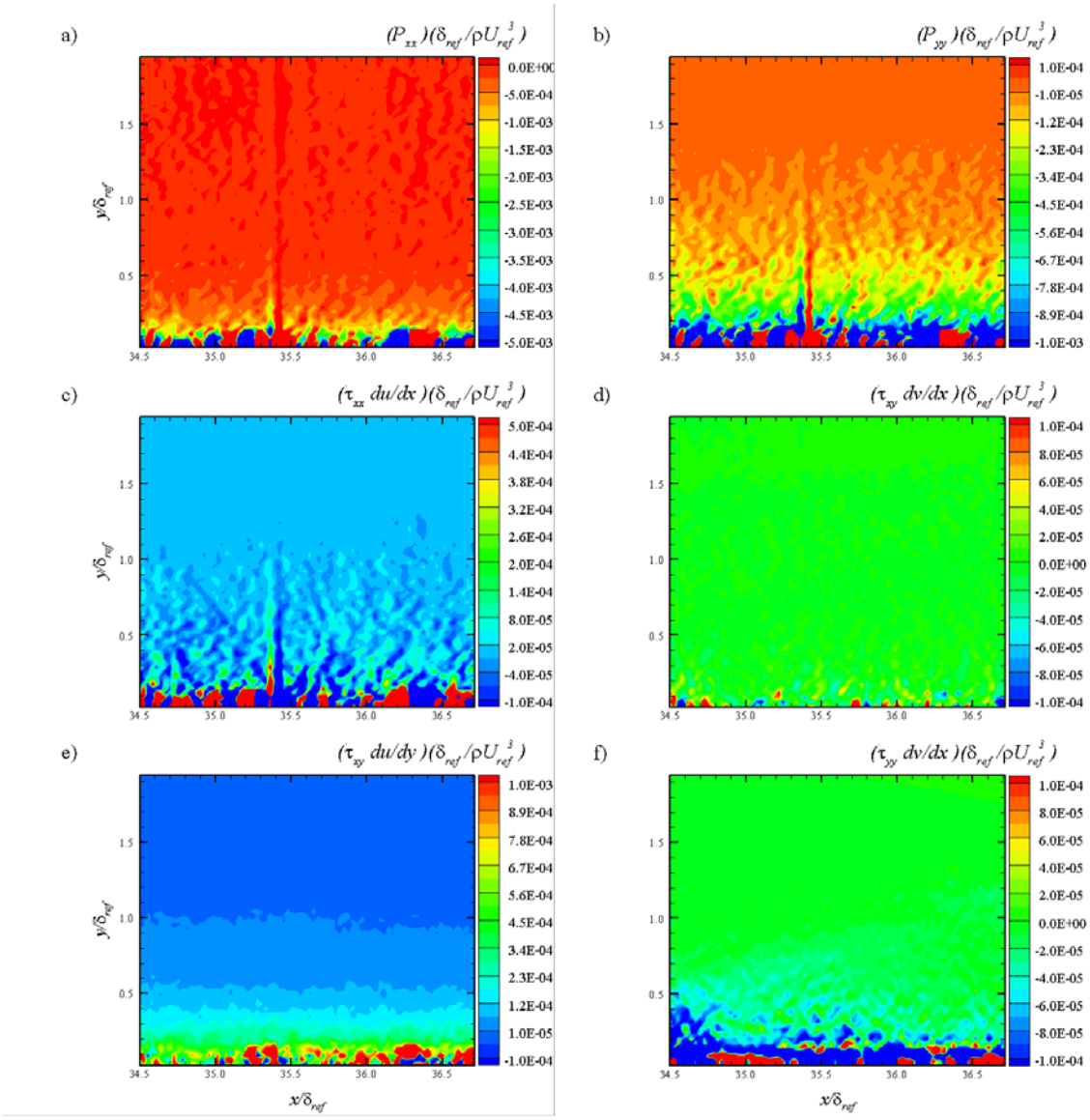

Figure 127: WPG Contours of P_{xx}, P_{yy} and Their Components at 2nd Measurement Location (Wall Normal Coordinate System)

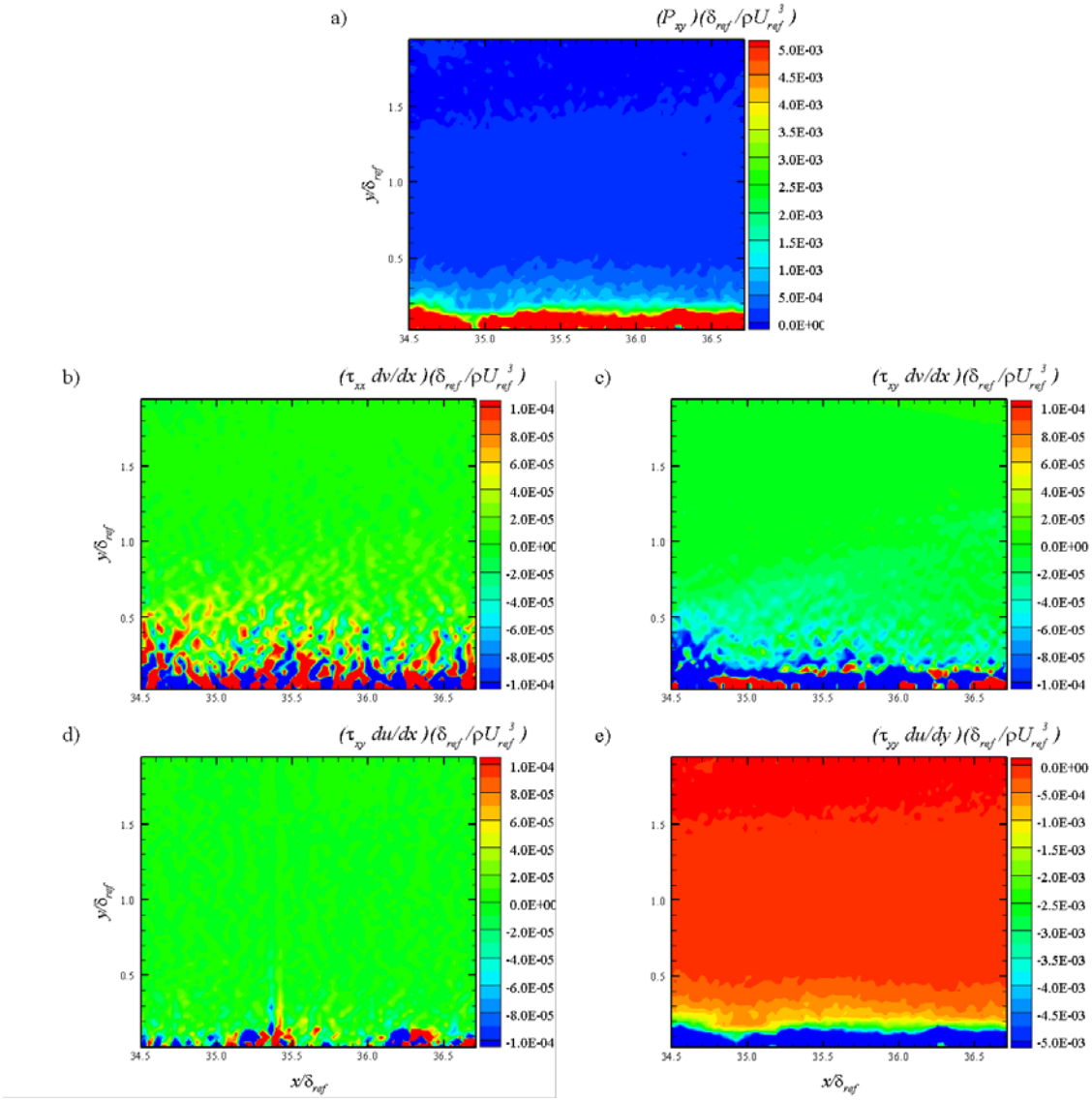

Figure 128: WPG Contours of P_{xy} and Its Components at 2nd Measurement Location (Wall Normal Coordinate System)

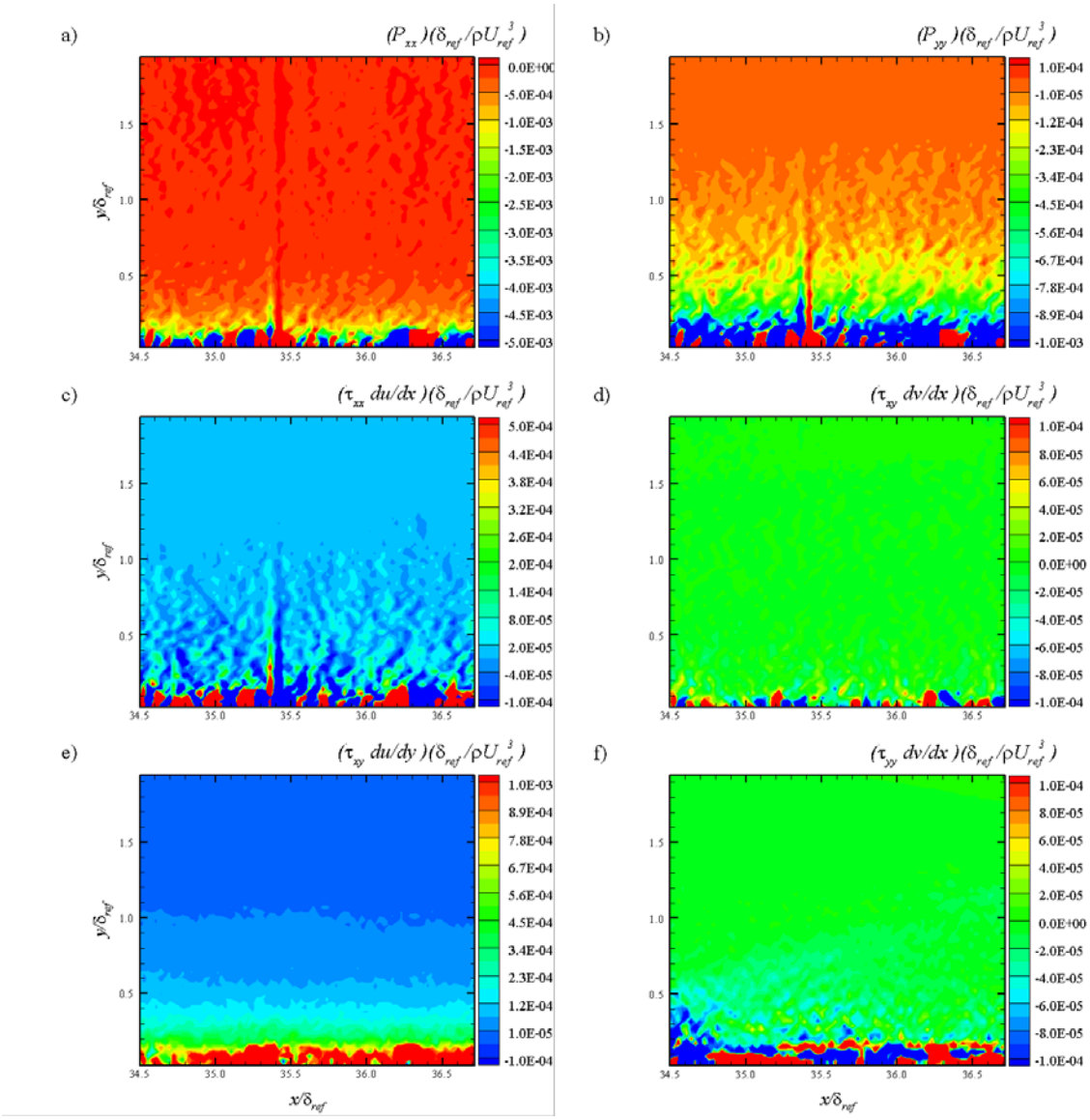

Figure 129: WPG Contours of P_{xx}, P_{yy} and Their Components at 2nd Measurement Location (Global Coordinate System)

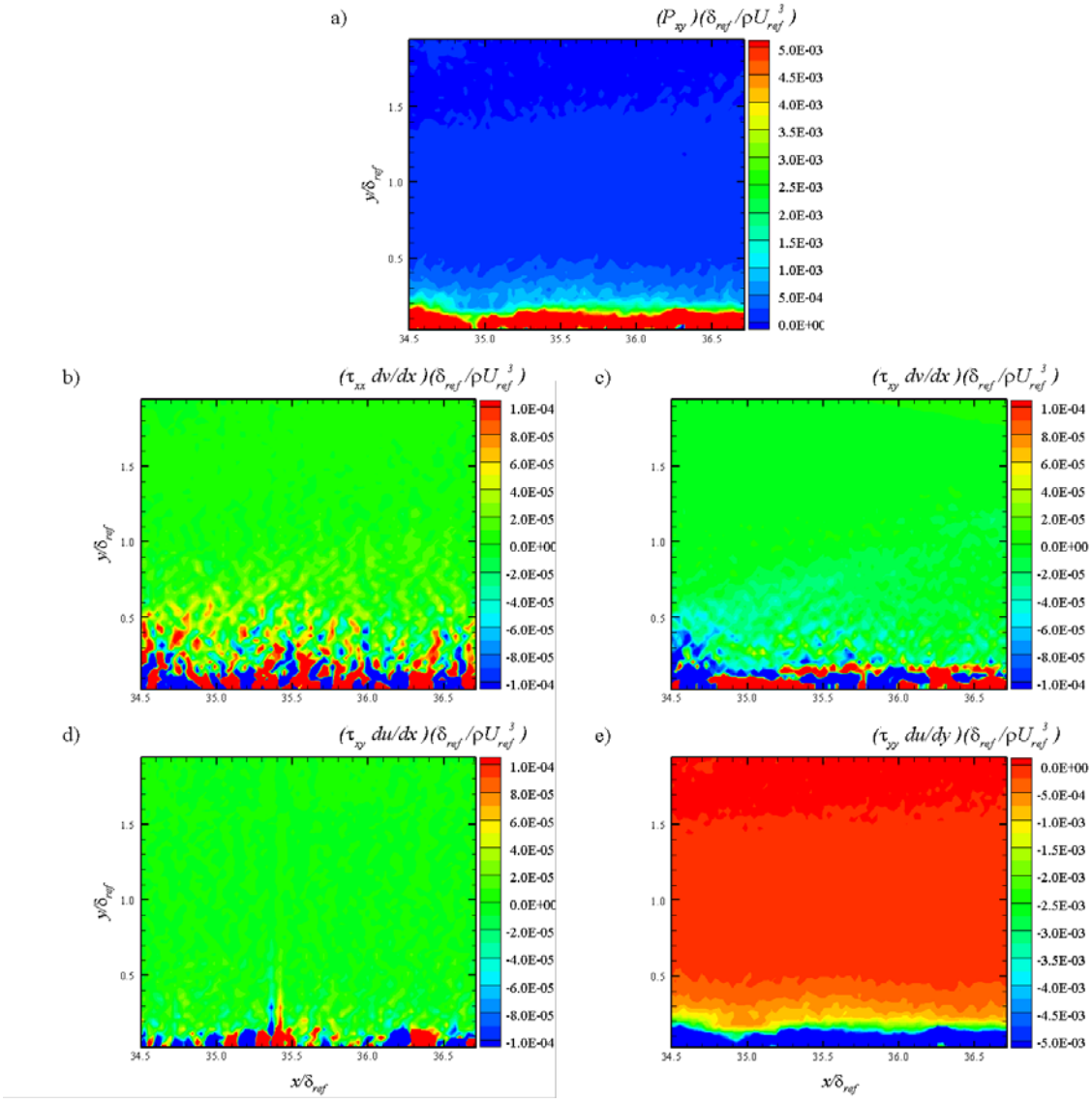

Figure 130: WPG Contours of P_{xy} and Its Components at 2nd Measurement Location (Global Coordinate System)

The contour plots for the turbulent stress production terms and their components for the SPG model are shown in Figure 131 and Figure 132 for the wall normal coordinate system and in Figure 133 and Figure 134 for the global coordinate system. Compared to the ZPG and WPG models, it can be seen that all of the turbulent stress production terms are reduced due to the wall curvature. The P_{xx} and P_{xy} production terms are much larger than the P_{yy} production term because of their dependence on the primary velocity gradient $d\bar{u}/dy$. When the velocity vectors are transformed into the global coordinate system, the axial turbulent stress production term and the transverse turbulent stress production terms become slightly larger compared to the wall normal coordinate system while the change in the turbulent shear stress production term is negligible between the two coordinate systems. Overall, similar trends are seen between all three pressure gradient models, however, all of the production terms are reduced for the WPG model and even further reduced for the SPG compared to the ZPG case.

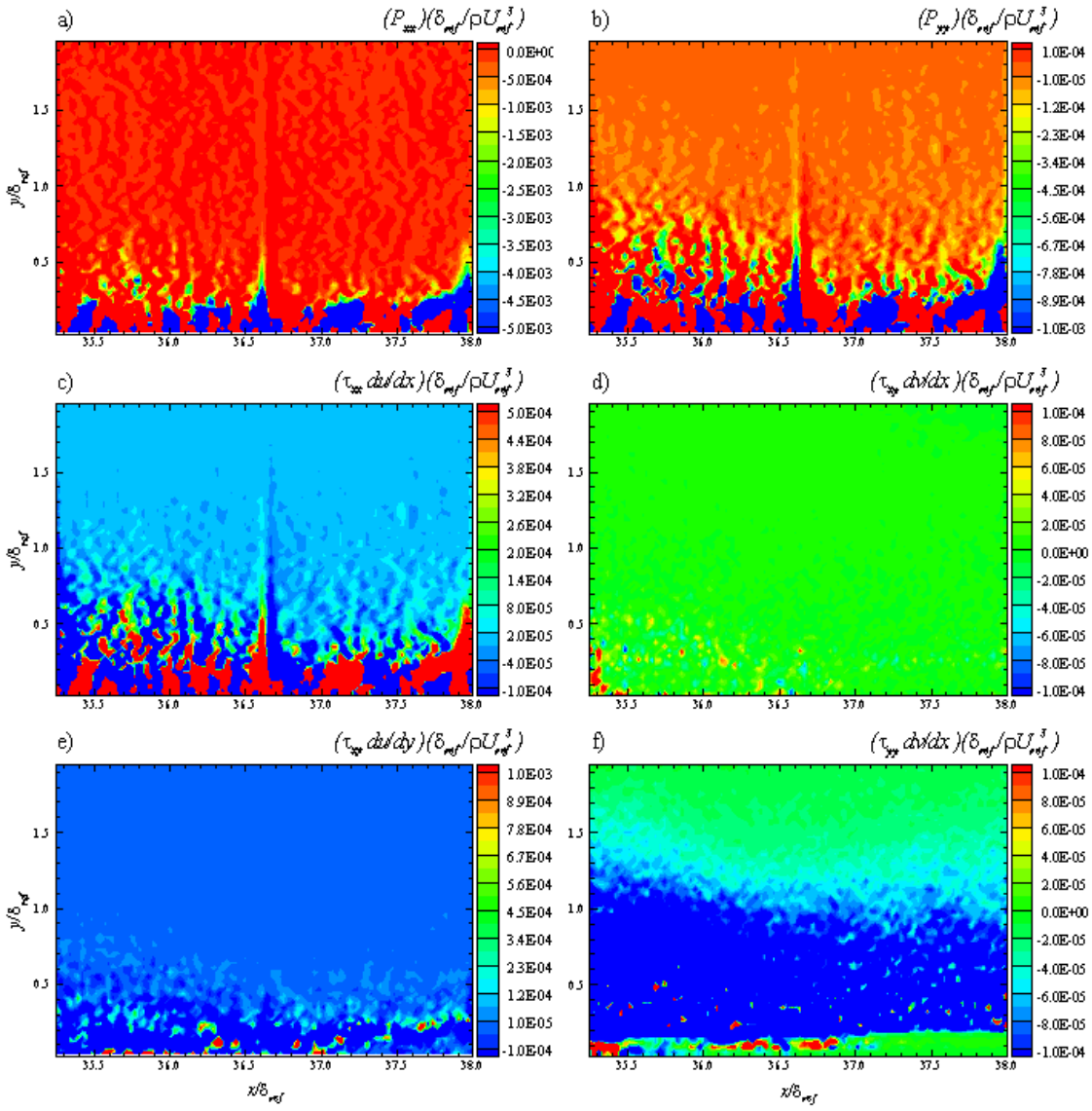

Figure 131: SPG Contours of P_{xx}, P_{yy} and Their Components at 2nd Measurement Location (Wall Normal Coordinate System)

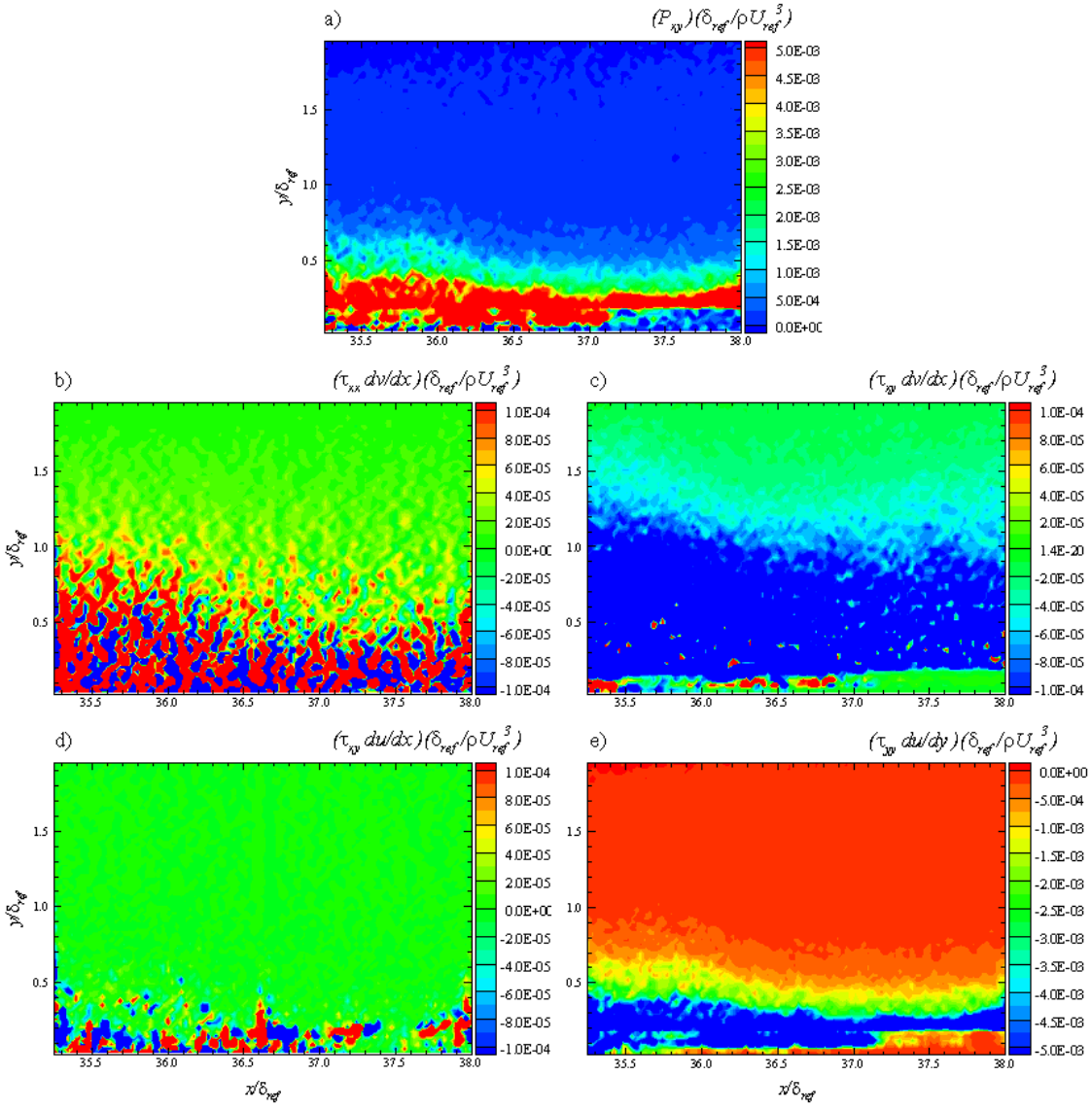

Figure 132: SPG Contours of P_{xy} and Its Components at 2nd Measurement Location (Wall Normal Coordinate System)

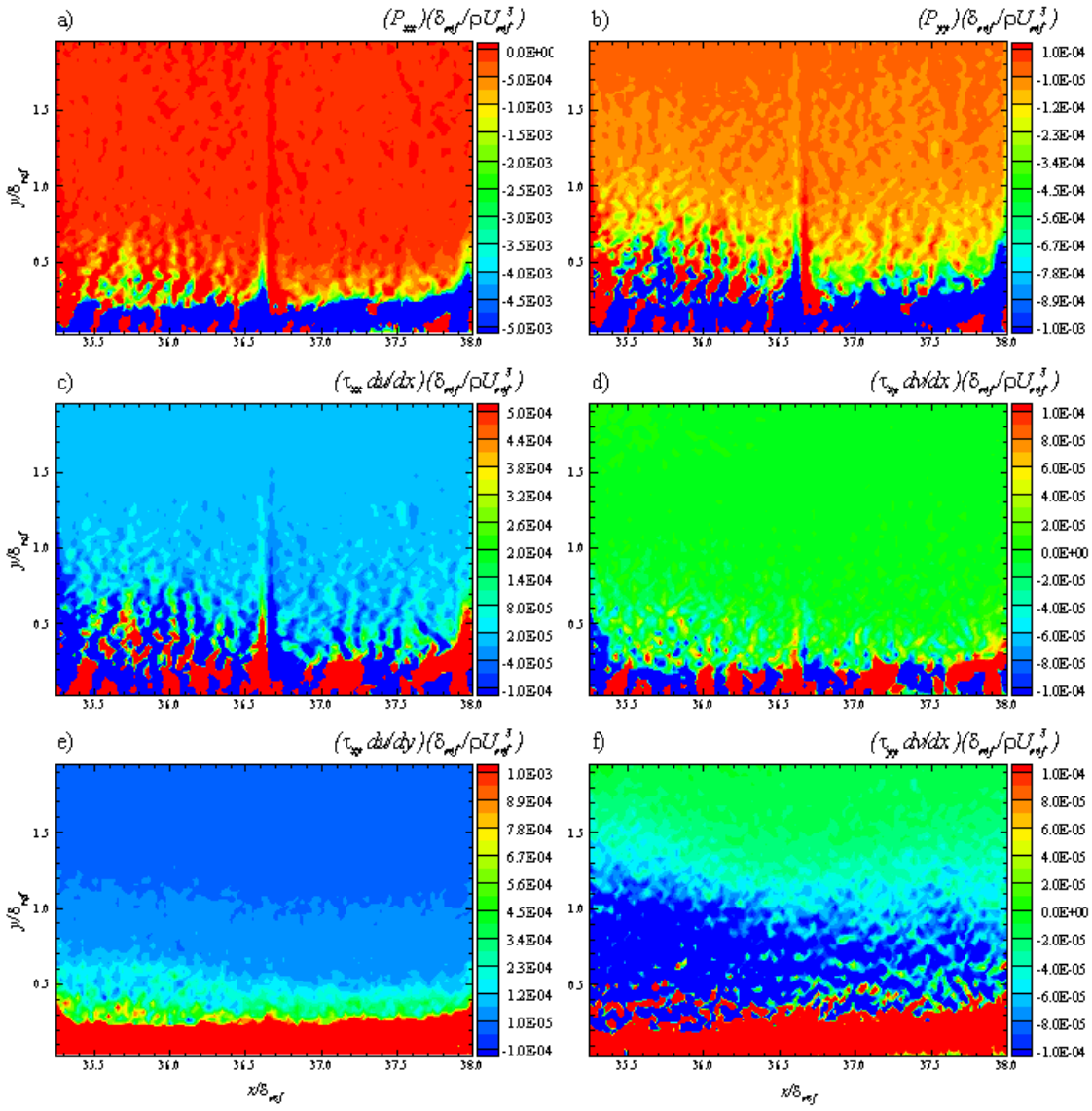

Figure 133: SPG Contours of P_{xx}, P_{yy} and Their Components at 2nd Measurement Location (Global Coordinate System)

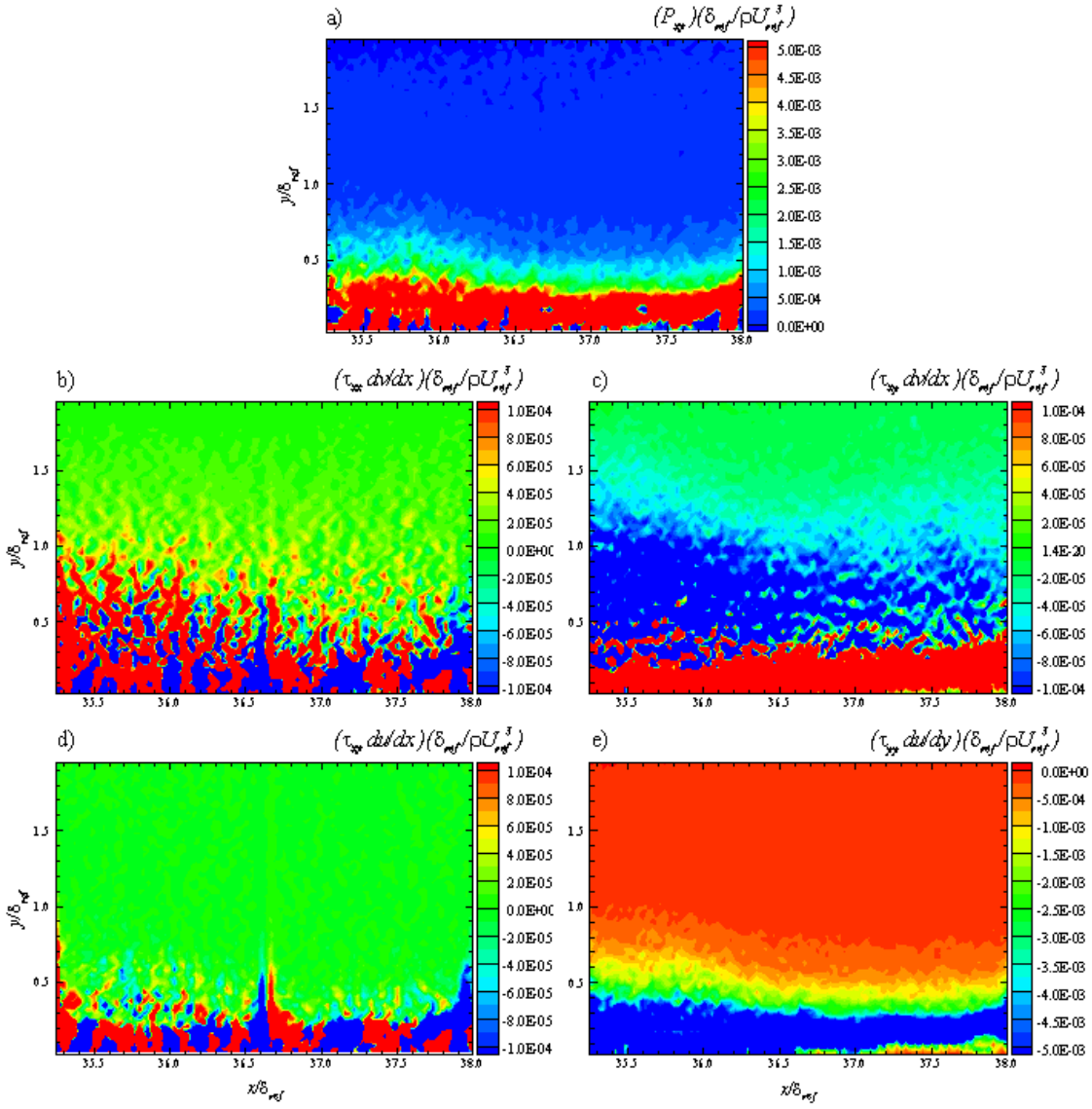

Figure 134: SPG Contours of P_{xy} and Its Components at 2nd Measurement Location (Global Coordinate System)

From the contour plots, turbulent stress production profiles were extracted normal to the wall for each pressure gradient model. The profiles for the axial turbulent stress production term are shown in Figure 135. The ZPG and the WPG cases exhibit very similar profiles. The WPG model actually has a slightly lower production

compared to the ZPG model. The profile for the SPG case in global coordinates show a similarly trend to the ZPG and WPG cases, with the axial production lower than the ZPG and WPG models except close to the wall. In the wall normal coordinate system, the SPG case produces an interesting result with the axial turbulent stress production actually changing signs which suggests that energy within the boundary layer is flowing in the opposite direction, back into the mean flow.

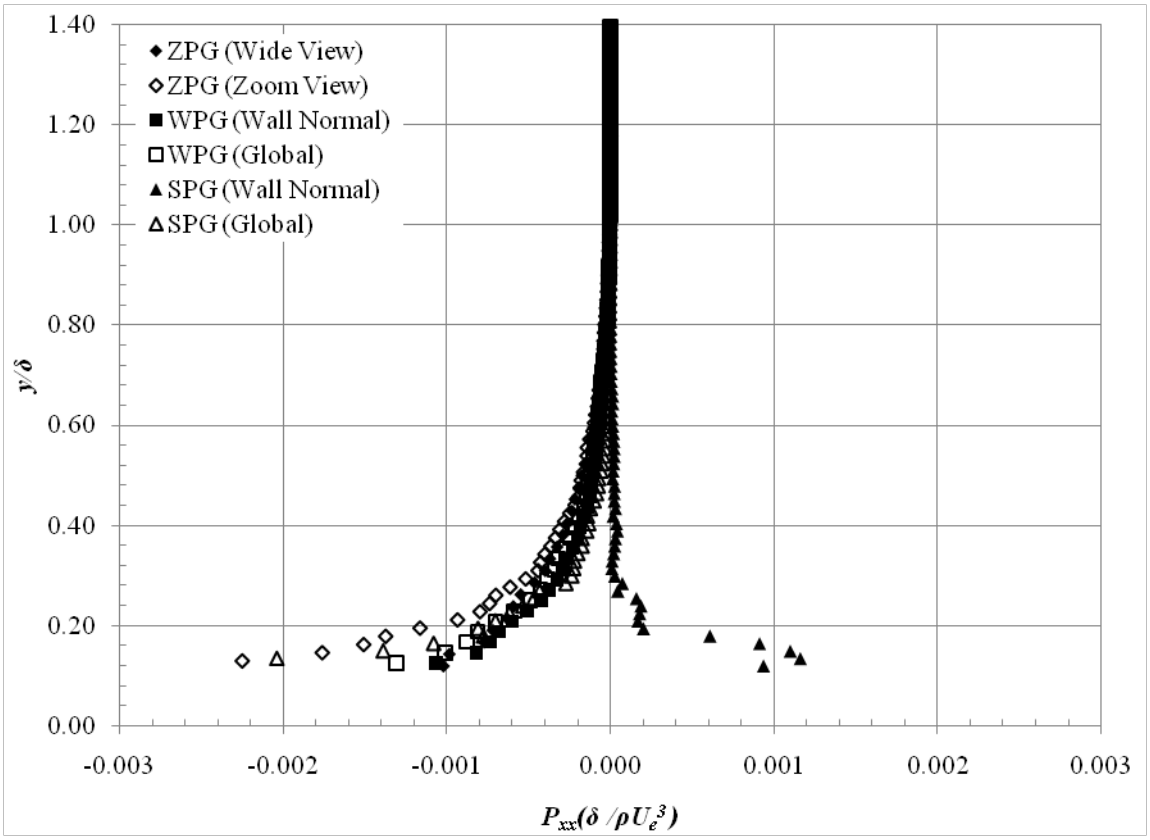

Figure 135: Axial Turbulent Stress Production, P_{xx} Profiles

The profiles for the transverse turbulent stress production term are shown in Figure 136. As discussed from the contour plots, the ZPG and WPG cases exhibit very similar trends with P_{yy} remaining very small throughout the field of view. The SPG case however shows a very different trend for the transverse turbulent stress production. For both the wall normal and global coordinate systems, the P_{yy} term increases approaching the wall. At approximately $0.40\, y/\delta$ the two SPG profiles begin to move in opposite directions with the wall normal profile continuing to increase and the global profile sharply decreasing and changing sign.

The turbulent shear stress production profiles are given in Figure 137 for each pressure gradient model. Again, the WPG model shows a decreased P_{xy} term compared to the ZPG case and the WPG profiles are very similar for each coordinate system. For the SPG case, the turbulent shear stress production is larger than the ZPG and WPG cases. In theory, the SPG case should exhibit a lower turbulent shear stress production because of the strong expansion over the wall curvature. The SPG P_{xy} profile is independent of the coordinate system as seen in the contour plots above.

The data from the present study were compared to previous lower Mach number data in order to address scientific question 4 described in Chapter I. All of the production terms from the present study exhibited changes of the same order and trend as the previous experiments.

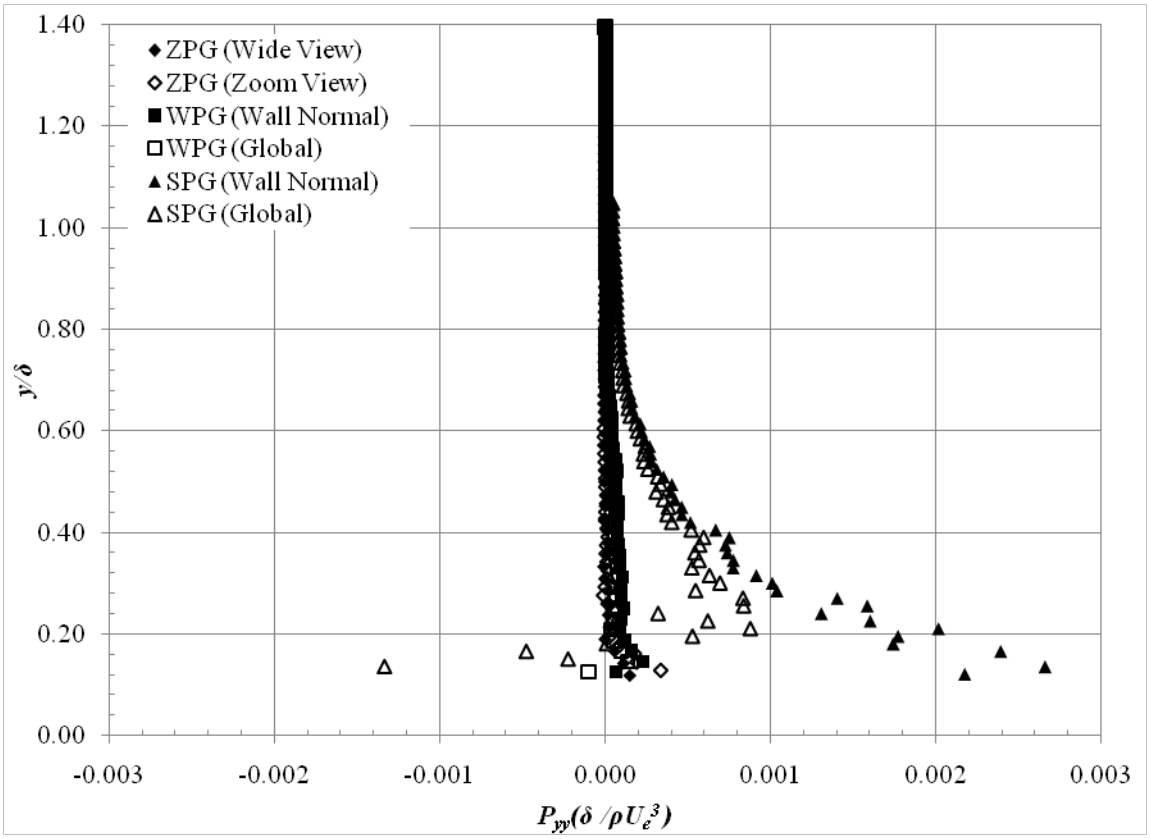

Figure 136: Transverse Turbulent Stress Production, P_{yy} Profiles

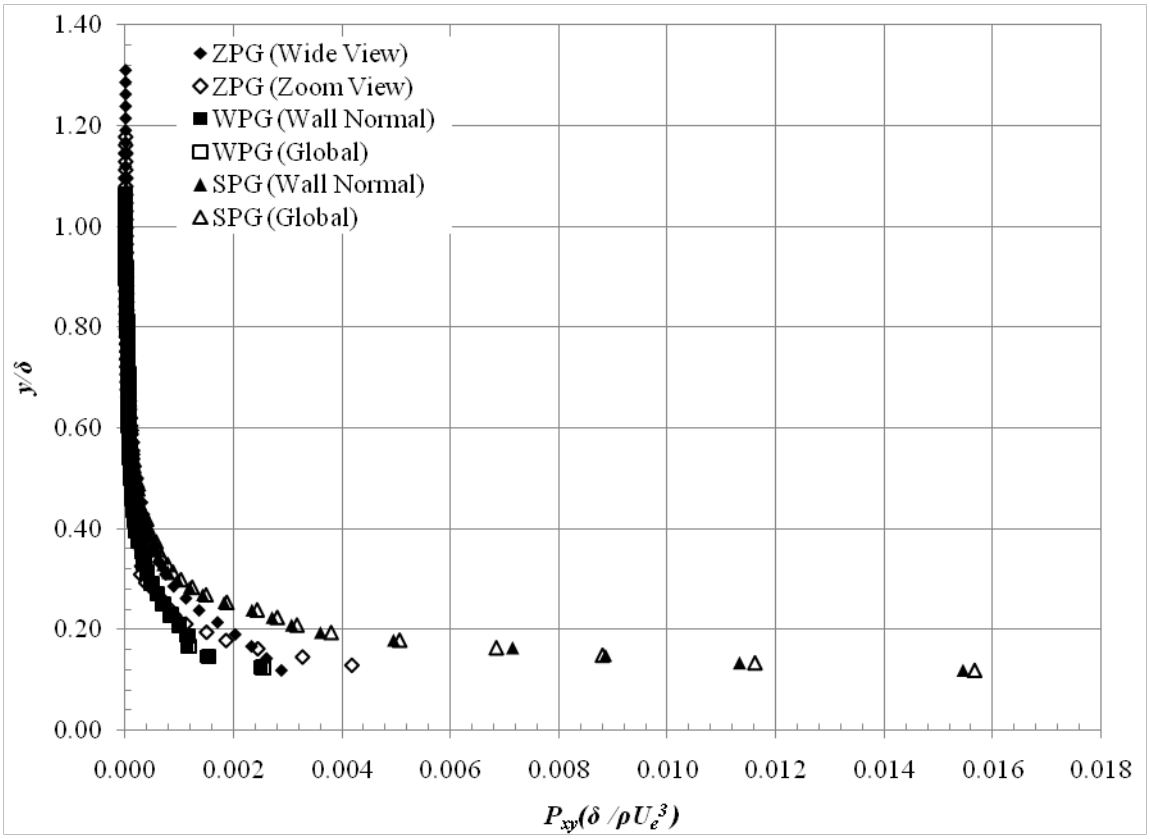

Figure 137: Turbulent Shear Stress Production, P_{xy} Profiles

Turbulent Stress Principal Axes Analysis

The purpose of these measurements were to determine the effect of favorable pressure gradients on the turbulent stress principal axes. These measurements addressed scientific question 3 described in Chapter I.

In order to gain additional insight into the turbulence evolution and production over the favorable pressure gradients, previous studies have examined the stress principal axes. A sketch of the turbulence stress orientation for the strong pressure gradient model is shown in Figure 138. The ordinate for the wall normal coordinate

system is represented by the arrow originating along the floor. For the first measurement location, this corresponds with the global wind tunnel coordinate system. For the second measurement location, the flow-turning angle ϕ represents the rotation angle from the global coordinate system to the wall normal coordinate system. The turbulent stress-turning angle α is the rotation angle from the global coordinate system to the turbulence stress principal axes.

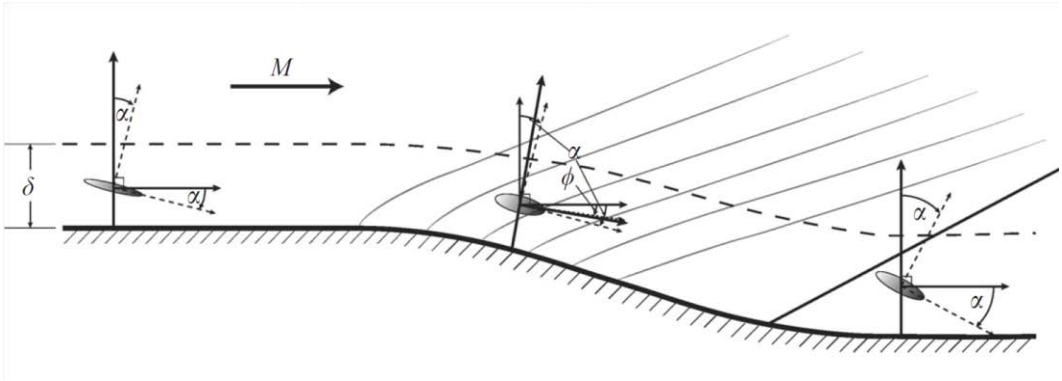

Figure 138: Sketch of Turbulence Stress Orientation[55]

Since the turbulence stress principal axes were not known *a priori*, the data were collected in the wall normal coordinate system as described above and transformed to the turbulence stress principal axes via the coordinate transformation given in (4.8)-(4.10), with the condition that $\overline{u'_\lambda v'_\lambda}$ is equal to zero.

$$\overline{u'_\lambda u'_\lambda} = \overline{u'u'}\cos^2\alpha - 2\overline{u'v'}\cos\alpha\sin\alpha + \overline{v'v'}\sin^2\alpha \tag{4.8}$$

$$\overline{v'_\lambda v'_\lambda} = \overline{v'v'}\cos^2\alpha + 2\overline{u'v'}\cos\alpha\sin\alpha + \overline{u'u'}\sin^2\alpha \tag{4.9}$$

$$\overline{u'_\lambda v'_\lambda} = \left(\overline{u'u'} - \overline{v'v'}\right)\cos\alpha\sin\alpha + \overline{u'v'}\left(\cos^2\alpha - \sin^2\alpha\right) \tag{4.10}$$

Contour plots were generated for the turbulent stress-turning angle α for each pressure gradient model and measurement location using the FORTRAN post-processing code. For each vector location, the velocity fluctuations were used to determine the turbulent stress-turning angle by scanning from -180 to 180 degrees until the $\overline{u'_\lambda v'_\lambda} = 0$ condition was satisfied. The contour plots for both fields of view of the ZPG model are shown in Figure 139. The turbulent stress-turning angle is somewhat intermittent in the freestream but becomes fairly consistent in the boundary layer. Again, below $0.3\ y/\delta_{ref}$ the turbulent stress-turning angle becomes widely varying. This conclusion is verified by the ZPG zoom view as well.

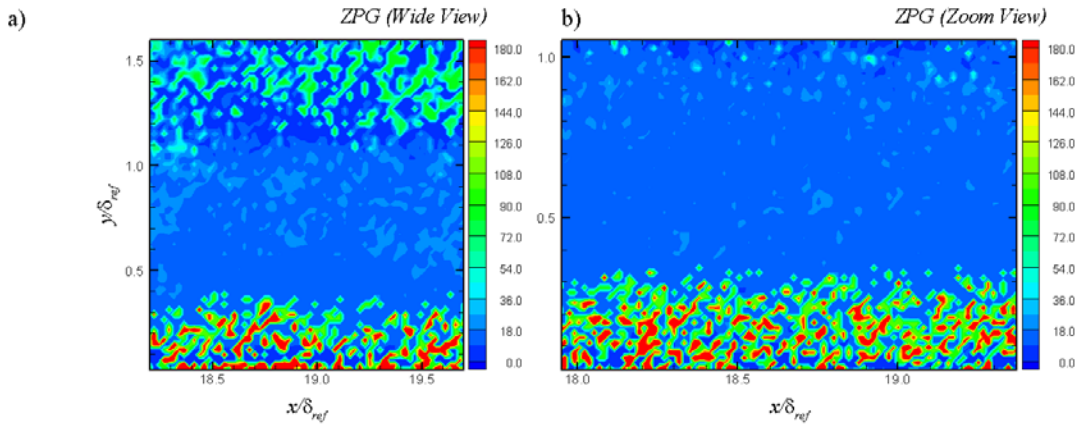

Figure 139: ZPG Contours of Turbulent Stress-Turning Angle at 1st Measurement Location

The contour plots for the WPG gradient in the wall normal and global coordinate systems are shown in Figure 140. The turbulent stress-turning angle is much different

depending on the location within the field of view. Outside of the boundary layer, α appears to be on the order of 90 degrees. Within the boundary layer, α is less than 20 degrees. As with the ZPG case, below approximately $0.3\ y/\delta_{ref}$, the turbulent stress-turning angle becomes erratic. The results are not significantly changed with the different coordinate systems.

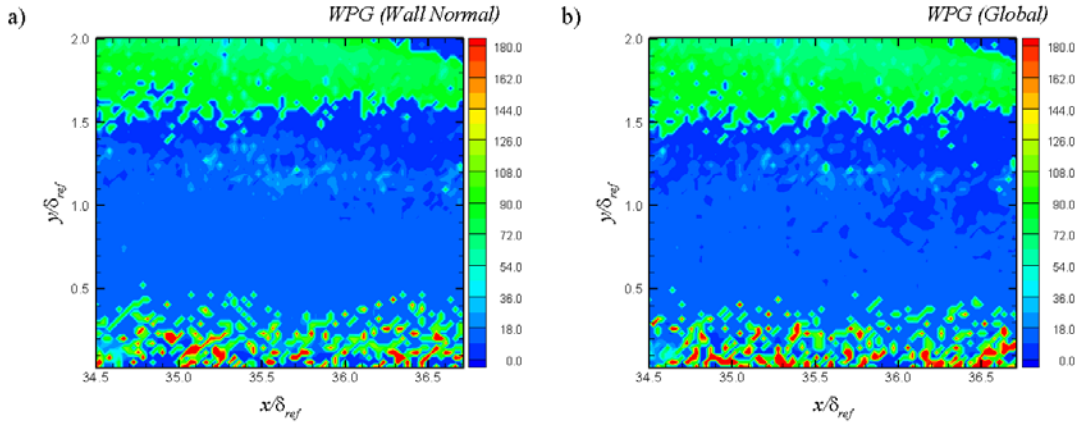

Figure 140: WPG Contours of Turbulent Stress-Turning Angle at 2nd Measurement Location

The contour plots of the turbulent stress-turning angle for the SPG model in the wall normal and global coordinate systems are shown in Figure 141. In wall normal coordinates above $1.0\ y/\delta_{ref}$, α is similar to the angle seen in the ZPG and WPG cases. Below approximately $1.0\ y/\delta_{ref}$, α becomes much larger until very near the wall which the turbulent stress-turning angle again becomes very intermittent. In the global coordinate system, α is significantly different over the SPG compared to the ZPG and WPG cases. Towards the freestream, the turbulent stress-turning angle is consistently

large and closer to the wall, becomes less uniform. It is obvious that the results for the turbulent stress-turning angle are greatly dependent on the coordinate system.

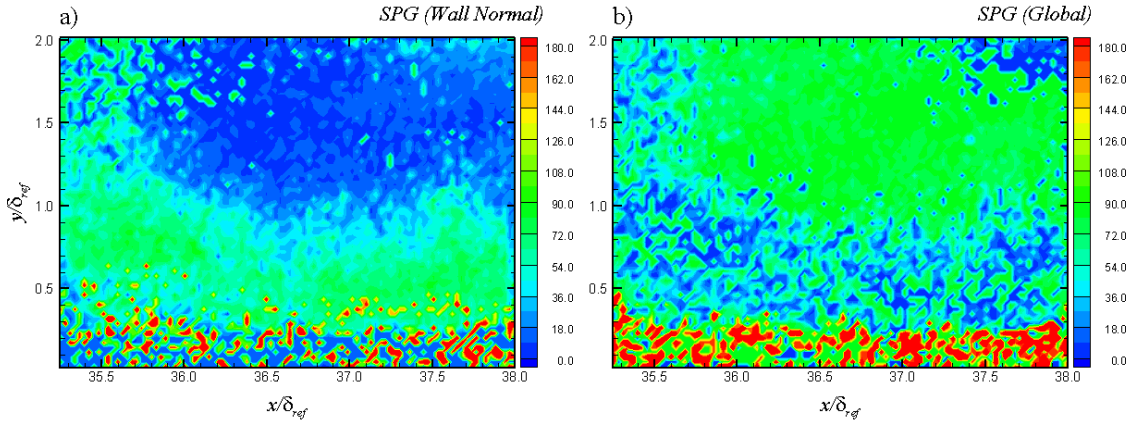

Figure 141: SPG Contours of Turbulent Stress-Turning Angle at 2nd Measurement Location

From the contours, profiles for the turbulent stress-turning angle were extracted normal to the wall; the profiles are shown in Figure 142 below. The ZPG model consistently exhibits a turbulent stress-turning angle near 20 degrees through the outer half of the boundary layer. The angle decreases towards 10 degrees through the inner half of the boundary layer. For the WPG model, the turbulent stress-turning angle is near 10 degrees throughout the entire boundary layer. There is a small increase near 0.85 y/δ and again near 0.20 y/δ. For the SPG case, the turbulent stress-turning angle is very consistently near -10 degrees through the outer half of the boundary layer. From 0.50 y/δ to 0.30 y/δ the angle is very scattered. Below 0.3 y/δ, the turbulent stress-

turning angle is positive and increases from near zero at 0.3 y/δ to approximately 16 degrees at 0.15 y/δ.

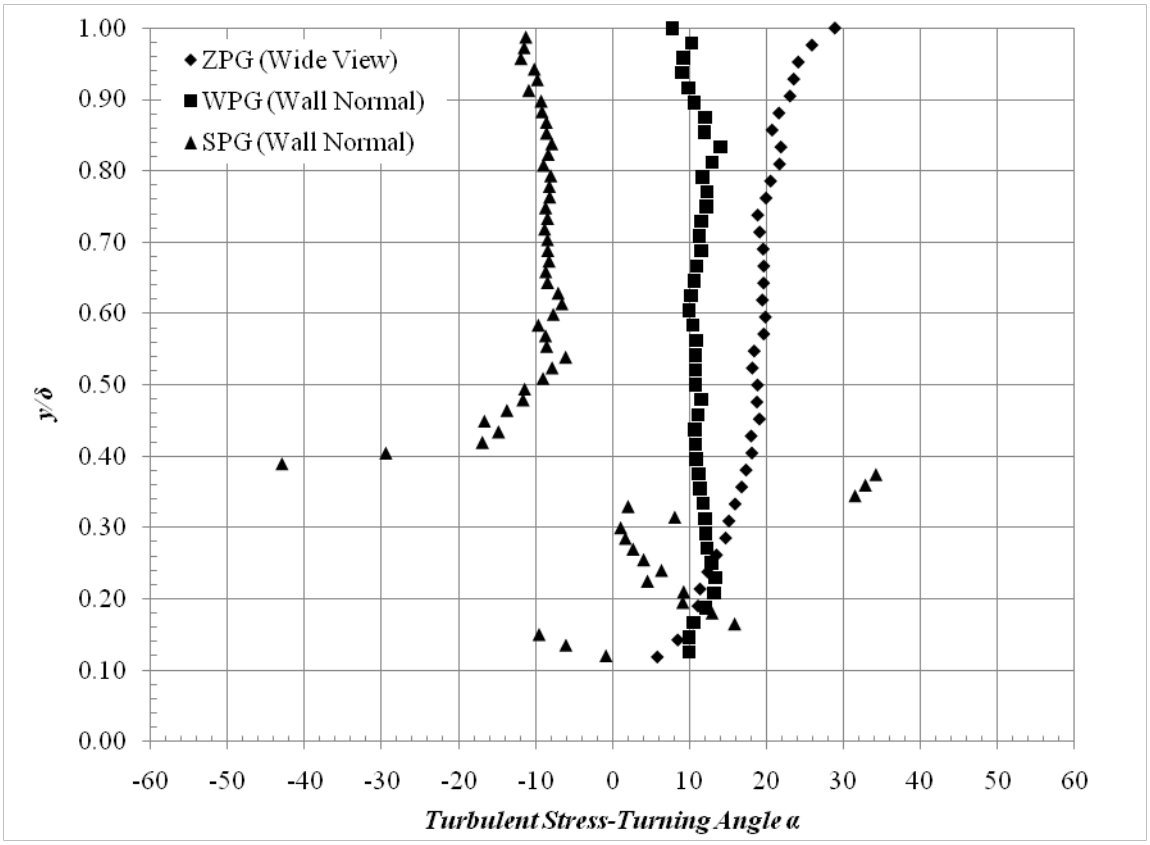

Figure 142: Turbulent Stress-Turning Angle Profiles

In the upper part of the boundary layer, the ZPG model had a turbulent stress-turning angle of approximately 18.8° while an angle of 10.8° and -9.0° was seen for the WPG and SPG cases specifically. These data were compared to the Mach 3 data from Ekoto et al to address scientific question 4 discussed in Chapter I. The turbulent stress-turning angles from the lower Mach number data were 12.7°, 10.0°, and 10.1° for the

ZPG, WPG, and SPG models respectively. This suggests that the turbulent stress turning angle is dependent of Mach number.

Reynolds Stress Quadrant Decomposition

The purpose of these measurements was to gain additional understanding of preferred orientation and events occurring within the boundary layer flow. These data addressed scientific question 2 described in Chapter I.

In order to learn more about the structure of turbulence within the supersonic boundary layer, Reynolds stress quadrant decomposition analyses were performed. This method is used to recognize the preferred orientation and events occurring at a specific location within the flow[56,57]. The velocity fluctuations measured from the PIV data are used for the quadrant decomposition technique by separating the data into four possible quadrants.

- Q1 $\left(u' > 0,\, v' > 0\right)$; faster moving fluid in an upward direction
- Q2 $\left(u' < 0,\, v' > 0\right)$; slower moving fluid in an upward direction
- Q3 $\left(u' < 0,\, v' < 0\right)$; slower moving fluid in a downward direction
- Q4 $\left(u' > 0,\, v' < 0\right)$; faster moving fluid in a downward direction

A sketch from Adrian (2000) shown in graphically depicts Q2 and Q4 events around a hairpin vortex.

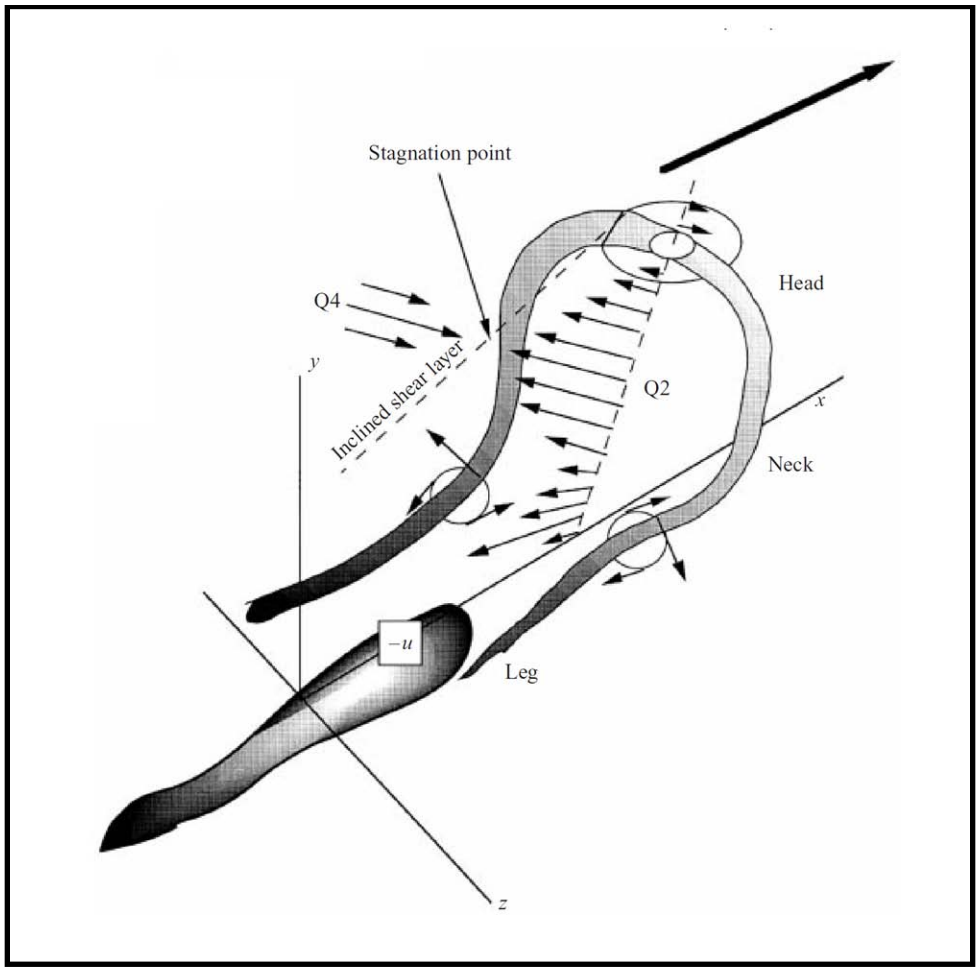

Figure 143: Sketch of a Hairpin Vortex and the Induced Motion[58]

An instantaneous shear angle is defined to better understand the organization of the large-scale, energy containing eddies.

$$\Psi = \tan^{-1}\left(\frac{v'}{u'}\right) \tag{4.11}$$

This instantaneous shear angle represents the angle of the velocity fluctuation with respect to the velocity vector direction. The quadrant decomposition was carried out for

several locations for each pressure gradient model including near the wall and into the freestream.

In the following discussion, only plots of the ZPG wide view, WPG in wall normal coordinates and SPG in wall normal coordinates were presented. The other cases displayed similar results are given in Appendix D for completeness.

The quadrant decomposition scatter plots as well as the instantaneous shear angle probability density functions for the ZPG wide view are shown belov for various locations normal to the wall. In the first two locations above the boundary layer, shown in Figure 144 and Figure 145, the velocity variations are small and all of the points are grouped near zero. Unlike previous studies though, the *u* fluctuating velocity is larger than the *v* fluctuating velocity which causes the group for form an ellipse rather than a circle. Regardless, in the freestream, the velocity fluctuations are near zero. The PDF of Ψ at $y/\delta_{ref} = 1.4$ shows a spike at approximately -5 degrees. This agrees with theory that the dominant quadrants should be Q2 and Q4, thus causing a negative instantaneous shear angle. At $y/\delta_{ref} = 1.2$ the scatter plot shows more outlying points compared to the $y/\delta_{ref} = 1.4$ plot, specifically in Q2. This shows that intermittency of the boundary layer edge as fluid from the boundary layer is periodically ejected into the freestream flow. Additionally, the instantaneous shear angle becomes very slightly more negative and more defined.

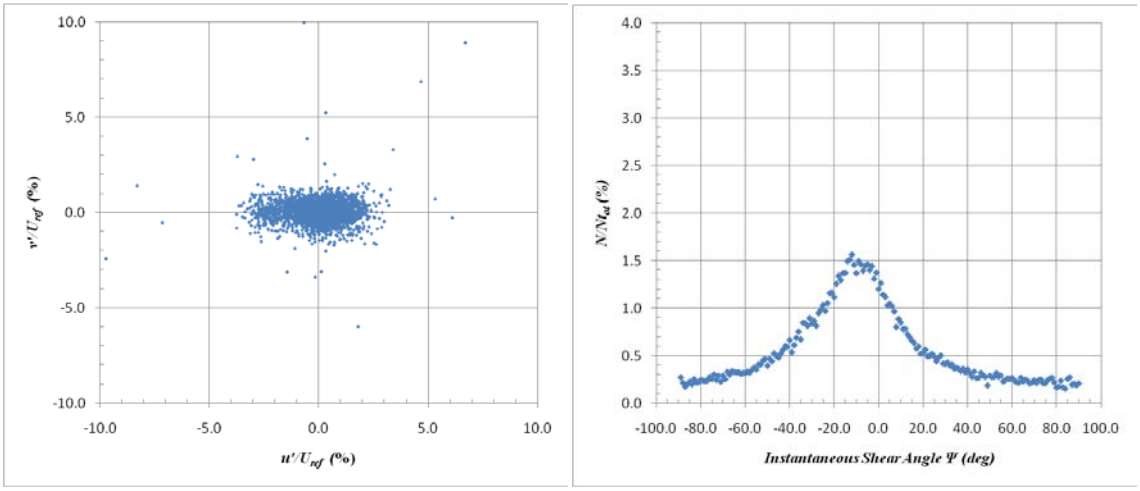

Figure 144: ZPG (Wide View) Quadrant Decomposition at y/δ_{ref} =1.4 at 1st Measurement Location

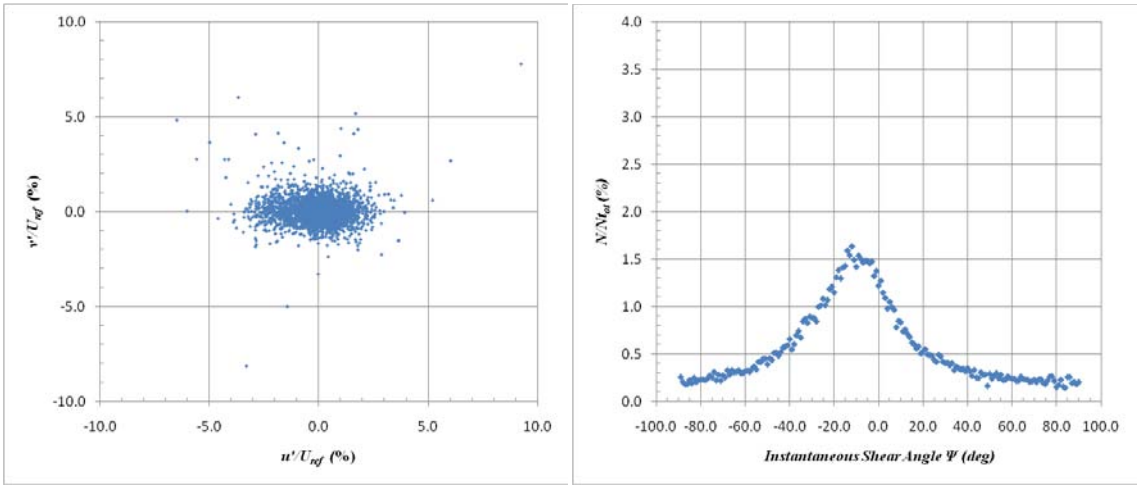

Figure 145: ZPG (Wide View) Quadrant Decomposition at y/δ_{ref} =1.2 at 1st Measurement Location

At the edge of the boundary layer, shown in Figure 146, the velocity fluctuations show additional scatter in the Q2 quadrant. It is interesting to note that the other quadrants do not show much difference from the freestream to the edge of the boundary

layer. The instantaneous shear angle PDF shows that Ψ again becomes slightly more negative and the peak increases near -8 degrees.

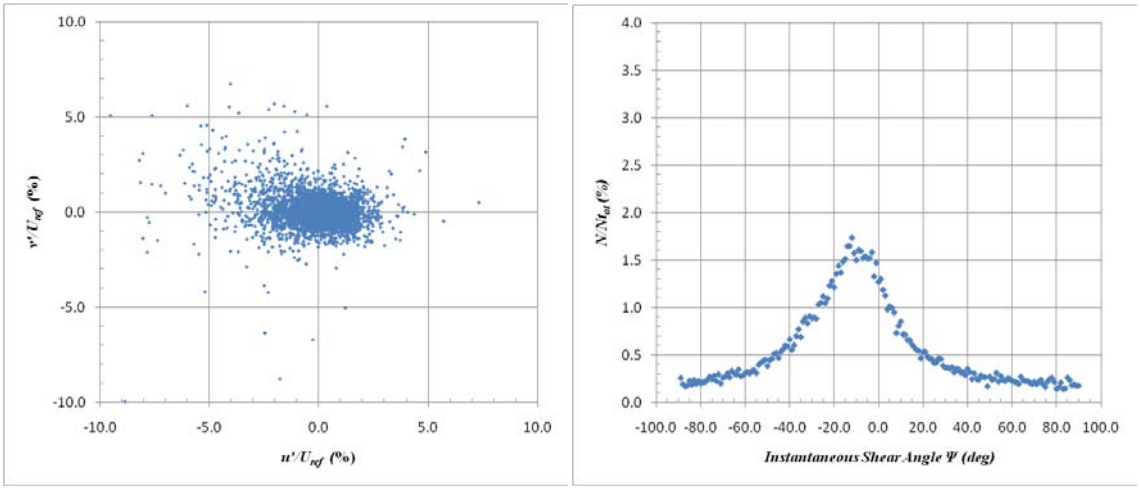

Figure 146: ZPG (Wide View) Quadrant Decomposition at y/δ_{ref} =1.0 at 1st Measurement Location

Figure 147 and Figure 148 show the quadrant decomposition for the ZPG wide view for $y/\delta_{ref} = 0.8$ and $y/\delta_{ref} = 0.6$ respectively. In the upper half of the boundary layer, the velocity fluctuations display a similar trend seen near the boundary layer edge. Significant scatter is seen in Q2 while the other three quadrants are relatively unchanged. The ellipse grouping begins to stretch in the *u* direction signifying that the *u* velocity fluctuations are strengthening. From the instantaneous shear angle PDFs, Ψ continues to become slightly more negative at each location and more defined as the peak of the PDF grows.

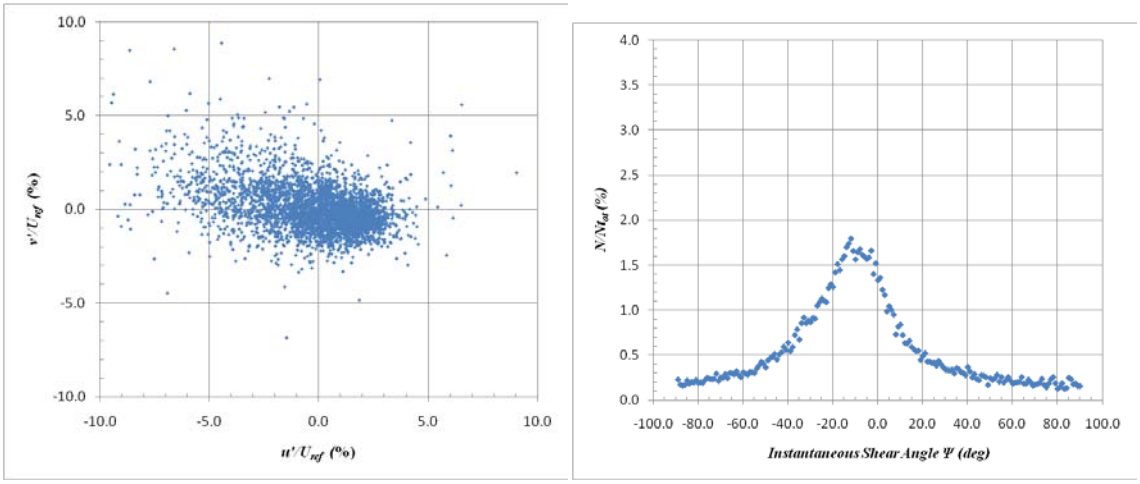

Figure 147: ZPG (Wide View) Quadrant Decomposition at y/δ_{ref} =0.8 at 1st Measurement Location

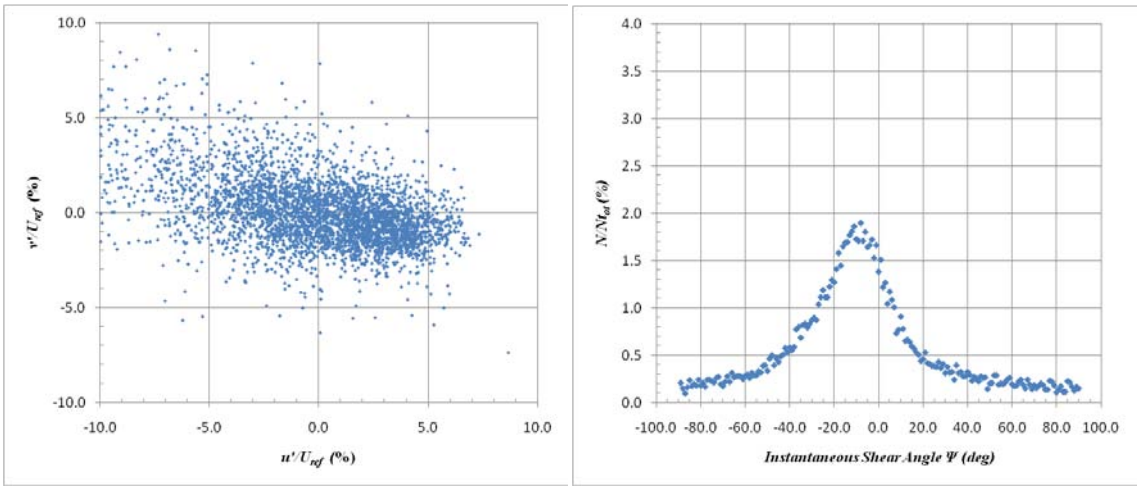

Figure 148: ZPG (Wide View) Quadrant Decomposition at y/δ_{ref} =0.6 at 1st Measurement Location

At $y/\delta_{ref} = 0.4$, shown in Figure 149, the velocity fluctuation scatter plot becomes much less grouped. From image to image, there are beginning to show significant changes in the velocity fluctuations in both the *u* and *v* velocities. The PDF

of the instantaneous shear angle shows the peak increasing and the angle remaining approximately the same as the previous location.

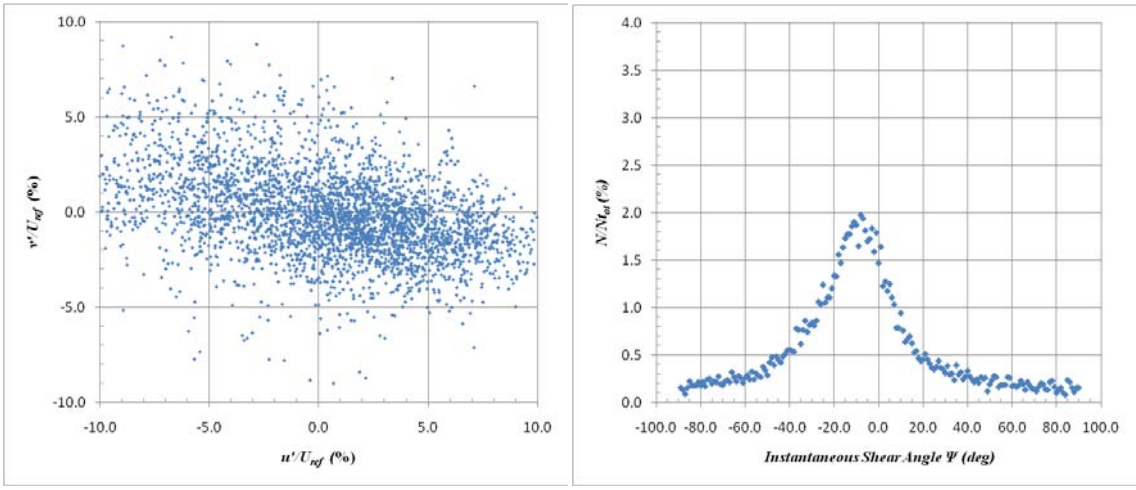

Figure 149: ZPG (Wide View) Quadrant Decomposition at y/δ_{ref} =0.4 at 1st Measurement Location

Figure 150 and Figure 151 show the quadrant decomposition results for the ZPG wide view at $y/\delta_{ref} = 0.2$ and $y/\delta_{ref} = 0.1$ respectively. The trend in the *u* and *v* velocity fluctuations is continued for these last two locations nearest the wall. The points become largely scattered in the Q2 and Q4 quadrants with only slight scattering in Q1 and Q3. The group clearly becomes more stretched closer to the wall signifying that the velocity fluctuations become significant. The PDF of the instantaneous shear angle show that the peak angle increases in magnitude, however the dominant angle moves slightly back towards zero, especially at $y/\delta_{ref} = 0.1$. The overall trend for the ZPG wide view quadrant decomposition is in agreement with previous work.

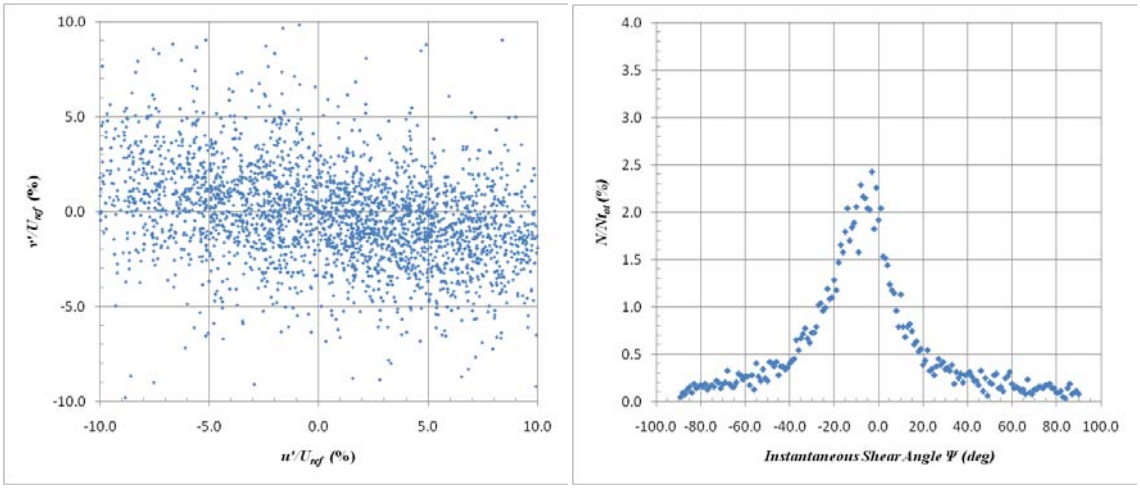

Figure 150: ZPG (Wide View) Quadrant Decomposition at y/δ_{ref} =0.2 at 1st Measurement Location

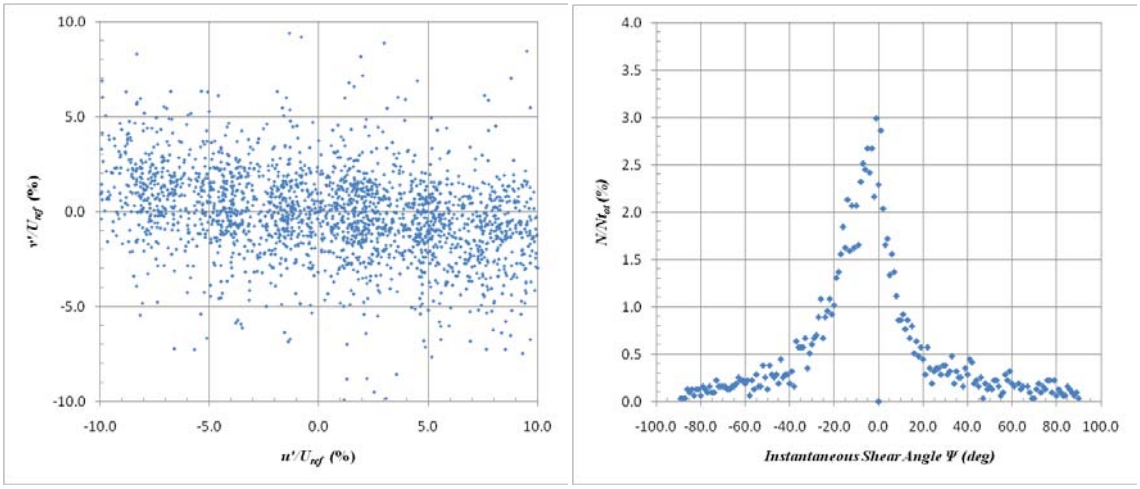

Figure 151: ZPG (Wide View) Quadrant Decomposition at y/δ_{ref} =0.1 at 1st Measurement Location

The quadrant decomposition plots for the WPG model in wall normal coordinates are given below. The same y-locations as the ZPG were analyzed. At $y/\delta_{ref} = 1.4$ and at $y/\delta_{ref} = 1.2$, seen in Figure 152 and Figure 153, the *u* and *v* velocity fluctuations

scatter plots show that the grouping is more circular than the ZPG case. However, at $y/\delta_{ref} = 1.2$ the scatter begins to increase in Q2 as seen before. The PDFs of the instantaneous shear angle show that Ψ is more uniformly spread compared to the ZPG case, but there a peak is still present at approximately -4 degrees. The magnitude of the peak instantaneous shear angle was much lower than the corresponding location on the ZPG model.

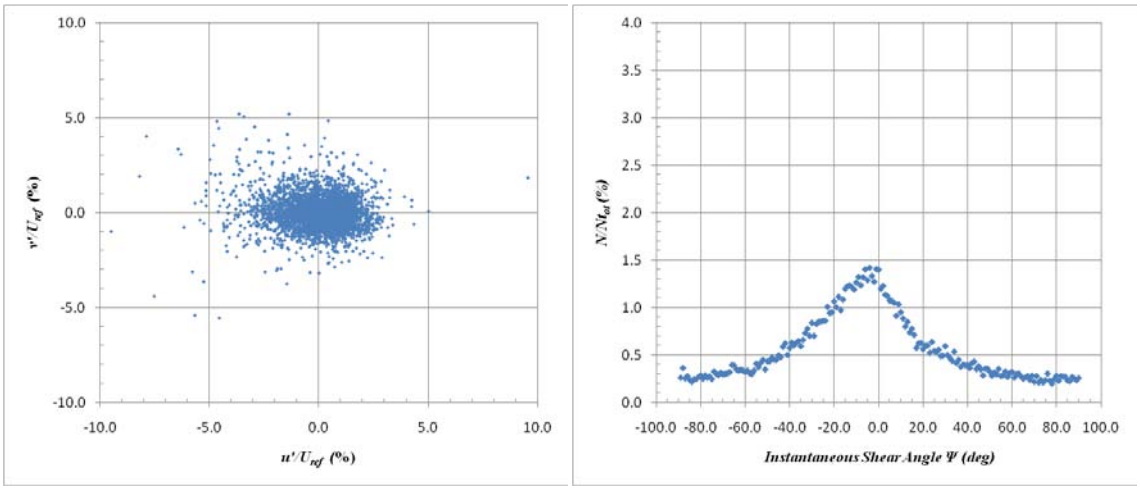

Figure 152: WPG Quadrant Decomposition at y/δ_{ref} =1.4 at 2nd Measurement Location (Wall Normal Coordinate System)

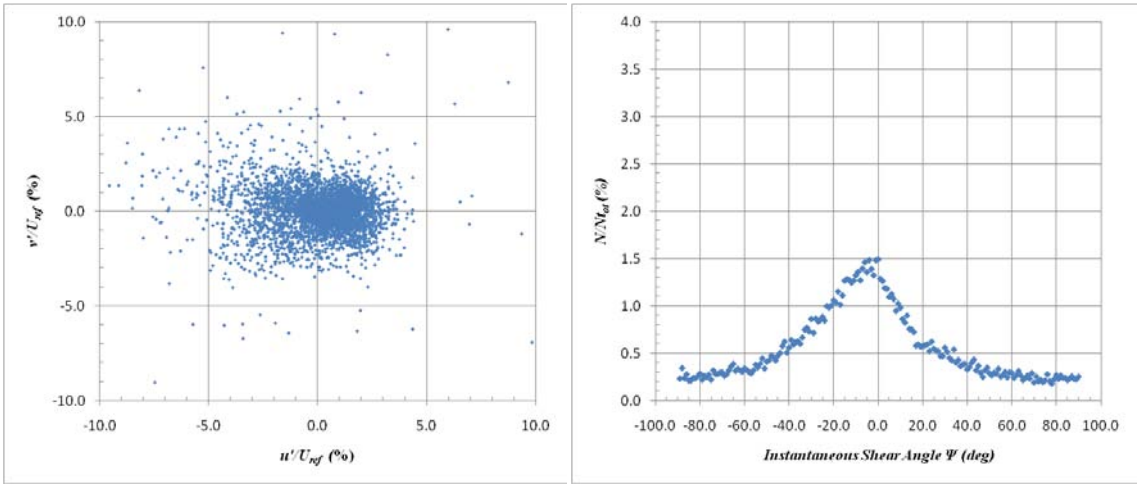

Figure 153: WPG Quadrant Decomposition at y/δ_{ref} =1.2 at 2nd Measurement Location (Wall Normal Coordinate System)

At $y/\delta_{ref} = 1.0$, shown in Figure 154, the velocity fluctuation scatter plot is slightly more spread out compared to the freestream locations. This again exhibits the Q2 events that eject the slower moving boundary layer fluid into the freestream flow. Additionally, the PDF of Ψ shows a slightly higher peak with a dominant angle that is slightly negative.

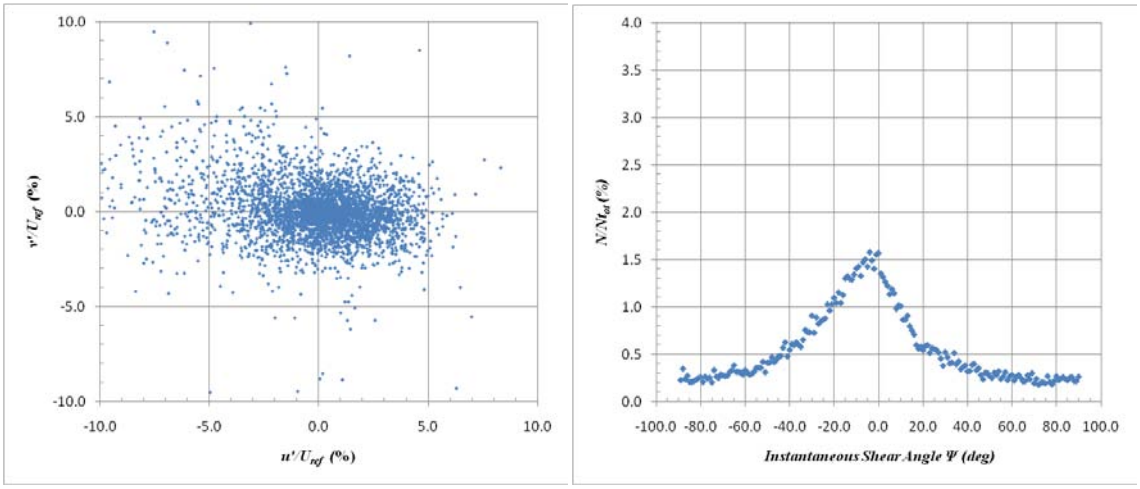

Figure 154: WPG Quadrant Decomposition at y/δ_{ref} =1.0 at 2nd Measurement Location (Wall Normal Coordinate System)

Figure 155 and Figure 156 show the quadrant decomposition results for the WPG model in wall normal coordinates at $y/\delta_{ref} = 0.8$ and $y/\delta_{ref} = 0.6$. The *u* an *v* velocity fluctuations continue to increase in scatter and extend into the Q2 and Q4 quadrants. The major change of velocity fluctuations occur in the streamwise direction as expected. For each successive location closer to the wall, the instantaneous shear angle PDF shows a larger, more defined peak.

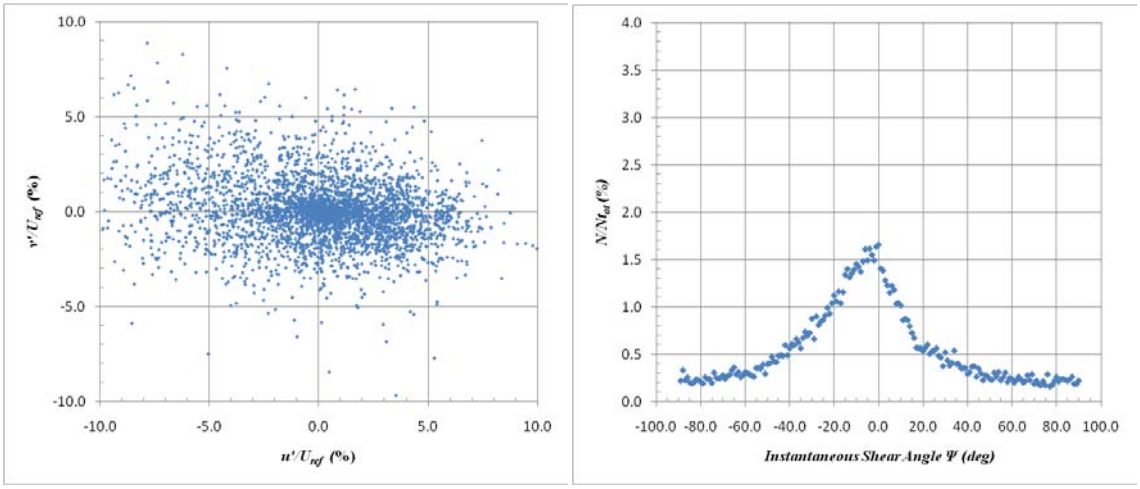

Figure 155: WPG Quadrant Decomposition at y/δ_{ref} =0.8 at 2nd Measurement Location (Wall Normal Coordinate System)

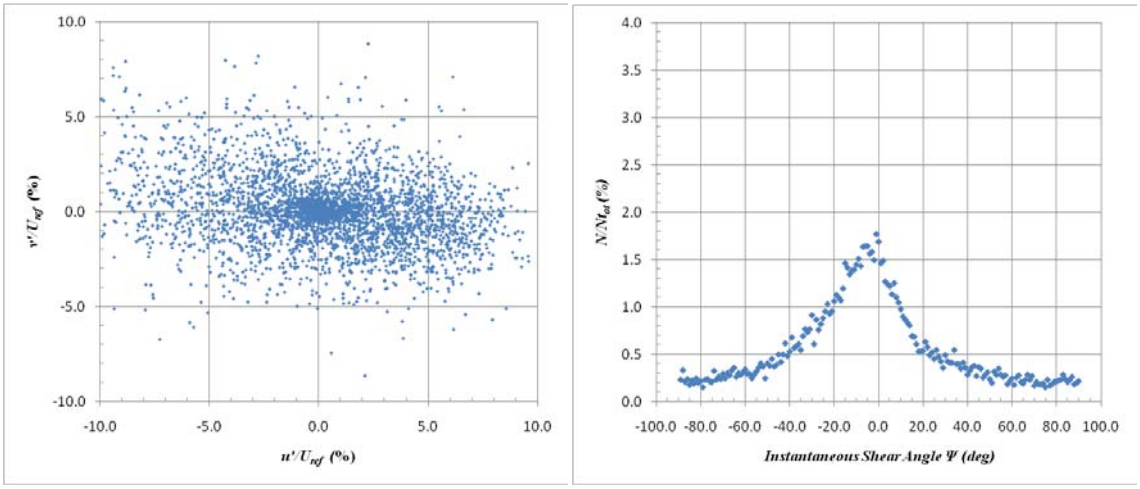

Figure 156: WPG Quadrant Decomposition at y/δ_{ref} =0.6 at 2nd Measurement Location (Wall Normal Coordinate System)

In the lower part of the boundary layer, the quadrant decomposition analyses exhibited a similar trend as previously observed. At $y/\delta_{ref} = 0.4$, seen in Figure 157, the velocity fluctuations increase in spread and the instantaneous shear angle becomes

more defined at a slightly negative value. For $y/\delta_{ref} = 0.2$ and $y/\delta_{ref} = 0.1$, shown in Figure 158 and Figure 159, both the velocity fluctuations scatter plot and the instantaneous shear angle PDF are very similar. At $y/\delta_{ref} = 0.1$, Ψ is approximately -2 degrees with a peak of just over 2%. Unlike the ZPG case, the *u* and *v* velocity fluctuations for the WPG in wall normal coordinates show a dense group near zero all the way to the wall. The reason that the peak instantaneous shear angle is closer to zero compared to the ZPG case is probable due to slight wall curvature and the wall normal coordinate system not corresponding to the global flow axes.

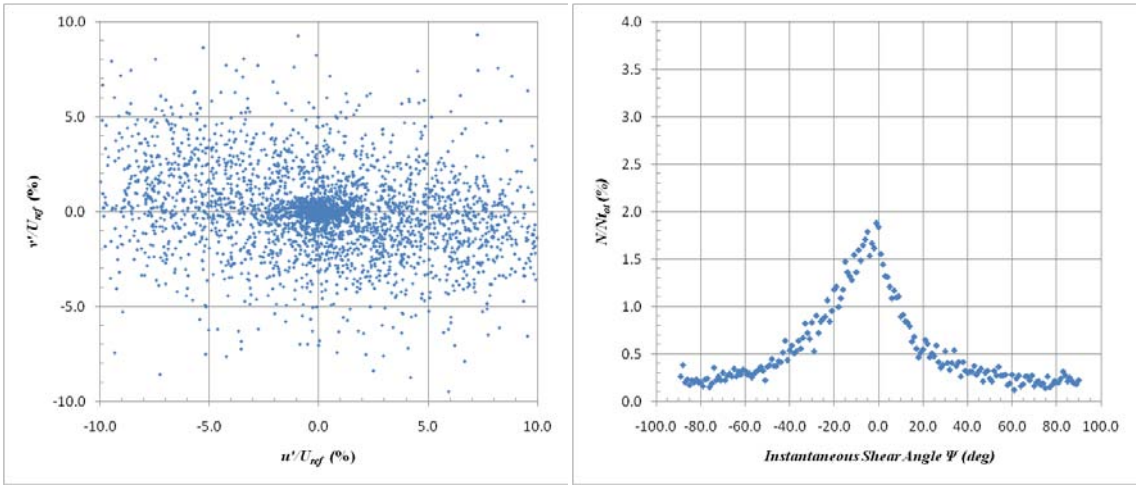

Figure 157: WPG Quadrant Decomposition at y/δ_{ref} =0.4 at 2nd Measurement Location (Wall Normal Coordinate System)

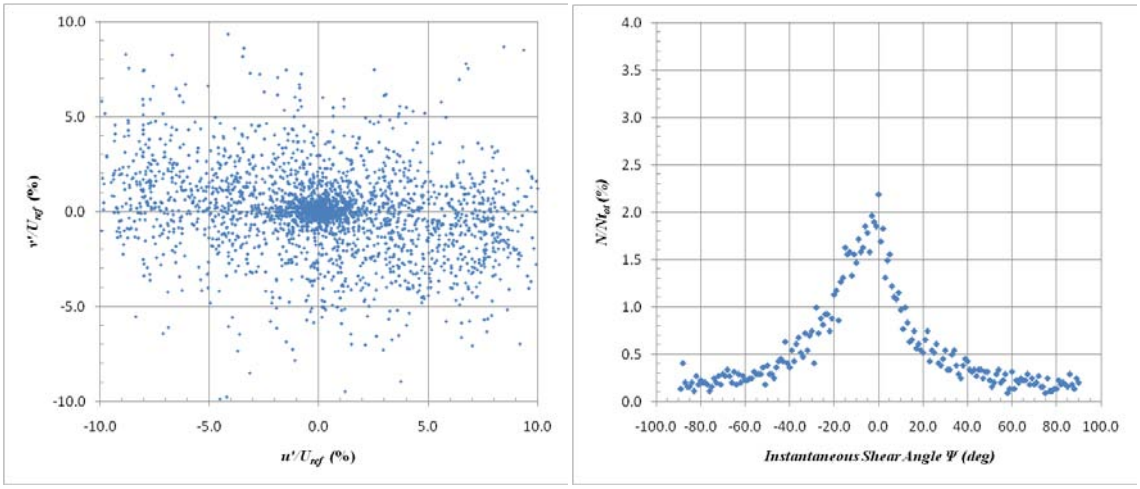

Figure 158: WPG Quadrant Decomposition at y/δ_{ref} =0.2 at 2nd Measurement Location (Wall Normal Coordinate System)

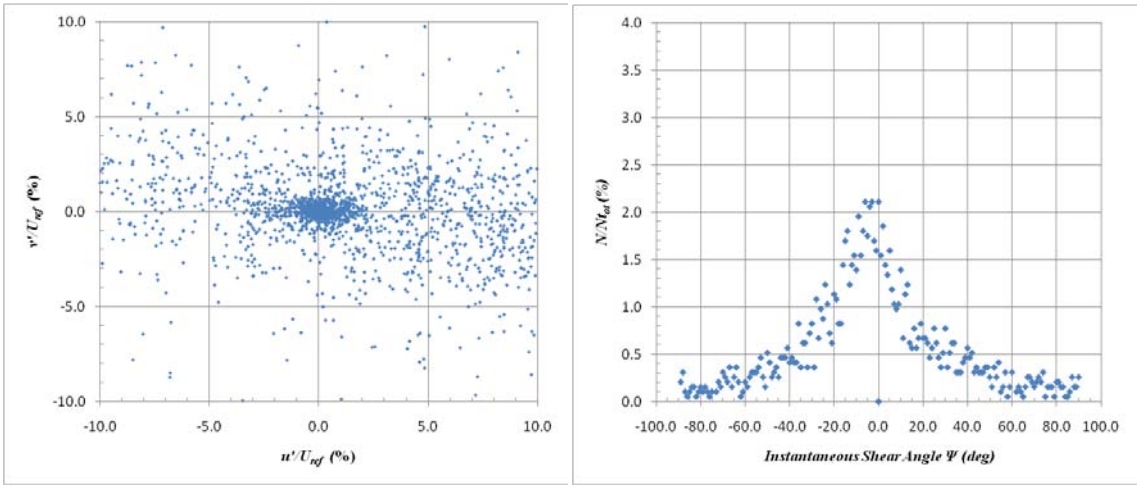

Figure 159: WPG Quadrant Decomposition at y/δ_{ref} =0.1 at 2nd Measurement Location (Wall Normal Coordinate System)

The quadrant decomposition plots for the SPG in wall normal coordinates are shown in Figure 160 through Figure 167. Overall, similar trends in the *u* and *v* velocity fluctuations are seen for the SPG model as were seen for the ZPG and WPG cases. As the interrogation location moves closer to the wall, the scatter in the velocity fluctuations

increases significantly with a small dense grouping remaining near zero all the way down to $y/\delta_{ref} = 0.1$. The most interesting result of the quadrant decomposition analysis for the SPG model is the shape of the curve of the instantaneous shear angle PDF. For each location, the peak angle is near zero. Unlike the ZPG and WPG cases, the peak is very sharp with a fairly even distribution of off-peak angles. This result is magnified at $y/\delta_{ref} = 0.1$ where the peak is largest and the off-peak values are very low.

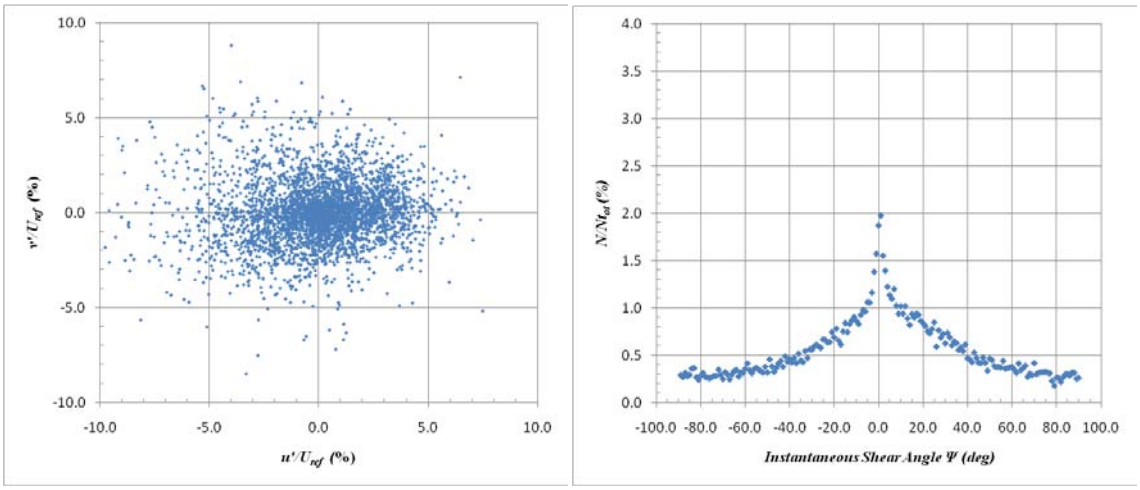

Figure 160: SPG Quadrant Decomposition at y/δ_{ref} =1.4 at 2nd Measurement Location (Wall Normal Coordinate System)

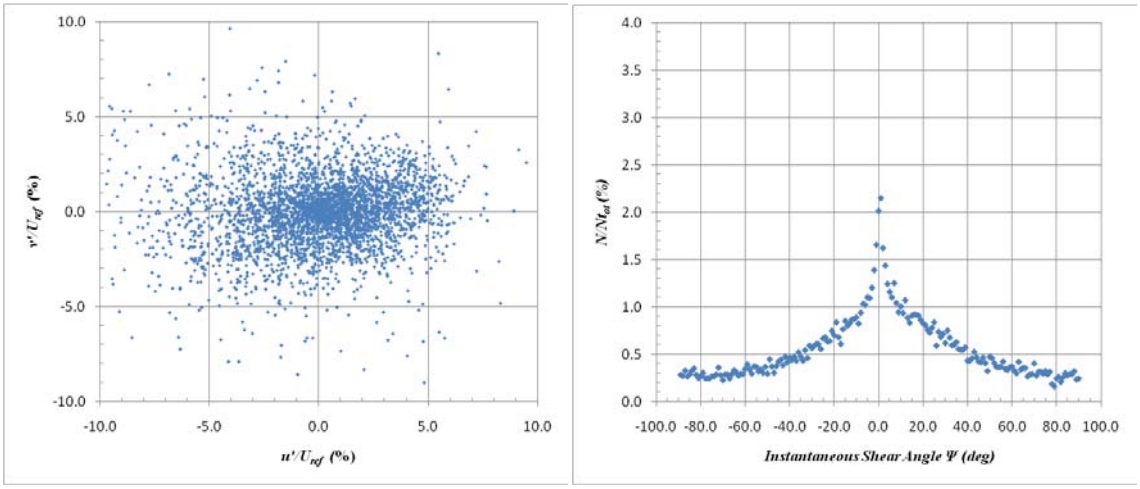

Figure 161: SPG Quadrant Decomposition at y/δ_{ref} =1.2 at 2nd Measurement Location (Wall Normal Coordinate System)

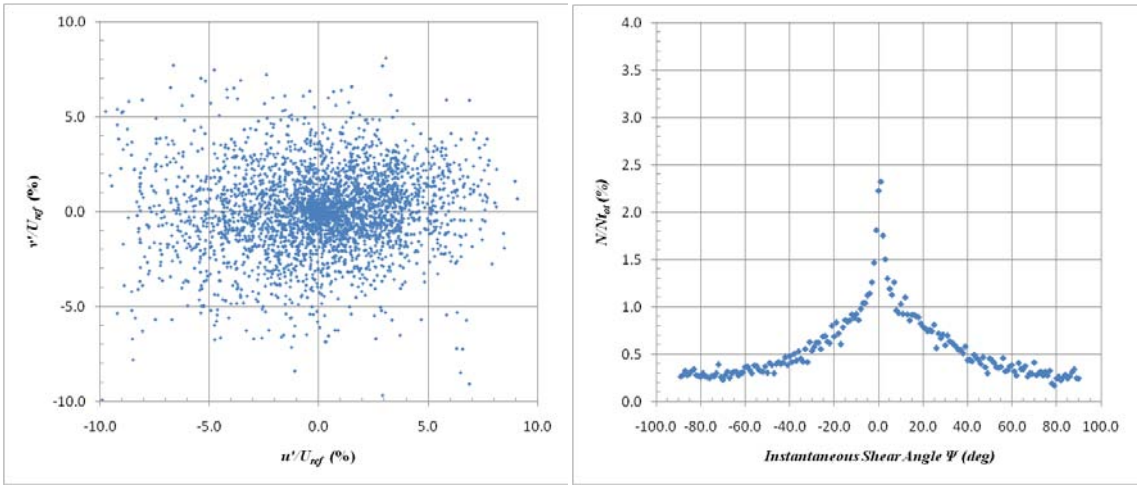

Figure 162: SPG Quadrant Decomposition at y/δ_{ref} =1.0 at 2nd Measurement Location (Wall Normal Coordinate System)

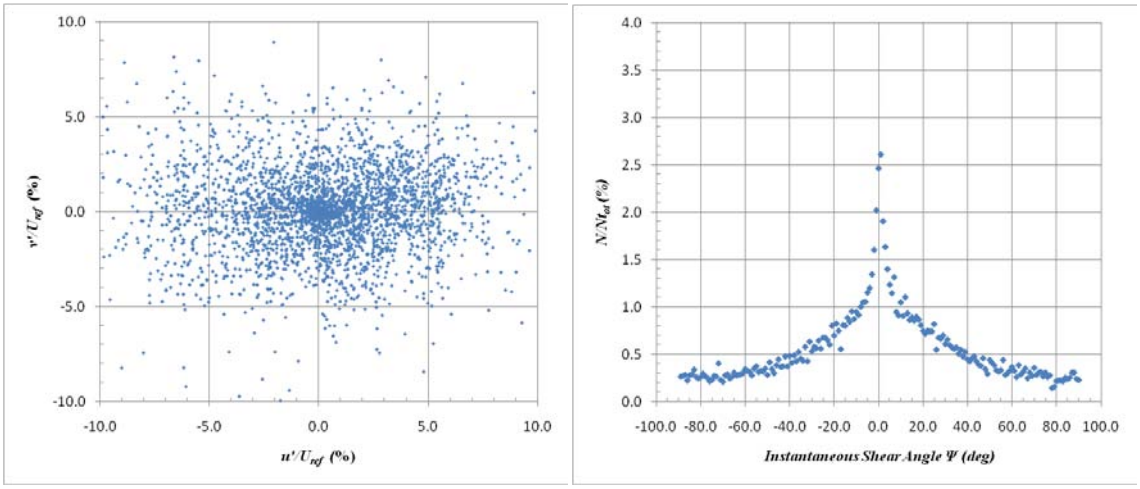

Figure 163: SPG Quadrant Decomposition at y/δ_{ref} =0.8 at 2nd Measurement Location (Wall Normal Coordinate System)

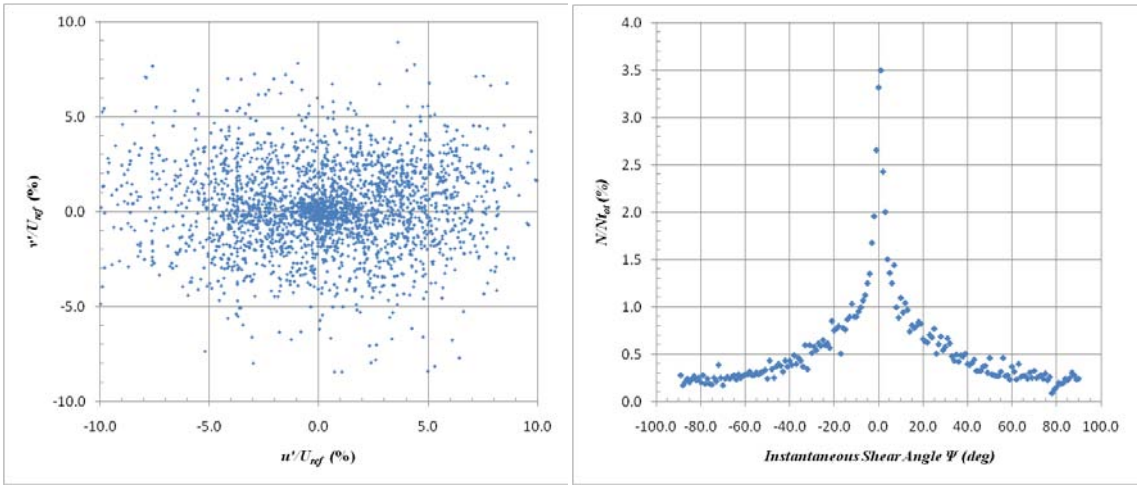

Figure 164: SPG Quadrant Decomposition at y/δ_{ref} =0.6 at 2nd Measurement Location (Wall Normal Coordinate System)

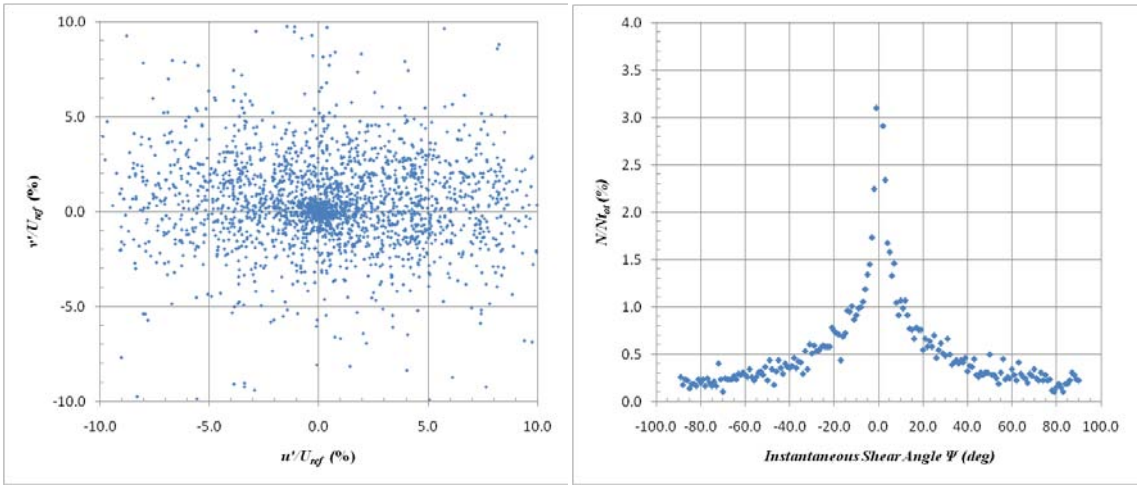

Figure 165: SPG Quadrant Decomposition at y/δ_{ref} =0.4 at 2nd Measurement Location (Wall Normal Coordinate System)

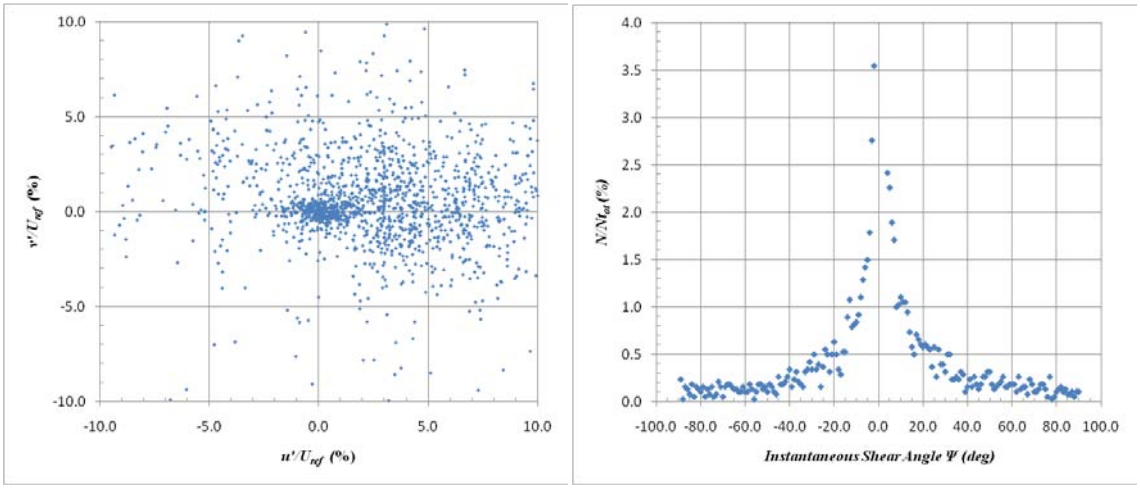

Figure 166: SPG Quadrant Decomposition at y/δ_{ref} =0.2 at 2nd Measurement Location (Wall Normal Coordinate System)

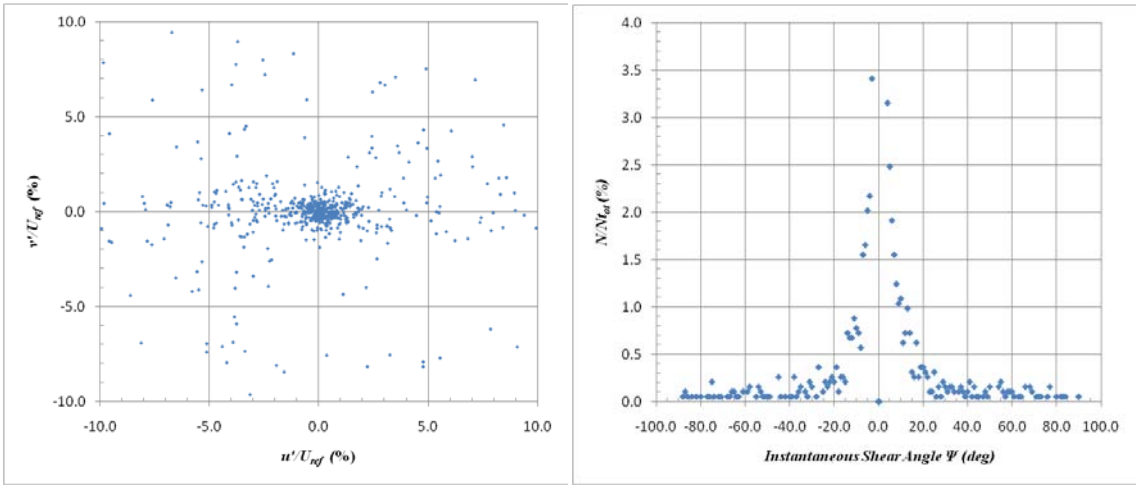

Figure 167: SPG Quadrant Decomposition at y/δ_{ref} =0.1 at 2nd Measurement Location (Wall Normal Coordinate System)

For the SPG case, the instantaneous shear angle is close to zero regardless of the interrogation location. This could be attributed to the wall normal coordinate system that is rotated from the global flow axis. The velocity fluctuation scatter plots do not show a preference to the Q2 and Q4 quadrants as seen in the ZPG and WPG cases. This illustrates that the boundary layer is not only ejecting slower fluid into the freestream, but it is also pushing faster fluid into the freestream. Additionally, fluid is moving down into the boundary layer from the freestream region regardless of the local instantaneous velocity relative to the average velocity.

These data were compared to lower Mach number data to address scientific question 4 described in Chapter I. The freestream in the present study is less isotropic than the lower Mach number data, signifying that the quadrant decomposition analysis is dependent on Mach number.

Two-Point Correlations

The purpose of these data was to gain additional understanding of the turbulent length scales within the boundary layer. These data addressed scientific question 2 described in Chapter I.

Two-point correlations were performed using the streamwise velocity fluctuations (*u*). This method is a well established way of quantifying the turbulent length scales within a turbulent flow[59,60]. A two-dimensional two-point correlation map was constructed directly across the entire range of wall-normal locations using the following equation.

$$R_{uu}\left(\Delta x, y, y_{ref}\right) = \frac{\overline{u\left(x, y_{ref}\right)u\left(x+\Delta x, y\right)}}{\sigma_u\left(y_{ref}\right)\sigma_u\left(y\right)}$$

where y_{ref} is the reference wall-normal location at which the correlation is computed, Δx is the in-plane streamwise separation, $\sigma_u\left(y_{ref}\right)$ is the rms of *u* at y_{ref} and $\sigma_u\left(y\right)$ is the rms of *u* at location *y*.

The two-point correlation maps computed for the ZPG, WPG, and SPG models are given in Figure 168, Figure 169, and Figure 170 respectively. From these it can clearly be seen that the correlation of the streamwise velocity fluctuations significantly decreases due to the favorable pressure gradients.

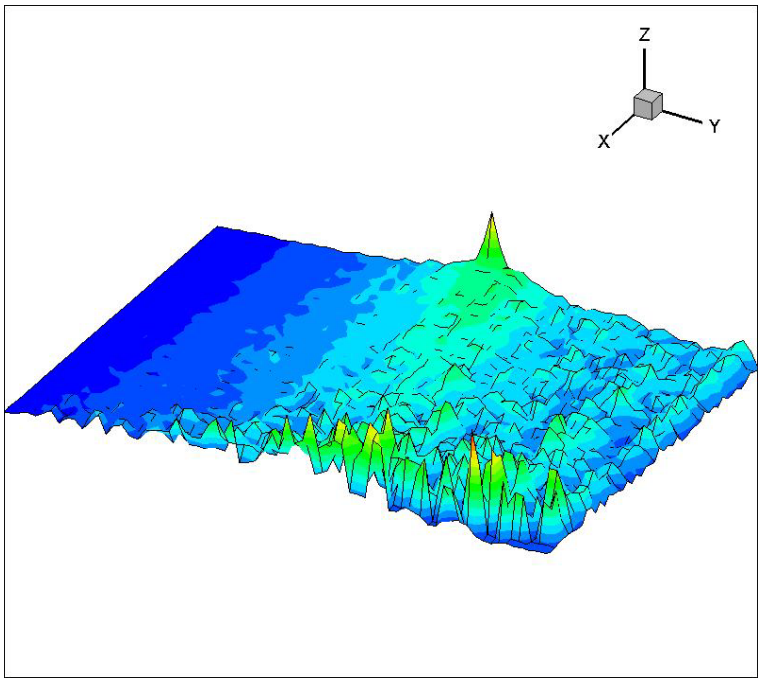

Figure 168: ZPG Streamwise Autocorrelation Map

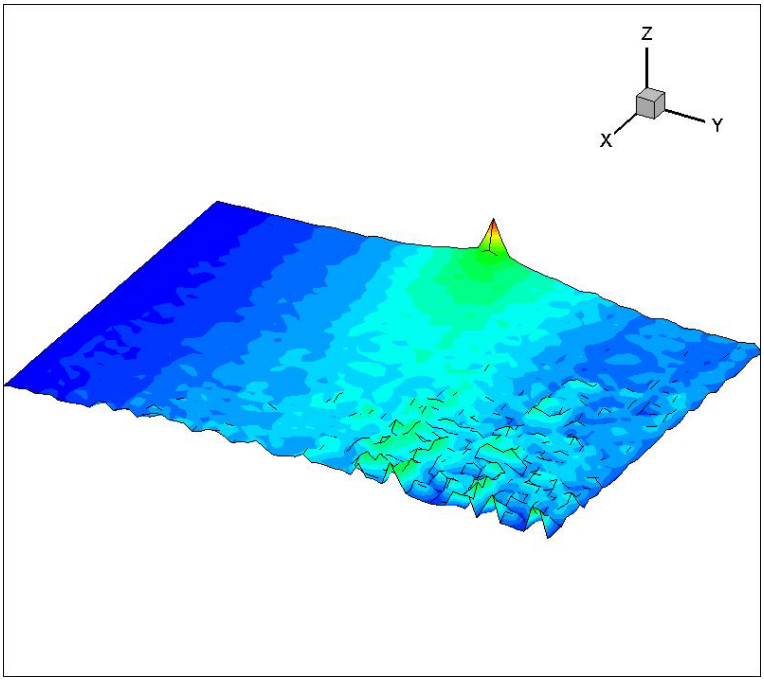

Figure 169: WPG Streamwise Autocorrelation Map

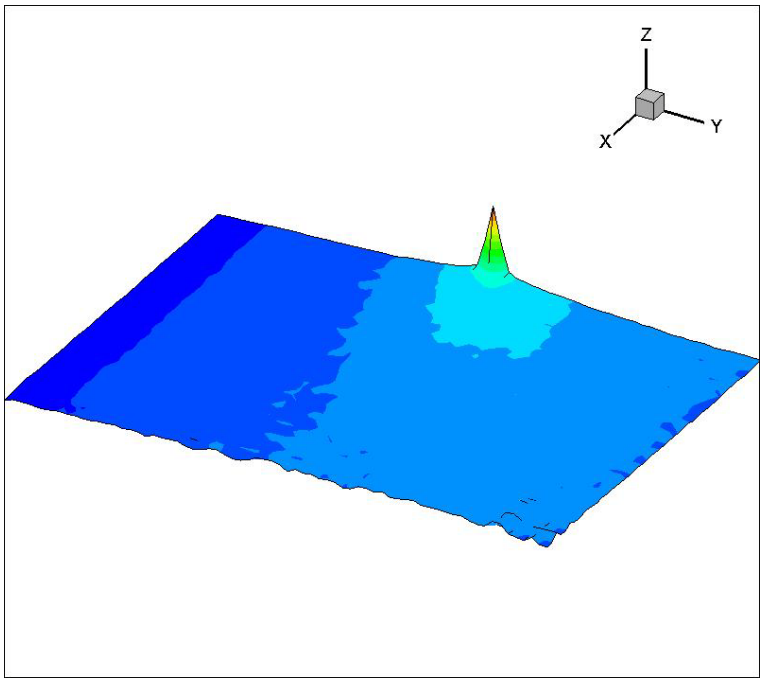

Figure 170: SPG Streamwise Autocorrelation Map

From the two-dimensional autocorrelation maps, the autocorrelation for each pressure gradient model at y_{ref} was plotted in Figure 171. Again, it can be seen that the autocorrelation for the SPG model is dramatically less than the ZPG and even the WPG cases. These results suggest that for the SPG case, the large structures within the boundary layer break up into smaller scales, therefore addressing scientific question 2.

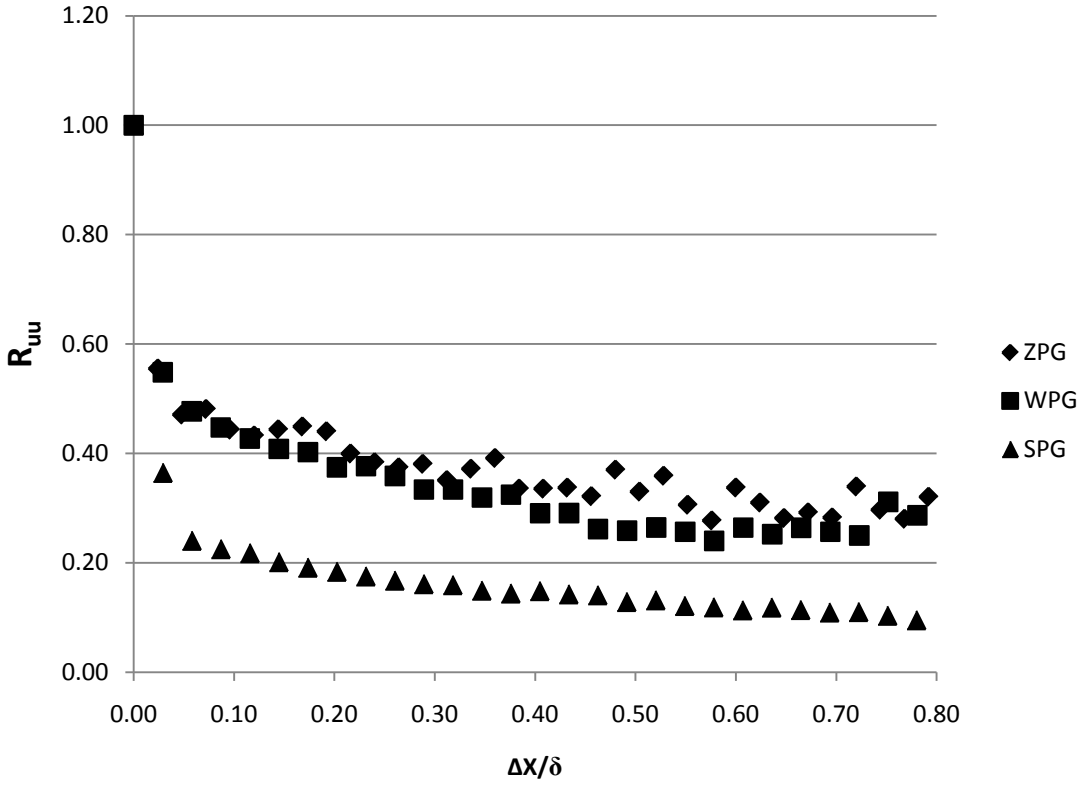

Figure 171: Streamwise Autocorrelation at y/δ=0.5

CHAPTER VI

CONCLUSIONS AND RECOMMENDATIONS

This final chapter is split into two main sections: conclusions and recommendations for the hypersonic boundary layer study over curvature-driven favorable pressure gradients, and conclusions and recommendations for the design and construction of the hypersonic wind tunnel facility (described in Appendix F).

Hypersonic Boundary Layer Study

Conclusions

The overarching research objective for the proposed research project is to improve our basic understanding and prediction capabilities of a high Mach high Reynolds number boundary layer over curvature driven pressure gradients. To address this objective, detailed studies of the influence of streamline curvature driven pressure gradients on a Mach 5.0, high Reynolds number (Re_θ =36,000) turbulent boundary layer were performed to answer the following scientific questions.

(1) How is state of the mean flow and turbulence statistics altered by curvature driven favorable pressure gradients?

(2) How is the structure of wall turbulence altered by curvature driven favorable pressure gradients; break-up, stretch or a combination of both?

(3) How are the Reynolds stress component production mechanisms altered by curvature driven favorable pressure gradients?

(4) What is the effect of Mach number on the above processes?

The important conclusions drawn from the analysis of the measured data in Chapter V are summarized below.

The first step in the study was to characterize the upstream flow boundary condition and assess the uncertainty in our measurements. This was important for two reasons. First, the upstream canonical equilibrium boundary provided the basis for comparison when assessing pressure gradient effects. Second, the upstream characterization provides the necessary inflow condition for future numerical simulation comparison. Our measurements demonstrated that the flow at the upstream measurement location, in the zero pressure gradient region (ZPG), was two-dimensional and independent of the installed pressure gradient model. The measured freestream Mach number was 4.88, and the freestream turbulence levels (axial and transverse) were 1.2%. Additionally, the ZPG case at this location was shown to agree with expected Van Driest II scaling, the law-of-the-wall, and the defect law. This comparison along with the spanwise survey validated the facility flow characteristics as well as the PIV measurement technique. Quantitative uncertainty analyses were also performed and summarized in Appendix C.

A flow visualization study was performed second to qualitatively examine the large-scale structures. Movies created from a series of instantaneous liquefaction images allowed for monitoring of the movement of the boundary layer structures and intermittency. Qualitative visual comparisons between the ZPG, WPG, and SPG models were performed. It was observed that the flow structure of the boundary layer changed

with the introduction of the favorable pressure gradients; the boundary layer became less intermittent and larger vortical structures were less easily discerned. This suggests that the dominant structural change was breakdown, not stretching. The large structures seen in the ZPG case are broken down into smaller scructures that are not as clearly seen in the flow visualization. However the qualitative flow visualization alone is not sufficient to determine the actual trend.

The third step in the study was to perform and analyze the velocity vectors for the WPG and SPG cases. Data were presented in wall normal and global coordinates. However, no significant difference was seen for the mean velocity fields. The mean velocity gradients were computed for each pressure gradient case using central differencing. Reductions in the primary velocity gradient $d\overline{u}/dy$ and the extra strain rate $d\overline{v}/dx$ due to the pressure gradients were seen while the extra strain rates $d\overline{u}/dx$ and $d\overline{v}/dy$ increased.

The *u* and *v* turbulence intensities were altered for the favorable pressure gradient models. The WPG showed a 3.8% decrease in axial turbulence intensity and a 18.9% decrease in transverse turbulence intensity compared to the ZPG case. The SPG showed a 13.6% decrease in axial turbulence intensity and a 15.2% increase in transverse turbulence intensity over the ZPG model. One of the most interesting results from the present study was the turbulent shear stress measurements over the pressure gradient models. As seen in previous work, it was expected that the turbulent shear stress should decrease with increasing favorable pressure gradient. For the WPG model, this effect was observed with a 35.5% decrease. However, for the SPG, not only did the turbulent

shear stress decrease, it changed sign and became slightly less than zero. This phenomenon was seen in previous studies at lower Mach numbers, but not to the extent observed in the present work[41,46]. Comparison to the Ekoto study indicated that the response of the Reynolds shear stress increased with Mach number.

The axial turbulent stress production P_{xx} decreased 40.4% with the WPG model and actually changed sign with a slight positive value for the SPG case. For the transverse turbulent stress production P_{yy}, the addition of the WPG did not have a large effect. However, the SPG case increased this production term significantly, approximately 450% of the ZPG value. The turbulent shear stress production term P_{xy} showed a decrease for the WPG and an increase for the SPG model compared to the ZPG of 51.9% and 32.8%, respectively. The effect of the favorable pressure gradient on the Reynolds stress production components is such that the axial turbulent stress production is decreased and the transverse turbulent stress production is increased. This trend is seen to a small extent for the WPG case and in the SPG to a larger extent. The results from the turbulent stress production terms are significant, however it is believed that the these terms cannot explain the large changes observed in the Reynolds stresses. The redistribution terms in the Reynolds transport equation become important in the favorable pressure gradient flows fields and help to drive the turbulence towards isotropy. The mean energy equation and the turbulent stress transport equation described in Chapter II are linked through identical production terms with opposide signs. Typically, energy cascades from the mean flow down into the turbulent structrure. However, the change in sign in the production terms suggest that the energy

is moving from the turbulence back into the mean flow though these linked terms. All three of the calculated production terms were compared to the Ekoto study. However, the data from that study is not presented as precisely as would be necessary for a completely accurate comparison. At a minimum, the production terms from the present study are of the same order and show similar trends as seen in the Ekoto study, leading to the conclusion that the production terms do not significantly depend on Mach number.

The turbulent stress principal axes analysis showed that the turbulent structure changed over the favorable pressure gradient models. The turbulent stress turning angle for the ZPG case was approximately 18.8 degrees at 0.5 y/δ. For the WPG model, the turbulent stress turning angle decreased slightly to 10.8 degrees at 0.5 y/δ. For the SPG model, the turbulent stress turning angle changed significantly, to -9.0 degrees at 0.5 y/δ. It is believed that this severe change in the turbulent stress turning angle may be due to the definition of α. Assuming small angles, the turning angle can be linearized as $\alpha \approx -\overline{u'v'}/\left(u'^2 - v'^2\right)$. For the SPG case, both the numerator and denominator are very close to zero, therefore making the angle ill-defined. Regardless, these results suggest that the curvature driven favorable pressure gradient greatly influences the structure of wall turbulence in the boundary layer. The turbulent stress principal axes are rotated relative to the mean flow direction by approximately 10 degrees and 30 degrees compared to the ZPG case for the WPG and SPG models, respectively. The 8.0 degree difference in turbulent stress turning angle between the WPG and ZPG models is much larger than that seen in the Ekoto study. Additionally, the SPG showed an additional change of approximately 20 degrees over the WPG model for the present study. The

results from Ekoto did not show such a severe change in turbulent stress turning angle, therefore suggesting that the turbulent stress turning angle is dependent on Mach number. The lower Mach number result may also be effected by the flow in that study being less isotropic than in the current study, therefore allowing Ekoto to better define the turbulent stress turning angle.

A quadrant decomposition analyses of the instantaneous velocity fields was performed. In the freestream, the velocity fluctuations are very small however, compared to previous studies at lower Mach numbers, the freestream is not as isotropic. Approaching the wall, the velocity fluctuations scatter plots become more ellipsoidal and stretch into the Q2 and Q4 quadrants as expected. This shows the presence of strong structures moving energy between the boundary layer and freestream flows. Additionally, the PDFs of the instantaneous shear angle at several interrogation locations show that nearer the wall, a specific shear angle becomes dominant; -14.0 degrees for the ZPG case, -6.0 degrees for the WPG case and 0.0 degrees for the SPG case. This signifies the alignment and organization of turbulent structures within the boundary layer. For the WPG case, the velocity fluctuations were generally decreased and the dominant instantaneous shear angle is smaller and less probable. For the SPG model, the velocity fluctuations are further decreased while the image-to-image intermittency increased. Additionally, for the SPG case, the instantaneous shear angle was very near zero throughout the entire boundary layer, suggesting that the large structures seen in the ZPG boundary layer have broken up, becoming more isotropic. These results suggest that the curvature driven favorable pressure gradients alter the basic structure of the

turbulent boundary layer. The WPG model decreased the instantaneous shear angle compared to the ZPG case, and the PDF was lower but looked qualitatively similar to the ZPG model. The SPG case however exhibited a very strong peak of the instantaneous shear angle near 0.0 degrees, signifying that the turbulent structure was fundamentally different compared to the ZPG and WPG models.

In summary, referring back to the four original questions, the following model is proposed for basic underlying processes. It was observed that as the flow experienced the favorable pressure gradient, the size and shape of the turbulence structures were altered, which, in turn, altered the statistical description. Specifically, referring back to Question 1, the change in sign of the axial stress production production, coupled with the fuller mean velocity profiles and reduced axial turbulence levels, indicated a reversal of energy flow, compared to the zero pressure gradient case, where turbulence energy was feeding back into the axial flow. From an energy spectra perspective, it was expected that, when compared to the zero pressure gradient flow, the magnutue of the axial energy at the low wave numbers (energy containing eddies) would be reduced. However, an opposite trend was seen for the transverse component. Thus, referring now to Questions 2 and 3, the shapes of the structures were reorganized, where it was shown that the principle stress axis oriention decreased (in a wall normal coordinate system) by 30 degrees for the strong pressure gradient. This reorganization was the primary driver in the apparent reduction of the Reynolds shear stress, as the net production was significantly higher. Other processes, such as pressure-strain and pressure-work may have played an important role. However, those effects were beyond the reach of our

measurement system. The nearly zero/slightly negative Reynolds shear stresses, the reduced autocorrelations and tighter quandrant decomposition maps indicated that the strong favorable pressure gradient boundary layer was populated with smaller, less correlated (i.e., more isotropic) structures, which would also suggest an alteration of the flow dissipation. However evidence for this proposition was not available in the present analysis. As for Question 4, direct comparison with the Ekoto et al study and the data summarized in Spina et al, demonstrate that the flow processes are dependent on the Mach number and the strength of the pressure gradient. In addition, Reynolds number effects cannot be ruled out.

Recommendations

Two addition questions were identified in the above summary. Specifically,

(1) Quantitatively, what happens to the rate of the dissipation?

(2) What are the roles of pressure-work and pressure-strain terms?

To address the first question, it is recommended that two-dimensional DFT analyses be performed on the particle image velocimetry data. These analysis would provide a for direct assessment of the energy spectra. Also, hot-wire/film measurements should be taken to provide time-resolved spectra and an estimate of the pressure-work (second question) term in the Reynolds Stress Transport equation. It is expected that this compressibility term will have a significant effect on the transport of turbulence at high Mach numbers, but experimental quantification is required to illustrate the impact. The pressure-work is enabled by a combination of the cross-wire/film and PIV

measurements[61]. Unfortunately, techniques to measure pressure-strain redistribution are currently unavailable; researchers must resort to numerical simulation. Hence, our understanding of the underlying mechanisms would be greatly enhanced by detailed direct numerical simulations, albeit at a lower Reynolds number. These studies would be able to see if the favorable pressure gradient characteristics quantified experimentally using particle image velocimetry can be reproduced numerically.

The present study only had a single discrete surface pressure tap downstream of the strong pressure gradient model. In order to further quantify the pressure effects of the favorable pressure gradient models, pressure sensitive paint should be utilized. PSP has been shown to effectively visualize surface pressure distributions on curved surfaces in previous studies and would be a useful technique to apply to the present experimental setup. Along the same lines, a series of schlieren images should be performed to further quantify the turbulent boundary layer over the favorable pressure gradient models. The present study performed flow visualizations using freestream oxygen liquefaction and the PIV laser system. Schlieren would also allow the quantification of the expansion lines from the favorable pressure gradient wall curvature and therefore direct calculation of the local pressure.

ACE Hypersonic Wind Tunnel Facility Development

Conclusions

A detailed description of the ACE hypersonic wind tunnel facility development was presented in Chapter VI. In this section, a brief summary of the facility development efforts will be presented along with several concluding remarks.

The actively controlled expansion hypersonic wind tunnel facility was built from the ground up at Texas A&M University. The infrastructure was assembled to allow the tunnel to have a nominal run time of approximately 50 seconds and a variable Mach number between 5.0 and 7.0. The cross sectional area was 22.86 cm x 35.56 cm (9.0 inches x 14.0 inches).

At the time of writing of this dissertation, the ACE hypersonic tunnel had progressed through many iterations and was running reliably[62]. The facility development was a significant part of the graduate research career and was included in the present dissertation to reflect that.

Recommendations

From the initial design, the ACE tunnel should undergo several modifications in order to improve the overall performance and efficiency of the facility. One of the major design flaws in the current setup is the interface between the settling chamber and the nozzle. For each Mach number setting, the spacing in the interface changes slightly and sometimes causes significant leaking. Although the leaking air comes from the higher pressured settling chamber and is upstream of the nozzle throat, this is not ideal and

wastes air. It is recommended that this interface be redesigned, probably by redesigning the entire settling chamber to allow for flexibility in Mach number while maintaining a solid seal.

The SISL test section discussed in detail in Chapter VI was designed specifically for the SISL model. However, since the SISL experiment was abandoned and other experiments were planned, the test section was converted to a straight test section by installing aluminum plates described above. In order to achieve the highest performance possible, it is recommended that the ACE test section be rebuild as a straight test section that would allow a wide range of models to be tested without worrying about odd upper and lower wall geometries.

The initial design of the diffuser proved to be very inefficient and a major obstacle during the shake down testing of the facility. The upstream converging section of the diffuser was determined to be too short and therefore inefficient. It is recommended that the diffuser be redesigned to allow for a much longer and therefore shallower converging diffuser section. Additionally, the diffuser proved to be a major source of leakage which increased the effective mass flow through the ejector and decreased performance. A major effort should be under taken to improve the overall diffuser design so that the ACE wind tunnel facility could operate in a much larger envelope than it currently can.

REFERENCES

[1] Bowersox, R., North, S. and Srinivasan, R., "High- Speed Free Shear Layers with Molecular Non-Equilibrium: An Example of the Fluids Information Triad (Invited)," AIAA Paper 2008-685, Jan. 2008.

[2] Smits, A. and Dussuage, J., *Turbulent Shear Layers in Supersonic Flow*, American Institute of Physics, Woodbury, New York, 1996.

[3] Anderson, J., *Hypersonic and High Temperature Gasdynamics*, American Institute or Aeronautics and Astronautics, Inc., Reston, VA, 2000.

[4] Olejniczak, J., and Candler, G., "Computation of Hypersonic Shock Interaction Flow Fields," AIAA Paper 1998-2446, June 1998.

[5] Thompson, M. "Flight Research: Problems Encountered and What They Should Teach Us," NASA SP-2000-4522, *Monographs in Aerospace History*, Number 22, 2000.

[6] Pope, S., *Turbulent Flows*, Cambridge University Press, Cambridge, UK 2000.

[7] Hinze, J., *Turbulence*, McGraw-Hill, New York, 1975.

[8] Schetz, J., *Boundary Layer Theory*, Prentice Hall, Englewood Cliffs, NJ, 1993.

[9] Wilcox, D., *Turbulence Modeling for CFD*, DCW Industries, La Canada, CA 2000.

[10] White, F., *Viscous Fluid Flow, 3rd Ed.*, McGraw Hill, New York, 2006.

[11] Morkovin, M., "Effects of Compressibility on Turbulent Flows," *The Mechanics of Turbulence*, Gordon and Breach Science Publisher, New York, 1961, pp. 367-380.

[12] Ristorcelli, J., and Blaisdell, Ga. “Validation of Pseudo-Sound Theory for the Pressure-Dilatation in DNS of Compressible Turbulence,” NASA CR-201748/ICASE Report 97-53, Langley Research Center, Hampton, VA, 1997.

[13] Kline, S., Reynolds, W., Schraub, F., and Runstadler, P., “The Structure of Turbulent Boundary Layers,” *Journal of Fluid Mechanics*, Vol. 30, 1967, pp. 741-773.

[14] Pantano, C. and Sarkar, S., “A Study of Compressibility Effects in High-Speed Turbulent Shear Layer using Direct Simulation,” *Journal of Fluid Mechanics*, Vol. 451, 2002, pp 329-371.

[15] Chapman, S. and Cowling, T., *The Mathematical Theory of Non-uniform Gases, 3rd Ed.*, Cambridge University Press, Cambridge, 1970.

[16] Bertin, J., *Hypersonic Aerothermodynamics*, American Institute of Aeronautics and Astronautics, Inc., Reston, VA., 1994.

[17] Clarke, J. and McChesney, M., *Dynamics of Real Gases*, Buttersworths Scientific Publications, London, 1964.

[18] Vincenti, W. and Kruger, C., *Introduction to Physical Gas Dynamics*, Krieger, Malabar, FL, 1965.

[19] Gnoffo, P., Gupta, R., and Shin, J., “Conservation Equations and Physical Models for Hypersonic Air Flows in Thermal and Chemical Non-equilibrium,” NASA Technical Paper 2867, Langley Research Center, Hampton, VA., 1989.

[20] Lee, J.-H., “Basic Governing Equations for the Flight Regimes of Aeroassisted Orbital Transfer Vehicles,” *Thermal Design of Aeroassisted Orbital Transfer*

Vehicles, Progress in Astronautics and Aeronautics, Volume 96, Ed. by H. Nelson, American Institute of Aeronautics and Astronautics, Inc., New York, 1985.

[21] Park, C., *Non-equilibrium Hypersonic Aerothermodynamics*, John Wiley & Sons, New York, 1990.

[22] Scalabrin, L., and Boyd, I., "Development of an Unstructured Navier-Stokes Solver for Hypersonic Non-Equilibrium Aerothermodynamics," AIAA Paper 2005-5203, June, 2005.

[23] Walters, R., Cinella, P., and Grossman, B., "Characteristic-Based Algorithms for Flows in Thermochemical Non-equilibrium," *AIAA Journal*, Vol. 30, No. 5, 1992, pp 1304-1313.

[24] Schlichting, H., *Boundary Layer Analysis*, Prentice Hall, Englewood Cliffs, NJ, 1993.

[25] Cebeci, T. and Smith, A.M.O., *Analysis of Turbulent Boundary Layers*, Applied Mathematics and Mechanics, No. 15, Academic Press Inc., New York, 1974.

[26] Van Driest, E.R., "Turbulent Boundary Layer in Compressible Fluids," *Journal of Aeronautical Sciences*, Vol. 18, 1956, pp. 145-160.

[27] Fernholz, I., Finley, M., and Mikulla, V., "A Further Compilation of Compressible Turbulent Boundary Layer Data with a Survey of Turbulence Data," *AGARDograph* 263, NATO, Technical Editing and Reproduction, London, Nov. 1981.

[28] Spina, E.F., Smits, A.J., and Robinson, S., "The Physics of Supersonic Turbulent Boundary Layers," *Annual Review of Fluid Mechanics*, Vol. 26, 1994, pp. 287-319.

[29] Smits, A.J., Spina, E.F., Alving, A.E., Smith, R.W., Fernando, E.M., and Donovan, J.F., "A Comparison of the Turbulence Structure of Subsonic and Supersonic Boundary Layers," *Physics of Fluids*, A Vol. 1, No. 11, 1989, pp. 1865-1875.

[30] Dussauge, J.P., Smith, R., Smits, A., Fernholtz, H., Finley, P., and Spina, E., "Turbulent Boundary Layers in Subsonic and Supersonic Flow," *AGARDograph* 335, NATO, Canada Communications Group, Hull, QC, Canada, July 1996.

[31] Bradshaw, P., "The Effect of Streamline Curvature on Turbulent Flow," *AGARDograph* 169, 1973.

[32] Clauser, F.H., "The Turbulent Boundary Layer," *Advanced Applied Mechanics*, Vol. 4, Academic Press Inc, New York, 1956, pp. 1-51.

[33] Coles, D., "The Law of the Wake in the Turbulent Boundary Layer," *Journal of Fluid Mechanics*, Vol. 1, 1956, pp. 191-226.

[34] Thomann, H., "The Effects of Axial Wall Curvature on Heat Transfer in Turbulent Boundary Layers to Short Regions of Concave Surface Curvature," *Journal of Fluid Mechanics*, Vol. 33, July 1968, pp. 283-292.

[35] Bradshaw, P., "The Analogy Between Streamline Curvature and Buoyancy in Turbulent Shear Flow," *Journal of Fluid Mechanics*, Vol. 36, 1969, pp. 177-191.

[36] Bradshaw, P., "The Effect of Mean Compression or Dilatation on the Turbulence Structure of Supersonic Boundary Layers," *Journal of Fluid Mechanics*, Vol. 63, No. 3, 1974, pp. 449-464.

[37] Shivaprasad, B.G., and Ramaprian, B.R., "Turbulence Measurements in Boundary Layers Along Mildly Curved Surfaces," *Journal of Fluids Engineering*, Vol. 100. No. 1, 1978, pp. 37-46.

[38] Kim, J., and Simon, T.W., "Measurements of the Turbulent Transport of Heat and Momentum in Convexly Curved Boundary Layers: Effects of Curvature, Recovery and Free-Stream Turbulence," *Journal of Turbomachinery*, Vol. 110, No. 1, 1988, pp. 80-87.

[39] Smith, D., and Smits, A., "The Effects of Streamline Curvature and Pressure Gradient on the Behavior of Turbulent Boundary Layers in Supersonic Flow," AIAA Paper 94-2227, June 1994.

[40] Hayakawa, K., Smits, A., and Bogdonoff, S., "Hot-Wire Investigation of an Unseparated Shock-Wave/Boundary Layer Interaction," *AIAA Journal*, Vol. 22, 1984, pp. 579-585.

[41] Luker, J., Hale, C., and Bowersox, R., "Experimental Analysis of the Turbulent Shear Stresses for Distorted Supersonic Boundary Layers," *Journal of Propulsion and Power*, Vol. 14, No. 1, 1998, pp. 110-118.

[42] Smith, D., and Smits, A., "The Rapid Expansion of a Turbulent Boundary Layer in a Supersonic Flow," *Theoretical Computational Fluid Dynamics*, Vol. 2, 1991, pp. 319-328.

[43] Donovan, J., Spina, E., and Smits, A., "The Structure of a Supersonic Turbulent Boundary Layers Subjected to Concave Surface Curvature," *Journal of Fluid Mechanics*, Vol. 259, Jan. 1994, pp. 1-24.

[44] Jayaram, M., Taylor, M., and Smits, A., "The Response of a Compressible Turbulent Boundary Layer to Short Regions of Concave Surface Curvature," *Journal of Fluid Mechanics*, Vol. 175, Feb. 1987, pp. 343-362.

[45] Dussauge, J.P., and Gaviglio, J., "The Rapid Expansion of a Supersonic Turbulent Flow: Role of Bulk Dilatation," *Journal of Fluid Mechanics*, Vol. 174, Jan. 1987, pp. 81-112.

[46] Arnette, S.A., Smimy, M., and Elliot, G.S., "The Effects of Expansions Regions on the Turbulence Structure of Compressible Boundary Layers," AIAA Paper 96-0656, Jan. 1996.

[47] Bowersox, R., and Buter, T., "Mass-Weighted Turbulence Measurements in a Mach 2.9 Boundary Layer with Mild Adverse and Favorable Pressure Gradient," *AIAA Journal*, Vol. 34, No. 12, 1996, pp. 2470-2483.

[48] Bowersox, R., Wier, R., Glawe, D., and Gogineni, S., "Measurements of Turbulent Flow Structure in Supersonic Curved Wall Boundary Layers," *Journal of Propulsion and Power*, Vol. 16, No. 1, 2000, pp. 153-154.

[49] Pope, A., Goin, K., *High-Speed Wind Tunnel Testing*, John Wiley & Sons, New York, 1965.

[50] Tilmann, C., and Bowersox, R., "On the Design and Construction of an Academic Mach 5 Wind Tunnel," AIAA Paper 99-0800, Jan. 1999.

[51] Ekoto, I., *Supersonic Turbulent Boundary Layers with Periodic Mechanical Non-Equilibrium*, Ph.D. Dissertation, Texas A&M University, College Station, TX, 2006.

[52] TSI Inc., “Model 9306A Six-Jet Atomizer Instruction Manual,” 1930099, Rev. B, Shoreview, MN, Feb. 2003.

[53] dPIV, 32-Bit PIV Analysis Code, Software Package, Ver. 2.1, Innovative Scientific Solutions Inc, Dayton, OH, 2005.

[54] Arnette, S., Samimy, M., and Elliott, G., "The Effects of Expansion on the Turbulence Structure of Compressible Boundary Layers," *Journal of Fluid Mechanics*, Vol. 367, 1998, pp. 67-105.

[55] Ekoto, I., Bowersox, R., Beutner, T., and Goss, L., "Response of Supersonic Turbulent Boundary Layers to Local and Global Mechanical Distortions," *Journal of Fluid Mechanics*, Vol. 630, 2009, pp. 225-265.

[56] Herrin, J., Dutton, J., “The turbulence structure of a reattaching axisymmetric compressible free shear layer,” *Physics of Fluids*, Vol. 9, 1997, pp. 3502-3512.

[57] Tuinstra, M, *A PIV Investigation on Shock Wave Boundary Layer Interaction*, M.S. Thesis, Delft University of Technology, The Netherlands, 2005.

[58] Adrian, R., Meinhart, C., and Tomkins, C., “Vortex Organization in the Outer Region of the Turbulent Boundary Layer,” *Journal of Fluid Mechanics*, Vol. 422, 2000, pp. 1-54.

[59] Ganapathisubramani, B., Hutchins, N., Hambleton, W., Longmire, E., and Marusic, I., “Investigation of Large-Scale Coherence in a Turbulent Boundary Layer Using Two-Point Correlations,” *Journal of Fluid Mechanics*, Vol. 524, 2005, pp. 57-80.

[60] Ganapathisubramani, B., “Statistical Properties of Streamwise Velocity in a Supersonic Turbulent Boundary Layer,” *Physics of Fluids*, Vol. 19, 2007, pp. 098108-1-098108-4.

[61] Bowersox, R., “Combined Laser Doppler Velocimetry and Cross-Wire Anemometry Analysis for Supersonic Turbulent Flow,” *AIAA Journal*, Vol. 34, No. 11, 1996, pp. 2269-2275.

[62] Semper, M., Tichenor, N., Bowersox, R., Srinvasan, R., and North, S., "On the Design and Calibration of an Actively Controlled Expansion Hypersonic Wind Tunnel," AIAA Paper 2009-799, Jan. 2009.

[63] Stoer, J., and Burlirsch, R., *Introduction to Numerical Analysis*, 2nd ed., Springer-Verlag, Berlin Germany, 1993.

ADDITIONAL REFERENCES

[64] Benedict, L., and Gould, R., "Towards Better Uncertainty Estimates for Turbulence Statistics," *Experiments in Fluids,* Vol. 22, 1996, pp. 129-136.

[65] Bowersox, R., *A Computer Program to Design Planar Nozzles with an Arbitrary Number of Expansion Reflections before Wave Cancellation*, Texas A&M University, College Station, TX, 2003.

[66] Van Driest, E., "Turbulent Boundary Layer in Compressible Fluids," *J. Aerospace Sciences*, Vol. 18, 1951, pp. 145-160.

[67] GASP Version 4.0 Users' Manual, Aerosoft Inc., Blacksburg, Virginia, 2001.

[68] Gridgen Users' Manual v 13.0, Pointwise Inc., Fort Worth, Texas, 1999.

[69] Spalart, P. R. and Allmaras, S. R., "A One Equation Turbulence Model for Aerodynamic Flows," *La Recherche Aerospatiale*, Vol. 1, 1994, pp. 5-21.

[70] Menter, F. R., "Zonal Two Equation $k-\omega$ Turbulence Models for Aerodynamic Flows," AIAA Paper 93-2906, July 1993.

[71] Wilcox, D. C., *Turbulence Modeling for CFD*, 2nd ed., DCW Industries, La Canada, CA, 1998.

[72] Wegener, P. and Lobb, K., "An Experimental Study of a Hypersonic Wind-Tunnel Diffuser," *Journal of Aeronautical Sciences*, Vol. 20, Feb. 1953, pp. 105–110.

[73] Bertram, M., "Investigation of the Pressure-Ratio Requirements of the Langley 11-Inch Hypersonic Tunnel with a Variable-Geometry Diffuser," NACA RM L50I13, Langley Research Center, Hampton, VA, 1950.

APPENDIX A

SOFTWARE PARAMETERS

CamWare Settings 227

dPIV Parameters 230

CamWare Settings

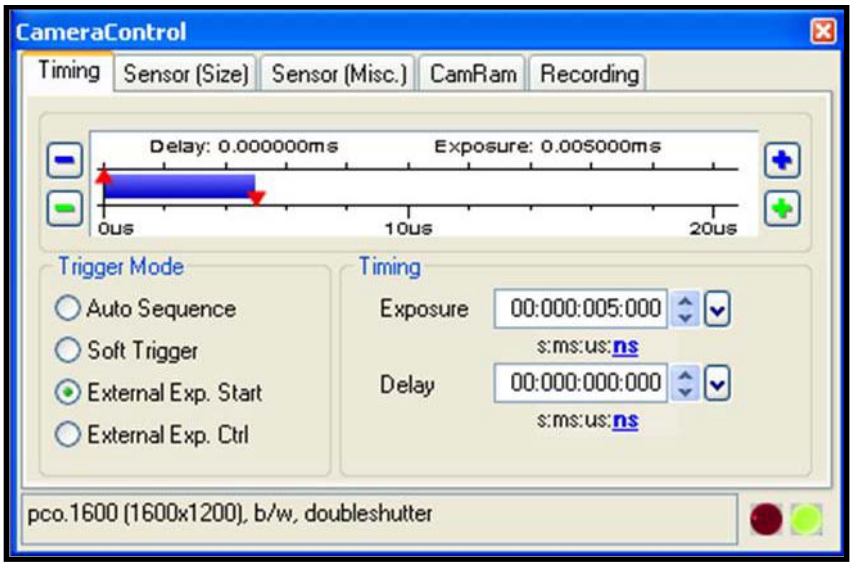

Figure A-1: CamWare camera control timing

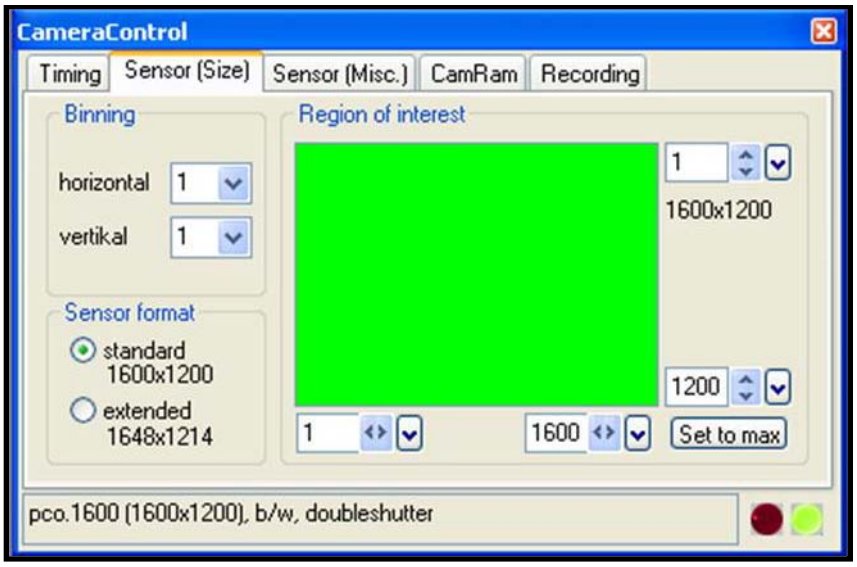

Figure A-2: CamWare camera control sensor (size) settings

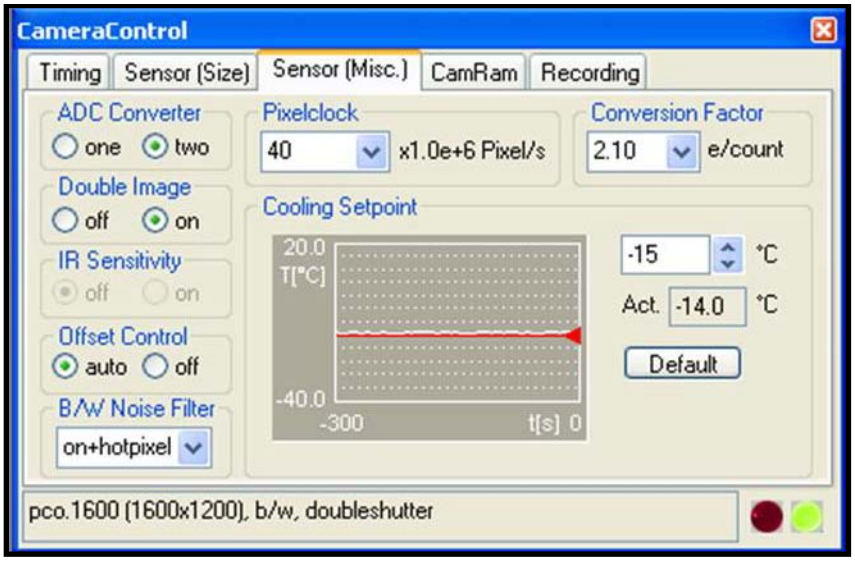

Figure A-3: CamWare camera control sensor (misc.) settings

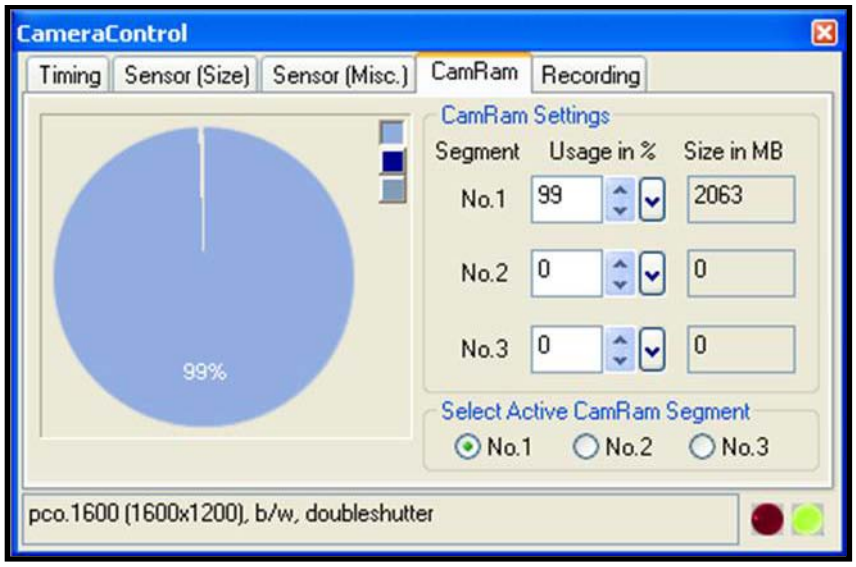

Figure A-4: CamWare camera control CamRam settings

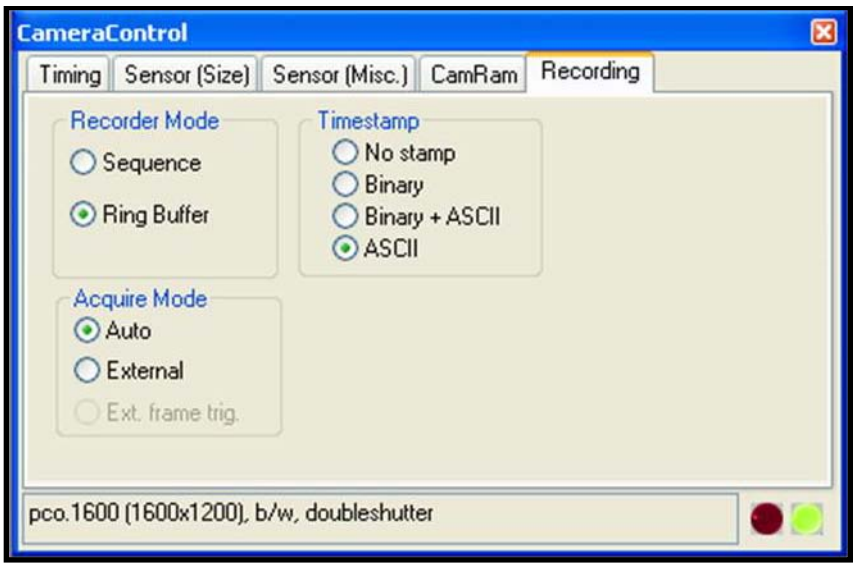

Figure A-5: CamWare camera control recording settings

dPIV Parameters

A pair of PIV images was loaded (Figure A-6) and processed to ensure proper pixel displacement and check for any major issues in the data.

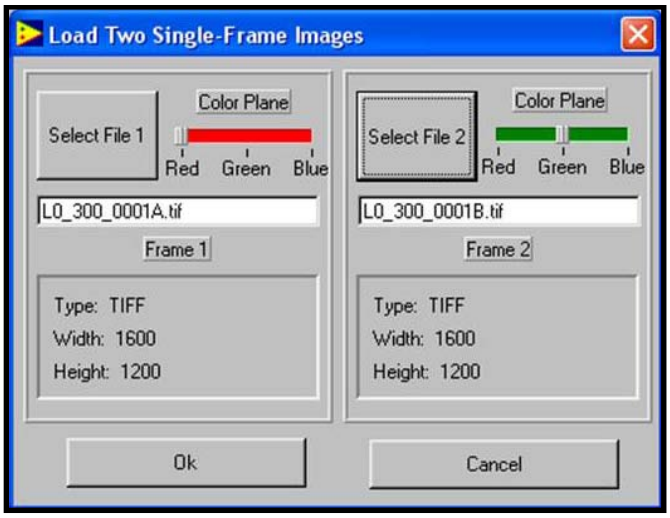

Figure A-6: dPIV image loading

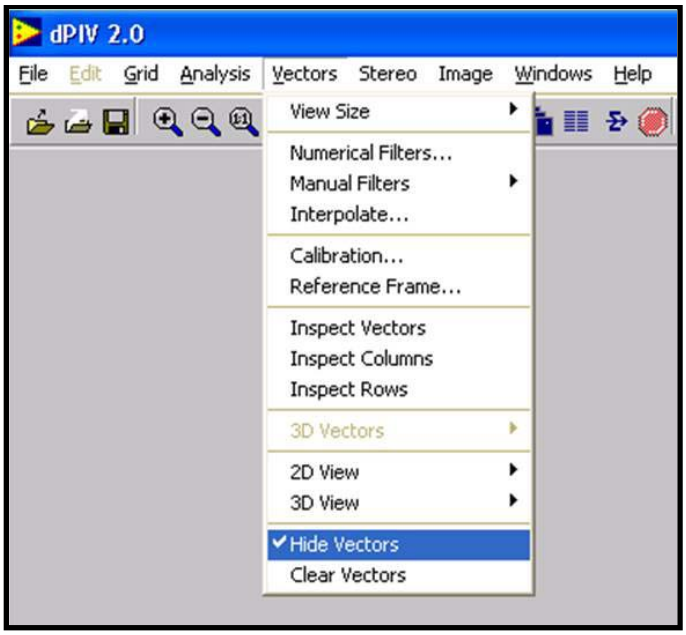

Figure A-7: dPIV hide vectors

Once the first pair of images was processed, the vector fields were hidden (Figure A-7). This is done to stop dPIV from drawing the vector field at the completion of each processing step in order to accelerate the batch processing completion. The correlation parameters utilized in dPIV are shown below (Figure A-8). The options outlined in red are those that were modified from default. Similar to the "Hide Vectors" option used before, setting "Display Vectors" to "off" halts dPIV from drawing the vectors as they are calculated, speeding up the process.

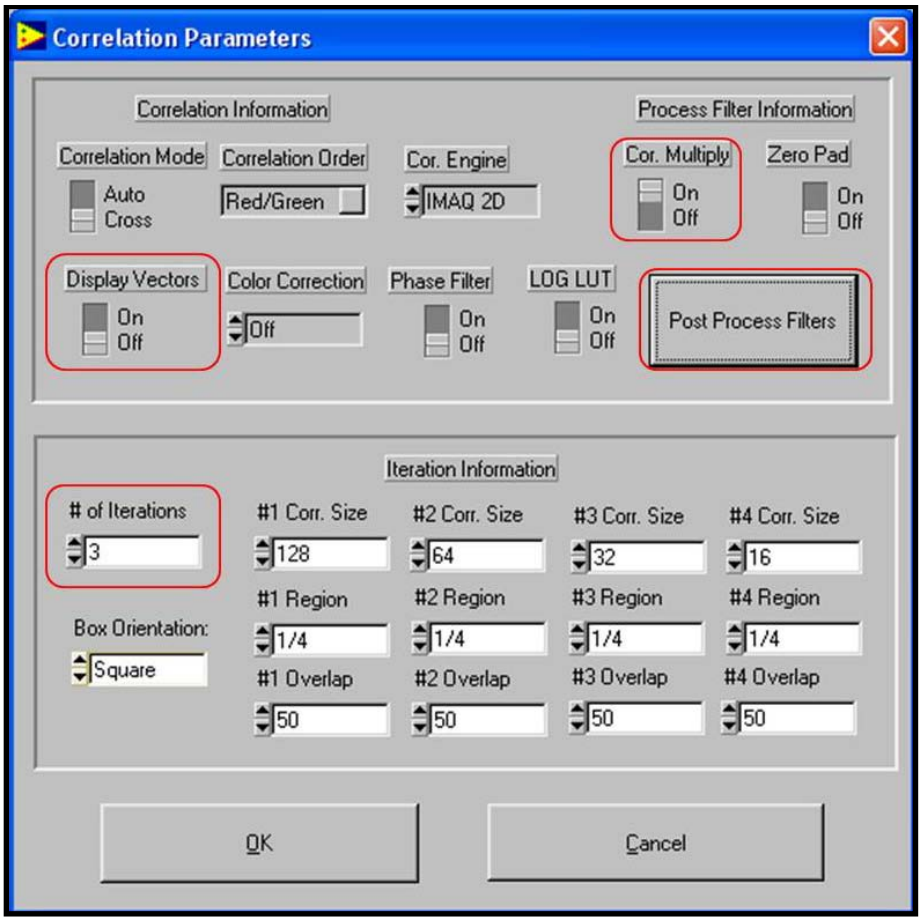

Figure A-8: dPIV correlation parameters

"Cor. Multiply" is set to "On" (Figure A-8) and "Upper", "Right" and "Lower" are activated (Figure A-9). Clicking "Post Process Filters" (Figure A-8) brings up the filter options (Figure A-10). "Consistency Filter" is set to "On" with default "Min. Num." of 2 and "Radius" of 2.

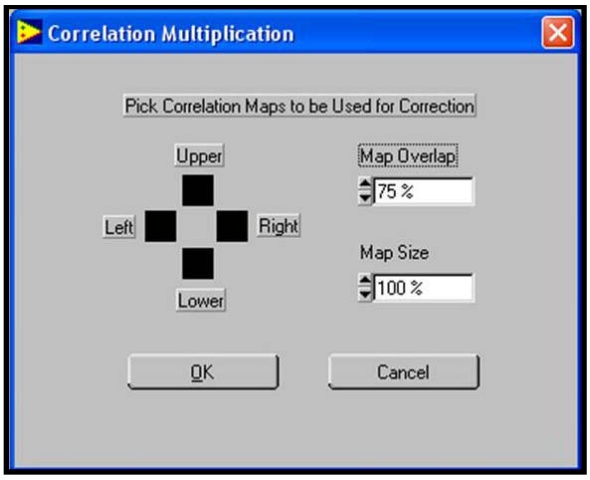

Figure A-9: dPIV correlation multiplication

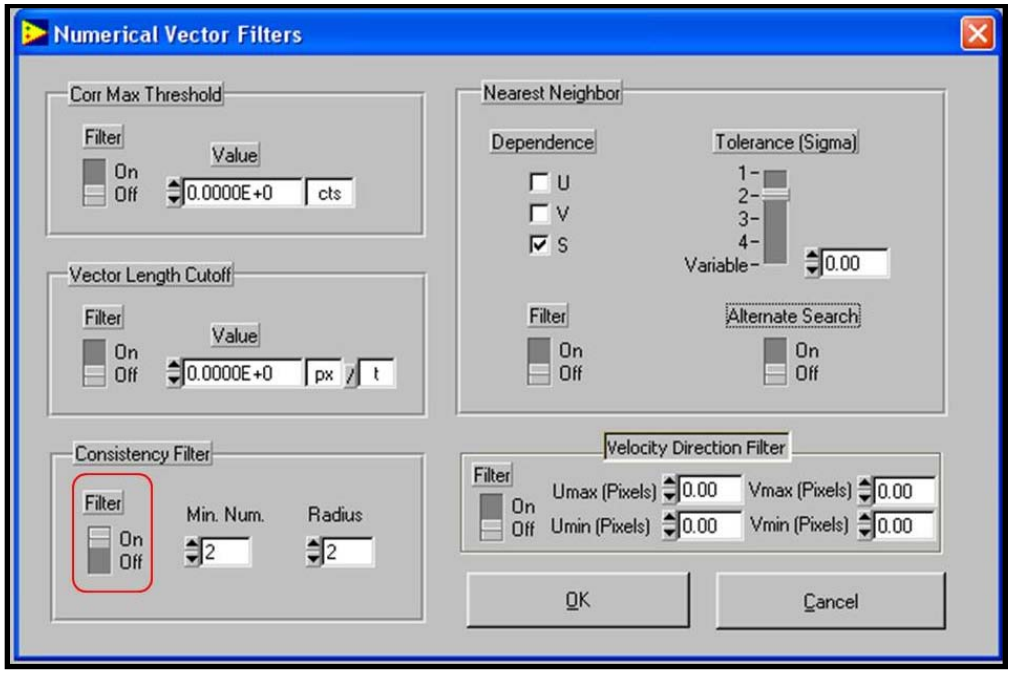

Figure A-10: dPIV post processing filters

APPENDIX B

PIV CODES

TAMU_PIV_INPUT.dat 235

TAMU_PIV_INPUT_QUAD.dat 236

TAMU_PIV_INPUT_CORR.dat 236

TAMU_PIV.f90 237

TAMU_PROFILE_IINPUT.dat 268

TAMU_PROFILE.f90 269

The purpose of this code is to read in the output files (.csv, or .dat) generated by dPIV and perform velocity averaging calculations as well as compute fluctuating velocities. The code also performs sigma filtering to remove spurious vectors.

TAMU_PROFILE.f90 was written to generate profiles by averaging columns of the final data set together into one well-resolved profile. The input file allows the user to specify the files from which to generate profiles as well as the left and right columns bounding the desired region to be averaged in the corresponding file.

**All codes must be run from the same directory as their target files*

TAMU_PIV_INPUT.dat

```
*********************************************************
*******     TAMU PIV Input File (PIV_INPUT.DAT)     *******
*******                                             *******
*******    VERSION: 2.128       DATE: 05/20/2010    *******
*********************************************************

File Name (15 Char. Max.)        run09
Number of Images                 345
Pixels / mm                      78.898
Delta T (uS)                     0.500
Pixels adjusted                  8
Clockwise Camera Rotation (deg)  10.49
Sigma                            2.0
Reference Velocity (m/s)         1.0
Reference Length (m)             1.0



PROGRAM UNITS (1 = on, 0 = off)
---------------------------------
Unit 1 - Mean Velocities                          1
Unit 2 - Fluctuating Velocities                   1
Unit 3 - Filtered Mean Velocities                 1
Unit 4 - Filtered Fluctuating Velocities          1
Unit 5 - Velocity Gradients                       1
Unit 6 - Normalization Unit                       0
Unit 7 - Include Camera Rotation                  0
Unit 8 - Stress Principal Axes Analyses           0
```

**Be sure that at least one decimal place is included in all variable inputs above (excluding File name and Number of Images)*

TAMU_PIV_INPUT_QUAD.dat

```
************************************************************
******* TAMU PIV Quadrant Decomposition Input File  *******
*******          (TAMU_PIV_INPUT_QUAD.DAT)          *******
************************************************************

Number of passes:    5

y(mm) locations:

0.85
1.70
2.805
3.40
5.10
```

TAMU_PIV_INPUT_CORR.dat

```
************************************************************
******* TAMU PIV Quadrant Decomposition Input File  *******
*******          (TAMU_PIV_INPUT_CORR.DAT)          *******
************************************************************

Number of passes:    5

y(mm) locations:

5.61
6.80
8.50
10.20
11.90
```

TAMU_PIV.f90

```
      !*****************************************************************
******************
      !     Program: TAMU_PIV
*
      !     Purpose: Calculate classical turbulence statistics from
processed PIV data    *
      !     Programmer: Nathan Tichenor
*
      !     Version: 2.132
*
      !     Date: 06/11/2010
*
      !*****************************************************************
******************

      PROGRAM TAMU_PIV


      ! INITIALIZE VARIABLES
      !*****************************************************************
******************

      CHARACTER(20) :: current_file, filename, file_number_char,
first_filename*25, full_filename*25, save_filename*27
      CHARACTER(10) :: dum*52, extension_1, extension_2, extension_3,
extension, end_stop, grad_save_filename*30,yrefc
      CHARACTER(20) :: profile_save_filename*40
      INTEGER :: num_images, start_file, vectors, file_number,
InputStatus, counter_X, counter_total, normal, pix_adj
      INTEGER :: num_X, num_Y, num_vectors, num_units,  seconds,
X_temp, Y_temp, first_Y, ios, z, prg, xref, yref, quad_repeat,
quad_number, corr_number
      REAL(8) :: pix_mm, pix_m, dt, sigma, U_ref, delta_ref, sign,
Y_max, test1, test2, dx, dy
      REAL(8) :: pix_mm_org, dt_org, rotation, dummy
      REAL(8) :: alpha_temp, uv_temp, Uinfavg, x_ref, y_ref
      INTEGER, DIMENSION(3) :: start_time, end_time, elapsed_time
      INTEGER, DIMENSION(:), ALLOCATABLE :: unit, unit_temp, ninf,
psi_location
      INTEGER, DIMENSION(:,:), ALLOCATABLE :: Xi, Yi
      REAL(8), DIMENSION(:), ALLOCATABLE :: Uinf, psi, psi_prob,
quad_location, corr_location
      REAL(8), DIMENSION(:,:,:), ALLOCATABLE :: num_good, filter,
num_good_avg, U_instant, V_instant, up_instant, vp_instant, Ruu, rhh
      REAL(8), DIMENSION(:,:), ALLOCATABLE :: X, Y, U, V, Ubar, Vbar,
uubar, vvbar, uvbar, Uavg, Vavg, uuavg, vvavg, uvavg, rhh_total
      REAL(8), DIMENSION(:,:), ALLOCATABLE :: Unorm, Vnorm, uunorm,
vvnorm, uvnorm, U_global, V_global
      REAL(8), DIMENSION(:,:), ALLOCATABLE :: alpha, uulambda,
vvlambda, uvlambda, up_rms, vp_rms
```

```
      REAL(8), DIMENSION(:,:), ALLOCATABLE :: dUdX, dUdY, dVdX, dVdY,
duudX, duudY, dvvdX
      REAL(8), DIMENSION(:,:), ALLOCATABLE :: dvvdY, duvdX, duvdY,
vorticity, strain
      REAL(8), DIMENSION(:,:), ALLOCATABLE :: txxdudx, txydudy,
txydvdx, tyydvdy, txydudx, tyydudy, txxdvdx, txydvdy
      REAL(8), DIMENSION(:,:), ALLOCATABLE :: productionxx,
productionyy, productionxy


      ! READ INPUT VARIABLES FROM PIV_INPUT.DAT
      !*************************************************************
*****************

      CALL itime(start_time)

      WRITE(*,*) "************************************************"
      WRITE(*,*) "***          TAMU PIV AVERAGING CODE           ***"
      WRITE(*,*) "***                                            ***"
      WRITE(*,*) "***   VERSION: 2.132      DATE: 06/11/2010    ***"
      WRITE(*,*) "************************************************"

      WRITE(*,*)
      WRITE(*,*)

      !WRITE(*,*) "READING INPUT VARIABLES FROM TAMU_PIV_INPUT.DAT"
      !WRITE(*,*)

      OPEN(UNIT=15, FILE='TAMU_PIV_INPUT.DAT', STATUS='OLD', IOSTAT =
ios)

      IF (ios /= 0) THEN

            WRITE(*,*) 'ERROR opening file TAMU_PIV_INPUT.DAT'
            WRITE(*,*) 'To continue, press any key, then [ENTER].'
            READ(*,*) end_stop

            STOP

      END IF

      READ(15,*)
      READ(15,*)
      READ(15,*)
      READ(15,*)
      READ(15,*)
      READ(15,*)

      READ(15,'(A32, A20)') dum, filename
      !WRITE(*,*) filename

      READ(15,'(A32, I8)') dum, num_images
      !WRITE(*,*) num_images
```

```
      READ(15,'(A32, F7.2)') dum, pix_mm
      pix_mm_org = pix_mm
      !WRITE(*,*) pix_mm

      READ(15,'(A32, F9.4)') dum, dt
      dt_org = dt
      dt = dt*0.000001;
      !WRITE(*,*) dt

      READ(15,'(A32, I8)') dum, pix_adj
      !WRITE(*,*) px_adj

      READ(15,'(A32,F9.4)') dum, rotation
      rotation = rotation*3.14159/180
      !WRITE(*,*) rotation
      !READ(*,*) dum
      !STOP

      READ(15,'(A32, F5.2)') dum, sigma
      !WRITE(*,*) sigma

      READ(15,'(A32, F6.2)') dum, U_ref
      !WRITE(*,*) U_ref

      READ(15,'(A32, F10.7)') dum, delta_ref
      !WRITE(*,*) delta_ref

      sign = -1

      num_units = 10

      READ(15,*)
      READ(15,*)
      READ(15,*)
      READ(15,*)
      READ(15,*)

      ALLOCATE(unit(num_units), unit_temp(num_units))

      DO i = 1, num_units
            READ(15,'(A51, I4)') dum, unit(i)
      END DO

      CLOSE(15)

      !WRITE(*,'(A12,A20,A17,I8)') "File name:", filename, "Number of
images:", num_images
      !WRITE(*,*)


      ! DETERMINE FILE TYPE
```

```
      !*****************************************************************
*****************

      extension_1 = "A.csv"
      extension_2 = "A.dat"
      extension_3 = "A.tif.dat"           !Added extension_3 to read
PPIV files


      first_filename = trim(adjustl(filename)) // '_0001' //
trim(adjustl(extension_1))
      first_filename = trim(adjustl(first_filename))

      OPEN(UNIT = 11, FILE = first_filename, STATUS = 'OLD', IOSTAT =
ios)        !Try to open first .CSV data file

      IF (ios /= 0) THEN

            GOTO 55

            WRITE(*,*) 'To continue, press any key, then [ENTER].'
            READ(*,*) end_stop

            STOP

      END IF

      !WRITE(*,*) 'USING .CSV FILE TYPE'
      !WRITE(*,*)

      extension = extension_1

      CLOSE(11)

      GOTO 65


55    first_filename = trim(adjustl(filename)) // '_0001' //
trim(adjustl(extension_2))
      first_filename = trim(adjustl(first_filename))

      !WRITE(*,*) first_filename

      !WRITE(*,*) extension_2

      OPEN(UNIT = 11, FILE = first_filename, STATUS = 'OLD', IOSTAT =
ios)        !Try to open first .DAT data file

      IF (ios /= 0) THEN

            GOTO 60

            WRITE(*,*)
```

```
            WRITE(*,*) 'ERROR cannot open data files. Ensure the file
name is correct.'
            WRITE(*,*)
            WRITE(*,*) 'To continue, press any key, then [ENTER].'
            READ(*,*) end_stop

            STOP

      END IF

      !WRITE(*,*) 'USING .DAT FILE TYPE'
      !WRITE(*,*)

      extension = extension_2

      CLOSE(11)

      GOTO 65


60    first_filename = trim(adjustl(filename)) // '_0001' //
trim(adjustl(extension_3))

      first_filename = trim(adjustl(first_filename))

      !WRITE(*,*) first_filename

      !WRITE(*,*) extension_3

      OPEN(UNIT = 11, FILE = first_filename, STATUS = 'OLD', IOSTAT =
ios)        !Try to open first .TIF.DAT data file

      IF (ios /= 0) THEN

            WRITE(*,*)
            WRITE(*,*) 'ERROR cannot open data files. Ensure the file
name is correct.'
            WRITE(*,*)
            WRITE(*,*) 'To continue, press any key, then [ENTER].'
            READ(*,*) end_stop

            STOP

      END IF

      !WRITE(*,*) 'USING .TIF.DAT FILE TYPE'
      !WRITE(*,*)

      extension = extension_3

      CLOSE(11)
```

```
      ! CALCULATE MATRIX SIZE
      !*****************************************************************
******************

65    CONTINUE
    !WRITE(*,*) "CALCULATING MATRIX SIZE..."
      !WRITE(*,*)

      !WRITE(*,*) first_filename

      counter_X = 0
      counter_total = 0

      OPEN(UNIT = 11, FILE = first_filename, STATUS = 'OLD')

      READ(11,*)

      IF (extension == extension_2) THEN

            READ(11,*)
            READ(11,*)

      END IF

      i = 1

      DO

            READ(11,*, IOSTAT = InputStatus) X_temp, Y_temp

            IF (i == 1) THEN
                  first_Y = Y_temp                          !Determine
first Y value (in pixels)
                  i = 2
            END IF

            IF (InputStatus < 0) EXIT

            IF (Y_temp == first_Y) THEN
                  counter_X = counter_X + 1                 !Counts
number of vectors per row
            ELSE
                first_Y = -1
            END IF

            counter_total = counter_total + 1         !Counts total
number of vectors

      END DO

      CLOSE(11)

      num_X = counter_X
```

```
      num_vectors = counter_total
      num_Y = num_vectors / num_X
      !Calculates number of vectors per column

      pix_m = pix_mm * 1000

      !WRITE(*,*) num_X
      !WRITE(*,*) num_Y
      !WRITE(*,*) num_vectors


      ! ALLOCATE ARRAYS
      !*************************************************************
*****************

      !WRITE(*,*) "ALLOCATING ARRAYS..."
      !WRITE(*,*)

      ALLOCATE(Xi(num_X, num_Y), Yi(num_X, num_Y), X(num_X, num_Y),
Y(num_X, num_Y), &
            &     U(num_X, num_Y), V(num_X, num_Y),Ubar(num_X, num_Y),
Vbar(num_X, num_Y), &
            &     Uavg(num_X, num_Y), Vavg(num_X, num_Y), uubar(num_X,
num_Y), vvbar(num_X, num_Y), uvbar(num_X, num_Y), &
            &     uuavg(num_X, num_Y), vvavg(num_X, num_Y),
uvavg(num_X, num_Y), &
            &     Unorm(num_X, num_Y), Vnorm(num_X, num_Y),
uunorm(num_X, num_Y), vvnorm(num_X, num_Y), &
            &     uvnorm(num_X, num_Y), U_global(num_X, num_Y),
V_global(num_X, num_Y), &
            &   alpha(num_X,num_Y), uulambda(num_X,num_Y),
vvlambda(num_X,num_Y), uvlambda(num_X,num_Y))

      ALLOCATE(up_rms(num_Y,num_images), vp_rms(num_Y,num_images))

      ALLOCATE(num_good(num_X, num_Y,4), filter(num_X, num_Y,4),
num_good_avg(num_X, num_Y,4))

      ALLOCATE(U_instant(num_X, num_Y, num_images), V_instant(num_X,
num_Y, num_images), &
        &   up_instant(num_X, num_Y, num_images), vp_instant(num_X,
num_Y, num_images), &
        &   Ruu(num_X, num_Y, num_images), rhh(num_X, num_Y,
num_images))

      ALLOCATE(Uinf(num_images), ninf(num_images), psi(num_images),
psi_location(200), psi_prob(200))

      ALLOCATE(dUdX(num_X, num_Y), dUdY(num_X, num_Y), dVdX(num_X,
num_Y), dVdY(num_X, num_Y), &
            &     duudX(num_X, num_Y), duudY(num_X, num_Y),
dvvdX(num_X, num_Y), dvvdY(num_X, num_Y), &
```

```
            &     duvdX(num_X, num_Y), duvdY(num_X, num_Y),
vorticity(num_X, num_Y), strain(num_X, num_Y), &
            &   txxdudx(num_X, num_Y), txydudy(num_X, num_Y),
txydvdx(num_X, num_Y), tyydvdy(num_X, num_Y), &
            &   txydudx(num_X, num_Y), tyydudy(num_X, num_Y),
txxdvdx(num_X, num_Y), txydvdy(num_X, num_Y), &
            &   productionxx(num_X, num_Y), productionyy(num_X, num_Y),
productionxy(num_X, num_Y), rhh_total(num_X,num_Y))


      DO m = 1, num_units - 1
            unit_temp(m) = 0
            DO i = m, num_units - 1
                  unit_temp(m) = unit_temp(m) + unit(i)
                  !WRITE(*,*) m, unit_temp(m)
            END DO
      END DO

    num_good = 0.0
    Ubar = 0.0
    Vbar = 0.0
    uubar = 0.0
    vvbar = 0.0
    uvbar = 0.0
    Uavg = 0.0
    Vavg = 0.0
    uuavg = 0.0
    vvavg = 0.0
    uvavg = 0.0
    alpha = 1.0e6
    Uinf = 0.0
    ninf = 0.0
      Uinfavg = 0.0
      up_rms = 0.0
      vp_rms = 0.0
      Ruu = 0.0
      rhh = 0.0
      rhh_total = 0.0

      psi_location = 0.0
      psi_prob = 0.0


      ! READ DATA FILES
      !*************************************************************
*****************

      WRITE(*,*) "READING DATA FILES..."
      WRITE(*,*)

      dummy = 20

      DO n = 1, num_images
```

```
          prg = (REAL(n)/REAL(num_images))*100

            IF (prg >= dummy) THEN

            !DO z = 1,300
            !    WRITE (*,*)
            !END DO
            WRITE(*,*) prg,"%"

            dummy = dummy + 20
          END IF

            file_number = n

            CALL Determine_filename (file_number, filename, extension,
full_filename)
            CALL Read_file (full_filename, end_stop, extension,
extension_2, num_X, num_Y, Xi, Yi, U, V, sign, pix_m, dt)

            DO i = 1, num_X
                  DO j = 1, num_Y
                      U_instant(i,j,n) = U(i,j)
                      V_instant(i,j,n) = V(i,j)
                  END DO
          END DO
        END DO

        WRITE(*,*)


        Y_max = MAXVAL (Yi)                     !Determine maximum Y
value (in pixels)

        DO i =1, num_X
              DO j =1, num_Y
              Yi(i,j) = Y_max - Yi(i,j)           !Flip Y coordinates
from PIV coordinate system to physical coordinate system
              END DO
        END DO

      DO i =1, num_X                                          !Convert
integer coordinates into real physical coordinates
          DO j =1, num_Y
          Yi(i,j) = Yi(i,j) + pix_adj
          X(i,j) = FLOAT(Xi(i,j)) / pix_mm
          Y(i,j) = FLOAT(Yi(i,j)) / pix_mm
          END DO
      END DO


        ! CALCULATE MEAN VELOCITIES
```

```
      !*****************************************************************
*****************

      IF (unit_temp(1) > 0) THEN

            WRITE(*,*) "CALCULATING MEAN VELOCITIES..."
            WRITE(*,*)

            !WRITE(*,*) num_images

            DO n = 1, num_images
            DO j = 1, num_Y
                     DO i = 1, num_X
                           IF (U_instant(i,j,n) /= 0.0) THEN
                                 num_good(i,j,1) = num_good(i,j,1) + 1
                                 Ubar(i,j) = Ubar(i,j) +
U_instant(i,j,n)
                                 Vbar(i,j) = Vbar(i,j) +
V_instant(i,j,n)
                           END IF
                     END DO
                END DO
            END DO

            DO i = 1, num_X
                  DO j = 1, num_Y
                        IF (num_good(i,j,1) == 0.0) THEN
                              Ubar(i,j)   = 0.0
                              Vbar(i,j)   = 0.0
                        ELSE
                            Ubar(i,j) = Ubar(i,j) / (num_good(i,j,1))
                              Vbar(i,j) = Vbar(i,j) / (num_good(i,j,1))
                        END IF
                  END DO
            END DO

      END IF


      ! CALCULATE FLUCTUATING VELOCITIES
      !*****************************************************************
*****************

      IF (unit_temp(2) > 0) THEN

            WRITE(*,*) "CALCULATING FLUCTUATING VELOCITIES..."
            WRITE(*,*)

            DO n = 1, num_images
            DO j = 1, num_Y
                     DO i = 1, num_X
                           IF (U_instant(i,j,n) /= 0.0) THEN
                                 num_good(i,j,2) = num_good(i,j,2) + 1
```

```
                                    up_instant(i,j,n) = U_instant(i,j,n)
- Ubar(i,j)
                                    vp_instant(i,j,n) = V_instant(i,j,n)
- Vbar(i,j)
                                    uubar(i,j) = uubar(i,j) +
(up_instant(i,j,n) * up_instant(i,j,n))
                                    vvbar(i,j) = vvbar(i,j) +
(vp_instant(i,j,n) * vp_instant(i,j,n))
                                    uvbar(i,j) = uvbar(i,j) +
(up_instant(i,j,n) * vp_instant(i,j,n))
                              END IF
                        END DO
                    END DO
               END DO

               DO i = 1, num_X
                     DO j = 1, num_Y
                           IF (num_good(i,j,2) == 0.0) THEN
                                 uubar(i,j) = 0
                                 vvbar(i,j) = 0
                                 uvbar(i,j) = 0
                           ELSE
                                 uubar(i,j) = uubar(i,j) /
(num_good(i,j,2)-1)
                                 vvbar(i,j) = vvbar(i,j) /
(num_good(i,j,2)-1)
                                 uvbar(i,j) = uvbar(i,j) /
(num_good(i,j,2)-1)
                           END IF
                     END DO
               END DO

      END IF


      ! CALCULATE FILTERED MEAN VELOCITIES
      !*************************************************************
******************

      IF (unit_temp(3) > 0) THEN

            WRITE(*,*) "CALCULATING FILTERED MEAN VELOCITIES..."
            WRITE(*,*)

            DO j = 1, num_Y
                  DO i = 1, num_X
                        filter(i,j,1) =  Ubar(i,j) + sigma *
sqrt(uubar(i,j))
                        filter(i,j,2) =  Ubar(i,j) - sigma *
sqrt(uubar(i,j))
                        filter(i,j,3) =  Vbar(i,j) + sigma *
sqrt(vvbar(i,j))
```

```
                        filter(i,j,4) =  Vbar(i,j) - sigma *
sqrt(vvbar(i,j))
                  END DO
            END DO

            DO n = 1, num_images
            DO j = 1, num_Y
                        DO i = 1, num_X
                              IF (  U_instant(i,j,n) /= 0.0 .AND. &
                                    & U_instant(i,j,n) <= filter(i,j,1)
.AND. &
                                    & U_instant(i,j,n) >= filter(i,j,2) )
THEN

                                    num_good(i,j,3) = num_good(i,j,3) + 1
                                    Uavg(i,j) = Uavg(i,j) +
U_instant(i,j,n)
                                    Vavg(i,j) = Vavg(i,j) +
V_instant(i,j,n)
                              END IF
                        END DO
                END DO
            END DO

            DO i = 1, num_X
                  DO j = 1, num_Y
                        IF (num_good(i,j,3) == 0.0) THEN
                              Uavg(i,j)   = 0
                              Vavg(i,j)   = 0
                        ELSE
                              Uavg(i,j) = Uavg(i,j) / num_good(i,j,3)
                              Vavg(i,j) = Vavg(i,j) / num_good(i,j,3)
                        END IF
                  END DO
            END DO

      ELSE

            DO i = 1, num_X
                  DO j = 1, num_Y
                        Uavg(i,j) = Ubar(i,j)
                        Vavg(i,j) = Vbar(i,j)
                  END DO
            END DO
      END IF


      ! CALCULATE FILTERED FLUCTUATING VELOCITIES
      !*************************************************************
******************

      IF (unit_temp(4) > 0) THEN
```

```
            WRITE(*,*) "CALCULATING FILTERED FLUCTUATING VELOCITIES..."
            WRITE(*,*)

            DO n = 1, num_images

                  DO i = 1, num_X
                      DO j = 1, num_Y

                          IF (  U_instant(i,j,n) /= 0.0 .AND. &
                              & U_instant(i,j,n) <= filter(i,j,1) .AND.
&
                              & U_instant(i,j,n) >= filter(i,j,2) )
THEN

                                  num_good(i,j,4) = num_good(i,j,4) + 1
                                  up_instant(i,j,n) = U_instant(i,j,n)
- Uavg(i,j)
                                  vp_instant(i,j,n) = V_instant(i,j,n)
- Vavg(i,j)
                                  uuavg(i,j) = uuavg(i,j) +
(up_instant(i,j,n) * up_instant(i,j,n))
                                  vvavg(i,j) = vvavg(i,j) +
(vp_instant(i,j,n) * vp_instant(i,j,n))
                                  uvavg(i,j) = uvavg(i,j) +
(up_instant(i,j,n) * vp_instant(i,j,n))
                              END IF

                      END DO
                  END DO

            END DO

            DO i = 1, num_X
                  DO j = 1, num_Y
                      IF (num_good(i,j,4) == 0.0) THEN
                            uuavg(i,j)  = 0
                            vvavg(i,j)  = 0
                            uvavg(i,j)  = 0
                      ELSE
                            uuavg(i,j) = uuavg(i,j) /
(num_good(i,j,4)-1)
                            vvavg(i,j) = vvavg(i,j) /
(num_good(i,j,4)-1)
                            uvavg(i,j) = uvavg(i,j) /
(num_good(i,j,4)-1)
                      END IF
                  END DO
            END DO

      ELSE

            DO i = 1, num_X
                  DO j = 1, num_Y
```

```
                        uuavg(i,j) = uubar(i,j)
                        vvavg(i,j) = vvbar(i,j)
                        uvavg(i,j) = uvbar(i,j)
                    END DO
                END DO
            END IF

        DO n = 1, num_images
            DO j = 1, num_Y

                DO i = 1, num_X-1
                    up_rms(j,n) = up_rms(j,n) +
(up_instant(i,j,n)*up_instant(i,j,n))
                    vp_rms(j,n) = vp_rms(j,n) +
(vp_instant(i,j,n)*vp_instant(i,j,n))
                END DO

                up_rms(j,n) = sqrt(up_rms(j,n)/num_X-1)
                vp_rms(j,n) = sqrt(vp_rms(j,n)/num_X-1)

            END DO
        END DO


          ! CALCULATE PRINCIPAL STRESS AXES
          !*************************************************************
******************
        IF (unit(8) > 0) THEN

            WRITE(*,*) "CALCULATING PRINCIPAL STRESS AXES..."
                WRITE(*,*)

              DO i = 1, num_X
                  DO j =1, num_Y

                      DO a = 0,360, 0.001
                          alpha_temp = a*3.14159/180
                          uv_temp = 0.5*(uuavg(i,j)-
vvavg(i,j))*sin(2*alpha_temp) + uvavg(i,j)*cos(2*alpha_temp)
                          !WRITE(*,*) a, alpha_temp, uv_temp

                          IF (ABS(uv_temp) <= 0.01) THEN              !
First try with toughest requirement
                            !WRITE(*,*) "IT WORKED!!!!"
                           !WRITE(*,*)
                           !WRITE(*,*)i, j, uuavg(i,j), vvavg(i,j),
uvavg(i,j),a, alpha_temp, alpha(i,j), uv_temp

                          uvlambda(i,j) = uv_temp
                          uulambda(i,j) = uuavg(i,j)*(cos(alpha_temp))**2
- 2*uvavg(i,j)*cos(alpha_temp)*sin(alpha_temp) +
vvavg(i,j)*(sin(alpha_temp))**2
```

```
                        vvlambda(i,j) = uuavg(i,j)*(sin(alpha_temp))**2
+ 2*uvavg(i,j)*cos(alpha_temp)*sin(alpha_temp) +
vvavg(i,j)*(cos(alpha_temp))**2
                        alpha(i,j) = alpha_temp*180/3.14159
                        GOTO 120
                      END IF

                      !WRITE(*,*) i, j, a, alpha_temp, uv_temp
                      !WRITE(*,*) uuavg(i,j), vvavg(i,j), uvavg(i,j)
                      !READ(*,*) dum
                      !STOP
                  END DO

                  DO a = 0,360, 0.001
                      alpha_temp = a*3.14159/180
                      uv_temp = 0.5*(uuavg(i,j)-
vvavg(i,j))*sin(2*alpha_temp) + uvavg(i,j)*cos(2*alpha_temp)

                      IF (ABS(uv_temp) <= 0.1) THEN                !
Then try with relaxed requirement
                        uvlambda(i,j) = uv_temp
                        uulambda(i,j) = uuavg(i,j)*(cos(alpha_temp))**2
- 2*uvavg(i,j)*cos(alpha_temp)*sin(alpha_temp) +
vvavg(i,j)*(sin(alpha_temp))**2
                        vvlambda(i,j) = uuavg(i,j)*(sin(alpha_temp))**2
+ 2*uvavg(i,j)*cos(alpha_temp)*sin(alpha_temp) +
vvavg(i,j)*(cos(alpha_temp))**2
                        alpha(i,j) = alpha_temp*180/3.14159
                        GOTO 120
                      END IF
                END DO

                DO a = 0,360, 0.001
                      alpha_temp = a*3.14159/180
                      uv_temp = 0.5*(uuavg(i,j)-
vvavg(i,j))*sin(2*alpha_temp) + uvavg(i,j)*cos(2*alpha_temp)

                      IF (ABS(uv_temp) <= 1.0) THEN                !
Finally try with loose requirement
                        uvlambda(i,j) = uv_temp
                        uulambda(i,j) = uuavg(i,j)*(cos(alpha_temp))**2
- 2*uvavg(i,j)*cos(alpha_temp)*sin(alpha_temp) +
vvavg(i,j)*(sin(alpha_temp))**2
                        vvlambda(i,j) = uuavg(i,j)*(sin(alpha_temp))**2
+ 2*uvavg(i,j)*cos(alpha_temp)*sin(alpha_temp) +
vvavg(i,j)*(cos(alpha_temp))**2
                        alpha(i,j) = alpha_temp*180/3.14159
                        GOTO 120
                      END IF
                END DO

120               CONTINUE
```

```
            END DO
         END DO
    END IF

125 CONTINUE


      ! CALCULATE VELOCITY GRADIENTS
      !*****************************************************************
******************

      IF (unit(5) > 0) THEN

            WRITE(*,*) "CALCULATING VELOCITY GRADIENTS..."
            WRITE(*,*)

            dx = (X(2,1) - X(1,1))/1000
            dy = (Y(1,2) - Y(1,1))/1000

            CALL Gradients2 (Uavg, num_X, num_Y, dUdX, dUdY, dx, dy)
            CALL Gradients2 (Vavg, num_X, num_Y, dVdX, dVdY, dx, dy)
            CALL Gradients2 (uuavg, num_X, num_Y, duudX, duudY, dx, dy)
            CALL Gradients2 (vvavg, num_X, num_Y, dvvdX, dvvdY, dx, dy)
            CALL Gradients2 (uvavg, num_X, num_Y, duvdX, duvdY, dx, dy)

            DO i = 1, num_X
                  DO j = 1, num_Y
                        vorticity(i,j) = dVdX(i,j) - dUdY(i,j)
                        strain(i,j) = dVdX(i,j) + dUdY(i,j)
                        txxdudx(i,j) = -uuavg(i,j) * dUdX(i,j)
                        txydudy(i,j) = -uvavg(i,j) * dUdY(i,j)
                        txydvdx(i,j) = -uvavg(i,j) * dVdX(i,j)
                        tyydvdy(i,j) = -vvavg(i,j) * dVdY(i,j)
                        txydudx(i,j) = -uvavg(i,j) * dUdX(i,j)
                        tyydudy(i,j) = -vvavg(i,j) * dUdY(i,j)
                        txxdvdx(i,j) = -uuavg(i,j) * dVdX(i,j)
                        txydvdy(i,j) = -uvavg(i,j) * dVdY(i,j)
                        productionxx(i,j) = -2*(txxdudx(i,j) +
txydudy(i,j))
                        productionyy(i,j) = -2*(txydvdx(i,j) +
tyydvdy(i,j))
                        productionxy(i,j) = -(txydudx(i,j) +
tyydudy(i,j) + txxdvdx(i,j) + txydvdy(i,j))

                  END DO
            END DO

      ELSE

            DO i = 1, num_X
                  DO j = 1, num_Y
                        dUdX(i,j) = 0
                        dUdY(i,j) = 0
```

```
                        dVdX(i,j) = 0
                        dVdY(i,j) = 0
                        duudX(i,j) = 0
                        duudY(i,j) = 0
                        dvvdX(i,j) = 0
                        dvvdY(i,j) = 0
                        duvdX(i,j) = 0
                        duvdY(i,j) = 0
                        vorticity(i,j) = 0
                        strain(i,j) = 0
                        txxdudx(i,j) = 0
                        txydudy(i,j) = 0
                        txydvdx(i,j) = 0
                        tyydvdy(i,j) = 0
                        txydudx(i,j) = 0
                        tyydudy(i,j) = 0
                        txxdvdx(i,j) = 0
                        txydvdy(i,j) = 0
                        productionxx(i,j) = 0
                        productionyy(i,j) = 0
                        productionxy(i,j) = 0
                    END DO
                END DO

            END IF


            ! PERFORM REYNOLDS STRESS QUADRANT DECOMPOSITION
            !*****************************************************************
**********

            IF (unit(9) > 1) THEN

                WRITE(*,*) "PERFORMING REYNOLDS STRESS QUADRANT
DECOMPOSITION..."
                WRITE(*,*)

               OPEN(UNIT = 52, FILE='TAMU_PIV_INPUT_QUAD.DAT', STATUS='OLD',
IOSTAT =  ios)

               IF (ios /= 0) THEN
                     WRITE(*,*) 'ERROR opening file TAMU_PIV_INPUT_QUAD.DAT'
                     WRITE(*,*) 'To continue, press any key, then [ENTER].'
                     READ(*,*) end_stop
                     STOP
               END IF

               READ(52,*)
               READ(52,*)
               READ(52,*)
               READ(52,*)
               READ(52,*)
```

```
            READ(52,'(17X, I20)') quad_number

            READ(52,*)
            READ(52,*)
            READ(52,*)

            ALLOCATE(quad_location(quad_number))

            DO i = 1, quad_number
                READ(52,*) quad_location(i)
            END DO

            CLOSE(52)

          DO k = 1, quad_number

              y_ref = quad_location(k)

              WRITE(yrefc,'(F6.3)') y_ref
              xref = num_X/2
              i = xref

              OPEN(UNIT = 55, FILE = trim(filename) // '_QUAD(' //
trim(yrefc) // ' mm).dat')

              DO j = num_Y, 1, -1

                  !WRITE(*,*) j, Y(i,j)

                  IF (Y(i,j) >= y_ref) THEN

                      DO n = 1, num_images

                          IF (up_instant(i,j,n) == 0.0) THEN
                              psi = 1000.0
                          ELSE
                              psi(n) =
(atan(vp_instant(i,j,n)/up_instant(i,j,n)))*180/3.14159
                          END IF

                          i_temp = 0

                          DO l = -89, 90
                              i_temp = i_temp + 1
                              !WRITE(*,*) i_temp, l
                              IF (psi(n) >= (l-1) .AND. psi(n) <= l) THEN
                                  psi_location(i_temp) = l
                                  psi_prob(i_temp) = psi_prob(i_temp) + 1

                                  !WRITE(*,*) n, i_temp, l,
psi_location(i_temp), psi_prob(i_temp)
                              END IF
                          END DO
```

```
                    END DO

                    WRITE(55,*) "X_ref(integer)  ", "Y_ref(mm)  ",
"Y_actual(mm)"
                    WRITE(55,*) xref, y_ref, Y(i,j)
                    WRITE(55,*)
                    WRITE(55,*) "i_temp  ", "psi_location  ", "psi_prob
"

                    DO i_temp = 1,200
                        WRITE(55,'(1X, I6, 2X, I6, 2X, E15.6)') i_temp,
psi_location(i_temp), psi_prob(i_temp)
                    END DO

                    WRITE(55,*)
                    WRITE(55,*)
                    WRITE(55,*) "Image  ", "u'  ", "v'  ", "Psi  "

                    DO n = 1, num_images
                        WRITE(55,'(1X, I6, 2X, E15.6, 2X, E15.6, 2X,
E15.6)') n, up_instant(i,j,n), vp_instant(i,j,n), psi(n)
                    END DO

                    GOTO 130

                END IF
            END DO

130         CONTINUE

            CLOSE(55)

        END DO
    END IF

135 CONTINUE


      ! PERFORM TWO-POINT CORRELATIONS
      !*****************************************************************
*****************

      IF (unit(10) > 0) THEN

          WRITE(*,*) "PERFORMING TWO-POINT CORRELATIONS..."
            WRITE(*,*)

          OPEN(UNIT = 55, FILE='TAMU_PIV_INPUT_CORR.DAT', STATUS='OLD',
IOSTAT =  ios)

          IF (ios /= 0) THEN
                WRITE(*,*) 'ERROR opening file TAMU_PIV_INPUT_CORR.DAT'
```

```
                WRITE(*,*) 'To continue, press any key, then [ENTER].'
                READ(*,*) end_stop
                STOP
            END IF

            READ(55,*)
            READ(55,*)
            READ(55,*)
            READ(55,*)
            READ(55,*)

            READ(55,'(17X, I20)') corr_number

            READ(55,*)
            READ(55,*)
            READ(55,*)

            ALLOCATE(corr_location(corr_number))

            DO i = 1, corr_number
                READ(55,*) corr_location(i)
            END DO

            CLOSE(55)


        xref = num_X / 2
        !yref = num_Y / 2

        img_count = 0

        DO k = 1, corr_number

            y_location = corr_location(k)
            WRITE(*,*) y_location

            WRITE(yrefc,'(F6.3)') y_location

            OPEN(UNIT = 29, FILE = trim(filename) // '_CORR(' //
trim(yrefc) // ' mm).dat')

            DO q = num_Y, 1, -1

                !WRITE(*,*) j, Y(i,j)

                IF (Y(xref,q) >= y_location) THEN

                    yref = q

                    imin = 1
                    imax = num_X-xref-1
                    jmin = 1
                    jmax = num_Y-yref-1
```

```
                    jlag = 1
                    ilag = imax-1

                    WRITE(29,*) 'TITLE = "Ruu_test2d.dat"'
                    WRITE(29,*) 'Variables = "deltaX (mm)","Y
(mm)","Lag number", "Ruu", "Ruu_norm"'
                    WRITE(29,*) 'ZONE I=', ilag, ', J=', num_Y, ',
F=POINT, DT=(DOUBLE,DOUBLE,DOUBLE,DOUBLE,DOUBLE)'
                    WRITE(29,'(A27,I6,2X,A14,E12.6,2X,A17,E12.6)') '#
INPUTS: X_ref(integer) = ', xref, ',  Y_ref(mm) = ', y_location, '
Y_actual(mm) = ', Y(xref,yref)

                    DO img = 1, num_images

                        img_count = img_count + 1
                        !WRITE(*,*) img_count

                        DO j = 1, num_Y
                            DO l = 0, ilag-1

                                iend = imax - l
                                sum = 0.0
                                numg = 0

                                DO i = xref, xref + iend

IF(ABS(up_instant(i,yref,img)*up_instant(i+l,j,img)) < 1e6) THEN
                                    sum = sum +
up_instant(i,yref,img)*up_instant(i+l,j,img)/(sqrt(uuavg(i,yref))*sqrt(
vvavg(i+l,j)))
                                    numg = numg + 1
                                    !WRITE(*,*) i, jj, sum,
up_instant(i,yref,n), up_instant(i+jj,yref,n), numg
                                END IF
                                END DO

                                !IF (j == 1) THEN
                                !READ(*,*) end_stop
                                !END IF

                                IF (numg-1 == 0) THEN
                                    rhh(l+1,j,img)=0
                                ELSE
                                    rhh(l+1,j,img) = 1./(numg-1)*sum
                                END IF

                                !WRITE(*,*) j,n,sum,rhh(j,n)
                                !READ(*,*) end_stop

                                rhh_total(l+1,j) = rhh_total(l+1,j) +
rhh(l+1,j,img)
```

```
                                !WRITE(*,*)
j,n,sum,rhh(j,n),rhh_total(j)
                                !READ(*,*) end_stop

                                !WRITE(*,*)
                                !WRITE(*,*) "j,sum,iend,rhh(j)"
                                !WRITE(*,*) j, sum, iend, rhh(j)
                                !READ(*,*) end_stop

                            END DO
                        END DO
                    END DO

                    DO j = 1, num_Y
                        DO l = 1, ilag
                            rhh_total(l,j) = rhh_total(l,j) / img_count
                        END DO
                    END DO

                    DO j = 1, num_Y
                        DO l = 1, ilag

WRITE(29,'(1X,E15.6,2X,E15.6,2X,I5,2X,E15.6,2X,E15.6)') X(xref+l-1,j)-
X(xref,j), Y(l,j), l, rhh_total(l,j), rhh_total(l,j)/rhh_total(1,yref)
                        END DO
                    END DO

                    GOTO 140

                END IF
            END DO

140     CONTINUE

        CLOSE(29)

        END DO

END IF


      ! NORMALIZE QUANTITIES
      !*****************************************************************
*****************

      IF (unit(6) > 1) THEN

            WRITE(*,*) "NORMALIZING VALUES..."
            WRITE(*,*)

            CALL Normalization (Unorm, Vnorm, uunorm, vvnorm, uvnorm,
Ubar, Vbar, uubar, vvbar, Uavg, Vavg, uuavg, vvavg, &
```

```
                  & uvavg, num_good, num_images, num_X, num_Y, U_ref,
unit)

      ELSE

            DO i = 1, num_X
                  DO j = 1, num_Y
                        Unorm(i,j) = Uavg(i,j)
                        Vnorm(i,j) = Vavg(i,j)
                        uunorm(i,j) = uuavg(i,j)
                        vvnorm(i,j) = vvavg(i,j)
                        uvnorm(i,j) = uvavg(i,j)
                  END DO
            END DO

      END IF

      DO k = 1, 4
            DO i = 1, num_X
                  DO j = 1, num_Y
                        num_good_avg(i,j,k) = num_good(i,j,k) /
num_images * 100
                  END DO
            END DO
      END DO

      DO i = 1, num_X
            DO j = 1, num_Y
                  !filtered_num_good_avg(i,j) = num_good(i,j,3) /
num_images * 100
            END DO
      END DO


      ! OUTPUT
      !*****************************************************************
*****************

      save_filename = trim(adjustl(filename)) // '_OUTPUT.dat'
      save_filename = trim(adjustl(save_filename))

      grad_save_filename = trim(adjustl(filename)) // '_GRADIENT.dat'
      grad_save_filename = trim(adjustl(grad_save_filename))

      20 FORMAT (1X, A9, A20, A1)
      22 FORMAT (1X, A389)
      25 FORMAT (1X, A7, I5, A5, I5, A294)
      27 FORMAT (1X, A12, 2X, A12, 2X, A12, 2X, A12, 2X, A12, 2X, A12,
2X, A12, 2X, A12, 2X, A12)
      28 FORMAT (A38, I6, A16, F7.2, A16, F9.4, A14, F9.2)
      30 FORMAT (1X, E15.6, 2X, E15.6, 2X, I5, 2X, I5, 2X, E15.6, 2X,
E15.6, 2X, E15.6, 2X, E15.6, 2X, E15.6, 2X, E15.6, 2X, E15.6, 2X, E15.6, 2X,
E15.6, 2X, E15.6, 2X, E15.6, 2X, E15.6, 2X, E15.6, 2X, E15.6, 2X,
```

```
E15.6, 2X, E15.6, 2X, E15.6, 2X, E15.6, 2X, E15.6, 2X, E15.6, 2X,
E15.6, 2X, E15.6, 2X, E15.6, 2X, E15.6, 2X, E15.6, 2X, E15.6, 2X,
E15.6, 2X, E15.6, 2X, E15.6, 2X, E15.6, 2X, E15.6, 2X, E15.6, 2X,
E15.6, 2X, E15.6, 2X, E15.6, 2X)

      WRITE(*,*) "SAVING TO ", adjustl(save_filename)
      WRITE(*,*)

      OPEN(UNIT = 23, FILE = save_filename)

      WRITE(23,20) 'TITLE = "', save_filename, '"'
    WRITE(23,22) 'Variables = "X (mm)","Y
(mm)","Xi","Yi","U_avg","V_avg","U_norm","V_norm","u''u''","v''v''","u'
'v''","dUdX","dUdY","dVdX","dVdY","duudX","duudY","dvvdX","dvvdY","duvd
X","duvdY","vorticity","strain","txxdudx","txydudy","txydvdx","tyydvdy"
,"txydudx","tyydudy","txxdvdx","txydvdy","productionxx","productionyy",
"productionxy","alpha","num_good","num_good/num_images", "filtered
num_good"'
      WRITE(23,25) 'ZONE I=', num_X, ', J=', num_Y, ', F=POINT,
DT=(DOUBLE,DOUBLE,DOUBLE,DOUBLE,DOUBLE,DOUBLE,DOUBLE,DOUBLE,DOUBLE,DOUB
LE,DOUBLE,DOUBLE,DOUBLE,DOUBLE,DOUBLE,DOUBLE,DOUBLE,DOUBLE,DOUBLE,DOUBL
E,DOUBLE,DOUBLE,DOUBLE,DOUBLE,DOUBLE,DOUBLE,DOUBLE,DOUBLE,DOUBLE,DOUBLE
,DOUBLE,DOUBLE,DOUBLE,DOUBLE,DOUBLE,DOUBLE,DOUBLE,DOUBLE)'
      WRITE(23,*)
      WRITE(23,28) '# INPUT VARIABLES: Number of images = ',
num_images, '  Pixels / mm = ',pix_mm_org, '  Delta T (us) = ', dt_org,
'  Uinfavg = ', Uinfavg
      WRITE(23,*)

      DO j = 1, num_Y
            DO i = 1, num_X
                  WRITE(23,30)
X(i,j),Y(i,j),Xi(i,j),Yi(i,j),Uavg(i,j),Vavg(i,j),Unorm(i,j),Vnorm(i,j)
,uunorm(i,j),vvnorm(i,j),uvnorm(i,j),dUdX(i,j),dUdY(i,j),dVdX(i,j),dVdY
(i,j),duudX(i,j),duudY(i,j),dvvdX(i,j),dvvdY(i,j),duvdX(i,j),duvdY(i,j)
,vorticity(i,j),strain(i,j),txxdudx(i,j),txydudy(i,j),txydvdx(i,j),tyyd
vdy(i,j),txydudx(i,j),tyydudy(i,j),txxdvdx(i,j),txydvdy(i,j),production
xx(i,j),productionyy(i,j),productionxy(i,j),alpha(i,j),num_good(i,j,1),
num_good_avg(i,j,1), num_good(i,j,3)
            END DO
      END DO

      CLOSE(23)

      CALL itime(end_time)


      elapsed_time(1) = end_time(1) - start_time(1)
      !Calculate elapsed time
      elapsed_time(2) = end_time(2) - start_time(2)
      elapsed_time(3) = ABS(end_time(3) - start_time(3))
```

```
      seconds = elapsed_time(1)*3600 + elapsed_time(2)*60 +
elapsed_time(3)

      1000 FORMAT (1X, A21, I2.2, ':', I2.2, ':', I2.2 )
      1002 FORMAT (1X, A21, A25)
      1001 FORMAT (1X, A21, I8)
      1005 FORMAT (1X, A21, I3, A6, I3, A8, I3, A8)

      WRITE(*,*) 'PROCESSING DONE !!'
      WRITE(*,*)
      WRITE(*,*)
      WRITE(*,*) 'SUMMARY'
      WRITE(*,*) '---------------------------'
      WRITE(*,1002) 'First file name   = ', first_filename
      WRITE(*,1002) 'Output file name  = ', save_filename
      WRITE(*,*)
      WRITE(*,1001) 'Number of Images  = ', num_images
      WRITE(*,1001) 'Number of Columns = ', num_X
      WRITE(*,1001) 'Number of Rows    = ', num_Y
      WRITE(*,1001) 'Number of Vectors = ', num_vectors
      WRITE(*,*)
      WRITE(*,1005) 'Processing time   = ', elapsed_time(1), 'hours',
elapsed_time(2), 'minutes', elapsed_time(3), 'seconds'
      WRITE(*,*)

      !WRITE(*,*) X(1,1)
      !WRITE(*,*) X(2,1)
      !WRITE(*,*) Y(1,1)
      !WRITE(*,*) Y(1,2)


      !WRITE(*,*) dx
      !WRITE(*,*) dy
      WRITE(*,*)
      WRITE(*,*)
      WRITE(*,*) 'To continue, press any key, then [ENTER].'
      READ(*,*) end_stop



      ! SUBROUTINES
      !*****************************************************************
*****************

      CONTAINS


    ! DETERMINE CURRENT FILE NAME
      !****************************************

      SUBROUTINE Determine_filename (file_number, filename, extension,
full_filename)
```

```
            ! INPUT = file_number, filename, extension
            !OUTPUT = full_filename

            INTEGER :: file_number
            CHARACTER(20) :: filename, file_number_char,
full_filename*25
            CHARACTER(10) :: extension

            !CHARACTER :: file_number_char, filename, extension,
full_filename

            !WRITE(*,*) "DETERMINING FILE NAMES AND READING FILES"
            !WRITE(*,*)

            !WRITE(*,*) file_number

            WRITE(file_number_char , '( I6 )' ) file_number

            IF (file_number < 10) THEN
                  full_filename = trim(adjustl(filename)) // '_000' //
trim(adjustl(file_number_char)) // trim(adjustl(extension))
                  full_filename = trim(adjustl(full_filename))
                  !PRINT '(A20)', full_filename
            END IF

            IF ((file_number >= 10) .AND. (file_number < 100)) THEN
                  full_filename = trim(adjustl(filename)) // '_00' //
trim(adjustl(file_number_char)) // trim(adjustl(extension))
                  full_filename = trim(adjustl(full_filename))
                  !PRINT '(A20)', full_filename
            END IF

            IF ((file_number >= 100) .AND. (file_number < 1000)) THEN
                  full_filename = trim(adjustl(filename)) // '_0' //
trim(adjustl(file_number_char)) // trim(adjustl(extension))
                  full_filename = trim(adjustl(full_filename))
                  !PRINT '(A20)', full_filename
            END IF

            IF ((file_number >= 1000) .AND. (file_number < 10000)) THEN
                  full_filename = trim(adjustl(filename)) // '_' //
trim(adjustl(file_number_char)) // trim(adjustl(extension))
                  full_filename = trim(adjustl(full_filename))
                  !PRINT '(A20)', full_filename
            END IF

      END SUBROUTINE Determine_filename


      ! READ CURRENT DATA FILE
      !*************************************************************
*****************
```

```
      SUBROUTINE Read_file (full_filename, end_stop, extension,
extension_2, num_X, num_Y, Xi, Yi, U, V, sign, pix_m, dt)

            ! INPUT = full_filename, end_stop, extension, extension_2,
num_X, num_Y
            !OUTPUT = Xi, Yi, U, V

            CHARACTER(20) :: full_filename*25
            CHARACTER(10) :: extension_2, extension, end_stop
            INTEGER :: IOSTAT, num_X, num_Y, ios
            REAL(8) :: pix_m, dt, sign
            INTEGER, DIMENSION(:,:) :: Xi, Yi
            REAL(8), DIMENSION(:,:) :: U, V

            !n = file_number

            OPEN(UNIT = 11, FILE = full_filename, STATUS = 'OLD',
IOSTAT = ios)

            IF (ios /= 0) THEN

                  WRITE(*,*) 'Error opening file, ',
adjustl(full_filename)
                  WRITE(*,*)
                  WRITE(*,*) 'To continue, press any key, then
[ENTER].'
                  READ(*,*) end_stop

                  STOP

            END IF

            READ(11,*)

            IF (extension == extension_2) THEN              !Account
for two additional header lines in Tecplot .DAT files
                  READ(11,*)
                  READ(11,*)
            END IF

            DO j = 1, num_Y
                  DO i = 1, num_X
                        READ(11,*,IOSTAT=ios) Xi(i,j), Yi(i,j), U(i,j),
V(i,j)
                        !WRITE(*,*) Xi(i,j,1), Yi(i,j,1), U(i,j,1),
V(i,j,1)
                        IF (ios /= 0) THEN
                              WRITE(*,*) 'ERROR in reading from
file...'  !File reading error message
                              WRITE(*,*) 'Filename = ', full_filename
                              WRITE(*,*) 'i= ', i, 'j= ', j
                              READ(*,*) end_stop
                              STOP
```

```
                        END IF
                        U(i,j) = U(i,j) / pix_m / dt
                        V(i,j) = V(i,j) / pix_m / dt * (sign)
                    END DO
                END DO

                IF (unit(7) == 1) THEN              !ROTATE MEAN VELOCITIES

                DO j = 1, num_Y
                        DO i = 1, num_X
                            U_global(i,j) =
U(i,j)*cos(rotation)+V(i,j)*sin(rotation)
                            V_global(i,j) = -
U(i,j)*sin(rotation)+V(i,j)*cos(rotation)
                        END DO
                    END DO

                DO j = 1, num_Y
                        DO i = 1, num_X
                            U(i,j) = U_global(i,j)
                            V(i,j) = V_global(i,j)
                        END DO
                    END DO

            END IF

              CLOSE(11)

        END SUBROUTINE Read_file


        !CALCULATE VELOCITY GRADIENTS
        !************************************************

        SUBROUTINE Gradients (vel, num_X, num_Y, dUdX, dUdY, dx, dy)

              ! INPUT = U, num_X, num_Y, dx
              !OUTPUT = dUdx, dUdy

              INTEGER :: num_X, num_Y
              REAL(8) :: dx, dy
              REAL(8), DIMENSION(:,:) :: vel, dUdX, dUdY

              DO j = 1, num_Y
                    DO i = 1, num_X - 1
                        IF (vel(i,j) == 0 .OR. vel(i+1,j) == 0) THEN
                              dUdX(i,j) = 0
                        ELSE
                              dUdX(i,j) = (vel(i+1,j) - vel(i,j)) / dx
                        END IF
                    END DO
              END DO
```

```
            DO j = 1, num_Y
                  dUdX(num_X,j) = dUdX(num_X-1,j)
            END DO

            DO i = 1, num_X
                  DO j = 1, num_Y - 1
                        IF (vel(i,j) == 0 .OR. vel(i,j+1) == 0) THEN
                              dUdY(i,j) = 0
                        ELSE
                              dUdY(i,j) = (vel(i,j+1) - vel(i,j)) / dy
                        END IF
                  END DO
            END DO

            DO i = 1, num_X
                  dUdY(i,num_Y) = dUdY(i,num_Y-1)
            END DO

      END SUBROUTINE Gradients



      SUBROUTINE Gradients2 (vel, num_X, num_Y, dUdX, dUdY, dx, dy)

            ! INPUT = U, num_X, num_Y, dx
            !OUTPUT = dUdx, dUdy

            INTEGER :: num_X, num_Y
            REAL(8) :: dx, dy
            REAL(8), DIMENSION(:,:) :: vel, dUdX, dUdY

            DO j = 1, num_Y
                  DO i = 2, num_X - 1
                        IF (vel(i-1,j) == 0 .OR. vel(i+1,j) == 0) THEN
                              dUdX(i,j) = 0
                        ELSE
                              dUdX(i,j) = (vel(i+1,j) - vel(i-1,j)) /
(2*dx)
                        END IF
                  END DO
            END DO

            DO j = 1, num_Y
                dUdX(1,j) = dUdX(2,j)
                  dUdX(num_X,j) = dUdX(num_X-1,j)
            END DO

            DO i = 1, num_X
                  DO j = 2, num_Y - 1
                        IF (vel(i,j-1) == 0 .OR. vel(i,j+1) == 0) THEN
                              dUdY(i,j) = 0
                        ELSE
```

```
                              dUdY(i,j) = (vel(i,j+1) - vel(i,j-1)) /
(2*dy)
                        END IF
                  END DO
            END DO

            DO i = 1, num_X
                dUdY(i,1) = dUdY(i,2)
                  dUdY(i,num_Y) = dUdY(i,num_Y-1)
            END DO

      END SUBROUTINE Gradients2


      !CALCULATE NORMALIZED VALUES
      !************************************************

      SUBROUTINE Normalization (Unorm, Vnorm, uunorm, vvnorm, uvnorm,
Ubar, Vbar, uubar, vvbar, Uavg, Vavg, uuavg, vvavg, &
                  & uvavg, num_good, num_images, num_X, num_Y, U_ref,
unit)

            INTEGER :: num_images, num_X, num_Y
            REAL(8) :: U_ref
            INTEGER, DIMENSION(:) :: unit
            REAL(8), DIMENSION(:,:) :: Ubar, Vbar, uubar, vvbar, Uavg,
Vavg, uuavg, vvavg, uvavg, Unorm, Vnorm, uunorm, vvnorm, uvnorm
            REAL(8), DIMENSION(:,:,:) :: num_good

            IF (unit(3) == 1) THEN
                  DO j = 1, num_Y
                        DO i = 1, num_X
                              Unorm(i,j) = Uavg(i,j) / U_ref
                              Vnorm(i,j) = Vavg(i,j) / U_ref
                        END DO
                  END DO

                  ELSE

                  DO j = 1, num_Y
                        DO i = 1, num_X
                              Unorm(i,j) = Ubar(i,j) / U_ref
                              Vnorm(i,j) = Vbar(i,j) / U_ref
                        END DO
                  END DO

            END IF

            IF (unit(4) == 1) THEN
                  DO j = 1, num_Y
                        DO i = 1, num_X
                              uunorm(i,j) = sqrt(uuavg(i,j)) / U_ref
                              vvnorm(i,j) = sqrt(vvavg(i,j)) / U_ref
```

```
                        uvnorm(i,j) = uvavg(i,j) / (U_ref**2)
                  END DO
            END DO

      ELSE

            DO j = 1, num_Y
                  DO i = 1, num_X
                        uunorm(i,j) = sqrt(uubar(i,j)) / U_ref
                        vvnorm(i,j) = sqrt(vvbar(i,j)) / U_ref
                        uvnorm(i,j) = uvavg(i,j) / (U_ref**2)
                  END DO
            END DO
      END IF

END SUBROUTINE Normalization


END PROGRAM TAMU_PIV
```

TAMU_PROFILE_INPUT.dat

```
**************************************************************************
*******   TAMU PROFILE Input File (TAMU_PROFILE_INPUT.DAT)    *******
*******                                  *******
*******        Version: 0.006      Date:05/20/2010          *******
**************************************************************************

Number of Files    6

Filename                 Left Bound (mm)       Right Bound (mm)
--------------------------------------------------------------------
File_1                      1.0              12.0
File_2                      1.0              12.0
File_3                      8.0              16.0
File_4                      8.0              16.0
File_5                      8.0              16.0
File_6                      8.0              16.0
```

TAMU_PROFILE.f90

```
      !*****************************************************************
******************
      !     Program: TAMU_PROFILE
*
      !     Purpose: Create Profiles from Processed PIV Data Output
from TAMU_PIV         *
      !     Programmer: Nathan Tichenor
*
      !     Version: 0.006
*
      !     Date: 05/20/2010
*
      !*****************************************************************
******************

      PROGRAM TAMU_PROFILE

      ! INITIALIZE VARIABLES
      !*****************************************************************
******************


      CHARACTER(60) :: input, output, skip, end_stop

      INTEGER :: i, j, k, m, num_X, num_Xc, num_Y, num_files, ios,
test, Xi_temp, Yi_temp
      REAL(8) :: L, R, Lx, Rx,  X_temp, Y_temp, U_temp, V_temp,
Unorm_temp, Vnorm_temp, uu_temp, vv_temp, uv_temp
      REAL(8) :: dudx_temp, dudy_temp, dvdx_temp, dvdy_temp
      REAL(8) :: dummy, txxdudx_temp, txydudy_temp, txydvdx_temp,
tyydvdy_temp, txydudx_temp, tyydudy_temp
      REAL(8) :: txxdvdx_temp, txydvdy_temp, productionxx_temp,
productionyy_temp, productionxy_temp
      REAL(8) :: alpha_temp, num_good_temp, num_good_avg_temp

      INTEGER, DIMENSION(:,:), ALLOCATABLE :: Xi, Yi
      REAL(8), DIMENSION(:,:), ALLOCATABLE :: X, Y, U, V, Unorm, Vnorm,
uu, vv, uv
      REAL(8), DIMENSION(:,:), ALLOCATABLE :: dudx, dudy, dvdx, dvdy
      REAL(8), DIMENSION(:,:), ALLOCATABLE :: txxdudx, txydudy,
txydvdx, tyydvdy, txydudx, tyydudy
      REAL(8), DIMENSION(:,:), ALLOCATABLE :: txxdvdx, txydvdy,
productionxx, productionyy, productionxy
      REAL(8), DIMENSION(:,:), ALLOCATABLE :: alpha, num_good,
num_good_avg
      REAL(8), DIMENSION(:),   ALLOCATABLE :: Xp, Yp, Up, Vp, Unp, Vnp,
uup, vvp, uvp
      REAL(8), DIMENSION(:),   ALLOCATABLE :: dudxp, dudyp, dvdxp,
dvdyp
```

```
      REAL(8), DIMENSION(:), ALLOCATABLE :: txxdudxp, txydudyp,
txydvdxp, tyydvdyp, txydudxp, tyydudyp
      REAL(8), DIMENSION(:), ALLOCATABLE :: txxdvdxp, txydvdyp,
productionxxp, productionyyp, productionxyp
      REAL(8), DIMENSION(:), ALLOCATABLE :: alphap, num_goodp,
num_good_avgp
      REAL(8), DIMENSION(:), ALLOCATABLE :: uulambda, vvlambda,
uvlambda
      INTEGER, DIMENSION(:),   ALLOCATABLE :: Yip



      ! READ INPUT VARIABLES FROM PROFILE_INPUT.DAT
      !*************************************************************
*****************


      WRITE(*,*) "***********************************************"
      WRITE(*,*) "***       TAMU PROFILE AVERAGING CODE        ***"
      WRITE(*,*) "***   Version: 0.006      Date:05/20/2010    ***"
      WRITE(*,*) "***********************************************"
      WRITE(*,*)
      WRITE(*,*)
      WRITE(*,*) "Saving profile data to:"
      WRITE(*,*)

      OPEN(UNIT=100, FILE='TAMU_PROFILE_INPUT.dat', STATUS='OLD',
IOSTAT =  ios)

      IF (ios /= 0) THEN

            WRITE(*,*) 'ERROR opening file TAMU_PROFILE_INPUT.DAT'
            WRITE(*,*) 'To continue, press any key, then [ENTER].'
            READ(*,*) end_stop

            STOP

      END IF

      READ(100,*)
      READ(100,*)
      READ(100,*)
      READ(100,*)
      READ(100,*)
      READ(100,*)

      READ(100,*) skip, skip, skip, num_files

      READ(100,*)
      READ(100,*)
      READ(100,*)

      m = 51
```

```
      DO k = 1, num_files ! Beginning of main DO loop

      READ(100,*) input, L, R
      input = trim(input)

      output = 'PROFILE_' // trim(input) // '.dat'
      input = trim(input) // '.dat'

      !WRITE(*,*) num_files
      !WRITE(*,*) input, L, R
      !WRITE(*,*) input, output

!stop

      OPEN(UNIT=k, FILE=input, STATUS='OLD')

      READ(k,*)
      READ(k,*)
      READ(k,*) skip, skip, num_X, skip, num_Y
      READ(k,*)
      READ(k,*)
      READ(k,*)


      ! ALLOCATE ARRAYS
      !*****************************************************************
*****************

      ALLOCATE(X(num_X, num_Y), Y(num_X, num_Y))
      ALLOCATE(Xi(num_X, num_Y), Yi(num_X, num_Y))
      ALLOCATE(U(num_X, num_Y), V(num_X, num_Y))
      ALLOCATE(Unorm(num_X, num_Y), Vnorm(num_X, num_Y))
      ALLOCATE(uu(num_X, num_Y), vv(num_X, num_Y), uv(num_X, num_Y))
      ALLOCATE(dudx(num_X, num_Y), dudy(num_X, num_Y), dvdx(num_X,
num_Y), dvdy(num_X, num_Y))
      ALLOCATE(txxdudx(num_X, num_Y), txydudy(num_X, num_Y),
txydvdx(num_X, num_Y), tyydvdy(num_X, num_Y))
      ALLOCATE(txydudx(num_X, num_Y), tyydudy(num_X, num_Y),
txxdvdx(num_X, num_Y), txydvdy(num_X, num_Y))
      ALLOCATE(productionxx(num_X, num_Y), productionyy(num_X, num_Y),
productionxy(num_X, num_Y))
      ALLOCATE(alpha(num_X, num_Y), num_good(num_X, num_Y),
num_good_avg(num_X, num_Y))

      ALLOCATE(Xp(num_Y), Yp(num_Y), Yip(num_Y))
      ALLOCATE(Up(num_Y), Vp(num_Y))
      ALLOCATE(Unp(num_Y), Vnp(num_Y))
      ALLOCATE(uup(num_Y), vvp(num_Y), uvp(num_Y))
      ALLOCATE(dudxp(num_Y), dudyp(num_Y), dvdxp(num_Y), dvdyp(num_Y))
      ALLOCATE(txxdudxp(num_Y), txydudyp(num_Y), txydvdxp(num_Y),
tyydvdyp(num_Y))
```

```
      ALLOCATE(txydudxp(num_Y), tyydudyp(num_Y), txxdvdxp(num_Y),
txydvdyp(num_Y))
      ALLOCATE(productionxxp(num_Y), productionyyp(num_Y),
productionxyp(num_Y))
      ALLOCATE(alphap(num_Y), num_goodp(num_Y), num_good_avgp(num_Y))
      ALLOCATE(uulambda(num_Y), vvlambda(num_Y), uvlambda(num_Y))


        X = 0
        Y = 0
        U = 0
        V = 0
       Unorm = 0
       Vnorm = 0
       uu = 0
       vv = 0
       uv = 0
       dudx = 0
       dudy = 0
       dvdx = 0
       dvdy = 0
      txxdudx = 0
      txydudy = 0
    txydvdx = 0
    tyydvdy = 0
    txydudx = 0
    tyydudy = 0
    txxdvdx = 0
    txydvdy = 0
    productionxx = 0
    productionyy = 0
    productionxy = 0
    alpha = 0
    num_good = 0
    num_good_avg = 0

       Xp = 0
       Yp = 0
      Yip = 0
       Up = 0
       Vp = 0
      Unp = 0
      Vnp = 0
      uup = 0
      vvp = 0
      uvp = 0
       dudxp = 0
       dudyp = 0
       dvdxp = 0
       dvdyp = 0
    txxdudxp = 0
      txydudyp = 0
    txydvdxp = 0
```

```
    tyydvdyp = 0
    txydudxp = 0
    tyydudyp = 0
    txxdvdxp = 0
    txydvdyp = 0
    productionxxp = 0
    productionyyp = 0
    productionxyp = 0
    alphap = 1e6
    num_goodp = 0
    num_good_avgp = 0

    alpha_temp = 0.0
    uv_temp = 0.0
    uulambda = 0.0
    vvlambda = 0.0
    uvlambda = 0.0



      ! POPULATE ARRAYS
      !*****************************************************************
******************


      DO j = 1, num_Y

            num_Xc = 0;

            DO i = 1, num_X

                  READ(k,*,IOSTAT=ios) X_temp, Y_temp, Xi_temp,
Yi_temp, U_temp, V_temp, Unorm_temp, Vnorm_temp, uu_temp, vv_temp,
uv_temp, dudx_temp, dudy_temp, dvdx_temp, dvdy_temp, dummy, dummy,
dummy, dummy, dummy, dummy, dummy, dummy, txxdudx_temp, txydudy_temp,
txydvdx_temp, tyydvdy_temp, txydudx_temp, tyydudy_temp, txxdvdx_temp,
txydvdy_temp, productionxx_temp, productionyy_temp, productionxy_temp,
dummy, num_good_temp, num_good_avg_temp

                  IF (X_temp .GE. L .AND. X_temp .LE. R) THEN

                        num_Xc = num_Xc + 1;

                        X(i,j) = X_temp
                        Y(i,j) = Y_temp
                        Xi(i,j) = Xi_temp
                        Yi(1,j) = Yi_temp
                        U(i,j) = U_Temp
                        V(i,j) = V_temp
                        Unorm(i,j) = Unorm_temp
                        Vnorm(i,j) = Vnorm_temp
                        uu(i,j) = uu_temp
                        vv(i,j) = vv_temp
```

```
                        uv(i,j) = uv_temp
                        dudx(i,j) = dudx_temp
                        dudy(i,j) = dudy_temp
                        dvdx(i,j) = dvdx_temp
                        dvdy(i,j) = dvdy_temp
                        txxdudx(i,j) = txxdudx_temp
                        txydudy(i,j) = txydudy_temp
                        txydvdx(i,j) = txydvdx_temp
                        tyydvdy(i,j) = tyydvdy_temp
                        txydudx(i,j) = txydudx_temp
                        tyydudy(i,j) = tyydudy_temp
                        txxdvdx(i,j) = txxdvdx_temp
                        txydvdy(i,j) = txydvdy_temp
                        productionxx(i,j) = productionxx_temp
                        productionyy(i,j) = productionyy_temp
                        productionxy(i,j) = productionxy_temp
                        !alpha(i,j) = alpha_temp
                        num_good(i,j) = num_good_temp
                        num_good_avg(i,j) = num_good_avg_temp
                !WRITE(*,*) productionxx(i,j), productionyy(i,j),
productionxy(i,j)

                        IF (ios /= 0) THEN
                              WRITE(*,*) 'Error populating array at:'
                              WRITE(*,*) 'i=', i
                              WRITE(*,*) 'j=', j
                              STOP
                        END IF

                  END IF

            END DO

      END DO


      ! GENERATE PROFILE AVERAGES
      !*************************************************************
******************


      DO j = 1, num_Y         ! Sum data across rows

            DO i = 1, num_X

                  Xp(j) =  Xp(j) + X(i,j)
                  Yp(j) =  Yp(j) + Y(i,j)
                 Yip(j) = Yi(1,j)
                  Up(j) =  Up(j) + U(i,j)
                  Vp(j) =  Vp(j) + V(i,j)
                 Unp(j) = Unp(j) + Unorm(i,j)
                 Vnp(j) = Vnp(j) + Vnorm(i,j)
                 uup(j) = uup(j) + uu(i,j)
```

```
              vvp(j) = vvp(j) + vv(i,j)
              uvp(j) = uvp(j) + uv(i,j)
         dudxp(j) = dudxp(j) + dudx(i,j)
         dudyp(j) = dudyp(j) + dudy(i,j)
         dvdxp(j) = dvdxp(j) + dvdx(i,j)
         dvdyp(j) = dvdyp(j) + dvdy(i,j)
    txxdudxp(j) = txxdudxp(j) + txxdudx(i,j)
    txydudyp(j) = txydudyp(j) + txydudy(i,j)
    txydvdxp(j) = txydvdxp(j) + txydvdx(i,j)
    tyydvdyp(j) = tyydvdyp(j) + tyydvdy(i,j)
    txydudxp(j) = txydudxp(j) + txydudx(i,j)
    tyydudyp(j) = tyydudyp(j) + tyydudy(i,j)
    txxdvdxp(j) = txxdvdxp(j) + txxdvdx(i,j)
    txydvdyp(j) = txydvdyp(j) + txydvdy(i,j)
productionxxp(j) = productionxxp(j) + productionxx(i,j)
productionyyp(j) = productionyyp(j) + productionyy(i,j)
productionxyp(j) = productionxyp(j) + productionxy(i,j)
!alphap(j) = alphap(j) + alpha(i,j)
num_goodp(j) = num_goodp(j) + num_good(i,j)
num_good_avgp(j) = num_good_avgp(j) + num_good_avg(i,j)

!WRITE(*,*) productionxxp(j), productionyyp(j), productionxyp(j)

         END DO

   END DO



   !WRITE(*,*) num_Xc


      Xp = Xp/num_Xc
      Yp = Yp/num_Xc
      Up = Up/num_Xc
      Vp = Vp/num_Xc
     Unp = Unp/num_Xc
     Vnp = Vnp/num_Xc
     uup = uup/num_Xc
     vvp = vvp/num_Xc
     uvp = uvp/num_Xc
   dudxp = dudxp/num_Xc
   dudyp = dudyp/num_Xc
   dvdxp = dvdxp/num_Xc
   dvdyp = dvdyp/num_Xc
txxdudxp = txxdudxp/num_Xc
txydudyp = txydudyp/num_Xc
txydvdxp = txydvdxp/num_Xc
tyydvdyp = tyydvdyp/num_Xc
txydudxp = txydudxp/num_Xc
tyydudyp = tyydudyp/num_Xc
txxdvdxp = txxdvdxp/num_Xc
txydvdyp = txydvdyp/num_Xc
```

```
    productionxxp = productionxxp/num_Xc
    productionyyp = productionyyp/num_Xc
    productionxyp = productionxyp/num_Xc
    !alphap = alphap/num_Xc
    num_goodp = num_goodp/num_Xc
    num_good_avgp = num_good_avgp/num_Xc

    WRITE(*,*) "CALCULATING PRINCIPAL STRESS AXES..."
    WRITE(*,*)

    DO j = 1, num_Y

        !write(*,*) j

        DO a = -45, 45, 0.0001
            alpha_temp = a*3.14159/180
            uv_temp = 0.5*(uup(j)-vvp(j))*sin(2*alpha_temp) +
uvp(j)*cos(2*alpha_temp)
            !WRITE(*,*) a, alpha_temp, uv_temp

            IF (ABS(uv_temp) <= 0.01) THEN              ! First try
with toughest requirement
                uvlambda(j) = uv_temp
                uulambda(j) = uup(j)*(cos(alpha_temp))**2 -
2*uvp(j)*cos(alpha_temp)*sin(alpha_temp) + vvp(j)*(sin(alpha_temp))**2
                vvlambda(j) = uup(j)*(sin(alpha_temp))**2 +
2*uvp(j)*cos(alpha_temp)*sin(alpha_temp) + vvp(j)*(cos(alpha_temp))**2
                alphap(j) = alpha_temp*180/3.14159
                GOTO 120
            END IF
        END DO

        DO a = -45, 45, 0.0001
            alpha_temp = a*3.14159/180
            uv_temp = 0.5*(uup(j)-vvp(j))*sin(2*alpha_temp) +
uvp(j)*cos(2*alpha_temp)

            IF (ABS(uv_temp) <= 0.1) THEN              ! Then try with
relaxed requirement
                uvlambda(j) = uv_temp
                uulambda(j) = uup(j)*(cos(alpha_temp))**2 -
2*uvp(j)*cos(alpha_temp)*sin(alpha_temp) + vvp(j)*(sin(alpha_temp))**2
                vvlambda(j) = uup(j)*(sin(alpha_temp))**2 +
2*uvp(j)*cos(alpha_temp)*sin(alpha_temp) + vvp(j)*(cos(alpha_temp))**2
                alphap(j) = alpha_temp*180/3.14159
                GOTO 120
            END IF

        END DO

        DO a = -45, 45, 0.0001
            alpha_temp = a*3.14159/180
```

```
            uv_temp = 0.5*(uup(j)-vvp(j))*sin(2*alpha_temp) +
uvp(j)*cos(2*alpha_temp)

            IF (ABS(uv_temp) <= 1.0) THEN              ! Finally try
with loose requirement
                uvlambda(j) = uv_temp
                uulambda(j) = uup(j)*(cos(alpha_temp))**2 -
2*uvp(j)*cos(alpha_temp)*sin(alpha_temp) + vvp(j)*(sin(alpha_temp))**2
                vvlambda(j) = uup(j)*(sin(alpha_temp))**2 +
2*uvp(j)*cos(alpha_temp)*sin(alpha_temp) + vvp(j)*(cos(alpha_temp))**2
                alphap(j) = alpha_temp*180/3.14159
                GOTO 120
            END IF

        END DO

120     CONTINUE

    END DO


      ! OUTPUT
      !*****************************************************************
******************


      61 FORMAT (3X, A6, 8X, A6, 8X, A6, 8X, A6, 10X, A6, 8X, A6, 8X,
A6, 8X, A6, 8X, A6, 8X, A6, 8X, A6, 8X, A6, 8X, A6, 8X, A8, 8X, A8, 8X,
A8, 8X, A8, 8X, A8, 8X, A8, 8X, A8, 8X, A8, 8X, A14, 8X, A14, 8X, A14,
8X, A7, 8X, A10, 8X, A21)
      62 FORMAT (1X, E12.6, 2X, I5, 2X, E12.6, 2X, E12.6, 2X, E12.6,
2X, E12.6, 2X, E12.6, 2X, E12.6, 2X, E12.6, 2X, E12.6, 2X, E12.6, 2X,
E12.6, 2X, E12.6, 2X, E12.6, 2X, E12.6, 2X, E12.6, 2X, E12.6, 2X,
E12.6, 2X, E12.6, 2X, E12.6, 2X, E12.6, 2X, E12.6, 2X, E12.6, 2X,
E12.6, 2X, E12.6, 2X, E12.6, 2X, E12.6)

      WRITE(*,*) output

      OPEN(UNIT=m, FILE=output, STATUS='REPLACE')

      WRITE(m,61) "Y", "Yi", "U", "V", "Unorm", "Vnorm", "u'u'",
"v'v'", "u'v'", "dUdX", "dUdY", "dVdX", "dVdY", "txxdudx", "txydudy",
"txydvdx", "tyydvdy", "txydudx", "tyydudy", "txxdvdx", "txydvdy",
"productionxx", "productionyy", "productionxy",
"alpha","num_good","num_good/num_images"
      !WRITE(m,61)

      DO i = 1, num_Y

            WRITE(m,62) Yp(i), Yip(i), Up(i), Vp(i), Unp(i), Vnp(i),
uup(i), vvp(i), uvp(i), dudxp(i), dudyp(i), dvdxp(i), dvdyp(i),
txxdudxp(i), txydudyp(i), txydvdxp(i), tyydvdyp(i), txydudxp(i),
tyydudyp(i), txxdvdxp(i), txydvdyp(i), productionxxp(i),
```

```
productionyyp(i), productionxyp(i), alphap(i), num_goodp(i),
num_good_avgp(i)

      END DO

      m = m+1;

      DEALLOCATE(X,Y,Xi, Yi, U,V,Unorm,Vnorm,uu,vv,uv)              !
Deallocate arrays to allow for multiple profile generations per
execution
      DEALLOCATE(Xp,Yp,Yip,Up,Vp,Unp,Vnp,uup,vvp,uvp,dudxp,dudyp,dvdxp,
dvdyp)
      DEALLOCATE(txxdudxp, txydudyp, txydvdxp, tyydvdyp, txydudxp,
tyydudyp, txxdvdxp, txydvdyp)
      DEALLOCATE(productionxxp, productionyyp, productionxyp)
      DEALLOCATE(alphap, num_goodp, num_good_avgp)

      CLOSE (k)

      END DO ! End of main DO loop

      WRITE(*,*)
      WRITE(*,*)

      WRITE(*,*) 'To continue, press any key, then [ENTER].'
      READ(*,*) end_stop


      END PROGRAM TAMU_PROFILE
```

APPENDIX C

PIV UNCERTAINTY ANALYSIS

Within any experimental research there will be inherent uncertainty within any measurements. The uncertainty analysis derermines the amount of error for each measurement, and the propagation error that results from multiple measurements that are used to determine a particular value. This section will identify and document all measurement and propagation error that exists for all measured values. Based on previous work, the present study uses the Euclidean (L_2) norm as the measure of error[61]. The L_2 norm is defined as[65]

$$\left\|x_i\right\|_2 = \left\|x_1, x_2, ..., x_n\right\|_2 = \left[\sum_{i=1}^{n} x_i^2\right]^{1/2}$$

For a given set of measurements, x_i. The total dimensional error is defined as

$$E_f = \left\|E_{x_i}\right\|_2 = \left[\sum_{i=1}^{n}\left(\frac{\partial f}{\partial x_i} E_{x_i}\right)^2\right]^{1/2}$$

Where f is a function dependent on x_i and E_x is the error associated over the various applicable measurements. The percent of nondimensional error is given by

$$\varepsilon_f = \frac{E_f}{f}$$

Which is the total error nondimensionalized by the mean value. The reduced data error bounds are estimated based on the linearized reduction equations and include

propagation of measurement errors. It has been assumed that all errors are random and have a Gaussian distribution.

There are two distinct areas where errors manifest in particle image velocimetry measurements. The first is experimental error, which include errors during correlation calculations as well as calibration. An example of calibration error is a slight misalignment of laser sheets or error when converting from pixel units to a real dimensional measurement. Each error is conservatively estimated at 1%. The second area is associated with flaws in the data sets. These include variable seed density or voids, laser reflections or seed accumulation on windows; these errors are unavoidable and will be greatest near the wall. These errors produce irregular correlations and are filtered during the correlation calculations. In the present experiment, use of the filter reduced the number of vectors by at most 40% (SPG case closest to the wall). Thus to determine the statistical unvertainty, the lowest extimate was used for the number of valid samples.

A confidence interval determines the level of certainty that the true mean lies within an error intercal from the calculated statistic. For normal distributions a 2 standard deviation or a 95% confidence interval is typical. For a 95% confidence interval, a given statistic will have the following error bound[66]: $\pm 1.96\sqrt{\mathrm{var}(x)}$. The error is calculated using the sample size according to the number of image pairs recorded, taking into account any vectors lost due to filtering. Estimated uncertainties are tabulated in Table C-1.

Table C-1: Quantity Uncertanties

Variable	Error
x, y	0.5 mm
$\bar{u}$	1.0 %
$\sqrt{\overline{u'^2}}$	5.0 %
$\sqrt{\overline{v'^2}}$	5.0 %
$\overline{u'v'}$	20.0 %

APPENDIX D

ADDITIONAL DATA PLOTS

Turbulent Stress Production Component Profile Plots 282

Reynolds Stress Quadrant Decomposition Plots (Global) ... 290

Turbulent Stress Production Component Profile Plots

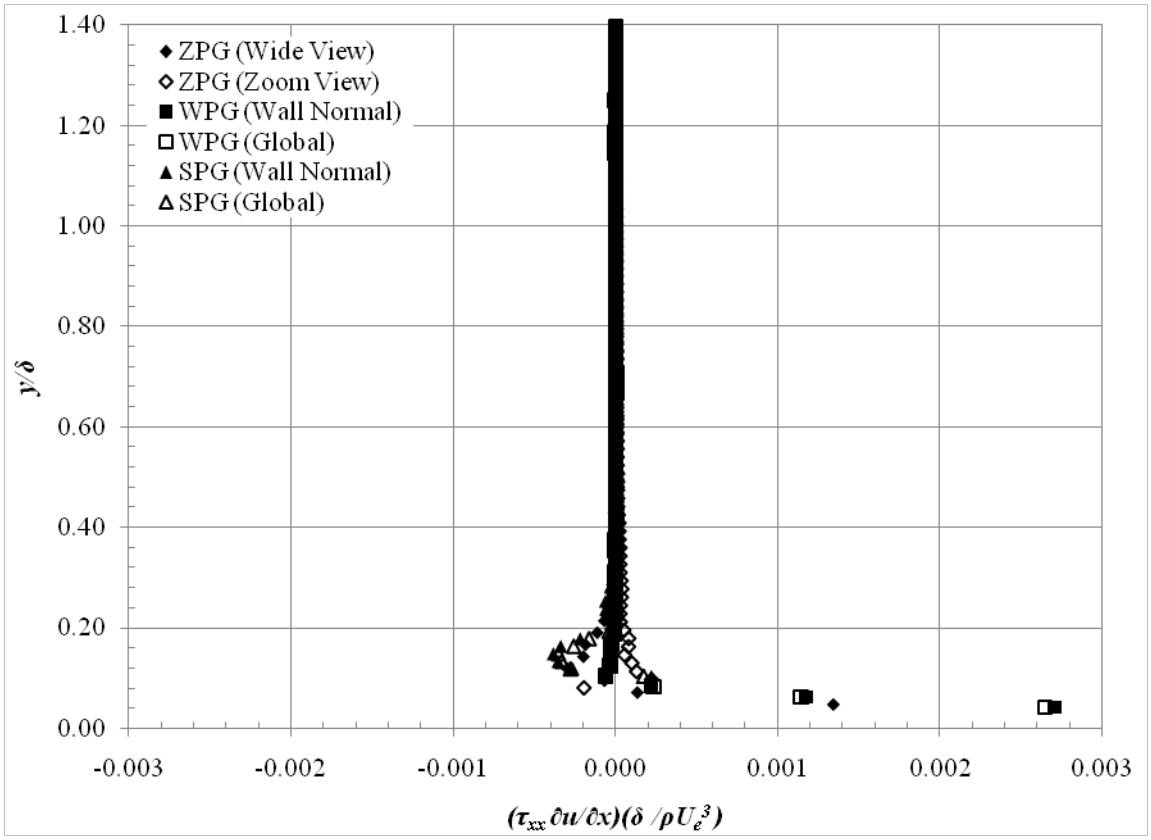

Figure D-1: Axial Turbulent Stress Production Component, ($\tau_{xx}\ \partial u/\partial x$) Profiles

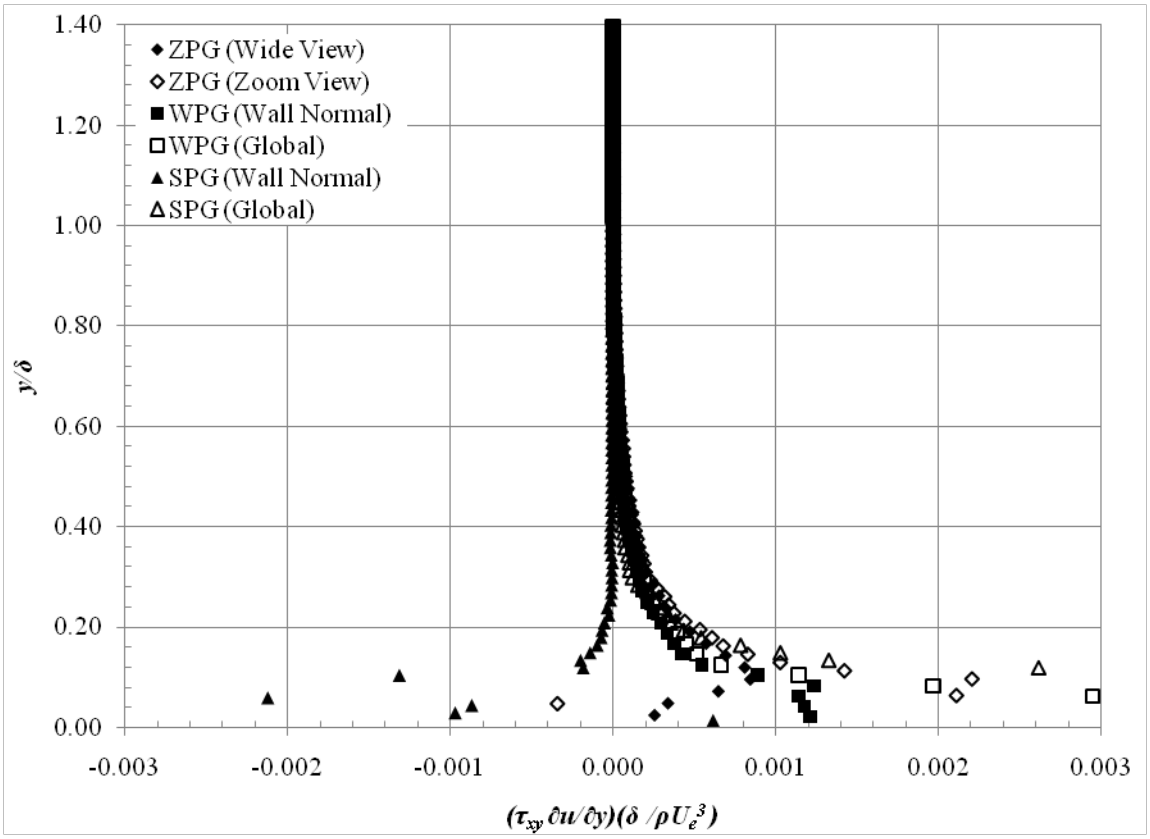

Figure D-2: Axial Turbulent Stress Production Component, (τ_{xy} ∂u/∂y) Profiles

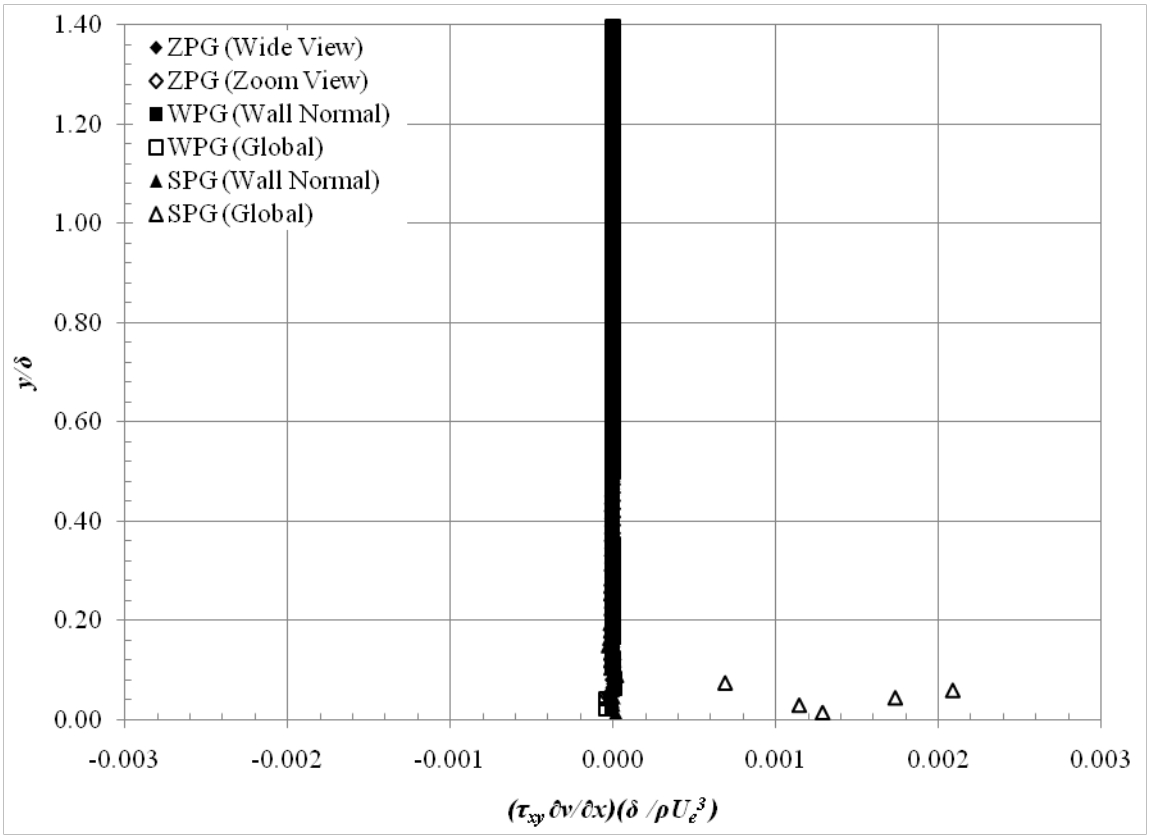

Figure D-3: Axial Turbulent Stress Production Component, (τ_{xy} ∂v/∂x) Profiles

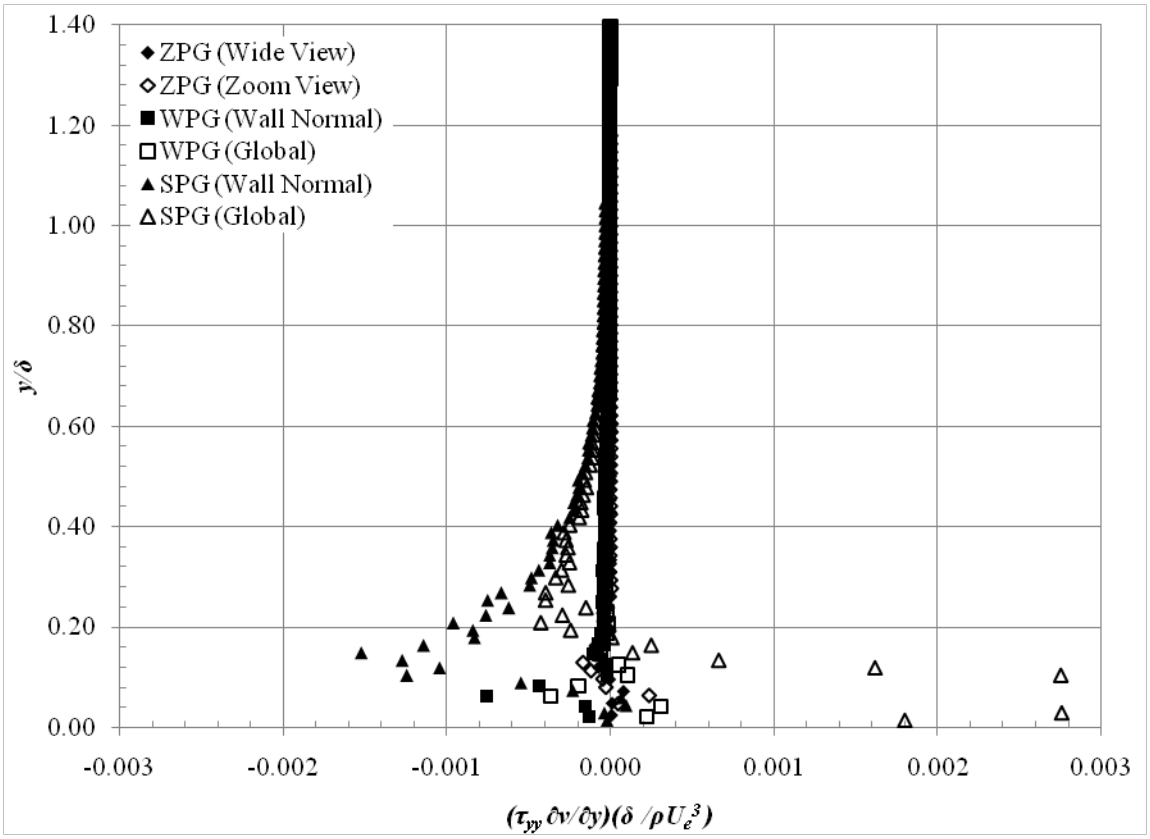

Figure D-4: Axial Turbulent Stress Production Component, (τ_{yy} ∂v/∂y) Profiles

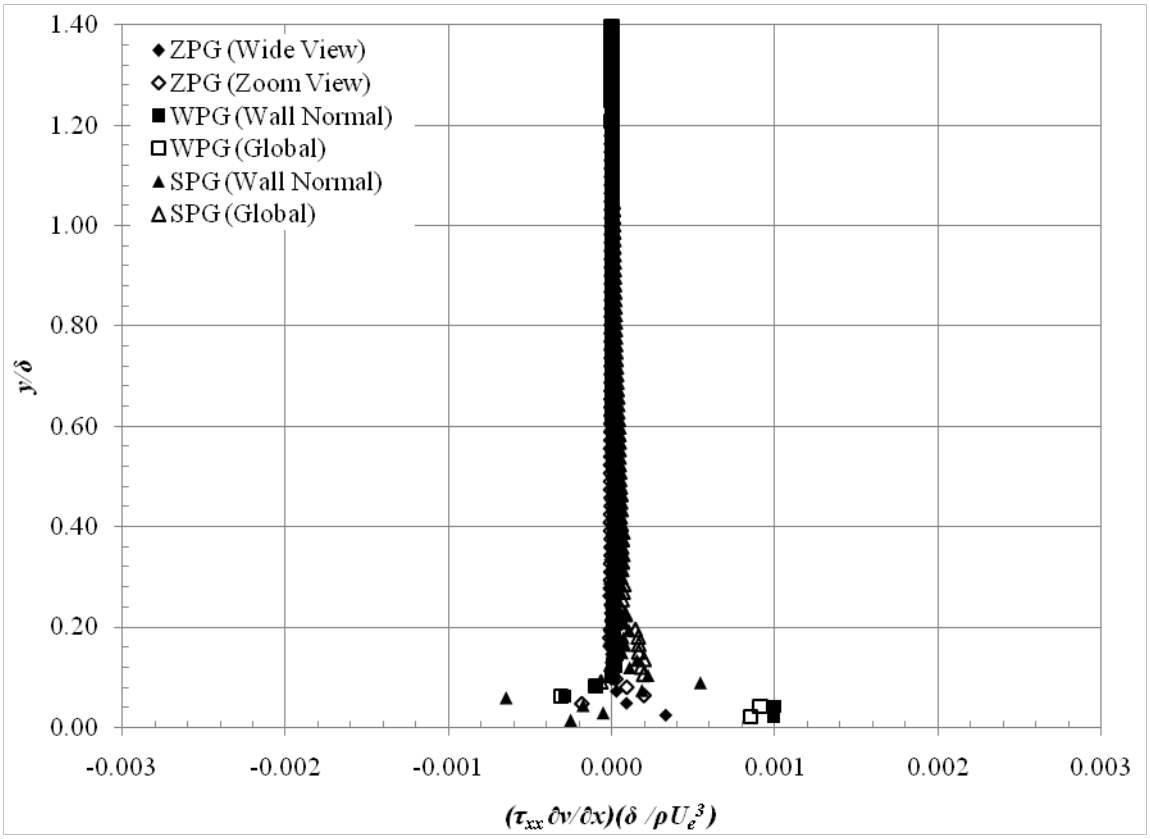

Figure D-5: Axial Turbulent Stress Production Component, (τ_{xx} ∂v/∂x) Profiles

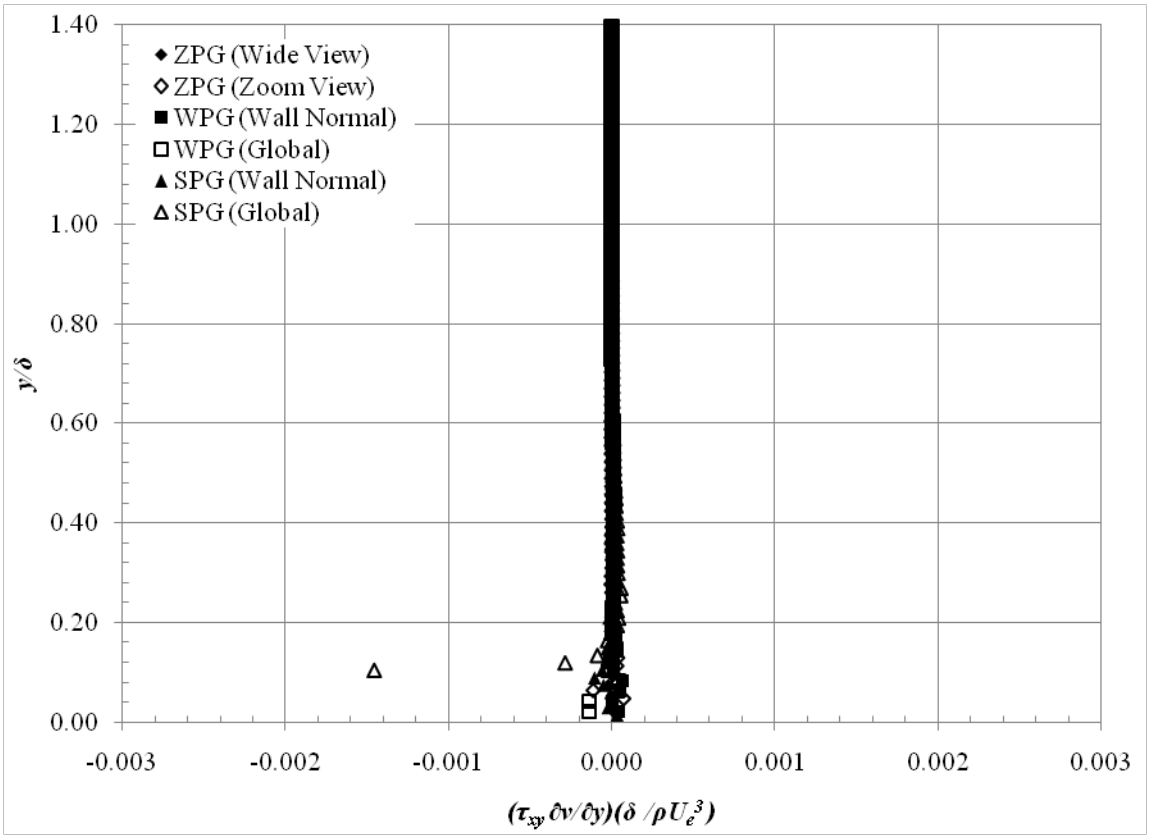

Figure D-6: Axial Turbulent Stress Production Component, ($\tau_{xy}\,\partial v/\partial y$) Profiles

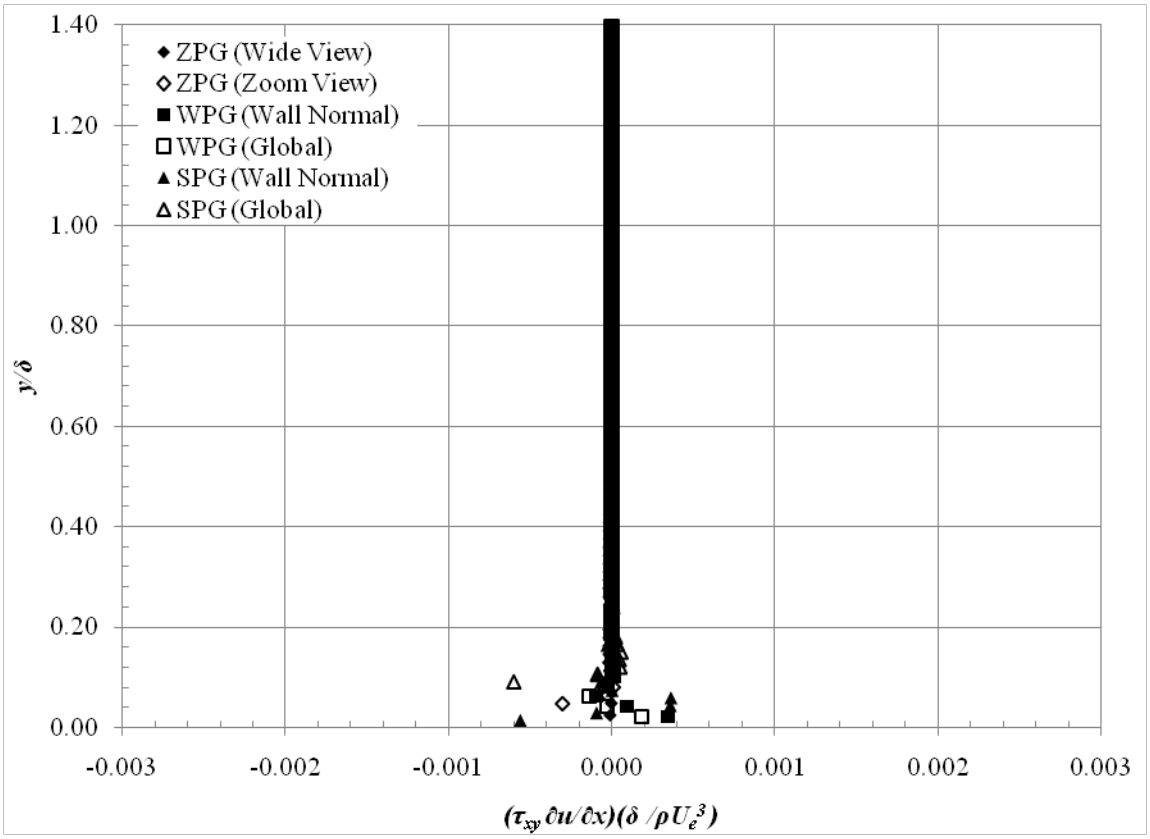

Figure D-7: Axial Turbulent Stress Production Component, (τ_{xx} ∂u/∂x) Profiles

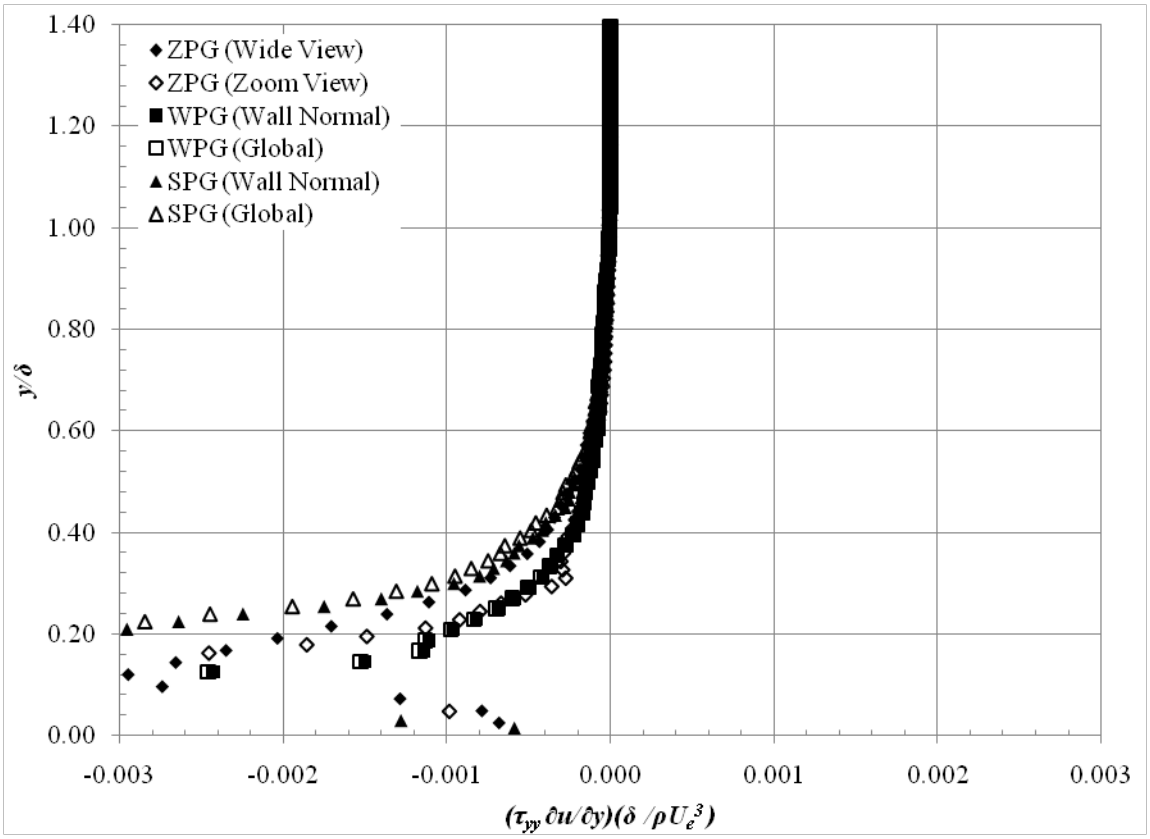

Figure D-8: Axial Turbulent Stress Production Component, ($\tau_{xx}\ \partial u/\partial x$) Profiles

Reynolds Stress Quadrant Decomposition Plots (Global)

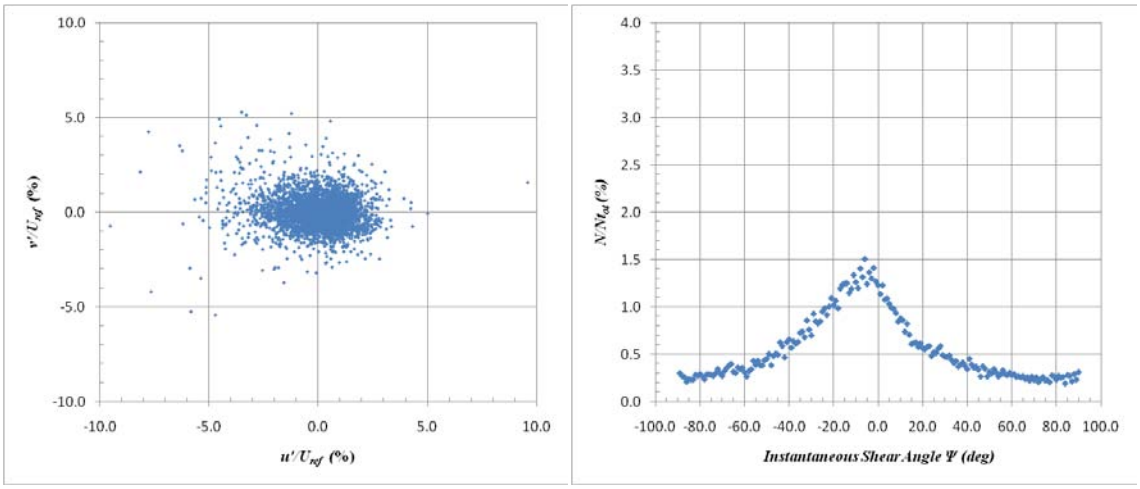

Figure D-9: WPG Quadrant Decomposition at y/δ_{ref} =1.4 at 2nd Measurement Location (Global System)

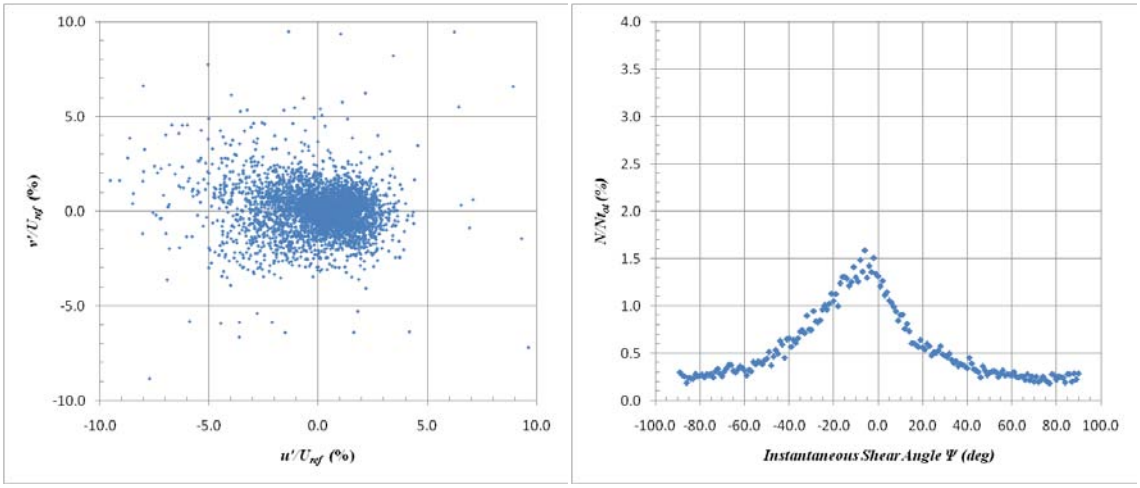

Figure D-10: WPG Quadrant Decomposition at y/δ_{ref} =1.2 at 2nd Measurement Location (Global System)

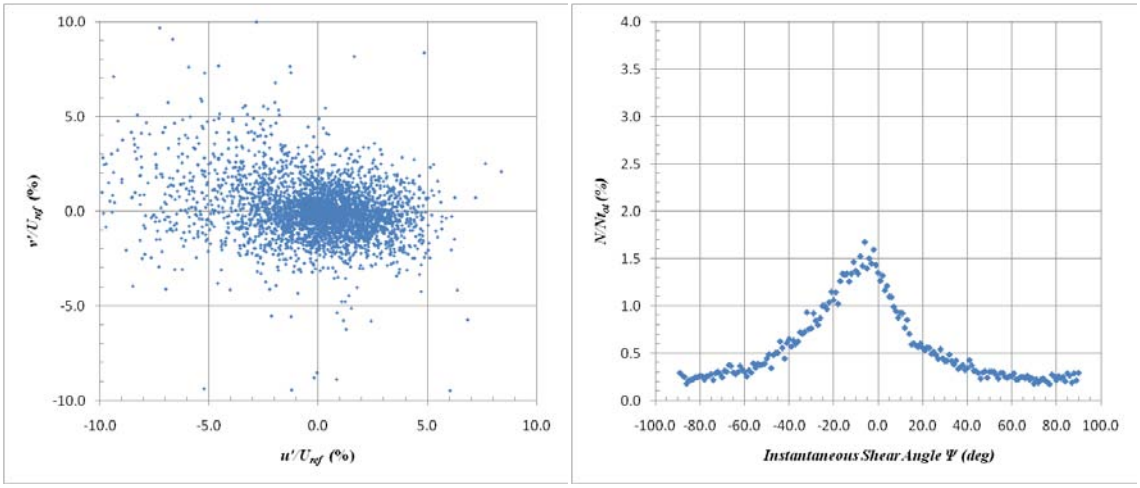

Figure D-11: WPG Quadrant Decomposition at y/δ_{ref} =1.0 at 2nd Measurement Location (Global System)

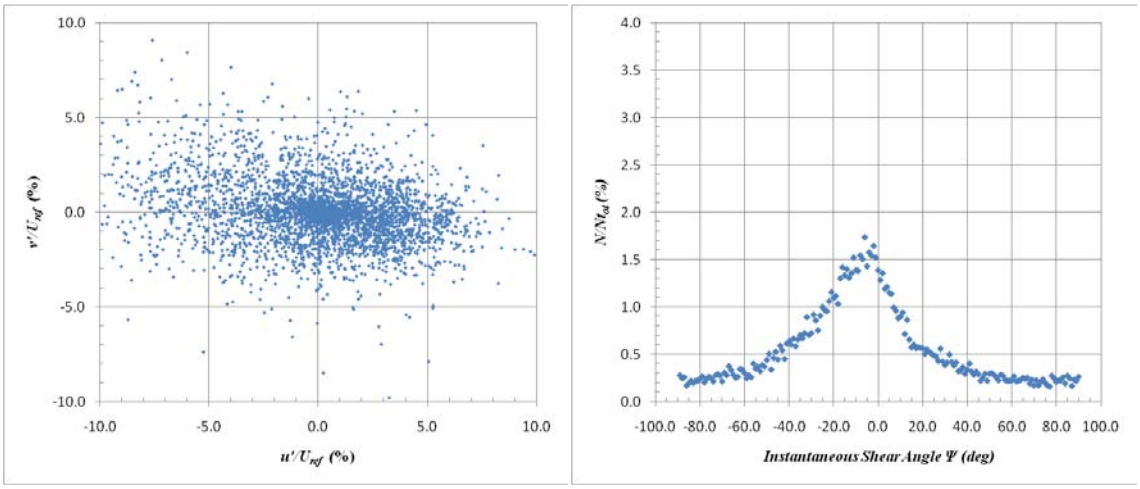

Figure D-12: WPG Quadrant Decomposition at y/δ_{ref} =0.8 at 2nd Measurement Location (Global System)

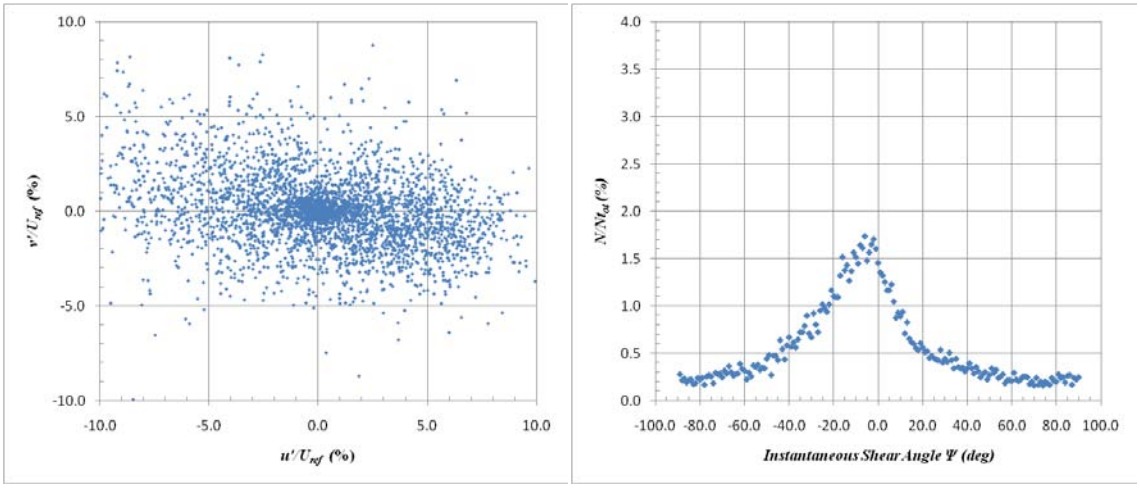

Figure D-13: WPG Quadrant Decomposition at y/δ_{ref} =0.6 at 2nd Measurement Location (Global System)

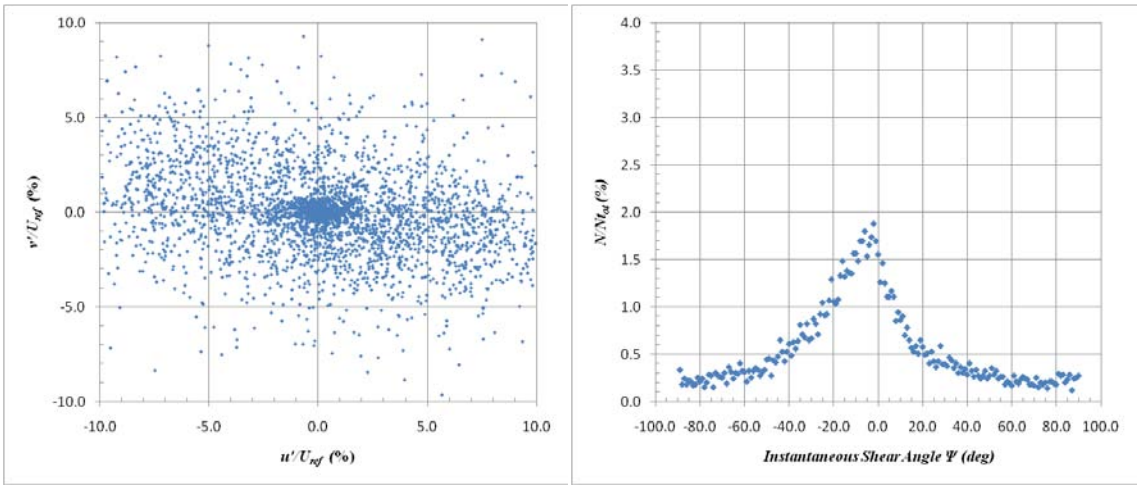

Figure D-14: WPG Quadrant Decomposition at y/δ_{ref} =0.4 at 2nd Measurement Location (Global System)

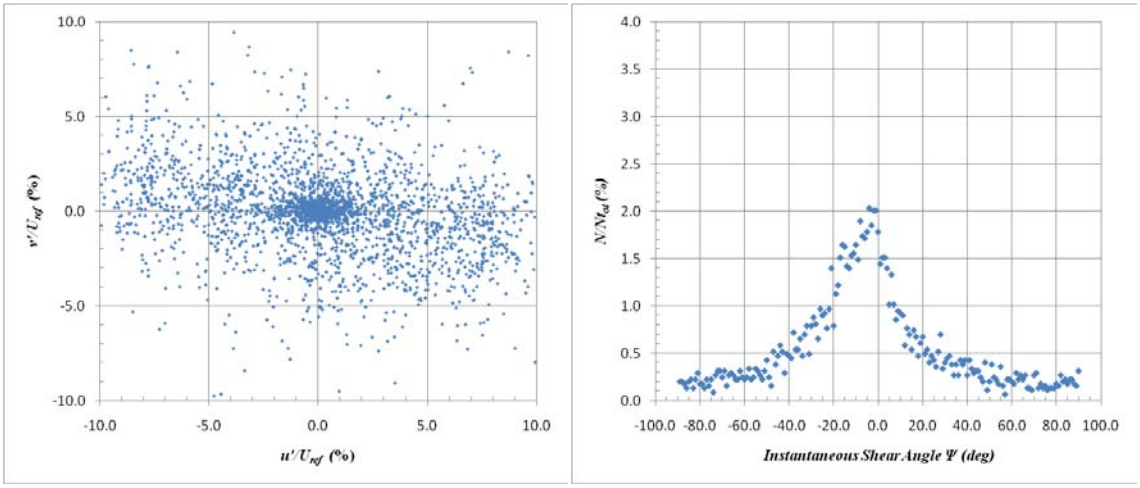

Figure D-15: WPG Quadrant Decomposition at y/δ_{ref} =0.2 at 2nd Measurement Location (Global System)

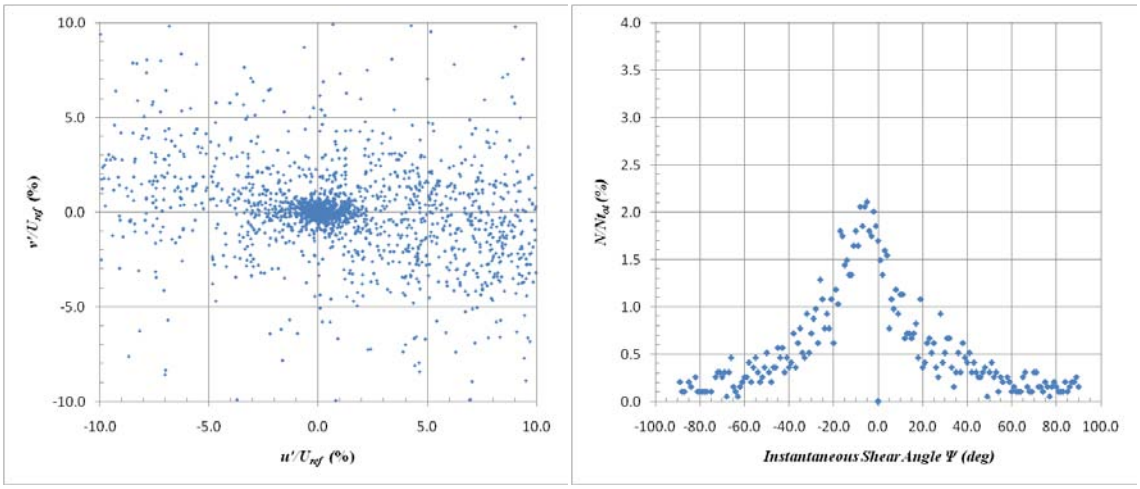

Figure D-16: WPG Quadrant Decomposition at y/δ_{ref} =0.1 at 2nd Measurement Location (Global System)

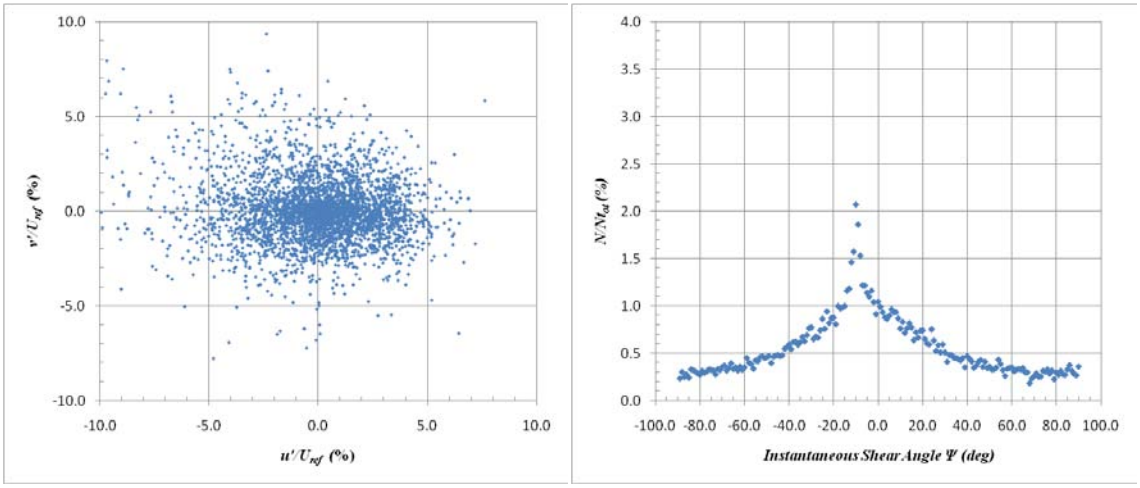

Figure D-17: SPG Quadrant Decomposition at y/δ_{ref} =1.4 at 2nd Measurement Location (Global System)

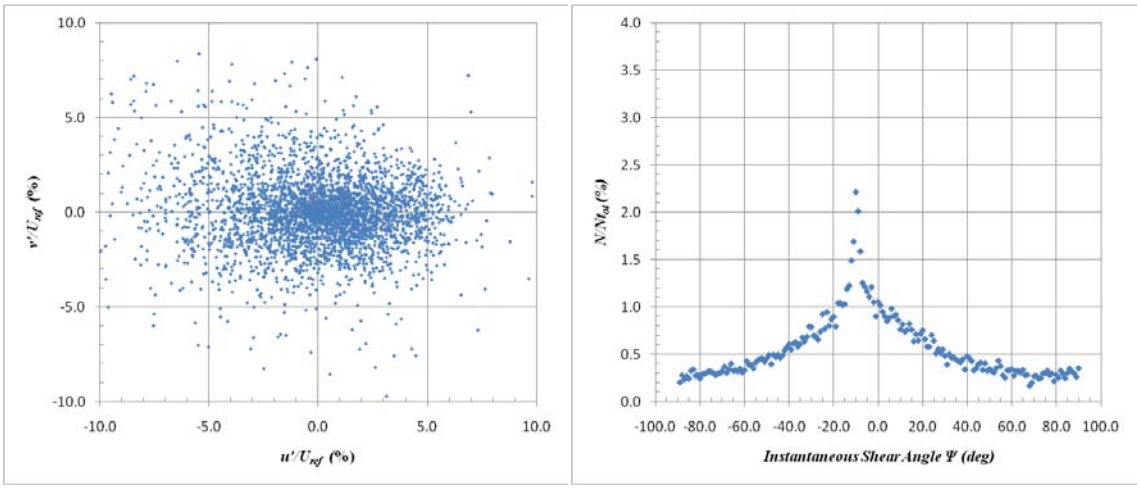

Figure D-18: SPG Quadrant Decomposition at y/δ_{ref} =1.2 at 2nd Measurement Location (Global System)

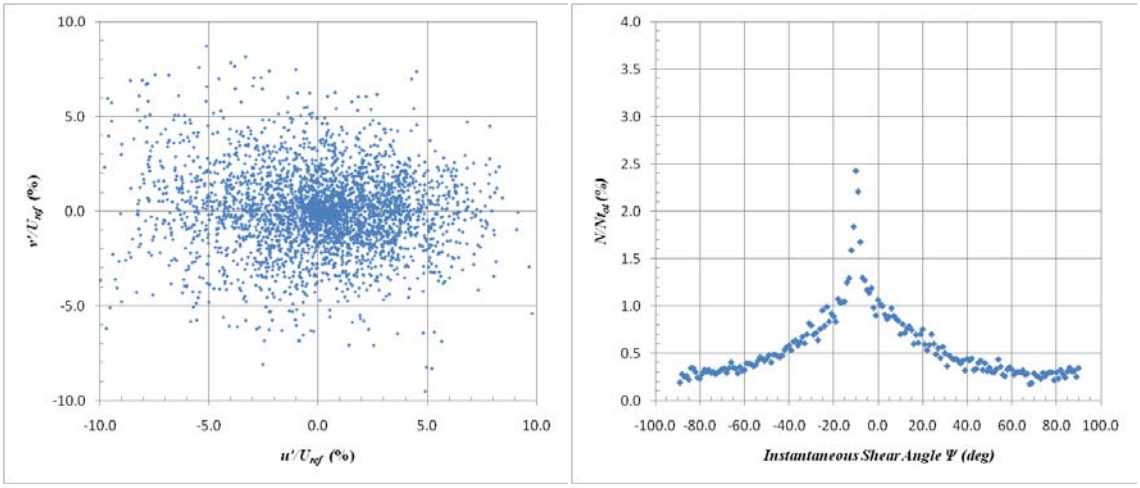

Figure D-19: SPG Quadrant Decomposition at y/δ_{ref} =1.0 at 2nd Measurement Location (Global System)

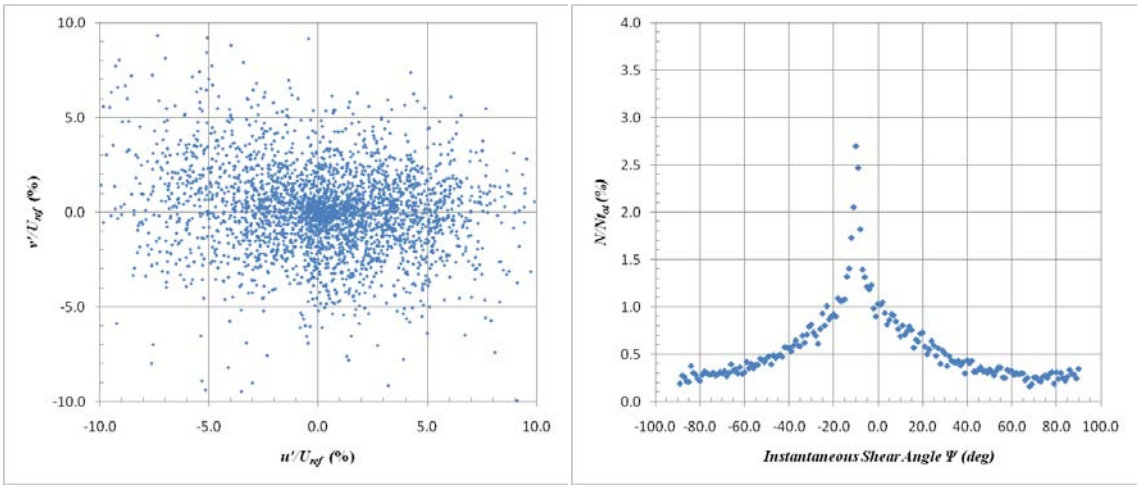

Figure D-20: SPG Quadrant Decomposition at y/δ_{ref} =0.8 at 2nd Measurement Location (Global System)

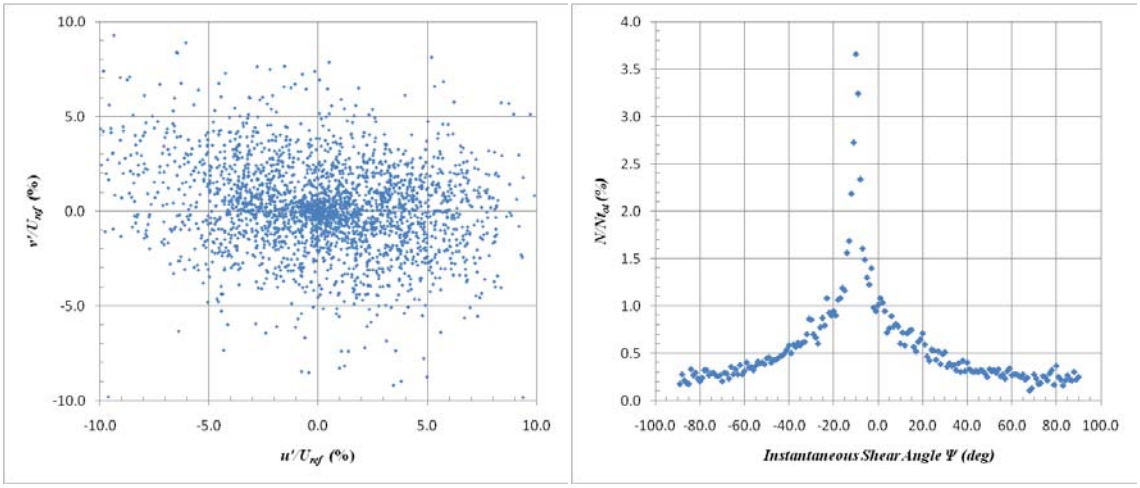

Figure D-21: SPG Quadrant Decomposition at y/δ_{ref} =0.6 at 2nd Measurement Location (Global System)

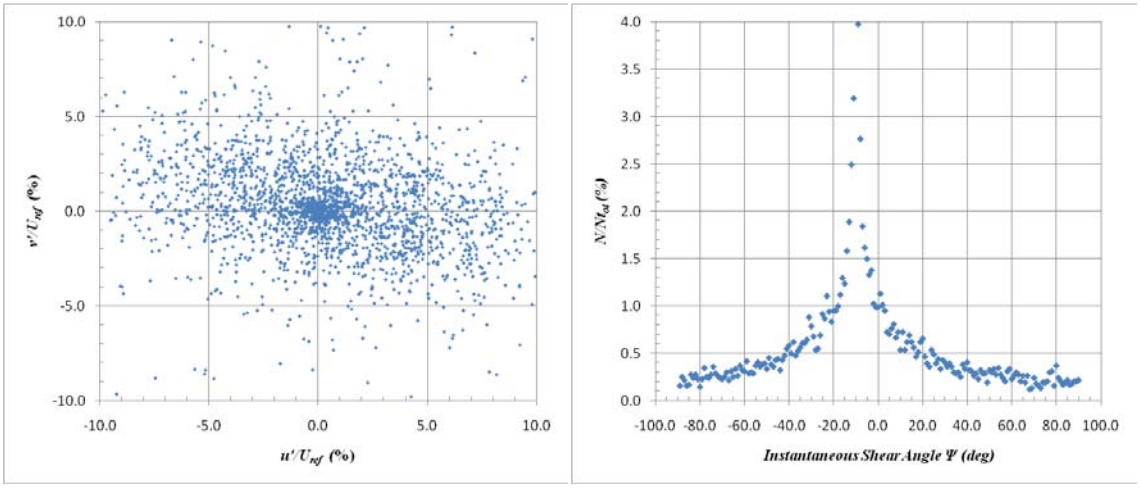

Figure D-22: SPG Quadrant Decomposition at y/δ_{ref} =0.4 at 2nd Measurement Location (Global System)

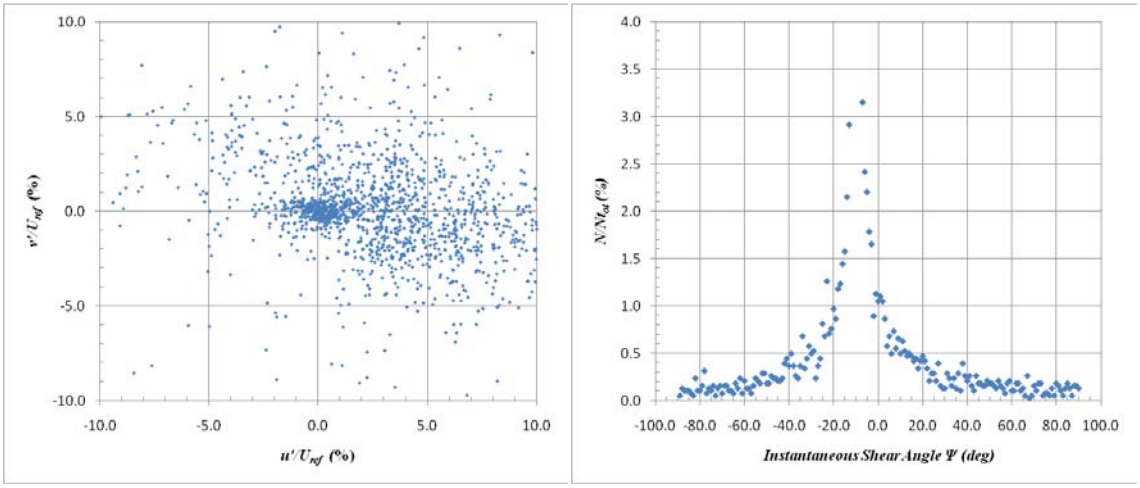

Figure D-23: SPG Quadrant Decomposition at y/δ_{ref} =0.2 at 2nd Measurement Location (Global System)

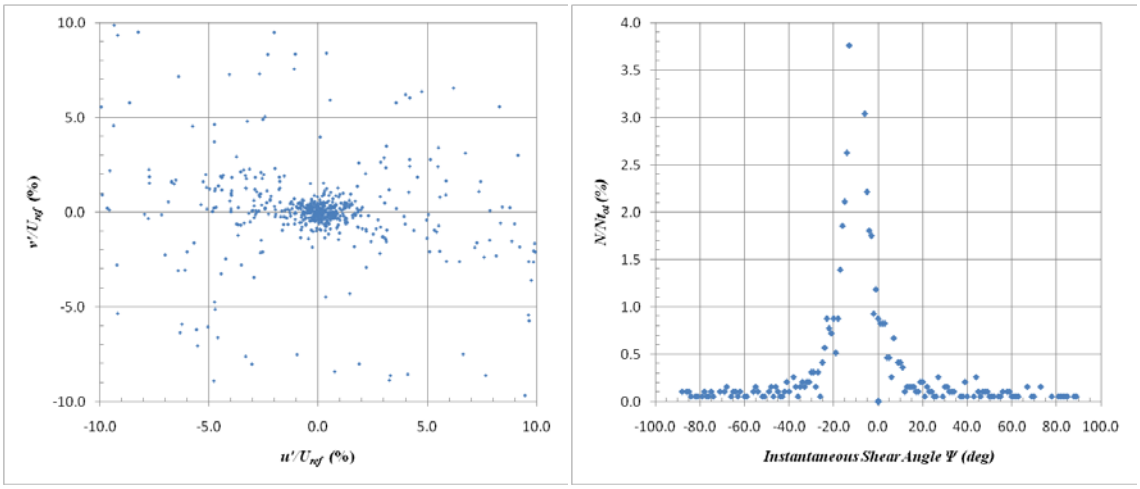

Figure D-24: SPG Quadrant Decomposition at y/δ_{ref} =0.1 at 2nd Measurement Location (Global System)

APPENDIX E

TABULATED PROFILE DATA

TABLE		Page
E-1	ZPG (Wide View)	299
E-2	ZPG (Zoom View)	301
E-3	WPG (Wall Normal Coordinates)	303
E-4	WPG (Global Coordinates)	305
E-5	SPG (Wall Normal Coordinates)	307
E-6	SPG (Global Coordinates)	309

Table E-1: ZPG (Wide View)

$\frac{y}{\delta}$	$\frac{U}{U_e}$	$\frac{\sqrt{\overline{u'^2}}}{U_e}$	$\frac{\sqrt{\overline{v'^2}}}{U_e}$	$\frac{\overline{u'v'}}{U_e^2}$	$\frac{d\bar{u}}{dx}\cdot\frac{\delta}{U_e}$	$\frac{d\bar{u}}{dy}\cdot\frac{\delta}{U_e}$	$\frac{d\bar{v}}{dx}\cdot\frac{\delta}{U_e}$	$\frac{d\bar{v}}{dy}\cdot\frac{\delta}{U_e}$	$P_{xx}\cdot\frac{\delta}{U_e^3}$	$P_{yy}\cdot\frac{\delta}{U_e^3}$	$P_{xy}\cdot\frac{\delta}{U_e^3}$	α
1.67	1.00	1.2E-02	1.0E-02	5.2E-06	-2.2E-04	3.0E-03	-1.4E-03	-3.0E-03	-2.9E-07	1.1E-06	-1.5E-08	7.6
1.64	1.00	1.1E-02	1.1E-02	3.1E-06	-3.2E-04	3.0E-03	-4.3E-04	-3.0E-03	-1.3E-07	-1.5E-07	3.9E-07	52.1
1.62	1.00	1.1E-02	1.2E-02	6.5E-06	-2.6E-04	8.9E-04	-3.5E-04	1.6E-03	-1.3E-07	5.8E-07	5.2E-08	56.8
1.59	1.00	1.1E-02	1.2E-02	5.3E-06	-2.9E-04	-1.1E-03	-9.4E-05	1.3E-03	-1.4E-07	8.5E-08	-1.5E-07	72.4
1.57	1.00	1.2E-02	1.2E-02	6.3E-06	-3.7E-04	-4.9E-04	7.9E-05	6.7E-05	-1.6E-07	-4.3E-07	6.0E-08	68.9
1.55	1.00	1.2E-02	1.2E-02	3.1E-06	-3.5E-04	3.0E-04	-3.2E-05	-8.2E-04	-1.1E-07	-3.1E-07	1.9E-08	77.1
1.52	1.00	1.2E-02	1.2E-02	3.0E-06	-5.2E-04	1.5E-04	2.1E-04	-6.1E-05	-2.2E-07	2.0E-07	1.0E-07	80.6
1.50	1.00	1.2E-02	1.3E-02	5.9E-06	-4.9E-04	2.4E-04	3.5E-04	7.1E-04	-1.6E-07	8.7E-07	1.5E-07	80.1
1.48	1.00	1.2E-02	1.3E-02	6.3E-06	-2.6E-04	-1.5E-04	-3.1E-05	1.1E-03	-9.0E-08	9.4E-07	-9.1E-09	79.1
1.45	1.00	1.2E-02	1.2E-02	5.6E-06	-1.8E-04	-8.5E-04	1.0E-04	2.3E-03	-7.2E-08	1.0E-06	-3.1E-07	73.2
1.43	1.00	1.1E-02	1.2E-02	5.9E-06	-2.0E-04	-4.8E-04	8.8E-05	1.5E-03	-1.4E-07	7.0E-07	-2.5E-07	75.2
1.40	1.00	1.1E-02	1.2E-02	3.5E-06	-2.7E-04	-2.2E-04	2.3E-04	-7.0E-04	-9.4E-08	-2.6E-07	-2.0E-07	67.8
1.38	1.00	1.1E-02	1.1E-02	3.1E-06	-3.6E-04	-6.9E-04	2.0E-04	-1.5E-03	-1.6E-07	-6.7E-07	-1.5E-07	66.4
1.36	1.00	1.1E-02	1.1E-02	1.5E-06	-6.1E-04	-1.1E-03	-2.2E-04	-5.3E-04	-2.3E-07	-1.9E-07	-1.8E-07	50.0
1.33	1.00	1.1E-02	1.1E-02	6.4E-07	-6.0E-04	-2.1E-04	2.7E-05	-9.5E-04	-1.8E-07	9.7E-08	-9.7E-09	85.1
1.31	1.00	1.1E-02	1.1E-02	3.6E-06	-4.4E-04	1.1E-03	1.0E-04	6.5E-05	-1.4E-07	7.3E-08	2.3E-07	57.0
1.29	1.00	1.1E-02	1.1E-02	2.4E-06	-4.7E-04	1.4E-03	2.6E-04	1.8E-03	-2.0E-07	3.2E-07	1.4E-07	38.6
1.26	1.00	1.1E-02	1.0E-02	3.1E-06	-3.9E-04	2.5E-03	3.5E-04	2.0E-03	-1.2E-07	3.6E-07	2.1E-07	16.7
1.24	1.00	1.1E-02	1.0E-02	5.0E-06	-3.7E-04	4.1E-03	4.6E-04	1.0E-03	-1.5E-07	1.0E-07	4.9E-07	27.3
1.21	1.00	1.1E-02	1.1E-02	4.7E-06	-4.4E-04	4.6E-03	2.2E-04	6.3E-04	-1.5E-07	-4.4E-08	6.3E-07	66.2
1.19	1.00	1.1E-02	1.1E-02	6.9E-06	-5.9E-04	5.9E-03	-4.5E-04	1.8E-03	-2.5E-07	5.8E-07	6.0E-07	47.6
1.17	1.00	1.1E-02	1.1E-02	5.9E-06	-5.1E-04	8.6E-03	-2.0E-05	1.9E-03	-2.5E-07	8.5E-07	9.2E-07	31.0
1.14	1.00	1.1E-02	1.1E-02	8.0E-06	-2.7E-04	1.2E-02	1.4E-04	3.5E-03	-2.6E-07	1.2E-06	1.5E-06	39.2
1.12	1.00	1.2E-02	1.1E-02	8.9E-06	-3.8E-04	1.5E-02	2.7E-04	3.3E-03	-3.6E-07	7.9E-07	1.9E-06	30.3
1.10	1.00	1.2E-02	1.2E-02	1.3E-05	-6.4E-04	1.9E-02	1.5E-04	1.7E-03	-7.2E-07	3.6E-07	2.6E-06	36.4
1.07	1.00	1.3E-02	1.2E-02	1.9E-05	-7.0E-04	2.5E-02	2.3E-05	1.8E-03	-1.2E-06	4.0E-07	3.7E-06	42.3
1.05	1.00	1.3E-02	1.3E-02	1.9E-05	-4.7E-04	3.0E-02	5.6E-04	3.0E-03	-1.3E-06	9.3E-07	4.7E-06	37.6
1.02	1.00	1.4E-02	1.3E-02	2.4E-05	-8.1E-04	3.9E-02	6.6E-04	3.6E-03	-2.2E-06	1.9E-06	6.0E-06	31.6
1.00	1.00	1.4E-02	1.3E-02	3.0E-05	-7.5E-04	4.7E-02	7.5E-04	1.5E-03	-3.2E-06	1.2E-06	7.9E-06	28.8
0.98	0.99	1.5E-02	1.3E-02	3.3E-05	-1.1E-03	5.5E-02	1.1E-03	1.5E-03	-4.2E-06	8.4E-07	9.6E-06	25.8
0.95	0.99	1.6E-02	1.4E-02	3.9E-05	-8.0E-04	6.5E-02	1.1E-03	3.0E-03	-5.5E-06	1.6E-06	1.2E-05	24.1
0.93	0.99	1.7E-02	1.4E-02	4.7E-05	-8.4E-04	7.2E-02	1.3E-03	3.8E-03	-7.5E-06	2.4E-06	1.5E-05	23.5
0.90	0.99	1.8E-02	1.5E-02	5.6E-05	-4.4E-04	8.1E-02	1.6E-03	2.2E-03	-9.5E-06	1.5E-06	1.9E-05	23.0
0.88	0.99	1.9E-02	1.6E-02	6.0E-05	-3.8E-04	9.3E-02	1.6E-03	1.2E-03	-1.2E-05	4.4E-07	2.4E-05	21.6
0.86	0.98	2.1E-02	1.6E-02	7.2E-05	-5.5E-04	1.0E-01	1.8E-03	9.0E-04	-1.5E-05	-1.1E-08	2.7E-05	20.7
0.83	0.98	2.2E-02	1.7E-02	8.7E-05	-2.4E-04	1.1E-01	1.5E-03	1.3E-03	-2.0E-05	3.5E-07	3.3E-05	21.8
0.81	0.98	2.3E-02	1.8E-02	9.7E-05	-8.4E-04	1.3E-01	1.8E-03	7.8E-04	-2.5E-05	4.7E-07	4.1E-05	21.6
0.79	0.98	2.5E-02	1.9E-02	1.1E-04	-1.2E-03	1.3E-01	2.0E-03	9.4E-04	-3.1E-05	2.9E-07	4.6E-05	20.5
0.76	0.97	2.6E-02	1.9E-02	1.3E-04	-1.6E-03	1.4E-01	1.2E-03	4.1E-03	-3.7E-05	3.0E-06	4.9E-05	19.9
0.74	0.97	2.7E-02	1.9E-02	1.4E-04	-1.7E-03	1.5E-01	1.6E-03	3.4E-03	-4.3E-05	1.5E-06	5.7E-05	18.8
0.71	0.97	2.8E-02	2.0E-02	1.5E-04	-1.2E-03	1.6E-01	2.0E-03	2.8E-03	-5.0E-05	1.6E-06	6.5E-05	19.1

$\frac{y}{\delta}$	$\frac{U}{U_e}$	$\frac{\sqrt{\overline{u'^2}}}{U_e}$	$\frac{\sqrt{\overline{v'^2}}}{U_e}$	$\frac{\overline{u'v'}}{U_e^2}$	$\frac{d\bar{u}}{dx}\cdot\frac{\delta}{U_e}$	$\frac{d\bar{u}}{dy}\cdot\frac{\delta}{U_e}$	$\frac{d\bar{v}}{dx}\cdot\frac{\delta}{U_e}$	$\frac{d\bar{v}}{dy}\cdot\frac{\delta}{U_e}$	$P_{xx}\cdot\frac{\delta}{U_e^3}$	$P_{yy}\cdot\frac{\delta}{U_e^3}$	$P_{xy}\cdot\frac{\delta}{U_e^3}$	α
0.69	0.96	3.0E-02	2.1E-02	1.7E-04	-1.5E-03	1.6E-01	2.1E-03	2.3E-03	-5.8E-05	1.8E-06	7.6E-05	19.5
0.67	0.96	3.1E-02	2.2E-02	1.9E-04	-2.1E-03	1.7E-01	1.5E-03	2.8E-03	-6.8E-05	2.0E-06	8.3E-05	19.6
0.64	0.95	3.2E-02	2.3E-02	2.1E-04	-1.5E-03	1.8E-01	1.6E-03	4.4E-03	-7.6E-05	3.3E-06	9.6E-05	19.6
0.62	0.95	3.4E-02	2.4E-02	2.3E-04	-1.2E-03	2.0E-01	1.2E-03	1.3E-03	-9.1E-05	-1.4E-06	1.1E-04	19.4
0.60	0.95	3.5E-02	2.5E-02	2.5E-04	-2.2E-03	2.1E-01	1.3E-03	-7.9E-05	-1.1E-04	-1.3E-07	1.3E-04	19.8
0.57	0.94	3.7E-02	2.7E-02	2.7E-04	-2.3E-03	2.1E-01	1.8E-03	2.8E-03	-1.2E-04	5.3E-06	1.5E-04	19.6
0.55	0.94	3.9E-02	2.7E-02	2.8E-04	-1.9E-03	2.2E-01	1.5E-03	6.2E-03	-1.3E-04	8.1E-06	1.6E-04	18.3
0.52	0.93	4.1E-02	2.8E-02	3.1E-04	-2.0E-03	2.3E-01	1.2E-03	3.5E-03	-1.5E-04	-8.3E-07	1.9E-04	18.1
0.50	0.92	4.3E-02	3.0E-02	3.4E-04	-1.5E-03	2.5E-01	4.7E-04	1.3E-03	-1.8E-04	-2.4E-06	2.3E-04	18.8
0.48	0.92	4.5E-02	3.2E-02	3.8E-04	-2.5E-04	2.6E-01	3.2E-04	3.8E-03	-1.9E-04	1.1E-05	2.6E-04	18.7
0.45	0.91	4.7E-02	3.4E-02	4.2E-04	3.9E-04	2.7E-01	8.8E-04	1.5E-03	-2.2E-04	1.9E-06	3.0E-04	19.0
0.43	0.91	5.0E-02	3.5E-02	4.4E-04	1.1E-03	2.8E-01	1.8E-04	9.4E-04	-2.4E-04	-3.2E-06	3.4E-04	18.0
0.40	0.90	5.2E-02	3.7E-02	4.8E-04	3.0E-05	2.9E-01	6.6E-04	4.0E-03	-2.6E-04	1.3E-05	3.8E-04	18.0
0.38	0.89	5.4E-02	3.8E-02	5.0E-04	-1.3E-03	3.0E-01	8.6E-04	5.7E-03	-2.9E-04	1.5E-05	4.3E-04	17.3
0.36	0.88	5.6E-02	4.0E-02	5.2E-04	-1.9E-03	3.2E-01	1.2E-03	4.5E-03	-3.3E-04	1.1E-05	5.1E-04	16.7
0.33	0.88	5.9E-02	4.2E-02	5.5E-04	-1.7E-03	3.4E-01	2.0E-03	2.5E-04	-3.7E-04	-7.3E-06	6.2E-04	15.9
0.31	0.87	6.3E-02	4.4E-02	5.7E-04	-8.4E-04	3.6E-01	1.4E-03	5.3E-04	-4.0E-04	-1.7E-06	7.4E-04	15.1
0.29	0.86	6.6E-02	4.6E-02	6.3E-04	4.4E-04	4.0E-01	2.1E-03	6.1E-03	-4.6E-04	2.1E-05	8.9E-04	14.6
0.26	0.85	7.0E-02	4.9E-02	6.4E-04	3.5E-04	4.4E-01	2.2E-03	8.1E-03	-5.5E-04	2.0E-05	1.1E-03	13.5
0.24	0.84	7.5E-02	5.2E-02	6.6E-04	2.4E-03	4.9E-01	5.6E-04	3.1E-03	-5.9E-04	2.0E-05	1.4E-03	12.3
0.21	0.83	8.0E-02	5.5E-02	6.9E-04	5.1E-03	5.6E-01	7.7E-04	1.4E-03	-6.3E-04	2.4E-05	1.7E-03	11.3
0.19	0.81	8.4E-02	5.7E-02	7.7E-04	7.7E-03	6.2E-01	8.7E-04	6.3E-03	-7.2E-04	6.1E-07	2.0E-03	11.1
0.17	0.80	8.7E-02	5.8E-02	8.0E-04	1.0E-02	7.1E-01	7.4E-04	1.3E-02	-7.7E-04	5.7E-05	2.3E-03	10.4
0.14	0.78	9.3E-02	5.7E-02	8.1E-04	7.7E-03	8.5E-01	-4.0E-04	1.9E-02	-9.8E-04	1.1E-04	2.6E-03	8.4
0.12	0.76	1.0E-01	5.4E-02	7.4E-04	9.7E-03	1.1E+00	-1.2E-03	2.6E-02	-1.0E-03	1.5E-04	2.9E-03	5.8
0.10	0.73	1.2E-01	4.9E-02	6.4E-04	-7.4E-04	1.3E+00	-2.3E-04	5.6E-03	-1.5E-03	8.2E-06	2.7E-03	3.0

Table E-2: ZPG (Zoom View)

$\frac{y}{\delta}$	$\frac{U}{U_e}$	$\frac{\sqrt{\overline{u'^2}}}{U_e}$	$\frac{\sqrt{\overline{v'^2}}}{U_e}$	$\frac{\overline{u'v'}}{U_e^2}$	$\frac{d\bar{u}}{dx}\cdot\frac{\delta}{U_e}$	$\frac{d\bar{u}}{dy}\cdot\frac{\delta}{U_e}$	$\frac{d\bar{v}}{dx}\cdot\frac{\delta}{U_e}$	$\frac{d\bar{v}}{dy}\cdot\frac{\delta}{U_e}$	$P_{xx}\cdot\frac{\delta}{U_e^3}$	$P_{yy}\cdot\frac{\delta}{U_e^3}$	$P_{xy}\cdot\frac{\delta}{U_e^3}$	α
1.18	1.00	9.4E-03	7.3E-03	5.7E-06	-5.0E-03	4.8E-03	-1.0E-03	2.3E-03	-9.5E-07	4.7E-07	1.9E-07	9.0
1.16	1.00	1.0E-02	7.5E-03	7.1E-06	-5.1E-03	4.8E-03	-2.4E-04	2.3E-03	-1.1E-06	2.1E-07	2.6E-07	8.5
1.15	1.00	1.1E-02	8.0E-03	8.8E-06	-4.6E-03	1.5E-02	-5.6E-04	-7.6E-04	-1.3E-06	-3.3E-08	9.9E-07	9.9
1.13	1.00	1.1E-02	8.1E-03	9.5E-06	-4.6E-03	1.8E-02	-4.3E-04	-6.0E-04	-1.4E-06	-1.3E-07	1.2E-06	10.2
1.11	1.00	1.1E-02	8.4E-03	1.1E-05	-4.9E-03	2.3E-02	-2.0E-04	-1.4E-03	-1.7E-06	-2.3E-07	1.7E-06	11.3
1.10	1.00	1.2E-02	8.8E-03	1.3E-05	-4.9E-03	2.6E-02	-5.9E-04	3.8E-04	-2.0E-06	7.6E-08	2.0E-06	12.6
1.08	1.00	1.2E-02	9.2E-03	1.4E-05	-5.1E-03	3.2E-02	-9.1E-04	1.2E-03	-2.4E-06	2.5E-07	2.6E-06	12.9
1.06	1.00	1.2E-02	9.5E-03	1.6E-05	-5.1E-03	3.6E-02	-8.4E-04	-1.9E-04	-2.8E-06	1.8E-08	3.2E-06	13.2
1.05	1.00	1.3E-02	9.4E-03	1.9E-05	-5.3E-03	3.9E-02	-4.7E-04	-4.1E-04	-3.2E-06	-5.0E-08	3.5E-06	12.7
1.03	1.00	1.3E-02	9.9E-03	2.0E-05	-5.1E-03	4.4E-02	-4.7E-04	1.3E-03	-3.6E-06	2.5E-07	4.4E-06	13.7
1.01	1.00	1.4E-02	1.0E-02	2.4E-05	-5.1E-03	5.3E-02	-3.6E-04	3.4E-04	-4.6E-06	9.9E-08	5.7E-06	14.3
1.00	1.00	1.5E-02	1.1E-02	2.8E-05	-5.3E-03	6.0E-02	-6.1E-04	5.6E-04	-5.7E-06	2.2E-07	7.0E-06	15.0
0.98	0.99	1.5E-02	1.1E-02	3.3E-05	-6.2E-03	6.5E-02	-7.7E-04	1.9E-03	-7.4E-06	5.5E-07	7.9E-06	14.8
0.97	0.99	1.6E-02	1.1E-02	3.8E-05	-7.3E-03	7.0E-02	-3.9E-04	3.9E-03	-9.4E-06	9.5E-07	9.2E-06	15.1
0.95	0.99	1.7E-02	1.2E-02	4.2E-05	-7.4E-03	7.4E-02	-2.2E-04	5.2E-03	-1.0E-05	1.3E-06	1.0E-05	14.7
0.93	0.99	1.8E-02	1.2E-02	4.6E-05	-6.6E-03	8.2E-02	-1.7E-04	4.0E-03	-1.2E-05	1.1E-06	1.2E-05	14.8
0.92	0.99	1.8E-02	1.2E-02	5.3E-05	-6.5E-03	9.1E-02	-3.8E-04	2.5E-03	-1.4E-05	7.7E-07	1.4E-05	15.1
0.90	0.99	1.9E-02	1.3E-02	5.8E-05	-6.8E-03	9.9E-02	-3.3E-04	1.7E-03	-1.6E-05	5.6E-07	1.6E-05	14.7
0.88	0.99	2.0E-02	1.3E-02	6.6E-05	-7.0E-03	1.0E-01	-2.4E-04	4.6E-03	-1.9E-05	1.5E-06	1.8E-05	14.9
0.87	0.98	2.1E-02	1.4E-02	7.2E-05	-6.8E-03	1.1E-01	-1.8E-04	4.3E-03	-2.1E-05	1.5E-06	2.0E-05	14.9
0.85	0.98	2.2E-02	1.4E-02	7.9E-05	-6.9E-03	1.1E-01	3.3E-04	2.3E-03	-2.4E-05	6.2E-07	2.2E-05	14.4
0.83	0.98	2.3E-02	1.4E-02	8.8E-05	-6.5E-03	1.2E-01	4.9E-04	1.3E-03	-2.7E-05	2.9E-07	2.4E-05	14.6
0.82	0.98	2.4E-02	1.5E-02	9.6E-05	-6.7E-03	1.2E-01	1.1E-03	-2.7E-04	-3.1E-05	-4.9E-07	2.8E-05	14.8
0.80	0.98	2.5E-02	1.5E-02	1.1E-04	-7.3E-03	1.3E-01	1.5E-03	2.2E-05	-3.6E-05	-6.1E-07	3.2E-05	14.9
0.78	0.97	2.6E-02	1.6E-02	1.2E-04	-7.6E-03	1.3E-01	1.8E-03	1.1E-03	-4.0E-05	7.2E-08	3.4E-05	15.0
0.77	0.97	2.6E-02	1.6E-02	1.2E-04	-7.5E-03	1.3E-01	2.0E-03	1.3E-03	-4.2E-05	6.8E-08	3.6E-05	14.9
0.75	0.97	2.7E-02	1.7E-02	1.3E-04	-6.7E-03	1.3E-01	1.8E-03	5.9E-05	-4.3E-05	-3.4E-07	3.8E-05	14.9
0.74	0.97	2.8E-02	1.7E-02	1.4E-04	-6.5E-03	1.3E-01	1.7E-03	-1.8E-03	-4.5E-05	-1.5E-06	4.0E-05	15.2
0.72	0.97	2.8E-02	1.8E-02	1.5E-04	-5.9E-03	1.3E-01	1.5E-03	-1.9E-03	-4.9E-05	-1.5E-06	4.3E-05	15.2
0.70	0.96	2.9E-02	1.8E-02	1.5E-04	-6.5E-03	1.4E-01	1.3E-03	8.2E-04	-5.3E-05	8.7E-08	4.7E-05	15.0
0.69	0.96	3.0E-02	1.8E-02	1.6E-04	-6.0E-03	1.5E-01	1.7E-03	1.4E-03	-5.9E-05	1.9E-07	5.2E-05	14.9
0.67	0.96	3.1E-02	1.9E-02	1.7E-04	-7.3E-03	1.7E-01	2.2E-03	-2.1E-03	-7.1E-05	-2.7E-06	6.2E-05	15.3
0.65	0.96	3.2E-02	1.9E-02	1.8E-04	-7.5E-03	1.7E-01	2.5E-03	-2.0E-03	-7.7E-05	-2.8E-06	6.7E-05	15.4
0.64	0.95	3.2E-02	2.0E-02	2.0E-04	-7.2E-03	1.7E-01	2.4E-03	1.3E-03	-8.2E-05	-5.1E-08	7.1E-05	15.5
0.62	0.95	3.3E-02	2.0E-02	2.1E-04	-7.1E-03	1.8E-01	2.4E-03	-1.6E-03	-9.3E-05	-2.3E-06	8.1E-05	15.8
0.60	0.95	3.4E-02	2.1E-02	2.2E-04	-7.1E-03	1.9E-01	2.8E-03	-7.3E-03	-1.0E-04	-7.5E-06	9.2E-05	15.7
0.59	0.94	3.5E-02	2.2E-02	2.3E-04	-7.3E-03	2.0E-01	2.7E-03	-6.4E-03	-1.1E-04	-7.0E-06	1.0E-04	15.7
0.57	0.94	3.7E-02	2.2E-02	2.6E-04	-7.4E-03	2.1E-01	2.4E-03	-2.8E-03	-1.3E-04	-4.5E-06	1.1E-04	15.8
0.56	0.94	3.8E-02	2.3E-02	2.8E-04	-7.5E-03	2.2E-01	3.1E-03	-1.8E-03	-1.4E-04	-4.0E-06	1.3E-04	15.5
0.54	0.93	3.9E-02	2.4E-02	2.9E-04	-6.5E-03	2.1E-01	2.6E-03	-7.4E-04	-1.5E-04	-2.2E-06	1.3E-04	15.4
0.52	0.93	4.0E-02	2.4E-02	3.0E-04	-6.2E-03	2.1E-01	2.9E-03	1.9E-03	-1.5E-04	5.4E-07	1.3E-04	15.2

$\frac{y}{\delta}$	$\frac{U}{U_e}$	$\frac{\sqrt{\overline{u'^2}}}{U_e}$	$\frac{\sqrt{\overline{v'^2}}}{U_e}$	$\frac{\overline{u'v'}}{U_e^2}$	$\frac{d\bar{u}}{dx}\cdot\frac{\delta}{U_e}$	$\frac{d\bar{u}}{dy}\cdot\frac{\delta}{U_e}$	$\frac{d\bar{v}}{dx}\cdot\frac{\delta}{U_e}$	$\frac{d\bar{v}}{dy}\cdot\frac{\delta}{U_e}$	$P_{xx}\cdot\frac{\delta}{U_e^3}$	$P_{yy}\cdot\frac{\delta}{U_e^3}$	$P_{xy}\cdot\frac{\delta}{U_e^3}$	α
0.51	0.93	4.1E-02	2.5E-02	3.2E-04	-7.2E-03	2.3E-01	2.7E-03	1.9E-03	-1.7E-04	7.3E-07	1.5E-04	15.1
0.49	0.92	4.3E-02	2.6E-02	3.4E-04	-6.9E-03	2.3E-01	2.7E-03	2.8E-03	-1.8E-04	1.4E-06	1.6E-04	15.3
0.47	0.92	4.4E-02	2.6E-02	3.5E-04	-6.7E-03	2.3E-01	2.6E-03	6.1E-03	-1.9E-04	6.9E-06	1.6E-04	14.9
0.46	0.92	4.5E-02	2.7E-02	3.6E-04	-6.6E-03	2.3E-01	9.7E-04	4.3E-03	-2.0E-04	6.5E-06	1.7E-04	14.7
0.44	0.91	4.6E-02	2.8E-02	3.8E-04	-6.6E-03	2.5E-01	9.6E-04	2.4E-03	-2.2E-04	1.8E-06	2.0E-04	14.8
0.42	0.91	4.8E-02	2.8E-02	4.2E-04	-7.4E-03	2.6E-01	2.4E-03	2.3E-03	-2.5E-04	3.2E-07	2.2E-04	14.9
0.41	0.90	4.9E-02	2.9E-02	4.3E-04	-8.8E-03	2.8E-01	2.9E-03	7.0E-03	-2.8E-04	9.7E-06	2.4E-04	14.4
0.39	0.90	5.1E-02	3.0E-02	4.5E-04	-8.6E-03	3.0E-01	1.9E-03	9.8E-03	-3.1E-04	1.6E-05	2.6E-04	14.2
0.38	0.89	5.2E-02	3.0E-02	4.8E-04	-8.3E-03	3.0E-01	7.8E-04	3.6E-03	-3.4E-04	7.0E-06	2.8E-04	14.1
0.36	0.89	5.4E-02	3.1E-02	5.1E-04	-9.5E-03	3.1E-01	8.6E-04	1.4E-03	-3.7E-04	3.7E-06	2.9E-04	13.8
0.34	0.88	5.5E-02	3.0E-02	5.2E-04	-9.0E-03	3.3E-01	8.1E-04	4.9E-03	-4.0E-04	8.4E-06	3.1E-04	13.1
0.33	0.88	5.7E-02	2.8E-02	5.2E-04	-7.9E-03	3.6E-01	1.7E-03	1.0E-02	-4.3E-04	1.6E-05	3.0E-04	11.4
0.31	0.87	6.0E-02	2.8E-02	5.3E-04	-8.1E-03	3.6E-01	1.2E-03	7.3E-03	-4.5E-04	9.7E-06	2.8E-04	10.4
0.29	0.87	6.3E-02	3.1E-02	6.0E-04	-8.8E-03	3.8E-01	1.5E-03	7.5E-05	-5.2E-04	-1.9E-06	3.7E-04	11.0
0.28	0.86	6.5E-02	3.5E-02	6.3E-04	-9.2E-03	4.2E-01	1.5E-03	-3.7E-03	-6.2E-04	-1.2E-05	5.3E-04	11.5
0.26	0.85	6.8E-02	3.8E-02	6.8E-04	-7.9E-03	4.6E-01	1.6E-04	4.9E-03	-7.0E-04	1.5E-05	6.7E-04	11.7
0.24	0.84	7.0E-02	4.0E-02	6.9E-04	-5.4E-03	4.9E-01	-6.1E-05	1.8E-02	-7.4E-04	6.0E-05	7.9E-04	11.5
0.23	0.84	7.2E-02	4.2E-02	7.1E-04	-5.3E-03	5.2E-01	-6.2E-04	2.3E-02	-8.0E-04	8.0E-05	9.0E-04	11.2
0.21	0.83	7.4E-02	4.4E-02	7.6E-04	-4.2E-03	5.8E-01	-1.2E-03	2.0E-02	-9.4E-04	7.8E-05	1.1E-03	11.5
0.19	0.82	7.8E-02	4.7E-02	7.9E-04	-5.9E-03	6.7E-01	-1.9E-04	6.3E-03	-1.2E-03	2.2E-05	1.5E-03	11.2
0.18	0.80	8.1E-02	4.9E-02	7.9E-04	-7.9E-03	7.6E-01	1.5E-03	1.8E-02	-1.4E-03	8.5E-05	1.9E-03	10.5
0.16	0.79	8.5E-02	5.3E-02	7.7E-04	-8.4E-03	8.7E-01	7.3E-04	3.1E-02	-1.5E-03	1.8E-04	2.4E-03	9.8
0.15	0.78	8.8E-02	5.7E-02	8.1E-04	-5.9E-03	1.0E+00	-1.4E-03	2.9E-02	-1.8E-03	1.9E-04	3.3E-03	9.9
0.13	0.76	9.3E-02	5.9E-02	8.6E-04	-1.2E-02	1.2E+00	-9.5E-05	4.6E-02	-2.3E-03	3.4E-04	4.2E-03	9.3

Table E-3: WPG (Wall Normal Coordinates)

$\frac{y}{\delta}$	$\frac{U}{U_e}$	$\frac{\sqrt{\overline{u'^2}}}{U_e}$	$\frac{\sqrt{\overline{v'^2}}}{U_e}$	$\frac{\overline{u'v'}}{U_e^2}$	$\frac{d\bar{u}}{dx}\cdot\frac{\delta}{U_e}$	$\frac{d\bar{u}}{dy}\cdot\frac{\delta}{U_e}$	$\frac{d\bar{v}}{dx}\cdot\frac{\delta}{U_e}$	$\frac{d\bar{v}}{dy}\cdot\frac{\delta}{U_e}$	$P_{xx}\cdot\frac{\delta}{U_e^3}$	$P_{yy}\cdot\frac{\delta}{U_e^3}$	$P_{xy}\cdot\frac{\delta}{U_e^3}$	α
1.46	1.00	1.0E-02	8.4E-03	-2.8E-05	-4.4E-03	-2.0E-02	-1.4E-02	-2.5E-02	-2.1E-06	-3.8E-06	-3.7E-06	61.7
1.44	1.00	1.1E-02	9.5E-03	-3.0E-05	-3.4E-03	-2.0E-02	-1.0E-02	-2.5E-02	-2.2E-06	-4.9E-06	-4.2E-06	61.5
1.42	1.00	1.1E-02	9.4E-03	-2.8E-05	-2.9E-03	-1.2E-02	-7.1E-03	-3.6E-03	-1.5E-06	-1.2E-06	-2.3E-06	63.6
1.40	1.00	1.1E-02	8.7E-03	-2.6E-05	-2.5E-03	-8.6E-03	-5.5E-03	1.2E-02	-1.2E-06	1.5E-06	-1.2E-06	67.1
1.37	1.00	1.1E-02	9.0E-03	-2.2E-05	-2.3E-03	-8.8E-03	-5.5E-03	1.9E-02	-1.1E-06	3.0E-06	-1.1E-06	67.7
1.35	1.00	1.1E-02	8.7E-03	-2.0E-05	-2.3E-03	-1.0E-02	-5.9E-03	1.9E-02	-1.1E-06	2.7E-06	-1.3E-06	71.4
1.33	1.00	1.1E-02	8.3E-03	-1.6E-05	-1.9E-03	-1.2E-02	-5.8E-03	2.3E-02	-8.8E-07	3.1E-06	-1.2E-06	74.6
1.31	1.00	1.1E-02	8.4E-03	-1.4E-05	-2.3E-03	-1.1E-02	-5.8E-03	2.7E-02	-9.5E-07	3.7E-06	-1.3E-06	75.8
1.29	1.00	1.1E-02	8.3E-03	-1.1E-05	-2.1E-03	-1.0E-02	-6.2E-03	3.1E-02	-8.3E-07	4.1E-06	-1.2E-06	78.5
1.27	1.00	1.1E-02	8.1E-03	-1.0E-05	-1.8E-03	-9.9E-03	-6.5E-03	3.6E-02	-6.9E-07	4.7E-06	-1.2E-06	79.8
1.25	1.00	1.1E-02	8.1E-03	-7.4E-06	-1.2E-03	-9.0E-03	-6.7E-03	3.5E-02	-4.2E-07	4.6E-06	-1.2E-06	82.5
1.23	1.00	1.1E-02	8.1E-03	-6.6E-06	-1.1E-03	-9.5E-03	-7.1E-03	3.9E-02	-4.5E-07	5.2E-06	-1.3E-06	83.5
1.21	1.00	1.1E-02	8.1E-03	-6.0E-06	-1.0E-03	-1.1E-02	-6.6E-03	4.3E-02	-4.2E-07	5.8E-06	-1.3E-06	84.0
1.19	1.00	1.1E-02	8.0E-03	-5.4E-06	-9.6E-04	-9.4E-03	-6.8E-03	4.4E-02	-3.7E-07	5.7E-06	-1.3E-06	85.0
1.17	1.00	1.1E-02	8.2E-03	-4.5E-06	-1.2E-03	-6.3E-03	-7.2E-03	4.2E-02	-3.2E-07	5.6E-06	-1.2E-06	85.6
1.15	1.00	1.1E-02	8.3E-03	-3.1E-06	-1.0E-03	-3.8E-03	-7.3E-03	4.0E-02	-3.0E-07	5.7E-06	-1.1E-06	87.0
1.12	1.00	1.2E-02	8.4E-03	-1.1E-06	-1.4E-03	9.8E-05	-7.6E-03	3.9E-02	-4.0E-07	5.6E-06	-9.8E-07	89.0
1.10	1.00	1.2E-02	8.9E-03	5.6E-07	-1.3E-03	4.4E-03	-7.9E-03	3.5E-02	-3.7E-07	5.8E-06	-7.6E-07	0.5
1.08	1.00	1.2E-02	9.3E-03	1.4E-06	-1.3E-03	9.9E-03	-7.8E-03	3.2E-02	-3.2E-07	5.7E-06	-2.9E-07	1.3
1.06	1.00	1.2E-02	9.4E-03	3.8E-06	-1.1E-03	1.6E-02	-7.7E-03	3.0E-02	-5.1E-07	5.5E-06	1.5E-07	3.1
1.04	1.00	1.3E-02	9.8E-03	4.7E-06	-2.1E-03	1.9E-02	-6.7E-03	2.8E-02	-9.7E-07	5.6E-06	7.0E-07	3.8
1.02	1.00	1.3E-02	9.9E-03	8.0E-06	-2.6E-03	2.7E-02	-6.7E-03	2.5E-02	-1.4E-06	5.1E-06	1.4E-06	5.7
1.00	1.00	1.4E-02	1.1E-02	1.1E-05	-3.2E-03	4.1E-02	-6.5E-03	2.0E-02	-2.3E-06	4.8E-06	3.5E-06	7.8
0.98	1.00	1.5E-02	1.2E-02	1.7E-05	-4.0E-03	5.2E-02	-6.2E-03	2.2E-02	-3.8E-06	6.5E-06	5.8E-06	10.3
0.96	1.00	1.6E-02	1.3E-02	1.6E-05	-5.8E-03	5.9E-02	-6.4E-03	2.6E-02	-4.8E-06	8.6E-06	7.8E-06	9.2
0.94	1.00	1.7E-02	1.3E-02	1.7E-05	-5.3E-03	7.4E-02	-6.8E-03	2.4E-02	-5.1E-06	8.5E-06	1.1E-05	9.0
0.92	1.00	1.8E-02	1.5E-02	2.0E-05	-4.5E-03	8.3E-02	-6.7E-03	2.3E-02	-6.4E-06	1.0E-05	1.6E-05	9.8
0.90	0.99	1.9E-02	1.6E-02	2.0E-05	-3.9E-03	9.2E-02	-5.7E-03	2.5E-02	-6.8E-06	1.3E-05	2.1E-05	10.7
0.87	0.99	2.0E-02	1.8E-02	2.4E-05	-5.3E-03	1.0E-01	-5.2E-03	2.2E-02	-9.3E-06	1.4E-05	3.0E-05	12.0
0.85	0.99	2.1E-02	1.8E-02	3.0E-05	-6.7E-03	1.0E-01	-5.2E-03	2.0E-02	-1.3E-05	1.4E-05	3.2E-05	12.0
0.83	0.99	2.2E-02	1.9E-02	3.7E-05	-5.7E-03	1.1E-01	-5.7E-03	2.1E-02	-1.4E-05	1.6E-05	3.6E-05	14.0
0.81	0.99	2.3E-02	1.9E-02	4.3E-05	-4.6E-03	1.2E-01	-5.7E-03	1.8E-02	-1.5E-05	1.4E-05	4.0E-05	13.0
0.79	0.98	2.4E-02	1.9E-02	5.1E-05	-5.6E-03	1.3E-01	-5.8E-03	1.4E-02	-2.0E-05	1.1E-05	4.4E-05	11.7
0.77	0.98	2.5E-02	1.9E-02	6.6E-05	-6.6E-03	1.4E-01	-5.5E-03	1.2E-02	-2.7E-05	9.3E-06	4.7E-05	12.3
0.75	0.98	2.7E-02	1.9E-02	7.8E-05	-5.7E-03	1.4E-01	-4.2E-03	1.4E-02	-3.1E-05	1.1E-05	5.1E-05	12.2
0.73	0.97	2.7E-02	1.9E-02	8.4E-05	-4.9E-03	1.6E-01	-4.3E-03	1.3E-02	-3.4E-05	1.0E-05	5.4E-05	11.5
0.71	0.97	2.9E-02	1.9E-02	9.9E-05	-6.0E-03	1.8E-01	-4.2E-03	1.3E-02	-4.6E-05	1.1E-05	6.4E-05	11.3
0.69	0.97	3.0E-02	2.0E-02	1.1E-04	-5.9E-03	1.8E-01	-5.1E-03	2.0E-02	-5.2E-05	1.7E-05	6.7E-05	11.5
0.67	0.96	3.2E-02	2.0E-02	1.3E-04	-5.1E-03	1.7E-01	-6.1E-03	2.9E-02	-5.3E-05	2.5E-05	6.0E-05	10.9
0.65	0.96	3.3E-02	2.0E-02	1.3E-04	-4.1E-03	1.8E-01	-6.2E-03	3.3E-02	-5.6E-05	2.8E-05	6.2E-05	10.6
0.62	0.96	3.4E-02	2.0E-02	1.4E-04	-3.6E-03	1.9E-01	-7.0E-03	3.7E-02	-6.3E-05	3.4E-05	6.7E-05	10.2

$\frac{y}{\delta}$	$\frac{U}{U_e}$	$\frac{\sqrt{\overline{u'^2}}}{U_e}$	$\frac{\sqrt{\overline{v'^2}}}{U_e}$	$\frac{\overline{u'v'}}{U_e^2}$	$\frac{d\bar{u}}{dx}\cdot\frac{\delta}{U_e}$	$\frac{d\bar{u}}{dy}\cdot\frac{\delta}{U_e}$	$\frac{d\bar{v}}{dx}\cdot\frac{\delta}{U_e}$	$\frac{d\bar{v}}{dy}\cdot\frac{\delta}{U_e}$	$P_{xx}\cdot\frac{\delta}{U_e^3}$	$P_{yy}\cdot\frac{\delta}{U_e^3}$	$P_{xy}\cdot\frac{\delta}{U_e^3}$	α
0.60	0.95	3.5E-02	2.1E-02	1.5E-04	-3.5E-03	1.8E-01	-7.8E-03	4.2E-02	-6.4E-05	3.9E-05	6.5E-05	10.0
0.58	0.95	3.6E-02	2.1E-02	1.6E-04	-3.1E-03	2.0E-01	-8.1E-03	3.9E-02	-7.3E-05	3.9E-05	7.3E-05	10.4
0.56	0.94	3.7E-02	2.2E-02	1.8E-04	-1.5E-03	2.1E-01	-9.9E-03	4.3E-02	-8.2E-05	4.7E-05	8.4E-05	10.8
0.54	0.94	3.9E-02	2.3E-02	2.0E-04	-1.6E-03	2.1E-01	-1.1E-02	5.2E-02	-8.8E-05	6.1E-05	8.6E-05	10.8
0.52	0.94	4.0E-02	2.4E-02	2.1E-04	-1.1E-03	2.2E-01	-1.0E-02	5.5E-02	-9.5E-05	6.8E-05	9.8E-05	10.8
0.50	0.93	4.1E-02	2.4E-02	2.2E-04	-8.1E-04	2.3E-01	-1.1E-02	4.9E-02	-1.0E-04	6.4E-05	1.1E-04	10.8
0.48	0.93	4.2E-02	2.5E-02	2.5E-04	-3.7E-04	2.3E-01	-1.0E-02	4.8E-02	-1.2E-04	6.8E-05	1.3E-04	11.5
0.46	0.92	4.3E-02	2.6E-02	2.6E-04	-2.6E-04	2.4E-01	-1.0E-02	5.5E-02	-1.2E-04	7.8E-05	1.3E-04	11.1
0.44	0.92	4.5E-02	2.6E-02	2.7E-04	2.8E-04	2.5E-01	-1.0E-02	5.1E-02	-1.4E-04	7.8E-05	1.4E-04	10.7
0.42	0.91	4.7E-02	2.8E-02	2.9E-04	-2.7E-03	2.7E-01	-8.9E-03	4.4E-02	-1.7E-04	7.3E-05	1.8E-04	10.8
0.40	0.90	4.8E-02	2.8E-02	3.1E-04	-1.8E-03	2.9E-01	-9.1E-03	4.2E-02	-1.8E-04	7.4E-05	2.0E-04	10.8
0.37	0.90	5.0E-02	3.0E-02	3.3E-04	1.1E-03	3.1E-01	-8.2E-03	4.3E-02	-2.0E-04	8.2E-05	2.4E-04	11.2
0.35	0.89	5.1E-02	3.1E-02	3.6E-04	1.1E-03	3.3E-01	-6.8E-03	4.0E-02	-2.3E-04	8.5E-05	3.0E-04	11.4
0.33	0.88	5.3E-02	3.3E-02	4.0E-04	1.2E-04	3.5E-01	-6.4E-03	4.0E-02	-2.7E-04	9.0E-05	3.4E-04	11.8
0.31	0.88	5.5E-02	3.4E-02	4.2E-04	1.2E-03	3.6E-01	-6.5E-03	4.2E-02	-2.9E-04	1.0E-04	3.9E-04	12.0
0.29	0.87	5.6E-02	3.6E-02	4.3E-04	1.1E-03	3.9E-01	-5.8E-03	3.4E-02	-3.3E-04	9.4E-05	4.8E-04	12.1
0.27	0.86	5.8E-02	3.8E-02	4.5E-04	9.1E-04	4.2E-01	-4.3E-03	3.2E-02	-3.7E-04	9.7E-05	5.8E-04	12.3
0.25	0.85	6.0E-02	3.9E-02	4.9E-04	2.3E-03	4.4E-01	-3.4E-03	3.5E-02	-4.2E-04	1.1E-04	6.8E-04	12.8
0.23	0.84	6.1E-02	4.1E-02	5.3E-04	3.3E-04	4.8E-01	-2.8E-03	2.8E-02	-5.1E-04	9.7E-05	8.3E-04	13.4
0.21	0.83	6.4E-02	4.3E-02	5.7E-04	1.1E-03	5.4E-01	-3.4E-03	2.3E-02	-6.0E-04	9.2E-05	9.7E-04	13.2
0.19	0.82	6.6E-02	4.3E-02	5.8E-04	1.4E-03	6.0E-01	-1.9E-03	2.9E-02	-6.8E-04	1.2E-04	1.1E-03	12.1
0.17	0.81	6.9E-02	4.2E-02	6.0E-04	4.8E-03	6.6E-01	-2.7E-03	4.3E-02	-7.3E-04	1.6E-04	1.1E-03	10.5
0.15	0.79	7.2E-02	4.5E-02	6.0E-04	5.7E-03	7.5E-01	-4.5E-03	5.7E-02	-8.2E-04	2.3E-04	1.5E-03	10.0
0.12	0.78	7.8E-02	5.2E-02	6.3E-04	5.8E-03	9.1E-01	-2.7E-03	2.4E-02	-1.1E-03	6.6E-05	2.5E-03	9.9

Table E-4: WPG (Global Coordinates)

$\frac{y}{\delta}$	$\frac{U}{U_e}$	$\frac{\sqrt{\overline{u'^2}}}{U_e}$	$\frac{\sqrt{\overline{v'^2}}}{U_e}$	$\frac{\overline{u'v'}}{U_e^2}$	$\frac{d\bar{u}}{dx}\cdot\frac{\delta}{U_e}$	$\frac{d\bar{u}}{dy}\cdot\frac{\delta}{U_e}$	$\frac{d\bar{v}}{dx}\cdot\frac{\delta}{U_e}$	$\frac{d\bar{v}}{dy}\cdot\frac{\delta}{U_e}$	$P_{xx}\cdot\frac{\delta}{U_e^3}$	$P_{yy}\cdot\frac{\delta}{U_e^3}$	$P_{xy}\cdot\frac{\delta}{U_e^3}$	α
1.46	1.00	1.0E-02	8.4E-03	-2.7E-05	-4.8E-03	-2.1E-02	-1.4E-02	-2.4E-02	-2.2E-06	-3.6E-06	-3.6E-06	63.4
1.44	1.00	1.1E-02	9.5E-03	-2.8E-05	-3.6E-03	-2.1E-02	-1.0E-02	-2.4E-02	-2.3E-06	-4.7E-06	-4.1E-06	63.1
1.42	1.00	1.1E-02	9.4E-03	-2.6E-05	-3.1E-03	-1.2E-02	-7.0E-03	-3.3E-03	-1.6E-06	-1.1E-06	-2.3E-06	64.8
1.40	1.00	1.1E-02	8.7E-03	-2.3E-05	-2.6E-03	-8.2E-03	-5.5E-03	1.2E-02	-1.2E-06	1.6E-06	-1.2E-06	68.7
1.37	1.00	1.1E-02	9.0E-03	-1.9E-05	-2.5E-03	-8.4E-03	-5.4E-03	1.9E-02	-1.1E-06	3.2E-06	-1.1E-06	69.6
1.35	1.00	1.1E-02	8.6E-03	-1.8E-05	-2.5E-03	-9.9E-03	-5.8E-03	1.9E-02	-1.1E-06	2.6E-06	-1.3E-06	73.6
1.33	1.00	1.1E-02	8.1E-03	-1.4E-05	-2.1E-03	-1.1E-02	-5.8E-03	2.3E-02	-8.7E-07	3.0E-06	-1.2E-06	77.1
1.31	1.00	1.1E-02	8.3E-03	-1.2E-05	-2.4E-03	-1.0E-02	-5.7E-03	2.7E-02	-9.4E-07	3.6E-06	-1.2E-06	78.4
1.29	1.00	1.1E-02	8.1E-03	-9.2E-06	-2.3E-03	-9.2E-03	-6.1E-03	3.1E-02	-8.3E-07	4.0E-06	-1.2E-06	81.1
1.27	1.00	1.1E-02	8.1E-03	-8.0E-06	-2.0E-03	-8.8E-03	-6.4E-03	3.6E-02	-6.8E-07	4.7E-06	-1.1E-06	81.9
1.25	1.00	1.1E-02	8.1E-03	-5.2E-06	-1.4E-03	-7.8E-03	-6.6E-03	3.5E-02	-4.2E-07	4.6E-06	-1.2E-06	84.7
1.23	1.00	1.1E-02	8.1E-03	-4.2E-06	-1.3E-03	-8.3E-03	-7.0E-03	4.0E-02	-4.4E-07	5.3E-06	-1.3E-06	85.8
1.21	1.00	1.1E-02	8.1E-03	-3.6E-06	-1.2E-03	-9.8E-03	-6.6E-03	4.4E-02	-4.1E-07	5.9E-06	-1.3E-06	86.3
1.19	1.00	1.1E-02	7.9E-03	-3.2E-06	-1.1E-03	-8.3E-03	-6.8E-03	4.4E-02	-3.7E-07	5.6E-06	-1.3E-06	87.0
1.17	1.00	1.1E-02	8.1E-03	-2.3E-06	-1.4E-03	-5.2E-03	-7.2E-03	4.2E-02	-3.3E-07	5.6E-06	-1.2E-06	87.8
1.15	1.00	1.1E-02	8.4E-03	-9.0E-07	-1.3E-03	-2.7E-03	-7.3E-03	4.0E-02	-3.3E-07	5.8E-06	-1.1E-06	89.1
1.12	1.00	1.2E-02	8.3E-03	1.1E-06	-1.6E-03	1.3E-03	-7.5E-03	3.8E-02	-4.6E-07	5.5E-06	-9.6E-07	0.9
1.10	1.00	1.2E-02	8.9E-03	2.6E-06	-1.5E-03	5.4E-03	-7.8E-03	3.5E-02	-4.6E-07	5.8E-06	-7.4E-07	2.4
1.08	1.00	1.2E-02	9.2E-03	3.4E-06	-1.5E-03	1.1E-02	-7.7E-03	3.1E-02	-4.2E-07	5.5E-06	-2.8E-07	3.3
1.06	1.00	1.2E-02	9.4E-03	6.2E-06	-1.3E-03	1.7E-02	-7.6E-03	2.9E-02	-6.5E-07	5.5E-06	1.8E-07	5.1
1.04	1.00	1.3E-02	9.7E-03	8.0E-06	-2.3E-03	2.0E-02	-6.6E-03	2.8E-02	-1.2E-06	5.5E-06	7.1E-07	6.4
1.02	1.00	1.3E-02	1.0E-02	1.1E-05	-2.8E-03	2.8E-02	-6.6E-03	2.4E-02	-1.7E-06	5.0E-06	1.5E-06	8.0
1.00	1.00	1.4E-02	1.1E-02	1.4E-05	-3.3E-03	4.2E-02	-6.3E-03	1.9E-02	-2.6E-06	4.6E-06	3.6E-06	9.7
0.98	1.00	1.5E-02	1.2E-02	2.1E-05	-4.1E-03	5.2E-02	-6.2E-03	2.1E-02	-4.3E-06	6.2E-06	6.0E-06	12.9
0.96	1.00	1.6E-02	1.3E-02	2.0E-05	-5.8E-03	6.0E-02	-6.3E-03	2.4E-02	-5.3E-06	8.2E-06	8.0E-06	11.4
0.94	1.00	1.7E-02	1.3E-02	2.1E-05	-5.6E-03	7.5E-02	-6.7E-03	2.2E-02	-5.9E-06	7.8E-06	1.2E-05	11.4
0.92	1.00	1.8E-02	1.5E-02	2.6E-05	-4.7E-03	8.3E-02	-6.5E-03	2.1E-02	-7.5E-06	9.4E-06	1.6E-05	13.1
0.90	0.99	1.9E-02	1.6E-02	2.5E-05	-4.1E-03	9.3E-02	-5.4E-03	2.2E-02	-7.9E-06	1.1E-05	2.2E-05	13.3
0.87	0.99	2.0E-02	1.8E-02	2.9E-05	-5.4E-03	1.0E-01	-5.1E-03	1.9E-02	-1.0E-05	1.2E-05	3.1E-05	14.5
0.85	0.99	2.1E-02	1.8E-02	3.6E-05	-6.9E-03	1.0E-01	-5.1E-03	1.7E-02	-1.4E-05	1.2E-05	3.2E-05	14.3
0.83	0.99	2.2E-02	1.9E-02	4.5E-05	-5.8E-03	1.1E-01	-5.6E-03	1.7E-02	-1.6E-05	1.3E-05	3.6E-05	16.2
0.81	0.99	2.3E-02	1.9E-02	5.2E-05	-4.8E-03	1.2E-01	-5.6E-03	1.4E-02	-1.8E-05	1.2E-05	4.0E-05	15.3
0.79	0.98	2.4E-02	1.9E-02	6.2E-05	-5.8E-03	1.3E-01	-5.5E-03	1.0E-02	-2.3E-05	8.4E-06	4.4E-05	13.9
0.77	0.98	2.5E-02	1.9E-02	7.7E-05	-6.7E-03	1.4E-01	-5.3E-03	8.7E-03	-3.0E-05	7.3E-06	4.8E-05	14.5
0.75	0.98	2.7E-02	1.9E-02	9.1E-05	-5.9E-03	1.4E-01	-4.0E-03	9.3E-03	-3.4E-05	7.8E-06	5.2E-05	14.1
0.73	0.97	2.7E-02	1.9E-02	9.9E-05	-5.1E-03	1.6E-01	-4.2E-03	7.8E-03	-3.9E-05	6.8E-06	5.5E-05	13.5
0.71	0.97	2.9E-02	2.0E-02	1.2E-04	-6.0E-03	1.8E-01	-4.0E-03	8.2E-03	-5.3E-05	7.7E-06	6.6E-05	13.4
0.69	0.97	3.0E-02	2.0E-02	1.3E-04	-6.0E-03	1.8E-01	-4.9E-03	1.5E-02	-6.0E-05	1.4E-05	6.9E-05	13.5
0.67	0.96	3.2E-02	2.0E-02	1.5E-04	-5.3E-03	1.7E-01	-6.0E-03	2.4E-02	-6.0E-05	2.1E-05	6.2E-05	12.9
0.65	0.96	3.2E-02	2.0E-02	1.6E-04	-4.3E-03	1.8E-01	-6.1E-03	2.8E-02	-6.5E-05	2.5E-05	6.3E-05	12.5
0.62	0.96	3.4E-02	2.1E-02	1.7E-04	-3.8E-03	1.9E-01	-6.9E-03	3.2E-02	-7.3E-05	3.0E-05	7.0E-05	12.0

$\frac{y}{\delta}$	$\frac{U}{U_e}$	$\frac{\sqrt{\overline{u'^2}}}{U_e}$	$\frac{\sqrt{\overline{v'^2}}}{U_e}$	$\frac{\overline{u'v'}}{U_e^2}$	$\frac{d\bar{u}}{dx}\cdot\frac{\delta}{U_e}$	$\frac{d\bar{u}}{dy}\cdot\frac{\delta}{U_e}$	$\frac{d\bar{v}}{dx}\cdot\frac{\delta}{U_e}$	$\frac{d\bar{v}}{dy}\cdot\frac{\delta}{U_e}$	$P_{xx}\cdot\frac{\delta}{U_e^3}$	$P_{yy}\cdot\frac{\delta}{U_e^3}$	$P_{xy}\cdot\frac{\delta}{U_e^3}$	α
0.60	0.95	3.5E-02	2.1E-02	1.8E-04	-3.7E-03	1.8E-01	-7.7E-03	3.7E-02	-7.4E-05	3.6E-05	6.7E-05	11.8
0.58	0.95	3.6E-02	2.1E-02	1.9E-04	-3.4E-03	2.0E-01	-8.0E-03	3.4E-02	-8.4E-05	3.5E-05	7.6E-05	12.2
0.56	0.94	3.7E-02	2.2E-02	2.1E-04	-1.8E-03	2.1E-01	-9.8E-03	3.7E-02	-9.6E-05	4.2E-05	8.7E-05	12.7
0.54	0.94	3.8E-02	2.3E-02	2.3E-04	-2.0E-03	2.1E-01	-1.1E-02	4.6E-02	-1.0E-04	5.6E-05	8.9E-05	12.6
0.52	0.93	4.0E-02	2.4E-02	2.5E-04	-1.4E-03	2.2E-01	-1.0E-02	4.8E-02	-1.1E-04	6.3E-05	1.0E-04	12.9
0.50	0.93	4.1E-02	2.5E-02	2.6E-04	-1.1E-03	2.3E-01	-1.1E-02	4.3E-02	-1.2E-04	5.8E-05	1.1E-04	12.6
0.48	0.92	4.2E-02	2.6E-02	2.8E-04	-4.6E-04	2.3E-01	-1.0E-02	4.1E-02	-1.4E-04	6.0E-05	1.3E-04	13.3
0.46	0.92	4.3E-02	2.6E-02	3.0E-04	-5.4E-04	2.4E-01	-1.0E-02	4.7E-02	-1.5E-04	7.1E-05	1.3E-04	13.0
0.44	0.91	4.5E-02	2.6E-02	3.2E-04	-5.1E-06	2.5E-01	-1.0E-02	4.4E-02	-1.6E-04	7.0E-05	1.5E-04	12.6
0.42	0.91	4.6E-02	2.8E-02	3.4E-04	-2.7E-03	2.7E-01	-8.9E-03	3.7E-02	-1.9E-04	6.4E-05	1.8E-04	12.8
0.40	0.90	4.8E-02	2.8E-02	3.6E-04	-2.0E-03	2.9E-01	-9.1E-03	3.5E-02	-2.2E-04	6.4E-05	2.0E-04	12.8
0.37	0.90	4.9E-02	3.0E-02	3.9E-04	7.7E-04	3.1E-01	-8.2E-03	3.5E-02	-2.4E-04	6.9E-05	2.5E-04	13.2
0.35	0.89	5.1E-02	3.2E-02	4.2E-04	9.1E-04	3.3E-01	-6.8E-03	3.1E-02	-2.7E-04	6.9E-05	3.1E-04	13.4
0.33	0.88	5.3E-02	3.3E-02	4.6E-04	-6.2E-05	3.5E-01	-6.8E-03	3.0E-02	-3.2E-04	7.3E-05	3.5E-04	13.7
0.31	0.88	5.4E-02	3.5E-02	4.9E-04	8.8E-04	3.6E-01	-6.4E-03	3.1E-02	-3.4E-04	8.0E-05	4.1E-04	14.0
0.29	0.87	5.6E-02	3.6E-02	5.0E-04	8.9E-04	3.9E-01	-5.9E-03	2.3E-02	-3.8E-04	6.4E-05	4.9E-04	14.2
0.27	0.86	5.8E-02	3.8E-02	5.2E-04	8.8E-04	4.2E-01	-4.6E-03	2.1E-02	-4.3E-04	6.5E-05	6.0E-04	14.2
0.25	0.85	5.9E-02	4.0E-02	5.7E-04	1.9E-03	4.4E-01	-3.1E-03	2.2E-02	-4.9E-04	7.4E-05	7.0E-04	14.9
0.23	0.84	6.1E-02	4.2E-02	6.1E-04	1.1E-04	4.8E-01	-2.9E-03	1.4E-02	-5.9E-04	5.2E-05	8.5E-04	15.5
0.21	0.83	6.3E-02	4.3E-02	6.6E-04	1.0E-03	5.4E-01	-3.4E-03	7.5E-03	-7.0E-04	3.6E-05	9.9E-04	15.4
0.19	0.82	6.6E-02	4.4E-02	6.8E-04	1.3E-03	6.0E-01	-2.3E-03	1.2E-02	-8.1E-04	5.5E-05	1.2E-03	14.3
0.17	0.81	6.9E-02	4.3E-02	7.1E-04	4.8E-03	6.6E-01	-3.0E-03	2.5E-02	-8.8E-04	9.6E-05	1.2E-03	12.5
0.15	0.79	7.2E-02	4.6E-02	7.2E-04	5.4E-03	7.5E-01	-4.5E-03	3.4E-02	-1.0E-03	1.4E-04	1.5E-03	12.1
0.12	0.77	7.8E-02	5.2E-02	7.6E-04	5.8E-03	9.0E-01	-2.9E-03	-4.8E-03	-1.3E-03	-1.0E-04	2.5E-03	12.1

Table E-5: SPG (Wall Normal Coordinates)

$\frac{y}{\delta}$	$\frac{U}{U_e}$	$\frac{\sqrt{\overline{u'^2}}}{U_e}$	$\frac{\sqrt{\overline{v'^2}}}{U_e}$	$\frac{\overline{u'v'}}{U_e^2}$	$\frac{d\bar{u}}{dx}\cdot\frac{\delta}{U_e}$	$\frac{d\bar{u}}{dy}\cdot\frac{\delta}{U_e}$	$\frac{d\bar{v}}{dx}\cdot\frac{\delta}{U_e}$	$\frac{d\bar{v}}{dy}\cdot\frac{\delta}{U_e}$	$P_{xx}\cdot\frac{\delta}{U_e^3}$	$P_{yy}\cdot\frac{\delta}{U_e^3}$	$P_{xy}\cdot\frac{\delta}{U_e^3}$	α
1.05	1.00	1.4E-02	1.3E-02	-7.7E-06	4.4E-03	5.0E-03	-3.9E-02	1.4E-01	1.6E-06	5.0E-05	-5.2E-06	-34.2
1.03	1.00	1.5E-02	1.3E-02	-9.6E-06	4.1E-03	5.0E-03	-3.9E-02	1.4E-01	1.8E-06	4.7E-05	-6.4E-06	-10.5
1.02	1.00	1.5E-02	1.3E-02	-9.2E-06	1.6E-03	1.1E-02	-3.9E-02	1.3E-01	6.7E-07	4.7E-05	-5.8E-06	-9.3
1.00	1.00	1.6E-02	1.4E-02	-1.1E-05	4.8E-04	1.9E-02	-3.9E-02	1.3E-01	5.5E-07	5.0E-05	-4.6E-06	-10.8
0.99	1.00	1.6E-02	1.4E-02	-1.3E-05	-3.3E-05	2.5E-02	-4.0E-02	1.3E-01	5.1E-07	5.1E-05	-3.7E-06	-11.2
0.97	1.00	1.7E-02	1.4E-02	-1.4E-05	-1.0E-03	3.0E-02	-4.0E-02	1.3E-01	-4.9E-08	5.5E-05	-2.7E-06	-11.5
0.96	1.00	1.7E-02	1.5E-02	-1.4E-05	-2.3E-04	4.1E-02	-4.0E-02	1.3E-01	6.0E-07	6.1E-05	-3.7E-07	-11.9
0.94	1.00	1.8E-02	1.5E-02	-1.5E-05	-7.5E-04	4.8E-02	-4.0E-02	1.3E-01	6.8E-07	6.1E-05	3.6E-07	-10.1
0.93	1.00	1.8E-02	1.6E-02	-1.6E-05	3.3E-04	4.7E-02	-4.1E-02	1.3E-01	1.6E-06	6.6E-05	1.0E-07	-9.7
0.91	1.00	1.9E-02	1.6E-02	-1.7E-05	5.8E-04	5.2E-02	-4.1E-02	1.4E-01	2.1E-06	7.3E-05	2.2E-06	-10.8
0.90	1.00	1.9E-02	1.6E-02	-1.8E-05	-1.9E-04	5.8E-02	-4.0E-02	1.3E-01	1.6E-06	7.1E-05	2.9E-06	-9.2
0.88	0.99	2.0E-02	1.7E-02	-1.9E-05	1.5E-03	6.2E-02	-4.1E-02	1.3E-01	3.3E-06	7.4E-05	4.2E-06	-9.1
0.87	0.99	2.0E-02	1.7E-02	-2.0E-05	3.4E-04	6.9E-02	-4.1E-02	1.3E-01	2.7E-06	7.8E-05	5.8E-06	-8.6
0.85	0.99	2.1E-02	1.7E-02	-2.2E-05	5.8E-04	7.2E-02	-4.0E-02	1.3E-01	3.4E-06	7.8E-05	7.5E-06	-8.5
0.84	0.99	2.2E-02	1.8E-02	-2.2E-05	-5.6E-04	7.5E-02	-4.0E-02	1.3E-01	2.9E-06	8.1E-05	8.0E-06	-7.9
0.82	0.99	2.2E-02	1.8E-02	-2.5E-05	2.8E-04	7.8E-02	-3.9E-02	1.3E-01	4.3E-06	8.3E-05	9.7E-06	-8.3
0.81	0.99	2.3E-02	1.8E-02	-2.8E-05	-7.6E-04	8.4E-02	-4.1E-02	1.3E-01	4.0E-06	8.6E-05	1.2E-05	-8.9
0.79	0.99	2.3E-02	1.9E-02	-2.8E-05	-3.5E-04	8.6E-02	-3.9E-02	1.3E-01	4.6E-06	9.3E-05	1.3E-05	-8.0
0.78	0.99	2.4E-02	1.9E-02	-3.1E-05	-1.1E-03	9.6E-02	-3.9E-02	1.3E-01	4.9E-06	9.6E-05	1.8E-05	-8.2
0.76	0.98	2.5E-02	2.0E-02	-3.3E-05	-1.8E-03	1.0E-01	-3.9E-02	1.3E-01	4.6E-06	1.0E-04	2.0E-05	-8.1
0.75	0.98	2.5E-02	2.0E-02	-4.0E-05	-2.1E-03	9.7E-02	-3.8E-02	1.3E-01	5.3E-06	9.8E-05	1.8E-05	-8.7
0.73	0.98	2.6E-02	2.0E-02	-3.8E-05	-9.6E-04	1.1E-01	-3.9E-02	1.3E-01	6.9E-06	1.1E-04	2.4E-05	-8.4
0.72	0.98	2.7E-02	2.1E-02	-4.1E-05	-1.5E-03	1.1E-01	-4.0E-02	1.4E-01	7.0E-06	1.2E-04	2.8E-05	-8.8
0.70	0.98	2.7E-02	2.2E-02	-4.3E-05	-1.1E-03	1.1E-01	-3.9E-02	1.3E-01	7.2E-06	1.3E-04	2.8E-05	-8.4
0.69	0.98	2.8E-02	2.2E-02	-4.3E-05	-6.6E-04	1.1E-01	-4.0E-02	1.3E-01	8.0E-06	1.3E-04	3.0E-05	-8.4
0.67	0.98	2.8E-02	2.3E-02	-4.3E-05	4.9E-04	1.2E-01	-4.0E-02	1.4E-01	1.2E-05	1.5E-04	3.9E-05	-8.2
0.66	0.97	2.9E-02	2.4E-02	-4.7E-05	2.1E-03	1.3E-01	-4.0E-02	1.4E-01	1.6E-05	1.6E-04	4.7E-05	-8.7
0.64	0.97	3.0E-02	2.4E-02	-5.0E-05	1.7E-03	1.3E-01	-3.8E-02	1.4E-01	1.6E-05	1.6E-04	5.1E-05	-8.4
0.63	0.97	3.1E-02	2.5E-02	-4.2E-05	2.6E-05	1.3E-01	-3.7E-02	1.4E-01	1.1E-05	1.8E-04	5.7E-05	-7.0
0.61	0.97	3.2E-02	2.6E-02	-3.8E-05	1.2E-03	1.4E-01	-3.9E-02	1.5E-01	1.3E-05	2.1E-04	6.1E-05	-6.6
0.60	0.97	3.2E-02	2.7E-02	-4.4E-05	2.1E-03	1.4E-01	-4.0E-02	1.5E-01	1.7E-05	2.2E-04	6.9E-05	-7.7
0.58	0.96	3.3E-02	2.8E-02	-5.4E-05	3.3E-03	1.3E-01	-3.9E-02	1.5E-01	2.2E-05	2.4E-04	7.4E-05	-9.6
0.57	0.96	3.4E-02	2.9E-02	-4.8E-05	4.6E-03	1.3E-01	-3.9E-02	1.6E-01	2.3E-05	2.7E-04	7.9E-05	-8.7
0.55	0.96	3.4E-02	3.0E-02	-4.5E-05	4.5E-03	1.5E-01	-3.6E-02	1.5E-01	2.5E-05	2.8E-04	1.0E-04	-8.5
0.54	0.96	3.5E-02	3.1E-02	-3.3E-05	5.1E-03	1.6E-01	-3.5E-02	1.5E-01	2.5E-05	2.8E-04	1.2E-04	-6.1
0.52	0.95	3.6E-02	3.2E-02	-3.6E-05	4.1E-03	1.6E-01	-3.5E-02	1.5E-01	2.2E-05	3.1E-04	1.3E-04	-7.8
0.51	0.95	3.7E-02	3.3E-02	-3.6E-05	2.5E-03	1.7E-01	-3.6E-02	1.6E-01	1.9E-05	3.6E-04	1.5E-04	-9.0
0.49	0.95	3.8E-02	3.5E-02	-3.9E-05	7.6E-04	1.9E-01	-3.5E-02	1.6E-01	1.5E-05	4.1E-04	2.0E-04	-11.4
0.48	0.95	3.8E-02	3.6E-02	-4.2E-05	3.3E-03	2.0E-01	-3.4E-02	1.5E-01	2.8E-05	4.0E-04	2.2E-04	-11.6
0.46	0.94	4.0E-02	3.7E-02	-4.3E-05	2.9E-03	1.8E-01	-3.7E-02	1.5E-01	2.6E-05	4.2E-04	2.1E-04	-13.7
0.45	0.94	4.0E-02	3.9E-02	-4.6E-05	2.9E-03	1.9E-01	-3.3E-02	1.5E-01	2.6E-05	4.6E-04	2.4E-04	-16.6

$\frac{y}{\delta}$	$\frac{U}{U_e}$	$\frac{\sqrt{\overline{u'^2}}}{U_e}$	$\frac{\sqrt{\overline{v'^2}}}{U_e}$	$\frac{\overline{u'v'}}{U_e^2}$	$\frac{d\bar{u}}{dx}\cdot\frac{\delta}{U_e}$	$\frac{d\bar{u}}{dy}\cdot\frac{\delta}{U_e}$	$\frac{d\bar{v}}{dx}\cdot\frac{\delta}{U_e}$	$\frac{d\bar{v}}{dy}\cdot\frac{\delta}{U_e}$	$P_{xx}\cdot\frac{\delta}{U_e^3}$	$P_{yy}\cdot\frac{\delta}{U_e^3}$	$P_{xy}\cdot\frac{\delta}{U_e^3}$	α
0.43	0.94	4.2E-02	4.0E-02	-4.5E-05	4.1E-03	2.2E-01	-3.3E-02	1.4E-01	3.4E-05	4.6E-04	3.0E-04	-14.8
0.42	0.93	4.3E-02	4.2E-02	-3.4E-05	1.5E-03	2.3E-01	-2.9E-02	1.4E-01	2.0E-05	5.2E-04	3.7E-04	-16.9
0.40	0.93	4.5E-02	4.4E-02	-5.6E-05	2.8E-03	2.2E-01	-3.1E-02	1.7E-01	4.0E-05	6.7E-04	3.9E-04	-29.4
0.39	0.93	4.6E-02	4.6E-02	-5.8E-05	3.0E-03	2.3E-01	-3.2E-02	1.7E-01	4.6E-05	7.5E-04	4.4E-04	-42.9
0.37	0.92	4.7E-02	4.8E-02	-6.4E-05	8.2E-04	2.5E-01	-3.0E-02	1.5E-01	3.3E-05	7.3E-04	5.3E-04	34.2
0.36	0.92	4.9E-02	5.0E-02	-6.3E-05	9.2E-04	2.4E-01	-2.6E-02	1.4E-01	2.8E-05	7.4E-04	5.6E-04	32.8
0.34	0.92	5.0E-02	5.1E-02	-3.5E-05	1.6E-03	2.5E-01	-2.8E-02	1.4E-01	2.3E-05	7.8E-04	6.0E-04	31.5
0.33	0.91	5.2E-02	5.3E-02	-3.9E-06	1.2E-03	2.6E-01	-2.4E-02	1.3E-01	1.3E-05	7.8E-04	6.9E-04	2.0
0.31	0.91	5.3E-02	5.5E-02	-2.6E-05	2.9E-04	2.7E-01	-2.1E-02	1.4E-01	1.1E-05	9.2E-04	7.8E-04	8.1
0.30	0.90	5.5E-02	5.8E-02	-5.8E-06	1.8E-03	2.9E-01	-1.8E-02	1.5E-01	2.9E-05	1.0E-03	9.6E-04	1.1
0.28	0.90	5.6E-02	6.0E-02	-1.4E-05	8.4E-03	3.3E-01	-2.0E-02	1.4E-01	7.5E-05	1.0E-03	1.2E-03	1.7
0.27	0.89	5.9E-02	6.3E-02	-2.3E-05	4.8E-03	3.5E-01	-1.9E-02	1.6E-01	4.7E-05	1.4E-03	1.4E-03	2.7
0.25	0.89	6.3E-02	6.6E-02	-3.6E-05	1.1E-02	4.0E-01	-1.4E-02	1.7E-01	1.6E-04	1.6E-03	1.8E-03	4.0
0.24	0.88	6.6E-02	7.0E-02	-7.1E-05	1.3E-02	4.6E-01	-1.2E-02	1.3E-01	1.9E-04	1.3E-03	2.3E-03	6.4
0.22	0.88	7.0E-02	7.4E-02	-5.6E-05	7.7E-03	4.9E-01	-1.7E-02	1.4E-01	1.8E-04	1.6E-03	2.7E-03	4.5
0.21	0.87	7.3E-02	7.8E-02	-1.2E-04	3.8E-03	5.1E-01	-1.5E-02	1.5E-01	1.7E-04	2.0E-03	3.1E-03	9.2
0.19	0.86	7.8E-02	8.2E-02	-1.1E-04	5.6E-03	5.2E-01	-1.8E-02	1.2E-01	2.0E-04	1.8E-03	3.6E-03	9.1
0.18	0.85	8.5E-02	8.7E-02	-9.8E-05	2.2E-02	6.3E-01	-1.1E-02	1.1E-01	6.1E-04	1.7E-03	4.9E-03	12.9
0.16	0.84	9.0E-02	9.2E-02	-7.3E-05	2.8E-02	8.3E-01	-1.1E-02	1.3E-01	9.1E-04	2.4E-03	7.1E-03	15.8
0.15	0.83	9.8E-02	9.5E-02	-1.2E-04	2.8E-02	9.4E-01	-9.3E-03	1.6E-01	1.1E-03	3.2E-03	8.9E-03	-9.5
0.13	0.81	1.1E-01	9.8E-02	-1.9E-04	2.8E-02	1.2E+00	-1.3E-02	1.4E-01	1.2E-03	2.7E-03	1.1E-02	-6.0
0.12	0.79	1.2E-01	9.7E-02	-8.8E-05	3.6E-03	1.6E+00	-1.2E-02	1.2E-01	9.3E-04	2.2E-03	1.5E-02	-0.8

Table E-6: SPG (Global Coordinates)

$\frac{y}{\delta}$	$\frac{U}{U_e}$	$\frac{\sqrt{\overline{u'^2}}}{U_e}$	$\frac{\sqrt{\overline{v'^2}}}{U_e}$	$\frac{\overline{u'v'}}{U_e^2}$	$\frac{d\bar{u}}{dx}\cdot\frac{\delta}{U_e}$	$\frac{d\bar{u}}{dy}\cdot\frac{\delta}{U_e}$	$\frac{d\bar{v}}{dx}\cdot\frac{\delta}{U_e}$	$\frac{d\bar{v}}{dy}\cdot\frac{\delta}{U_e}$	$P_{xx}\cdot\frac{\delta}{U_e^3}$	$P_{yy}\cdot\frac{\delta}{U_e^3}$	$P_{xy}\cdot\frac{\delta}{U_e^3}$	α
1.05	1.00	1.4E-02	1.3E-02	2.3E-06	-2.8E-03	2.8E-02	-3.9E-02	1.3E-01	-1.3E-06	4.7E-05	-2.3E-06	11.0
1.03	1.00	1.5E-02	1.3E-02	9.1E-06	-3.0E-03	2.8E-02	-3.9E-02	1.3E-01	-2.0E-06	4.6E-05	-4.9E-06	9.7
1.02	1.00	1.5E-02	1.3E-02	8.7E-06	-5.3E-03	3.5E-02	-3.8E-02	1.2E-01	-3.3E-06	4.6E-05	-3.3E-06	9.7
1.00	1.00	1.6E-02	1.4E-02	7.9E-06	-6.6E-03	4.0E-02	-3.8E-02	1.2E-01	-4.0E-06	4.8E-05	-2.4E-06	8.4
0.99	1.00	1.6E-02	1.4E-02	6.8E-06	-7.1E-03	4.7E-02	-3.9E-02	1.2E-01	-4.4E-06	4.9E-05	-1.3E-06	6.7
0.97	1.00	1.7E-02	1.4E-02	7.6E-06	-7.9E-03	5.4E-02	-3.9E-02	1.2E-01	-5.5E-06	5.2E-05	-3.7E-08	6.5
0.96	1.00	1.7E-02	1.5E-02	8.5E-06	-7.2E-03	6.3E-02	-3.8E-02	1.2E-01	-5.6E-06	5.5E-05	2.2E-06	7.2
0.94	1.00	1.8E-02	1.5E-02	8.4E-06	-7.7E-03	6.9E-02	-3.9E-02	1.2E-01	-6.2E-06	5.9E-05	3.4E-06	6.4
0.93	0.99	1.8E-02	1.5E-02	1.0E-05	-7.0E-03	6.9E-02	-3.9E-02	1.2E-01	-6.2E-06	6.0E-05	2.6E-06	6.4
0.91	0.99	1.9E-02	1.6E-02	1.1E-05	-6.7E-03	7.5E-02	-4.0E-02	1.2E-01	-6.4E-06	6.4E-05	4.1E-06	6.6
0.90	0.99	1.9E-02	1.6E-02	1.3E-05	-7.4E-03	8.0E-02	-3.9E-02	1.2E-01	-7.8E-06	6.4E-05	5.2E-06	7.0
0.88	0.99	2.0E-02	1.7E-02	1.4E-05	-6.1E-03	8.3E-02	-4.0E-02	1.2E-01	-7.2E-06	6.6E-05	6.1E-06	6.7
0.87	0.99	2.0E-02	1.7E-02	1.6E-05	-7.0E-03	9.0E-02	-4.1E-02	1.2E-01	-9.0E-06	7.1E-05	8.2E-06	7.3
0.85	0.99	2.1E-02	1.8E-02	1.8E-05	-6.5E-03	9.4E-02	-4.0E-02	1.1E-01	-9.4E-06	7.1E-05	1.0E-05	7.6
0.84	0.99	2.2E-02	1.8E-02	2.0E-05	-7.6E-03	9.5E-02	-3.9E-02	1.1E-01	-1.1E-05	7.1E-05	9.9E-06	7.4
0.82	0.99	2.2E-02	1.8E-02	2.2E-05	-6.7E-03	9.9E-02	-3.9E-02	1.1E-01	-1.1E-05	7.2E-05	1.1E-05	7.4
0.81	0.98	2.3E-02	1.8E-02	2.0E-05	-7.8E-03	1.0E-01	-3.9E-02	1.1E-01	-1.2E-05	7.4E-05	1.3E-05	6.1
0.79	0.98	2.3E-02	1.8E-02	2.6E-05	-7.3E-03	1.1E-01	-3.8E-02	1.2E-01	-1.3E-05	8.1E-05	1.4E-05	7.3
0.78	0.98	2.4E-02	1.9E-02	2.9E-05	-7.9E-03	1.2E-01	-3.7E-02	1.1E-01	-1.6E-05	8.2E-05	1.8E-05	7.6
0.76	0.98	2.5E-02	1.9E-02	3.1E-05	-8.7E-03	1.2E-01	-3.8E-02	1.1E-01	-1.8E-05	8.7E-05	2.1E-05	7.7
0.75	0.98	2.5E-02	2.0E-02	2.9E-05	-8.8E-03	1.2E-01	-3.7E-02	1.1E-01	-1.8E-05	8.7E-05	1.9E-05	6.5
0.73	0.98	2.6E-02	2.0E-02	3.5E-05	-7.6E-03	1.3E-01	-3.8E-02	1.1E-01	-1.9E-05	9.5E-05	2.5E-05	7.9
0.72	0.97	2.7E-02	2.1E-02	3.6E-05	-8.3E-03	1.3E-01	-3.8E-02	1.2E-01	-2.1E-05	1.1E-04	2.9E-05	7.8
0.70	0.97	2.7E-02	2.2E-02	4.5E-05	-8.0E-03	1.3E-01	-3.8E-02	1.1E-01	-2.4E-05	1.1E-04	3.0E-05	9.2
0.69	0.97	2.8E-02	2.2E-02	4.7E-05	-7.4E-03	1.3E-01	-3.8E-02	1.1E-01	-2.4E-05	1.1E-04	3.2E-05	8.9
0.67	0.97	2.9E-02	2.3E-02	4.8E-05	-6.4E-03	1.4E-01	-3.9E-02	1.2E-01	-2.4E-05	1.3E-04	4.3E-05	9.6
0.66	0.96	3.0E-02	2.5E-02	4.7E-05	-5.1E-03	1.5E-01	-4.0E-02	1.2E-01	-2.3E-05	1.5E-04	5.2E-05	9.4
0.64	0.96	3.0E-02	2.5E-02	5.1E-05	-5.1E-03	1.5E-01	-3.8E-02	1.1E-01	-2.5E-05	1.4E-04	5.3E-05	9.2
0.63	0.96	3.1E-02	2.5E-02	6.3E-05	-6.6E-03	1.6E-01	-3.6E-02	1.1E-01	-3.3E-05	1.5E-04	6.0E-05	10.8
0.61	0.96	3.2E-02	2.7E-02	7.2E-05	-5.5E-03	1.6E-01	-3.9E-02	1.3E-01	-3.4E-05	1.9E-04	6.7E-05	13.1
0.60	0.96	3.2E-02	2.8E-02	7.4E-05	-4.9E-03	1.6E-01	-4.0E-02	1.2E-01	-3.4E-05	2.0E-04	7.4E-05	13.8
0.58	0.95	3.3E-02	2.9E-02	7.3E-05	-3.4E-03	1.6E-01	-3.8E-02	1.2E-01	-3.0E-05	2.2E-04	8.2E-05	14.4
0.57	0.95	3.4E-02	3.0E-02	8.8E-05	-1.7E-03	1.6E-01	-3.8E-02	1.3E-01	-3.2E-05	2.5E-04	8.9E-05	18.1
0.55	0.95	3.4E-02	3.1E-02	9.3E-05	-2.3E-03	1.7E-01	-3.7E-02	1.2E-01	-3.7E-05	2.3E-04	1.1E-04	18.7
0.54	0.95	3.5E-02	3.2E-02	1.2E-04	-1.6E-03	1.9E-01	-3.5E-02	1.1E-01	-4.6E-05	2.4E-04	1.4E-04	23.2
0.52	0.94	3.6E-02	3.3E-02	1.3E-04	-2.6E-03	1.9E-01	-3.5E-02	1.1E-01	-5.5E-05	2.6E-04	1.5E-04	27.0
0.51	0.94	3.7E-02	3.5E-02	1.3E-04	-4.2E-03	1.9E-01	-3.6E-02	1.3E-01	-6.0E-05	3.2E-04	1.7E-04	30.7
0.49	0.94	3.8E-02	3.7E-02	1.4E-04	-5.7E-03	2.1E-01	-3.3E-02	1.2E-01	-7.6E-05	3.4E-04	2.1E-04	36.0
0.48	0.93	3.9E-02	3.7E-02	1.7E-04	-2.6E-03	2.1E-01	-3.4E-02	1.1E-01	-7.8E-05	3.1E-04	2.3E-04	35.2
0.46	0.93	4.0E-02	3.9E-02	1.9E-04	-3.9E-03	2.0E-01	-3.5E-02	1.1E-01	-8.8E-05	3.5E-04	2.3E-04	39.5
0.45	0.93	4.0E-02	4.0E-02	2.2E-04	-4.1E-03	2.1E-01	-3.2E-02	1.1E-01	-1.0E-04	3.9E-04	2.5E-04	42.0

$\frac{y}{\delta}$	$\frac{U}{U_e}$	$\frac{\sqrt{\overline{u'^2}}}{U_e}$	$\frac{\sqrt{\overline{v'^2}}}{U_e}$	$\frac{\overline{u'v'}}{U_e^2}$	$\frac{d\bar{u}}{dx}\cdot\frac{\delta}{U_e}$	$\frac{d\bar{u}}{dy}\cdot\frac{\delta}{U_e}$	$\frac{d\bar{v}}{dx}\cdot\frac{\delta}{U_e}$	$\frac{d\bar{v}}{dy}\cdot\frac{\delta}{U_e}$	$P_{xx}\cdot\frac{\delta}{U_e^3}$	$P_{yy}\cdot\frac{\delta}{U_e^3}$	$P_{xy}\cdot\frac{\delta}{U_e^3}$	α
0.43	0.92	4.2E-02	4.1E-02	2.5E-04	-2.7E-03	2.3E-01	-3.2E-02	1.0E-01	-1.3E-04	3.8E-04	3.2E-04	43.2
0.42	0.92	4.3E-02	4.3E-02	2.6E-04	-3.7E-03	2.4E-01	-2.8E-02	1.0E-01	-1.4E-04	4.1E-04	3.9E-04	-43.7
0.40	0.92	4.5E-02	4.5E-02	2.6E-04	-3.1E-03	2.4E-01	-2.9E-02	1.2E-01	-1.4E-04	5.2E-04	4.0E-04	-43.4
0.39	0.91	4.6E-02	4.7E-02	2.7E-04	-3.1E-03	2.6E-01	-3.1E-02	1.3E-01	-1.5E-04	6.0E-04	4.6E-04	-40.8
0.37	0.91	4.7E-02	4.9E-02	2.8E-04	-4.2E-03	2.7E-01	-2.7E-02	1.1E-01	-1.8E-04	5.7E-04	5.6E-04	-37.4
0.36	0.91	4.9E-02	5.1E-02	3.0E-04	-2.4E-03	2.6E-01	-2.5E-02	1.0E-01	-1.8E-04	5.5E-04	6.0E-04	-37.3
0.34	0.90	5.0E-02	5.2E-02	3.5E-04	-9.3E-04	2.8E-01	-2.7E-02	9.4E-02	-2.0E-04	5.7E-04	6.6E-04	-36.4
0.33	0.90	5.2E-02	5.5E-02	3.7E-04	-1.5E-03	2.9E-01	-2.5E-02	8.4E-02	-2.2E-04	5.3E-04	7.8E-04	-33.7
0.31	0.89	5.3E-02	5.7E-02	3.6E-04	-1.2E-03	3.0E-01	-2.2E-02	9.3E-02	-2.3E-04	6.3E-04	8.8E-04	-31.5
0.30	0.89	5.5E-02	6.0E-02	4.1E-04	3.9E-04	3.0E-01	-1.9E-02	9.7E-02	-2.4E-04	7.0E-04	1.0E-03	-28.2
0.28	0.88	5.6E-02	6.2E-02	4.6E-04	5.4E-03	3.4E-01	-2.4E-02	6.8E-02	-2.7E-04	5.5E-04	1.2E-03	-26.4
0.27	0.88	5.9E-02	6.5E-02	5.9E-04	1.7E-03	3.7E-01	-2.3E-02	8.5E-02	-4.4E-04	8.4E-04	1.5E-03	-28.5
0.25	0.87	6.2E-02	6.8E-02	6.4E-04	6.6E-03	4.2E-01	-1.8E-02	8.1E-02	-4.7E-04	8.4E-04	1.9E-03	-28.9
0.24	0.87	6.5E-02	7.2E-02	6.7E-04	1.1E-02	4.8E-01	-1.6E-02	3.1E-02	-5.4E-04	3.2E-04	2.4E-03	-27.5
0.22	0.86	6.9E-02	7.6E-02	7.1E-04	4.2E-03	4.9E-01	-1.7E-02	4.9E-02	-6.2E-04	6.2E-04	2.8E-03	-26.9
0.21	0.85	7.3E-02	7.9E-02	7.1E-04	3.4E-03	5.1E-01	-1.3E-02	6.3E-02	-7.0E-04	8.8E-04	3.2E-03	-27.1
0.19	0.84	7.7E-02	8.3E-02	7.9E-04	8.0E-03	5.6E-01	-2.2E-02	3.7E-02	-8.1E-04	5.3E-04	3.8E-03	-28.1
0.18	0.83	8.4E-02	8.9E-02	8.4E-04	1.9E-02	6.6E-01	-2.0E-02	1.7E-03	-7.8E-04	1.0E-05	5.1E-03	-31.2
0.16	0.82	8.9E-02	9.3E-02	1.0E-03	2.3E-02	8.0E-01	-2.1E-02	-3.1E-02	-1.1E-03	-4.7E-04	6.8E-03	-34.2
0.15	0.81	9.7E-02	9.7E-02	1.1E-03	2.7E-02	9.4E-01	-1.9E-02	-2.3E-02	-1.4E-03	-2.2E-04	8.8E-03	-44.8
0.13	0.80	1.1E-01	9.9E-02	1.1E-03	2.5E-02	1.2E+00	-1.6E-02	-7.0E-02	-2.0E-03	-1.3E-03	1.2E-02	30.5
0.12	0.78	1.2E-01	9.8E-02	1.6E-03	5.2E-03	1.6E+00	-1.4E-02	-1.6E-01	-4.8E-03	-3.3E-03	1.6E-02	15.4

APPENDIX F

ACE HYPERSONIC WIND TUNNEL FACILITY DEVELOPMENT

The following appendix describes in detail the design and development of an experimental hypersonic wind tunnel facility. This system was initially going to the be the facility used for the present study, however due to time constraints and facility setbacks, it was decided to obtain the data in the smaller SHR tunnel located in the laboratory. Since the design and development of the ACE facility was such a large part of the graduate studies, it is included in the present dissertation.

Infrastructure

The 10.16 cm (4 inch) pipeline described in the above chapter was reduced to a 7.62 cm (3 inch) pipeline before being split into separate lines for the two stages of the ejector. The reduction interface was located inside of the heater room and is shown below in Figure F-1.

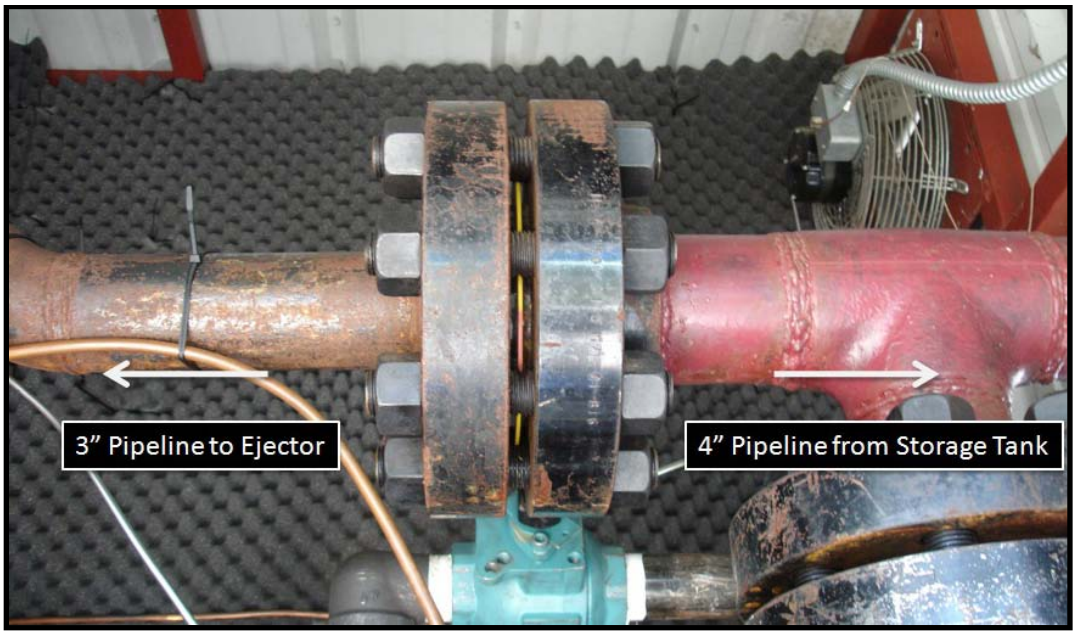

Figure F-1: 4" Pipeline Reduction Interface

The 7.62 cm (3 inch) high pressure line was then split to each stage of the ejector using welded pipe fittings and hammer unions to reduce to the correct pipe sizes. The Tee section can be seen in Figure F-2.

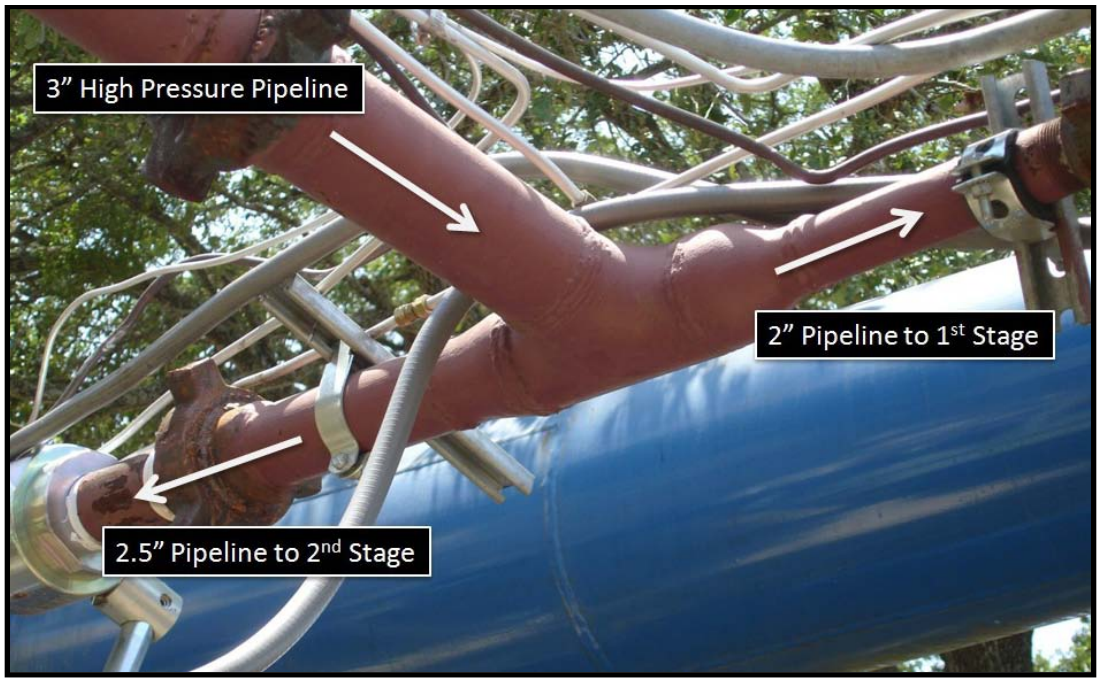

Figure F-2: 3" Tee Section

Each of the air ejector inlet lines was isolated from the high pressure 10.16 cm (4 inch) pipeline with a high pressure ball valve. For the first stage of the ejector, a Warren W36 series 5.08 cm (2 inch) high pressure full port ball valve was used. This ball valve had a rated pressure of 24.81 MPa (3600 psig) at 311 K (100 °F) and is shown in Figure F-3.

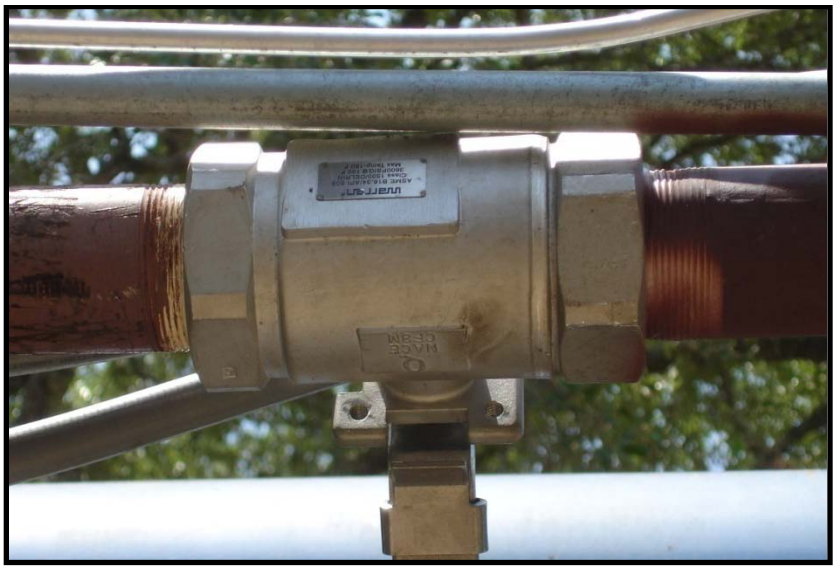

Figure F-3: First Stage Ball valve

For the second stage of the ejector, a Triad Process Equipment VS 260 series full port 6.35 cm (2.5 inch) high pressure ball valve was used. This valve had a 316 stainless steel body, ball and stem and had 6.35 cm (2.5 inch) NPT female connections. The rated pressure for the valve was 41.36 MPa (6000 psig) with a maximum operating temperature of 478 K (400 °F) and an overall length of 16.00 cm (6.30 inches). The ball valve mounted inline is shown in Figure F-4.

Figure F-4: Second Stage Ball Valve

The high pressure air from the 7.62 cm (3 inch) pipeline was regulated down to the ejector operating pressures using a series of regulators. For the first stage, two stainless steel Stra-Val dome loaded pressure regulators were used in series. The upstream Stra-Val regulator (pre-regulator), serial number 9207-1, had 5.08 cm (2 inch) FNPT inlet and outlet connections and a Cv value of 51.4. This regulator reduced the upstream high pressure air down to approximately 6.48 MPa (940 psig). A second Stra-Val regulator, serial number 25-6131-2, had a Cv value of 23.0 and also had 5.08 cm (2 inch) FNPT inlet and outlet connections. This regulator reduced the 6.48 MPa (940 psig) output pressure from the first regulator down to the ejector first stage operating pressure of approximately 0.90 MPa (130 psig). Both of the first stage pressure

regulators can be seen in Figure F-5 and the entire ejector first stage air supply line is shown in Figure F-6.

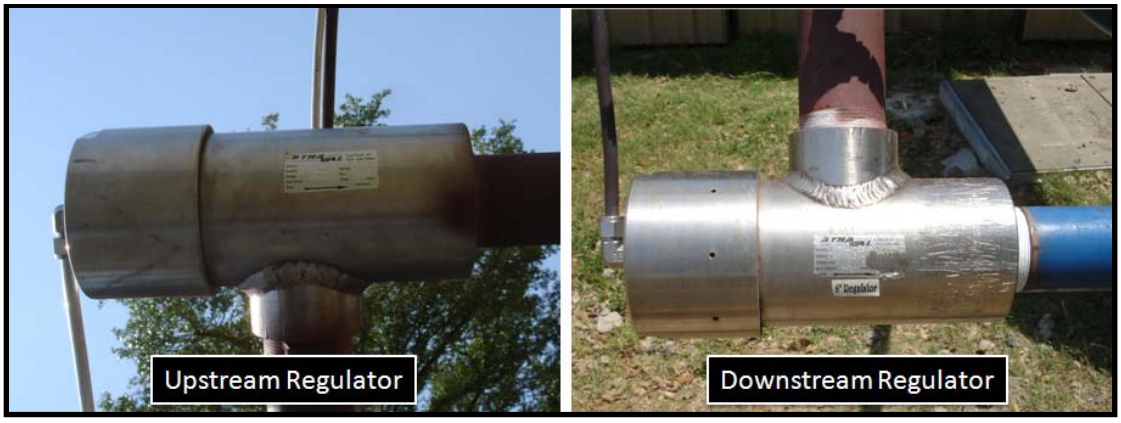

Figure F-5: Ejector 1st Stage Regulators

Figure F-6: Ejector 1st Stage Air Supply Line

For the second stage, two stainless steel Stra-Val dome loaded pressure regulators were also used in series. The upstream Stra-Val regulator, serial number 9228-1, had a 6.35 cm (2.5 inch) FNPT inlet and outlet connections and a Cv value of 61.8. This regulator also reduced the upstream high pressure air down to approximately 5.72 MPa (830 psig). A second Stra-Val regulator had a Cv value of 91.4 and had a 6.35 cm (2.5 inch) FNPT inlet and a 10.16 cm (4 inch) 600# flanged outlet. This regulator reduced the 5.72 MPa (830 psig) output pressure from the first regulator down to the ejector second stage operating pressure of approximately 0.97 MPa (140 psig). Each of

the second stage pressure regulators can be seen in Figure F-7 and the entire ejector second stage air supply line is shown in Figure F-8.

Figure F-7: Ejector 2nd Stage Regulators

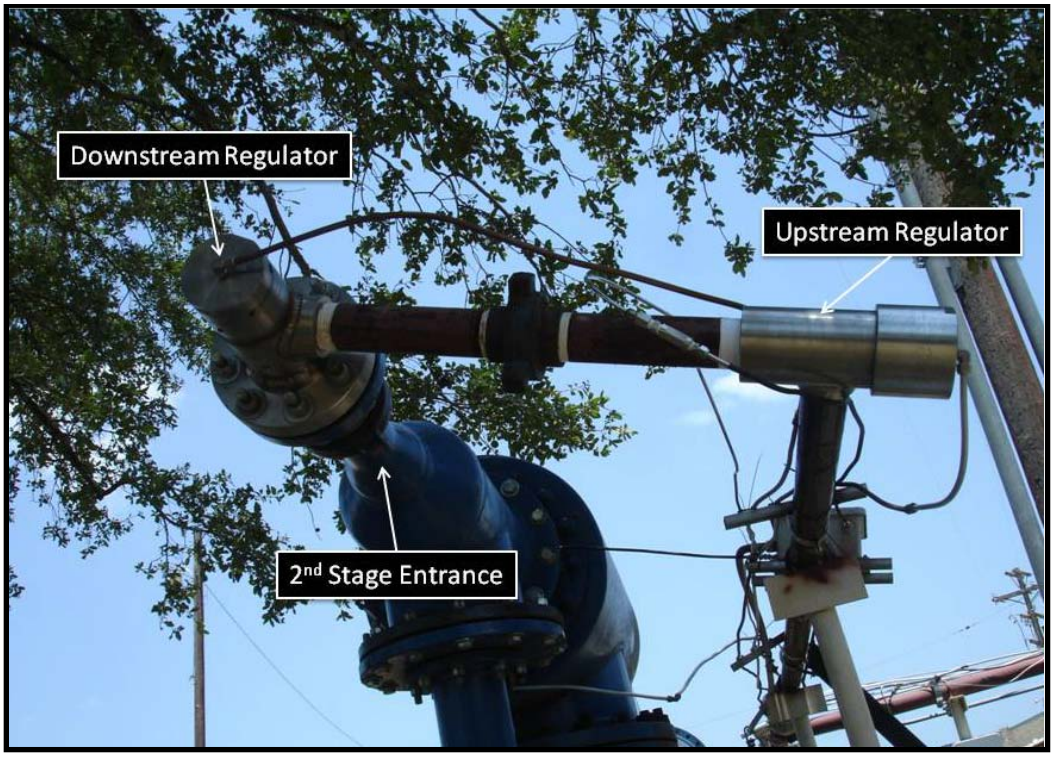

Figure F-8: Ejector 2nd Stage Air Supply Line

The air ejector has a pressure rating of only 1.38 MPa (200 psig). In order to prevent over-pressuring the system, a rupture disk was mounted to each stage inlet line. Originally, 15.24 cm (6 inch) Zook Enterprises SFAZ series rupture disks were used. These disks were scored, forward-acting disks that were ordered for 1.31 MPa (190 psig) with 0% manufacturing range. However, the safe operating pressure for this series is 85% of the marked pressure, 1.11 MPa (161.5 psig) in this case. Because of this very low margin between the ejector operating pressure and the safe operating pressure of the rupture disks, many disks were ruptured during the shake-down testing of the new high-speed experimental facility. At approximately $300.00 for each disk, this became very expensive. In an effort to reduce the occurrence of rupturing disks, the rupture disks were replaced with 15.24 cm (6 inch) Zook Enterprises URA series rupture disks. These disks were scoreless, reverse-acting disks that allowed higher cycle life compared to scored disks. These disks were also ordered for 1.31 MPa (190 psig) with 0% manufacturing range, however the URA series allows for a working pressure up to 90% of the rated burst pressure, 1.18 MPa (171 psig) in this case. Therefore, the allowable pressure margin between the ejector working pressure and the safe operating disk pressure was significantly increased. Both the SFAZ and the URA series rupture disks are shown in Figure F-8 for comparison.

Figure F-8: Zook Rupture Disks

With the new rupture disks installed, breaking the disks became much less common during the shake-down phase and virtually non-existent during the test phase of the high-speed experimental faculty development. Figure F-9 shows the first stage rupture disk system while the second stage rupture disk system can be seen in Figure F-10.

Figure F-9: First Stage Rupture Disk System

Figure F-10: Second Stage Rupture Disk System

Initially, the 5.08 cm (2 inch) stainless steel pipeline and the 10.16 cm (4 inch) carbon steel pipeline were independent of each other. However, in an effort to increase run time of the high-speed experimental facility, a bypass line was installed that coupled the two pipelines. This line was placed in the heater room upstream of the heater. It was meant to offset some of the pressure loss through the 10.16 cm (4 inch) pipeline by supplying additional air close to the ejector inlet lines. To prevent air from flowing from the 10.16 cm (4 inch) line into the 5.08 cm (2 inch) line, a Check-All model CNMSS check valve was installed. The valve was made of type 316 stainless steel and had 7.62 cm (3 inch) male NPT pipe threads on both sides. It was 13.97 cm (5.50 inches) long and had an orifice diameter of 5.14 cm (2.025 inches). The maximum rated pressure of the check valve was 20.68 MPa (3000 psig) at 311 K (100 °F) and a rated Cv value of 89.0. Also, in order to allow the bypass to be opened and closed, another Cameron WKM Dynaseal

5.08 cm (2 inch) full bore 3-piece ball valve was used. A sample picture of the check valve style can be seen in Figure F-11 and picture of the bypass line is shown in Figure F-12.

Figure F-11: Sample of Check-All Check Valve

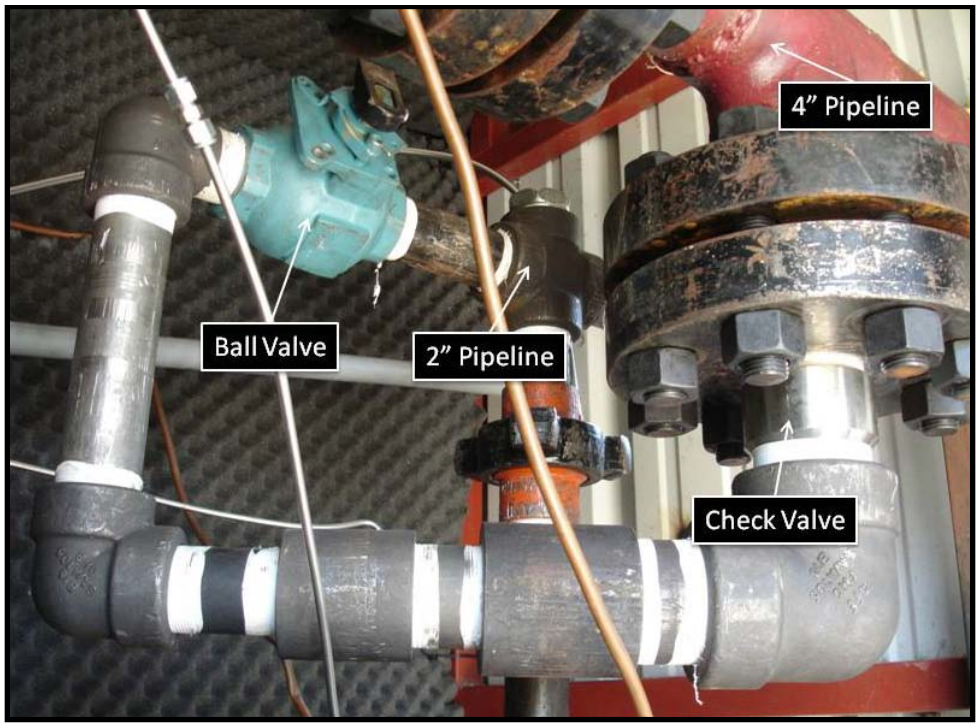

Figure F-12: Bypass Line

After the air is regulated down to approximately 1.25 MPa (180 psig), it flows through the heater and into the laboratory through 7.62 cm (3 inch) carbon steel pipe. Inside the lab, the pipe is split between the various wind tunnel facilities. For the high-speed experimental wind tunnel test facility discussed in this dissertation, a 7.62 cm (3 inch) KTM EB12 full bore ball valve was installed to isolate the tunnel from the pipeline and is shown in Figure F-13.

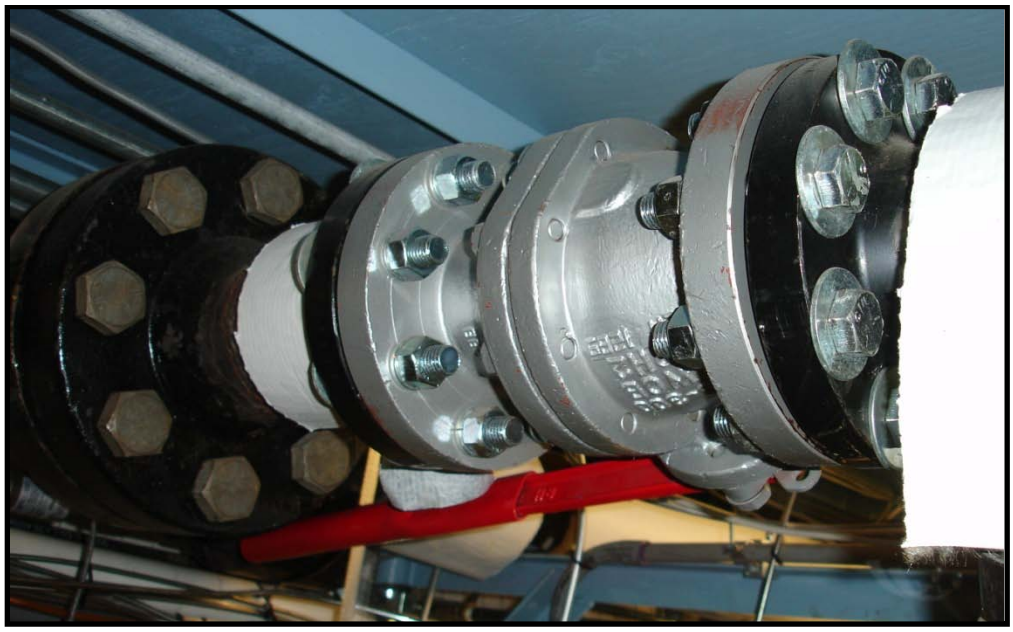

Figure F-13: KTM 3" Ball Valve

This ball valve had a carbon steel body and a stainless steel stem and ball. It had an ASME Class 300 pressure rating and 7.62 cm (3 inch) 300# flanged connections. When the experimental facility was not in use, this valve remained closed as an additional safety measure.

A large, 1 micron filter was installed downstream of the 7.62 cm (3 inch) ball valve. The filter was given to Texas A&M University by NASA Langley along with the other Mach 6 Quiet Tunnel equipment. The filter has ten rolled stainless steel filter cartridges in an enclosed case[52,58]. The filter is shown in Figure F-14 and a picture showing the filter cartridges is given in Figure F-15.

Figure F-14: 1 Micron Filter

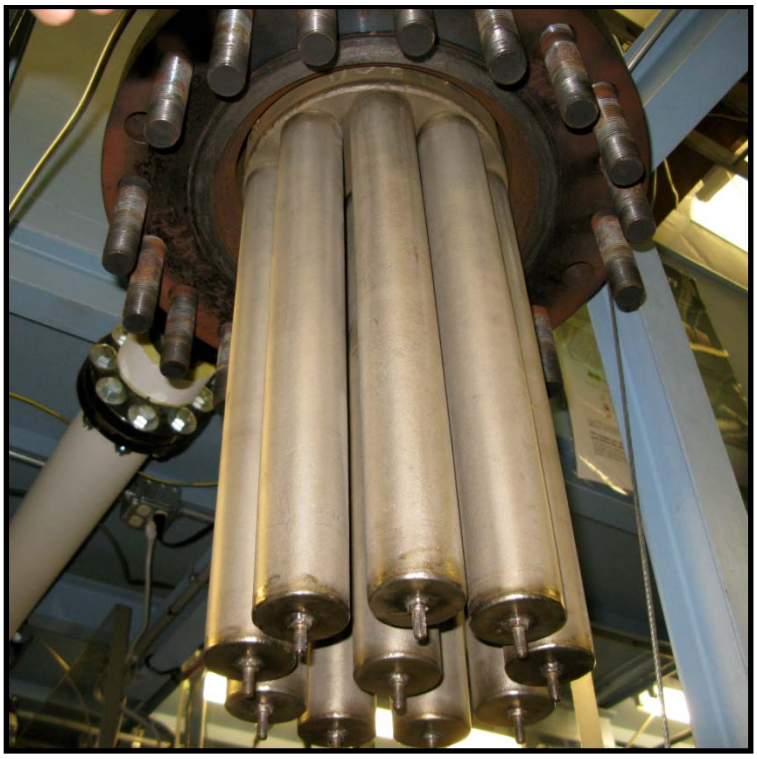

Figure F-15: 1 Micron Filter Cartridges

Immediately after the filter exit, the 7.62 cm (3 inch) pipe is reduced down to a 5.08 cm (2 inch) pipe size. A 5.08 cm (2 inch) cross was placed in line to allow for the installation of another Stra-Val safety relief valve. The valve had a set pressure of 1.38 MPa (200 psig) to prevent the air line within the lab from over pressurizing. The exhaust port of the valve was plumbed outside for added safety. The safety relief valve is shown in Figure F-16.

Figure F-16: Safety Relief Valve

After the filter, the air in the 5.08 cm (2 inch) line moved through a manifold and two Stra-Val dome loaded pressure regulators in parallel similar to ones used elsewhere in the system. Both regulators had a 5.08 cm (2 inch) FNPT inlet and outlet and were used to regulate the incoming 1.24 MPa (180 psig) air down to the operating pressure for the high-speed experimental facility. With this configuration, the tunnel experienced the oscillations discuss previously, but at the time, it was thought that these two regulators were the source of the oscillation. Because of this, a new set of higher precision regulators were ordered.

The new regulators were 5.08 cm (2 inch) Leslie Controls Inc. pressure reducing valves model GPK-1. These regulators allowed for higher precision and greater control which was thought would eliminate the pressure oscillations. The valves were air

loaded domed regulators made out of cast iron, had 6.35 cm (2.5 inch) 250# flanged connections and had a maximum pressure of 1.72 MPa (250 psig) at 505 K (450 °F). They were connected in parallel and each had a maximum rated Cv value of 82.6. However, even with the higher precision regulators installed in the system, the pressure oscillations were still present. At this point, it was still unknown that the heater room Stra-Val regulator was the source of the oscillations.

One final attempt to correct the pressure oscillation was made. A custom made Stra-Val dome loaded pressure regulator, serial number 10244-1, was ordered. This regulator had a 6.35 cm (2.5 inch) FNPT inlet and a 7.62 cm (3 inch) FNPT outlet and a Cv value of 73.1. This regulator was the final configuration for the high speed experimental facility and is shown in Figure F-17.

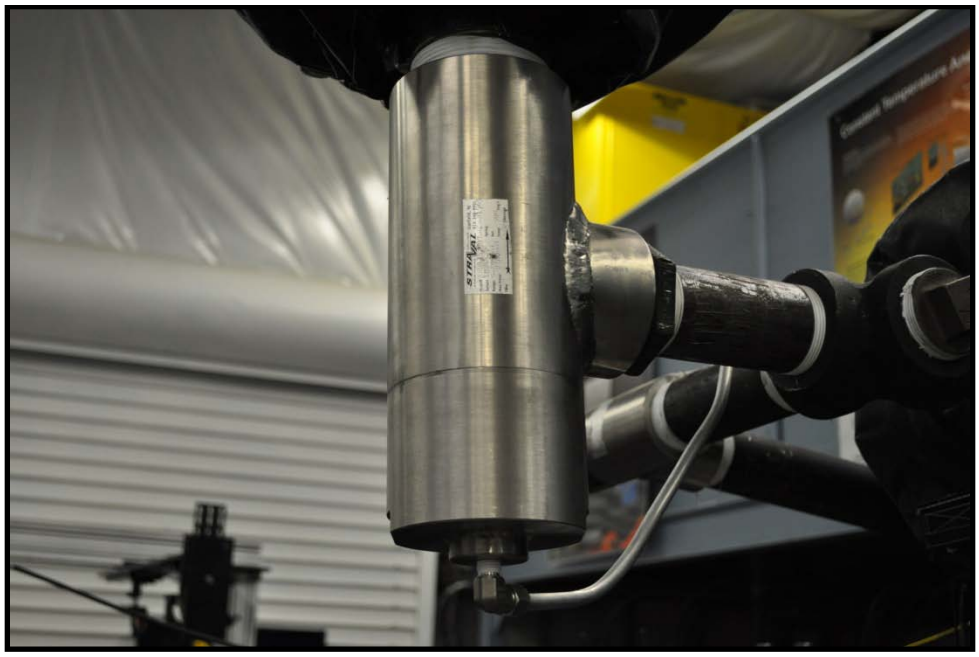

Figure F-17: 2.5" x 3" Stra-Val Regulator

Even with this regulator installed into the system, the pressure oscillations were still seen. At this point, it was realized that the regulators inside the laboratory were not the source, but instead the second Stra-Val regulator in the heater room. This second regulator was removed from the system and the oscillations were no longer seen.

After the final regulator, the air passed through a 4.88 m (16 feet) long, 10.16 cm (4 inch) stainless steel corrugated hose that was reinforced with stainless steel braiding. The hose was model UFBX from US Hose Corporation and had 10.16 cm (4 inch)-600# welded stainless steel flanged connections on each end. The braided hose can be seen in Figure F-18.

Figure F-18: 4" Stainless Steel Braided Hose

To better distribute the air flowing into the high speed facility, a stainless steel pipe manifold was designed the fabricated. Using a series of type 304 stainless steel pipe fittings and flanges, the 10.16 cm (4 inch) flanged inlet was split into four separate 3.81 cm (1.5 inch) flanged outlets. A SolidWorks drawing of the manifold is shown in Figure F-19.

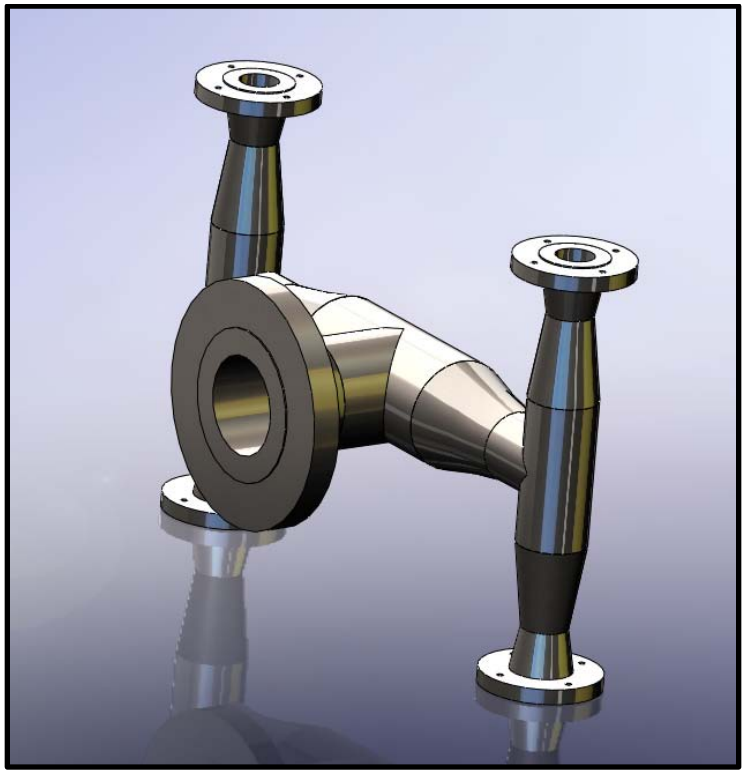

Figure F-19: SolidWorks Drawing of Manifold

After the manifold, the air flowed into four 3.81 cm (1.5 inch) braided stainless steel hoses from US Hose Corporation, model UFBX. Each of these hoses was 91.44 cm (36 inches) long and had swivel 3.81 cm (1.5 inch)-150# flanged connections and was

attached directly to the settling chamber. This design allowed for greater flexibility when assembling and operating the system and also provided a more even delivery of the air to the chamber itself. The manifold with the attached braided hoses can be seen in Figure F-20.

Figure F-20: Manifold with Attached Braided Hoses

Ejector

Description

For this project, a Fox brand 2-stage air ejector was purchased, shown in Figure F-21. This ejector system had a 61 cm (24 inch) diameter inlet pipe, a 76 cm (30 inch) exit diameter and was used to provide the vacuum side to the high-speed experimental wind tunnel facility.

Figure F-21: Fox 2-Stage Air Ejector

The ejector was designed to require approximately 21.5 kg/sec of air at 0.86 MPa (125 psig), which would allow the high-speed experimental facility a run time of approximately 50 seconds. A diagram of the manufacturer's designed specifications for the ejector is shown in Figure F-22.

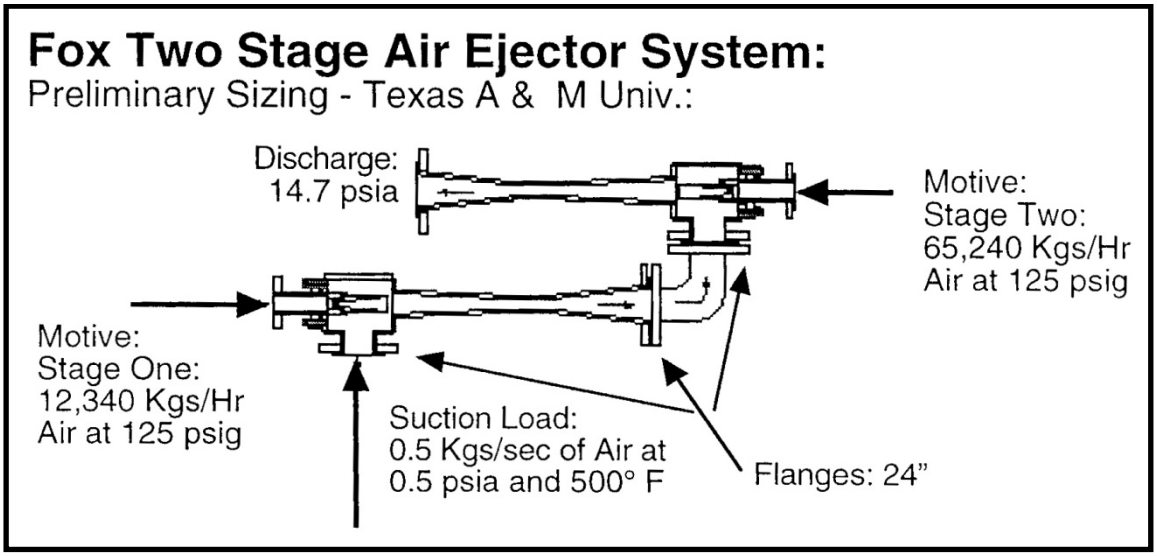

Figure F-22: Fox Air Ejector Manufacturer Design Specifications

The manufacturer also provided a representational cross section of the ejector to provide additional understanding into the operation of the system; it is shown in Figure F-23.

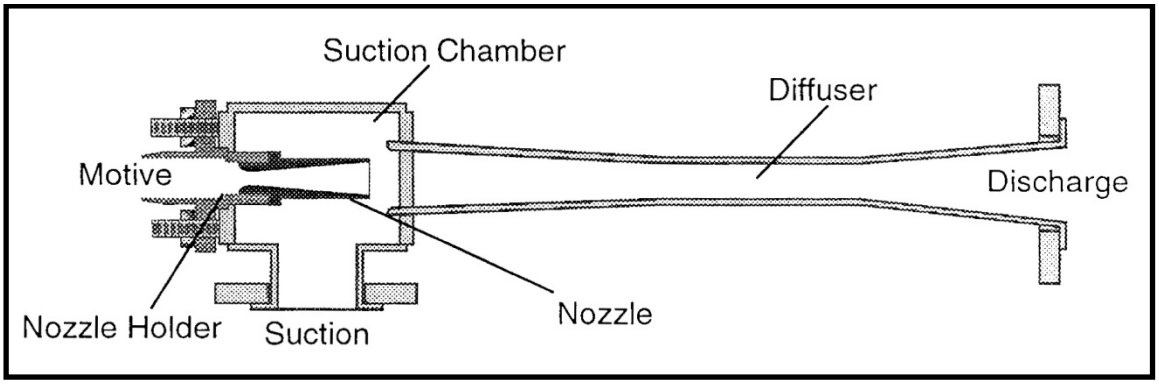

Figure F-23: Fox Air Ejector Representational Cross Section

The theoretical ejector performance at the designed operating conditions was supplied by the manufacturer for various suction flow rates based on a small scale prototype unit. The theoretical performance is plotted for a suction flow rate up to 3.0 kg/s in Figure F-24. The high-speed experimental facility was designed to operate with a mass flow of approximately 0.5 kg/s which means, based on the supplied theoretical performance curve, the ejector should pull a steady vacuum of 3.33 kPa (25 Torr).

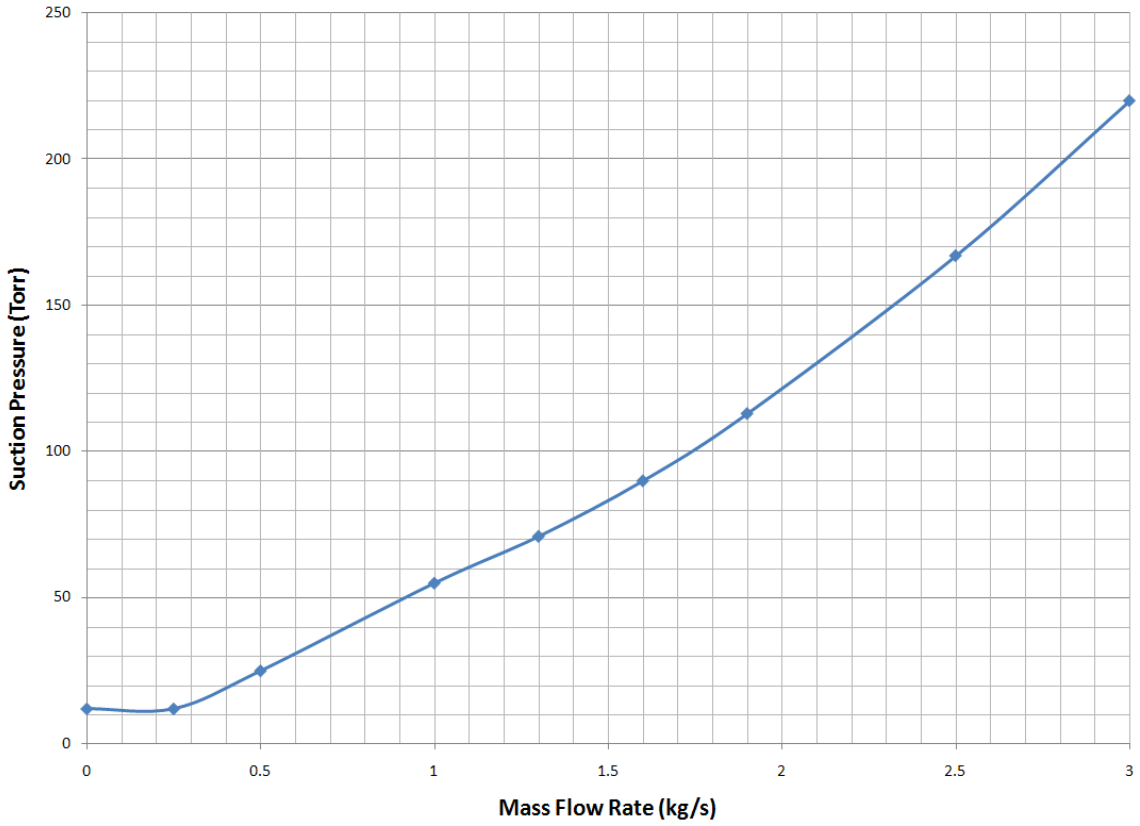

Figure F-24: Fox 2-Stage Air Ejector Suction Pressure Performance (Theoretical)

Calibration

Before the high-speed experimental facility was installed, the air ejector system was tested and calibrated. The goal of the ejector calibration was to verify the theoretical performance provided by the manufacturer and to provide additional data points for future knowledge. To accurately calibrate the ejector, a mass flow plate was designed and built that bolted directly to the ejector suction entrance; the location where the high-speed experimental wind tunnel would connect to the ejector system. The flange interface was a 60.96 cm (24 inch) 150# flange. A SolidWorks drawing and a picture of the mass flow plate are shown in Figure F-25 and Figure F-26 respectively.

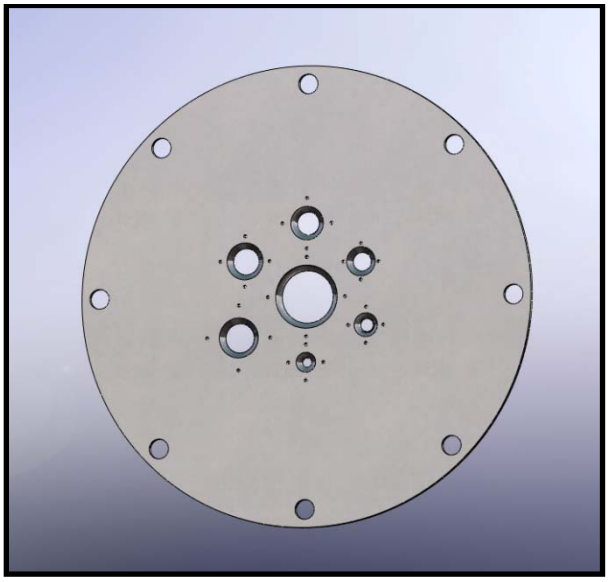

Figure F-25: SolidWorks Drawing of Mass Flow Plate

Figure F-26: Picture of Mass Flow Plate

The plate was constructed of 1.27 cm (0.5 inch) carbon steel and had a 81.28 cm (32 inch) diameter. The bolt pattern matched the 60.96 cm (24 inch) 150# flange hole pattern and a series of tapered holes were machined into the plate to allow the mass flow into the ejector to be controlled. Using the choked mass flow equation,

$$\dot{m} = \frac{Ap_t}{\sqrt{T_t}}\sqrt{\frac{\gamma}{R}}\left(\frac{\gamma+1}{2}\right)^{-\frac{\gamma+1}{2(\gamma-1)}}$$

the tapered holes were sized to allow a certain known mass flow. The designed mass flow values along with the corresponding hole diameters are given in Table F-1.

Table F-1: Mass Flow Plate Hole Sizes

Mass Flow (kg/s)	Hole Diameter (cm)
0.05	1.633
0.10	2.310
0.20	3.266
0.30	4.000
0.40	4.619
0.50	5.164
1.60	9.238

For each tapered hole, four bolt holes were drilled and tapped with 1/4”-20 threads. Aluminum cover plates were also designed and machined to cover each tapered hole in the mass flow plate. Four thru holes were drilled in each cover plate corresponding to the four mounting holes in the mass flow plate around each hole. To ensure a tight seal when covered, 0.32 cm (0.125 inch) rubber sheeting was cut to the size of each hole cover plate and attached using spray adhesive. Each hole cover plate was then bolted to the mass flow plate using 3.81 cm (1.5 inch) long 1/4”-20 hex head bolts which were sealed using bonded rubber washers. A bead of silicone was laid around the face of the 60.96 cm (24 inch) 150# ejector pipe flange and allowed to cure before the mass flow plate was bolted to the ejector. All of these measures ensured that the entire apparatus was completely sealed and prevented any leaks to allow additional

mass flow into the ejector. With this design, multiple holes were uncovered in various configurations to allow a high fidelity of mass flow levels into the ejector for calibration.

ACE Tunnel

The Actively Controlled Expansion (ACE) Hypersonic Wind Tunnel design consisted of (1) an actively controlled expansion nozzle, (2) a test section for calibration or experiments, (3) a diffuser and (4) the necessary infrastructure to drive the facility. The design methodology consisted of a combination of classical methods and high fidelity computational fluid dynamics.

Tunnel Operating Conditions

The ACE tunnel was designed to provide a continuously variable Mach number over a range of 5.0 to 7.0. The facility was sized to fit within the available infrastructure in the TAMU-NAL (described below) and the nozzle exit geometry was chosen to be 22.86 cm x 35.56 cm (9.0 inches x 14.0 inches). The available flow conditions are summarized in Table F-2.

Table F-2: ACE Hypersonic Wind Tunnel Operating Conditions

Mach No.	Total Pressure (MPa)	Total Temperature (K)	Run Time (sec)	Test Section (sq. cm.)
5.0 – 7.0	0.14 – 1.03	300 - 533	50	22.86 x 35.56

Setling Chamber

Air from the four 3.81 cm (1.5 inch) stainless steel braided hoses fed into the ACE tunnel settling chamber through four 3.81 cm (1.5 inch) holes in the upper and lower surfaces. The entrance holes were located 10.80 cm (4.25 inches) from the back wall and 9.53 cm (3.75 inches) from the centerline of the settling chamber. The settling chamber was constructed from type 304 stainless steel that was 3.81 cm (1.5 inches) thick for the top, bottom and back walls and 2.54 cm (1.0 inch) thick for the side walls. The settling chamber had overall outer dimensions of 33.83 cm L x 40.64 cm W x 11.94 cm H (13.32 inches x 16.0 inches x 4.7 inches). The inside height was 4.32 cm (1.7 inches) while the inside width was 35.56 cm (14.0 inches). An overall SolidWorks drawing of the settling chamber is shown in Figure F-27.

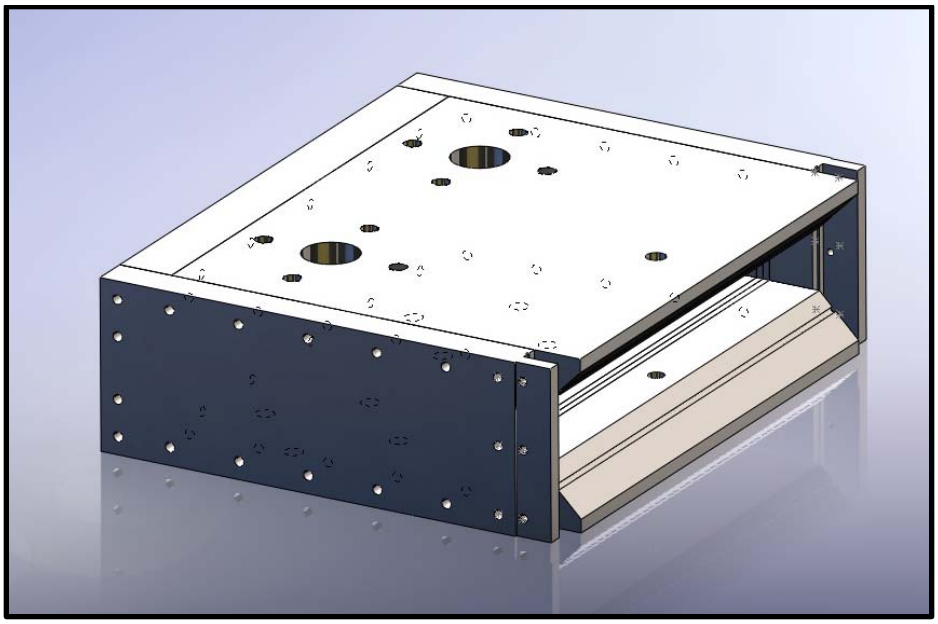

Figure F-27: Overall SolidWorks Drawing of ACE Settling Chamber

A series of channels were machined into the upper and lower settling chamber plates to allow for the installation of flow conditioners. The initial design, shown in Figure F-28, included five channels that were 0.64 cm (.025 inches) wide and 0.64 cm (0.25 inches) deep.

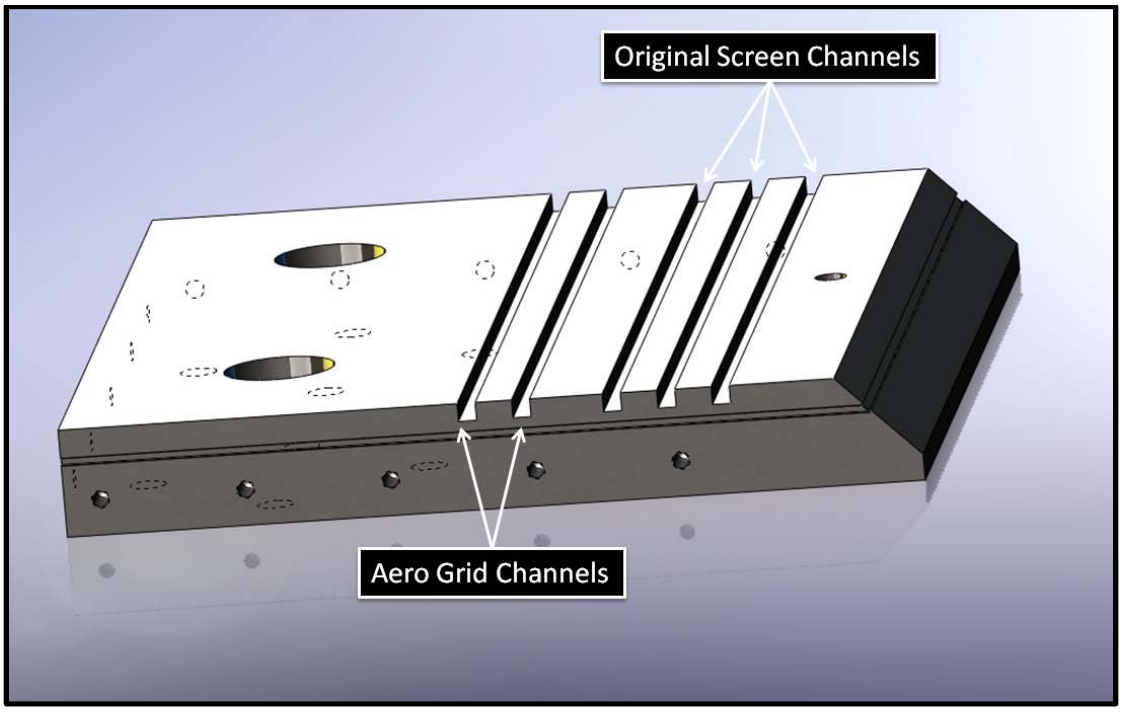

Figure F-28: Original Settling Chamber Channels

However, to allow for the wire mesh screens (discussed below), the last three channels were widened to 0.95 cm (.375 inches). Additionally, to allow the mesh screen frames to sit below all flow surfaces, three 0.95 cm (.375 inch) channels were machined in each of the settling chamber side plates in line with the widened channels in the upper

and lower plates. SolidWorks drawings and pictures of the modified top plate and side plate are shown in Figure F-29 and Figure F-30 respectively.

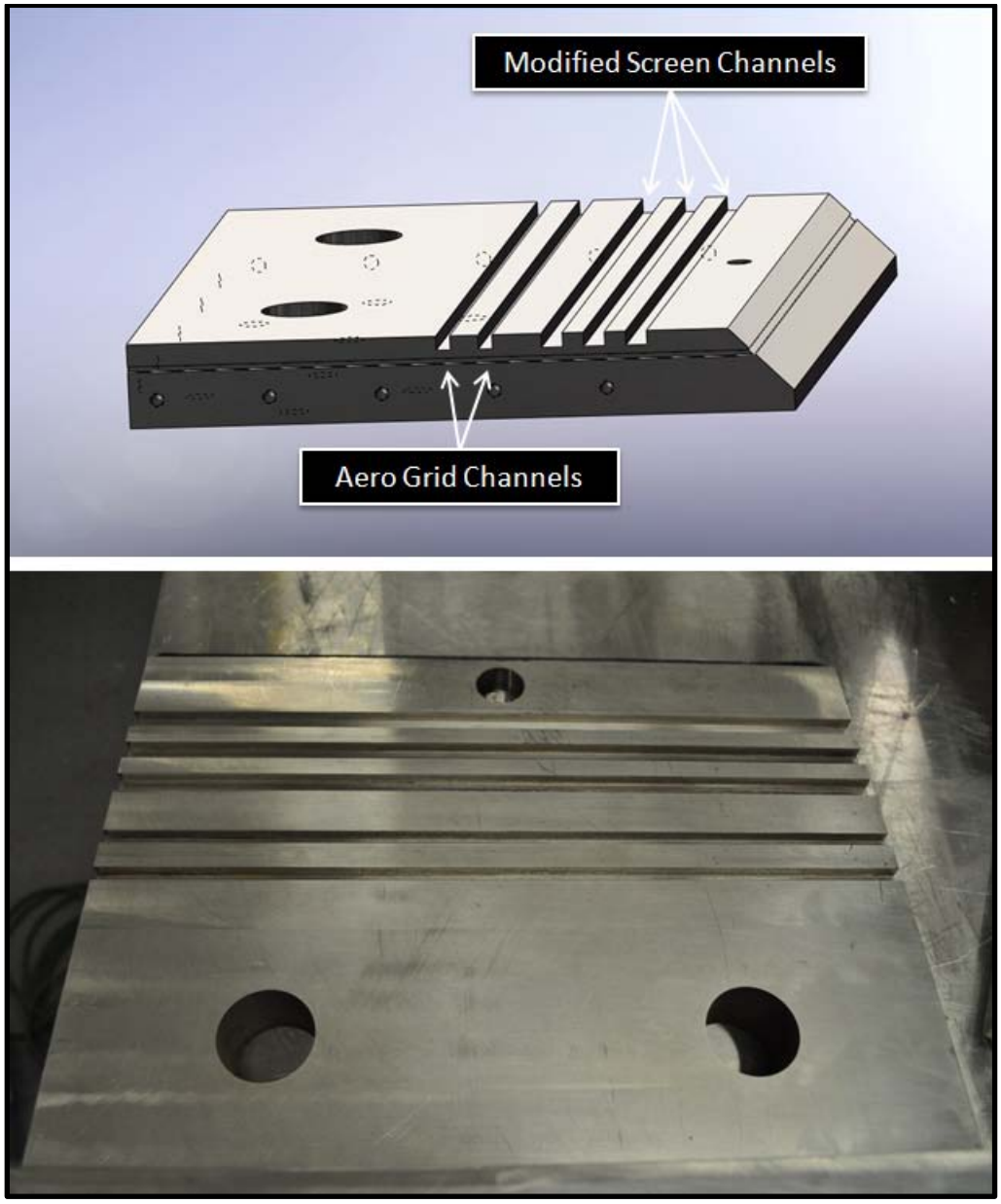

Figure F-29: Modified Top Settling Chamber Plate Channels

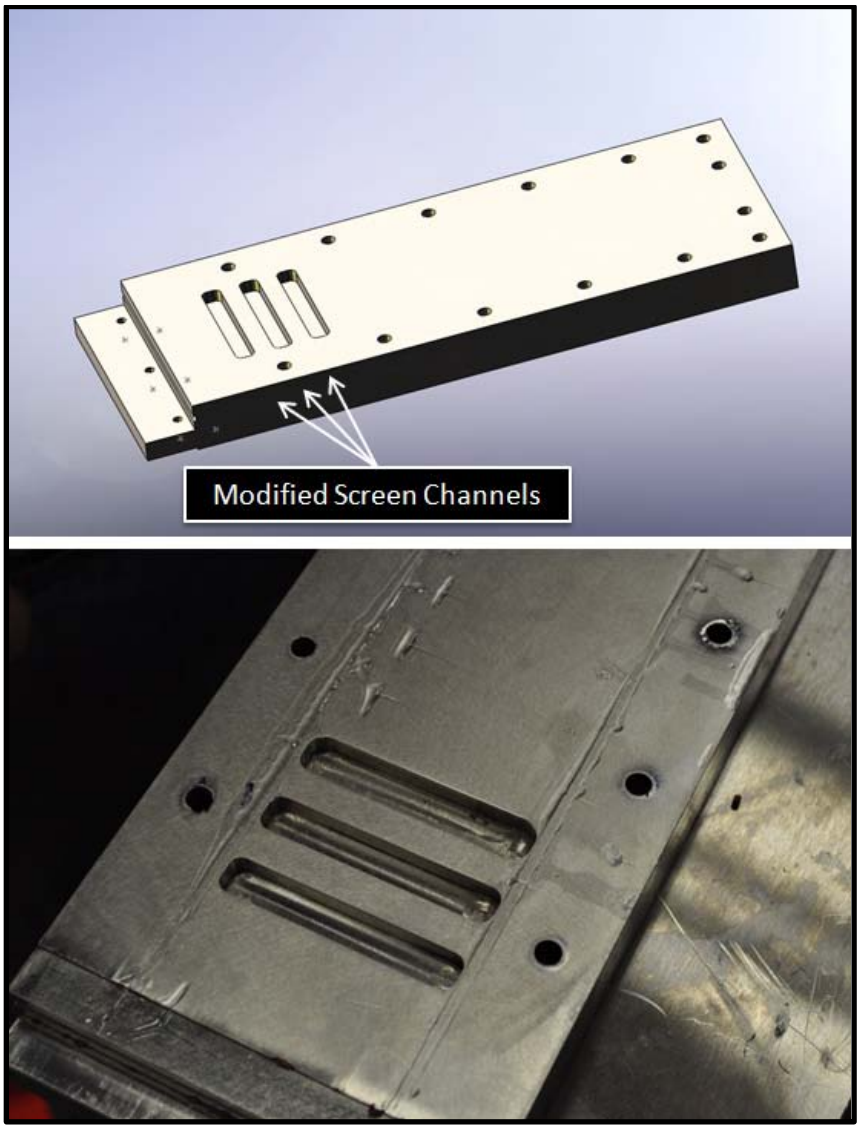

Figure F-30: Modified Side Settling Chamber Plate Channels

In the upper and lower plates, three holes were drilled and tapped near the settling chamber exit. These holes were designed as access ports for instrumentation or for other future needs and were drilled and tapped for 0.64 cm (0.25 inch) NPT threads. The outside holes were used for the settling chamber instrumentation (discussed below)

and the center hole was used for the PIV seeding system (also discussed below). A SolidWorks drawing of the settling chamber access holes are shown in Figure F-31.

Figure F-31: SolidWorks Drawing of Settling Chamber Access Holes

However, during the PIV setup, it was determined that the originally designed center hole was too small and reduced seeding performance. Because of this, the center access hole was drilled and tapped to a larger 1.91 cm (0.75 inch) NPT threaded hole size for the upper and lower plates. This allowed for a much larger area to introduce seed particles into the flow. A SolidWorks drawing as well as a photograph showing the modified settling chamber plate can be seen in Figure F-32.

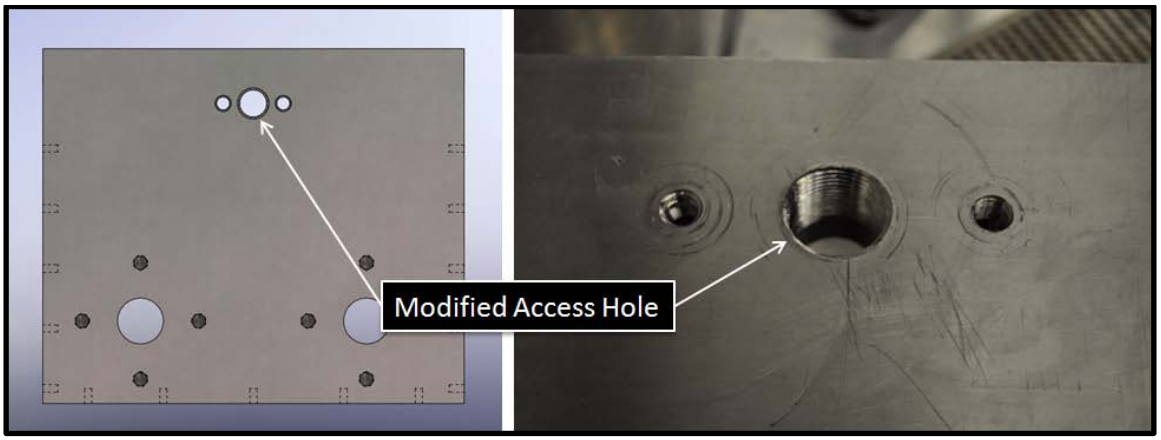

Figure F-32: Modified Settling Chamber Top Plate Access Hole

In order to produce a more uniform and evenly distributed flow entering the nozzle, a series of flow conditions were inserted into the settling chamber. Two perforated plates, or aero grids were installed immediately downstream of the air inlets. These plates are constructed of 0.64 cm (0.25 inch) type 304 multipurpose stainless steel and are 35.56 cm (14.0 inches) wide and 5.59 cm (2.2 inches) tall. In each plate, approximately 650 0.32 cm (0.125 inch) diameter holes were drilled to redistribute the air evenly. Both plates have approximately the same number of holes; however the pattern on each plate is different so that the holes do not line up which further improves the uniformity of the incoming air. A SolidWorks drawing and a photograph of the two perforated plates are shown in Figure F-33 and Figure F-34 respectively.

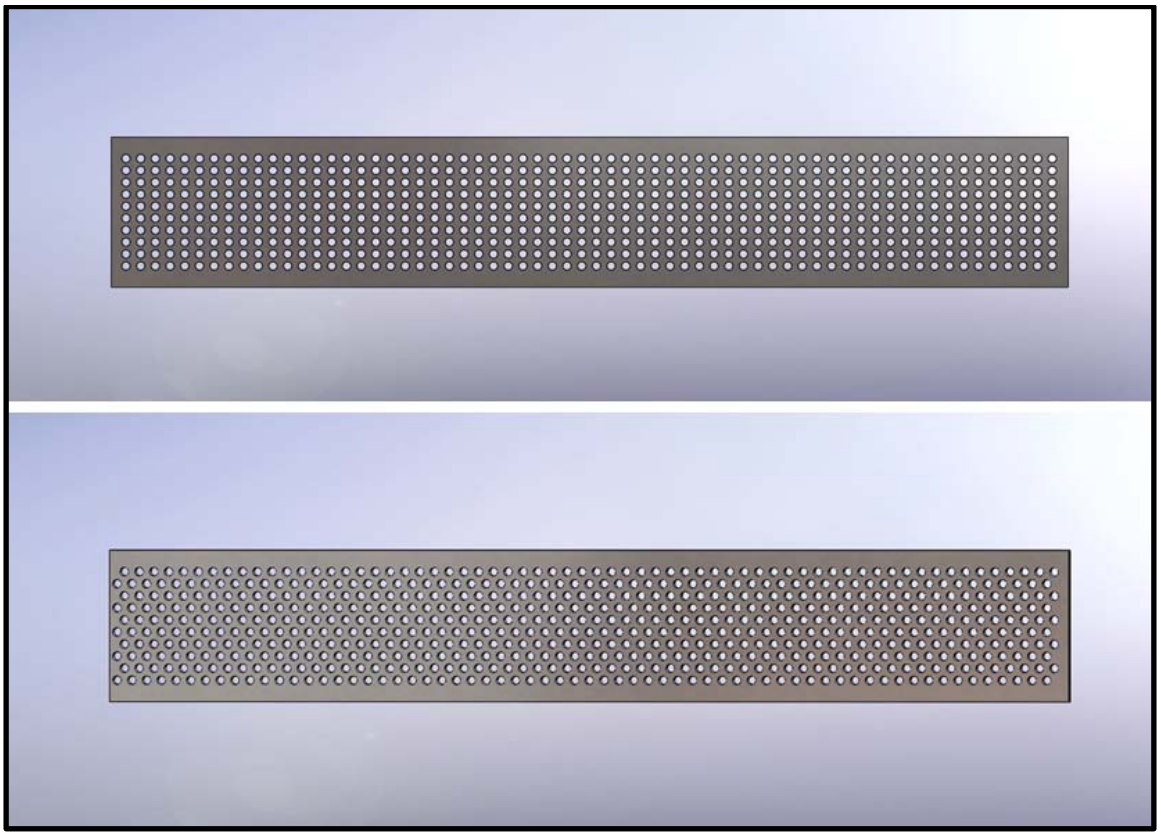

Figure F-33: SolidWorks Drawings of Settling Chamber Perforated Plates

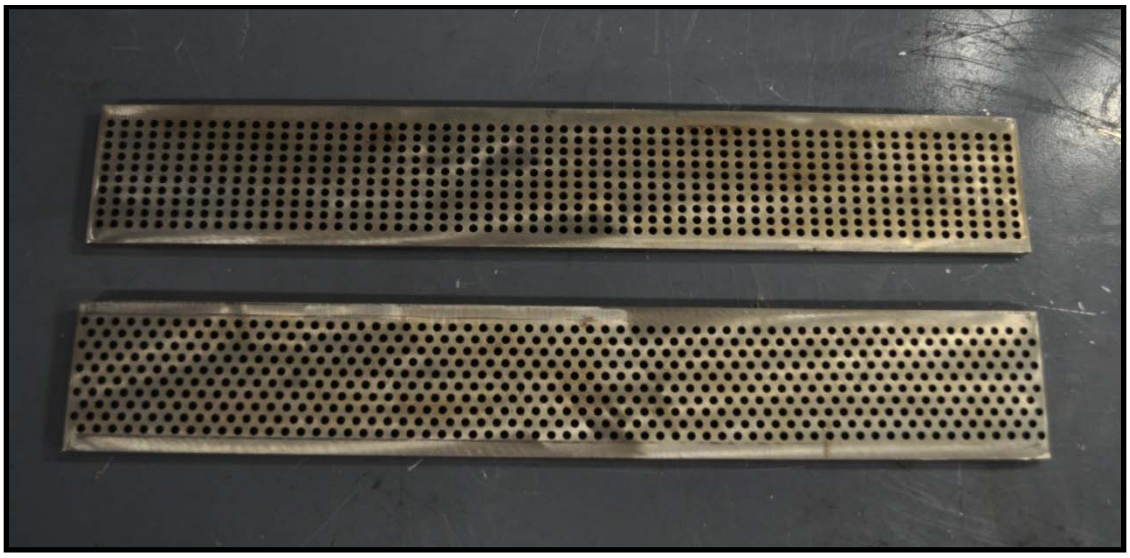

Figure F-34: Photograph of Settling Chamber Perforated Plates

Downstream of the two perforated plates, three mesh screens were installed to reduce flow turbulence. To hold the screens, three frames were designed and fabricated. Each frame was constructed in two pieces which screwed together and sandwiched the mesh in between. Each frame piece was machined from 0.48 cm (0.1875 inch) type 304 multipurpose stainless steel. Once side of the frame was drilled and tapped and the other side was countersunk to accommodate 4-40 flat head screws. A SolidWorks drawing of a stainless steel mesh frame is shown in Figure F-35.

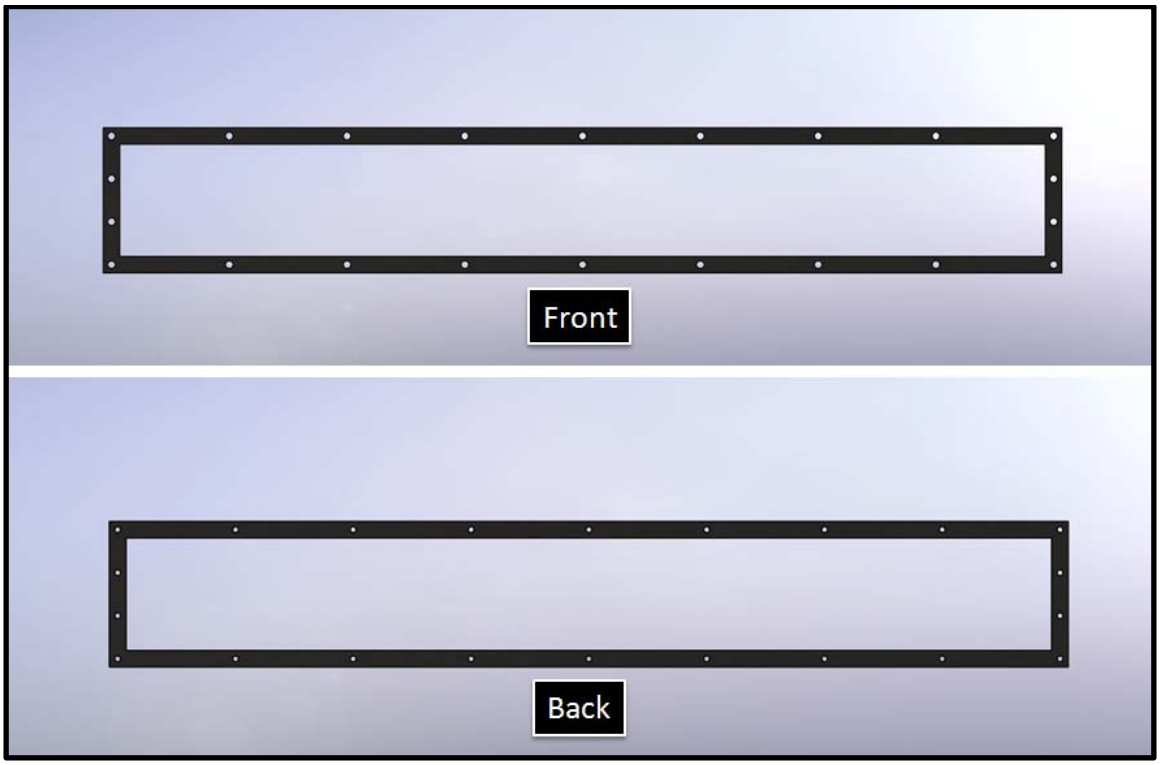

Figure F-35: SolidWorks Drawing of Settling Chamber Mesh Frame

Three type 304 stainless steel mesh sizes were chosen and installed in decreasing order. The largest mesh was located just downstream of the last perforated grid and had a mesh size of 7.87 grids per centimeter (20 grids per inch) with a square size of 863.6 µm (0.034 inches), a wire diameter of 406.4 µm (0.016 inches) and had a 46.2% open area. The middle mesh had a mesh size of 23.62 grids per centimeter (60 grids per inch) with a square size of 228.6 µm (0.009 inches), a wire diameter of 190.5 µm (0.0075 inches) and had a 30.5% open area. The smallest and final mesh had a mesh size of 59.06 grids per centimeter (150 grids per inch) with a square size of 104.1 µm (0.0041

inches), a wire diameter of 59.06 µm (0.0026 inches) and had a 37.8% open area. A picture of the three settling chamber mesh sizes can be seen in Figure F-36.

Figure F-36: Settling Chamber Mesh Sizes

Once all of the perforated plates and mesh screens were installed, the settling chamber was sealed using a single piece of 2.4mm (0.093 inch) diameter viton O-ring cord stock shown in Figure F-37.

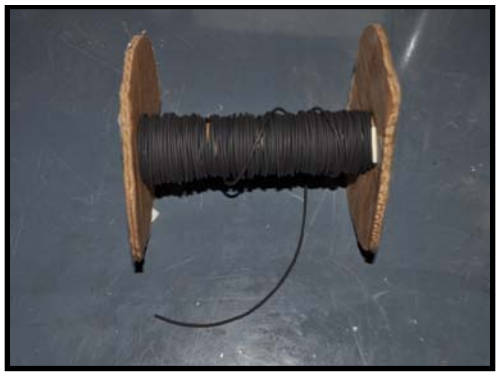

Figure F-37: Settling Chamber O-Ring Stock

The five plates were then bolted together using 38 1/4-28 grade 8 bolts. An exploded SolidWorks drawing of the settling chamber is shown in Figure F-38 and photographs of the assembly of the settling chamber are shown in Figure F-39 and Figure F-40.

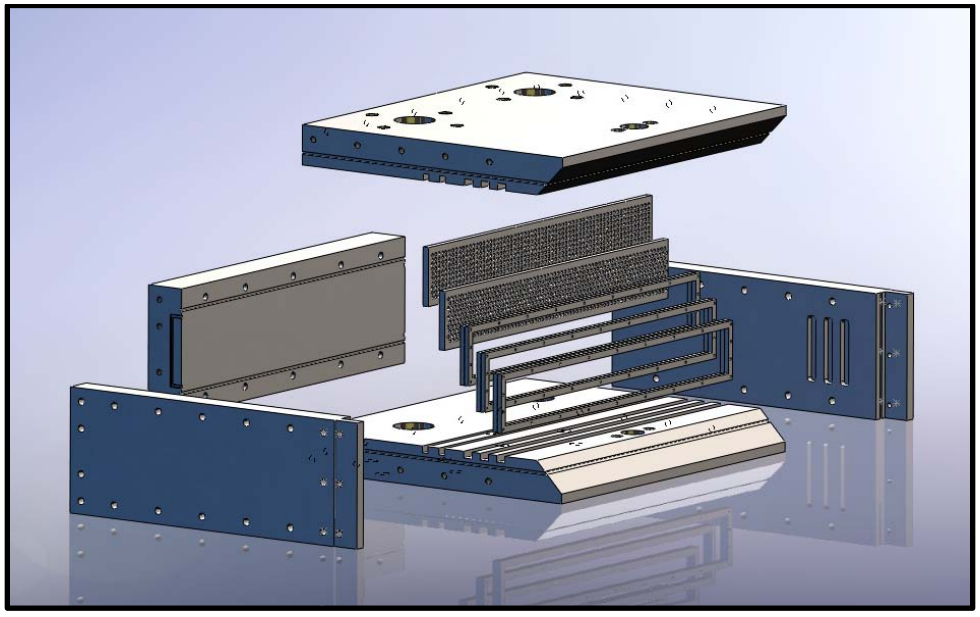

Figure F-38: SolidWorks Drawing of Settling Chamber (Exploded View)

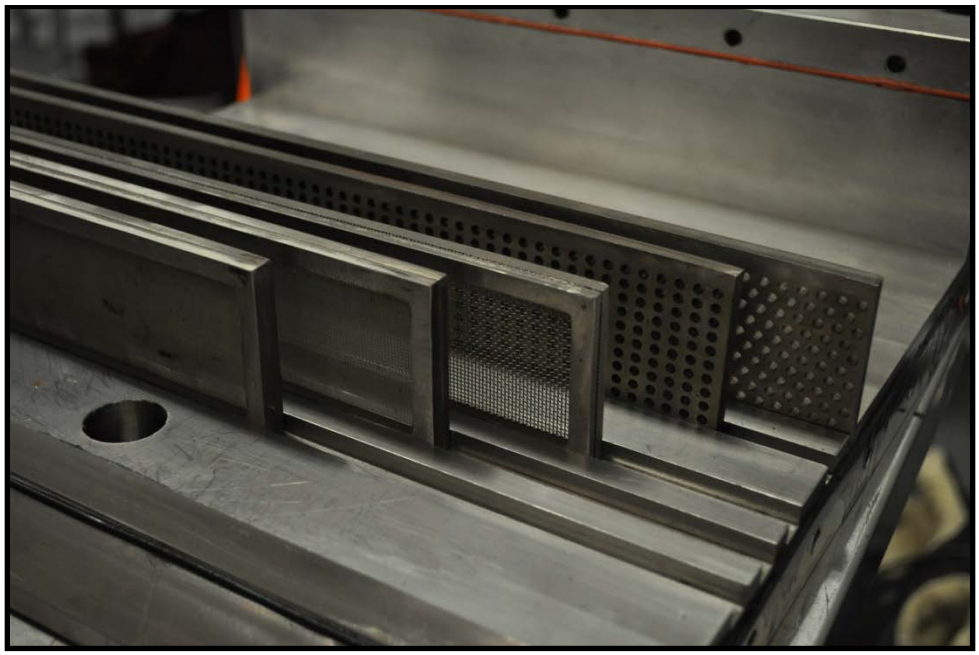

Figure F-39: Settling Chamber Assembly (Top View)

Figure F-40: Settling Chamber Assembly (Side View)

Nozzle

A combination of the method of characteristics, with viscous corrections, and CFD were used to design the ACE nozzle. The method of characteristic nozzle design was performed with an in-house written computer program[62]. The computer program allows for multiple reflections of the expansion fan off of the centerline and upper wall before cancellation at the wall. This measure was included to control the initial expansion angle, which was required to (1) prevent flow separation near the throat and (2) control the rate of acceleration to prevent or minimize the formation of a vortex pair along the centerline on each side of the wind tunnel[53]. This vortex pair results in significant flow distortions and an hourglass shaped uniform flow region. The vortex pair structure is captured with modern finite volume CFD (the CFD methods are described below). The trade-off analysis was centered on minimizing both the nozzle length and the effect of the vortex pair. After numerous iterations, the Mach 7.0 supersonic wall contour shown in Figure F-41 was designed. The characteristic mesh consisted of 100 characteristics and seven reflections, followed by the wave cancellation. The dark half diamond structure near the throat in Figure F-41 shows the intersection points of the characteristic lines. The zoomed images in Figure F-42 and Figure F-43 better show the intersection points while the finite radius curvature of the throat is visible in Figure F-43. The dashed line in Figure F-41 shows the estimated boundary layer thickness[66].

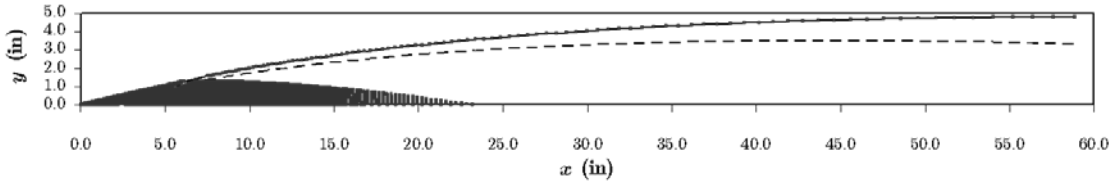

Figure F-41: Full Nozzle MOC

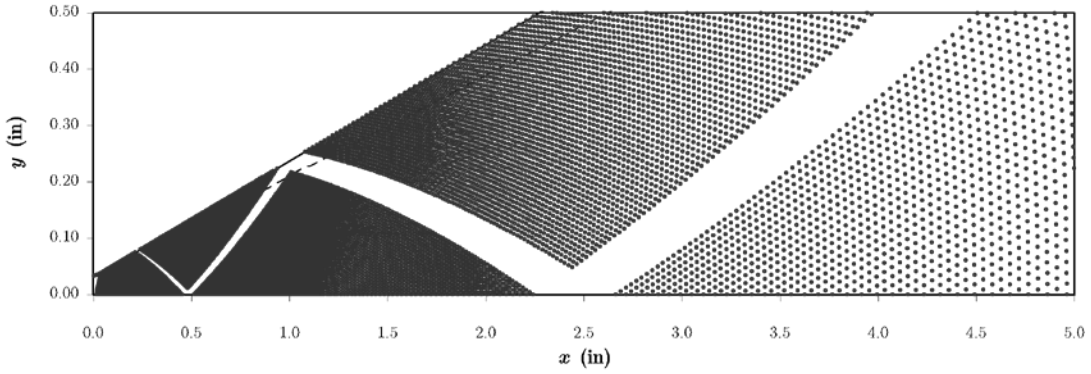

Figure F-42: Throat Region Nozzle MOC (not to scale)

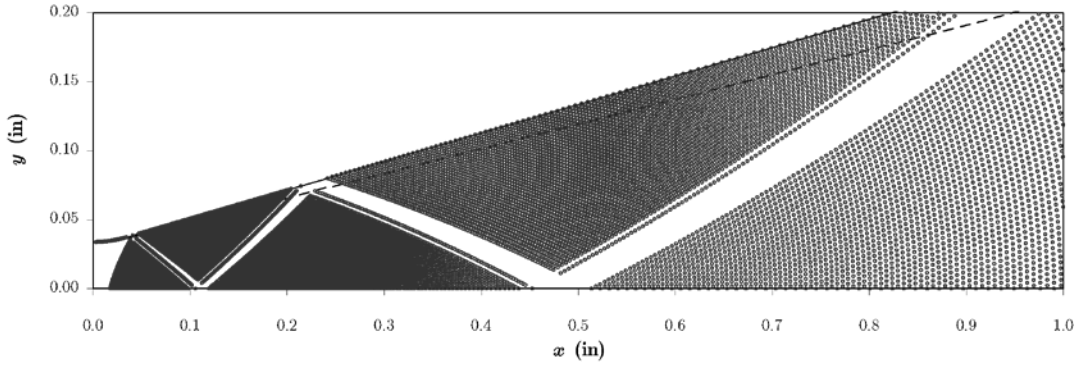

Figure F-43: Zoomed Throat Region Nozzle MOC (not to scale)

As indicated, the maximum core flow region was at x = 101.6 cm (40 inches). Hence, the nozzle was truncated at this location; the local wall angle was 2.0 degrees at this location. To operate the tunnel at lower Mach numbers, the nozzle planes were rotated up. To adjust the Mach number from 7.0 to 5.0 requires a 0.2° rotation. High fidelity CFD simulations demonstrated the exit flow was uniform over a range of 5.0 to 7.0; a contributing factor to the uniform flow was the large number of expansion reflections. The nozzle planes were designed to float between the side walls, with O-ring seals and a flexure was connected to the downstream end. These two measures allowed the nozzle to be actively moved during a tunnel run in the future. The flow response time, estimated as the nozzle length divided by the speed of sound, was on the order of 5 – 10 msec.

The nozzle flow was computed using the GASP flow solver[67]. GASP was a compressible, structured grid, multi-block code with a suite of integrated turbulence models. The solver had the support for using overlapping grids and time-accurate solutions could be obtained using either explicit or implicit methods. For the static configuration simulations, three different structured grids corresponding to M = 5, 6 and 7 were generated using the Gridgen software package[68]. The flow domain starts at the throat of the nozzle and includes only one-quarter of the total nozzle cross-section. This is possible due to the symmetry of the nozzle in the lateral and transverse directions. The static flow conditions at the throat were specified at the inlet boundary condition. Adiabatic wall conditions were used on the nozzle internal surfaces and extrapolation boundary conditions were specified at the exit. Symmetry boundary conditions were

used on the lateral and transverse symmetry planes. The simulations were performed using both parabolic and elliptic methods. Turbulence effects were simulated using the one-equation[69], two-equation models[70] and Wilcox's stress-Reynolds stress transport model[71]. Sample Mach number contour results for the M = 5 case are shown in Figure F-44 while results for the M = 7 case are shown in Figure F-45. The grey scale contours in the lateral and transverse cross-sectional plane shows contours of density gradient. Mach number profiles for the M = 7 case are given in Figure F-46 and are for the exit plane in both directions of symmetry.

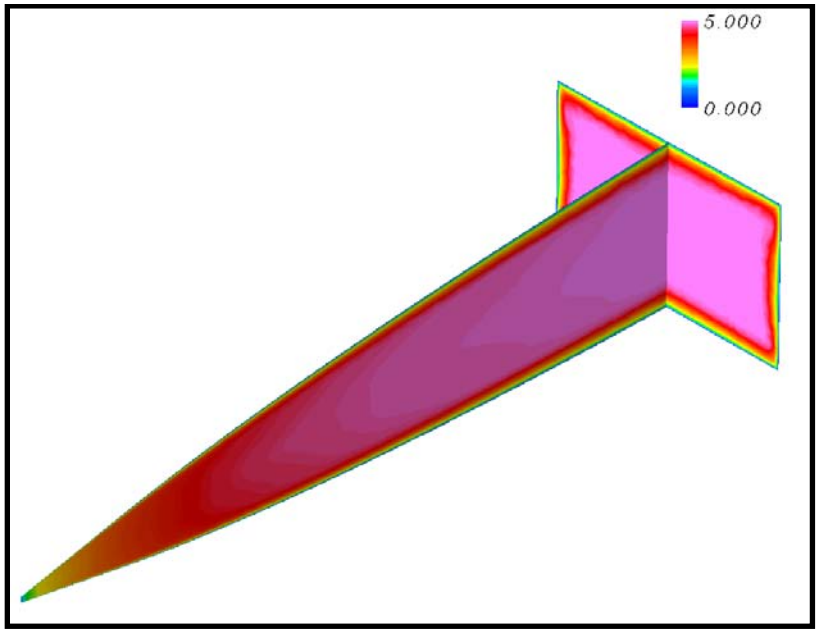

Figure F-44: Mach 5.0 Nozzle CFD Results

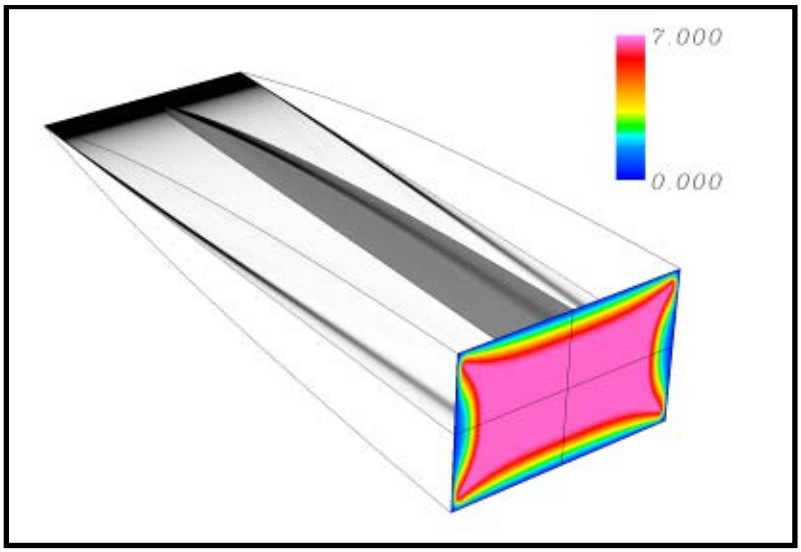

Figure F-45: Mach 7.0 Nozzle CFD Results

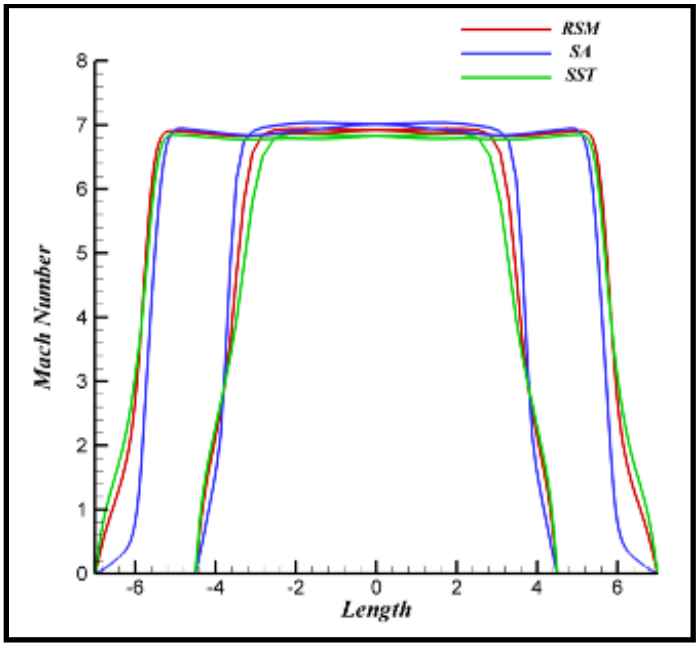

Figure F-46: Mach 7.0 Nozzle CFD Exit Mach Number Profile Results

The actuating ACE nozzle was also simulated using the GASP flow solver. A two-dimensional grid composed of two blocks was generated using Gridgen. The primary block was the nozzle domain and the second block was the overlapping block used for interpolation. The two blocks are shown in Figure F-47 where the nozzle block is in black and the overlap block is shown in red. Only one half of the nozzle domain was simulated, as the flow was considered symmetric about the nozzle centerline. Choked conditions at the throat were specified at the inlet of the overlapping block and symmetry conditions were specified for the overlapping block at the tunnel centerline.

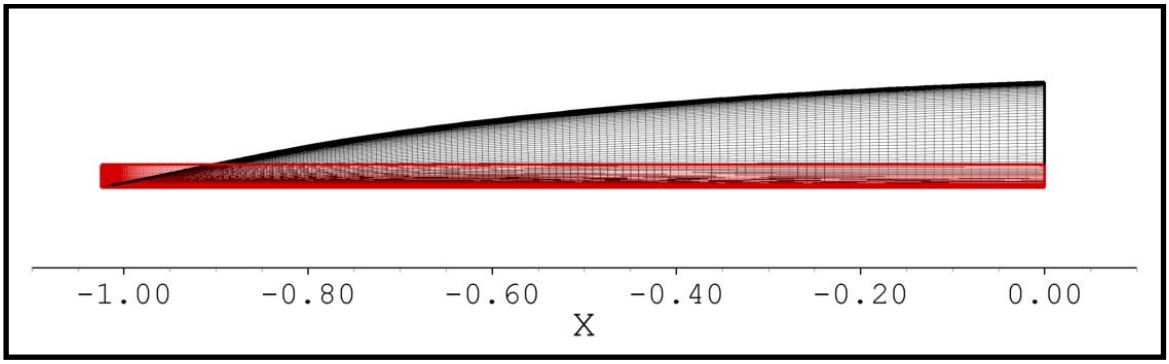

Figure F-47: Two-dimensional grid for the nozzle.

The corresponding surfaces of the nozzle block were set using interpolation from the overlapping block. Adiabatic wall conditions were used for the nozzle wall and extrapolation was applied at the nozzle exit. Turbulence was modeled using Menter's two-equation SST model[70]; the implicit method was used for time integration. A sinusoidal oscillation with a frequency of 10 Hz was used in the simulations and new interpolation coefficients were computed at every 10th time step of the simulation.

The results from a half-cycle of the simulation are shown in Figure 226. At the beginning of the cycle, the throat of the nozzle was at the minimum point, i.e., the exit Mach number was at a maximum. As the cycle progressed, the nozzle block was subjected to solid-body rotation, at the specified rate, about the wall point on the exit plane. Information was interpolated between the nozzle block and the overlapping block at each time step. The change in Mach number can be seen in the sequence of images in Figure F-48. The line plot of the Mach number at the exit plane of the nozzle is also shown. As expected, the Mach number varied from ~7 to ~5 during the half-cycle.

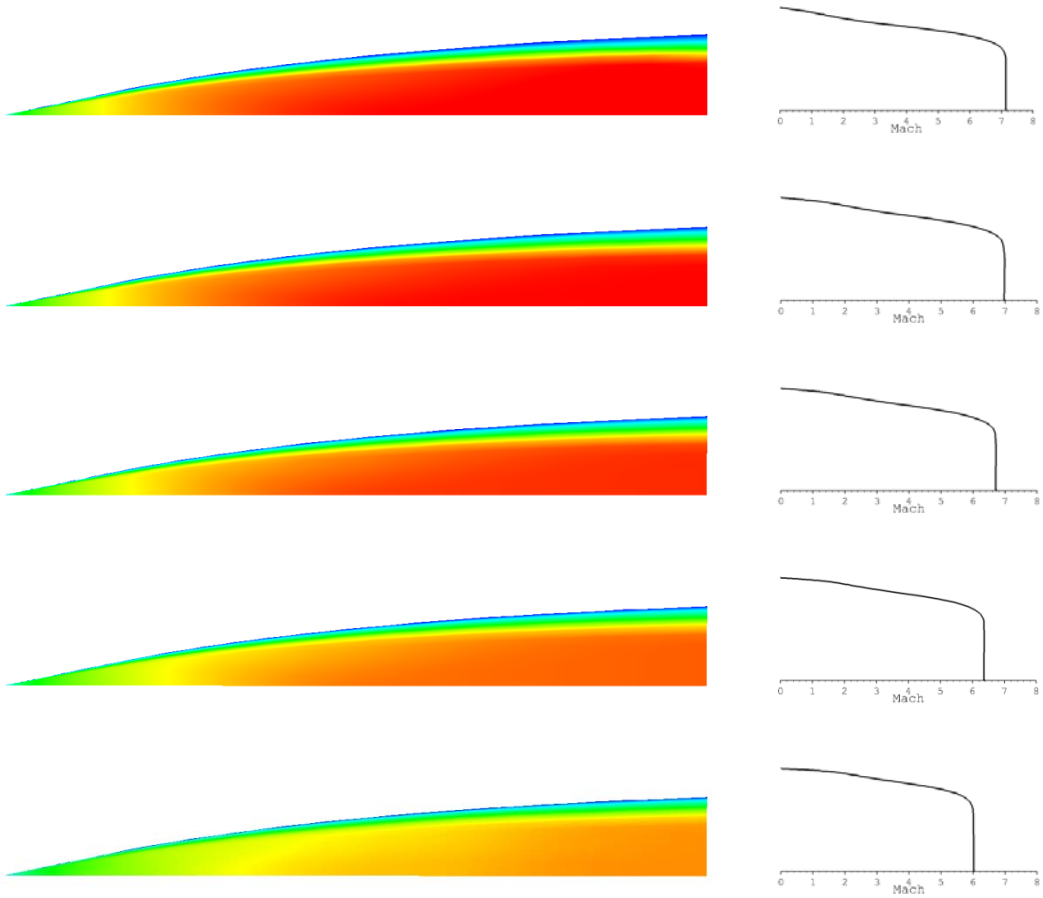

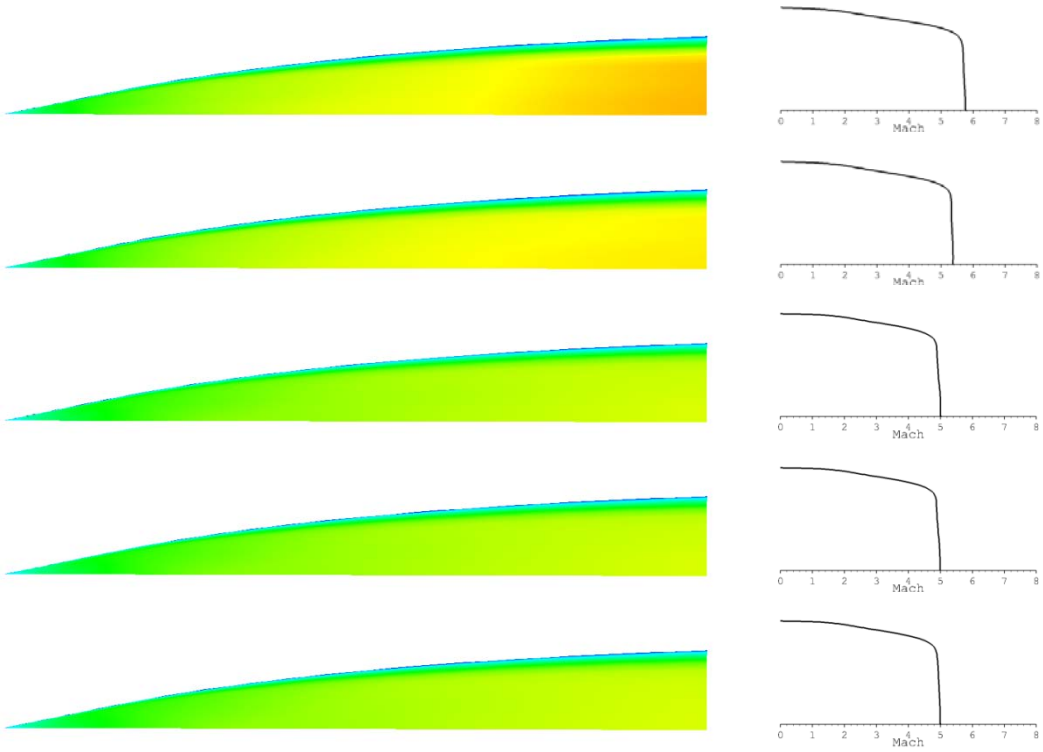

Figure F-48: Contours of the Flow Mach Number in the Nozzle During Actuation

The mechanical realization of the CFD results was designed entirely in-house at Texas A&M University. The final nozzle plane geometry was imported directly into the SolidWorks and the planes were machined from solid plates of type 304 stainless steel on a CNC milling machine. A SolidWorks drawing of the ACE nozzle plane is shown in Figure F-49.

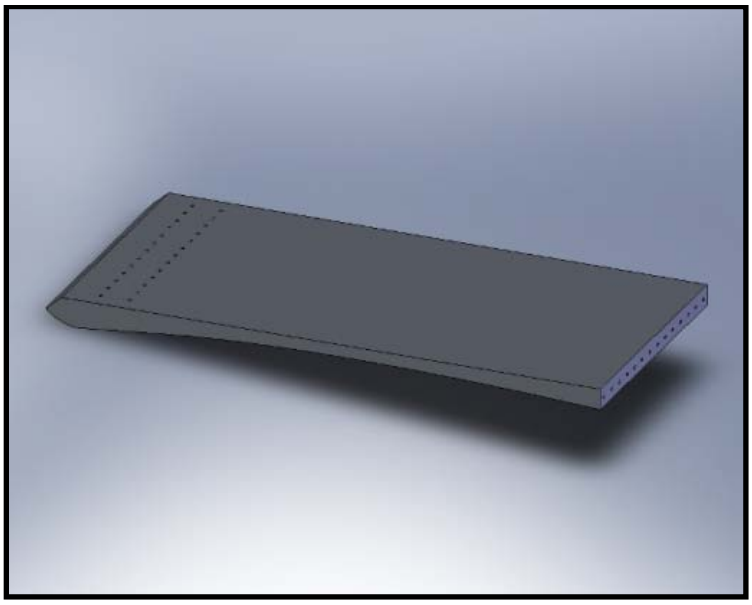

Figure F-49: SolidWorks Drawing of Nozzle Plane

After the initial machining, the planes were carefully examined using an Infinite series Cimcore/Romer portable coordinate measuring machine (CMM) model 5024, shown in Figure F-50 and was compared to the original geometry. Any deviations from the original design were then removed with a second fine-machining pass. A picture of the fabrication of the nozzle plane using the CNC milling machine is shown in Figure F-51.

Figure F-50: Cimcore/Romer CMM

Figure F-51: CNC Machining of ACE Nozzle Plane

The sidewalls of the ACE nozzle were made from type 304 stainless steel plates that sealed the nozzle by compressing the O-rings embedded in the edges of the nozzle planes. A SolidWorks drawing and a photograph of the nozzle assembly is shown in Figure F-52 and Figure F-53. The inclusion of the O-rings on the planes themselves allowed the planes to move when switching Mach number without breaking the overall seal.

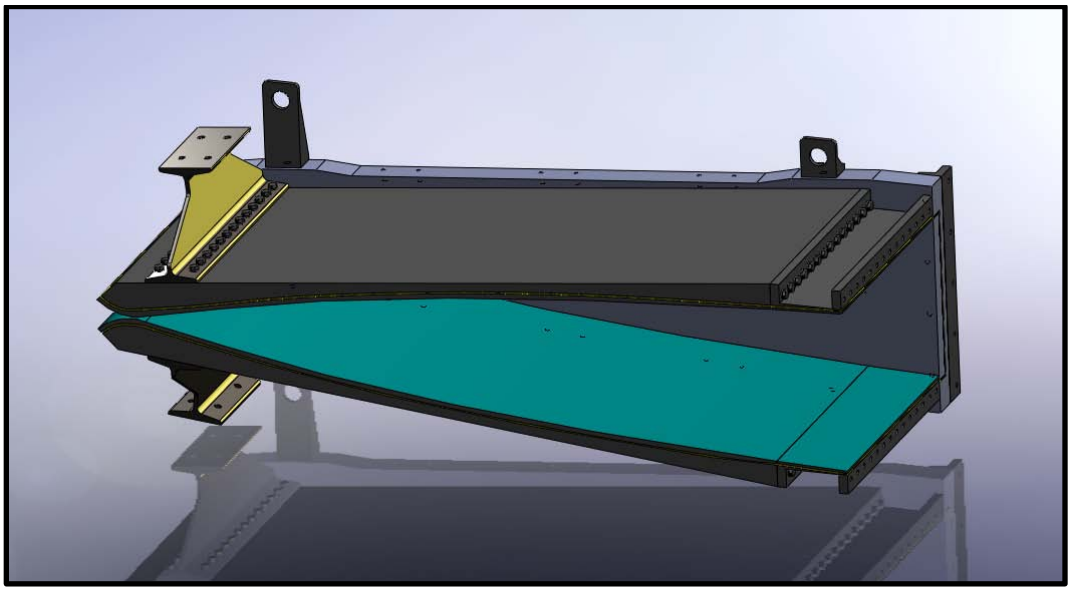

Figure F-52: SolidWorks Drawing of Nozzle Assembly

Figure F-53: Picture of Nozzle Assembly

To ensure a complete seal and for an added measure of safety, the sidewalls were clamped together using 5.08 cm x 7.62 cm (2 inch x 3 inch) steel rectangular tubing and 3.175 cm (1.25 inch) threaded rod shown in Figure F-54.

Figure F-54: ACE Nozzle Clamps

The ACE nozzle was designed such that the Mach number is varied by adjusting the throat height of the nozzle; the exit dimensions are constant regardless of the condition being tested. To achieve this result, the flexure shown in Figure F-55 was designed.

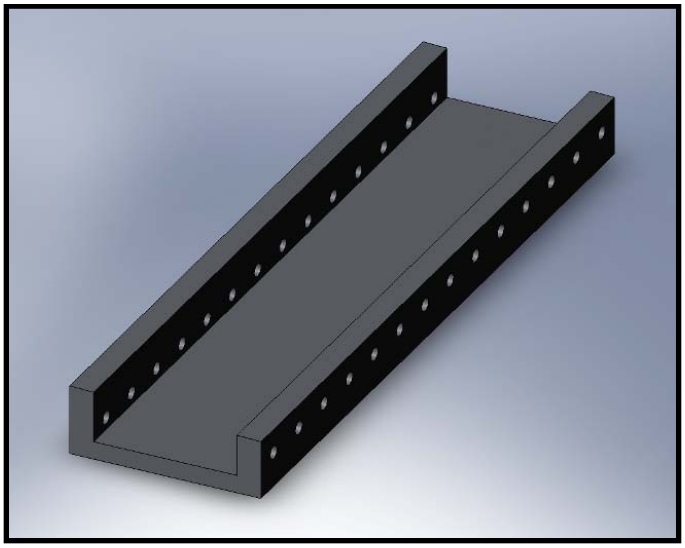

Figure F-55: SolidWorks Drawing of Nozzle Flexure

This flexure was fixed to the exit of the nozzle plane and to the nozzle frame, and bends such that the throat section of the nozzle is allowed to move while the exit section is bolted in place. A SolidWorks drawing of a flexure connected to a nozzle plane is shown in Figure F-56 and a photograph of the nozzle throat fixture with fixed shims is given in Figure F-57.

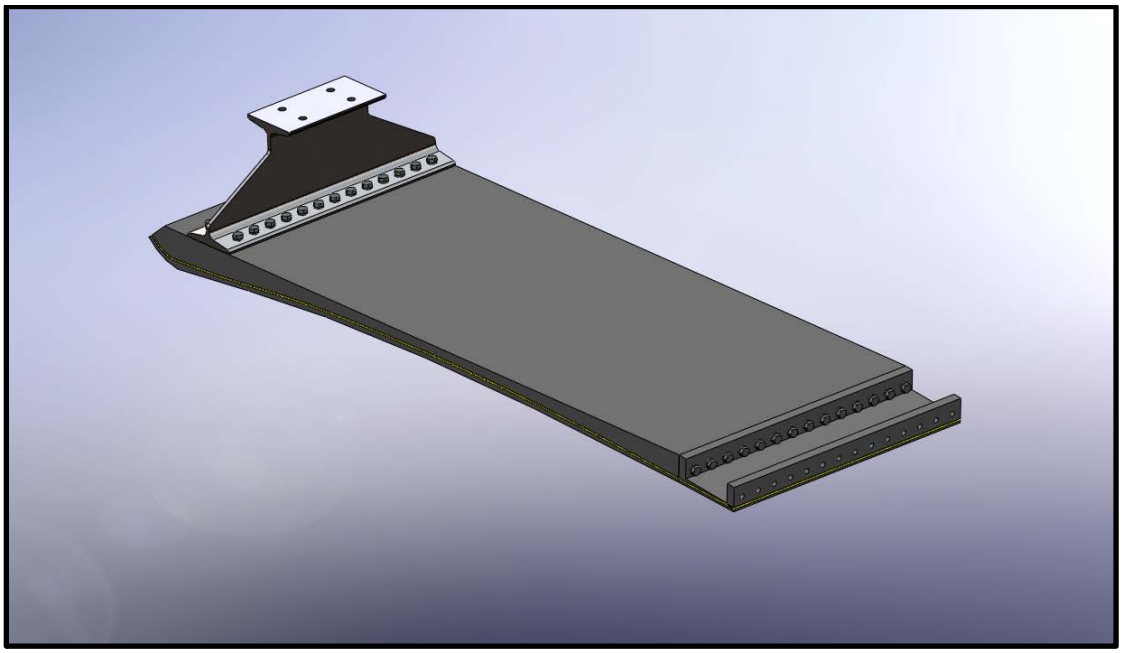

Figure F-56: SolidWorks Drawing of Nozzle Flexure and Plane

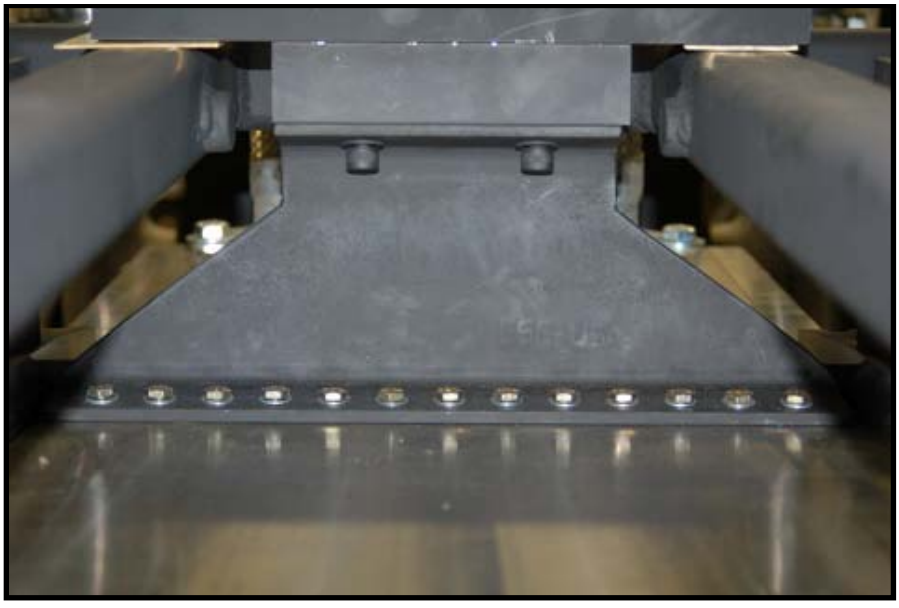

Figure F-57: Nozzle Throat Fixture with Fixed Shims

To align and calibrate the nozzle for testing, the centerline was first carefully determined through laser alignment. A JDS Uniphase Helium : Neon laser model 1507-1 was mounted to laboratory mounts and rails which were connected to the nozzle alignment plate. The entire setup was mounted to a scissor jack and is shown in Figure F-58. The laser mounting system was verified to be level and plumb relative to the nozzle frame before calibration.

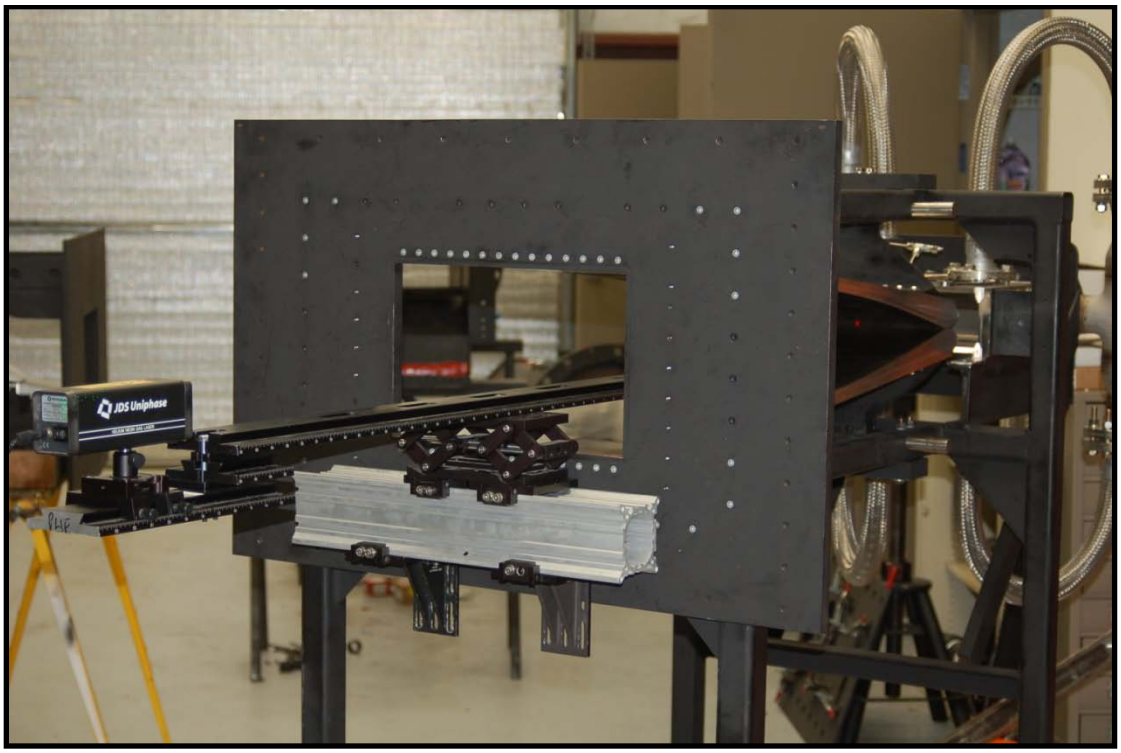

Figure F-58: Laser Nozzle Alignment Setup

The nozzle plains were then lowered using brass shims until the two sides barely touched. The laser beam was verified to be centered at the nozzle throat which is shown

in Figure F-59. Careful measurements of the shims were made and new nozzle blocks were machined from carbon steel. The blocks were designed to allow the nozzle plains to touch at the centerline when shims were not added to the system. With this calibration, the nozzle throat height was set to a known value by simply adding shims that were half the throat height to each nozzle plain.

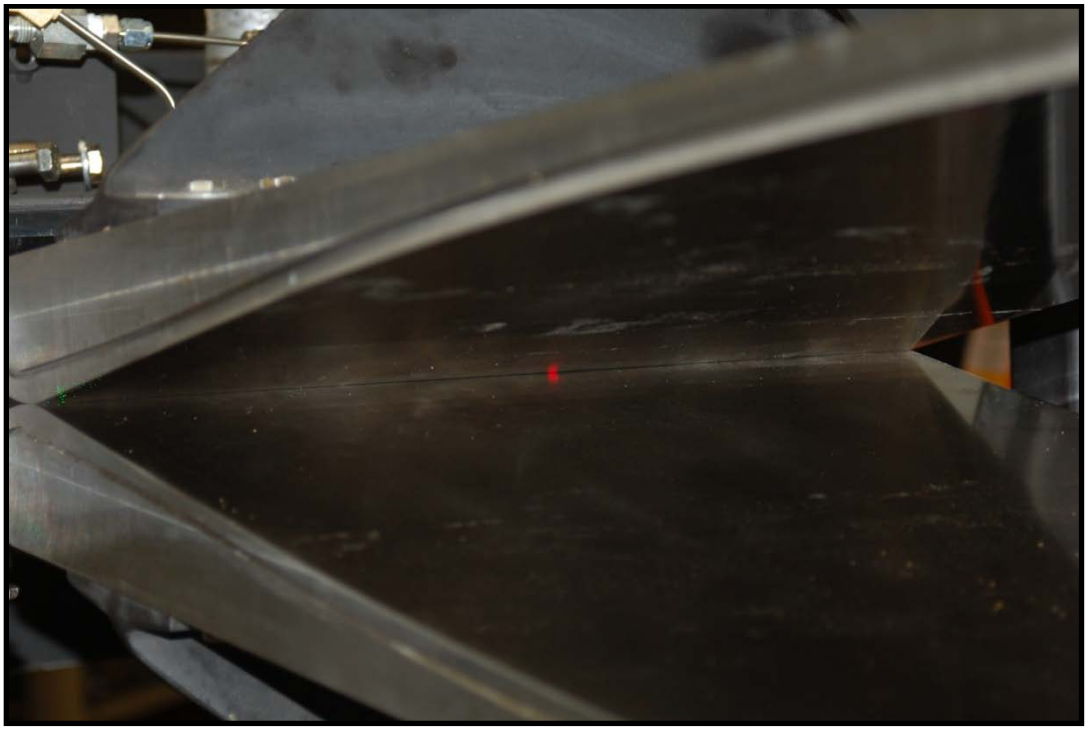

Figure F-59: Alignment Laser Beam at Nozzle Throat

The nozzle was contained entirely on a custom-designed frame made from 5.08 cm (2 inch) carbon steel square tubing with a 0.64 cm (0.25 inch) wall thickness. The frame supported the nozzle assembly, front alignment plate, settling chamber, and air delivery manifold. A SolidWorks drawing of the frame is shown in Figure F-60.

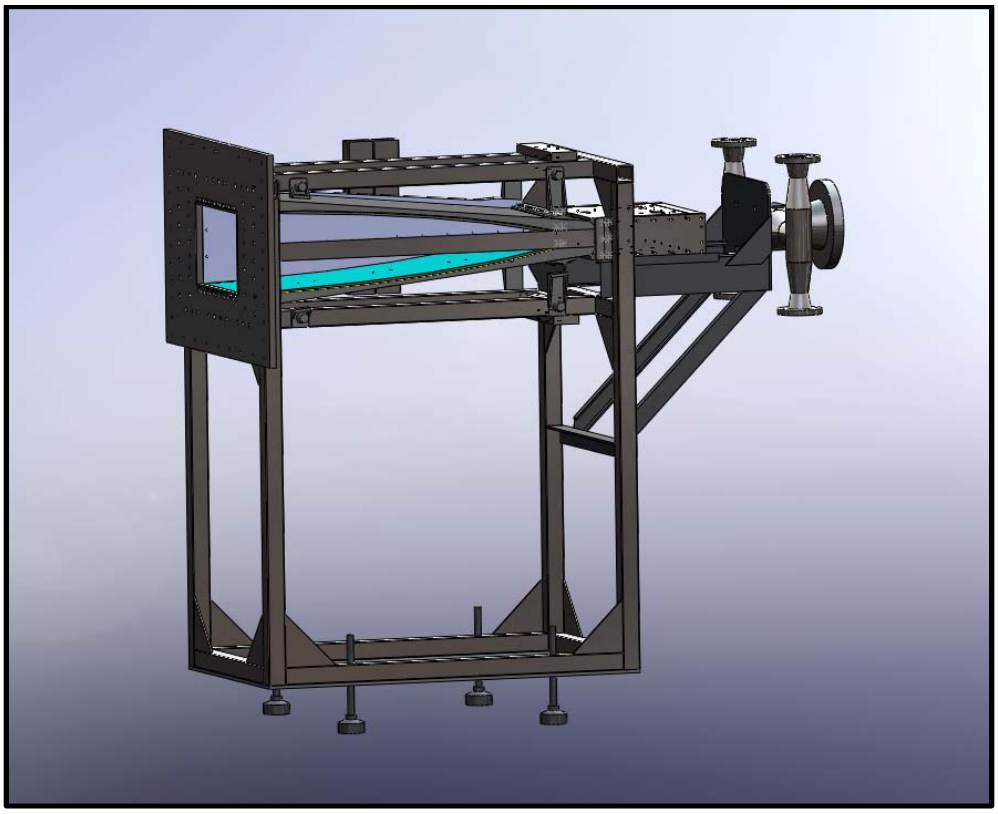

Figure F-60: SolidWorks Drawing of ACE Nozzle Frame

Originally, swivel feel were mounted to the base of the nozzle stand. This configuration allowed for height adjustment but did not allow for lateral movement. This proved to make alignment of the nozzle to the test section extremely difficult. To fix this problem, heavy duty industrial casters (Model 50) were purchased from Caster City. They were 15.24 cm (6 inch) diameter casters made from ductile steel. Two casters were swivel casters and two were V groove rigid casters and each caster had a maximum load capacity of 1591 kg (3500 lbs). Sample pictures of both styles are shown in Figure F-61.

Figure F-61: Nozzle Stand Caster Styles

To ensure proper alignment, a 121.92 cm (48 inch) long piece of 3.81 cm x 3.81 cm x 0.64 cm (1.5 inch x 1.5 inch x 0.25 inch) carbon steel angle was welded approximately 15.24 cm (6 inches) from the long edge of a 1.22 m x 2.44 m (4 feet x 8 feet) sheet of 0.95 cm (0.375 inch) carbon steel. This sheet was then anchored to the concrete floor of the laboratory in the correct location to allow proper alignment of the nozzle to the rest of the high speed experimental facility. A picture of the nozzle stand on the steel caster plate is shown in Figure F-62. This final caster configuration allowed the nozzle to be unbolted from the facility and manually separated while maintaining proper alignment and positioning.

Figure F-62: Nozzle Stand on Steel Caster Plate

Once the settling chamber was placed on the nozzle support stand, a spring system was designed to maintain the seal between the settling chamber and nozzle. The spring clamps were made from 7.62 cm x 7.62 cm x 0.635 cm (3 inches x 3 inches x 0.25 inches) carbon steel angle. Three 0.95 cm (0.375 inch) holes were drilled in each piece of the angle and 3/8”-16 nuts were welded over the holes. The angle was bolted to the sides of the settling chamber and the nozzle with a designed 0.635 cm (0.25 inch) space in between. Socket head bolts were then used to clamp the two pieces of angle iron together which was able to maintain the necessary force needed to seal the settling chamber and nozzle interface. A picture of the spring clamp system is shown in Figure F-63 and a photograph of the nozzle with one of the side plates removed is given in Figure F-64.

Figure F-63: Settling Chamber / Nozzle Spring System

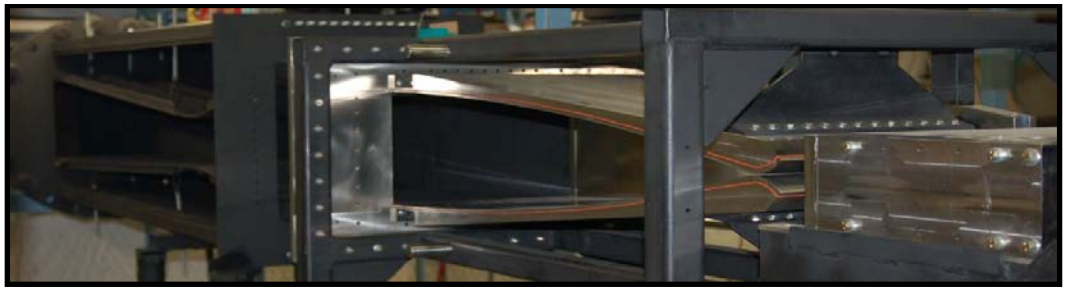

Figure F-64: Open View of Installed ACE Nozzle with Embedded O-Ring

Calibration Test Section Design

For the initial calibration experiments, a surrogate test section was designed to measure exit Mach number of the nozzle. As Figure F-65 shows, the test section was 35.56 cm (14.0 inches) wide, approximately 60.96 cm (24.0 inches) long and continued the 2° divergence angle of the nozzle exit to avoid compression waves which would have resulted from parallel walls. The test section upper and lower frames were

constructed of 5.08 cm x 5.08 cm x 0.635 cm (2 inches x 2 inches x 0.25 inches) carbon steel square tubing welded to 35.56 cm x 60.96 cm x 0.95 cm (14 inches x 24 inches x 0.375 inches) carbon steel plates. Thru holes were drilled in the square tubing every 5.08 cm (2 inches) to accommodate 1/4”-20 fasteners for installation. A SolidWorks drawing of a tubing frame section of the calibration test section is shown in Figure F-65.

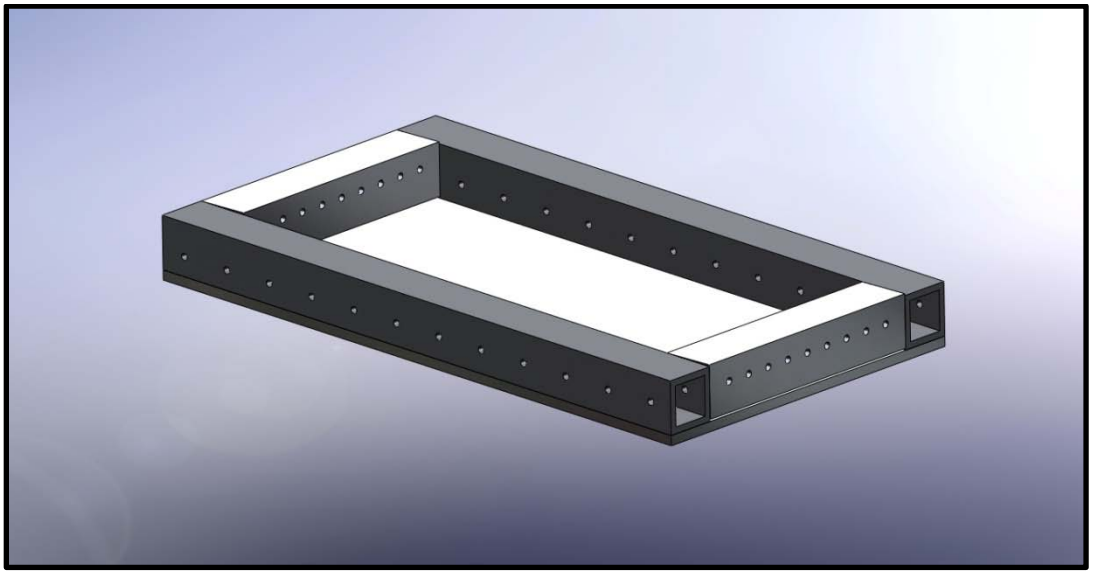

Figure F-65: Calibration Test Section Tubing Frame

The side plates of the calibration test section were fabricated from 0.95 cm (0.375 inch) carbon steel plate and 0.64 cm (0.25 inch) holes were drilled near the upper and lower edges to attach the upper and lower frame sections. To seal the test section, 0.32 cm (0.125 inch) O-ring grooves were also machined on the inner surfaces of the side plates, seen in Figure F-66.

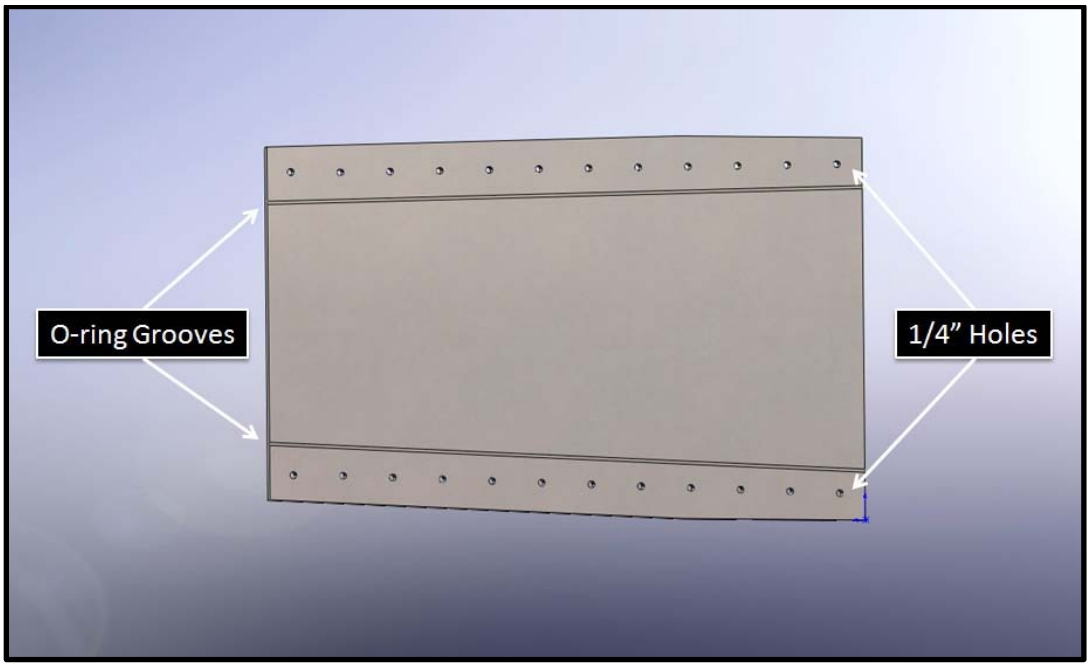

Figure F-66: Calibration Test Section Side Plate

One issue with this design that was discovered later was the test section/diffuser interface. The final experimental test section was designed to have a 30.48 cm (12.0 inches) exit height, but for simplicity and abbreviated length, the calibration test section had approximately a 25.4 cm (10.0 inches) exit height. It was discovered that the continued divergence of the test section and the abrupt 2.54 cm (1.0 inch) step on each side of the interface increased the entrance Mach number of the diffuser greatly and thereby decreased its performance. To compensate for this, false floors were fabricated from 0.64 cm (0.25 inches) carbon steel plate welded to 0.79 cm (0.3125 inches) carbon steel round bar. The false floors were bolted to the diverging test section walls to change the 2° divergence angle to a straight and parallel cross section, thereby limiting the Mach number. These plates extended from approximately the center of the test section to

30.48 cm (12.0 inches) inside of the diffuser. The full test section, including the false floor plates can be seen in an exploded view in Figure F-67 and assembled in Figure F-68.

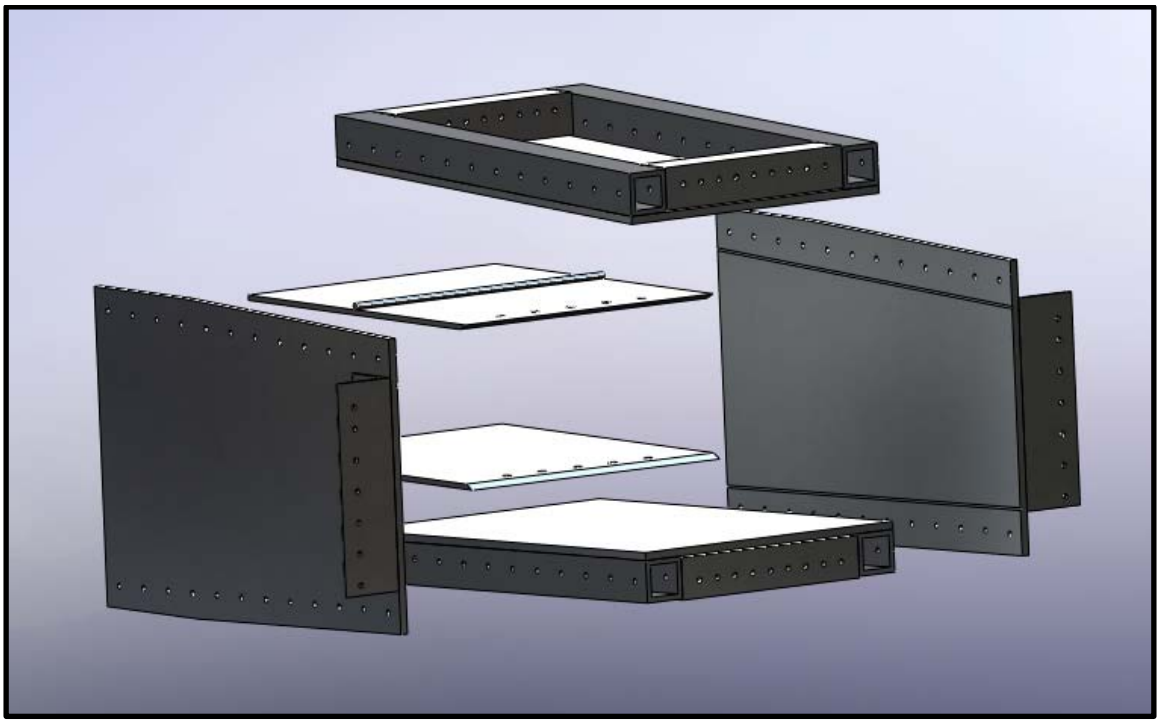

Figure F-67: Calibration Test Section (Exploded View)

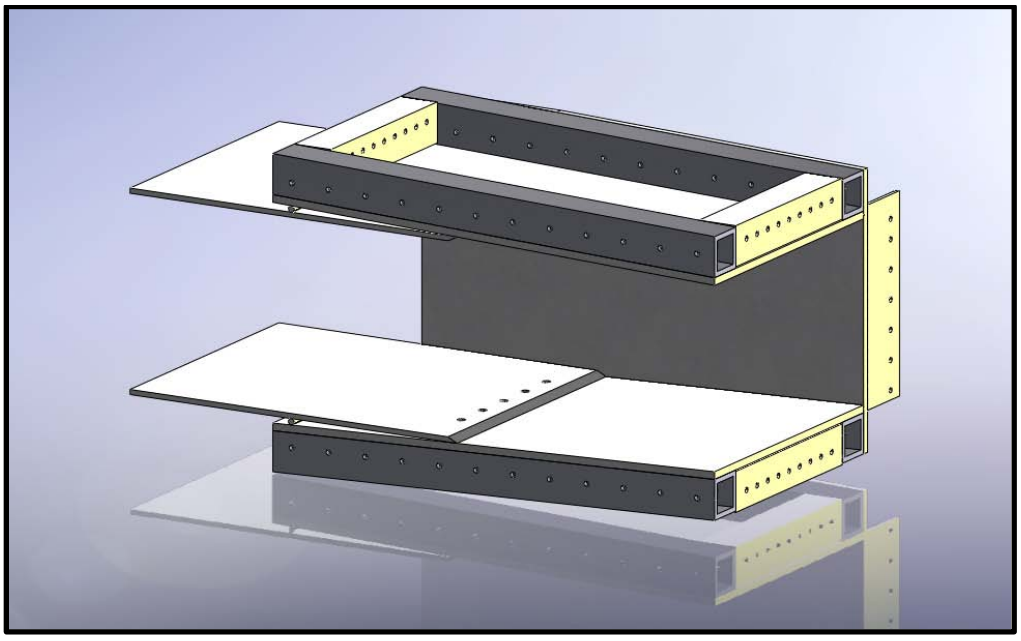

Figure F-68: SolidWorks Drawing of Calibration Test Section

Approximately 20.32 cm (8 inches) from the nozzle exit, a pitot (stagnation) probe was installed into the centerline of the tunnel from the ceiling and a static port was added in the floor. The test section was then sealed with a combination of silicone O-rings, RTV, and JB Weld along the seams connecting the nozzle and test section interface. The calibration test section mounted in the ACE tunnel is shown in Figure F-69.

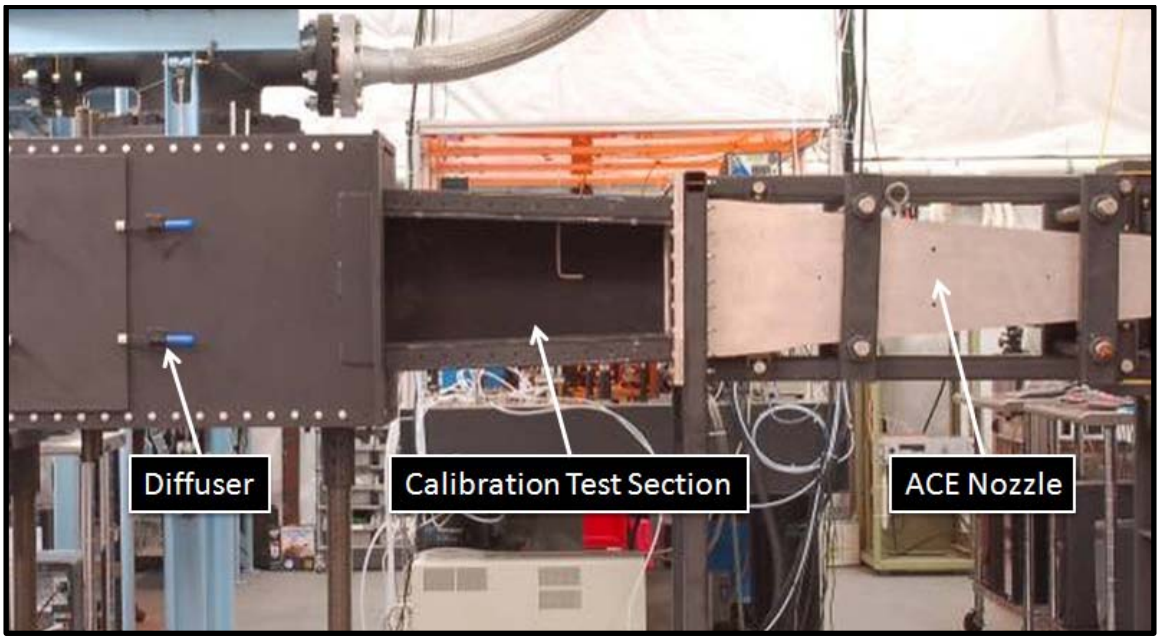

Figure F-69: Calibration Test Section Connected to ACE Nozzle and Diffuser

SISL Test Section Design

To perform the original shock induced shear layer experiment, a new test section for the high speed experimental facility was designed and constructed. The contours of the upper and lower surfaces of the test section were designed using CFD tools to maximize tunnel efficiency when the SISL model was installed. The use of the CFD simulations allowed for iteration is the design of the test section before every cutting metal. The CFD results from the design of the SISL test section are discussed below in the SISL model section.

Based on the CFD simulation results, the dimensions of the SISL test section were finalized. In order for ACE tunnel to start properly with the large SISL model installed, the test section had to be designed specifically for the SISL model. This

resulted in unconventional test section construction. The profile of the internal contour of the SISL test section is shown in Figure F-70. Immediately after the nozzle, the upper and lower walls of the test section continue the 2° divergence angle seen at the end of the nozzle geometry. The upper surface has an initial section that is 13.87 cm (5.46 inches) long then opened sharply with a 17.96 cm (7.07 inches) section at 18°. After the sharp rise, the upper surface of the test section ended with a section that was 43.79 cm (17.24 inches) long at 3° below horizontal. The lower surface of the test section was composed to two sections. First, a 50.57 cm (19.91 inches) long section at 2° followed by a 24.16 cm (9.51 inches) section at 4.37°. This geometry allows the test section inlet height match the nozzle exit height of 22.86 cm (9.0 inches) and test section exit height to match the diffuser inlet height of 30.48 cm (12.0 inches).

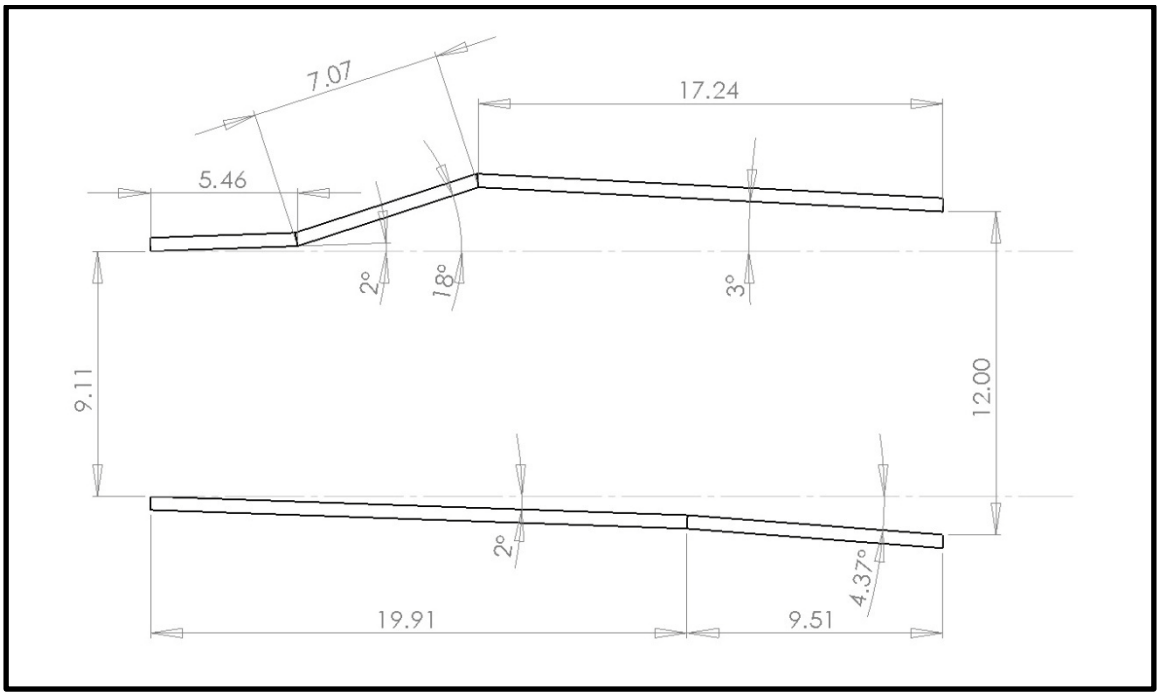

Figure F-70: Profile of SISL Test Section Contour

The CFD simulations showed the need for the upper wall to rapidly open in order to create a strong expansion region of the flow which aided in sucking the messy flow created from oblique shock waves off of the SISL model downstream into the diffuser. The particular design was chosen to allow proper inlet and exit dimensions as well as to accommodate a sufficient SISL model size.

Once the test section design was finalized, fabrication began. The test section was approximately 77.47 cm (30.5 inches) long from flange to flange. The test section surfaces were constructed of 1.27 cm (0.5 inch) carbon steel plate and were cut using a water jet cutter system. This system allowed accurate production of two-dimensional parts with high tolerances. Large cutouts were cut into the side plates as well as 1” holes

near the upper and lower edges. The cutout areas were designed to allow for installation of the SISL model and to allow for a large opening for internal tunnel access. The 2.54 cm (1.0 inch) diameter holes were cut to accommodate 2.54 cm (1.0 inch) threaded rod that was used to close the test section walls. In order to seal the test section, 0.48 cm (0.1875 inches) wide O-ring grooves were machined into the outside surface of each test section side plate, which can be seen in Figure F-71.

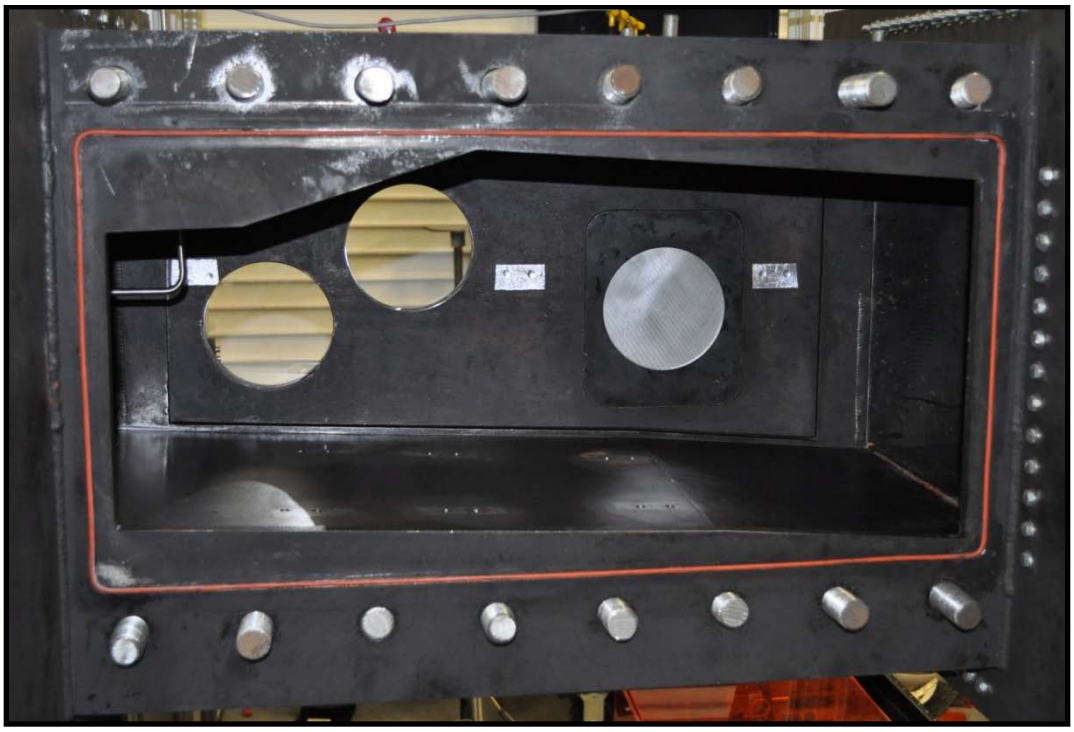

Figure F-71: SISL Test Section Side Plate

The lower surface of the SISL test section was constructed of two carbon steel plates. To ensure proper fit, these pieces were cut using a water jet cutter as well. The upper surface of the SISL test section was contracted of a small solid carbon steel plate,

followed by a plate in which a window access port was machined. This access port was designed to accommodate a 10.16 cm (4 inch) optical glass flat. A lip that had an internal diameter of 8.89 cm (3.5 inches) and was 0.32 cm (0.125 inches) thick was machined into the plate on which the window rested. To maintain an air tight seal, a 0.48 cm (0.1875 inches) O-ring grove was machined into the internal perimeter of the access port. A retaining frame was designed and fabricated to mount into the access port using 10 #10-24 bolts. The retaining ring also had a lip with a 8.89 cm (3.5 inches) diameter that was 0.64 cm (0.25 inches) thick to hold the window tight. The access port and the retaining ring are shown in Figure F-72.

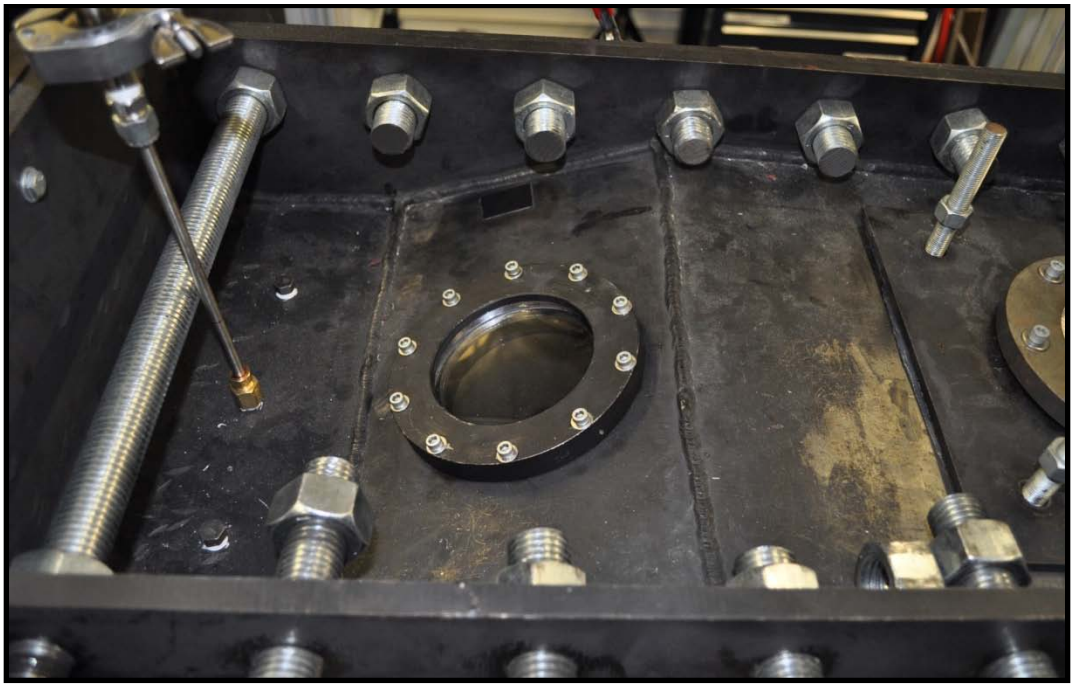

Figure F-72: 4" Window Access Port and Retaining Ring

The final plate for the upper test section surface was cut to size and included a large opening for a pressure relief plate. The hole was 15.24 cm (6.0 inches) wide and 20.32 cm (8.0 inches) long and four 3/8”-16 tapped holes were drilled into the plate. A 25.4 cm x 25.4 cm (10 inches x 10 inches) pressure plate fabricated from 0.64 cm (0.25 inches) carbon steel was placed over the plate and held in place by vacuum grease. This prevented the test section from ever pressurizing because it would simply start leaking from this pressure plate.

The side plates, upper and lower surface plates, and the end plates were carefully welded together to ensure proper sealing. These plates are shown in an exploded SolidWorks drawing in Figure F-73 as well as assembled in Figure F-74.

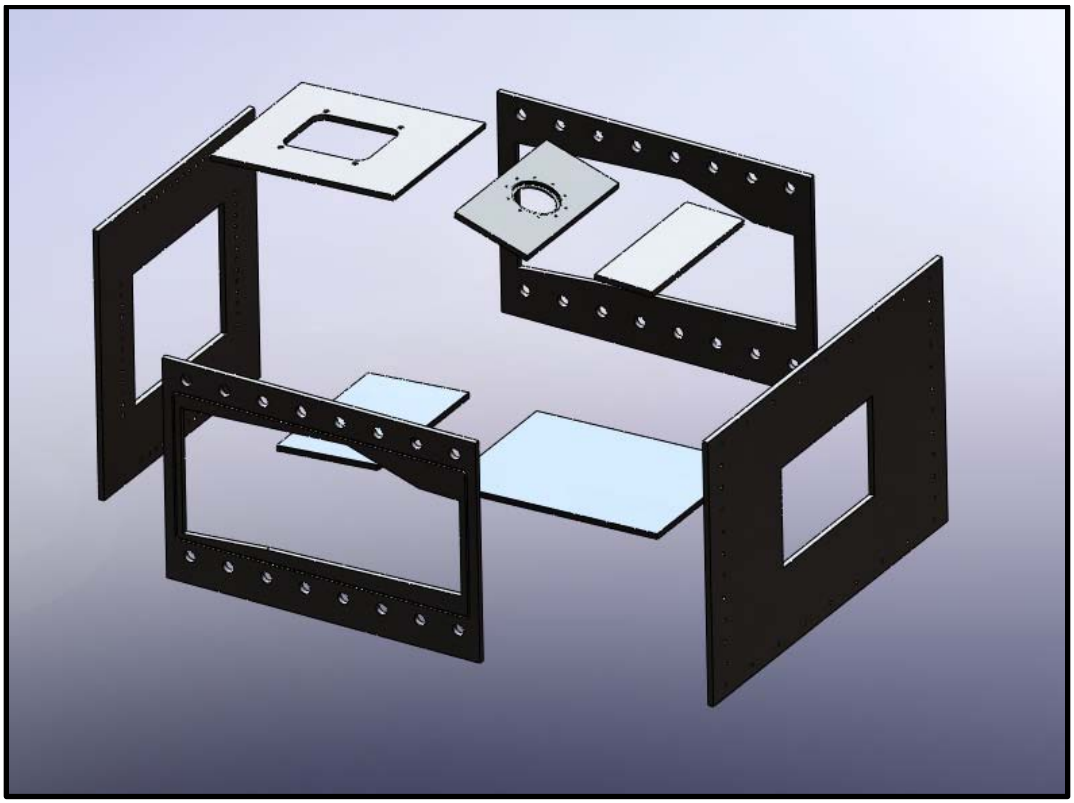

Figure F-73: SISL Test Section Welded Parts (Exploded View)

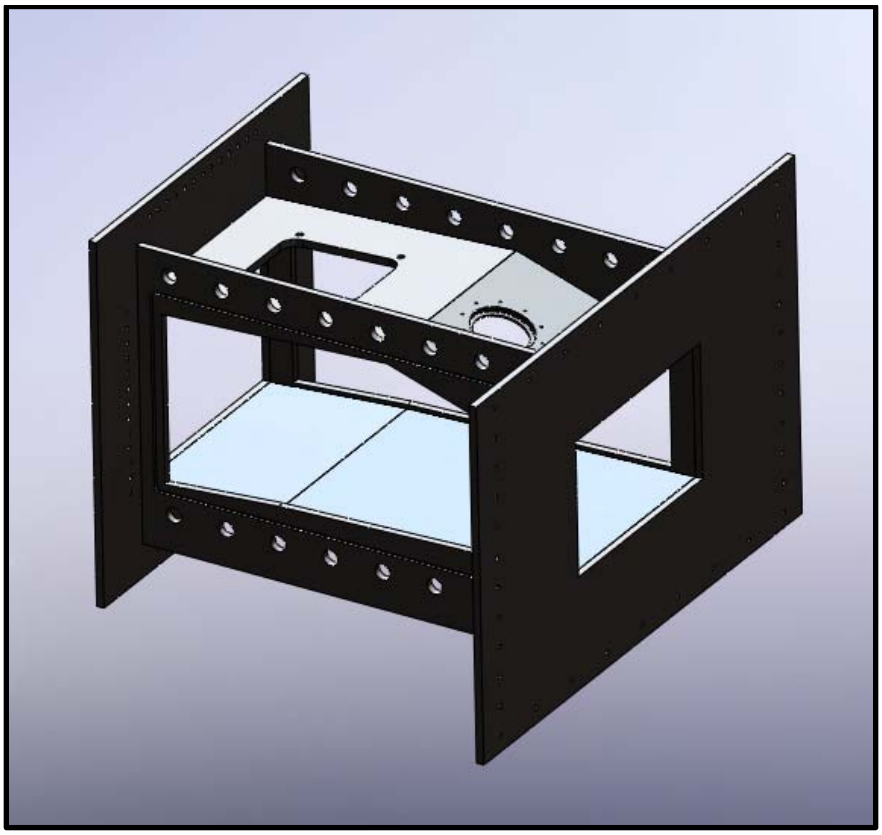

Figure F-74: SISL Test Section Welded Parts

To close the large cutouts in the welded test section walls, side panel plates were designed and fabricated from 1.91 cm (0.75 inches) carbon steel plate. Using a water jet cutter, the two dimensional features of the side panel were cut out, including two window locations, a large 16.51 cm x 20.32 cm (6.5 inches x 8 inches) access hole, and 2.54 cm (1.0 inch) thru holes corresponding to the holes cut into the welded side plates to allow 2.54 cm (1.0 inch) threaded rod from mounting. The two window mounting locations were determined specifically to allow optical access for the SISL model areas of interest. The holes were then machined out to accommodate 15.24 cm (6.0 inches) optical flats following a similar design to the window access location in the upper surface. A 0.32 cm (0.125 inches) lip with an internal diameter of 12.7 cm (5.0 inches) was machined into the plate for each location to allow the windows to rest securely in place. A SolidWorks drawing and a photograph of one of the SISL test section side panels are shown in Figure F-75.

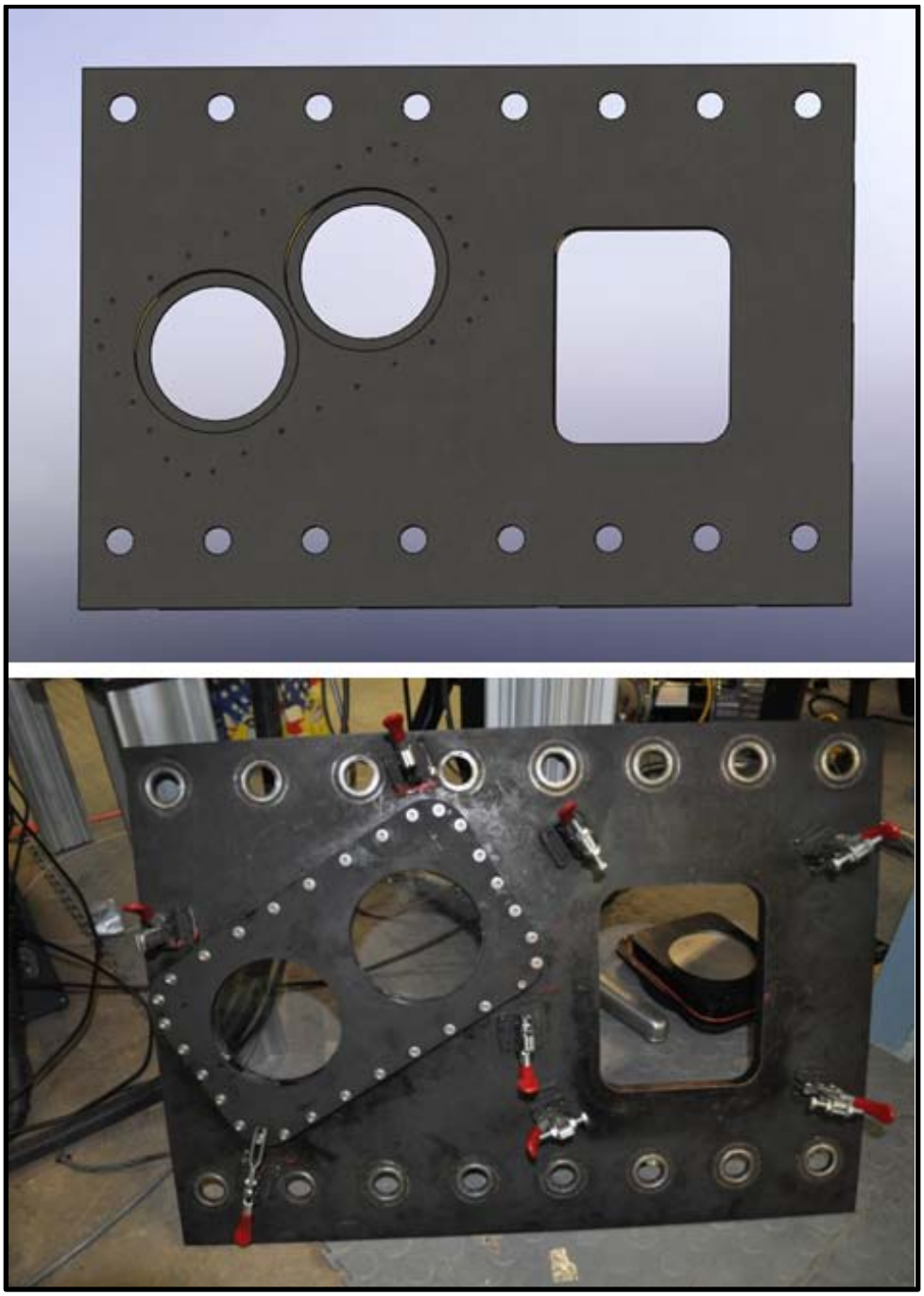

Figure F-75: SISL Test Section Side Panel

Window holders with overall dimensions of 35.56 cm x 20.32 cm x 1.59 cm (14 inches x 8 inches x 0.625 inches) were designed for each side to mount 15.24 cm (6.0 inches) windows to the SISL test section side panels. Lips that were 0.32 cm (0.125 inches) thick with an internal diameter of 12.70 cm (5.0 inches) were used to securely hold the windows in place. To ensure a proper seal, 0.48 cm (0.1875 inches) O-ring grooves were machined into the inner perimeter of the holder rings and a 0.32 cm (0.125 inches) O-ring groove was cut into the holder face that rests against the test section side panel. The holders were mounted to the side panels with 30 #10-24 mounting bolts. A SolidWorks drawing and a photograph of one of the window holders is shown in Figure F-76.

Figure F-76: SISL Test Section Side Panel Window Holder

To seal the access hole in each side panel, access doors machined from carbon steel were designed to fit flush to the inner surface of the test section. The overall dimensions were 24.13 cm x 20.32 cm x 2.86 cm (9.5 inches x 8.0 inches x 1.125 inches). To seal the hole, a 0.48 cm (0.1875 inches) O-ring grove was cut into the surface that presses against the test section side panels. A SolidWorks drawing of the side access door is shown in Figure F-77.

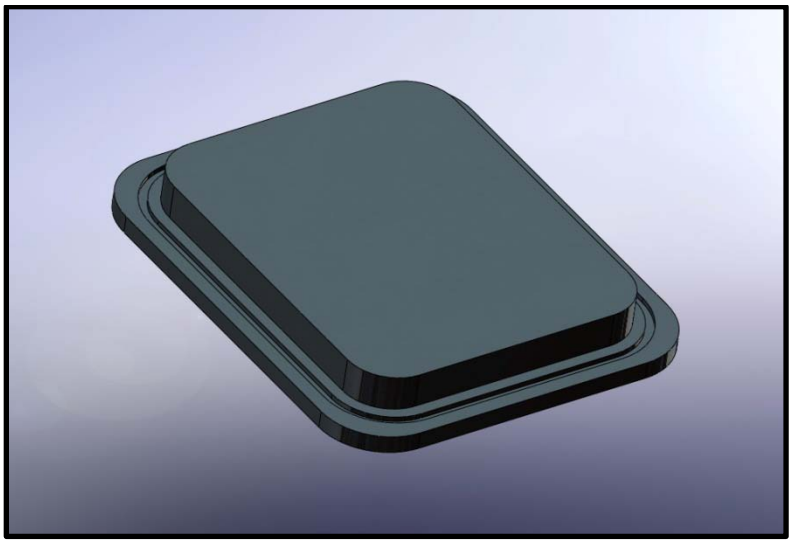

Figure F-77: SISL Test Section Side Access Door

Low profile hold-down clamps were welded around the window locations as well as the access holes to allow the window holders and access doors to be quickly secured without bolts if needed. The clamps had a holding capacity of 80 lbs each and an overall length of 13.97 cm (5.5 inches) and maximum holding height of 1.59 cm (0.625 inches). A technical drawing of the clamps is given in Figure F-78.

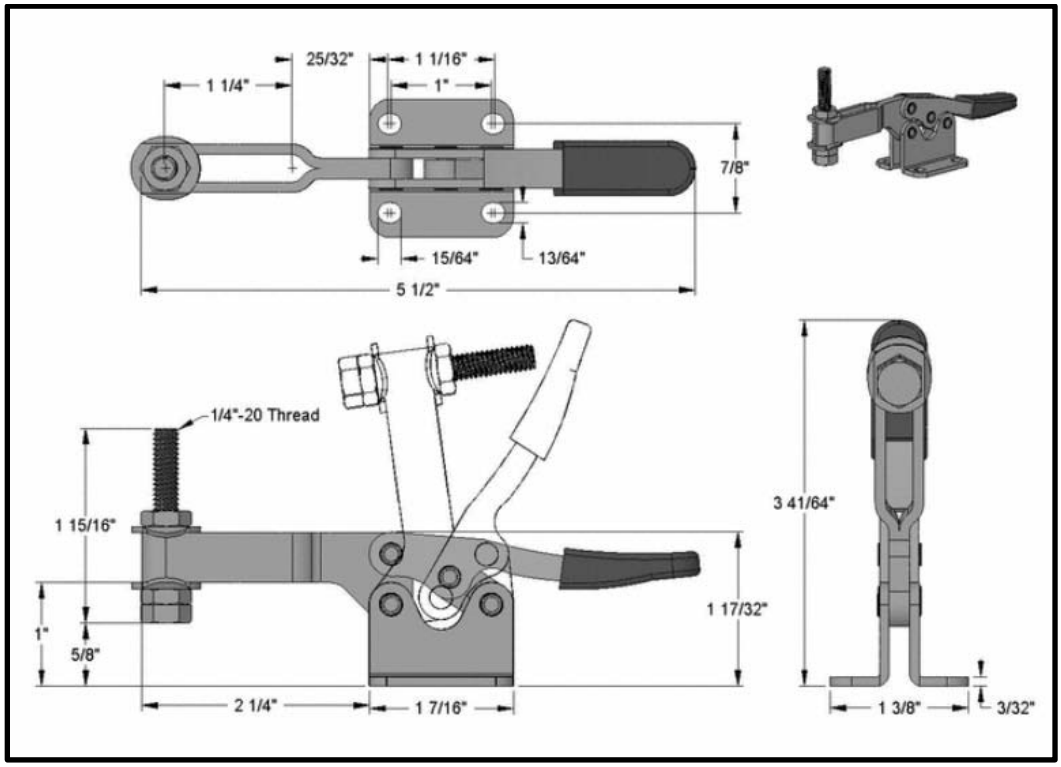

Figure F-78: SISL Test Section Hold-Down Clamp Specifications

A SolidWorks drawing of the assembled SISL test section is shown in Figure F-79 and a picture of the SISL test section mounted in the ACE tunnel is shown in Figure F-80.

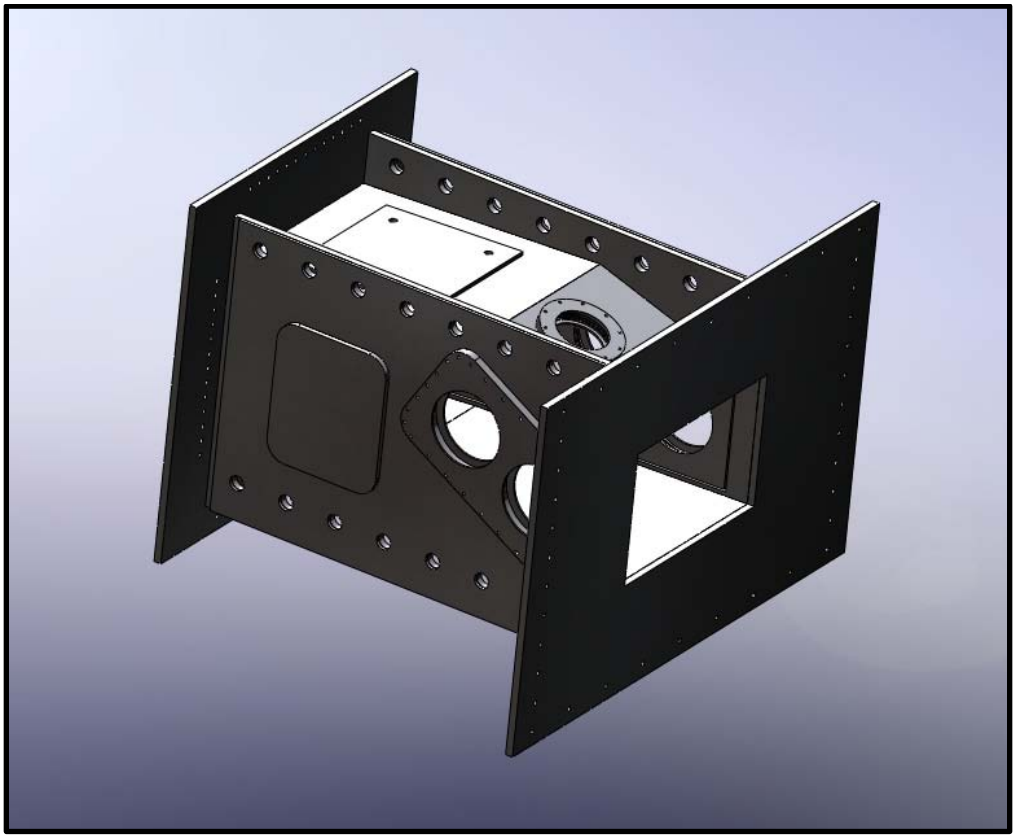

Figure F-79: Assembled SISL Test Section

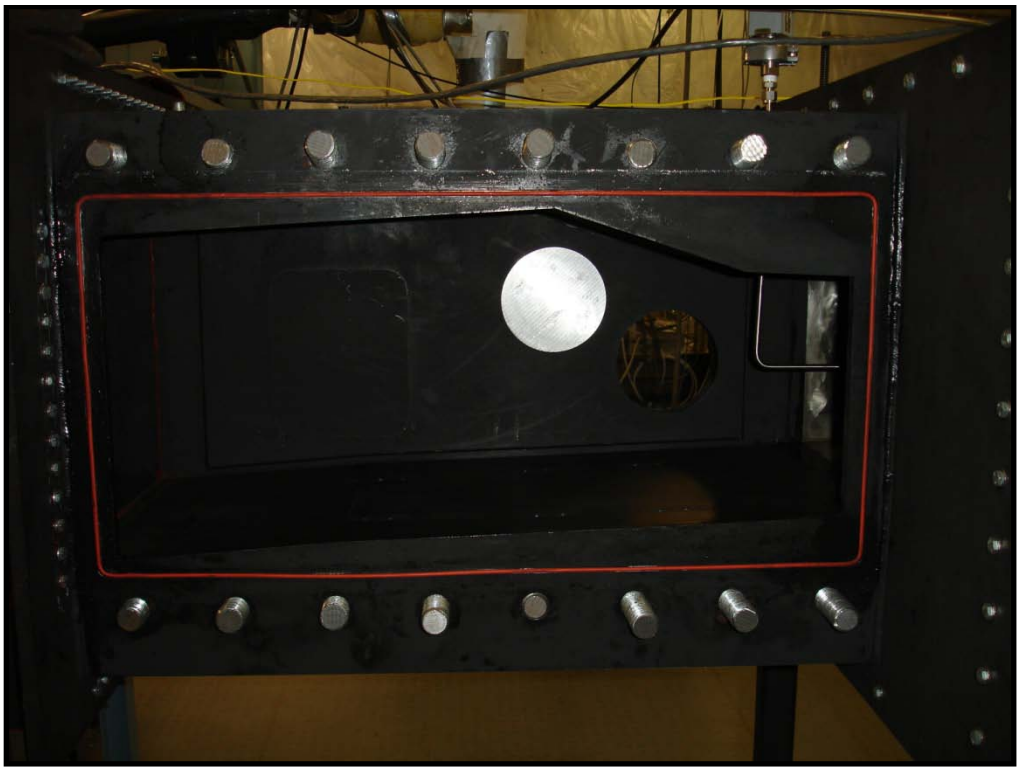

Figure F-80: SISL Test Section in the ACE Tunnel

SISL Test Section Modification

When the shock induced shear layer experiment was abandoned, the SISL test section had to be slightly modified from the original design to perform alternate experiments. The upper surface of the SISL test section was intentionally designed with a steep opening angle to allow for the large SISL model, however subsequent models were much smaller and therefore this expansion region in the test section was not needed to enable the tunnel to operate. Additionally, by leaving this expansion region, the hypersonic flow would continue to accelerate through the expansion therefore increasing the Mach number seen by the diffuser. This would decrease diffuser efficiency and

possibly decrease run time. To solve this issue, a false ceiling plate was designed SISL test section.

The false ceiling plate was designed and fabricated from 1.27 cm (0.5 inch) 6061 aluminum stock. The plate was 35.56 cm (14 inches) wide and 60.96 cm (24 inches) long. A 16° angle was machined to the upstream edge and a 37° angle was machined into the downstream edge to allow for a seamless transition to the original test section surfaces and to match the same 2° divergence angle present in the test section floor surface. Additionally, a slot that was 11.43 cm (4.5 inches) long and 1.27 cm (0.5 inches) wide was machined in the plate, approximately 40.64 cm (16.0 inches) from the leading edge to allow the PIV laser sheet to enter into the test section for diagnostic measurements. A SolidWorks drawing and a photograph of the false ceiling plate is shown in Figure F-81 and a diagram showing the profile view of the installed plate is given in Figure F-82.

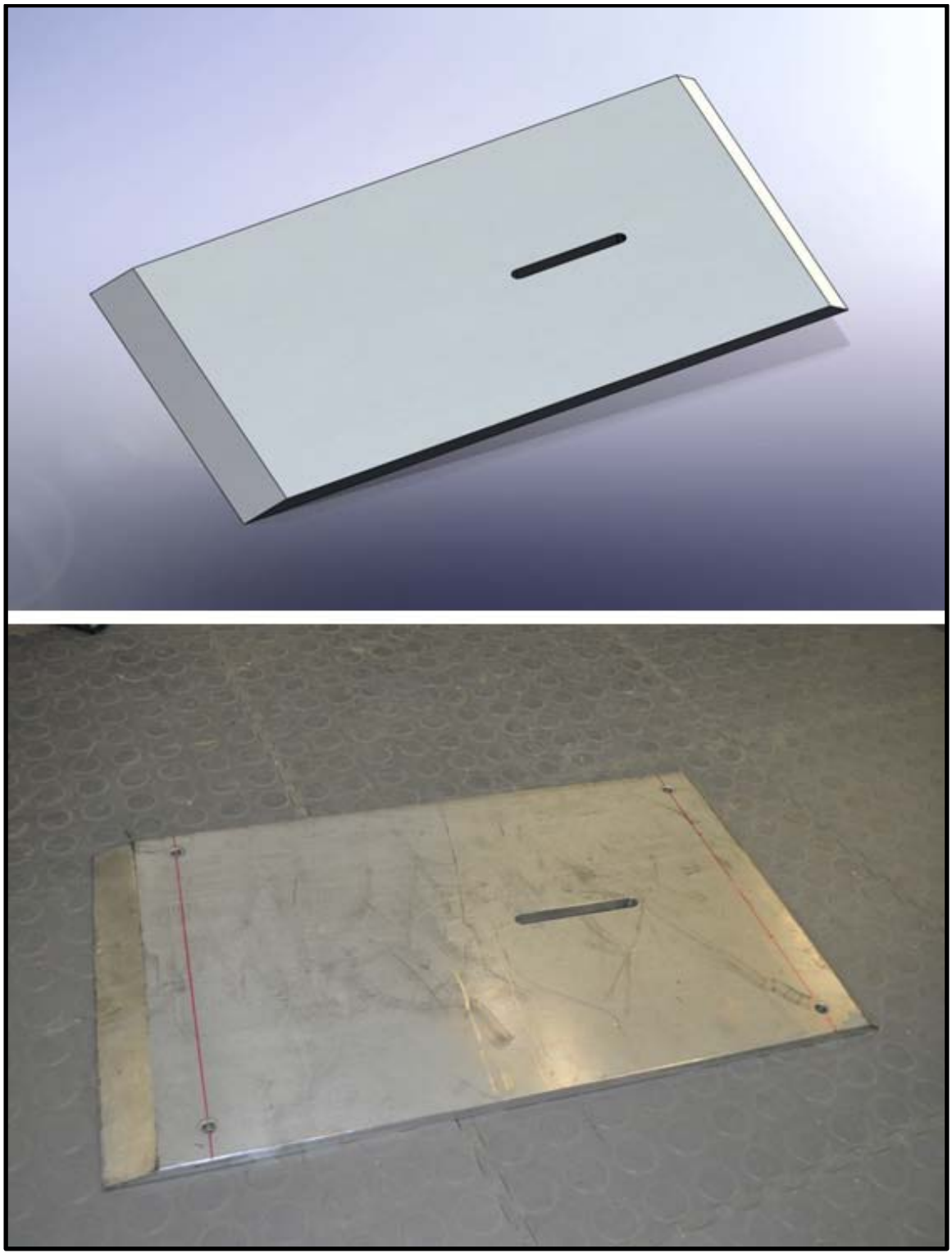

Figure F-81: False Ceiling Plate

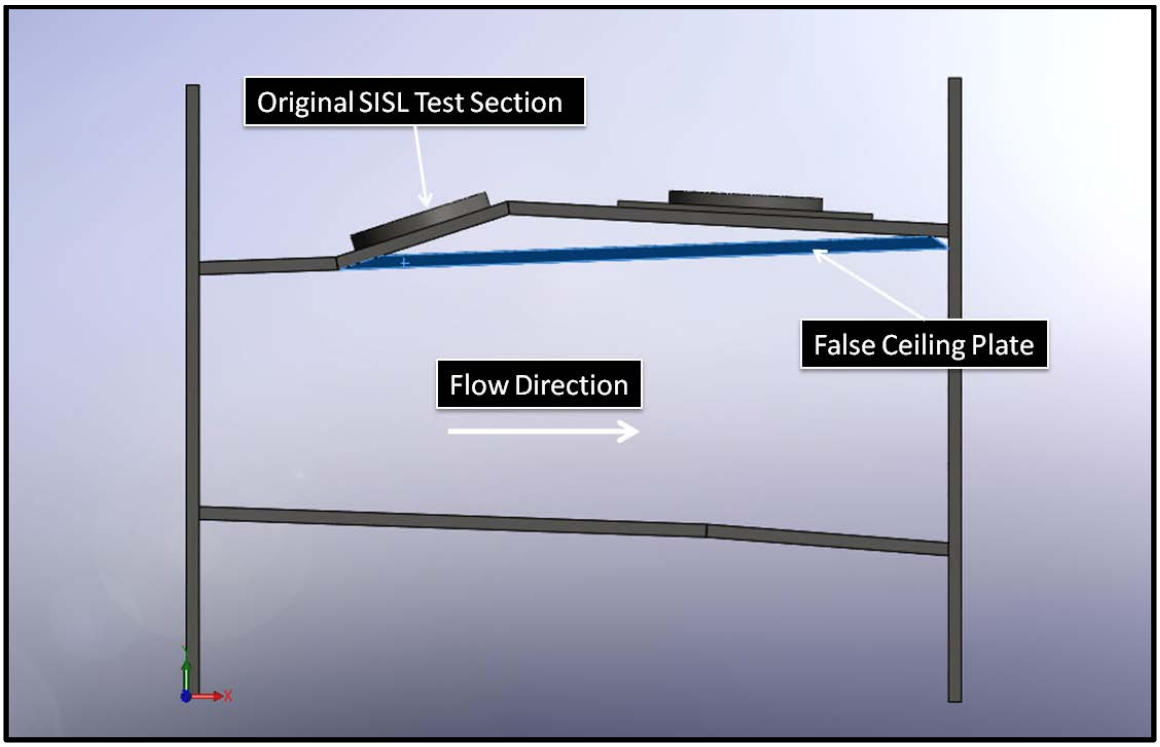

Figure F-82: Test Section False Ceiling Plate Diagram

In order to probe the flow in the desired location using PIV, new optical access locations had to be added to the external structure of the SISL test section. For laser sheet access, the original SISL test section pressure plate was modified. The blank plate was machined to accommodate a 10.16 cm (4 inch) window blank. The design was similar to the other window holders with a 0.32 cm (0.125 inches) thick, 7.62 cm (3 inch) diameter lip which the window rested on and a 0.48 cm (0.1875 inches) O-ring groove for sealing. A mating window holder was also designed and fabricated to securely hold the window in plate. The holder was bolted to the modified pressure plate using six 1/4”-20 bolts. A SolidWorks drawing and a photograph of the modified pressure plate and new window holder are given in Figure F-83.

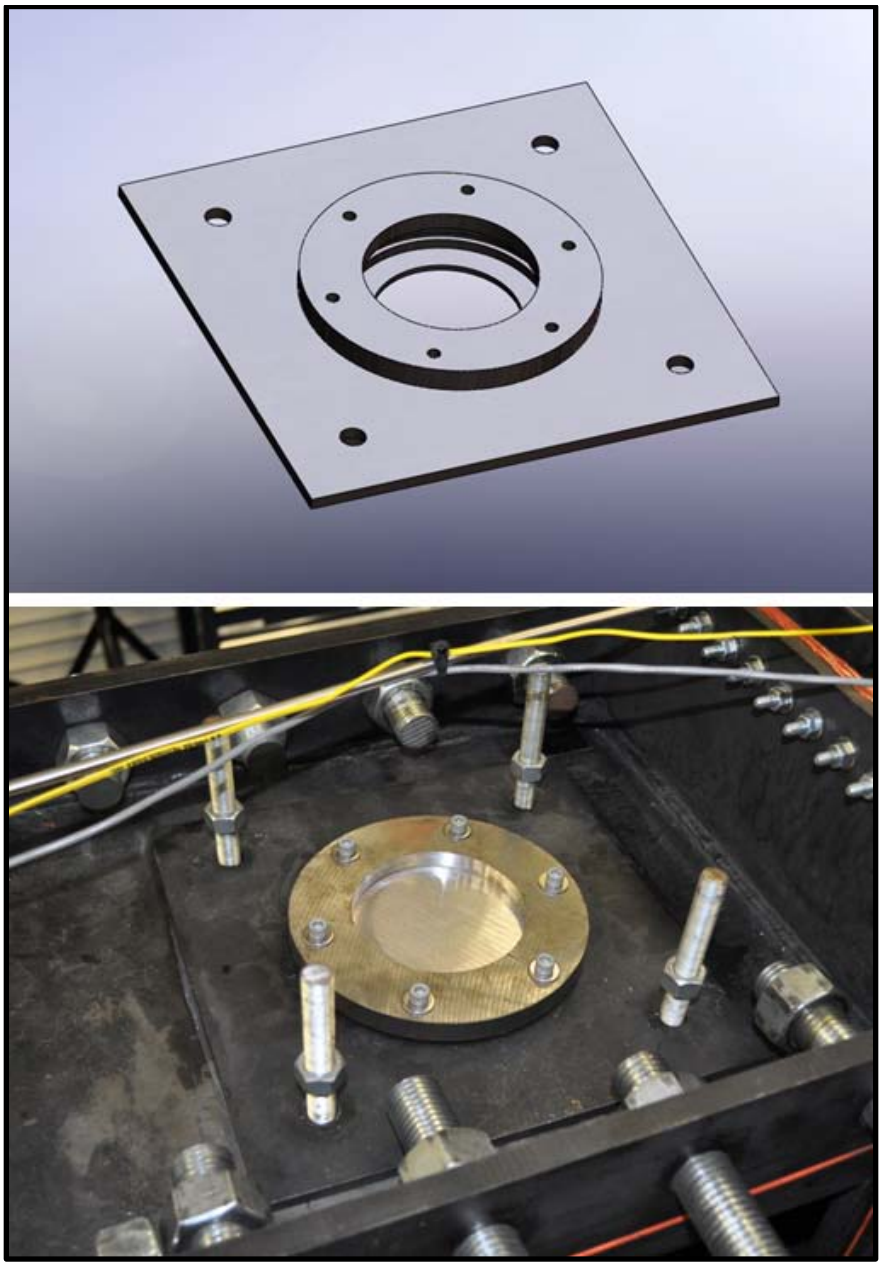

Figure F-83: Modified Pressure Plate with Window Holder

In addition to the false ceiling plate and the modified pressure plate, the side access doors designed for the SISL test section were modified to allow for camera optical access. The originally designed side window locations were not adequate to

perform PIV measurements on the flat plate experiment. The original access doors were modified to accommodate 15.24 cm (6.0 inches) optical flats. Again following previously discussed designs, a 0.32 cm (0.125 inches) lip with an internal diameter of 12.70 cm (5.0 inches) was machined into the access doors as well as a 0.48 cm (0.1875 inches) O-ring groove for sealing. A carbon steel window holder for the 15.24 cm (6.0 inches) windows was designed and fabricated for each side and was mounted to the access door using six 1/4”-20 bolts. A SolidWorks drawing of the modified side access door and new 15.24 cm (6.0 inches) window holder as well as a photograph of the installed hardware in the modified SISL test section are shown in Figure F-84 and Figure F-85 respectively.

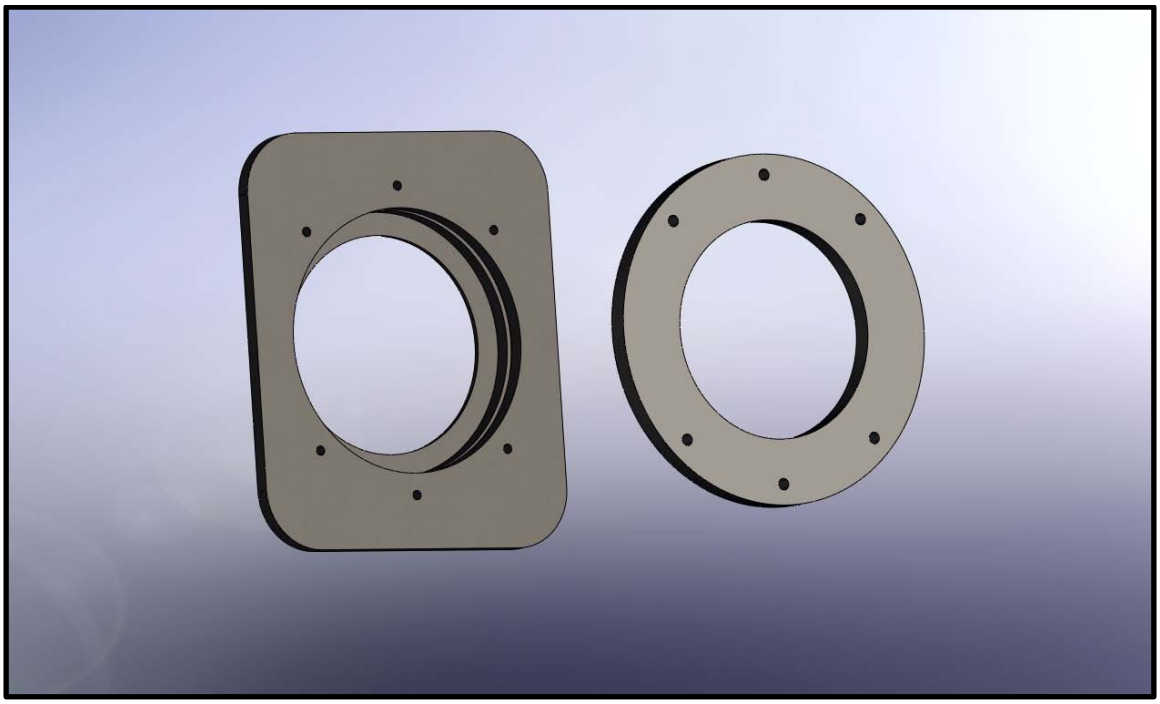

Figure F-84: Modified Side Access Door with Window Holder

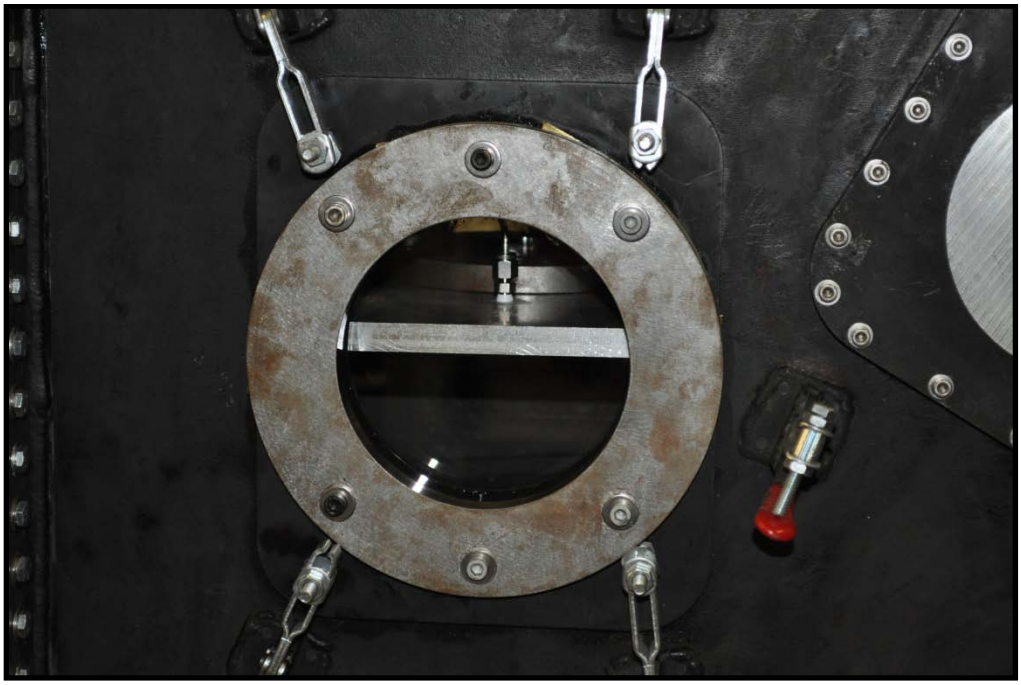

Figure F-85: Installed Side Access Door with Window Holder

The above described modifications to the SISL test section hardware enabled PIV laser diagnostic testing on the hypersonic flat plate boundary layer experiment in the desired location. A SolidWorks drawing of the assembled modified SISL test section given in Figure F-86 and a picture of the installed test section in the high speed experimental facility is shown in Figure F-87.

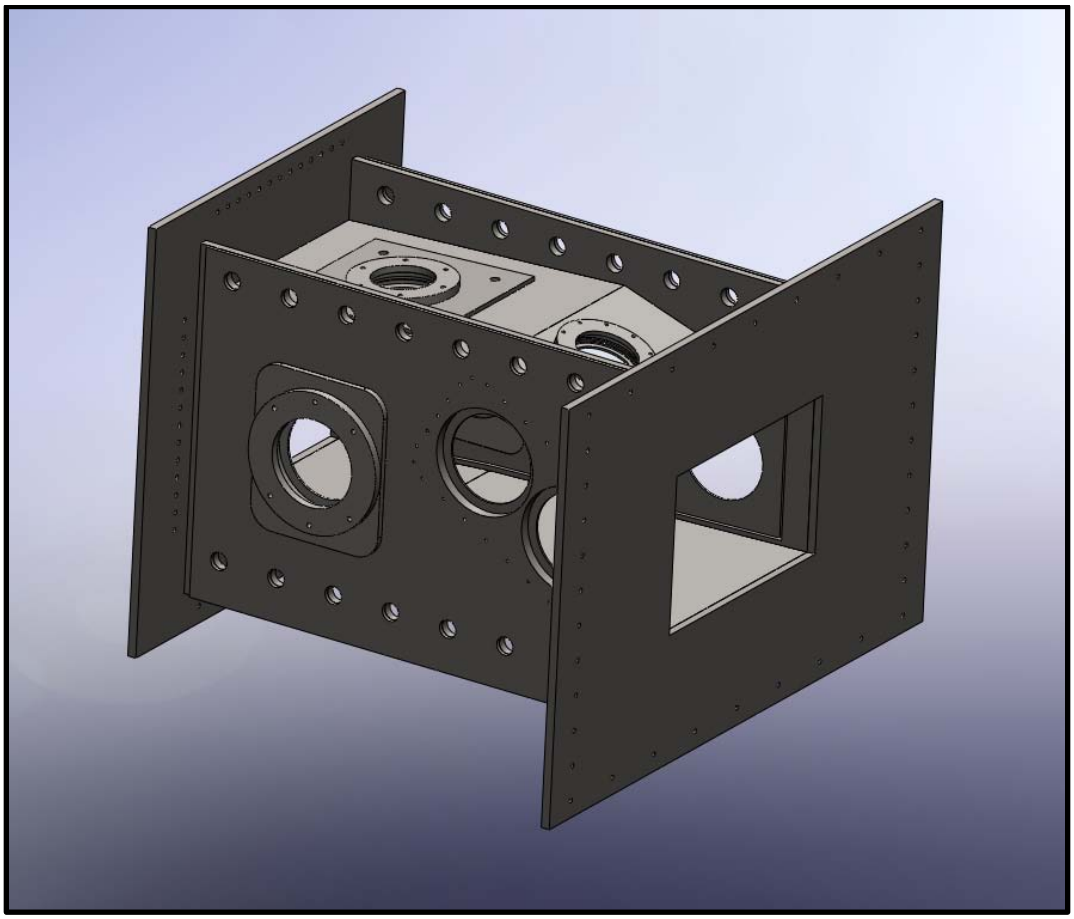

Figure F-86: Assembled Modified SISL Test Section

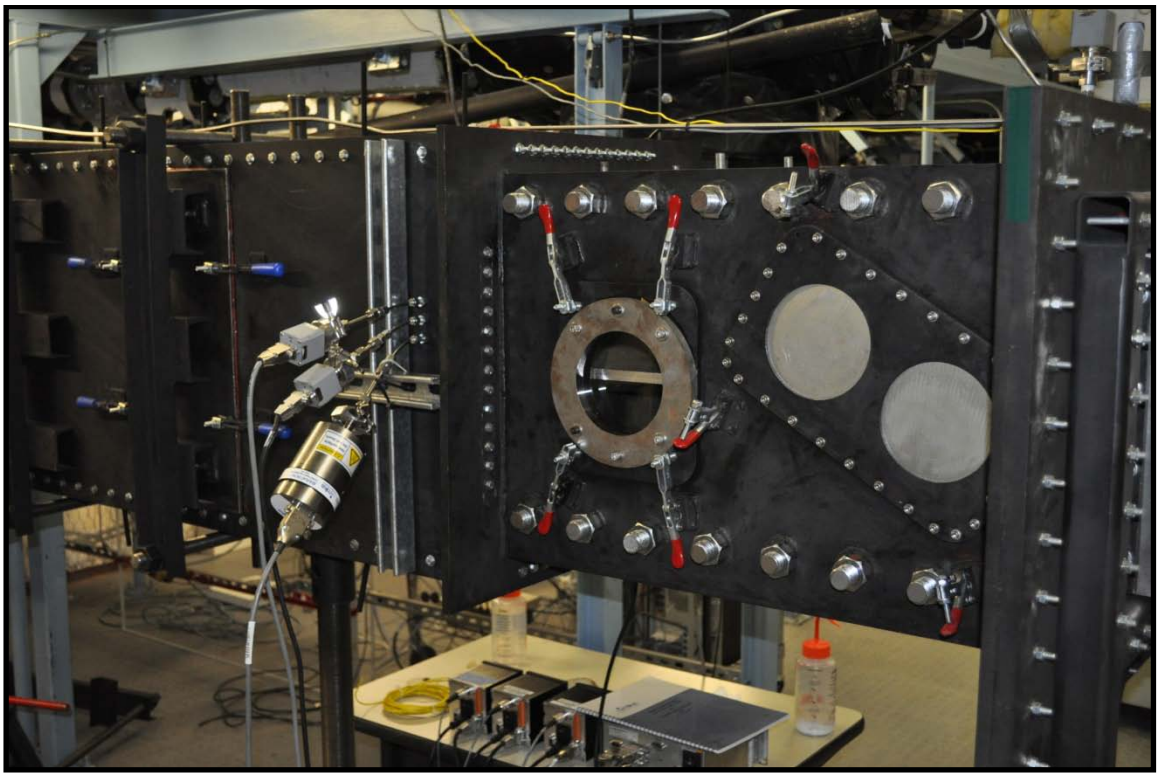

Figure F-87: Installed Modified SISL Test Section

Diffuser Design

For the ACE hypersonic tunnel, a variable throat diffuser was designed following Wegener and Lobb (1953) and Bertram (1952) with the geometry chosen to match Bertram[72,73]. The diffuser was constructed of a variable section and a fixed section. The variable section was constructed using an upper and lower frame connected to thick steel plates at each end. Within the frame structure, two inner diffuser planes were designed to allow the diffuser throat height to be varied. The inlet and exit heights were 30.48 cm (12.0 inches) each and the diffuser throat height was able to be adjusted from 10.16 to 30.48 cm (4.0 to 12.0 inches). The overall width was a constant 35.56 cm (14.0 inches)

for the entire length. The adjustable section of the diffuser was 223.52 cm (88.0 inches) long and provided the majority of the flow diffusion while the fixed section of the diffuser is 127.00 cm (50.0 inches) long and diverges at a half angle of three degrees. A sketch of the overall diffuser dimensions is shown in Figure F-88.

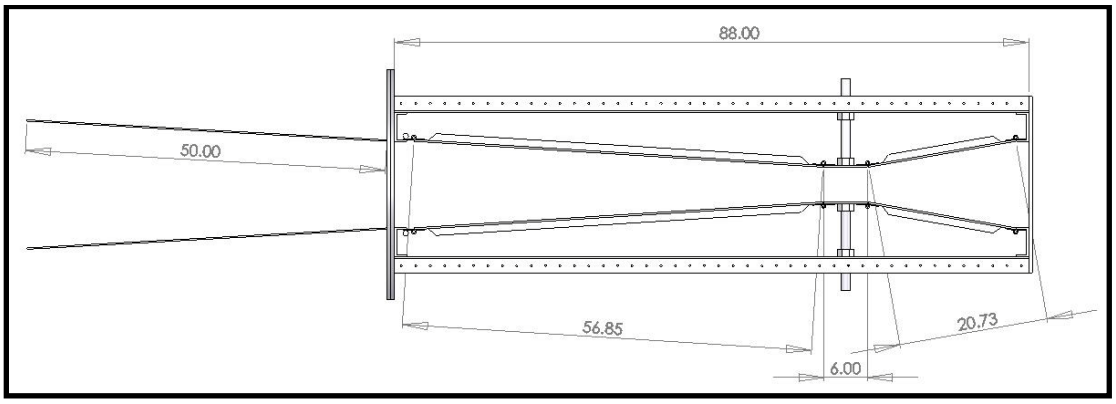

Figure F-88: Sketch of Overall Diffuser Dimension (inches)

After the overall dimensions of the diffuser were determined, CFD simulations were performed on the entire ACE tunnel to verify that the specified diffuser design would perform as required. The results are presented in Figure F-89.

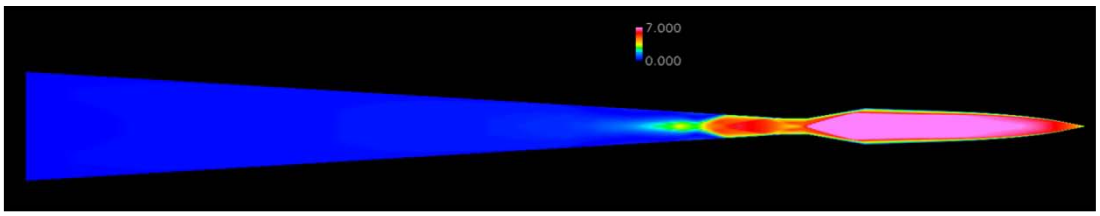

Figure F-89: CFD Simulation of ACE Tunnel

The outer frame structure of the diffuser was fabricated from 5.08 cm x 5.08 cm x 0.32 cm (2 inches x 2 inches x .125 inches) carbon steel tubing and 5.08 cm x 5.08 cm x 0.32 cm (2 inches x 2 inches x .125 inches) carbon steel angle. The tubing and angle was cut to length with 45 degree cuts at each end, and 0.64 cm (0.25 inches) diameter thru holes were drilled in each piece every two inches for fasteners. The tubing was used for the long, side lengths while the angle was used for the end sections; the frame had a total width of 35.56 cm (14.0 inches) and a total length of 223.52 cm (88 .0 inches). A SolidWorks drawing of the tubing frame for the high speed experimental facility diffuser is given in Figure F-90.

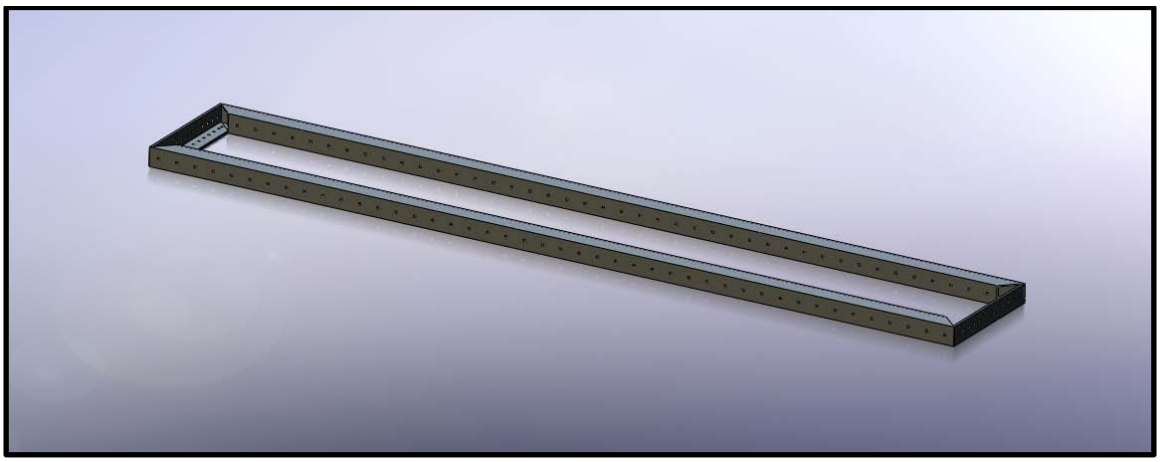

Figure F-90: Diffuser Tubing Frame

For the frame surface, 0.64 cm (0.25 inches) carbon steel plate was cut to size, including slots for the threaded rod used for throat adjustment, using a water jet cutter system. The slots were sized to allow lateral movement of the threaded rods as the

throat was adjusted. A dimensioned drawing of the frame plate showing the slot cutouts is presented in Figure F-91.

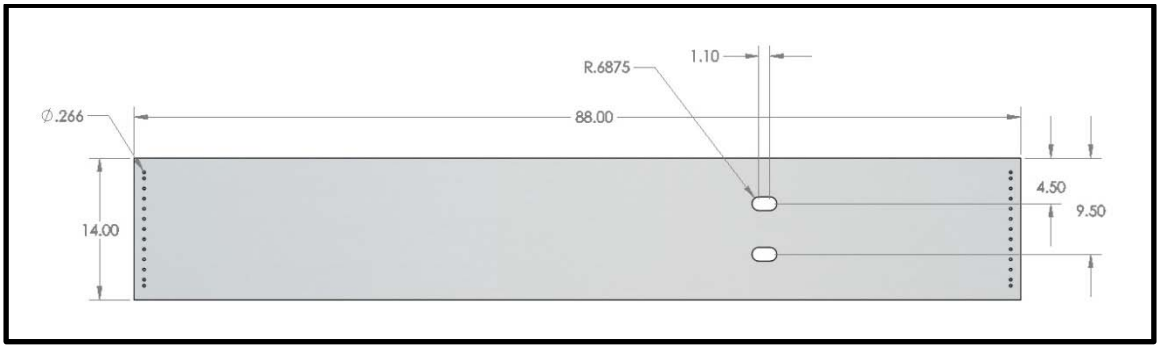

Figure F-91: Dimensioned Frame Plate

The plate was then welded to the square tubing frame and seven 7.25# steel C-channel ribs were welded to the tubing the plate for additional support. A SolidWorks drawing of one of the diffuser frame structures is shown in Figure F-92.

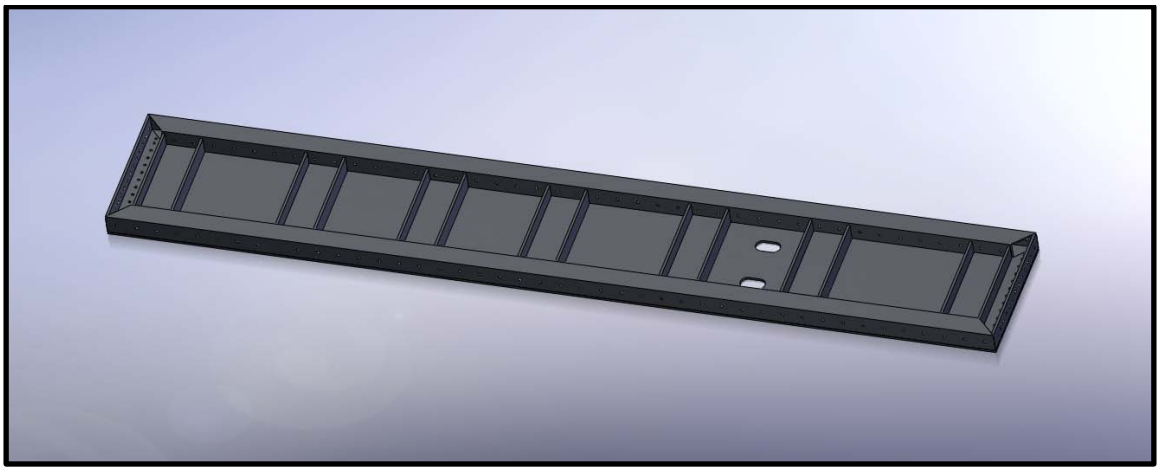

Figure F-92: Diffuser Completed Frame Structure

Two identical frame sections were fabricated to make the upper and lower surfaces of the diffuser. The ends of the frame sections were connected using 1.27 cm (0.5 inch) steel carbon steel plates cut again using a water jet cutter system. The upstream plate was the test section / diffuser interface plate, and the downstream plate was the diffuser / ejector interface plate. Both plates are shown in Figure F-93.

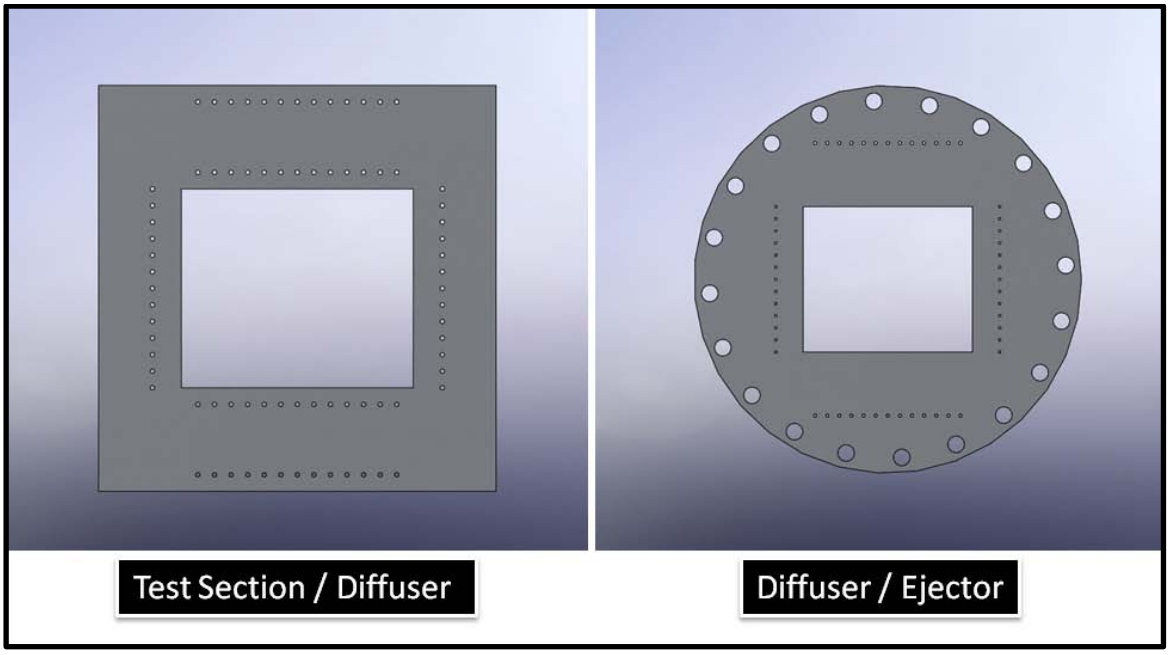

Figure F-93: Diffuser Interface Plates

The test section / diffuser interface plate was 60.96 cm (24.0 inches) wide and 62.23 cm (24.5 inches) tall and had a cutout size of 35.56 cm x 30.48 cm (14.0 inches x 12.0 inches). For connecting the various components, six rows of 0.64 cm (0.25 inches) thru holes were drilled in the plate. The inside set of holes on the upper and lower section are counter bored for 1/4”-20 socket head bolts and are used to attach the upper and

lower diffuser frame sections. The outside set of holes on the upper and lower section of the plate is for the connection to the test section. The set of holes on either side of the center cutout are for the assembly of the diffuser side walls discussed below.

The diffuser / ejector flange allowed the rectangular cross section of the variable throat diffuser to connect to the round ejector piping. The plate had a diameter of 32" and the hole pattern of a 60.96 cm (24 inches) pipe flange as well as two sets of thru holes for tapped 1/4"-20 bolt connections were cut into the plate using a water jet cutter. Like the test section / diffuser interface plate, a 35.56 cm (14.0 inches) wide, 30.48 cm (12.0 inches) tall rectangular hole was cut into the center of the plate for the airflow. The pre-existing flange welded to the ejector piping was rotated by 13.5 degrees, so this was accounted for in the design of the diffuser / ejector interface plate to ensure that the diffuser was level. The two sets of bolt holes were tapped for 1/4"-20 connections and were used to attach the upper and lower diffuser frame sections as well as the diffuser side plates. A SolidWorks drawing of the two frame sections bolted to the two interface plates is shown in Figure F-94.

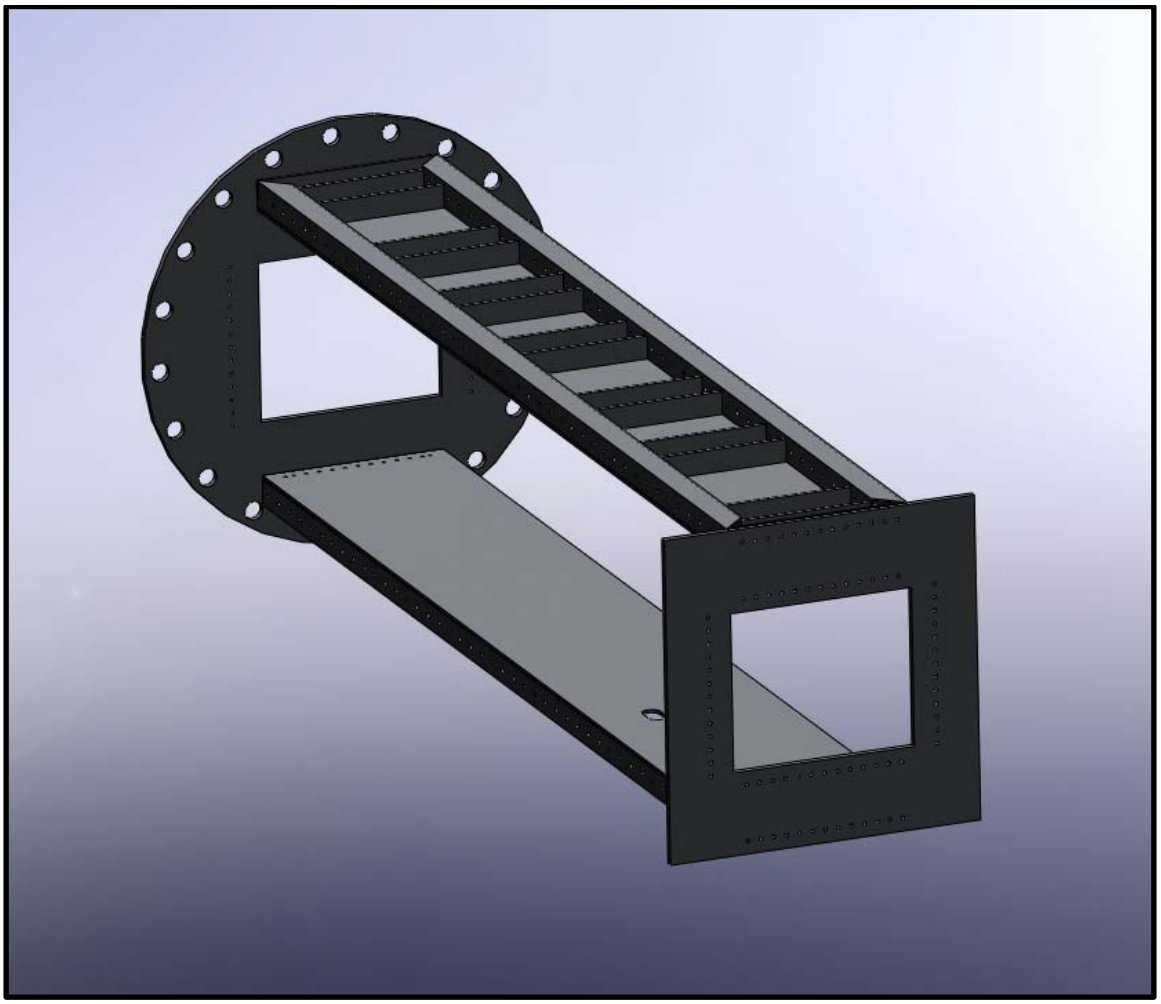

Figure F-94: Diffuser Frame with Interface Plates

The inner surfaces of the diffuser were constructed of 0.64 cm (0.25 inches) carbon steel plates and were reinforced with four 2.54 cm (1.0 inch) carbon steel angle lengths. Each diffuser inner plane was constructed of three plates. A SolidWorks drawing showing a view of a single inner diffuser plate is given in Figure F-95.

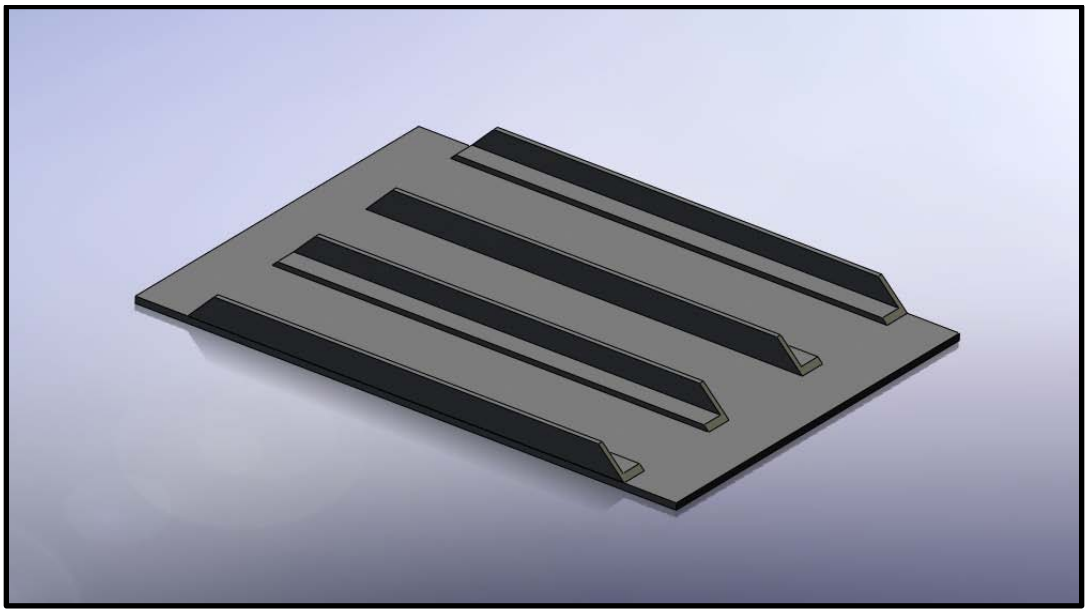

Figure F-95: SolidWorks Drawing of a Single Diffuser Inner Plate

The plate immediately after the test section was 52.65 cm (20.73 inches) long and provided the converging section of the diffuser. This plate was welded to a 15.24 cm (6.0 inches) long throat plate that remained parallel to the tunnel waterline at all times. After the throat plate, a long 144.40 cm (56.85 inches) plate provided the initial diverging area.

To enable the adjustment of the throat height, two 3.18 cm (1.25 inches) nuts were welded to each throat plate. These were located 11.43 cm (4.5 inches)from each edge of the plate and are shown welded to the throat section in Figure F-96.

Figure F-96: Diffuser Throat Section

The three plates of each internal surface were connected using a piano hinge at each joint. The piano hinge was cut to length and welded in place. Initially, a piano hinge was chosen with a 0.31 cm (0.120 inches) leaf thickness, 7.62 cm (3 inch) open width, 0.95 cm (0.375 inches) pin diameter and 5.08 cm (2 inch) knuckle length. However, after multiple throat adjustments, the think hinge leafs began to bend. The diffuser was disassembled and the hinges were replaced. The new hinge was stronger, with a 0.46 cm (0.180 inches) leaf thickness, 7.62 cm (3 inch) open width, 1.27 cm (0.5 inch) pin diameter and 5.08 cm (2 inch) knuckle length. A picture of the final piano hinge stock used for the diffuser is shown in Figure F-97.

Figure F-97: Diffuser Piano Hinge Stock

The internal surface of the diffuser was connected to the outer frame by 7.25# carbon steel C-channel. The channel was connected to each end of the diffuser plane assembly using the above described piano hinge stock. Holes were drilled in the edge of each piece of channel and 1/4”-20 bolts were used to mount the inner plane assembly to the upper and lower diffuser frames. A SolidWorks drawing of the diffuser inner plane is shown in Figure F-98 and a photograph of the fabrication of this section is shown in Figure F-99. At the downstream end of the diffuser inner planes, six 1.27 cm (0.5 inch) holes were drilled in the plates to allow the pressure to equalize above and below the adjustable planes.

Figure F-98: SolidWorks Drawing of Diffuser Inner Plane

Figure F-99: Fabrication of Diffuser Inner Plane

The inner planes were mounted to the upper and lower frame sections interface plates using the attached steel C-channel at the upstream and downstream ends of the adjustable diffuser section. Also, the large 3.18 cm (1.25 inches) threaded rods used for

the throat adjustment added stability and strength to the assembly. A SolidWorks drawing of the adjustable diffuser section is shown in Figure F-100 and a photograph of the installed diffuser in the high speed experimental facility is shown in Figure F-101.

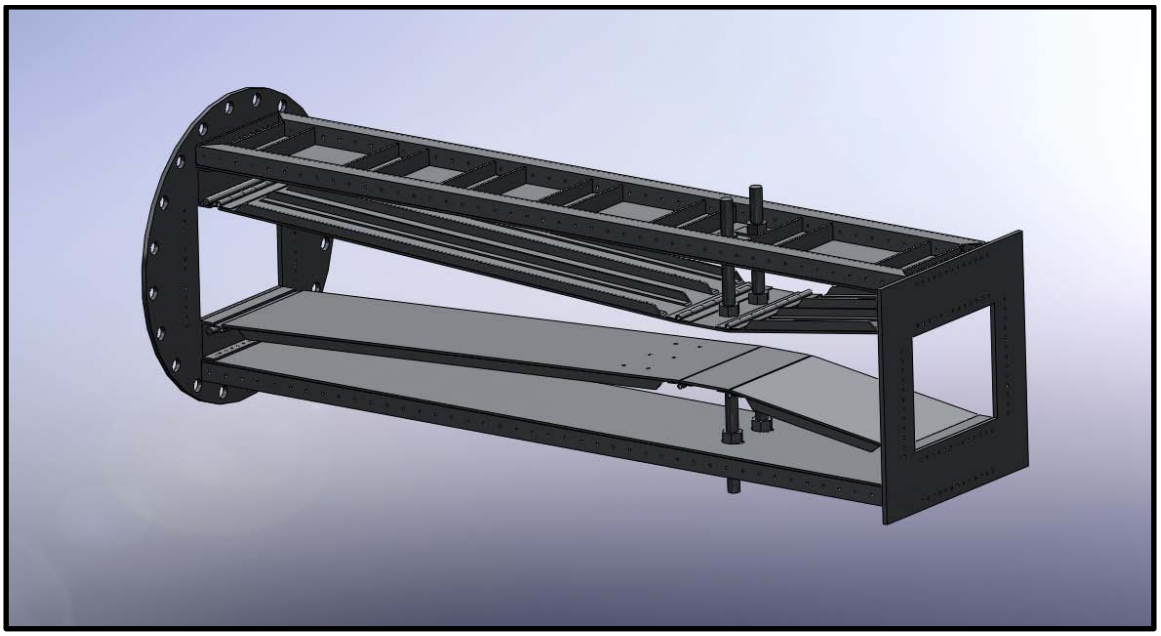

Figure F-100: SolidWorks Drawing of Assembled Diffuser Adjustable Section

Figure F-101: Installed Diffuser

The side plates of the diffuser were constructed of 0.64 cm (0.25 inch) carbon steel plate with overall dimensions of 223.52 cm x 62.23 cm (88 inches x 24.5 inches). A large cutout with dimensions of 49.53 cm x 20.32 cm (19.5 inches x 8 inches) was removed from each plate to allow easy access to the 3.18 cm (1.25 inch) threaded rod connections to the throat plates. In each plate, 88 0.64 cm (0.25 inches) thru holes were cut near the upper and lower edges to mount the side plates to the diffuser frame sections. A SolidWorks drawing of the diffuser side wall is shown in Figure F-102.

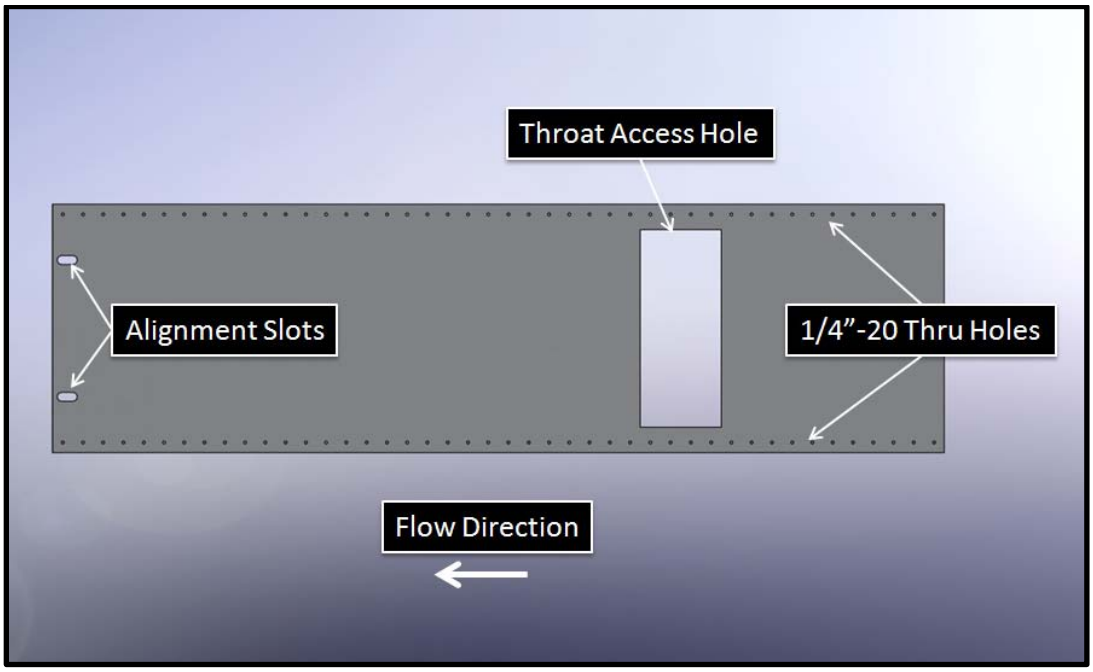

Figure F-102: Diffuser Side Wall

For added safety, the access doors as well as the side plates were clamped in place using 5.4# carbon steel channel and 2.54 cm (1.0 inch) threaded rod. High temperature RTV was used to seal the entire diffuser. A picture showing the complete diffuser assembly is shown in Figure F-103.

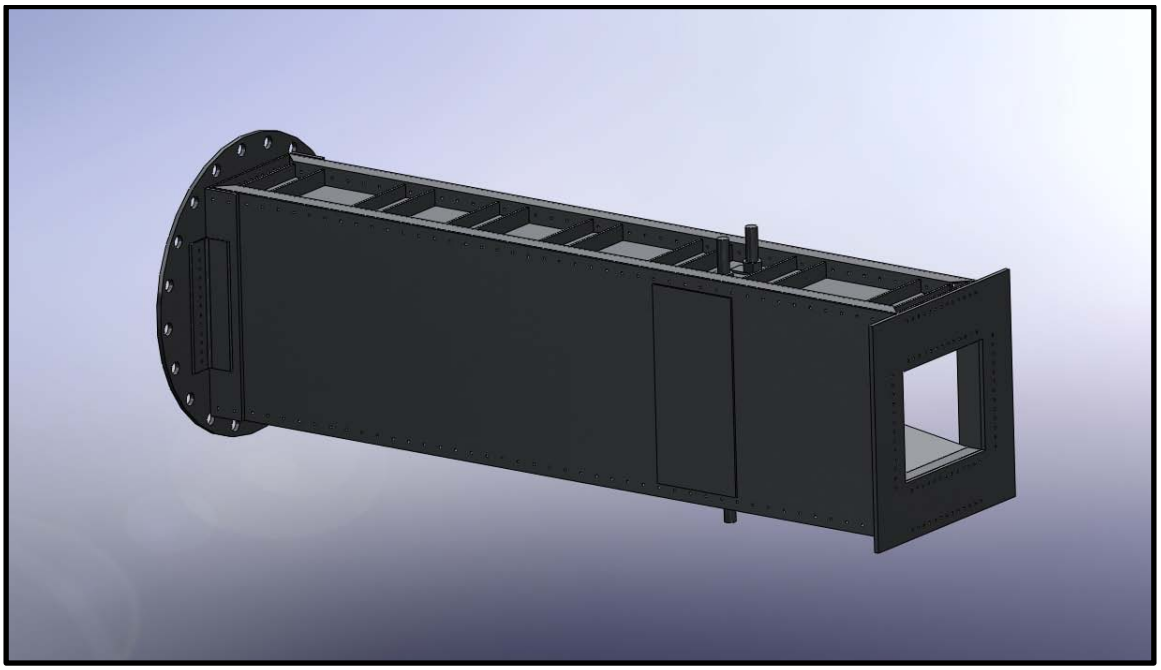

Figure F-103: Complete Diffuser Assembly

Calibration

Comparison of the CFD to the Wegener and Lobb study indicated that the current models provide a reasonable, albeit conservative, estimate of the unstart pressure ratio, shown in Figure F-104.

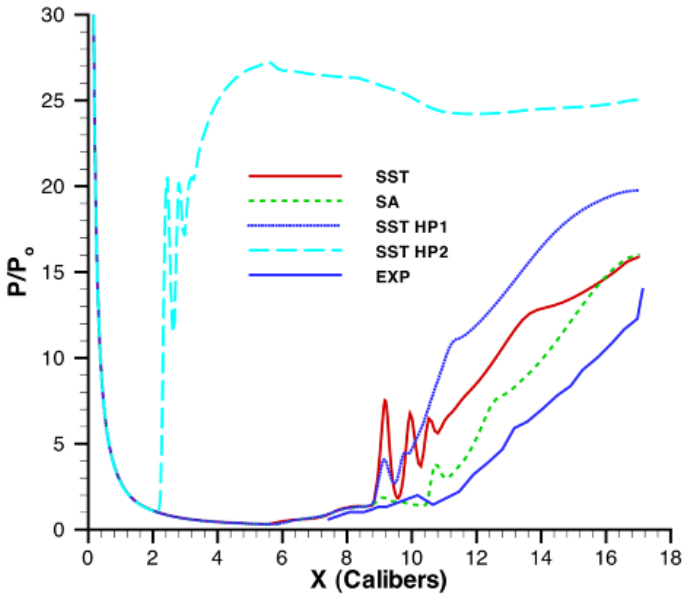

Figure F-104: Simulation Results for Wegener and Lobb (1953) Study[72]

The diffuser throat height was determined based on conservation of mass and optimizing the operating conditions. As the throat height was adjusted, the downstream diffusion angle changed. The measurements described are shown in Figure F-105 and Figure F-106 below.

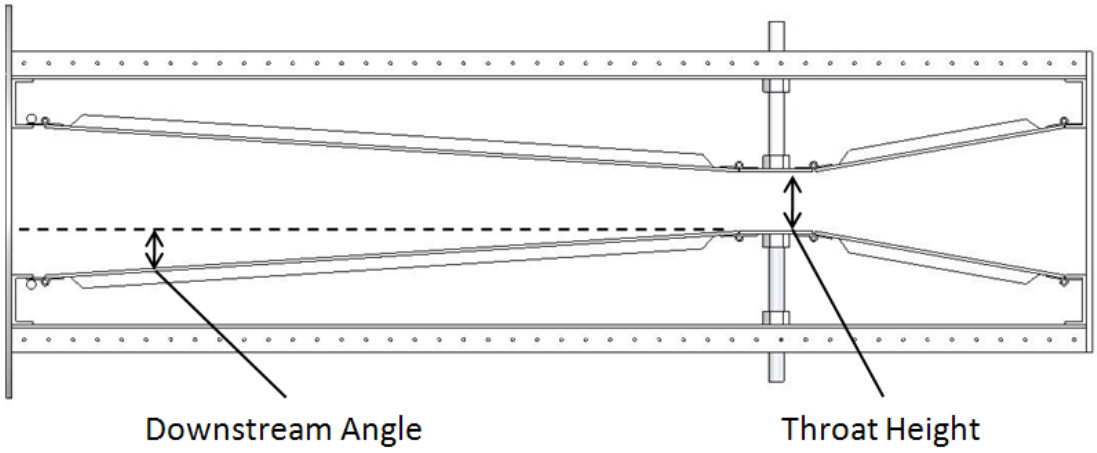

Figure F-105: Labeled Diffuser Sketch

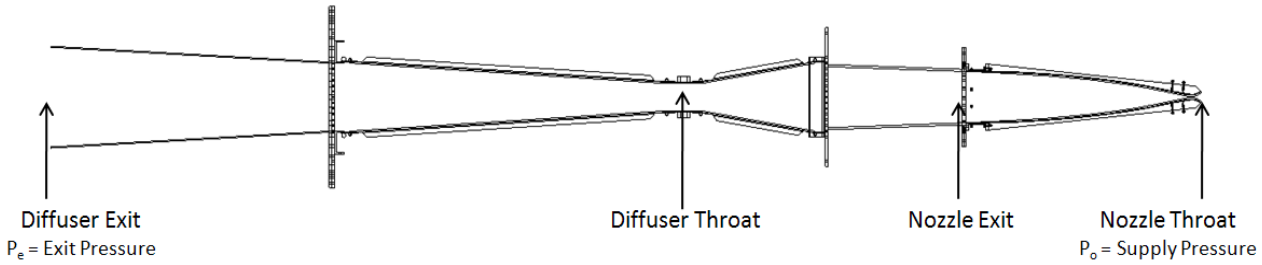

Figure F-106: Labeled Sketch of Full Tunnel Assembly

The throat height can be adjusted continuously from 10.16 cm to 30.48 cm (4.0 inches to 12.0 inches), where the 30.48 cm (12.0 inch) throat height allows the upper and lower surfaces to be parallel throughout the diffuser length. The throat heights and the corresponding downstream diffusion angles are presented in Table F-3.

Table F-3: Diffuser Throat Height and Corresponding Downstream Diverging Diffuser Angle

Throat Height (in)	Downstream Angle (deg)
4	4.0
5	3.5
6	3.0
7	2.5
8	2.0
9	1.5
10	1.0
11	0.5
12	0.0

By running the tunnel at various Mach numbers and closely monitoring the pressures throughout the system, the required pressure ratios to start and run the tunnel were determined. The required pressure ratio to start the tunnel is higher than the pressure ratio required to run the tunnel. This trend is shown in Figure F-107. For a given Mach number, the initial pressure ratio must be at or above the starting condition line. Once the tunnel is started it will remain started until the pressure ratio drops below the unstart condition line.

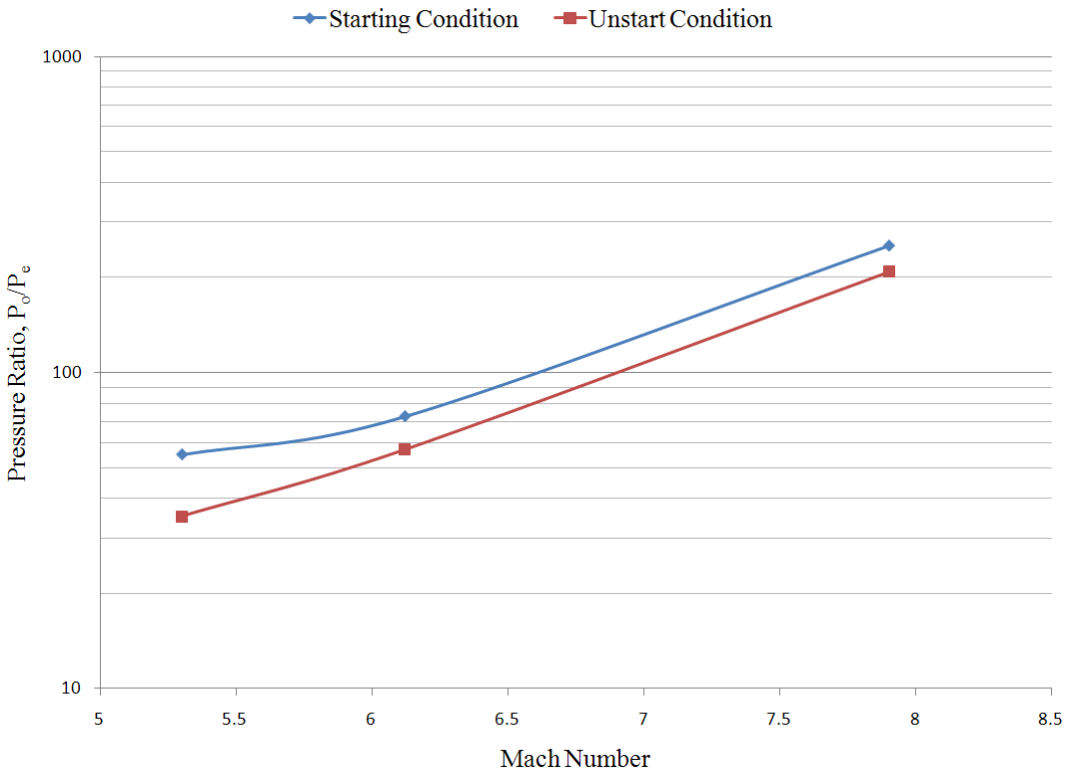

Figure F-107: Required Starting and Unstarting Pressure Ratios vs. Mach Number

Initial calibrations were conducted to measure the ejector performance. The experimental results were compared to the theoretical values and it was determined that the ejector is performing above specifications. The tunnel was then run for various Mach numbers and mass flow rates. Based on these data, the diffuser figure of merit was calculated for each Mach number and is given in Table F-4. The diffuser figure of merit, *f*, is defined as the minimum running pressure ratio P_{diff}/P_{t1} over the normal shock pressure ratio P_{t2}/P_{t1}. It can be seen that the diffuser seems to be most efficient near Mach 6. However, the current diffuser figure of merit is suboptimal. The calibration data to date are for cold, unheated air, at approximately 300K. These data are shown in

dashed lines in Figure F-108. The required diffuser pressure for the hot cases, at 530K, were calculated and are shown as solid lines on the same figure. Figure F-108 clearly shows the operating requirements for the ACE tunnel. The tunnel will run for a given Mach number if that Mach number line is above the available measured ejector pressure at the desired mass flow rate. Therefore, it can be seen that for the cold, unheated cases that have been performed to date, only very low mass flow rates will allow the tunnel to run. With the air heated, a much wider range of mass flow rates will be acceptable to run. It is believed that the poor diffuser performance is the result of the mismatch in heights between the test section exit and the diffuser inlet, which results in fewer shock reflections in the contraction and hence lowers pressure recovery.

Table F-4: Diffuser Figure of Merit for Given Mach Number

Mach Number	*f*
~ 5	58%
~ 6	64%
~ 7	53%

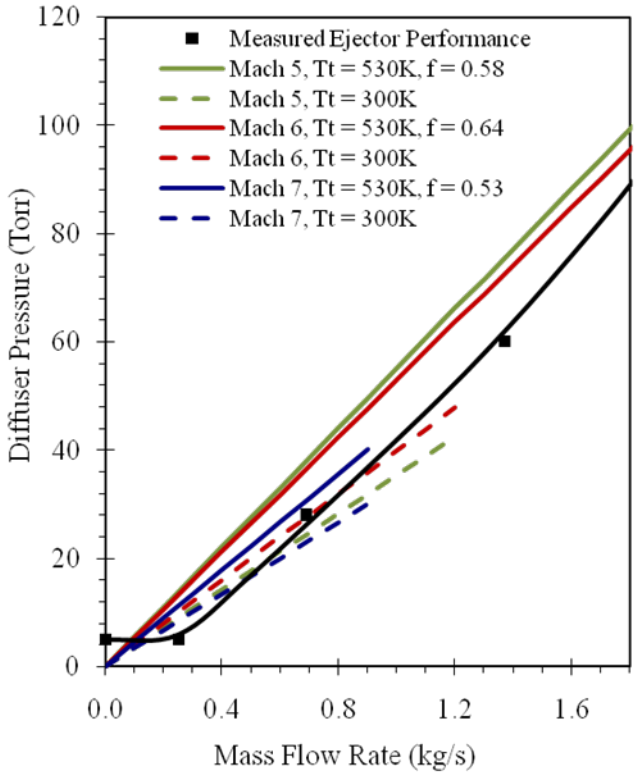

Figure F-108: Diffuser Exit Pressure vs. Mass Flow Rate

APPENDIX G

SAFE OPERATING PROCEDURES

SHR Safe Operating Procedures 421

ACE Safe Operating Procedures 423

Run Number _____ **SHR** Date _____

Item #	Supersonic Tunnel Safety Check List	Initial
	Initialization	
1	Three operators are required to run ALL high-speed facilities	
2	Notify one of the primary contacts of run plans	
	Main Tank and Primary Line Ball Valves	
3	Pressurize main supply tank (TANK-1) to 2300 psig	
4	Close secondary tank ball valve (BV-3) {blue ball valve on back end}	
5	Visually check pop-off safety valve (SV-1) for integrity	
6	Check BV-2 actuator pressure in compressor building (100 psi) {verify shop air is on and pressurized to >120psi, then open ball valve behind dryer}	
7	Energize the actuator (ACT-2) for the secondary on/off ball valve (BV-4) {switch on panel in compressor building, 2" tank actuator}	
8	Energize main control panel in lab	
9	Activate yellow warning light	
10	Open green ball valve to gauge panel {ball valve above gauges in lab}	
11	Cycle BV-4 and verify operation with an operator at the control panel	
	Prepare the Ejector (not used for the supersonic tunnel)	
12	Open BV-3 {ball valve on back end}	
	Heater	
13	Rotate main switch on heater to "On"	
14	Verify setpoint temperature	
15	Close heater room door half-way	
16	Close bypass valve	
	Tunnel Valves	
17	Cycle tunnel on/off valve (BV-5) {heater room actuator}	
18	Verify that the supersonic tunnel ball valve (BV-6) is open	
19	Verify that the hypersonic tunnel ball valve (BV-7) is closed	
20	Set heater room regulator to operating condition Mach3: 25 psig gauge -> 100 psig tunnel Mach5: 85 psig gauge -> 390 psig tunnel	
21	Fire 3, 2-second horn blasts	
22	**Run the Supersonic Tunnel**	
	Verify all operators have eye and hearing protection	
23	Energize main control panel	
24	Set warning light to red	

25	Enable DAQ recording	
26	Turn ON the control panel switches in the following order	
27	Tank actuator 2” (TANK-1) switch	
	Heater room tunnel Actuator (ACT-2) switch	
	Wait 15 seconds	
	Heater max temp	
	Perform Run	
	Standard Shut-Down	
	Turn OFF the control panel switches in the following order	
1	Heater max temp	
	Tank actuator (TANK-1) switch	
	Heater room tunnel actuator (ACT-2) switch	
	De-energize main control panel	
2	Rotate heater switch to "Off"	
3	Depressurize tunnel control regulator (REG-3) {close ball valve above dryer, then bleed off air using ball valve}	
4	Manually close supersonic tunnel ball valve (BV-7)	
5	Manually close secondary tank ball valve (BV-3)	
6	De-energize ACT-1 (in compressor building) {2” switch on panel in compressor building}	
7	Set warning light to green	
8	**Emergency Shut-Down**	
	De-energize main control panel with red safety switch, which will	
1	Close the main tank ball valve (BV-1)	
	Close tunnel on/off ball valve (BV-5)	
	Shut off power to the air heater	
	Depressurize REG-3	
2	Manually close the ball valves	
3	Supersonic tunnel ball valve (BV-7)	
	Tank main ball valve (BV-1)	
	De-energize ACT-1	
4	Once situation is safe, set warning light to green	
5	Reset switches on main control panel to OFF position	
6	Notify primary contacts to perform a safety review before running again	
7		

Notes:

Run Number _____ ACE Date _____

	Hypersonic Tunnel Safety Check List	Initial
	Initialization	
	Two operators are required to run the hypersonic facility	
	Notify one of the primary contacts of run plans	
	Close main red gate valve on tank, drain HPV-5	
	Cycle 2” and 4” actuators once daily prior to starting up compressors	
	Open main red gate valve on tank	
	Pressurize the main supply tank (minimum 1900 PSI)	
	Main Tank and Primary Line Ball Valves	
	Visually check the pop-safety valve integrity	
	Turn on Husky compressor to 2” and 4” actuators	
	Turn on power to 2” and 4” actuators	
	Prepare the Ejector	
	Visually verify the rupture disks’ integrity	
	Check for obstructions, etc. directly at and downstream of ejector exit	
	Remove ejector outlet cover	
	Slowly open the 1^{st} and 2^{nd} stage ejector ball valves	
	Heater Building	
	Turn on the heater, reset overtemp (if necessary) and check set points	
	Open or close bypass line as required	
	Tunnel Valves	
	Open & close appropriate butterfly valves	
	Close supersonic tunnel ball valve	
	Cycle heater room actuator	
	Open main hypersonic ball valve	
	Open & close appropriate tunnel ball valves	
	Instrumentation	
	Check all control regulators and set to appropriate values	
	Verify Data Acquisition System (DAQ) is operational	
	Run the Hypersonic Tunnel	
	Verify all personnel have protective equipment	
	Verify all-clear from video surveillance	
	Set warning light to red, fire 3 short horn blasts, wait 10 seconds	
	Enable DAQ recording	
	Energize main control panel	
	Turn ON the tunnel in the following order	
	Heater control switch (wait for elements to heat up)	
	2” tank actuator switch (wait for pressure)	

	4” tank actuator switch	
	Ejector control regulator ball valves switch	
	Heater room actuator switch (when diffuser pressure < 10 torr)	
	Standard Shut-Down	
	Turn OFF the tunnel in the following order	
	Ejector control regulator ball valves switch	
	4” tank actuator switch	
	2” tank actuator switch	
	Heater room tunnel actuator switch (after pressure is drained)	
	De-energize main control panel	
	Depressurize all control regulators	
	Manually close hypersonic ball valve	
	Manually close tunnel ball valves	
	Manually close butterfly valves	
	Manually close ejector ball valves	
	Manually close the main tank gate valve and 2” ball valve	
	Turn off warning light	
*	**Emergency Shut-Down**	
	Emergency shut down as follows	
	Depressurize ejector outlet control regulators	
*	Switch off master power switch with red cover	
*	Follow remaining standard shut down procedures	
*	Notify primary contacts to perform a safety review before running again	

Notes:

VITA

Name: Nathan Ryan Tichenor

Address: Department of Aerospace Engineering
Texas A&M University
H.R. Bright Building, Rm. 701
3141 TAMU
College Station, TX 77843-3141

Email Address: nathantichenor@gmail.com

Education: B.S., Aerospace Engineering, Texas A&M University, 2005
M.S., Aerospace Engineering, Texas A&M University, 2007
Ph.D., Aerospace Engineering, Texas A&M University, 2010